Transactions of the ASME, Journal of Heat Transfer (ISSN 0022-1481) is published monthly by The American Society of Mechanical Engineers, Three Park Avenue, New York, NY 10016. Periodicals postage paid at New York, NY and additional mailing offices. POSTMASTER: Send address changes to Transactions of the ASME, Journal of Heat Transfer, c/o THE AMERICAN SOCIETY OF MECHANICAL ENGINEERS, 22 Law Drive, Box 2300, Fairfield, NJ 07007-2300. **CHANGES OF ADDRESS** must be received at Society headquarters seven weeks before they are to be effective. Please send old label and new address.
 INDEXED by Applied Mechanics Reviews and Engineering Information, Inc. Canadian Goods & Services Tax Registration #126148048.

Journal of Heat Transfer

Published Monthly by ASME

VOLUME 127 • NUMBER 3 • MARCH 2005

RESEARCH PAPER

(**Contents continued on inside back cover**)

This journal is printed on acid-free paper, which exceeds the ANSI Z39.48-1992 specification for permanence of paper and library materials. ♾™
♲ 85% recycled content, including 10% post-consumer fibers.

Journal of Heat Transfer **Volume 127, Number 3** **MARCH 2005**

The ASME Journal of Heat Transfer is abstracted and indexed in the following:

Applied Science and Technology Index, Chemical Abstracts, Chemical Engineering and Biotechnology Abstracts (Electronic equivalent of Process and Chemical Engineering), Civil Engineering Abstracts, Compendex (The electronic equivalent of Engineering Index), Corrosion Abstracts, Current Contents, E & P Health, Safety, and Environment, Ei EncompassLit, Engineered Materials Abstracts, Engineering Index, Enviroline (The electronic equivalent of Environment Abstracts), Environment Abstracts, Environmental Engineering Abstracts, Environmental Science and Pollution Management, Fluidex, Fuel and Energy Abstracts, Index to Scientific Reviews, INSPEC, International Building Services Abstracts, Mechanical & Transportation Engineering Abstracts, Mechanical Engineering Abstracts, METADEX (The electronic equivalent of Metals Abstracts and Alloys Index), Petroleum Abstracts, Process and Chemical Engineering, Referativnyi Zhurnal, Science Citation Index, SciSearch (The electronic equivalent of Science Citation Index), Theoretical Chemical Engineering

Flow Visualization and Flow Pattern Identification With Power Spectral Density Distributions of Pressure Traces During Refrigerant Condensation in Smooth and Microfin Tubes

Leon Liebenberg
Associate Professor,
e-mail: lieb@up.ac.za
Department of Mechanical and Aeronautical Engineering,
University of Pretoria,
Pretoria, 0002, South Africa

John R. Thome
Professor,
e-mail: john.thome@epfl.ch
Laboratory of Heat and Mass Transfer,
Faculty of Engineering Science,
Swiss Federal Institute of Technology-Lausanne (EPFL), Lausanne 1015, Switzerland

Josua P. Meyer
Professor and Head:
e-mail: jmeyer@up.ac.za
Department of Mechanical and Aeronautical Engineering,
University of Pretoria,
Pretoria, 0002, South Africa

This paper presents a flow pattern identifier of the prevailing flow regime during refrigerant condensation inside smooth- and microfin tubes. The power spectral density distribution of the fluctuating condensing pressure signal was used to identify the prevailing flow regime, as opposed to the traditional (and subjective) use of visual-only methods, and/or smooth-tube flow regime maps. The prevailing flow regime was observed by using digital cameras and was validated with the use of the conventional smooth-tube flow regime transition criteria, as well as a new flow regime map for microfin-tube condensation. Experimental work was conducted for condensing refrigerants R-22, R-407C, and R-134a at an average saturation temperature of 40°C with mass fluxes ranging from 300–800 kg/m^2 s, and with vapor qualities ranging from 0.05–0.15 at condenser outlet to 0.85–0.95 at condenser inlet. Tests were conducted with one smooth-tube condenser and three microfin-tube condensers (with helix angles of 10°, 18°, and 37° respectively). The power spectral density distributions of the condensing pressure signals distinguish the annular and intermittent (slug and plug) flows. A very low resonant frequency (<40 Hz) and low power spectral density amplitude of the pressure oscillation denoted stratified and wavy flows. As the annular flow regime was approached, the oscillations became larger and their frequencies increased (typically 40–120 Hz). Intermittent flow showed the most distinct character of all flow regimes. Its trace consisted of large amplitude pressure pulses occurring at fairly constant frequencies (approximately 50, 60, 80, 100, and 120 Hz). As the transition from intermittent to annular flow began, the pressure fluctuations became less regular and the amplitude dropped sharply. [DOI: 10.1115/1.1857942]

Introduction

Numerous flow pattern maps have been proposed over the years for predicting two-phase flow regime transitions in horizontal tubes under adiabatic and diabatic conditions [1]. Kattan et al. [2–5] proposed the first comprehensive flow-boiling model for evaporation inside horizontal tubes based on the local flow pattern and a newly developed diabatic flow pattern map. Their new approach resulted in very significant improvements in the accuracy and reliability of heat transfer predictions compared to previous methods. As a consequence, several new condensation heat transfer models based on local flow pattern have been proposed by Shao and Granryd [6] and Cavallini et al. [7]. El Hajal et al. [8] adapted the flow-boiling two-phase flow pattern map, originally developed by Kattan et al. for condensation inside horizontal tubes. El Hajal et al. [8] and Thome/Collier [9,10] proposed a new log-mean method for predicting void fractions for pressures ranging from atmosphere up to near the critical pressure. This was prompted by the high reduced pressures of interest for condensation, and because of the sensitivity of flow pattern transitions, heat transfer coefficients, and pressure drop to void fraction. The Thome map [9] is a modification of the Steiner [11] map, which in turn is a modification of the original Taitel and Dukler [12] map. El Hajal et al. [8] simplified the implementation of the map by bringing the Rouhani and Axelsson [13] void fraction equation into the method to eliminate its iterative solution scheme. Also, the changes proposed by Zürcher et al. [14] were implemented to ensure better prediction of the transition curves from annular to stratified/wavy flow, and from stratified/wavy to wavy flow.

El Hajal et al. [8] and Thome [9] show that for condensation, saturated vapor enters a condenser tube and forms either: (i) A thin liquid film around the perimeter of the tube as an annular flow or (ii) a liquid layer in the bottom of the tube and a gravity-controlled condensing film around the upper perimeter as a stratified or stratified/wavy flow. Therefore, the transition curve from annular and intermittent flow to stratified/wavy flow can be supposed to reach its minimum value and then continue on horizontally to the vapor quality of 1.0. This means that a saturated vapor enters at $x=1.0$ and goes directly into either the annular flow regime or the stratified/wavy flow regime, depending on whether the mass flux is greater or less than the transition curve. This is shown in Fig. 3 and is discussed later on in the paper.

Thome [9] obtains the transition between intermittent flow and annular flow as a vertical line given by x_{IA}, which is determined by setting the Martinelli parameter X_{tt} equal to 0.34, as

$$x_{IA}=\left\{\left[0.2914\left(\frac{\rho_V}{\rho_L}\right)^{-1/1.75}\left(\frac{\mu_L}{\mu_V}\right)^{-1/7}\right]+1\right\}^{-1} \quad (1)$$

The use of completely visual observations for determining flow pattern transitions has the disadvantage of sometimes being subjective. Differences in interpretation of visual observations are no doubt a major reason experimenters have reported different flow

Manuscript received November 7, 2003; revision received September 19, 2004. Review conducted by: R. M. Manglik.

patterns under essentially similar flow conditions. The development of a simple qualitative means for distinguishing between flow patterns is therefore desirable [1].

To construct a flow pattern map for visualization purposes, it is sufficient to assume a fixed value of mass flux in the general range of interest. Thome [9] and Liebenberg [15] note that the choice of the value of mass flux affects the void fraction calculation but is not significant for the principal transition curves of interest for most refrigerant condensation studies and therefore has no impact on x_{IA}, the vapor quality for transition from annular to intermittent flow.

Hubbard and Dukler [16] showed that the analysis of the frequency of the fluctuations in pressure drop between two nearby wall locations might be used to distinguish between flow patterns for air-water flow. They found that all of the spectral distributions were seen to fall into three broad categories, characterized by the manner in which the energy in the wall pressure fluctuation was distributed among the frequencies observed. They classified horizontal air-water flow into three regimes: Separated flow, intermittent flow, and dispersed flow. Hubbard and Dukler also found that the character of a pressure trace is distinguished only by two variables, the amplitude of the fluctuations and their frequency. Although certain types of flow could be detected from the time traces of the wall pressure oscillations without the need to consider the power spectrum (i.e., slug flow and slug-annular flow), their traces had characteristic rectangular pressure pulses corresponding to slugs. However, the pressure-time records did not suffice to distinguish other regimes (i.e., from the traces alone, it was difficult to discriminate between stratified or wavy flows and dispersed flow). Therefore, in order to discriminate between flow regimes, an investigation was made of the additional information that could be obtained from the power spectral density (PSD) distribution of the fluctuating wall pressure. In Hubbard and Dukler's work, the wall pressure fluctuations appeared to be stationary, by virtue of the fact that a random pressure signal's statistical properties are unaffected by any translation of time. This technique could therefore be used because the pressure signal was of a stationary nature, viz. the random pressure signal's statistical properties were unaffected by any translation of time.

Jones and Zuber [17] analyzed the frequency spectrum of the output of a gamma densitometer to evaluate the statistical nature of air-water flow. They also employed a digital Fourier analyser to obtain probability density functions and PSDs of void fraction fluctuations. Their results include a simplification of overall flow pattern classification suggested by the statistical data and the development of an objective flow pattern discriminator for the three major classifications: Bubbly, slug, and annular flows. The data suggest that in the overall view, slug flow is simply a transitional flow, periodically fluctuating between bubbly flow and annular flow, and thus is simply a recurring time combination of these latter two independent regimes.

Weisman et al. [18] also concluded that pressure drop fluctuations would furnish a very convenient means of flow analysis. However, the complex requirements for good spectral analyses led the researchers to the development of some relatively simple criteria that can be readily applied to oscillograph traces of the pressure drop.

This paper presents the PSD characteristics of condensing refrigerants R-22, R-407C, and R-134a, for both a smooth-tube and a selection of microfin-tube condensers. The paper also displays the use of the PSD distribution of the condensing pressure signal to detect the prevailing flow regime in both smooth tubes and microfin tubes, verified by visual observations and by a newly developed flow pattern identification transition criterion for microfin-tube condensation.

Experimental Facility

The Vapor Compression Loop. The main system components were a reciprocating compressor (10 kW nominal cooling capacity) with suction accumulator, water-cooled condenser, a manually adjustable expansion valve, and a water-heated evaporator, as shown in Fig. 1(*a*).

The test condenser consisted of eight coaxial tube condenser sections connected in series, and labeled A through H in Fig. 1(*a*). The outer tube of each test section was of hard-drawn copper tubing with an inside diameter of 17.27 mm and an outside diameter of 19.05 mm, cf. Fig. 1(*b*). The inner tubes were either smooth- or microfin tubes as listed in Table 1. In Table 1, the length of the smooth-tube condenser was based on that of a typical commercial heat pump with similar heating capacities. Condenser lengths for microfin tubes were calculated from estimates of the average enhanced heat transfer factors, for all tested mass fluxes and vapor qualities, of several researchers, as summarized in Liebenberg [15]. These factors were 1.09, 1.33, and 2.0, respectively, for the 10°, 18°, and 37° helix-angled microfin tubes. Thus, the 10° microfin-tube length was made 12 m/1.09=11 m, and so forth for the other microfin tubes.

Cooling water flowed in the annulus and refrigerant in the inner tube in a counterflow direction. Spacers between the tubes prevented tube sagging. Refrigerant mass flow rate through the condensers was controlled by means of a refrigerant bypass line, which was connected in parallel with the test condenser. A water-cooled aftercondenser was used to ensure that only liquid refrigerant entered the Coriolis-type mass flow meter. Sight glasses before and after the refrigerant Coriolis flow meter were used to verify that only liquid (i.e., subcooled) refrigerant flowed through it. All test sections were thermally insulated with foam rubber.

The pressures of the condensing refrigerant were measured with a large-dial pressure gauge, as well as strain-gauge-type pressure transducers situated at the inlet and outlet of each of the condenser subsections. Temperatures were measured with resistance temperature detectors (RTDs) at all the refrigerant and water inlets and outlets, for both the condenser and evaporator. At each of the measurement locations, two RTDs were positioned, one at each side of the inner tube. Six minivideo cameras provided visual observations through specially manufactured high-pressure sight glasses [cf. Fig. 1(*b*)]. Care was taken to ensure that the inner diameter of the sight glasses was the same as the inner diameter of the inner tubes.

The Water Loops. Two main water loops were used, one flowing through the condensing side (i.e., the chilled water loop) and the other through the evaporating side (i.e., the hot water loop). On the condensing side, the water temperature was kept constant in a 1000 liter capacity insulated reservoir connected to a 15 kW chiller. A centrifugal pump pumped the chilled water to the coaxial tube condenser. The flow rate of the water through the test sections was measured with a Coriolis mass flow meter. After passing through the condenser, the water returned to the reservoir of the chiller unit.

A similar flow loop was used on the evaporating side, also with an insulated 1000 liter reservoir, but connected to a 12 kW electric resistance heater. Increasing or decreasing the temperature and flow rate of the water through the evaporator and condenser altered the refrigerant density at the compressor inlet and thus the refrigerant mass flow.

Experimental Ranges. Table 2 shows the ranges of experimental parameters covered, while Table 3 presents the experimental uncertainties that were calculated by a propagation-of-error analysis [19].

Data Acquisition. Data were gathered by a computerized data acquisition system that displayed all measured quantities in real time. In addition, secondary quantities, such as flow regime, refrigerant quality, heat transfer coefficient, and various dimensionless groups, were output to the screen. This allowed close monitoring of system parameters until they reached target values. Data were acquired only when energy balances of better than 1%

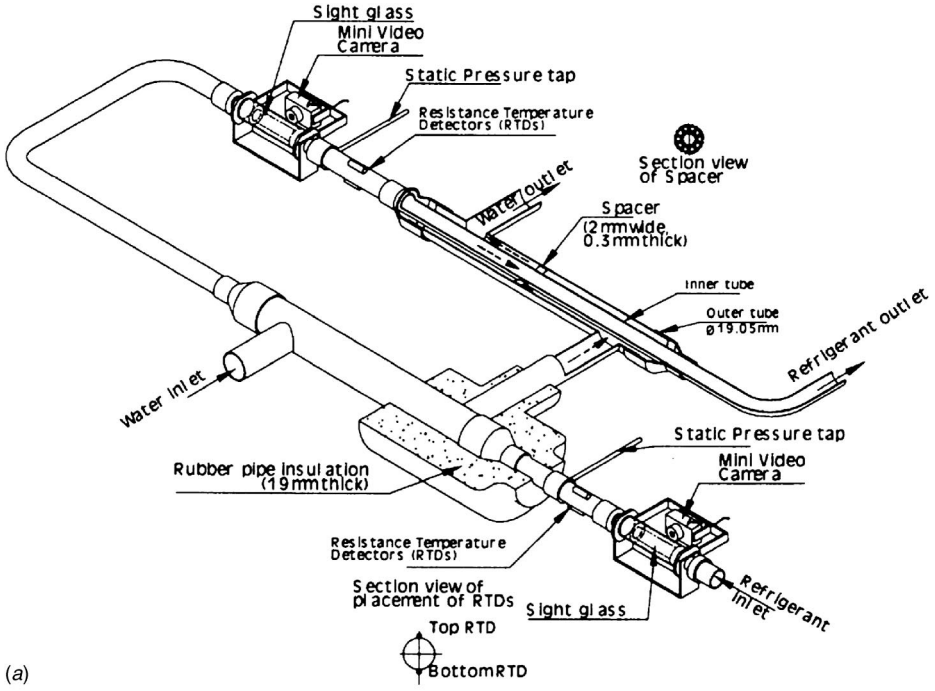

(*a*)

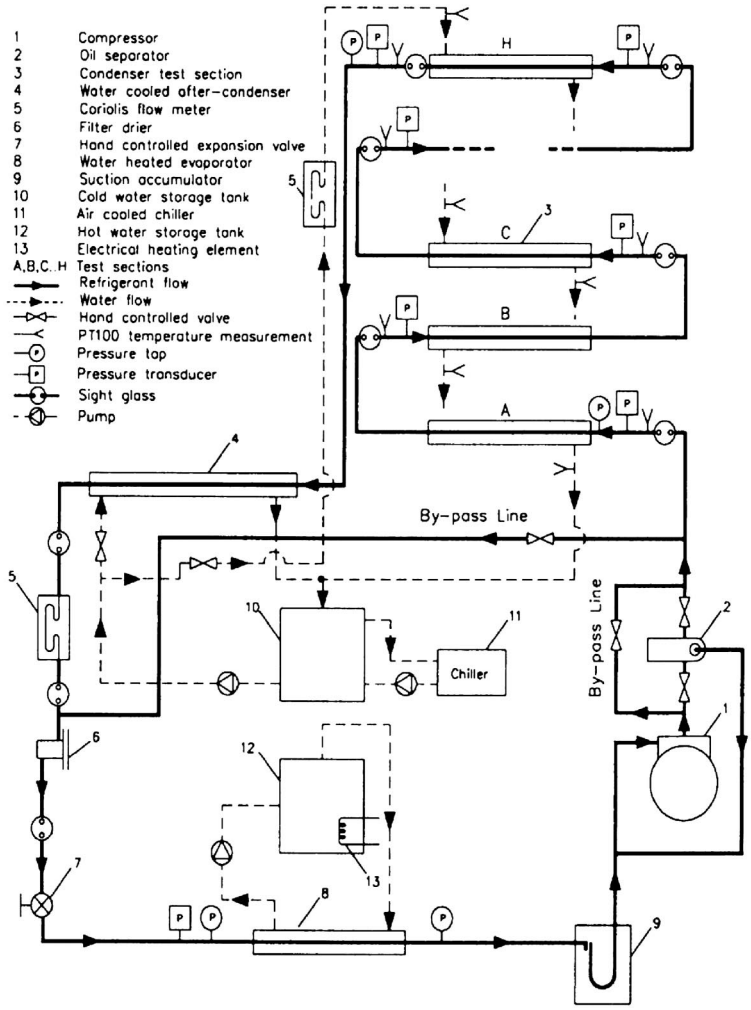

(*b*)

Fig. 1 Experimental setup: (*a*) subsection of test condenser and (*b*) entire system

Table 1 Geometric parameters of experimental inner tubes

Parameter/tube type	Smooth	Microfin	Microfin	Microfin
Helix angle (°)	—	10	18	37
Apex angle (°)	—	40	40	40
Number of fins (-)	—	60	60	60
Fin base thickness (mm)	—	0.16	0.1661	0.1585
Outside diameter (mm)	9.52	9.65	9.55	9.55–9.575
Inside diameter (mm)	8.11	9.081	8.936	8.668
Tube wall thickness (mm)	1.3	0.292	0.302–0.312	0.445–0.447
Fin height (mm)	—	0.194–0.216	0.198–0.2197	0.182–0.229
Overall condenser length (m)	12	11	9	6
Condenser subsection length (m)	1.5	1.375	1.12	0.75
Distance between pressure taps	1.4	1.3	1.0	0.65

were achieved, which was usually attained after a period of 10–15 min upon implementing a change in setup, depending on the required mass flux and vapor quality.

Data Reduction

Analysis of Pressure Trace. Pressure traces were sampled at eight points along the path of the condensing refrigerant and subsequent frequency and amplitude analyses were performed. Figure 2 shows that the character of a pressure trace is distinguished by the amplitude of the fluctuations and their frequency. It is apparent that certain types of flow can be detected from the time traces of the wall pressure oscillations without the need to consider the power spectrum (i.e., stratified/wavy flows); their traces have characteristic ''triangular'' pulses with much larger amplitudes than the other flow patterns. However, the pressure-time records do not suffice to distinguish the other regimes, i.e., from the traces alone, it is difficult to distinguish between annular and intermittent (slug and plug) flows. Therefore, in order to discriminate between flow regimes, an investigation was made of the additional infor-

Table 2 Ranges of experimental quantities covered

Experimental quantity	Range covered
Refrigerant mass flux kg/(m^2 s)	300, 400, . . . ,800
Overall condensing heat transfer coefficient W/(m^2 °C)	1000–8000
Vapor quality (total, nominal) -	0.05–0.9
Condensation temperature (nominal) °C	40

Table 3 Instrumentation ranges and uncertainty

Quantity	Equipment	Range	95% uncertainty: Low mass flux (300 kg/m^2 s)	95% uncertainty: High mass flux (800 kg/m^2 s)
Refrigerant temperature	Resistance detector, Pt—100	−27–95°C	0.14 K	0.04
Water temperature	Resistance detector, Pt—100	−27–95°C	0.11 K	0.04
Saturation temperature	—	—	0.12 K	0.02
Log-mean temperature difference			±2.1%	
Temperature difference (water)			±0.438%	
Pressure	*Gems Sensor*, UK	0–4000 kPa	0.28%	0.18%
Refrigerant mass flow rate	Coriolis flow meter: *Micro Motion inc*., Boulder, CO Sensor CMF050M320NB Transmitter RFT9739E4SBB	0–0.9 kg/s (nominal range) 1.9 kg/s (maximum)	0.31%	0.15%
Water mass flow rate	Coriolis flow meter: *Micro Motion inc*., Boulder, CO Sensor CMF025M009NB Transmitter RFT9739R2SBS	0–0.3 kg/s (nominal range) 0.6 kg/s (maximum)	0.15%	0.40%
Annulus heat transfer coefficient			±4%	±5%
Average heat transfer coefficient			±7%	±40%
Local heat transfer coefficient			±15%	
Annulus heat transfer coefficient			±9%	±11%
Average quality	—	—	4.58%	1.46%
Viscosity	—	—	0.10%	0.10%
Density	—	—	0.03%	0.04%
Tube length	Tape measure	0–10 m	±0.11%	
Tube diameter	Dial calliper	0.01–20 mm	±0.125%	
Uncertainty in water heat capacity measurement			±3.39%	

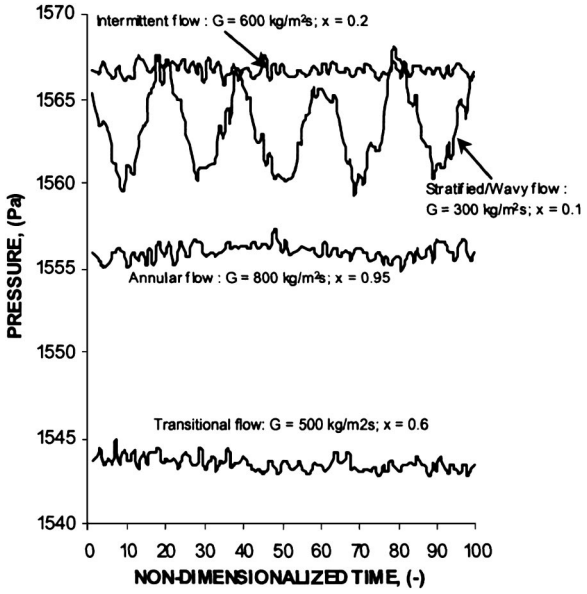

Fig. 2 Sample wall pressure (gauge pressure) traces for condensing R-407C in a smooth tube

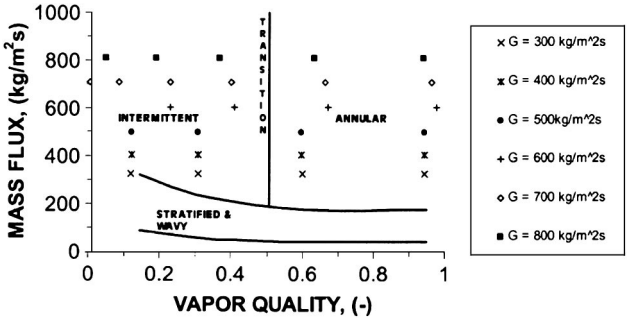

Fig. 3 Experimental data plotted with Thome [8,9] flow regime transitions for condensing R-407C in a smooth tube at 40°C

mation that could be obtained from the PSD distribution of the fluctuating wall pressure.

The pressure traces are typical examples of signals that are neither periodic nor transient (from a statistical point of view), thus rendering classical Fourier series analysis ineffective. As suggested by Webster [20], a PSD distribution of the pressure traces would render a suitable generalized harmonic analysis.

The data acquisition software was adapted to incorporate automatic sampling of pressure traces, using the power spectrum function, defined as

$$S_{xx}(f)=X^*(f)X(f)=|X(f)|^2 \tag{2}$$

where $X(f)=F\{X(t)\}$ is the Fourier transform of the pressure signal, and $X^*(f)$ is the complex conjugate of $X(f)$. All of these pressure trace amplitudes and frequencies were analyzed with the fast Fourier transform (FFT) technique [20].

The power spectrum was eventually computed as

$$S_{xx}=\frac{1}{n^2}|F\{\mathbf{X}\}|^2 \tag{3}$$

with S_{xx} representing the output sequence power spectrum, and n being the number of samples in the input sequence **X**. To enable usage of the FFT, the number of samples would have to be a valid power of 2, i.e., $n=2^m$ for $m=1,2,3\ldots$. Therefore, **X** essentially represents the amplitude spectra of the pressure traces.

After numerous preliminary experiments on the experimental setup, it was found that the frequency range of interest did not exceed 120 Hz. The user-defined maximum frequency scale was however set to 140 Hz. Considering that the maximum observable frequency was 120 Hz, a Nyquist folding frequency of twice that (i.e., 240 Hz) would be required to avoid the effect of aliasing. The closest larger valid power of two (i.e., $2^8=256$) was thus selected as the number of samples to be gathered per second, using 1024 (or 2^{10}) samples. This resulted in sampling periods of $1024/256=4$ s. No effect of the system compressor or alternating current equipment was found in the pressure traces at frequencies below 140 Hz.

Deduction of Vapor Quality. The average sectional vapor quality was calculated from

$$x_{\mathrm{TS},i}=\frac{i_{\mathrm{TS},i}-i_L}{i_L-i_V} \text{ with } i_L \text{ and } i_V \text{ measured at } T_{\mathrm{TS},i}$$
$$x_{\mathrm{TS},o}=\frac{i_{\mathrm{TS},o}-i_L}{i_L-i_V} \text{ with } i_L \text{ and } i_V \text{ measured at } T_{\mathrm{TS},o} \tag{4}$$

The average vapor quality of each test subsection was then calculated as $x=(x_{\mathrm{TS},i}+x_{\mathrm{TS},o})/2$.

Experimental Results

Flow Regimes in Smooth Tubes. Figure 3 shows the experimental flow regime map for condensing R-407C in a smooth tube, using the El Hajal et al. and Thome [8,9] transition equations. The Thome flow regime transitions varied very little among the refrigerants R-22, R-134a, and R-407C and also between different mass fluxes. It was therefore decided to use the flow regime transitions for 500 kg/m^2 s (i.e., midway between the lowest and highest experimental mass fluxes, being $x_{\mathrm{IA}}=0.48$) as the applicable flow transitions at all mass fluxes [15].

Figure 3 also shows that all the data points fall in the annular and intermittent (i.e., slug/plug flow) flow regimes. As the vapor quality decreases, the experimental points move from the annular flow region, through the transitional region, and into the intermittent flow region.

Figure 4 shows video-captured images of condensing R-134a at 300, 500, and 800 kg/m^2 s in the smooth-tube condenser, where the progression from one flow regime to the next is apparent. The images are superimposed on the Thome flow regime transitions to facilitate ease of interpretation. It is apparent that in the intermittent flow regime, a thick liquid layer covers the lower part of the condenser tube with a thin liquid film present in the upper part. Heat transfer is therefore no longer dominated by vapor shear, but rather by gravity forces.

The experimental observations of Figs. 3 and 4 show that the Thome flow regime map [8,9] is an accurate flow regime predictor, a fact that has not previously been independently verified. It was also found that the Thome transitions from annular to intermittent flow are very close to a vapor quality of 48% (for all mass fluxes), for all three the tested refrigerants. The intermittent flow regime, which includes both slug and plug flow, could clearly be observed, and again, visual observations concur with the Thome et al. map predictions. Although the visual observations cannot depict the exact point of transition, the annular-intermittent flow transitional range of 40% to 50% certainly seems appropriate, thus validating the Thome predictions.

Flow Regimes in Microfin Tubes. Figure 5 shows flow observations at 500 kg/m^2 s for condensing R-22 inside the four experimental tubes. (Similar trends for condensing R-134a and R-407C were observed and are therefore not presented here, but are available from Liebenberg [15].) At the highest vapor qualities (i.e., $x\simeq 0.9$), the flow in the microfin tubes is annular with a

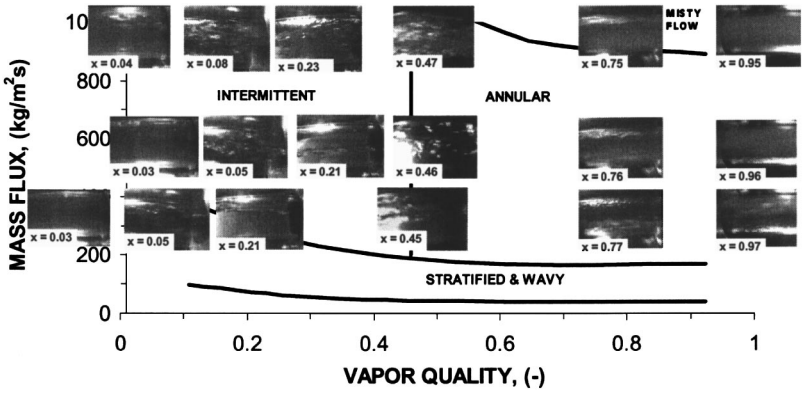

Fig. 4 Video images of condensing R-134a at 300, 500, and 800 kg/m^2 s in a smooth tube, superimposed on the flow transitions of the Thome et al. [8,9] map. Mass flux (300, 500, and 800 kg/m^2 s) is plotted against vapor quality.

stable, and apparently very thin, annular film. The flow has a twisting (or swirling) nature, induced by the helix angle of the microfins, as expected. Heat transfer would therefore be controlled by vapor shear in this regime. It is further expected that the microfins are very effective at mixing the liquid-vapor interface due to their proximity to this interface. Also, surface tension drainage is expected to have a large effect at these high vapor qualities.

As the condensation process progresses, liquid accumulates at the bottom of the horizontal condenser tube. But, different to the smooth-tube counterpart at equivalent vapor quality, the microfin tubes generate prominent secondary swirling flows (e.g., $x=0.44$ for 10° helix angle), and at these vapor qualities the liquid does not accumulate in a pool as it does with the smooth tube. Rather, the microfins ensure that some liquid is carried to the top of the tube and held there by the capillary action of the fins and the swirling energy of the flow. The liquid is therefore redistributed around the circumference, and this changes the flow pattern from an intermittent flow regime to an annular flow regime, thus further enhancing the heat transfer. Elongated slugs form at the lower vapor qualities (cf. $x=0.2$ for the 18° microfin tube), and eventually, very prominent waves are formed (cf. $x=0.05$, for the 10° microfin tube). It appears that the slug frequency, slug length, wave amplitude, and the wave frequency are stochastic in nature. Eventually the refrigerant becomes a subcooled liquid without the appearance of occasional bubbles, as was the case with the smooth tube.

It is apparent that the microfins delay the transition from annular flow to intermittent flow (by approximately $x=15-20\%$), which enhances the heat transfer relative to the smooth-tube counterpart. The visual observations furthermore showed that the intermittent flow regime is neither uniform nor steady.

New Flow Regime Transition Criterion for Microfin-Tube Condensation. Figure 6(*a*) plots the variation of void fraction, calculated by the Rouhani and Axelsson [13] and Thome [9] ''logarithmic-mean'' methods, with average vapor quality for condensing R-407C in all three microfin tubes. The trends for condensing R-134a and R-22 (and for different helix angles) are near identical and are therefore not reproduced here, but are available in Liebenberg [15]. However, the slopes of the curves change at a vapor quality of approximately 25% for all three the refrigerants (the comparative vapor quality was 30% for the smooth tube). This vapor quality depicts the transition from stratified/wavy/intermittent flow to annular flow.

Another observation from Fig. 6(*a*) is that the void fractions were almost always greater than 0.5, even at the lowest vapor qualities (as was the case for the smooth tube). As was the case for the smooth tube, if it is considered that the difference between the liquid and vapor densities was large for all three refrigerants tested under the experimental conditions, it can then be assumed that, in the mass flux range tested (300–800 kg/m^2 s), an annular flow configuration should exist over most of the tube length where condensation occurs. This was the case as attested to by the earlier visual observations. It is therefore apparent that analysis techniques and correlation methods that are applicable to annular flow are of particular interest for this study.

Figure 6(*b*) presents a plot of the void fraction for the three tested refrigerants against the Froude rate on a logarithmic scale, where the Froude rate parameter is defined as [21]:

$$Ft=[(G^2x^3)/[(1-x)\rho_V^2 gD_i]]^{1/2} \tag{5}$$

Figure 6(*b*) shows the smooth-tube results compared to only the 18° microfin-tube case, due to identical trends that were observed for the other helix-angled microfin tubes. The void fraction data are seen to collapse neatly with respect to the Froude rate parameter, and that the slope changes at a Froude rate (Ft) of 10 (compared to $Ft=20$ for the smooth tube), again indicating the change in flow pattern from stratified/wavy/intermittent to annular. The transitional Froude numbers were calculated by plotting the local heat transfer coefficients against the Froude numbers, as reported in Liebenberg [15].

Figures 5, 6(*a*), and 6(*b*) show the similarity of flow regimes between microfin tubes and smooth tubes. There is a similar change in flow characteristics at a Froude rate of 10–20 and at vapor qualities in the vicinity of 30%, cf. Fig. 6(*b*). Under the last-mentioned conditions, the flow pattern changes from stratified/wavy/intermittent to annular flow, implying that the Froude rate is a suitable predictor of the transition between the annular and intermittent/stratified/wavy flow regimes.

Although the Thome flow regime map [8] predicts the similar transition in the vapor quality range of 48–52% for the smooth tube, it must be acknowledged that the stratified-intermittent transition region is one of poor precision. The fact however remains that the microfin tubes cause a delay in transition from annular to intermittent flow and it would therefore make sense to adapt the Thome smooth-tube transition criterion for annular to intermittent flow.

Recognizing that the Lockhart–Martinelli parameter, Eq. (6), is essentially a ratio of viscous dissipation to inertial energy, and that the Froude rate parameter, Eq. (5), is a ratio of gravitational energy dissipation to inertial energy, implies that these two parameters could be used together in order to predict transition from annular flow (where viscous forces dominate) to intermittent flow (where gravitational forces dominate). The Lockhart–Martinelli parameter is defined as [22]:

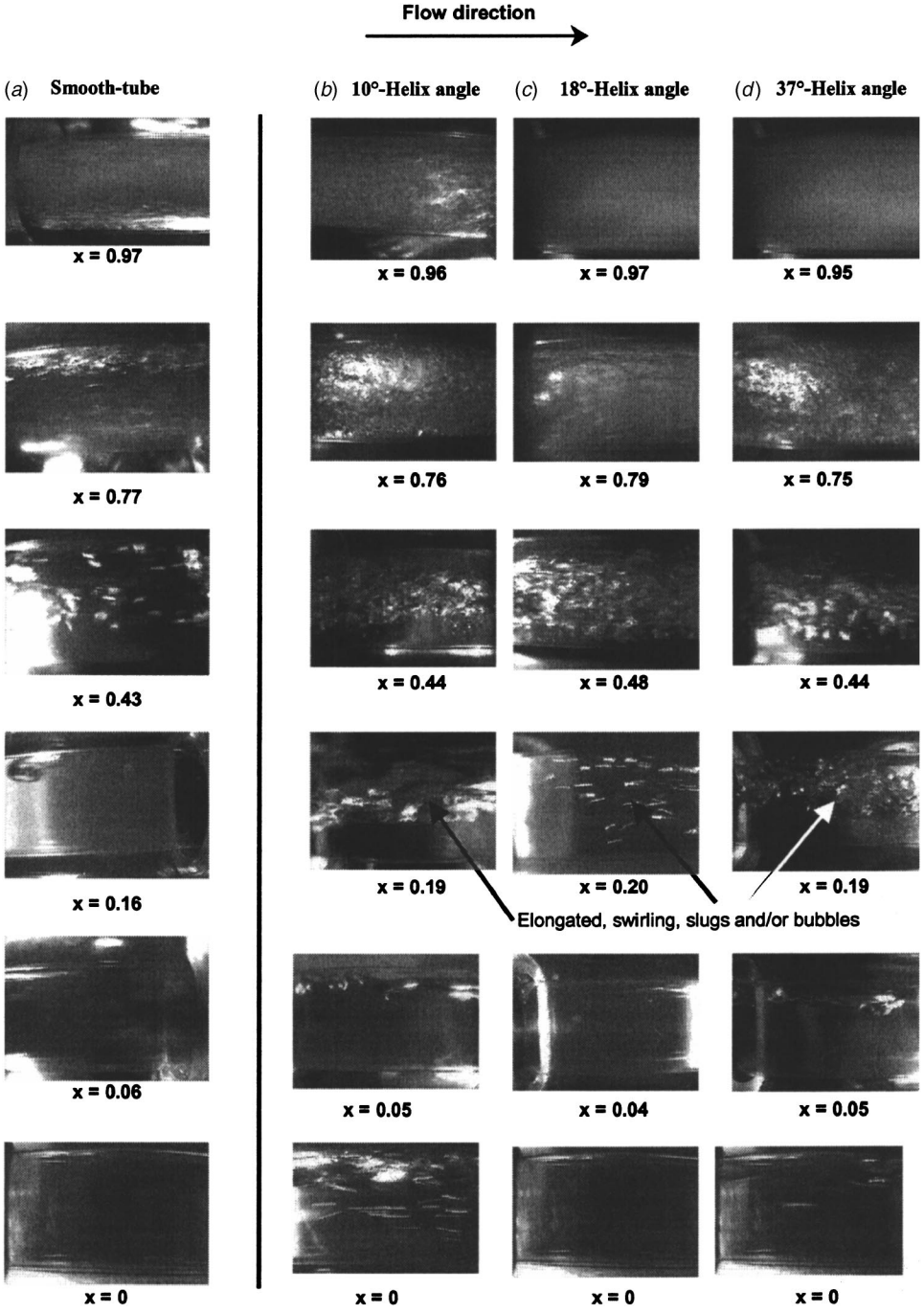

Fig. 5 Flow observations at 500 kg/m^2 s for condensing R-22 inside (*a*) a smooth tube, and microfin tubes with varying helix angles: (*b*) 10°, (*c*) 18°, and (*d*) 37°

$$X_{tt}=\left(\frac{\rho_V}{\rho_L}\right)^{0.5}\left(\frac{\mu_L}{\mu_V}\right)^{0.1}\left(\frac{1-x}{x}\right)^{0.9} \tag{6}$$

Graham et al. [21] showed the relative independence between gravitational and viscous effects as the flow field transitions from one region of dominance to the other.

Figure 7 shows the variation of Martinelli parameter (X_{tt}) with Froude rate (Ft) for all test points for all three refrigerants in all three microfin tubes as well as for the smooth tube. All the data points were logarithmically regressed to

$$X_{tt}=-0.3696\ln(\mathrm{Ft})+1.5465 \tag{7}$$

Using the pre-established Froude rate transitional value of 10 [cf. Fig. 6(*b*)] into Eq. (7), gives a value of $X_{tt}=0.695$. When this value is equated to Eq. (6), and the resulting equation is rearranged to make the vapor quality the object of the equation, gives

$$x_{\mathrm{IA}}=\left\{\left[0.595\left(\frac{\rho_V}{\rho_L}\right)^{-1/1.75}\left(\frac{\mu_L}{\mu_V}\right)^{-1/7}\right]+1\right\}^{-1} \tag{8}$$

The vapor quality determined by Eq. (8) therefore gives the transition between intermittent and annular flow, and will be used to adapt the Thome flow regime map for use with microfin-tube condensation (cf. Fig. 8). The transitional vapor qualities obtained by the use of Eq. (8) give values of 32% for all three microfin

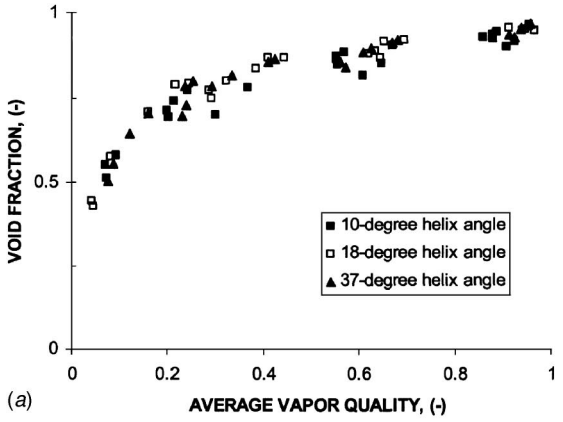

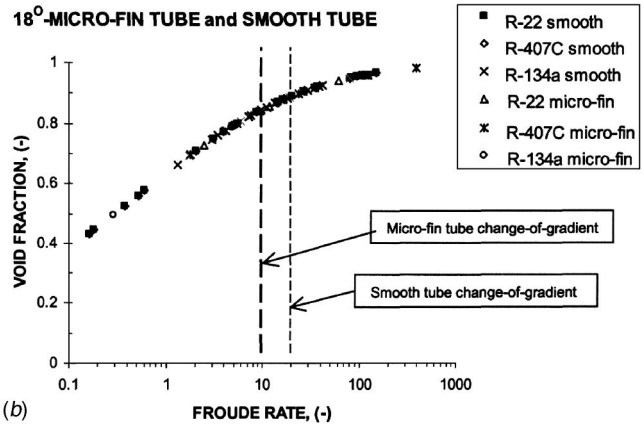

Fig. 6 (*a*) **Void fraction versus average vapor quality for all three microfin tubes for condensing R-407C (condensing R-134a and R-22 showed near-identical trends, and are therefore not shown here); (*b*) Comparison of smooth-tube and 18° microfin tube void fractions versus Froude rate parameters. The transitional Froude numbers were calculated by plotting the local heat transfer coefficients against the Froude numbers, as reported in Liebenberg [15].**

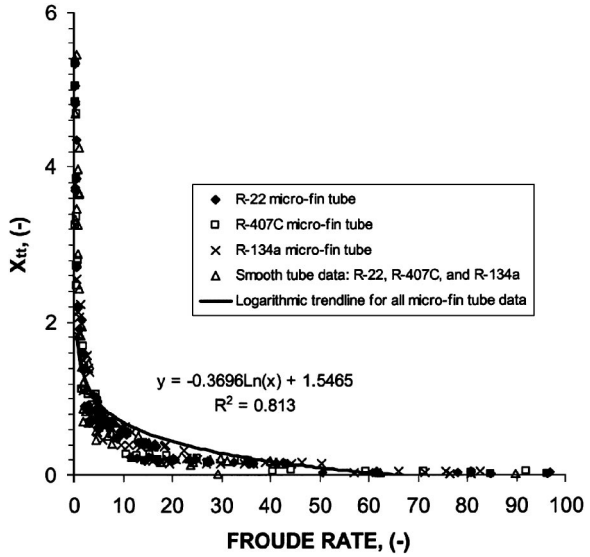

Fig. 7 Martinelli parameter (Xtt) versus Froude rate parameter for R22, R-407C, and R-134a condensing in the three test microfin tubes (10, 18, and 37-helix angles)

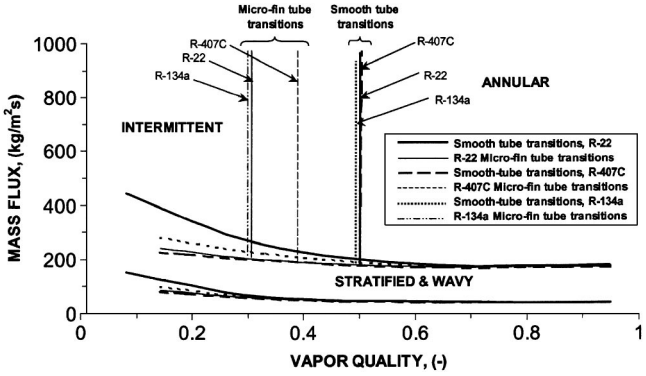

Fig. 8 Comparison of experimental Thome et al. flow pattern transitions in a smooth tube, versus those in microfin tubes with condensing R-22, R-407C, and R-134a

tubes using R-22, 39% for R-407C, and 30% for R-134a. Therefore, the transitional vapor qualities have shifted from approximately 48% for smooth tubes (cf. Fig 3) to 30–39% for microfin tubes, thus correctly reflecting the delay in the transition from annular to intermittent flow by 9–18% for the microfin-tube condensers.

Regarding the transitions from intermittent and annular flow to stratified/wavy flow, the smooth-tube case displayed the highest mass flux transition values, compared to the microfin tubes. For the microfin tubes, little difference was predicted, although R-134a ensured the lowest transitional mass fluxes, followed by R-22, and then R-407C. It was only at vapor qualities below approximately 35% where the transitional curves showed diverging tendencies. These variations are directly attributed to the varying reduced pressures among the refrigerants, since high values of reduced pressure imply similar densities of the liquid and vapor phases, which further imply higher values of vapor density and viscosity, and lower values of liquid density and viscosity. Condensing R-134a had a reduced pressure of 0.26, R-22 had a value of 0.31, and R-407C had a value 0.36, thus meaning that at a given mass flux, the size of the vapor quality range occupied by annular flow was greater at lower reduced pressure, implying that the most annular flow was observed for R-134a, followed by R-22, with R-407C showing the least amount of annular flow, [15]. The flow transitions are represented in Fig. 8.

Power Spectral Densities

The pressure signals obtained from the pressure transducers were sampled as earlier explained, and their respective PSD distributions were calculated in real time. Liebenberg [15] shows that there are distinct similarities between the PSDs of R-407C, R-22, and R-134a. Therefore, only the salient characteristics and harmonics are shown for both the smooth-tube (Fig. 9) and microfin tubes (Fig. 10).

Smooth-Tube- and Microfin-Tube Results. Figure 9 shows that the high vapor qualities are associated with power spectra that are focused at either 40 or 120 Hz. Visual observations show that this corresponds to stable annular flow. As the vapor quality reduces, cf. Fig. 9(*b*), the amplitudes of the harmonics reduce in magnitude but that harmonic frequency of the higher vapor quality flow is retained (i.e., 40 and 120 Hz). This flow regime is indicative of an unstable annular flow where a thick liquid film should be apparent.

When a vapor quality of around 40–50% is attained, the PSD distributions change and now cover the entire band of frequencies, with at least eight dominant harmonics occurring (typically, 5, 20, 50, 60, 80, 100, 110, and 120 Hz). When compared with the visual observations, the flow is of an intermittent (slug and plug) nature. Figure 9(*c*) indicates that these harmonics characterize the fluctu-

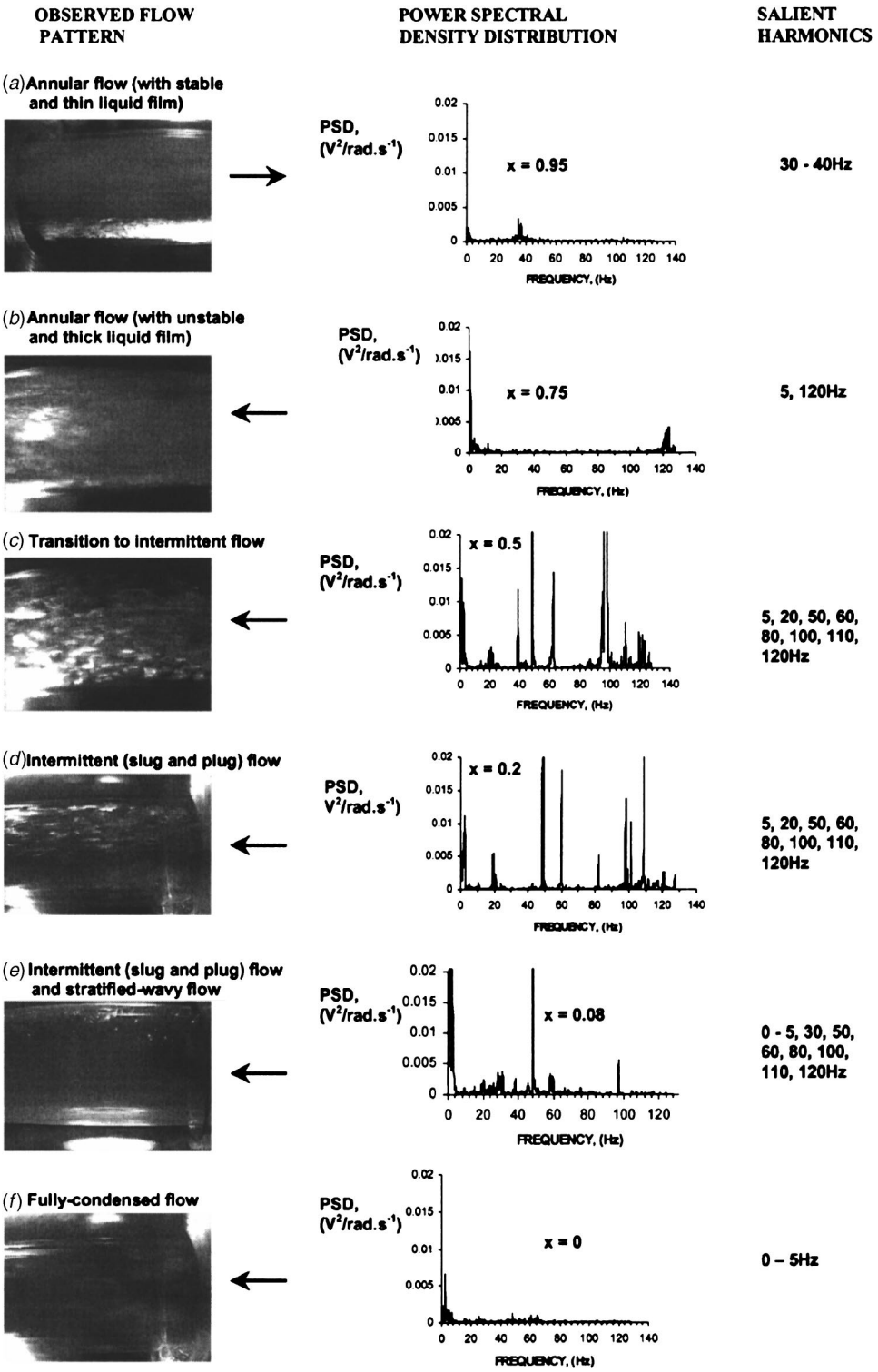

Fig. 9 Summary of typical PSD distributions (versus harmonic frequency) for the different observed flow regimes in the smooth tube (for 500 kg/m^2 s, for all three refrigerants). Arrows indicate flow directions.

ating nature of the slugs and plugs, and are also indicative of the flow's periodic transition to annular (thick-film) flow. In the transitional region between intermittent (i.e., slug and plug) and annular flow, the wide range of frequencies covered by the PSD, suggest a recurring time combination of the intermittent and annular flow regimes.

At low vapor qualities (i.e., $x<30\%$) and low mass fluxes ($G<500\,\mathrm{kg/m^2\,s}$), the flow is of a highly intermittent nature, as suggested in Fig. 9(*d*). The same harmonics as in the previous higher vapor quality region are retained, but the PSD amplitudes have decreased. At vapor qualities lower than 20%, many of the previous harmonics have disappeared, cf. Fig. 9(*e*), and the harmonics are now typically concentrated around 0–5, 30, 50, 60, and 100 Hz. The amplitudes also drop off significantly with increasing

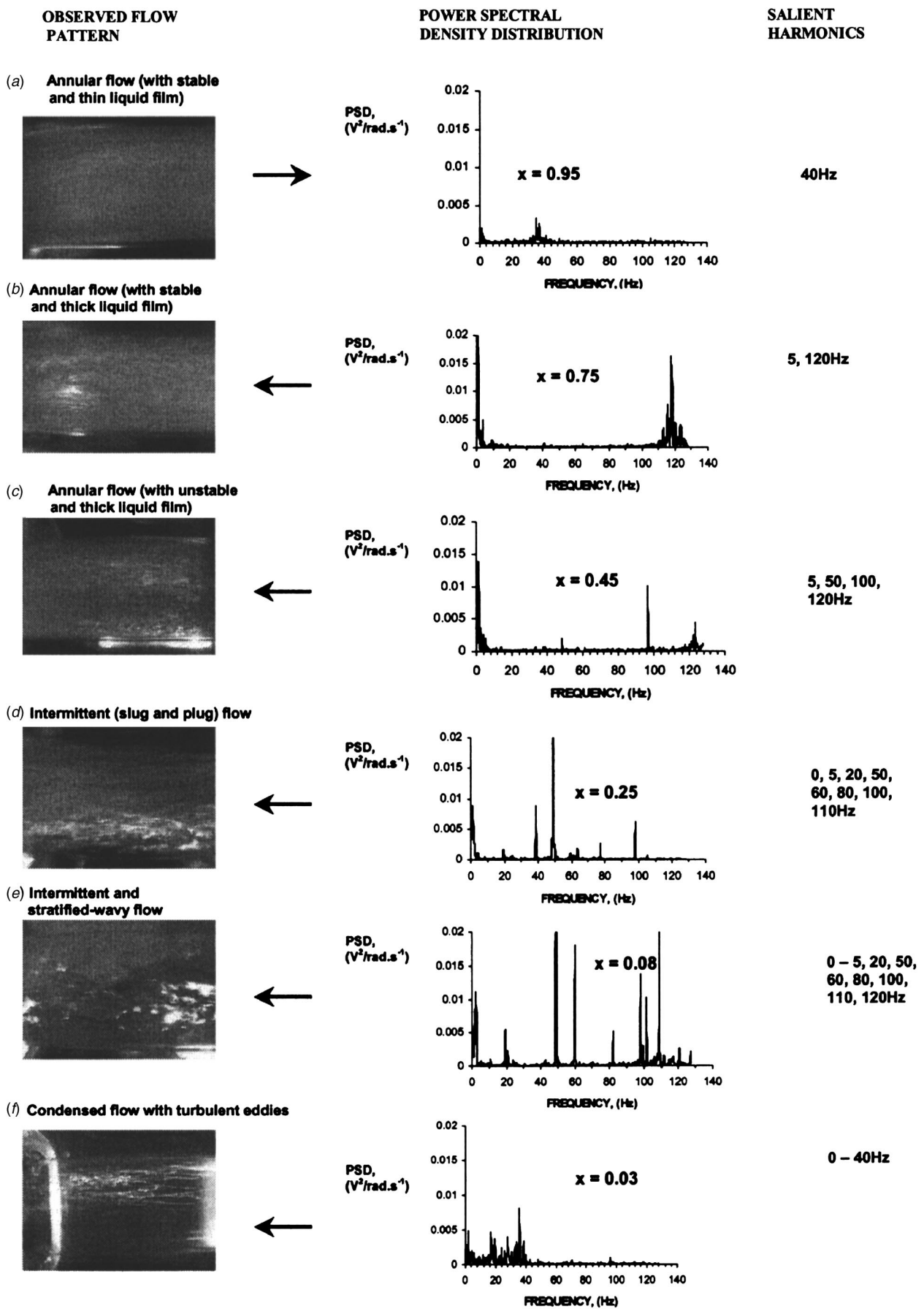

Fig. 10 Summary of typical PSD distributions (versus harming frequency) for the different observed flow regimes in the three microfin tubes for all three the tested refrigerants. Horizontal arrows show flow directions.

frequency. These latter spectral phenomena coincide with visually observed stratified and wavy flow patterns, with the occasional formations of bubbles.

Subcooled flow of refrigerant is characterized by power spectra with distributions centred on 0–5 Hz, again, with their amplitude dropping off at a very steep gradient as the frequency increases, cf., Fig. 9(*f*). Also to be noted is the fact that the condensing flow did not demonstrate harmonics beyond 120 Hz. Liebenberg [15] shows that high mass fluxes are associated with lower amplitudes than is the case for smaller mass fluxes, which is ascribed to the diminishing size in bubbles/slugs as the mass flux increases.

Figure 10 shows that the microfin-tubes' PSD distributions of the pressure trace reflect the prevailing flow regime, as was the case with the smooth tube. There is little difference between the PSDs of the smooth and the microfin tube, mostly the transition from annular to intermittent flow, which is delayed for the case of the microfin tube; for the smooth tube, transition already occurs at around 50% vapor quality, while this is delayed to around 25%–30% for the microfin tube, as correctly predicted by Eq. (8). However, at low vapor qualities (i.e., $x<20\%$) and low mass fluxes ($G<500\,\mathrm{kg/m^2\,s}$), the flows tend to become stratified with the appearance of stochastic waves and elongated, swirling bubbles. The same harmonics as in the previous higher vapor quality region are retained, with similar PSD amplitudes. At vapor qualities around 10%, the flow of refrigerant is characterized by power spectra similar to that of the previous vapor quality. Also, at the lowest vapor qualities and at the highest mass fluxes, the appearance of turbulent eddies is common, cf., Fig. 10(*f*). These eddies apparently cause significant pressure fluctuations and these are characterized by a PSD distribution with harmonics occurring in the full range of 0–40 Hz.

Conclusion

Refrigerants R-22, R-407C, and R-134a were condensed in one smooth and three microfin tubes, each with varying helix angle. The flow regime map of El Hajal et al. and Thome [8,9] was found to correlate the smooth-tube experimental data accurately. The flow regimes that were observed for the microfin tubes were similar to those for smooth-tube condensation. However, the most important comparative flow regime observation was that the transition from annular to intermittent flow occurred at vapor qualities from 30–39% compared to 48% for smooth-tube condensation. The microfins therefore effectively delay the transition from annular to intermittent flow, which in itself would bring about an increase in the measured heat transfer coefficients.

A new transitional criterion for microfin-tube condensation was compared with the captured visual observations of the condensing flow patterns, and good agreement was obtained. The visual observations and flow regime map predictions were corroborated by the PSD distributions of the condensing pressure signals. All three test refrigerants in all three microfin tubes showed a steep climb in PSD harmonics to occur at 25–30% vapor qualities, depicting the change in flow pattern from annular to intermittent.

The microfin tubes cause a distinct swirling motion that is especially apparent at low vapor qualities. Also, at high mass fluxes and low vapor qualities, swirling turbulent eddies were present; these were not noticeable with smooth-tube condensation. This is again confirmed by the PSD distributions of the microfin tubes, that show a range of activity spanning 0–40 Hz (implying the presence of the eddies), where the smooth tube at similar vapor qualities only displayed frequency peaks around 0–5 Hz.

Acknowledgments

Wolverine Inc., Alabama, USA supplied the experimental microfin tubes, and the authors are indebted to Mr. Petur Thors who arranged for the kind donation. The research work was performed with a South African National Research Foundation grant, under Grant No. 2053287.

Nomenclature

D = diameter, D_i (inner); D_o (outer) m
F = fast Fourier transform
Ft = Froude rate$=[(G^2x^3)/\{(1-x)\rho_V^2 g D_i\}]^{1/2}$ -
G = mass velocity $\mathrm{kg/m^2\,s}$
g = acceleration due to gravity $\mathrm{m/s^2}$
i = specific enthalpy J/kg
$\dot{m}$ = mass flow rate kg/s
n = number of samples -
p = pressure Pa
$S_{xx}(f)$ = power spectrum function of power signal $\mathrm{V^2/rad\cdot s^{-1}}$
T = temperature, T_w (water); T_{sat} (saturation) °C
x = vapor quality mol/mol
x_{IA} = vapor quality depicting transition between annular and intermittent flows, mol/mol
$\mathbf{X}$ = normalized pressure signal, using Hamming window technique
$X(f)$ = fourier transform of pressure signal
$X^*(f)$ = complex conjugate of $X(f)$
$X(t)$ = time-domain referred pressure signal
X_{tt} = Lockhart-Martinelli parameter for turbulent flow$=[(1-x)/x]^{0.9}(\rho_V/\rho_L)^{0.5}(\mu_L/\mu_V)^{0.1}$ -

Greek Letters

μ = dynamic viscosity $\mathrm{Ns/m^2}$
ρ = density $\mathrm{kg/m^3}$

Subscripts

i = inside, inlet
IA = intermittent annular
L = liquid phase
max = maximum
o = outside, outlet
TS = test section
V = vapor phase

References

[1] Liebenberg, L., Bergles, A. E., and Meyer, J. P., 2000, "A Review of Refrigerant Condensation in Horizontal MicroFin Tubes," **40**, *Proc. ASME Advanced Energy Systems Division*, pp. 155–168.
[2] Kattan, N., Thome, J. R., and Favrat, D., 1998a, "Flow Boiling in Horizontal Tubes. Part 1: Development of a Diabatic Two-Phase Flow Pattern Map," ASME J. Heat Transfer, **120**(1), pp. 140–147.
[3] Kattan, N., Thome, J. R., and Favrat, D., 1998b, "Flow Boiling in Horizontal Tubes. Part 3: Development of a New Heat Transfer Model Based on Flow Patterns," ASME J. Heat Transfer, **120**(1), pp. 156–165.
[4] Kattan, N., Thome, J. R., and Favrat, D., 1995a, "Measurement and Prediction of Two-Phase Flow Patterns for New Refrigerants Inside Horizontal Tubes," ASHRAE Trans., **101**(2), SD-95-17-4.
[5] Kattan, N., Thome, J. R., and Favrat, D., 1995b, "Boiling of R-134a and R-123 in a Microfin Tube," *Proc. 19th Int. Congress of Refrigeration*, The Hague, Vol. IVa, pp. 337–344.
[6] Shao, D. W., and Granryd, E., 2000, "Flow Pattern, Heat Transfer and Pressure Drop in Flow Condensation; Part I: Pure and Azeotropic Refrigerants," HVAC&R Res., **6**(2), pp. 175–195.
[7] Cavallini, A., Censi, G., Del Col, D., Doretti, L., Longo, G. A., and Rossetto, L., 2002, "In-Tube Condensation of Halogenated Refrigerants," ASHRAE Trans., **108**(1), pp. 146–161.
[8] El Hajal, J., Thome, J. R., and Cavallini, A., 2003, "Condensation in Horizontal Tubes, Part 1: Two-Phase Flow Pattern Map," Int. J. Heat Mass Transfer, **46**, pp. 3349–3363.
[9] Thome, J. R., 2003, "Update on Kattan-Thome-Favrat Flow Boiling Model and Flow Pattern Map," *Proc. 5th International Conference on Boiling Heat Transfer*.
[10] Collier, J. G., and Thome, J. R., 1994, *Convective Boiling and Condensation*, Clarendon, Oxford.
[11] Steiner, D., 1993, "Heat Transfer to Boiling Saturated Liquids," *VDI-Wärmeatlas* (VDI Heat Atlas), edited by Verein Deutscher Ingenieure, VDI-Geseelschaft Verfahrenstechnik und Chemieingenieurswesen (GCV), Düsseldorf.
[12] Taitel, Y., and Dukler, A. E., 1976, "A Model for Predicting Flow Regime Transitions in Horizontal and Near-Horizontal Gas-Liquid Flow," AIChE J., **22**(1), pp. 47–55.
[13] Rouhani, Z., and Axelsson, E., 1970, "Calculation of Volume Void Fraction in

the Subcooled and Quality Region,'' Int. J. Heat Mass Transfer, **13**, pp. 383–393.
[14] Zürcher, O., Thome, J. R., and Favrat, D., 1999, ''Evaporation of Ammonia in a Smooth Horizontal Tube: Heat Transfer Measurements and Predictions,'' ASME J. Heat Transfer, **121**, pp. 89–101.
[15] Liebenberg, L., 2002, ''A Unified Prediction Method for Smooth and Microfin Tube Condensation Performance,'' Ph.D. thesis, Department of Mechanical Engineering, Rand Afrikaans University, South Africa.
[16] Hubbard, M. G., and Dukler, A. E., 1966, ''The Characterization of Flow Regimes for Horizontal Two-phase Flow: Statistical Analysis of Wall Pressure Fluctuations,'' *Proc. 1966 Heat Transfer and Fluid Mechanics Institute*, pp. 100–121.
[17] Jones, O., and Zuber, Z., 1974, ''Statistical Methods for Measurement and Analyses of Two-Phase Flow,'' *Heat Transfer 1974: Proc. 5th International Heat Transfer Conference*, pp. 200–204.
[18] Weisman, J., Duncan, D., Gibson, J., and Crawford, T., 1979, ''Effect of Fluid Properties and Pipe Diameter on Two-Phase Flow Patterns in Horizontal Lines,'' Int. J. Multiphase Flow, **5**, pp. 437–462.
[19] Kline, S. J., and Mc Clintock, F. A., 1953, ''Describing Uncertainties in Single-Sample Experiments,'' Mech. Eng. (Am. Soc. Mech. Eng.), **75**, pp. 3–8.
[20] Webster, J. G. (Editor-in-Chief), 1999, *The Measurement, Instrumentation, and Sensors Handbook*, CRC Press, New York.
[21] Graham, D. M., Kopke, H. R., Wilson, M. J., Yashar, D. A., Chato, J. C., and Newell, T. A., 1999, ''An Investigation of Void Fraction in the Annular/Stratified Flow Regions in Smooth, Horizontal Tubes,'' ACRC TR-44, Air Conditioning and Refrigeration Center, University of Illinois at Urbana–Champaign.
[22] Lockhart, R. W., and Martinelli, R. C., 1949, ''Proposed Correlation of Data for Isothermal Two-Phase, Two-Component Flow in Pipes,'' Chem. Eng. Prog., **45**(1), pp. 39–48.

Condensation of Zeotropic Mixtures in Horizontal Tubes: New Simplified Heat Transfer Model Based on Flow Regimes

D. Del Col
e-mail: davide.delcol@unipd.it

A. Cavallini
e-mail: alcav@unipd.it

Dipartimento di Fisica Tecnica,
Università di Padova,
I-35131, Padova, Italy

J. R. Thome
e-mail: john.thome@epfl.ch
Laboratory of Heat and Mass Transfer,
Faculty of Engineering Science and Technology,
Ecole Polytechnique Fédérale de Lausanne,
CH-1015 Lausanne, Switzerland

The need for optimal design of heat exchangers with in-tube condensation of zeotropic refrigerant mixtures has pushed the research of predictive methods in the last years. Some procedures have been developed, based on the Colburn and Drew (1937, Trans. AIChemE ***33****, pp. 197–215) analysis, that require significant numerical effort and the diffusivity properties of the mixture to calculate the mass transfer resistance in the process and, hence, are rarely used for heat exchanger design. Proposing a modified version of the well-known simplified approach of Silver (1947, Trans. Inst. Chem. Eng.* ***25****, pp. 30–42) and Bell and Ghaly (1973, AIChE Symp. Ser.* ***69****, pp. 72–79) to include the effects of interfacial roughness and nonequilibrium effects, the present study extends the flow-pattern-based model of Thome, El Hajal, and Cavallini (2003, Int. J. Heat Mass Transfer* ***46****, pp. 3365–3387) for condensation of pure fluids and azeotropic mixtures to zeotropic mixtures. By implementing this within the above flow-pattern-based heat transfer model, it leads to an improved method for accurately predicting local mixture heat transfer coefficients, maintaining a clear relationship between flow regime and heat transfer, and achieving both the goals of higher prediction accuracy and low calculation effort. The method has been verified for refrigerant mixtures (both halogenated and hydrocarbon) having temperature glides of 3.5–22°C, that is temperature differences between the dew point and bubble point temperatures (at a fixed pressure and bulk composition).* [DOI: 10.1115/1.1857951]

1 Introduction

Mixture condensation differs from pure vapor condensation in two ways. First, the temperature of the condensing process changes through the condenser, and second, mass transfer effects are introduced in addition to those of heat transfer. During the condensation of a zeotropic mixture in a tube, the less volatile component condenses more readily causing the composition and temperature in the vapor and liquid phases to vary along the length of the tube. The mass fraction of the more volatile component in each phase increases along the flow direction, while the temperature of the bulk vapor decreases.

As the condensation process in this case is nonisothermal, both liquid and vapor phase sensible effects are present. The condensate already laid down must be further cooled, and the remaining vapor must be cooled down to remain in near equilibrium at the interface where further condensation is taking place. As stated by Bell and Ghaly [1], the sensible heat removal from the vapor is particularly significant because of the low heat transfer coefficients commonly associated with this process. As a result from the continuous changes in the compositions of both phases during the process, there are mass transfer resistances in both the vapor and liquid phases coupled to the heat transfer processes. The resistance to mass transfer in the vapor phase is a critical aspect of the problem, where the lack of applicable mass transfer data and the complexity of the computational procedure are big obstacles for the search of the exact solution of the problem.

Colburn and Drew [2] derived the basic transport equations for condensation of a miscible binary mixture. Since then, significant developments have been made to Colburn-Drew method so that this approach is used for rigorous design of multicomponent condensers when possible [3,4].

Manuscript received October 31, 2003; revision received November 17, 2004. Review conducted by: J. N. Chung.

Cavallini et al. [5] applied the Colburn and Drew film method to a tube-in-tube condenser with superheated vapor entering the tube. During the condensation process of the binary mixture, at a given point, the total condensing molar flux was related to the condensing molar flux of each component as a function of the total molar concentration, the mass transfer coefficient in the gas-phase, and the mole fractions of the pure components in the vapor phase at liquid-vapor interface temperature and at bulk gas temperature. The vapor-side mass transfer coefficient was obtained from the Reynolds analogy, as a function of the binary diffusion coefficient. This procedure was pretty complex to implement and is not easy to extend to ternary mixtures, mainly because of the need for the diffusion coefficients.

Although the Colburn approach presents the advantage of being a more physically realistic treatment of the phenomenon, the principal method of industrial design practice is an approximate general method, which was first devised by Silver [6] and then extended by Bell and Ghaly [1]. It is based on the equilibrium cooling curve and heat transfer considerations alone.

These different approaches are discussed and compared in Webb [3] and Webb et al. [7]. Silver [6] and then Bell and Ghaly [1] proposed a simplified method to account for the mass transfer thermal resistance, under the hypothesis that complete mixing both in the liquid and in the vapor phase is reached and overall equilibrium is maintained. According to Bell and Ghaly [1], the mass transfer resistance is proportional to the sensible heat transfer resistance in the vapor phase. Bell and Ghaly focused on the heat transfer problem because reasonable estimates of its resistance can be made from available information, and it is possible to bound the heat transfer problem in the conservative direction. Therefore, the key assumption in the Bell and Ghaly [1] procedure is that the effect of the mass transfer resistance in the vapor phase can be replaced by a conservative estimate of the heat transfer resistance in the vapor. Their assumptions lead to writing the over-

Table 1 Condensation heat transfer database of zeotropic mixtures

Authors	Data points	Mixture (mass fraction)	d [mm]	T_{sat} [°C]	ΔT_{gl} [°C] *	$(T_{sat}-T_w)$ [°C]	G [kg/(m^2 s)]
Cavallini et al. (1999)	38	R407C	8.0	38 – 49	4.9	4.5 - 13	104 - 755
Cavallini et al. (2000)	43	R125/236ea (46/54%)	8.0	39 - 57	21.2	6.5 - 18	102 - 753
	31	R125/236ea (63/37%)	8.0	36 - 55	16.9	5.5 - 13.5	96 - 751
	24	R125/236ea (28/72%)	8.0	35 - 56	21.9	5.7 - 13.9	98 - 743
Lee (1994)	27	R22/124 (20/80%)	7.5	19 - 44	5.5	9.4 - 19.3	215 - 305
	26	R22/124 (50/50%)	7.5	22 - 39	6.7	10.9 - 19.2	167 - 369
	24	R22/124 (80/20%)	7.5	22 - 37	3.6	7.7 - 15.8	174 - 358
Kim et al. (1996)	213	R290/600 (25/75%)	8.0	45 - 54	10.5	2.8 - 6.9	65 - 154
	205	R290/600 (50/50%)	8.0	44 - 55	12.2	3.5 - 6.9	57 - 172
	241	R290/600 (75/25%)	8.0	46 - 54	8.2	3.5 - 7.3	89 - 191

(*) Values of ΔT_{gl} are mean values since the temperature glide varies with saturation pressure.

all thermal resistance as the sum of two thermal resistances in series. The first resistance is for convective heat transfer in the vapor phase from the bulk vapor temperature to the temperature at the interface, and the second resistance is across the condensate film itself

$$R_T=\frac{1}{\alpha_p}+\frac{đq_{SV}}{đq_T}\frac{1}{\alpha_G} \tag{1}$$

where R_T is the overall thermal resistance for the zeotropic mixture, α_G is the heat transfer coefficient of the vapor phase, α_p is the pure fluid condensation heat transfer coefficient evaluated using the mixture properties, and $(đq_{SV}/đq_T)$ is the ratio between the sensible heat duty removed by cooling the vapor and the total transferred heat flow rate.

This paper tackles the need for predicting the local condensation data of miscible zeotropic mixture more accurately than in the past. From a literature review on this matter it can be seen that a complete theoretical method is not accessible in most cases due to the large numerical effort requested. A long debate is available in the literature on the relative merits of the two approaches, namely, the Colburn film method and the simplified method. As stated by Webb [3], the application of the theoretical methods, first proposed by Colburn, requires full specifications on the mixture and the availability of diffusivity data. This is why the application of this approach is, at present, limited to simple mixtures and geometries. For all the reasons described above, the present paper does not address the discussion of a theoretical approach to the treatment of condensation of zeotropic mixtures.

Furthermore, this paper adopts the heat transfer model developed by Thome et al. [8] for the computation of the local heat transfer coefficient during pure vapor condensation. This model is based on simplified flow structures of the flow regimes and includes the effect of liquid-vapor interfacial roughness on heat transfer. The model was compared by Thome et al. to experimental heat transfer coefficients for pure fluids and quasi-azeotropic mixtures. The objective of the present paper is to extend their flow-pattern-based model to condensation of zeotropic mixtures. For this purpose, the simplified approach is applied, as suggested by Bell and Ghaly [1], assuming that the sensible heat of the vapor is transferred from the vapor-liquid interface by a convective heat transfer process. The heat transfer coefficient is calculated from a correlation for the geometry involved, assuming only the vapor phase is present and using vapor physical properties and local vapor flow rate. This assumption overestimates the heat transfer resistance because the two-phase coefficients are generally much higher than the vapor single-phase value actually calculated; in the end, it does not care about the mass transfer resistance because its effect on the heat transfer coefficient is accounted for in the solution of the heat transfer problem.

The present study assumes that a cooling or condensation curve is available, as requested in the equilibrium method by Bell and Ghaly [1]. Specifically, this work addresses the case of a vapor mixture whose behavior during the process is well reproduced by an integral condensation curve. The integral curve describes condensation in a device where vapor and condensate follow a parallel path with complete mixing so that overall equilibrium is maintained.

Other condensation curves may be defined, for instance, differential condensation curves. A differential curve should be used when vapor and condensate are separated within the condenser and depart from equilibrium. The reference to a differential condensation curve may be more realistic and give a better description of a horizontal condenser when the liquid condensate forms a layer at the bottom of the tube [3], but this curve is not usually available in the design. For instance, at low values of mass velocity, the process very likely departs from the ideal behavior depicted by the integral condensation curve. This situation will be discussed in more detail later by providing a proper correction for specific flow regimes when vapor and condensate are separated.

The development of a new procedure for calculating the local heat transfer coefficient needs, of course, a database for validating the model. Several experimental studies have been presented in the literature with data for zeotropes. Unfortunately, most of those data are not easy to handle due to discrepancies or large uncertainties in the reduction procedure. Nevertheless, this new procedure will be validated against test data from independent laboratories relative to halogenated and hydrocarbon refrigerants.

2 Heat Transfer Database

The database of condensation heat transfer coefficients available for the current study covers four mixture systems representing ten different zeotropic mixture compositions, with a wide range of temperature glides and test conditions. The definition of the temperature glide used in the present paper has been introduced by the refrigeration industry to mean the boiling range, which is defined as the difference between the dew point and bubble point temperatures at a fixed pressure and bulk composition. The experimental database used in the current study includes contributions from three different laboratories, as described in Table 1, and covers HCFCs, HFCs, and HCs (hydrocarbons). Several other experimental studies have been conducted in the recent years on condensation of zeotropic mixtures. Unfortunately, some studies are not useful for future comparison mainly due to lack of information or nonuniform definition of the heat transfer coeffi-

cient. In fact, the isobaric condensation process occurs over a temperature range that leads to uncertainty in the determination of the heat transfer coefficient when the mixture temperature is not precisely known.

2.1 Data Set by Cavallini et al. [9,10]. The main set of data used in the present work is the one by Cavallini et al., covering R407C [9] and three mixtures of R125/R236ea [10]. R407C is a ternary zeotropic refrigerant blend of R32, R125, and R134a (23/25/52% by mass), characterized by a temperature glide of around 5°C at test conditions. The R407C experimental data refer to the pressure 1.7 ± 0.1 MPa. Average vapor quality ranges from 0.2 to 0.8, while the change of vapor quality occurring in the test section varies between 15% and 25%.

The other blends tested by Cavallini et al. [10] present higher values of temperature glide and are obtained by mixing two HFC fluids having far different saturation conditions, R125 and R236ea. R125 in the present case is the ''high-pressure'' fluid, whereas R236ea can be considered a ''low-pressure'' fluid. The mixtures tested are blends of R125 and R236ea, condensing at 28/72%, 46/54%, and 63/37% mass bulk composition at saturation pressures of 810 ± 100 kPa, 1160 ± 100 kPa, and 1430 ± 100 kPa, respectively, with corresponding temperature glides of 21.5, 18, and 21°C. The experimental runs were carried out at mass velocity from 100 to 750 kg/(m^2 s), at temperatures ranging from 60 to 40°C. Average vapor quality ranged from 0.1 to 0.9, while the change in vapor quality that occured in the test section varied between 15% and 25%.

The test section used by Cavallini et al. is a counter flow, horizontal tube-in-tube condenser, with the refrigerant condensing in the inner tube, against cold water flowing in the annulus. The test section includes (i) a precondensing section, approximately 300 mm long, where the refrigerant achieves a fully developed flow regime, and (ii) the measuring section, an 8 mm inside diameter smooth tube approximately 1.0 m long, instrumented with thermocouples embedded in the tube wall to measure the wall temperature.

Experimental heat transfer coefficients were reduced from the measured values of saturation temperature and wall temperature. It was estimated from a propagation of error analysis that the heat transfer coefficients were measured to an accuracy of $\pm 5.0\%$ at typical test conditions.

As zeotropic mixtures may present a shift in composition during two-phase processes, a check on the actual mass composition was carried out by using an in-line gas chromatograph. It was observed that the HFC-125/236ea composition varied by less than 3% (by mass) for each component at high mass velocities [400 and 750 kg/(m^2 s)]. A higher shift from nominal composition was found at lower mass velocities. The same trend was found for all three mass compositions, and the authors stated that a possible reason for the higher shift at low mass velocity was the effect of the postcondenser installed in the experimental test rig.

Cavallini et al. [10] reported experimental data to show a heat transfer penalty, mainly caused by the mass transfer thermal resistance buildup, when varying the mass composition of the mixture. By testing the pure R125 and R236ea, the authors showed that at quality 0.5 and same mass velocity the heat transfer coefficient for pure R236ea is around 85% higher than that for pure R125. The heat transfer coefficients for the mixture were always lower than the values calculated by a kind of ideal mixing rule from the values pertaining to the pure components at the same flow condition, with up to 30% heat transfer penalty.

Data by Cavallini et al. [9,10] were taken as reference data in the development of the present model, which will be described in Section 3. As already stressed, several experimental reports have been published in the recent years presenting heat transfer data during condensation of zeotropic mixtures, but lack of information on the data reduction procedure or operating conditions very often prevent use of those data. As reported in Table 1, data sets from two other laboratories are considered in the paper.

2.2 Data Sets by Independent Researchers. The data set by Lee [11] refers to the mixture R22/124 at three different mass compositions (20/80,50/50,80/20%). Test data were taken in a 7.5 mm inside diameter tube. Saturation temperatures ranged between 20 and 40°C and mass velocities between 170 and 370 kg/(m^2 s). The temperature glide for these three mixtures ranged between 3.6 and 6.7°C. Their test condenser, which was a counterflow tube-in-tube heat exchanger, was composed of four test sections. The sectional heat transfer length of each test section was 1.04 m, and the total heat transfer length of the test condenser was 4.16 m.

T-type thermocouples were used for all temperature measurements in their experimental system. Refrigerant temperatures were measured at the inlet and outlet of the test condenser by using thermocouples inserted in the middle of the tube. Five thermocouples were used to measure the coolant temperatures at the inlet and outlet of the test condenser and at the three U-bends connecting two adjacent test sections. The annulus heat transfer coefficient was determined by the Wilson plot technique. The tube side heat transfer coefficient was obtained from the overall and annulus heat transfer coefficients.

The data set by Kim et al. [12] includes heat transfer data on the mixtures of propane and butane. These two hydrocarbons were blended at three different mass compositions, leading to three mixtures with temperature glides ranging from 8 to 12°C. The test condenser, made of two copper tubes with inner diameters of 8 and 13.8 mm, respectively, was inserted in a heat pump system. It was designed for counterflow heat exchange; the refrigerant flowed inside the inner tube and the secondary heat transfer fluid (ethyl alcohol) flowed through the annulus. The condenser had 12 straight sections in which the refrigerant passage was connected by a U-bend. The total length of the condenser was 9.6 m. Temperature and pressure of the refrigerant and secondary fluid were measured in this return bend. For the temperature measurements, T-type sealed thermocouples were used. Temperature differences of secondary fluid were measured using four element thermopiles. The heat transfer and the temperature difference between the refrigerant and the secondary fluid were measured in each subsection, and thus the overall heat transfer coefficient was obtained. Annulus side heat transfer coefficients were obtained from the liquid-to-liquid heat transfer by using a modified Wilson plot technique. The internal local heat transfer coefficients were obtained from the overall and the external heat transfer coefficients.

3 New Model Based on Flow Regime

3.1 Pure Vapor Condensation Model. The condensation model proposed by Thome et al. [8] is based on a flow pattern map for condensation in horizontal plain tubes [13]. In this map flow patterns are classified as fully stratified, stratified-wavy, intermittent, annular, and mist flow. Intermittent flow refers to the plug and slug flow regimes, and it is essentially a stratified-wavy flow pattern with large amplitude waves that wash the top of the tube. This flow pattern map incorporates a logarithmic mean void fraction (LMε) method for calculation of vapor void fractions spanning the entire range from low pressures up to pressures near the critical point [13]. Furthermore, the condensation model by Thome et al. [8] assumes three simplified geometries for describing annular, stratified-wavy, and fully stratified flow, as shown in Fig. 1. For annular flow, for the sake of simplicity, a uniform liquid film thickness of δ is assumed and the actual larger thickness of the film at the bottom as compared to the top due to gravity is ignored. Utilizing a void fraction equation, the cross-sectional areas of the vapor and the liquid phases are determined. From the total flow rate and the local vapor quality, the mass flow rate of the liquid is calculated. Then, using the liquid density and the cross-sectional area occupied by the liquid, the mean velocity of the liquid is determined for the film, and turbulent flow heat transfer to the film can be correlated based on the mean velocity of the liquid film.

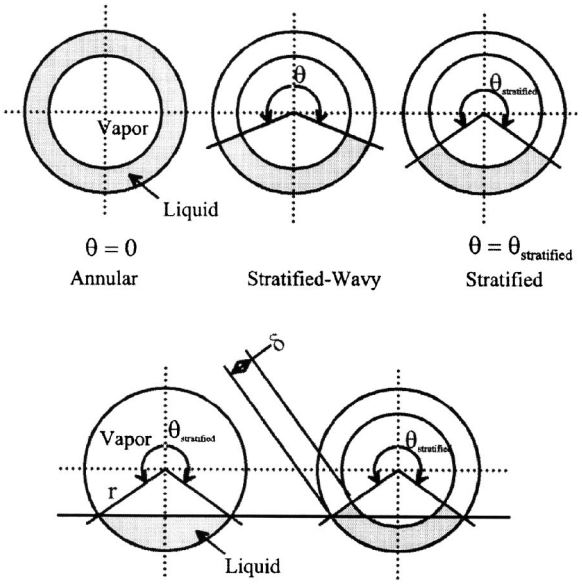

Fig. 1 Top: simplified flow structures for two-phase flow patterns. Bottom: actual geometry (left) and equivalent simplified geometry (right) for fully stratified flow.

Figure 1 shows the actual geometry of a fully stratified flow (left) and its equivalent geometry (right) with the same angle of stratification and cross-sectional area occupied by the liquid, but with the liquid distributed as a truncated annular ring of uniform thickness δ. In stratified-wavy flow the top perimeter of the tube is not wetted by the stratified liquid, but only by the condensate that forms on this part of the exposed tube perimeter. Here, once again, for simplicity the stratified liquid is assumed to form an annular truncated ring as shown in Fig. 1. Thus the angle θ varies between its maximum value of θ_{strat} at the threshold to fully stratified flow and its minimum value of zero at the threshold to annular flow.

In the model, the convective heat transfer coefficient is applied to the stratified perimeter subtended by $(2\pi-\theta)$, while Nusselt film condensation is applied to the upper wall subtended by θ with the condensate flowing downward into the stratified liquid below. For annular flow, however, convective condensation heat transfer occurs around the entire perimeter without any Nusselt film condensation. For simplicity's sake, the annular flow structure is also assumed to apply to the intermittent flow regime, which has a very complex flow structure.

In the model the two heat transfer mechanisms of convective condensation and film condensation are applied to their respective heat transfer surface areas, as shown in Fig. 2. The convective condensation heat transfer coefficient α_c is applied to the perimeter wetted by the axial flow of liquid film, which refers to the entire perimeter in annular, intermittent, and mist flows, but only part of the perimeter in stratified-wavy and fully stratified flows.

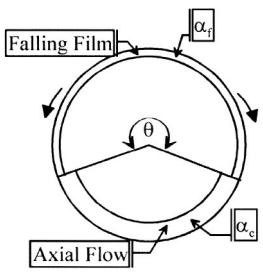

Fig. 2 Schematic of the convective and falling film boundaries in the heat transfer model

The axial film flow is assumed to be turbulent. The film condensation heat transfer coefficient α_f is applied to the perimeter that would otherwise be dry in an adiabatic two-phase flow and hence is the upper perimeter of the tube for stratified-wavy and fully stratified flows. The coefficient α_f is obtained by applying the Nusselt falling film theory to the inside of the horizontal tube, which assumes the falling film is laminar. The effect of axial shear on this falling film is ignored. Heat transfer coefficients for stratified types of flow are known to be a function of the saturation-to-wall temperature difference, whereas those for annular flow are not, as experimentally shown by several researchers. This effect is included through the Nusselt falling film heat transfer equation in the model.

The expression for the local condensing heat transfer coefficient of the pure fluid α_p is

$$\alpha_p = \frac{\alpha_f \theta + (2\pi - \theta)\alpha_c}{2\pi} \tag{2}$$

where θ is the falling film angle around the top perimeter of the tube. For annular, intermittent, and mist flows, $\theta=0$. For fully stratified flow, $\theta=\theta_{\text{strat}}$. The equations for calculating the angle θ_{strat} are reported in Thome et al. [8]. For stratified-wavy flow, the stratified angle θ is obtained by assuming a quadratic interpolation between its maximum value of θ_{strat} at G_{strat} and its minimum value of 0 at G_{wavy}

$$\theta = \theta_{\text{strat}} \left(\frac{G_{\text{wavy}} - G}{G_{\text{wavy}} - G_{\text{strat}}} \right)^{0.5} \tag{3}$$

The values of G_{strat} and G_{wavy} are determined from their respective transition equations in the flow pattern map [13]. The following two equations are given for computing α_c and α_f in Eq. (2):

$$\alpha_c = 0.003\, \text{Re}_L^{0.74}\, \text{Pr}_L^{0.5} \frac{\lambda_L}{\delta} f_i \tag{4}$$

$$\alpha_f = 0.728 \left[\frac{\rho_L(\rho_L - \rho_V) g h_{LV} \lambda_L^3}{\mu_L d (T_{\text{sat}} - T_w)} \right]^{1/4} \tag{5}$$

The equations for computing the liquid thickness δ are reported in Thome et al. [8]. The term f_i in Eq. (4) represents an interfacial roughness parameter, which will be further discussed.

3.2 Application of the Bell and Ghaly Procedure. During condensation of zeotropic mixtures, the heat transfer mechanisms are the same that occur during condensation of a pure fluid, convective condensation, and film condensation. Clearly, these mechanisms are affected by the zeotropic characteristics of the blend. Because the condensation process is nonisothermal, there are both liquid and vapor phase sensible heat effects. As already stated, sensible heat removal from the vapor is particularly significant because of the low heat transfer coefficients associated with this process. Besides, since compositions of both phases are continuously changing, there are diffusion resistances in both the vapor and the liquid phases that are coupled to the heat transfer processes. The mass transfer resistance in the vapor phase is the most crucial point in this process and, according to the Bell and Ghaly approach [1], it is proportional to the sensible heat transfer resistance in the vapor phase. By adopting this approach, the heat transfer coefficients that are calculated for convective condensation α_c and for film condensation α_f of a pure fluid can be corrected through an estimate of the heat transfer resistance in the vapor.

In the simplified procedure proposed by Bell and Ghaly [1], the heat transfer coefficient of the mixture is calculated as a function of the heat transfer coefficient of the condensate, the heat transfer coefficient of the vapor phase flowing alone in the duct, and the ratio between the sensible heat duty removed by cooling the vapor and the total transferred heat flow rate [Eq. (1)]. The total thermal resistance is given as the sum of two resistances in series: the first one at liquid-vapor interface concerns only the sensible cooling

flux, whereas the second one across the liquid film concerns the total heat flux, covering both sensible and latent effects. For the first component, the pure fluid model can be used in the calculation. The second component is obtained from the ratio of sensible to total heat duty ($đq_{SV}/đq_T$). To a good approximation, this ratio can be expressed as follows:

$$(đq_{SV}/đq_T) \approx x c_{pG} (\mathrm{d}T/\mathrm{d}h) \tag{6}$$

where x is vapor quality and c_{pG} is specific heat of the vapor phase. If the ratio $(\mathrm{d}T/\mathrm{d}h)$ remains approximately constant during the condensation process, this ratio can be written as a function of the temperature glide and the enthalpy change of isobaric condensation

$$\mathrm{d}T/\mathrm{d}h \approx \Delta T_{gl}/\Delta h_m \tag{7}$$

This last expression provides a significant simplification in the implementation of the procedure, with no significant change in the final results. By substituting Eqs. (6) and (7) into Eq. (1), it leads to the expression of the overall thermal resistance for the mixture

$$R_T = \frac{1}{\alpha_p} + x c_{pG} \left(\frac{\Delta T_{gl}}{\Delta h_m} \right) \frac{1}{\alpha_G} \tag{8}$$

The term $1/\alpha_p$ in Eq. (8) represents the condensate layer resistance, and it can be computed by a pure fluid model using the liquid mixture properties. The last term represents the simplified expression of the Bell and Ghaly correction and in the following will be named as Bell and Ghaly resistance (R) of the heat transfer mechanism.

3.3 Extension of the Pure Fluid Model to Zeotropic Mixtures. Similar to the procedure for pure fluids [Eq. (2)], the local heat transfer coefficient for the mixture is obtained from an interpolation of the film condensation coefficient $\alpha_{f.m}$ and the convective condensation coefficient $\alpha_{c.m}$, by accounting for the different areas pertaining to the two mechanisms

$$\alpha_m = \frac{\alpha_{f.m}\theta + (2\pi - \theta)\alpha_{c.m}}{2\pi} \tag{9}$$

where θ is the falling film angle around the top perimeter of the tube (Fig. 2) and its computation has already been discussed. The convective condensation heat transfer coefficient is obtained from the Bell and Ghaly approach, as follows:

$$\alpha_{c.m} = \left(\frac{1}{\alpha_c} + R_c \right)^{-1} \tag{10}$$

where α_c is computed from the equations for the pure fluid model. The appropriate Bell and Ghaly resistance R_c can be calculated as follows:

$$R_c = x c_{pG} \frac{\Delta T_{gl}}{\Delta h_m} \frac{1}{\alpha_G^O} \tag{11}$$

The resistance in (11) is a function of the vapor phase heat transfer coefficient referred to the vapor-liquid interface. Thome et al. [8] introduced an interfacial roughness correction factor to act on the convective coefficient α_c and to account for the increase in the heat transfer coefficient due to the action of the interfacial shear between the condensate and the vapor. Thome et al. [8] argued that the shear of the high-speed vapor is transmitted to the liquid film across the interface and hence increases the magnitude and number of the waves generated at the interface, which, in turn, increases the available surface area for condensation, tending to increase heat transfer. Based on this reasoning, the same correction factor acting on α_c should be applied to the vapor heat transfer coefficient that appears in the Bell and Ghaly [1] resistance of the axial flow. Therefore the vapor coefficient in Eq. (11) can be written as

$$\alpha_G^O = \alpha_G f_i \tag{12}$$

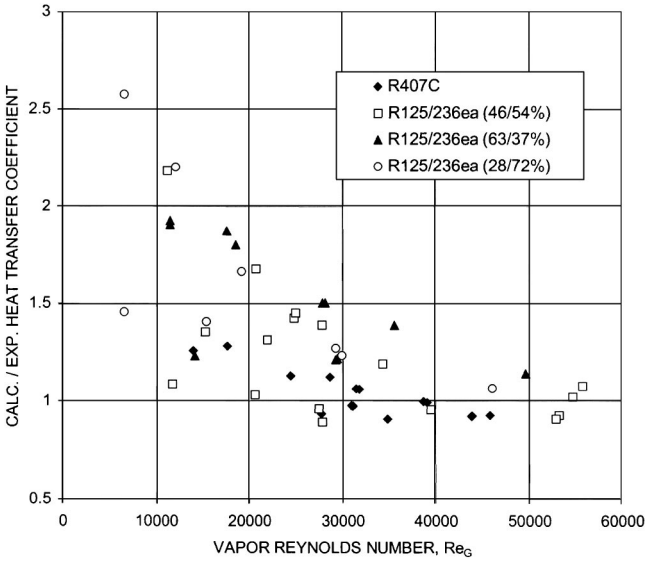

Fig. 3 Ratio of calculated-to-experimental heat transfer coefficient vs vapor Reynolds number in stratified flow regime. The predicted values are obtained *without* using the mixture factor F_m. Data by Cavallini et al. [9,10].

where the interfacial roughness factor f_i is computed from the following equations [8]:

$$f_i = 1 + \left(\frac{u_G}{u_L} \right)^{1/2} \left[\frac{(\rho_L - \rho_G) g \delta^2}{\sigma} \right]^{1/4} \quad G > G_{\mathrm{strat}}$$
$$f_i = 1 + \left(\frac{u_G}{u_L} \right)^{1/2} \left[\frac{(\rho_L - \rho_G) g \delta^2}{\sigma} \right]^{1/4} \frac{G}{G_{\mathrm{strat}}} \quad G < G_{\mathrm{strat}} \tag{13}$$

where u_G and u_L are the mean velocities of the vapor and liquid phases, respectively, both referred to the respective cross-sectional area

$$u_G = \frac{Gx}{\rho_G \varepsilon} \qquad u_L = \frac{G(1-x)}{\rho_L (1-\varepsilon)}$$

The vapor heat transfer coefficient α_G in Eq. (12) can be computed with the Dittus and Boelter [14] equation

$$\alpha_G = \frac{\lambda_G}{d} 0.023 \, \mathrm{Re}_G^{0.8} \, \mathrm{Pr}_G^{0.33} \tag{14}$$

by adopting the following expression for the Reynolds number of the vapor phase:

$$\mathrm{Re}_G = \frac{\rho_G u_G d}{\mu_G} \tag{15}$$

The Bell and Ghaly procedure [1] is applied to the film condensation component in the same way as it was seen for the convective term, but without interfacial roughness of the laminar falling film. The heat transfer coefficient in the stratified type of flow is a function of the saturation-to-wall temperature difference, and this effect is incorporated in the expression for α_f. After comparing the procedure with the Bell and Ghaly correction to the data set by Cavallini et al. [9,10], it was seen that the model strongly overpredicted experimental heat transfer coefficients in the fully stratified and stratified-wavy flow regimes, while instead the model captured the annular flow data very well. Figure 3 reports the comparison between experimental data characterized by stratified flow and the model when only the Bell and Ghaly correction is applied. The ratio of calculated to experimental heat transfer coefficient is plotted versus the vapor Reynolds number, which is a

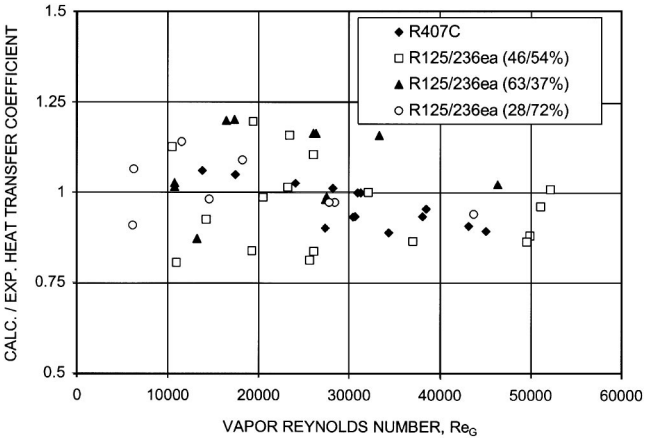

Fig. 4 Ratio of calculated-to-experimental heat transfer coefficient vs vapor Reynolds number in stratified flow regime. The mixture factor F_m is used in the prediction. Data by Cavallini et al. [9,10].

key parameter, for the data points by Cavallini et al. [9,10] falling within the fully stratified and wavy-stratified flow regime zones.

The overprediction of data in Fig. 3 may be explained by looking back at the main assumption of the Bell and Ghaly approach [1], which is the overall equilibrium between the liquid and vapor phases. Notably, the condensation process inside a tube departs from this equilibrium when the liquid condensate forms a stratified layer at the bottom of the tube. For this reason, it was found that after applying the Bell and Ghaly method, the film condensation component must be further corrected with an empirical mixture factor F_m acting on the resistance of the falling film

$$\alpha_{f.m} = F_m \left(\frac{1}{\alpha_f} + R_f \right)^{-1} \tag{16}$$

The heat transfer coefficient α_f is calculated from the pure vapor model [Eq. (5)], while the Bell and Ghaly resistance R_f can be determined in the form

$$R_f = x c_{pG} \frac{\Delta T_{gl}}{\Delta h_m} \frac{1}{\alpha_G} \tag{17}$$

where no interfacial roughness factor applies to the vapor phase heat transfer coefficient because the falling film is supposed to be smooth. The nonequilibrium mixture factor F_m in Eq. (16) accounts for nonequilibrium effects in stratified flow regimes, and it is experimentally derived as a function of vapor quality, mass velocity, temperature glide, and saturation-to-wall temperature difference

$$F_m = \exp\left[-0.25(1-x) \left(\frac{G_{\text{wavy}}}{G} \right)^{0.5} \frac{\Delta T_{\text{gl}}}{T_{\text{sat}} - T_w} \right] \tag{18}$$

Values of F_m range between 0 and 1 and go to 1 for azeotropic mixtures. F_m decreases when stratification is enhanced (low mass velocity and low vapor quality). In fact, the nonequilibrium between the two phases (vapor and liquid) increases with the flow stratification.

The mass transfer resistance depends on the temperature glide, and that is why F_m decreases when increasing ΔT_{gl}. Finally, the effect of the saturation-to-wall temperature difference is the opposite to the one in the Nusselt theory. Given the saturation temperature, when the wall temperature decreases, the vapor of the more volatile component accumulates near the interface and acts as an incondensable. When this temperature difference increases, the more volatile component begins to condense and this decreases the thermal resistance of the diffusion layer. That is the reason why the factor F_m should increase with the saturation-to-wall temperature difference, leading to an increase in the heat transfer coefficient. This trend of the heat transfer coefficient with the temperature difference was experimentally illustrated during condensation of zeotropic mixtures on the outside of plain tubes [15].

All these effects are accounted for in Eq. (18). Figure 4 reports the comparison of the procedure to experimental data by Cavallini et al. [9,10] relative to stratified flows. The ratio of calculated to experimental heat transfer coefficient is plotted versus vapor Reynolds number. This shows the capability of the model to catch the trend of experimental data for fully stratified and stratified-wavy flow regimes. Figure 4 should be compared to Fig. 3, where no F_m correction was used in the calculation of $\alpha_{f \cdot m}$. The adoption of the mixture factor significantly improves the accuracy of prediction.

4 Comparison to Entire Experimental Database

The extension of the pure fluid model to mixtures was primarily developed using the heat transfer database of Cavallini et al. [9,10], mainly because those heat transfer data were obtained from direct measurement of the wall temperature. In fact, both Lee [11] and Kim et al. [12] used a Wilson plot technique in the determination of the experimental heat transfer coefficient. That is why all the comparisons reported in the following are made to the Cavallini data sets first, and second to the data sets by Lee [11] and Kim et al. [12], called hereafter "independent researchers." Both vapor and condensate phase compositions change during condensation, raising the question of evaluation of physical properties for the mixtures. This is a relatively minor problem for mixtures of closely related components, and no significant effect to the prediction was found. Thermodynamic and thermophysical properties were determined from Refprop 7.0 [16].

Figure 5 depicts a comparison of the new procedure to the database by Cavallini et al. [9,10]. There are four mixtures represented, with temperature glides between 5 and 22°C and a wide range of operating conditions. For instance, the mass velocity varies between 100 and 750 kg/(m^2 s). Almost all the data points are predicted within $\pm 20\%$ and most within $\pm 10\%$.

Figure 6 reports the comparison of the model to the data plotted versus the vapor phase Reynolds number. Data at low Reynolds number are more difficult to predict because in this situation nonequilibrium effects between the vapor and liquid phases are more likely present and more influential. A low-vapor Reynolds number means low values of vapor quality and mass velocity. Besides, the possible presence of liquid subcooling in part of the test section makes experimental testing and reduction of experimental data very complex.

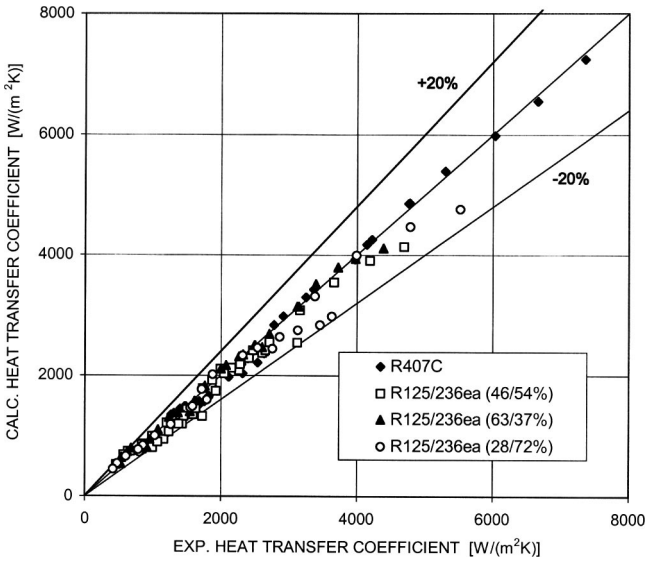

Fig. 5 Comparison of model to data by Cavallini et al. [9,10]

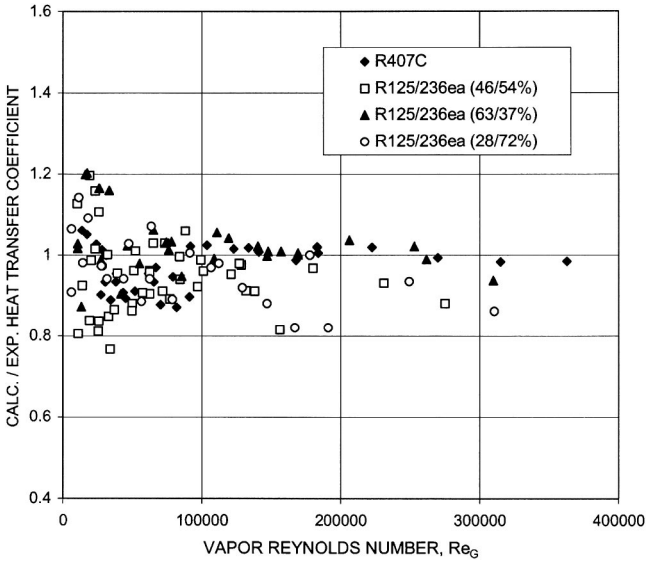

Fig. 6 Ratio of calculated-to-experimental heat transfer coefficient vs vapor Reynolds number. Data by Cavallini et al. [9,10].

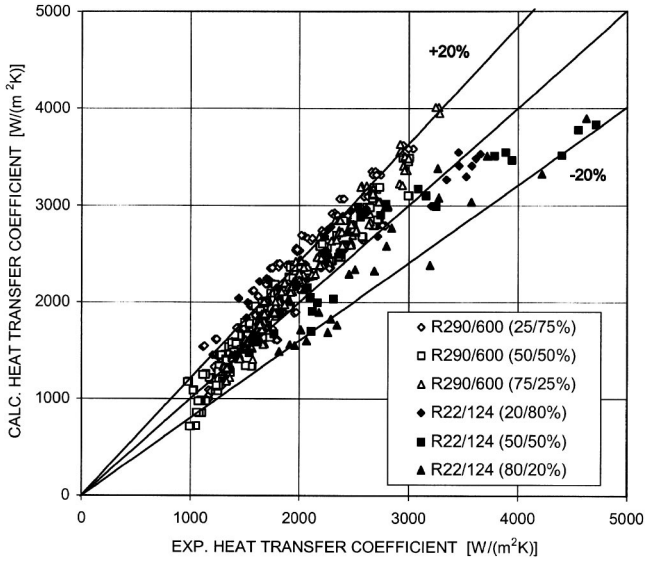

Fig. 7 Comparison of model to data by Lee [11] and by Kim et al. [13]

A comparison of the procedure to the data sets by independent researchers is depicted in Fig. 7. Six mixtures are reported, three of halogenated refrigerants and three of hydrocarbons, and their heat transfer coefficients are measured in two different laboratories. The comparison shows a good agreement, although the model seems to overestimate the data points relative to hydrocarbons.

Figures 5 and 7 provide only a statistical view of the accuracy of the model in the prediction of the local heat transfer coefficient. However, in order to be useful as a method for the optimization of heat exchangers, it is important that the method respects the characteristic trends in the data (i.e., the effect of the individual variables on the local heat transfer coefficient). Hence, the same data are shown in a more detailed graphical presentation in the following graphs in which the ratio of calculated to experimental heat transfer coefficients are plotted versus the most important parameters. Again, first the graphs are shown for the data sets by Cavallini et al. [9,10] as they are taken as reference for the development of the model, and second, the figures are reported for the data sets of independent researchers.

In Fig. 8 the data (by Cavallini et al. [9,10]) are plotted versus vapor quality, and the ratio of calculated to experimental heat transfer coefficient remains roughly the same over the range of vapor qualities. This means that the model is correctly capturing the slope of α_m versus x as G changes. In Fig. 8 the same data are also plotted versus mass velocity. As there are essentially four values of mass velocity, it is possible to calculate the average deviation for each value of mass velocity, where the deviation is defined as $(\alpha_{\text{calc}}-\alpha_{\text{exp}})/\alpha_{\text{exp}}$. It comes out that the average deviation is around $+7\%$ at 100 kg/(m^2 s), -7% at 200 kg/(m^2 s), -3.7% at 400 kg/(m^2 s), and -2.9% at 750 kg/(m^2 s). On the whole, the model is able to capture the experimental trend with a satisfactory agreement. Finally, Fig. 8 illustrates the comparison to Cavallini et al. data [9,10] by plotting the ratio of heat transfer coefficients by flow regime (S=fully stratified, S-W=stratified wavy, I=intermittent, A=annular). The model can work nearly uniformly well for all the flow regimes. In fact, the average deviation for data points falling within the annular region is -5%, in the intermittent region is -2%, and finally in the wavy-stratified region is -1%.

Figure 9 depicts the comparison of the model to the data by independent researchers. Data points refer to mixtures of R22 and R124 and mixtures of R290 and R600. Calculated-to-experimental ratios are plotted versus vapor quality, mass velocity, and flow regime. As one can see, the deviation is quite evenly distributed over the range of vapor qualities, and thus the model is correctly capturing the slope. The data by Lee [11] are predicted with an average deviation of -0.5%, whereas the hydrocarbon data by Kim et al. [13] are predicted with an average deviation of $+9.6\%$. The average overprediction of hydrocarbon data is only of 4% in the stratified-wavy flow regime, while it reaches 13% in the annular and intermittent region.

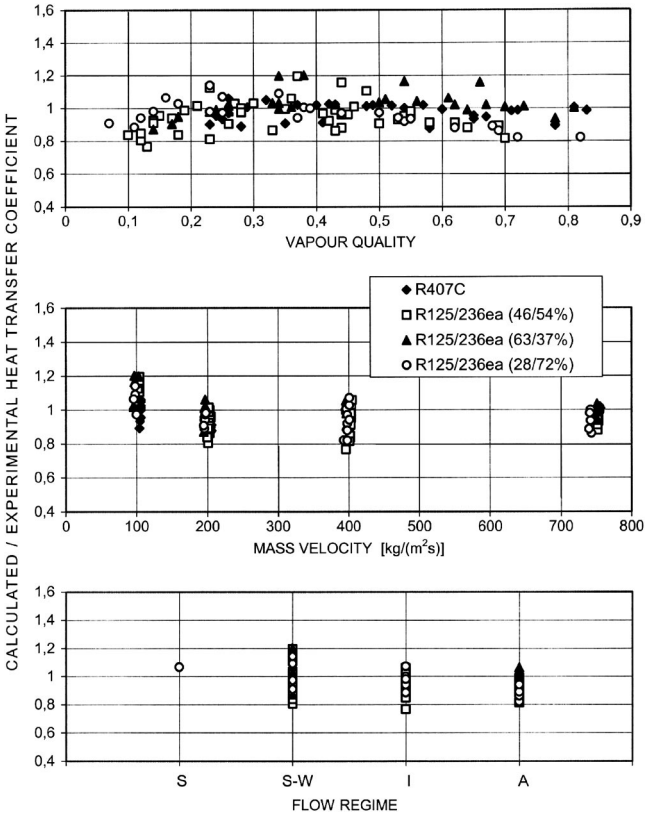

Fig. 8 Comparison of model to data by Cavallini et al. [9,10] by vapor quality, mass velocity, and flow pattern

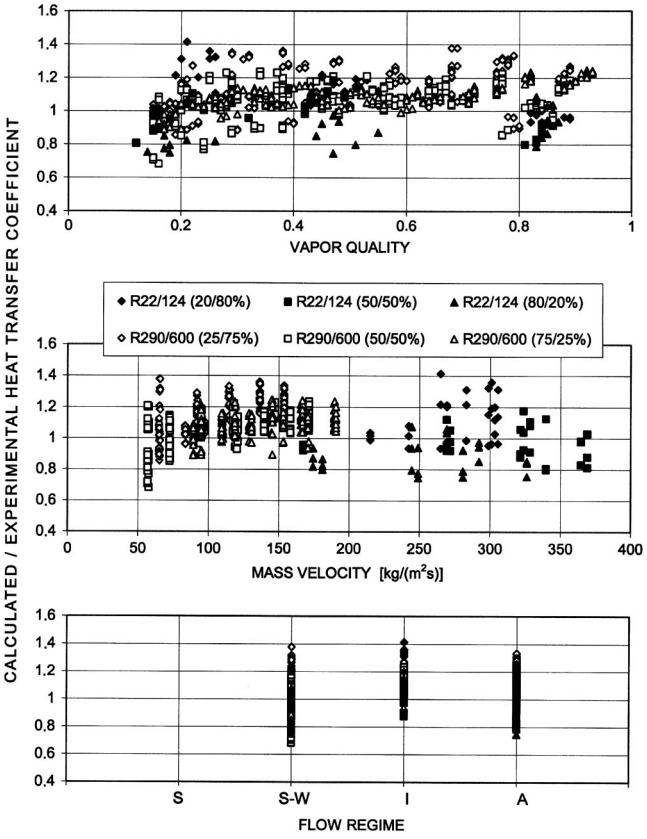

Fig. 9 Comparison of model to data by Lee [11] and Kim et al. [13] by vapor quality, mass velocity, and flow pattern

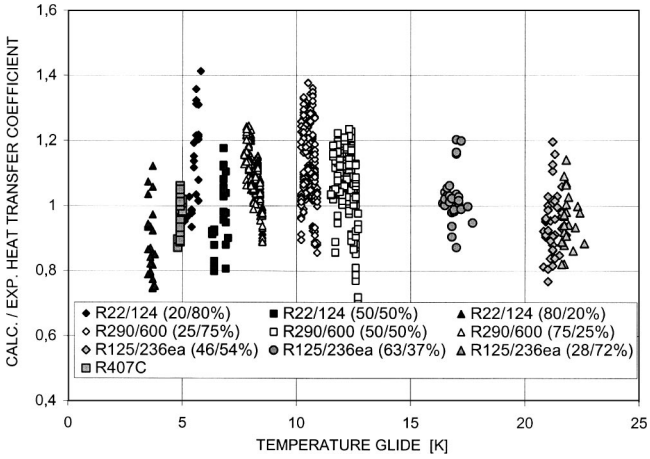

Fig. 10 Comparison of model to all data by temperature glide

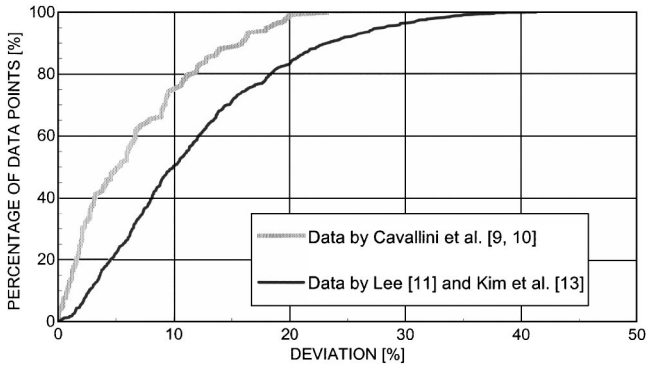

Fig. 11 Percentage of data points predicted to a certain deviation vs deviation

Figure 10 summaries the comparison of the model to all data versus temperature glide, ranging from 3.5 to 22°C. One can see that the deviation does not present any particular anomalous trend with the temperature glide.

The overall predictive performance of the model is shown in Fig. 11, in the form of percentage of data points (*y*-axis) falling within the deviation (*x*-axis). Notably, the method predicts 75% of the refrigerant heat transfer coefficients measured by Cavallini et al. [9,10] (136 points) to within ±10% and 98% to within ±20%. It also predicts 50% of the halogenated plus hydrocarbon refrigerant heat transfer coefficients measured by independent researchers (736 points) to within ±10% and 85% to within ±20%.

Table 2 provides a statistical summary of the comparison of the new procedure to the experimental database. For each source, the data are classified by fluid and by flow regime to show their distribution. It can be seen that the average deviation between calculated and experimental values in the comparison to the Cavallini data sets [9,10] is within −11.7% and +7.2% for all the flow regimes. For the mixtures tested by Lee [11] and Kim et al. [12] the average deviation is between plus and minus 20% for most of the flow regimes. Only the data points referred to the intermittent flow regime of the mixtures R22/124 (20/80%) and R290/600 (25/75%) present higher values of average deviation.

Table 2 Mean and standard deviations by flow regime and source (S=stratified, SW=stratified wavy, I=intermittent, A=annular)

Authors	Mixture	Number of points				Average deviation					Standard deviation				
		S	SW	I	A	S	SW	I	A	all	S	SW	I	A	all
Cavallini et al. (1999)	R407C		16	10	12		-4.3	-0.5	-4.1	-3.3		5.9	3.8	5.3	5.3
Cavallini et al. (2000)	R125/236ea (46/54%)		17	15	11		-3.6	-5.0	-8.2	-5.3		12.6	7.4	4.6	9.3
	R125/236ea (63/37%)		11	10	10		7.2	-0.2	1.0	2.8		11.0	4.5	3.3	7.8
	R125/236ea (28/72%)	1	7	8	8	6.4	0.1	-1.6	-11.7	-4.1	-	8.4	5.6	4.7	8.2
Lee (1994)	R22/124 (20/80%)		3	6	18		8.1	31.9	6.0	12.0		11.4	7.0	10.5	14.5
	R22/124 (50/50%)		4	6	16		-7.8	0.4	-3.7	-3.3		7.8	10.3	11.2	10.5
	R22/124 (80/20%)		7	1	16		-20.6	5.8	-8.5	-11.4		3.8	-	10.3	10.9
Kim et al. (1996)	R290/600 (25/75%)		129	12	72		8.5	32.2	18.1	13.1		10.9	3.4	10.1	12.2
	R290/600 (50/50%)		105	27	73		1.6	16.2	11.2	7.0		10.9	4.6	5.8	10.4
	R290/600 (75/25%)		64	57	120		1.0	9.0	12.9	8.8		4.9	4.9	5.5	7.2

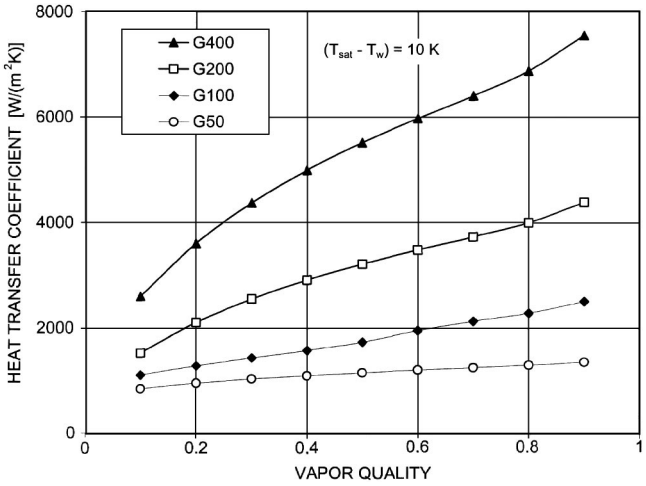

Fig. 12 Simulation of model for condensation of R290/600 (50/50% by mass) at 0.9 MPa in a 8 mm inside diameter tube

5 Simulation for Condensation of a Zeotropic Mixture

Figure 12 illustrates the predicted trends in the local heat transfer coefficient as a function of vapor quality and mass velocity. The heat transfer has been simulated for the mixture R290/600 at 50/50% by mass condensing at 0.9 MPa in an 8 mm dia tube, assuming a saturation-to-wall temperature difference of 10 K. The temperature glide is equal to 12.4 K.

At the highest flow rate [400 kg/(m^2 s)], the flow enters in the annular flow regime and converts to intermittent flow at vapor quality at about 0.55; it leaves in this same regime. At 200 kg/(m^2 s), the flow presents roughly the same behavior, but the heat transfer coefficient is of course lower as compared to the previous case. At 100 kg/(m^2 s), the flow enters in annular flow but it soon passes through wavy-stratified flow. At the lowest flow rate, 50 kg/(m^2 s), the flow is first in the stratified-wavy and then in the fully stratified regime.

6 Conclusions

The model by Thome et al. [8] for local condensation heat transfer coefficient of pure fluids and azeotropic mixtures, which is based on flow patterns and simplified flow structures, has been extended to zeotropic mixtures by modifying the approach of Bell and Ghaly [1]. The additional heat transfer resistance created by the mixture is applied to both the convective and the film coefficients, including the effect of interfacial roughness on the vapor heat transfer coefficient acting on the convective film. A nonequilibrium mixture factor is also introduced in the calculation of the film heat transfer coefficient, to account for nonequilibrium phenomena in the stratified flow regimes. This new procedure is easy to implement and does not require as much computational effort as the theoretical methods, but it still provides accurate predictions of the local heat transfer data.

The procedure has been compared against a wide heat transfer database, obtained in three different laboratories, which includes ten different mixtures with temperature glides ranging from 3.5 to 22°C. The method predicts 98% of the refrigerant heat transfer coefficients measured by Cavallini et al. [9,10] (136 points) to within ±20% and predicts 85% of the halogenated plus hydrocarbon refrigerant heat transfer coefficients measured by independent researchers (736 points) to within ±20%.

Acknowledgment

Davide Del Col received partial support for this project as an ERCOFTAC Scientific Visitor to the Laboratory of Heat and Mass Transfer at the EPFL in Lausanne.

Nomenclature

c_p = specific heat capacity, J/(kg K)
d = diameter, m
G = mass velocity, kg/(m^2 s)
G_{strat} = stratified flow transition mass velocity, kg/(m^2 s)
G_{wavy} = wavy flow transition mass velocity, kg/(m^2 s)
h = specific enthalpy, J/kg
h_{LV} = differential latent heat, J/kg
q = heat flow rate, W
R = thermal resistance, (m^2 K)/W
T = temperature, K
u_G = mean vapor velocity, m/s
u_L = mean liquid velocity, m/s
x = vapor mass quality, [-]
α = heat transfer coefficient, W/(m^2 K)
α_c = pure fluid convective condensation heat transfer coefficient, W/(m^2 K)
$\alpha_{c.m}$ = mixture convective condensation heat transfer coefficient, W/(m^2 K)
α_f = pure fluid Nusselt film condensation coefficient on top perimeter of fluid, W/(m^2 K)
$\alpha_{f.m}$ = mixture Nusselt film condensation coefficient on top perimeter, W/(m^2 K)
δ = liquid film thickness of annular ring, m
ΔT_{gl} = temperature glide, K
λ = thermal conductivity, W/(m K)
μ = viscosity, kg/(m s)
ρ = density, kg/m^3
σ = surface tension, N/m

Subscripts

G = vapor phase
L = liquid phase
m = mixture
s = sensible
sat = saturation
T = total
w = wall

References

[1] Bell, K. J., and Ghaly, M. A., 1973, "An Approximate Generalized Design Method for Multicomponent/Partial Condenser," AIChE Symp. Ser., **69**, pp. 72–79.
[2] Colburn, A. P., and Drew, T. B., 1937, "The Condensation of Mixed Vapors," Trans. AIChemE, **33**, pp. 197–215.
[3] Webb, D. R., 1995, "Condensation of Vapor Mixtures," *Heat Exchangers Design Handbook*, Begell House, New York, pp. 2.6.3-7–2.6.3-11.
[4] Taylor, R., and Krishna, R., 1993, *Multicomponent Mass Transfer*, Wiley, New York, pp. 435–440.
[5] Cavallini, A., Censi, G., Del Col, D., Doretti, L., Longo, G. A., and Rossetto, L., 2002, "A Tube-in-Tube Water/Zeotropic Mixture Condenser: Design Procedure Against Experimental Data," Exp. Therm. Fluid Sci., **25**, pp. 495–501.
[6] Silver, L., 1947, "Gas Cooling With Aqueous Condensation," Trans. Inst. Chem. Eng., **25**, pp. 30–42.
[7] Webb, D. R., Fahrner, M., and Schwaab, R., 1996, "The Relationship Between the Colburn and Silver Methods of Condenser Design," Int. J. Heat Mass Transfer, **39**(15), pp. 3147–3156.
[8] Thome, J. R., El Hajal, J., and Cavallini, A., 2003, "Condensation in Horizontal Tubes, Part 2: New Heat Transfer Model Based on Flow Regimes," Int. J. Heat Mass Transfer, **46**, pp. 3365–3387.
[9] Cavallini, A., Del Col, D., Doretti, L., Longo, G. A., and Rossetto, L., 1999, "Condensation of R-22 and R-407C Inside a Horizontal Tube," *Proc. of 20th Int. Congress of Refrigeration*, IIR/IIF, France.
[10] Cavallini, A., Censi, G., Del Col, D., Doretti, L., Longo, G. A., Rossetto, L., and Zilio C., 2000, "Analysis and Prediction of Condensation Heat Transfer of the Zeotropic Mixture R-125/236ea," *Proc. of the ASME Heat Transfer Division*, ASME, New York, HTD-Vol. 366-4, pp. 103–110.
[11] Lee, C.-C., 1994, "Investigation of Condensation Heat Transfer of R124/22 Nonazeotropic Refrigerant Mixtures in Horizontal Tubes," Ph.D. thesis, National Chiao Tung University, Taiwan.
[12] Kim, M. S., Chang, Y. S., and Ro, S. T., 1996, "Performance and Heat Transfer of Hydrocarbon Refrigerants and Their Mixtures in a Heat Pump System," *Proc. of IIR Meeting of Comm. B1, B2, E1, E2*, Aarhus, IIR, France, pp. 477–486.
[13] El Hajal, J., Thome, J. R., and Cavallini, A., 2003, "Condensation in Horizon-

tal Tubes, Part 1: Two-Phase Flow Pattern Map,'' Int. J. Heat Mass Transfer, **46**, pp. 3349–3363.
[14] Dittus, F. W., and Boelter, L. M. K., 1930, *Publications on Engineering*, University of California, Berkeley, Vol. 2, p. 443.
[15] Signe, J. C., Bontemps, A., and Marvillet, Ch., 1995, ''Condensation of R134a/R23 Outside a Bundle of Smooth and Enhanced Surface Tubes,'' *Proc. of Eurotherm Seminar 47*, Elsevier, Paris, pp. 146–153.
[16] National Institute of Standard and Technology, 2002, *NIST Thermodynamic Properties of Refrigerants and Refrigerant Mixtures Database* (REFPROP), Ver. 7.0, Gaithersburg.

Experimental Determination of the Effect of Disjoining Pressure on Shear in the Contact Line Region of a Moving Evaporating Thin Film

Sashidhar S. Panchamgam
Shripad J. Gokhale
Joel L. Plawsky

The Isermann Department of Chemical and Biological Engineering, Rensselaer Polytechnic Institute, Troy, NY 12180

Sunando DasGupta
Department of Chemical Engineering, Indian Institute of Technology, Kharagpur, PIN—721302, India

Peter C. Wayner, Jr.[1]
The Isermann Department of Chemical and Biological Engineering, Rensselaer Polytechnic Institute, Troy, NY 12180
e-mail: wayner@rpi.edu

The thickness and curvature profiles in the contact line region of a moving evaporating thin liquid film of pentane on a quartz substrate were measured for the thickness region, $\delta<2.5$ μm. The critical region, $\delta<0.1$ μm, was emphasized. The profiles were obtained using image-analyzing interferometry and an improved data analysis procedure. The precursor adsorbed film, the thickness, the curvature, and interfacial slope (variation of the local "apparent contact angle") profiles were consistent with previous models based on interfacial concepts. Isothermal equilibrium conditions were used to verify the accuracy of the procedures and to evaluate the retarded dispersion constant in situ. The profiles give fundamental insight into the phenomena of phase change, pressure gradient, fluid flow, spreading, shear stress, and the physics of interfacial phenomena in the contact line region. The experimental results demonstrate explicitly, for the first time with microscopic detail, that the disjoining pressure controls fluid flow within an evaporating completely wetting thin curved film. [DOI: 10.1115/1.1857947]

Keywords: Contact Line, Dispersion Constant, Evaporation, Oscillating Meniscus, Ultrathin Film

Introduction

The intermolecular interactions between a thin film of liquid, its vapor, and a solid surface have been extensively studied because of their importance to many equilibrium and nonequilibrium phenomena. For example, understanding the dynamics of the contact line region, where the liquid, vapor, and solid intersect, is important for optimizing lab-on-a-chip processes and boiling as well as adsorption, spreading, evaporation, condensation, wetting, and stability. Furthermore, the ability to understand and control these interactions is growing in importance as chemical self-assembly processes related to phase change are being explored to produce new classes of materials. Herein, we study the dynamics of the moving evaporating contact line region to enhance our understanding of these processes.

The free energy of a very thin film of liquid on a solid substrate is different from that of a bulk fluid because the long-range intermolecular force field is a function of the thickness and curvature of the film. Derjaguin and co-workers pioneered the use of the disjoining pressure concept to model this variation in force with film thickness in the study of the mechanics and thermodynamics of very thin films [1–4]. Of particular interest to our work, they measured the stability and equilibrium thickness of adsorbed ultrathin films as a function of an interfacial temperature jump [1]. In addition, using a vapor/air bubble pressed against a liquid film on a glass substrate, the presence of a liquid-vapor interfacial pressure jump has also been experimentally demonstrated (e.g., [5]). Using adsorption isotherms and the disjoining pressure concept, Derjaguin et al. [4] demonstrated theoretically that thin film transport is capable of accelerating the evaporation rate from capillaries. In 1972, Potash and Wayner [6] built upon Derjaguin's work and developed a Kelvin-Clapeyron model to describe evaporation from an extended meniscus on a vertical flat plate. The model included both the curved (evaporating) and the adjacent flat, equilibrium, adsorbed thin film regions. The combined effects of disjoining pressure, capillarity, and the temperature on the vapor pressure were demonstrated. For the experimental results presented herein, the disjoining pressure in the adsorbed flat thin film region is the boundary condition at the leading edge of a moving evaporating meniscus. For a completely wetting, pure, isothermal fluid, the sum of the disjoining pressure and capillary pressure can lead to fluid flow and phase change in the direction of a decrease in film thickness [6–10]. The Kelvin-Clapeyron model has been used frequently to theoretically describe liquid-vapor phase change processes, contact line motion, and stability in heat transfer (e.g., [6–30]).

Extensive experimental research on interfacial phenomena has been done using interferometry and ellipsometry. For example, Wayner and co-workers [10–12,15–17,25–27,31–34] used ellipsometry and/or interferometry techniques to study liquid-vapor interfacial phenomena during phase change for both wetting and nonwetting systems. Blake [5] used double wavelength interferometry to investigate equilibrium-wetting films of alkanes on α Alumina. Chen and Wada [35] studied the isothermal spreading dynamics of a drop edge using a laser light interference microscopy method. Cazabat and coworkers [36–38] used ellipsometric measurements to study the spreading of drops of polydimethylsiloxane (PDMS) on silicon. Kavehpour et al. [39] used phase-shifting laser feedback interferometer (psLFI) to study the dynamics of a precursor layer in front of the contact line of a spreading viscous nonvolatile drop on smooth substrates. Churaev et al. [40] used interference microscopy to study the spreading of surfactant solutions. Dussaud and Troian [41] used laser shadowgraphy to visualize the spreading films of volatile liquids during evaporation. Kihm and Pratt used a Fizeau interferometer to obtain contour mapping of thin liquid films [42].

Various researchers have studied evolution and instabilities of

[1]Corresponding author.

Manuscript received March 1, 2004; revision received September 10, 2004. Review conducted by: J. H. Lienhard V.

liquid-vapor interfaces [43–51]. For example, de Gennes presented a unified model of dry spreading by considering a precursor film around a spreading drop [43] and showed a scaling analysis of the upward flow of a wetting fluid [44]. Dussan et al. [45] and Marsh et al. [46] experimentally validated a theoretical expression for the slope of a fluid interface by using an asymptotic form of the slope at the contact line as the boundary condition. Oron et al. [47] presented a comprehensive review on evolution of thin films. Instabilities of the liquid-vapor interfaces due to Marangoni stresses developed either due to imposed temperature gradient [48] or concentration gradient [49,50] along the interface have also been studied. Kavehpour et al. [51] showed evidence of Marangoni instabilities in pure fluids due to localized evaporation near the contact line region and developed onset stability criteria.

In the present study, a vertical constrained vapor bubble (VCVB) was used that enabled us to look at capillary flow in a sharp 90 deg corner. Such a situation is important because it is related to the behavior of liquid films in the grooves of heat transfer devices and other systems where fluid motion is based on capillary transport. For example, Stephan and Busse [18] have presented a model for the calculation of the radial heat transfer coefficient in heat pipes with open grooves and have shown why the assumption of an interface temperature equal to the saturation temperature of the vapor leads to a large overprediction of the radial heat transfer coefficient. Swanson and Peterson [19] developed a mathematical model of the evaporating extended meniscus in a V-shaped channel to investigate the effects of wedge half-angle and vapor mass transfer on meniscus morphology, fluid flow, and heat transfer. Ayyaswamy et al. [52] obtained solutions to the two-dimensional equations of motion governing steady laminar flow in a triangular groove with the free surface governed by surface tension forces. Xu and Carey [53] used an analytical model to predict the heat transfer characteristics of film evaporation on a microgroove surface assuming that the evaporation takes place only from the thin film region of the meniscus. Khrustalev and Faghri [54] developed a mathematical model to describe heat transfer through thin liquid films in the evaporator region of heat pipes with capillary grooves. Wu and Peterson [55] studied a wickless micro heat pipe. They successfully used the Young-Laplace equation to describe the internal fluid dynamics of this integrated device. An analytical prediction of the axial dry-out point for evaporating liquids in axial microgrooves and the experimental verification of the predicted locations of the dry-out points were also accomplished [56]. From these works it was concluded that the longitudinal groove design was crucial to increase the heat transport capacity of these miniature devices and that the small grooves provided the necessary capillary force for the liquid to flow back into the evaporative zone. However, due to the experimental difficulties associated with measurements in small regions, experimental data on the details of a moving evaporating curved thin film in grooves are insufficient.

Herein, we study a relatively large wickless heat pipe with four corner grooves, which should be a very effective passive fin heat exchanger based on capillarity in a microgravity environment. The results from scheduled experiments on the International Space Station will be compared to these earth-based results. However, in addition to this applied use, the transparent experimental cell design has also the following two basic uses, which we demonstrate herein: (i) Under equilibrium conditions, the cell can be used to determine the equilibrium interfacial properties of an extended meniscus and (ii) under nonequilibrium conditions, the cell can be used to study fluid flow and transport processes in the contact line region. The results are needed to understand the operation of a relatively large wickless heat pipe. First, we present data on the isothermal meniscus in mechanical and phase equilibrium. The vertical curvature gradient in the thicker region agrees with the Kelvin equation. The transition to the flat adsorbed thin film region agrees with the augmented Young-Laplace equation. Kinetic theory tells us that there is an enormous exchange flux with a net value of zero at equilibrium. Next, we heated the meniscus and obtained, after a period of time, a stationary meniscus with different values of the curvature and the adsorbed flat thin film regions from the equilibrium values. This stationary extended meniscus is at mechanical equilibrium with the vapor because it is not moving. However, the pressure gradient in the liquid does not agree with the Kelvin equation. As described in, e.g., [6–9,13,18,19], a Kelvin-Clapeyron model is needed to describe phase change at the liquid-vapor interface for this nonisothermal steadily evaporating extended meniscus. Since the film at the leading edge appears flat at the start and during subsequent motion, there is no apparent viscous flow in the flat film portion of the nonisothermal meniscus. There is phase change in the flat portion of the moving meniscus. Therefore, at the start, the stationary flat thin region is in phase equilibrium where the Kelvin effect is offset by the Clapeyron effect. We emphasize that all subsequent experiments and conclusions are relative to this reference steady-state stationary meniscus. Next, we present data on the nonsteady state by following the motion during the transition from one steady state to another steady state. Previously, Zheng et al. [32] presented data on an unstable oscillating, evaporating thin film of pentane where moving velocities of the oscillating film were obtained. A force balance for the oscillating meniscus based on intermolecular and shape-governed forces was used to describe the oscillating velocities. However, the details of the region below a film thickness of 0.1 μm were not adequately addressed because of the relatively high velocity. Therefore, the important effect of disjoining pressure was only inferred. Herein, we present experimental data on the thickness, interfacial slope (a measure of contact angle), and curvature profiles of a moving, evaporating, thin liquid film of pentane on a quartz surface with emphasis on the region where the film thickness δ is below 0.1 μm. The profiles were measured using image-analyzing interferometry and an improved data analysis procedure. These profiles provide fundamental insights into the phenomena of phase change, pressure gradient, fluid flow, spreading, shear stress, and the general physics behind interfacial phenomena in the contact line region. We note that the measured shape signifies a combined effect of the contact line motion and phase change at the interface. The measured precursor adsorbed film, the interfacial slope (variation of the local ''apparent contact angle''), and the curvature profiles are consistent with previous concepts based on interfacial models (e.g., [6,9,17]). The unique experimental results demonstrate, explicitly with microscopic detail, that the disjoining pressure controls the movements of the contact line and fluid flow within an evaporating completely wetting meniscus.

The present study is a significant improvement over the results presented in Ref. [32] because of two major advances in the measurement and data analysis techniques. The previous study [32] did not evaluate thicknesses below the zeroth dark fringe ($\sim$0.1 μm). The present method, using a relative reflectivity concept, extended the evaluation of film thicknesses to the transition and adsorbed flat film regions. Furthermore, the thicknesses were determined at every pixel and not just at the maxima and minima of the interferogram (as was done in the previous study). The data were numerically analyzed to obtain the slope, the curvature, and the curvature gradient at every pixel location. The present study thus captured substantially more information about the important transport processes occurring in the contact line region ($\delta<0.1$ μm) and confirms the previous concepts presented in [6–23]. Also, the current imaging technique is significantly simpler than ellipsometry, which can also measure thickness below the zeroth dark fringe, as the circularly polarized light (for ellipsometry) would not be perpendicular to the sidewalls of the cuvette, thereby introducing significant complexity and errors.

Due to the complex, transient, large temperature gradients in the system, a theoretical analysis of the details of the three-dimensional temperature and heat flux fields is beyond the scope of this paper. Instead, a simpler control volume approach is used

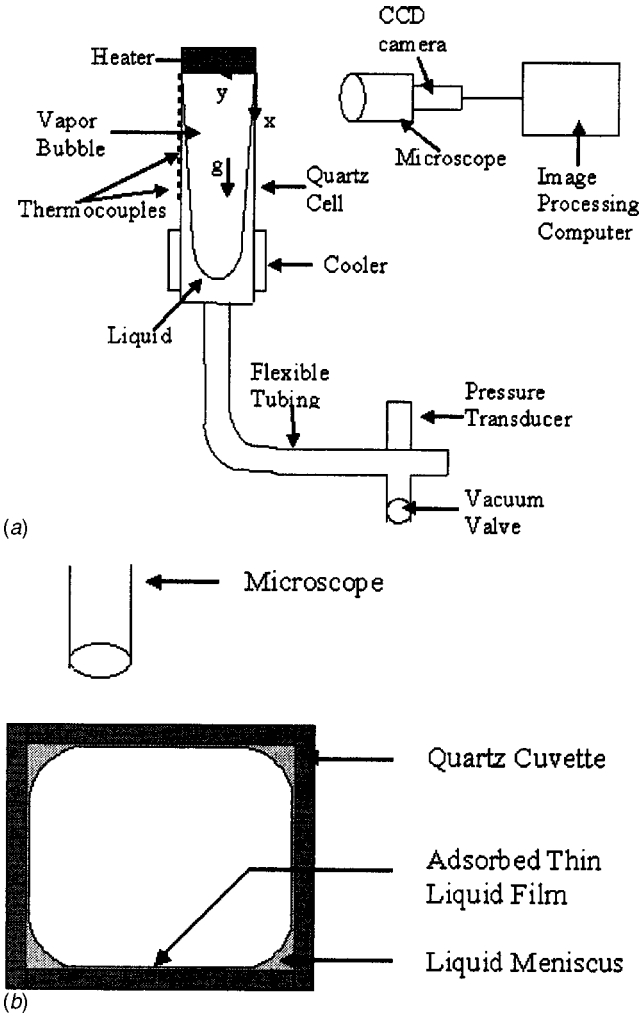

Fig. 1 (*a*) Schematic diagram of the experimental setup and (*b*) cross-sectional view of the quartz cuvette (inside dimensions 3 mm×3 mm). Acceleration due to gravity *g* is acting perpendicular to the cross section.

to discuss the results. The main objective of this paper is to present new experimental techniques, observations, and data.

Experimental Setup

A schematic representation of the Vertical Constrained Vapor Bubble (VCVB) [33] is shown in Fig. 1(*a*). A detailed analysis of the theoretical accuracy of the procedure and the resulting measurements is given in [33]. A vertical cuvette, made of fused silica (square cross section, inside dimensions 3 mm×3 mm, outside dimensions 5.5 mm×5.5 mm, length 43 mm) was attached to a length of pyrex tubing. A cross section of the cuvette is shown schematically in Fig. 1(*b*). To minimize the presence of impurities and dust particles, the system was thoroughly cleaned inside a glove box purged with dry nitrogen. The silica cuvette and the pyrex tubing were repeatedly rinsed with the working fluid before use. They were then heated in an oven at 100°C for 1 h to remove any adsorbed film on the silica surface. Once the system was cleaned, a thermoelectric heater was attached to the top of the cell. Four thermoelectric coolers, one on each side of the cell, were attached using a high thermal conductivity epoxy at a distance of 25 mm from the heater. Although external thermocouples could not give an accurate measurement of the internal temperature distribution, they were attached at intervals of 2 mm to give the trend in the temperature distribution along the axial direction, which responds to the heat input Q_{in}. The other end of the pyrex tubing was attached to a three-way vacuum valve. One end of this valve was connected to a pressure transducer, another end was connected to a vacuum pump, and the third end was connected to a reservoir of the working fluid.

The heat transfer working fluid used in these experiments was pentane (Fluka Chemicals) with a boiling point of 34°C and a stated purity greater than 99.8%. The setup was first evacuated and then partially filled with the requisite amount of the working liquid. This procedure ensured that the only materials inside the cell were the liquid and vapor phases of the working fluid. The vapor pressure was used to check the purity within ±25 mm of Hg (At 25°C, transducer pressure, $P_v = 537$ mm of Hg). The entire cuvette assembly was mounted on an aluminum base plate, and the base plate was attached to a precision, three-way translation stage on an air-buffered vibration control bench. The translation stage allowed us to focus the microscope at any desired position along the extended meniscus formed in the corners of the cuvette.

Experimental Procedure

In the VCVB, liquid from the pool at the bottom of the cuvette rises along the corners of the cuvette due to capillary and disjoining pressure forces and thereby forms a continuous extended meniscus in the four corners of the cuvette [see Fig. 1(*b*)]. To operate the system, power was applied to the heater and to the thermoelectric coolers. The liquid near the heater evaporated (evaporating section), the vapor near the cooler condensed (condensing section), and the condensate returned to the zone of evaporation as a result of the change in interfacial profile. Thus, the axial pressure gradient in the corner meniscus was a function of the heat input and heat rejection at a particular setting. The contact line of the corner meniscus was made to recede toward the corner by increasing the heat input at the start of a cycle and to advance by subsequently decreasing the heat input in the cycle. The meniscus was always preceded by an adsorbed thin film. Meniscus movement was observed through a microscope and analyzed using the image analyzing system. An improved image analysis technique [34] was used to analyze the images.

In the current study, monochromatic light ($\lambda = 546$ nm) from a mercury light source was used to illuminate the cuvette through the objective of the microscope. Naturally occurring interference fringes appeared [Fig. 2(*a*)], which were due to the reflection of light from the liquid-vapor and the liquid-solid interfaces. A Charged Couple Device (CCD) camera with a maximum frame rate of 30 frames/s was used to capture interference images of the receding and advancing menisci. The captured images were digitized using a data acquisition card (DT3155-MACH Series Frame Grabber).

Data Analysis

The images of the interference fringes were analyzed with the Image-Pro Plus software (version 4.1). The image captured from the microscope through the CCD camera was digitized into 640 (horizontal)×480 (vertical) pixels and assigned one of 256 possible gray values representing intensity from 0 (black) to 255 (white). The gray value at each pixel is a measure of the reflectivity. Thus each microscopic pixel acts as an individual light sensor to measure the local film thickness. With the 50× objective in the microscope and the CCD camera used in the experiments, each of 640×480 pixels represented the average reflectivity of a region of 0.177 μm length. From each image a plot of the pixel gray value G versus pixel position y was extracted. The experimentally obtained gray value plot for the interference fringes [Fig. 2(*a*)] of the corner meniscus under isothermal conditions at $x = 1.1$ mm is shown in Fig. 2(*b*). For comparison, the profile at $x = 14.93$ mm is given in Fig. 2(*c*). The reader should note that all the images correspond to the corner meniscus at a particular cross section of the cuvette [see Fig. 1(*b*)] and not near the nose of the bubble.

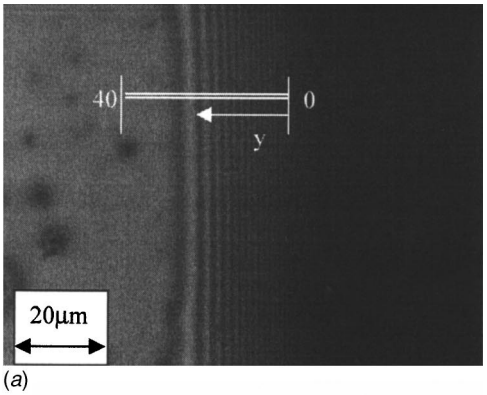

(*a*)

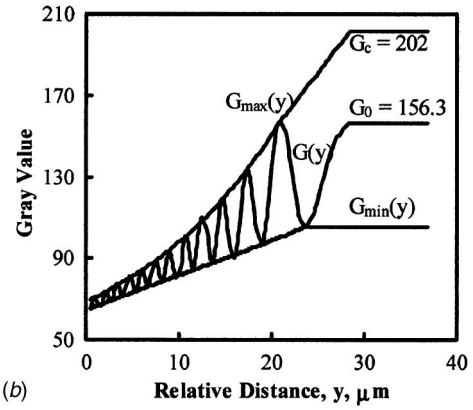

(*b*)

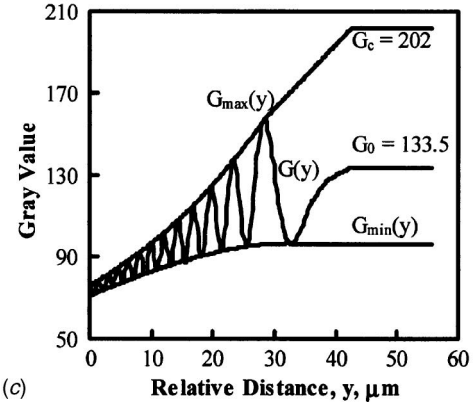

(*c*)

Fig. 2 (*a*) Fringe pattern for an equilibrium isothermal extended corner meniscus of pentane at $x=1.1$ mm ($Q_{in}=0$); (*b*) gray value profile for pentane at $x=1.1$ mm ($Q_{in}=0$, $\delta_0=48.9$ nm); and (*c*) gray value profile for pentane at $x=14.93$ mm ($Q_{in}=0$, $\delta_0=60.2$ nm)

A computer program written in MATLAB scanned the peaks and valleys and filtered the noise from the real peaks and valleys. It then calculated a relative gray value $\bar{G}$ at each pixel position based on the following relation [34]

$$\bar{G}(y)=\frac{G(y)-G_{\min}(y)}{G_{\max}(y)-G_{\min}(y)} \tag{1}$$

where $G_{\min}(y)$ and $G_{\max}(y)$ were determined from the interpolated envelopes to the various order minima and maxima. The presence of stray light necessitated the use of a relative gray value $\bar{G}$, as defined in Eq. (1). This also implicitly took into account the increase in the absorption of light due to an increase in the liquid film thickness and changes in the interfacial slope. The envelopes were drawn by fitting the respective maxima and minima with polynomials of third order corresponding to an error of less than 2%. The interpolated envelopes corresponding to the dark and bright fringes of the corner meniscus shown in Fig. 2(*a*) are shown in Fig. 2(*b*). It was found that for most of the data, a third-order polynomial was sufficient to fit these envelopes, and the evaluated film thickness profiles were found to be independent for higher orders of this polynomial. The value of $G_{\min}(y)$ for positions ahead of the zeroth dark fringe was taken to be the value at the zeroth dark fringe. The value of $G_{\max}(y)$ in the adsorbed flat film region was taken to be equal to the measured gray value G_c of the bare quartz surface of the cuvette. This gray value corresponded to a film thickness equal to zero and was measured using a dry cell with the same light intensity. A linear interpolation was used to connect the gray value of the first bright fringe and this value of G_c at the beginning of the adsorbed section as shown in Fig. 2(*b*). The constant gray value in the flat adsorbed film region is G_0. Near the pool of the liquid (farther from the top of the cuvette, $x=14.93$ mm), the constant gray value in the flat adsorbed film region of the meniscus G_0 decreased as shown in Fig. 2(*c*). This shows an increase in the value of the adsorbed film thickness δ_0 near the pool of the liquid at the bottom, which is expected.

The next step was to relate the relative gray value to the reflectivity RL by using the following relation [57] so that the film thickness could be evaluated

$$RL(y)=\bar{G}(y)[RL_{\max}-RL_{\min}]+RL_{\min} \tag{2}$$

Since the gray value at each pixel location was known from the experimental data, the reflectivity of the liquid film could be calculated at each pixel position using Eq. (2). The reflectivity of a thin liquid film of refractive index n_1, on a solid surface of refractive index n_s was related to the film thickness δ, according to Eq. (3).

$$RL=\frac{\alpha+\beta\cos 2\varphi_1}{\kappa+\beta\cos 2\varphi_1} \tag{3}$$

where

$$\varphi_1=\frac{2\pi n_1\delta}{\lambda},\quad \alpha=r_1^2+r_2^2,\quad \beta=2r_1r_2$$
$$\kappa=1+r_1^2r_2^2,\quad r_1=\frac{n_1-n_v}{n_1+n_v},\quad r_2=\frac{n_s-n_1}{n_s+n_1} \tag{4}$$

The equation shows that the reflectivity changes cyclically with the minima and maxima according to

$$RL_{\max}=\left(\frac{r_1+r_2}{1+r_1r_2}\right)^2=\frac{\alpha+\beta}{\kappa+\beta} \tag{5}$$

$$RL_{\min}=\left(\frac{r_1-r_2}{1-r_1r_2}\right)^2=\frac{\alpha-\beta}{\kappa-\beta} \tag{6}$$

Combining Eqs. (2) and (3), the film thickness at each pixel location was related to the gray value at that pixel location according to Eq. (7)

$$2\varphi_1=\cos^{-1}\left\{\frac{\beta+\kappa[1-2\bar{G}(y)]}{\beta[2\bar{G}(y)-1]-\kappa}\right\} \tag{7}$$

Thus, the film thickness at each pixel location was obtained based entirely on the experimental data. The fact that the extended meniscus profile merged smoothly to an adsorbed flat film was utilized to estimate the adsorbed film thickness from the gray value data, the gray value corresponding to a bare surface, and the peak and valley envelopes. Figure 3 is an example of the film thickness profile of the corner meniscus for the gray values represented in Fig. 2, which showed that the capillary meniscus merges smoothly to an adsorbed flat thin film region, $\delta=\delta_0$. The thickness at the zero-order fringe is $\delta=0.1$ μm. The error in the film thickness

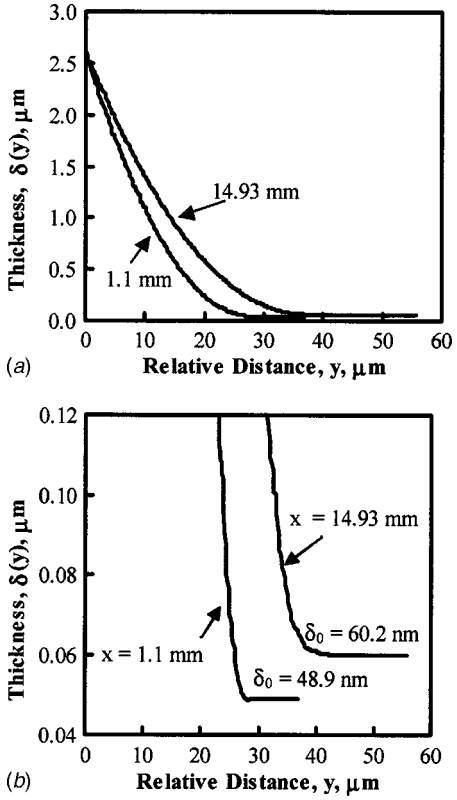

Fig. 3 (*a*) Comparison of thickness profiles at $x=1.1$ and 14.93 mm ($Q_{in}=0$), and (*b*) comparison of thickness profiles at $x=1.1$ and 14.93 mm near contact line region ($Q_{in}=0$)

measurement was estimated to be ± 0.01 μm in the transition and capillary region of the film and $\pm 10\%$ in the adsorbed film region.

Once the film thickness was obtained at every pixel, the slope ($d\delta/dy$) of the film thickness profile (local tangent angle) and the curvature were obtained at pixel number p by fitting a second order polynomial to the film thickness at pixel numbers $p-1$, p, and $p+1$. The terms $d\delta/dy$ and $d^2\delta/dy^2$ were then obtained at pixel number p based on this fitted polynomial between the three points. The curvature at pixel position p was then calculated using the following relation:

$$K=\frac{\dfrac{d^2\delta}{dy^2}}{\left[1+\left(\dfrac{d\delta}{dy}\right)^2\right]^{3/2}} \tag{8}$$

Next, the pixel numbers p, $p+1$, and $p+2$ were used and the process was repeated to obtain the slope and curvature at pixel position $p+1$. Since the distance between two successive pixels represented a length of 0.177 μm, a second-order polynomial to the film thicknesses at three consecutive pixel positions was found to be highly satisfactory (with very small error, coefficient of regression greater than 0.99). Thus, the technique successfully evaluated the thickness, slope, and curvature at every pixel position. This technique captured the variations of these quantities as a function of position. This would not be possible if one polynomial (of even higher orders) was fitted to the complete film thickness profile and used to obtain the slope and curvature. Also, a check using a five-point method did not change the results in a significant way. In addition, we lose details when we average over a larger length. All the experimental data of the corner meniscus during isothermal and nonisothermal conditions were analyzed using this improved image analysis technique. The curvature profiles

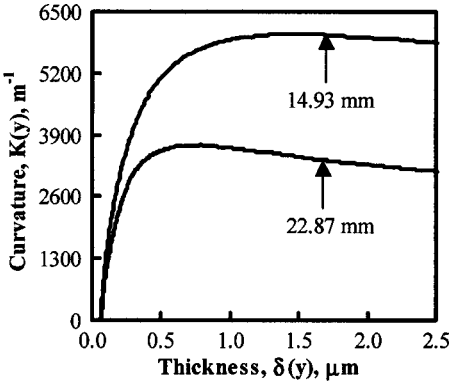

Fig. 4 Curvature profiles of the isothermal corner meniscus at two axial locations, $x=14.93$ and 22.87 mm ($Q_{in}=0$)

for the isothermal corner meniscus calculated using the experimental data and Eq. (8) at different axial locations x are plotted in Fig. 4. Figure 4 shows that the curvature of the isothermal corner meniscus is zero in the adsorbed flat film region ($\delta=\delta_0$). The curvature increased with an increase in the film thickness and became relatively constant in the thicker part of the corner meniscus ($\delta>1$ μm). In addition, the average value of the curvature for $\delta>1$ μm (K_T) increased with an increase in the hydrostatic head (decrease in the distance from the top of the cuvette, x).

The experimental technique could be verified by analyzing the data for the effect of hydrostatics on the curvature of the isothermal meniscus at equilibrium because the capillary pressure would balance the hydrostatic pressure if there were no contribution from the dispersion force. Writing a hydrostatic pressure balance for the thicker portion ($\Pi=0$) of the isothermal corner meniscus at two different axial locations along the cell, we find Eqs. (9)–(11)

$$P_l|_x-P_l|_{x_0}=\rho g(x-x_0) \tag{9}$$

$$(P_v-P_l)|_x-(P_v-P_l)|_{x_0}=\rho g(x_0-x) \tag{10}$$

$$\sigma(K_{T,x_0}-K_{T,x})=\rho g(x-x_0) \tag{11}$$

In the experimental system described here, as we go toward the bottom of the cell (increase in x), the hydrostatic head decreases, and hence the meniscus curvature ($K_{T,x}$) decreases. According to Eq. (11), a plot of ($K_{T,x_0}-K_{T,x}$) versus $-(\rho g/\sigma)(x_0-x)$ should be a straight line with slope equal to one. The data in Fig. 5 show excellent agreement with this hypothesis with an accuracy of data fitting of 98.4%. Thus, the experimental/analytical technique could be used to measure and analyze accurately the curvature of the corner meniscus of the wetting fluid.

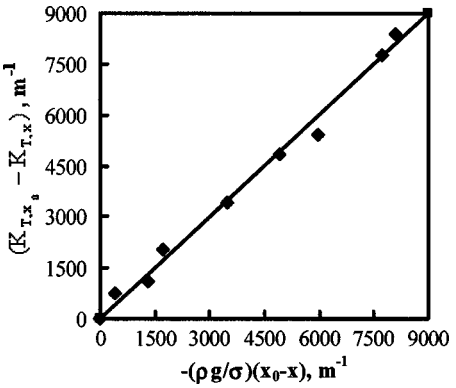

Fig. 5 Curvature versus $-(\rho g/\sigma)(x_0-x)$; ($K_{T,x_0}=10{,}863\ m^{-1}$ at $x=1.1$ mm)

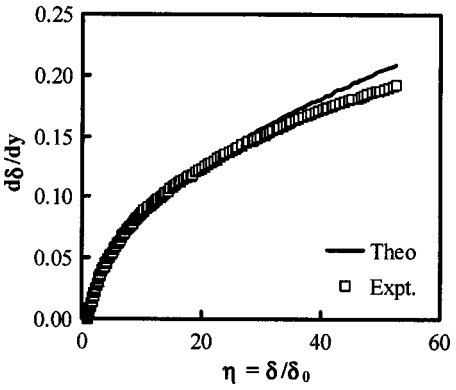

Fig. 6 Comparison between theoretical [Eq. (12)] and experimentally obtained slopes of a liquid-vapor interface of pentane on quartz in a VCVB at $x=1.11$ mm ($Q_{in}=0$)

Also, to justify the algorithms used in the evaluation of the slope, we compared the experimentally obtained slope of an isothermal pentane meniscus with the analytical expression derived by DasGupta et al. [10] for a stationary isothermal meniscus that is given below

$$\frac{d\delta}{dy}=(K_T\delta_0)^{1/2}\sqrt{2\eta+\frac{2}{3}\frac{\alpha^4}{\eta^3}-\frac{8}{3}\alpha} \tag{12}$$

where δ_0 is the adsorbed thin film thickness in *m*, η is the dimensionless thickness along the interface, defined as $\eta=\delta/\delta_0$, and α is a dimensionless variable defined as $\alpha^4=-B/\sigma K_T\delta_0^4$, which for an isothermal stationary meniscus is equal to 1. Using Eq. (12) for an isothermal pentane meniscus in the VCVB at a length $x=1.11$ mm, a comparison of the experimentally obtained slopes and the theoretical slopes is made and is shown in Fig. 6. As shown in Fig. 6, an excellent agreement is obtained between the experimental and theoretical slopes of the interface, which justifies the algorithm used in the evaluation of the slope and hence the curvature of the interface.

Including the effects of the capillary and the dispersion forces, the isothermal part of the excess interfacial free energy per unit volume (interfacial pressure jump) could be calculated from the experimental data using the following equation (e.g., [10,58,59])

$$\begin{aligned} P_v-P_l&=\sigma K-\frac{A}{6\pi\delta^3} \quad \delta\leqslant 20 \text{ nm} \\ P_v-P_l&=\sigma K-\frac{B}{\delta^4} \quad \delta\geqslant 40 \text{ nm} \end{aligned} \tag{13}$$

where P_v is the vapor pressure, P_l is the pressure inside the liquid, K is the curvature of the liquid-vapor interface, σ is the surface tension, and δ is the film thickness of the liquid. For our experimental conditions, we find that we are in the retarded film thickness, $\delta\geqslant 40$ nm. The second term on the right-hand side of the equation describes the van der Waals interactions and is defined in the thicker case as

$$\frac{\partial\Delta G^{vdw}}{\partial\delta}=\frac{B}{\delta^4}=-\Pi \tag{14}$$

where ΔG^{vdw} is the excess interfacial free energy per unit area due to the van der Waals interactions. ΔG^{vdw} includes the contributions from dipolar (purely entropic) and dispersion interactions. A is the Hamaker constant, and B is the retarded dispersion (Hamaker) constant for thicker films. Negative values of the Hamaker and dispersion constants signify that an adsorbed thin film in the microscopic region would be stable and would reduce the free energy of the system. Therefore, the thickness of the adsorbed thin film decreases with an increase in the hydrostatic head as shown in Fig. 3(*b*).

The value of the ideal dispersion constant is a function of the bulk refractive indices and the dielectric constants of the three phases. Since our experimental system was not ideal because it was designed to study transport phenomena using a fluid with a high vapor pressure, we evaluate the dispersion constant using experimental data. Since the corner meniscus was near equilibrium isothermal conditions, the augmented Young-Laplace model [Eq. (13)] can be written for both the thin adsorbed film region ($K=0$) and the thicker portion of the corner meniscus ($\Pi=0$)

$$P_v-P_l(y)=\sigma K(y)-\frac{B}{\delta^4}=\text{constant} \tag{15}$$

and

$$\sigma K_T=-\frac{B}{\delta^4}=\text{constant} \tag{16}$$

Although, we found that the experimental values of B were a weak function of the adsorbed film thickness, an average value of B is considered adequate in calculating disjoining pressure of the thin film during receding and advancing movement of the meniscus during the nonisothermal studies. We also assume that the process of phase change does not effect the value of B. Using the values of the thickness of the thin adsorbed film (δ_0) and the curvature in the thicker part of the meniscus K_T for the experimental system at isothermal conditions, the average dispersion constant B_{avg} was found to be equal to -1.195×10^{-27} Jm over a thickness range of 48 nm$<\delta_0<$55 nm. We also note that, an error in the measured adsorbed film thickness due to interfacial temperature jumps could result in a larger than expected value of the dispersion constant. As described in previous studies [26] a possible uncontrollable interfacial temperature jump of the order of 10^{-4} K could cause an error in thickness of δ_0 of 100% and a large error in B. Although further studies are needed to quantify these effects and so achieve a better understanding of the value of the dispersion constant, we emphasize that an error incorporated in the value of the dispersion constant does not effect the conclusions given below because they depend on the change of Π from the hydrostatic and/or the nonisothermal, steady-state reference measurement.

Advancing and Receding Menisci

First, a reference steady-state stationary evaporating meniscus was set by fixing the heat input rate at $Q_{in}=0.039$ W. Then the contact line of the corner meniscus was made to receed towards the walls of the cuvette by changing the heater power from 0.039 W to 0.068 W (time, $t=0$ s) and to advance away from the wall by changing the heat input back to 0.039 W ($t\approx30$ s). Note that there is fluid flow and evaporation in the reference meniscus at $Q_{in}=0.039$ W. During this process, the contact line of the meniscus first recedes due to additional evaporation and then advances back to its original position due to a decrease in evaporation (with some possible condensation in the flat adsorbed film) as shown in Fig. 7. Meniscus recession occurs from $t=0$ s to $t\approx30$ s and advancement during $30<t<67$ s. Here the receding meniscus for $t<10$ s and the advancing meniscus for $t>50$ s is considered due to significant changes in the meniscus profiles in these regions. Figures 7(*a*)–7(*c*) represent the fringe pattern of the receding meniscus of pentane at $t=2.92$, 6.05, and 10.13 s, respectively and Figs. 7(*d*)–7(*g*) represent the advancing meniscus at $t=52.63$, 56.71, 61.47, and 66.44 s, respectively. Using the image-analyzing technique discussed earlier, the captured images of the receding and advancing films were analyzed to obtain the variation in thickness, slope, curvature, and pressure profiles.

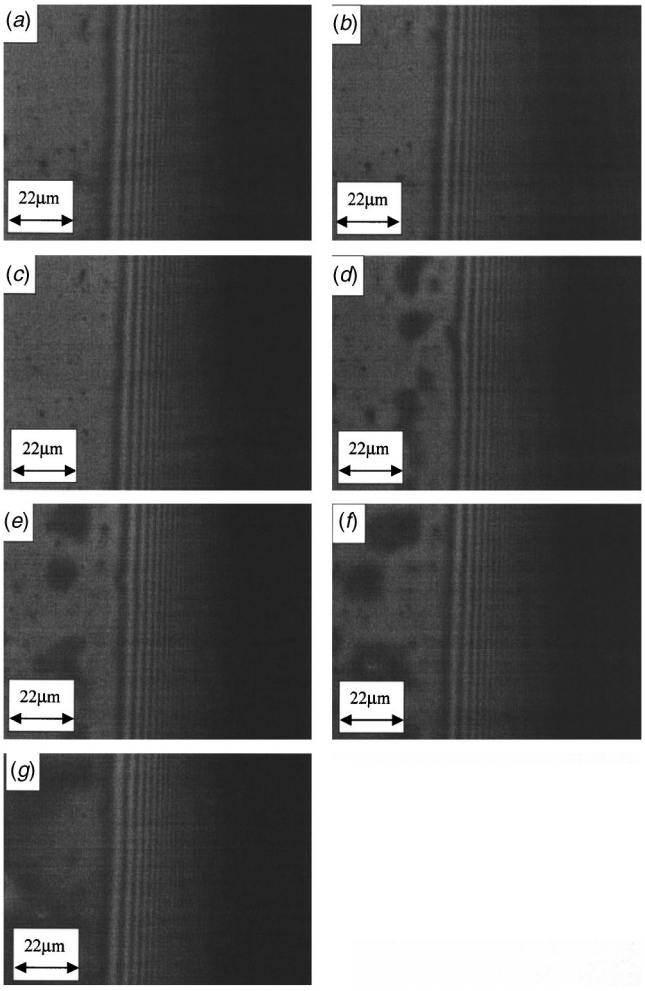

Fig. 7 Fringe pattern for receding and advancing menisci, Receding meniscus: (*a*) 2.92 s, (*b*) 6.05 s, (*c*) 10.13 s; Advancing meniscus: (*d*) 52.63 s, (*e*) 56.71 s, (*f*) 61.47 s, and (*g*) 66.44 s

Film Thickness Profiles

Gray value profiles for the interference fringe pattern (Fig. 7) of the receding meniscus at two instants ($t=2.92$ and 10.13 s) are shown in Fig. 8. During the film recession, the gray value profile changes and its value in the adsorbed thin film region increases (thinner adsorbed film). The corresponding thickness profiles of the receding meniscus at three instants of time ($t=2.92$, 6.05, and 10.13 s) are presented in Fig. 8. Table 1 and Fig. 9 clearly show that the adsorbed film thickness decreased (from 50.4 nm at $t=0$ s to 36.7 nm at 10.13 s) as the film receded toward the corner. The profiles of the advancing meniscus (due to change in heat input from 0.068 W to 0.039 W) at four instants of time ($t=52.63$, 56.71, 61.47, and 66.44 s) are presented in Fig. 10. The advancement of the film was associated with an increase in the adsorbed film thickness from 40 nm to 55.5 nm. The complete results are presented in Table 1, where the states (advancing or receding) of the meniscus are also shown. A plot of the change in the adsorbed film thickness with time is presented in Fig. 11. The data show that the value of δ_0 decreases as the film recedes and increases as the film advances. The slopes for the data represented in Fig. 7 are plotted in Fig. 12. It is evident that the slope of the film thickness profile is zero in the adsorbed, thinner flat film region. The slope then increased rapidly along the thickness profile. As can be seen from the figure, the slope increased at a given value of δ as the film receded toward the corner and the slope decreased with the advancement of the meniscus. This observation is consistent with the results obtained by Zheng et al. [32] and Zheng [60]. We note that since there is no bulge in the thickness profile, Marangoni flows and instabilities appear to be absent in this portion of the meniscus.

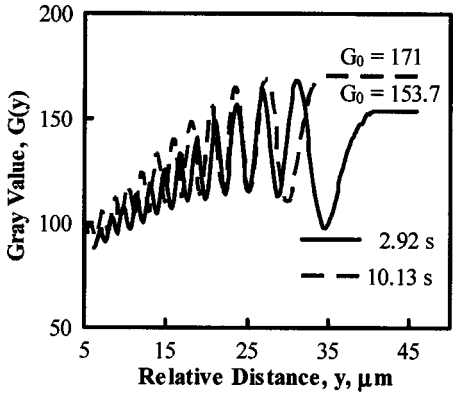

Fig. 8 Gray value profiles of the pentane meniscus at $x \approx 10$ mm during recession, at $t=2.92$ s, $\delta_0=45.7$ nm and at $t=10.13$ s, $\delta_0=36.7$ nm (nonisothermal)

Curvature Profiles

The curvature profiles for the receding and the advancing menisci were calculated using Eq. (8). The curvature profiles for the data presented in Fig. 7 are shown in Fig. 13. The shapes are significantly different from the equilibrium shapes presented in Fig. 4. The curvature approached a relatively constant value in the thick film region at any given instant. In the flat part of the film, the value of the curvature was zero. It then increased rapidly and passed through a maximum. High curvature and curvature gradients near the contact line region were suggested previously by the numerical modeling results of Potash and Wayner [6], Truong and Wayner [61] and others (eg., [9,18,20,22,62,63]), but had not been observed in a transient situation before. The increase in curvature with thickness in the thinner region results from the decrease in disjoining pressure with thickness as indicated by Eq. (9). The maximum values of the curvature and the nearly constant values of the curvature at the thicker end of the film are presented in Table 1. As can be seen from Table 1, the maximum and constant curvature near the thicker region increased when the film receded and decreased when the film advanced. DasGupta et al. [10,17] also experimentally obtained a curvature maximum in the contact line region of a steady-state evaporating thin film for a completely wetting case, but for a stationary film. Note that as the film receded, the curvature around $\delta=0.5$ μm (maximum curvature) and the constant curvature in the thicker region increased, which served to increase the curvature gradient and, hence, the potential for fluid flow. After $t \approx 20$ s, the decrease in the adsorbed film thickness (Fig. 11) and curvature are smaller as the profile adjusts to a new steady state with evaporation. During advancing (time increasing), the maximum curvature decreased due to enhanced spreading, as can be seen in Fig. 13(*b*). This served to decrease the curvature gradient and, hence, the potential for flow. The increased curvature and curvature gradients near the microregion of the meniscus led to extremely high capillary forces and a strong liquid flow toward the interface, as is also the case during evaporation in a steady-state meniscus. Thus, with the experimental technique used herein, the presence of a curvature maximum in the contact line region for both receding and advancing menisci was demonstrated.

Pressure

Based on the experimentally measured thickness and curvature profiles, we calculated the pressure at every pixel using the augmented Young-Laplace equation (13). There are two fundamental

Table 1 Parameters for receding and advancing menisci (θ_r is the apparent contact angle at δ=0.1 μm)

	Time (s)	δ_0 (nm)	$K_{0.1\,\mu m}$ (m^{-1})	K_{max} (m^{-1})	K_T (m^{-1})	Velocity U_i (μm/s)	Contact angle θ_r (deg)	τ_0 (N/m^2)
0.039 W to 0.068 W	0	50.4	6030	6786	4585	–	1.20	−0.47
(Receding meniscus)	0.34	50.0	5000	7271	4629	−1.95	1.13	−0.80
	1.29	46.6	6590	7333	4855	−0.35	1.33	−0.90
	2.92	45.7	5911	7416	4895	−0.54	1.28	−1.07
	3.33	45.6	5816	7564	4954	−0.87	1.29	−1.31
	4.35	45.3	5890	7607	4985	−0.35	1.31	−1.24
	4.69	45.1	5287	8094	5024	−1.56	1.23	−1.43
	6.05	44.9	5140	8991	5088	−0.91	1.18	−1.88
	7.07	44.8	5234	9082	5137	−0.17	1.22	−1.65
	7.41	43.9	5109	9328	5207	−1.04	1.22	−1.86
	8.09	42.5	4990	9470	5284	−0.52	1.19	−2.53
	8.77	39.9	5091	9554	5367	−0.78	1.24	−3.79
	10.13	36.7	4790	9643	5528	−0.52	1.21	−5.08
0.068 W to 0.039 W	52.63	40.0	2831	9159	6311	–	0.86	−5.25
(Advancing meniscus)	52.97	41.9	2811	9248	6268	0.52	0.84	−4.17
	54.67	42.0	2889	9202	6089	0.26	0.84	−3.92
	56.71	42.5	3279	8985	5881	0.61	0.97	−3.68
	58.75	42.3	3844	8878	5878	0.35	1.04	−3.08
	60.79	42.4	4314	8725	5549	0.52	1.17	−3.25
	61.47	46.3	4329	8552	5458	0.78	1.08	−2.86
	64.87	47.3	4728	8303	5262	0.47	1.10	−2.16
	65.89	49.0	4276	7298	5226	1.21	1.04	−1.79
	65.96	49.6	4360	6900	5126	7.81	1.05	−1.18
	66.23	50.8	4709	6835	5128	1.95	1.11	−0.86
	66.44	55.5	5305	6936	5185	1.73	1.10	−0.69

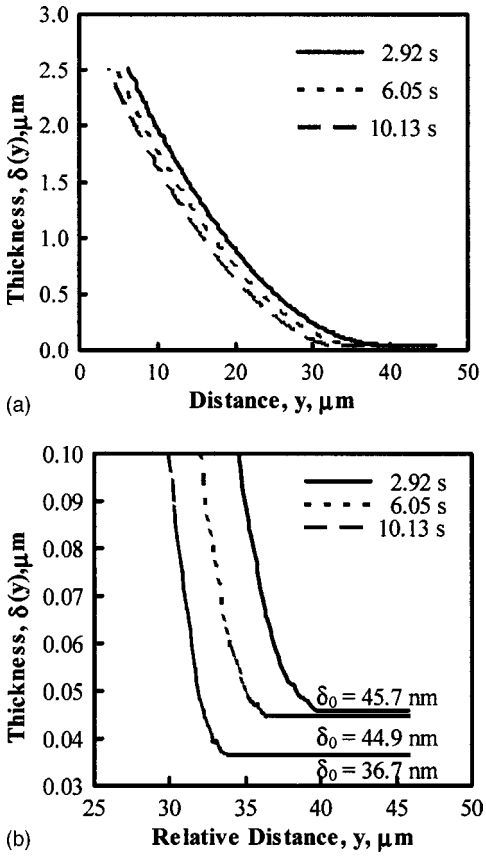

Fig. 9 (*a*) Thickness profiles of the pentane meniscus at $x \approx 10$ mm during recession (nonisothermal) and (*b*) comparison of thickness profiles of the pentane meniscus at $x \approx 10$ mm during recession near the contact line region (nonisothermal)

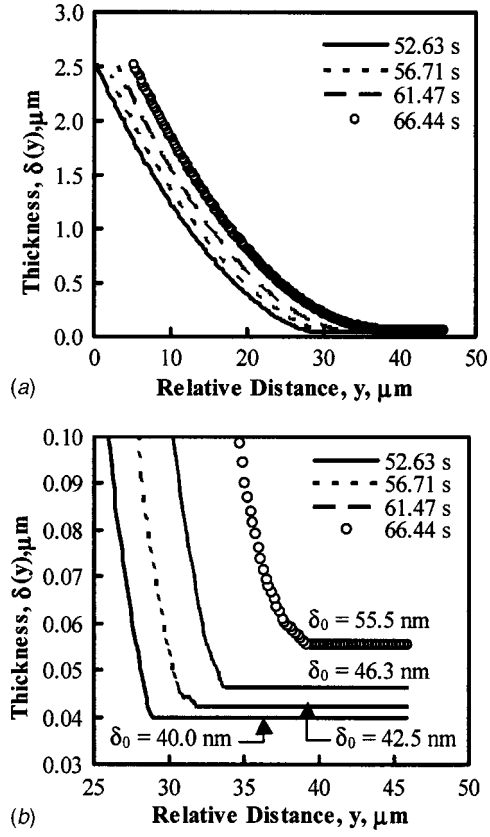

Fig. 10 (*a*) Thickness profiles of the pentane meniscus at $x \approx 10$ mm during advancement (nonisothermal) and (*b*) comparison of thickness profiles of the pentane meniscus at $x \approx 10$ mm during advancement near the contact line region (nonisothermal)

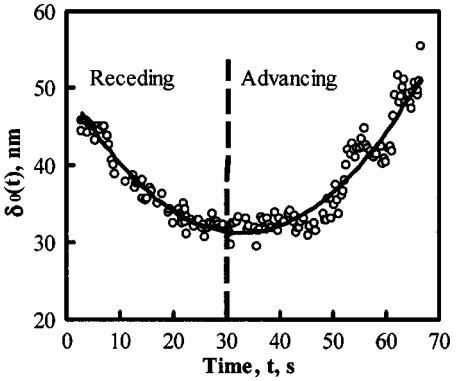

Fig. 11 Adsorbed thickness δ_0 versus time during receding and advancing movements of the pentane meniscus at $x \approx 10$ mm from the top of the cuvette (nonisothermal). Open circles represent data point and solid line shows the trend in the data.

properties we need for this calculation, the dispersion constant for the system and the interfacial tension. The interfacial tension was experimentally obtained using a Fisher surface tensiomat® and was found to be equal to 0.0171 N/m, and the experimental value of the average dispersion constant, $B_{avg} = -1.195 \times 10^{-27}$ Jm, was used for the pressure calculation. Also the variation of surface tension with temperature was found to be $\partial\sigma/\partial T \approx -0.1106 \times 10^{-3}$ (N/m °C) [64].

Plots of P_1 against distance y for both receding and advancing menisci are shown in Fig. 14. Note that the pressure roughly followed changes in the curvature in the region where the disjoining pressure effect is small. The horizontal regions for large values of

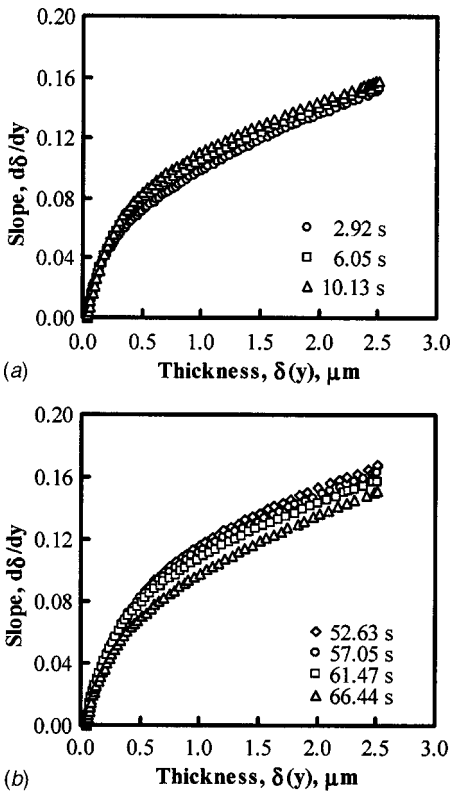

Fig. 12 (*a*) Slope profiles for the receding meniscus of pentane at $x \approx 10$ mm (nonisothermal) and (*b*) slope profiles for the advancing meniscus of pentane at $x \approx 10$ mm (nonisothermal)

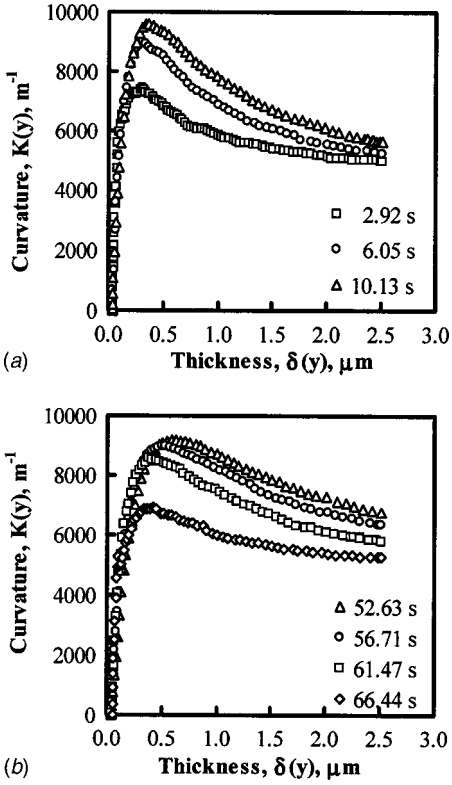

Fig. 13 (*a*) Curvature profiles for the receding meniscus of pentane at $x \approx 10$ mm (nonisothermal) and (*b*) curvature profiles for the advancing meniscus of pentane at $x \approx 10$ mm (nonisothermal)

y show the effect of disjoining pressure. As the film receded [Fig. 14(*a*)], the pressure gradients closest to the flat thin film (contact line) increased. As the film advanced [Fig. 14(*b*)], the pressure gradient decreased and the whole curve flattened. These plots show the forces driving the motion of the fluid and how differences in those forces at different regions of the film caused flow toward or from the contact line.

Average Shear Stress

The liquid-vapor interfacial velocity was also used to characterize the movement of the meniscus. Herein, the location of the point $\delta = 0.1$ μm, *C*, was taken as the reference point and the velocities were calculated based on the movement of this point of the meniscus between times t_{i-1} to t_i by

$$U_i = \frac{c_i - c_{i-1}}{t_i - t_{i-1}} \tag{17}$$

If the liquid-vapor interfacial velocity was positive, then it indicated that the contact line moved toward the flat film (advancement). Velocity calculated from Eq. (17) represents the velocity of a control volume of the liquid-vapor interface, starting from the adsorbed thin film to a thickness of 0.1 μm. This is obvious from Figs. 9(*b*) and 10(*b*), where the thickness profiles for the receding and advancing movements of the meniscus are parallel to each other, indicating a constant velocity over the entire control volume for a given instant. We note that for $\delta > 0.1$ μm, we observed more complicated velocity profiles. However, the area of interest in this paper is restricted to $\delta_0 < \delta < 0.1$ μm for the nonisothermal experiments.

In a related work Zheng et al. [32,60] presented the following force balance method for an oscillating film. Figure 15 illustrates the macroscopic interfacial force balance that relates viscous losses to interfacial forces and the apparent contact angle in an

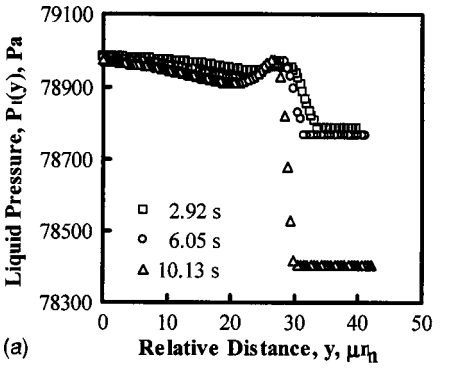

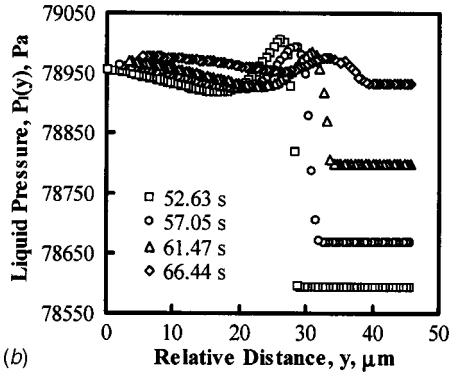

Fig. 14 (*a*) Liquid pressure versus distance for the receding meniscus of pentane at $x \approx 10$ mm (nonisothermal, $P_v = 593$ mm of Hg at $T_{quartz, x \approx 10\ mm} = 31.5°C$) and (*b*) liquid pressure versus distance for the advancing meniscus of pentane at $x \approx 10$ mm (nonisothermal)

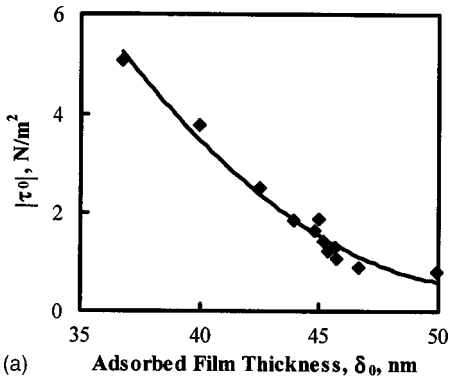

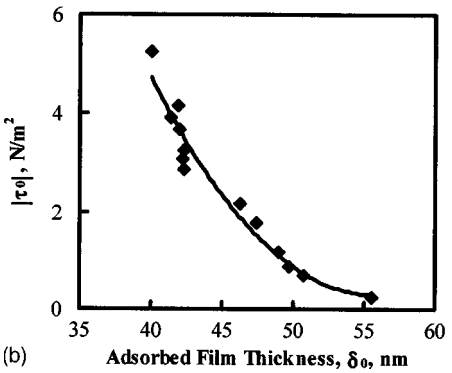

Fig. 16 (*a*) Absolute value of average shear stress during recession against δ_0 and (*b*) absolute value of average shear stress during advancement against δ_0. A parabolic profile is fitted to show the trend in $\tau_0(\delta_0)$.

evaporating meniscus for the control volumes between δ_0 and δ_r. Due to the extremely small momentum of the system, we can assume that the sum of the forces acting on the interfaces of the control volume is balanced. Therefore, using the augmented Young-Laplace equation, the interfacial force balance between δ_r (measured at $\delta_r = 0.1\ \mu$m) and the flat liquid film on the quartz surface (at δ_0) is

$$\sigma_{lv,r}\cos\theta_r + \sigma_{ls,r} + (\sigma_{lv,r}K_r + \Pi_r)\delta_r = [\tau_0 L_0 + \sigma_{lv,0} + \sigma_{ls,0} + (\sigma_{lv,0}K_0 + \Pi_0)\delta_0] \quad (18)$$

where τ_0 is the average shear stress that the solid exerts on the fluid over the length L_0. The product $\tau_0 L_0$ represents a shear force per unit contact line length perpendicular to L_0 and is assumed to be positive toward the adsorbed thin film. Π_0 is the disjoining pressure at δ_0, and θ_r is the value of the apparent contact angle at 0.1 μm. The sum $(\Pi_0\delta_0 + \sigma_{lv,0}K_0\delta_0)$ represents the "suction" at δ_0 due to interfacial forces. The disjoining pressure or free energy per unit volume Π_0, represents the force per unit area at the contact line and is positive for a completely wetting fluid. The value of the apparent contact angle is a function of the location because of the curvature K.

Assuming that $\sigma_{lv,r} = \sigma_{lv,0} = \sigma_l$, $\sigma_{ls,r} = \sigma_{ls,0} = \sigma_{ls}$, Eq. (18) can be simplified as

$$[\tau_0 L_0 + \Pi_0\delta_0 + \sigma_l K_0\delta_0] = \sigma_l(\cos\theta_r - 1) + (\sigma_l K_r + \Pi_r)\delta_r \quad (19)$$

To overcome the difficulty of measuring the disjoining pressure at the thicker end of the control volume the film thickness δ is taken to be the thickness at the first destructive interference fringe, 0.1 μm, where the disjoining pressure Π_r is negligible.

Equation (19) can be rewritten to get the average shear stress over the control volume as

$$\tau_0 = \frac{\sigma_l(\cos\theta_r + K_r\delta - 1) - \Pi_0\delta_0}{L_0} \quad (20)$$

From Eq. (20), we can calculate the average surface shear stress between the adsorbed film thickness δ_0, and the reference thickness δ_r. The results are presented in Table 1.

From Table 1 we see that the average shear stress over the control volume has a negative sign for both advancing and receding menisci. This demonstrates that the liquid adjacent to the solid surface is flowing toward the contact line while evaporating in both cases. Figure 16 shows the absolute average shear stress of the receding and advancing menisci as a function of the adsorbed film thickness δ_0. As shown in Fig. 16 and Table 1, the average absolute value of the shear stress at the wall increases as the meniscus recedes (decrease in δ_0 with more evaporation) and decreases as the meniscus advances (increase in δ_0 with less evaporation). The increase in the average shear stress during recession is due to the decrease in the adsorbed film thickness, which increases the van der Waals interactions between the wall and the liquid film. Hence any further recession causes an increase in

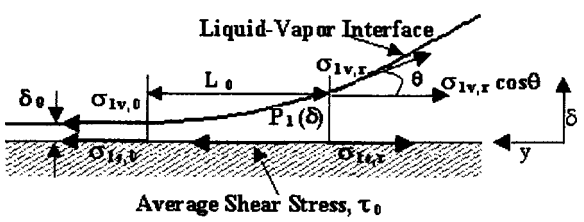

Fig. 15 Schematic of the control volume of an evaporating corner meniscus for macroscopic interfacial force balance

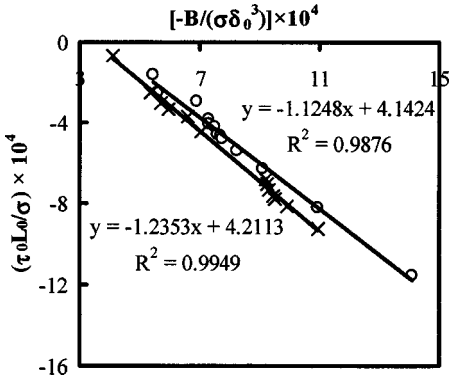

Fig. 17 Dimensionless shear stress, $\tau_0 L_0/\sigma$, versus dimensionless disjoining pressure, $-B/\sigma\delta_0^3$. × represents receding meniscus and ○ represents advancing meniscus.

shear stress as shown in Fig. 16(*a*). During advancing, the average shear stress decreases as the meniscus advances [Fig. 16(*b*)], due to an increase in the adsorbed film thickness, which causes a decrease in the van der Waals interactions.

Equation (20) can be made dimensionless by multiplying both sides by (L_0/σ) resulting in

$$\frac{\tau_0 L_0}{\sigma} = (\cos\theta_r + K_r\delta_r - 1) - \frac{-B}{\sigma\delta_0^3} \tag{21}$$

A plot of $\tau_0 L_0/\sigma$ against $-B/\sigma\delta_0^3$ is shown in Fig. 17 for both receding and advancing menisci. The data fits to a straight line of slope ≅1 with an error of 2–4%. Also, the value of the intercept $(\cos\theta_r + K_r\delta_r - 1)$ is approximately constant for both receding and advancing movements of the meniscus. This shows that $\tau_0 L_0/\sigma$ depends mainly on $-B/\sigma\delta_0^3$ and the effect of $(\cos\theta_r + K_r\delta_r - 1)$ is approximately constant and relatively small compared to $-B/\sigma\delta_0^3$ (Table 2).

Thus, the experimentally measured force field (disjoining pressure, curvature, and contact angle) and inferred average shear stress help describe the physics behind the advancing and receding meniscus. We find that changes in the disjoining pressure controls the motion of the extended meniscus and fluid flow in the meniscus.

Table 2 Shear stress for receding and advancing menisci

	Time (s)	L_0 (μm)	$\tau_0 L_0/\sigma$ (10^{-4})	$\cos\theta_r + K_r\delta_r - 1$ (10^{-4})	$-B/\sigma\delta_0^3$ (10^{-4})
0.039 W to 0.068 W	0	5.84	−1.61	3.84	5.45
(Receding meniscus)	0.34	5.49	−2.56	3.05	5.60
	1.29	5.66	−2.97	3.91	6.88
	2.92	6.19	−3.88	3.43	7.31
	3.33	5.31	−4.06	3.26	7.32
	4.35	5.84	−4.23	3.27	7.49
	4.69	5.49	−4.60	2.99	7.59
	6.05	4.25	−4.68	3.00	7.68
	7.07	4.96	−4.78	2.98	7.76
	7.41	4.96	−5.39	2.84	8.23
	8.09	4.25	−6.28	2.82	9.10
	8.77	3.72	−8.24	2.74	10.97
	10.13	3.90	−11.56	2.56	14.12
0.068 W to 0.039 W	52.63	3.01	−9.24	1.71	10.94
(Advancing meniscus)	52.97	3.19	−7.78	1.73	9.50
	54.67	3.54	−7.62	1.81	9.43
	56.71	4.07	−7.32	2.00	9.32
	58.75	3.72	−7.06	2.19	9.25
	60.79	4.07	−6.81	2.41	9.22
	61.47	3.54	−4.48	2.56	7.04
	64.87	3.54	−3.70	2.88	6.58
	65.89	4.78	−3.31	2.64	5.95
	65.96	6.02	−3.04	2.67	5.71
	66.23	6.19	−2.50	2.84	5.34
	66.44	4.60	−0.63	3.46	4.09

Conclusions

A system consisting of an evaporating meniscus of pentane on a quartz surface in a vertical constrained vapor bubble was studied. Image-analyzing interferometry with an improved data analysis technique was successfully used to measure the profile of the moving contact line region of evaporating corner meniscus of pentane. Isothermal equilibrium experiments verified the accuracy of the curvature measurement process. To characterize the system, the value of the dispersion constant for the thickness of use was evaluated in situ.

Nonisothermal experiments were also performed. The meniscus was made to recede and advance by increasing and decreasing the heat inputs. The motion was due to a change in heat input, and the meniscus was stable after a long period of time at the particular heat fluxes studied. The advancing and receding menisci were analyzed to obtain the film thickness, curvature, and pressure profiles as a function of time. A maximum in the curvature profile of the liquid-vapor interface was observed, and it decreased as the meniscus advanced (lower heat flux) and increased as the meniscus receded (higher heat flux). An increase in the adsorbed film thickness was associated with the advancing stage and a decrease with the receding stage. Using the augmented Young-Laplace equation, pressure profiles were calculated as a function of time that demonstrated the cause of fluid flow toward or away from the contact line. Shear stress on the wall was correlated with changes in the van der Waals interactions between the wall and the liquid film. The results indicate that the changes in the disjoining pressure control the motion of the extended meniscus and fluid flow therein.

Acknowledgments

This material is based on the work supported by the National Aeronautics and Space Administration under Grant No. NAG3-2351 and No. NAG3-2383. Any opinions, findings, and conclusions or recommendations expressed in this publication are those of the authors and do not necessarily reflect the view of the NASA.

Nomenclature

A = Hamaker constant, J
B = dispersion constant, Jm
g = acceleration due to gravity, m/s^2
G = average gray value
G = gray value
G_c = gray value of the bare surface
G_0 = constant gray value corresponding to adsorbed thickness of δ_0
ΔG^{vdw} = change in Gibbs free energy
K = curvature, m^{-1}
L = order of the fringe
L_0 = control volume length, m
n = refractive index
p = pixel number
P = pressure, Pa
r_1, r_2 = coefficients defined in Eq. (4)
RL = reflectivity
Q_{in} = heat input, W
T = temperature, K
U = velocity, m/s
x = axial location, mm
y = distance, μm

Greek Symbols.

α, β, κ = coefficients defined in Eqs. (4) and (12)

δ = film thickness, μm
δ_0 = adsorbed thin film thickness, nm
Δ = difference
λ = wavelength, nm
Π = disjoining pressure, N/m^2
ρ = density of the liquid, kg/m^3
σ = surface tension of the liquid, N/m
φ_1 = parameter defined in Eq. (4)
θ_r = apparent contact angle (tangent angle) at δ=0.1 μm, deg
τ_0 = average shear stress, N/m^2

Subscripts

avg = average
i = ith instant
l = liquid
max = maximum
min = minimum
R = reference state
s = solid
T = thicker portion
x = axial distance, mm
v = vapor

References

[1] Derjaguin, B. V., and Zorin, A. M., 1957, ''Optical Study of the Adsorption and Surface Condensation of Vapors in the Vicinity of Saturation on a Smooth Surface,'' *Proc. of 2nd Int. Congr. Surface Activity* (London) **2**, Butterworths Scientific Publications Ltd., London, England, pp. 145–152.
[2] Derjaguin, B. V., and Shcherbakov, L. M., 1961, ''Effect of Surface Forces on Phase Equilibria of Polymolecular Layers and Contact Angles,'' Colloid J. USSR, **23**, pp. 33–43.
[3] Derjaguin, B. V., and Churaev, N. V., 1976, ''The Definition of Disjoining Pressure and Its Importance in the Equilibrium and Flow of Thin Films,'' Colloid J. USSR, **38**, pp. 438–448.
[4] Derjaguin, B. V., Nerpin, S. V., and Churaev, N. V., 1965, ''Effect of Film Transfer Upon Evaporation of Liquids From Capillaries,'' Bull Rilem, **29**, pp. 93–98.
[5] Blake, T. D., 1975, ''Investigation of Equilibrium Wetting Films of n-Alkanes on α-Alumina,'' J. Chem. Soc., Faraday Trans. 1, **71**, pp. 192–208.
[6] Potash, Jr., M., and Wayner, Jr., P. C., 1972, ''Evaporation From a Two-Dimensional Extended Meniscus,'' Int. J. Heat Mass Transfer, **15**, pp. 1851–1863.
[7] Wayner, Jr., P. C., Kao, Y. K., and LaCroix, L. V., 1976, ''The Interline Heat-Transfer Coefficient of an Evaporating Wetting Film,'' Int. J. Heat Mass Transfer, **19**, pp. 487–492.
[8] Wayner, Jr., P. C., 1991, ''The Effect of Interfacial Mass Transport on Flow in Thin Liquid Films,'' Colloids Surf., **52**, pp. 71–84.
[9] Moosman, S., and Homsy, S. M., 1980, ''Evaporating Menisci of Wetting Fluids,'' J. Colloid Interface Sci., **73**, pp. 212–223.
[10] DasGupta, S., Plawsky, J. L., and Wayner, Jr., P. C., 1995, ''Interfacial Force Field Characterization in a Constrained Vapor Bubble Thermosyphon,'' AIChE J., **41**, pp. 2140–2149.
[11] Wayner, Jr., P. C., 1994, ''Mechanical and Thermal Effects in the Forced Spreading of a Liquid Film With a Finite Contact Angle,'' Colloids Surf., A, **89**, pp. 89–95.
[12] Wayner, Jr., P. C., 2002, ''Nucleation, Growth and Surface Movement of a Condensing Sessile Droplet,'' Colloids Surf., A, **206**, pp. 157–165.
[13] Holm, F. W., and Goplen, S. P., 1979, ''Heat Transfer in the Meniscus Thin Film Region,'' ASME J. Heat Transfer, **101**, pp. 543–547.
[14] Dhir, V. K., 2001, ''Numerical Simulations of Pool-Boiling Heat Transfer,'' AIChE J., **47**, pp. 813–835.
[15] Renk, F. J., and Wayner, Jr., P. C., 1979a, ''An Evaporating Ethanol Meniscus, Part I: Experimental Studies,'' ASME J. Heat Transfer, **101**, pp. 55–58.
[16] Renk, F. J., and Wayner, Jr., P. C., 1979b, ''An Evaporating Ethanol Meniscus, Part II: Analytical Studies,'' ASME J. Heat Transfer, **101**, pp. 59–62.
[17] DasGupta, S., Kim, I. Y., and Wayner, Jr., P. C., 1994, ''Use of the Kelvin-Clapeyron Equation to Model an Evaporating Curved Microfilm,'' ASME J. Heat Transfer, **116**, pp. 1007–1015.
[18] Stephan, P., and Busse, C. A., 1992, ''Analysis of the Heat Transfer Coefficient of Grooved Heat Pipe Evaporator Walls,'' Int. J. Heat Mass Transfer, **35**, pp. 383–391.
[19] Swanson, L. W., and Peterson, G. P., 1995, ''The Interfacial Thermodynamics of Micro Heat Pipes,'' ASME J. Heat Transfer, **115**, pp. 195–201.
[20] Morris, S. J. S., 2001, ''Contact Angles for Evaporating Liquids Predicted and Compared With Existing Experiments,'' J. Fluid Mech., **432**, pp. 1–30.
[21] Bankoff, S. G., 1990, ''Dynamics and Stability of Thin Heated Liquid Films,'' ASME J. Heat Transfer, **112**, pp. 538–546.
[22] Ajaev, V. S., and Homsy, G. M., 2001, ''Steady Vapor Bubbles in Rectangular Microchannels,'' J. Colloid Interface Sci., **240**, pp. 259–271.
[23] Anderson, D. M., and Davis, S. H., 1995, ''The Spreading of Volatile Liquid Droplets on Heated Surfaces,'' Phys. Fluids, **7**, pp. 248–265.
[24] Shanahan, M. E. R., 2001, ''Condensation Transport in Dynamic Wetting,'' Langmuir, **17**, pp. 3997–4002.
[25] Zheng, L., Wang, Y.-X., Plawsky, J. L., and Wayner, Jr., P. C., 2002, ''Effect of Curvature, Contact Angle, and Interfacial Subcooling on Contact Line Spreading in a Microdrop in Dropwise Condensation,'' Langmuir, **18**, pp. 5170–5177.
[26] Gokhale, S. J., Plawsky, J. L., and Wayner, Jr., P. C., 2003, ''Experimental Investigation of Contact Angle, Curvature and Contact Line Motion in Dropwise Condensation and Evaporation,'' J. Colloid Interface Sci., **259**, pp. 354–366.
[27] Gokhale, S. J., Plawsky, J. L., and Wayner, Jr., P. C., 2003, ''Effect of Interfacial Phenomena on Dewetting in Dropwise Condensation,'' Adv. Colloid Interface Sci., **104**, pp. 175–190.
[28] Ehrhard, P., and Davis, S. H., 1991, ''Nonisothermal Spreading of Liquid Drops on Horizontal Plates,'' J. Fluid Mech., **229**, pp. 365–388.
[29] Burelbach, J. P., Bankoff, S. G., and Davis, S. H., 1990, ''Steady Thermocapillary Flows of Thin Liquid Layers, II. Experiments,'' Phys. Fluids A, **2**, pp. 322–333.
[30] Sharma, A., 1998, ''Equilibrium and Dynamics of Evaporating or Condensing Thin Fluid Domains: Thin Film Stability and Heterogeneous Nucleation,'' Langmuir, **14**, pp. 4915–4928.
[31] Karthikeyan, M., Huang, J., Plawsky, J. L., and Wayner, Jr., P. C., 1998, ''Experimental Study and Modeling of the Intermediate Section of the Nonisothermal Constrained Vapor Bubble,'' ASME J. Heat Transfer, **120**, pp. 166–173.
[32] Zheng, L., Plawsky, J. L., Wayner, Jr., P. C., and DasGupta, S., 2004, ''Stability and Oscillations in an Evaporating Corner Meniscus,'' ASME J. Heat Transfer, **126**, pp. 169–178.
[33] Zheng, L., Wang, Y.-X., Plawsky, J. L., and Wayner, Jr., P. C., 2002, ''Accuracy of Measurements of Curvature and Apparent Contact Angle in a Constrained Vapor Bubble Heat Exchanger,'' Int. J. Heat Mass Transfer, **45**, pp. 2021–2030.
[34] Gokhale, S. J., Plawsky, J. L., Wayner, Jr., P. C., and DasGupta, S., 2004, ''Inferred Pressure Gradient and Fluid Flow in a Condensing Sessile Droplet Based on the Measured Thickness Profile,'' Phys. Fluids, **16**(6), pp. 1942–1955.
[35] Chen, J. D., and Wada, N., 1992, ''Edge Profiles and Dynamic Contact Angles of a Spreading Drop,'' J. Colloid Interface Sci., **148**, pp. 207–222.
[36] Heslot, F., Fraysee, N., and Cazabat, A. M., 1989, ''Molecular Layering in the Spreading of Wetting Liquid Drops,'' Nature (London), **338**, pp. 640–642.
[37] Heslot, F., Cazabat, A. M., and Levinson, P., 1989, ''Dynamics of Wetting on Tiny Drops: Ellipsometric Study of the Late Stages of Spreading,'' Phys. Rev. Lett., **62**(11), pp. 1286–1289.
[38] Heslot, F., Cazabat, A. M., Levinson, P., and Fraysee, N., 1990, ''Experiments on Wetting on the Scale of Nanometers: Influence of the Surface Energy,'' Phys. Rev. Lett., **65**(5), pp. 599–602.
[39] Kavehpour, H. P., Ovryn, B., and McKinley, G. H., 2003, ''Microscopic and Macroscopic Structure of the Precursor Layer in Spreading Viscous Drops,'' Phys. Rev. Lett., **91**(19), p. 196104.
[40] Churaev, N. V., Esipova, N. E., Hill, R. M., Sobolev, V. D., Starov, V. M., and Zorin, Z. M., 2001, ''The Superspreading Effect of Trisiloxane Surfactant Solutions,'' Langmuir, **17**, pp. 1338–1348.
[41] Dussaud, A. D., and Troian, S. M., 1998, ''Dynamics of Spontaneous Spreading With Evaporation on a Deep Fluid Layer,'' Phys. Fluids, **10**, pp. 23–38.
[42] Kihm, K. D., and Pratt, D. M., 1999, ''Contour Mapping of Thin Liquid Film Thickness Using Fizeau Interferometer,'' *Proc. of 33rd, National Heat Transfer Conference*, Albuquerque, Aug. 15–17, ASME, New York, N.Y., pp. 500–509.
[43] de Gennes, P. G., 1985, ''Wetting: Statics and Dynamics,'' Rev. Mod. Phys., **57**, pp. 827–863.
[44] Joanny, J. F., and de Gennes, P. G., 1986, ''Upward Creep of a Wetting Fluid: A Scaling Analysis,'' J. Phys. (Paris), **47**, pp. 121–127.
[45] Dussan, E. B. V., Rame, E., and Garoff, S., 1991, ''On Identifying the Appropriate Boundary Conditions at a Moving Contact Line: An Experimental Investigation,'' J. Fluid Mech., **230**, pp. 97–116.
[46] Marsh, J. A., Garoff, S., and Dussan, E. B. V., 1993, ''Dynamic Contact Angles and Hydrodynamics Near a Moving Contact Line,'' Phys. Rev. Lett., **70**(18), pp. 2778–2781.
[47] Oron, A., Davis, S. H., and Bankoff, S. G., 1997, ''Long-Scale Evolution of Thin Liquid Films,'' Rev. Mod. Phys., **69**(3), pp. 931–980.
[48] Cazabat, A. M., Heslot, F., Carles, P., and Troian, S. M., 1992, ''Hydrodynamic Fingering Instability of Driven Wetting Films,'' Adv. Colloid Interface Sci., **39**, pp. 61–75.
[49] Hosoi, A. E., and Bush, J. W. M., 2001, ''Evaporative Instabilities in Climbing Films,'' J. Fluid Mech., **442**, pp. 217–239.
[50] Fanton, X., and Cazabat, A. M., 1998, ''Spreading and Instabilities Induced by a Solutal Marangoni Effect,'' Langmuir, **14**, pp. 2554–2561.
[51] Kavehpour, P., Ovryn, B., and McKinley, G. H., 2002, ''Evaporatively-Driven Marangoni Instabilities of Volatile Liquid Films Spreading on Thermally Conductive Substrates,'' Colloids Surf., A, **206**, pp. 409–423.
[52] Ayyaswamy, P. S., Catton, I., and Edwards, D. K., 1974, ''Capillary Flow in Triangular Grooves,'' ASME J. Appl. Mech., **41**, pp. 332–336.
[53] Xu, X., and Carey, V. P., 1990, ''Film Evaporation From a Micro-Grooved Surface-An Approximate Heat Transfer Model and Its Comparison With Experimental Data,'' J. Thermophys. Heat Transfer, **4**, pp. 512–520.

[54] Khrustalev, D., and Faghri, A., 1995, ''Thermal Characteristics of Conventional and Flat Miniature Axially-Grooved Heat Pipes,'' ASME J. Heat Transfer, **117**, pp. 1048–1054.
[55] Wu, D., and Peterson, G. P., 1991, ''Investigation of the Transient Characteristics of a Micro Heat Pipe,'' J. Thermophys. Heat Transfer, **5**, pp. 129–134.
[56] Anand, S., De, S., and DasGupta, S., 2002, ''Experimental and Theoretical Study of Axial Dry Out Point for Evaporation From V-Shaped Microgrooves,'' Int. J. Heat Mass Transfer, **45**, pp. 1535–1543.
[57] Vasicek, A., 1960, *Optics of Thin Films*, Interscience Publishers Inc., New York.
[58] Israelachvili, J. N., 1992, *Intermolecular and Surface Forces*, Second Edition, Academic Press, New York.
[59] Dzyaloshinskii, I. E., Liftshitz, E. M., and Pitaevskii, L. P., 1961, ''The General Theory of van der Waals Forces,'' Adv. Phys., **10**, pp. 165–209.
[60] Zheng, L., 2002, ''Study of Microscale Transport Processes and the Stability of the Thin Film in a Loop Constrained Vapor Bubble,'' Ph.D. thesis, Rensselaer Polytechnic Institute, Troy, NY.
[61] Troung, J. G., and Wayner, Jr., P. C., 1987, ''Effect of Capillary and van der Waals Dispersion Forces on the Equilibrium Profile of a Wetting Liquid: Theory and Experiment,'' J. Chem. Phys., **87**, pp. 4180–4188.
[62] Kalliadasis, S., and Chang, H.-C., 1994, ''Apparent Dynamic Contact Angle of an Advancing Gas-Liquid Meniscus,'' Phys. Fluids, **6**, pp. 12–23.
[63] Sharma, A., 1993, ''Equilibrium Contact Angles and Film Thicknesses in the Apolar and Polar Systems: Role of Intermolecular Interactions in Coexistence of Drops With Thin Films,'' Langmuir, **9**, pp. 3580–3586.
[64] 2003, *CRC Handbook of Chemistry and Physics*, 84 Edition, CRC Press, Cleveland.

Satish G. Kandlikar[1]
e-mail: sgkeme@rit.edu

Wai Keat Kuan

Abhijit Mukherjee

Thermal Analysis and Microfluidics Laboratory,
Department of Mechanical Engineering,
Rochester Institute of Technology,
76 Lomb Memorial Dr.,
Rochester, NY 14623

Experimental Study of Heat Transfer in an Evaporating Meniscus on a Moving Heated Surface

A stable meniscus is formed by a circular nozzle dispensing water over a heated circular face of a rotating cylindrical copper block. The nozzle is offset from the axis of rotation of the copper block and thus a moving meniscus is formed on the surface. The water flow rate, heater surface temperature, and the speed of rotation are controlled to provide a stable meniscus with continuous evaporation of water without any meniscus breakup. The study provides an important insight into the role of the evaporating liquid-vapor interface and transient heat conduction around a nucleating bubble in pool boiling.
[DOI: 10.1115/1.1857948]

Introduction

Heat transfer at the liquid-vapor interface with a moving contact line on a heated surface is of great interest in boiling studies. The meniscus region heat transfer is not well understood, and a direct measurement of heat flux under an evaporating meniscus is useful in providing insight into the associated heat transfer phenomena. The heat transfer around a nucleating bubble is in many respects similar to the advancing and receding motion of the meniscus on a heated surface.

A novel technique is presented in this paper by which we can access the liquid-vapor interface and the contact line region (defined as the region where the liquid-vapor interface meets the heater surface). Figure 1 presents a comparison between a moving meniscus and a nucleating bubble. As the bubble grows, the liquid-vapor interface advances into the liquid; the receding liquid front of a moving meniscus represents this region of the bubble ebullition cycle. As the bubble grows to its departure size, its footprint on the heater surface rapidly shrinks as the liquid front advances over the region that formed the bubble base during the bubble growth period. This region of rewetting is represented by the advancing liquid front of a moving meniscus.

Figure 2 shows the details of a wedge of thin liquid film on a heated surface. Three regions are identified here: (i) *Nonevaporating Adsorbed Thin-Film Region*. In this region, liquid is adsorbed on the heater surface and forms a nonevaporating layer. The molecular forces have controlling influence, and the disjoining pressure reduces the pressure in the liquid and enables it to reside in a supersaturated liquid state. (ii) *Evaporating Thin-Film Region*. Evaporation occurs at the liquid-vapor interface, and liquid is fed from the bulk liquid through the intrinsic meniscus region. Here both the disjoining pressure and the capillary forces play a role. (iii) *Intrinsic Meniscus Region*. The fluid mechanics in this region is governed by the conventional equation of capillarity.

Previous studies on meniscus mainly focused on stationary menisci, which were formed inside or at the outlet end of a capillary or a small diameter tube, or at a straight edge between two intersecting surfaces. The focus of most of these studies [1–23] was the microscale and macroscale heat transfer and fluid mechanics in the vicinity of the stationary contact line region.

A clear influence of the meniscus velocity on heat flux was demonstrated in their early experiments by Kandlikar and Kuan [24,25]. In their experiments, heat flux was found to increase linearly with the meniscus velocity from 0 to 0.38 m/s. Further increase in velocity caused a meniscus breakdown. The variation of advancing and receding contact angles with meniscus velocity was also studied over the range of parameters investigated.

The advantages of studying the meniscus geometry are fairly obvious: (i) the liquid-vapor interface and the contact line region can be viewed clearly without any obstruction from the highly active boiling phenomena occurring around a bubble in pool boiling, and (ii) under stable operating conditions, the liquid flow rate provides a direct measurement of the heat transfer rate over the wetted region bounded by the advancing and receding interfaces.

Literature Review

As mentioned earlier, previous studies on meniscus mainly focused on stationary menisci, which were formed inside or at the outlet end of a capillary or a small diameter tube, or at a straight edge formed between two intersecting surfaces.

In 1978, Wayner [1] stated that viscous flow in a thin film in the immediate vicinity of the interline (junction of solid-liquid-vapor) significantly affects the complete profile of an evaporating meniscus. This change as a function of heat flux was theoretically analyzed based on the premise that fluid flow was caused by the London–van der Waals dispersion force. In their analysis, the change in the apparent contact angle from its intrinsic value was attributed to viscous effects only and did not include a surface roughness effect. The extended meniscus was divided into three zones: (i) the immediate vicinity of the interline (the thin film region), where the thickness of the liquid can vary from a monolayer to approximately 500 Å; (ii) the inner intrinsic meniscus region, where the thickness range is approximately $0.05–10 \times 10^{-6}$ m; and (iii) the outer intrinsic meniscus region, where the thickness is greater than 10^{-5} m.

Holm and Goplen [2] stated in 1979 that very high heat transfer rates have been observed near the triple interline, the junction of the vapor, the evaporating thin film, and the nonevaporating adsorbed thin film. Dropwise condensation was used as an example that exhibits surface heat transfer coefficients that are approximately one order-of-magnitude greater than the coefficients resulting from film condensation. At the same time, Holm and Goplen demonstrated that the extent of interline dispersion at any time can be controlled by using capillary grooves partially filled with a liquid as a means of forming the triple interline region. The heat transfer is augmented by the flow of the liquid into the groove under the action of capillary forces—a passive process. Because

[1]Corresponding author.

Manuscript received August 20, 2003; revision received December 15, 2004. Review conducted by: J. N. Chung.

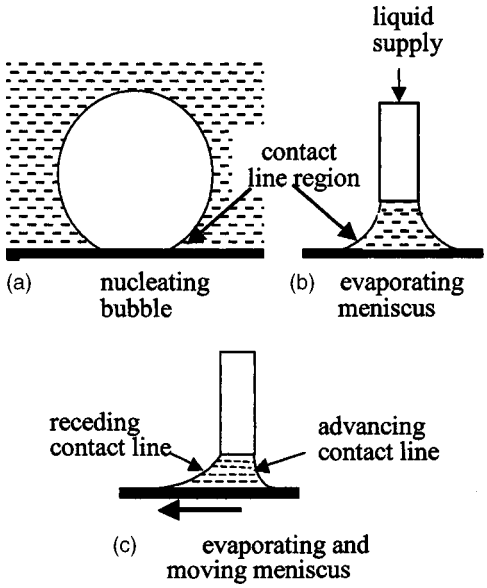

Fig. 1 Similarity between a nucleating bubble and an evaporating meniscus in the contact line region

of the small physical dimensions associated with a meniscus, the local characteristics of the combined heat and mass transfer processes were deduced from overall characteristics, such as (i) total heat transfer from a grooved plate, (ii) overall temperature drops in the walls separating the grooves, and (iii) the temperature difference between the top of the wall and the surrounding vapor.

In 1992, Swanson and Herdt [3] formulated a mathematical model describing the evaporating meniscus in a capillary tube incorporating the full three-dimensional Young-Laplace equation, Marangoni convection, London–van der Waals dispersion forces, and nonequilibrium interface conditions. The governing equations and boundary conditions were cast in terms of five coupled nonlinear ordinary differential equations and solved numerically. The model was tested using various values of the dimensionless superheat and dispersion number.

In 1994, Hallinan et al. [4] determined the effects of evaporation from the thin film region of a liquid-vapor meniscus within the micropores of a heat pipe wick on the interfacial shape, temperature distribution, and pressure distribution.

Khrustalev and Faghri [5] developed a mathematical model of the evaporating liquid-vapor meniscus in a capillary slot in 1996. The model consists of two-dimensional steady-state momentum conservation and energy equations for both the vapor and liquid phases and incorporates the existing simplified one-dimensional model of the evaporating microfilm. A constant wall temperature is assumed in the analysis because the solid wall thermal conductivity is significantly higher than that of liquid.

Kim and Wayner [6] experimentally and theoretically evaluated the microscopic details of fluid flow and heat transfer in the contact line region of an evaporating curved liquid film in 1996. In their experiment, the evaporating film thickness profiles were measured optically using null ellipsometry and image analyzing interferometry. The pressure field was obtained from the thickness profiles using the augmented Young-Laplace equation. Using the liquid pressure field, the evaporative mass flux profile was obtained from a Kelvin-Clapeyron model for the local vapor pressure. An evaporating meniscus was formed in the circular experimental cell with octane as the working fluid.

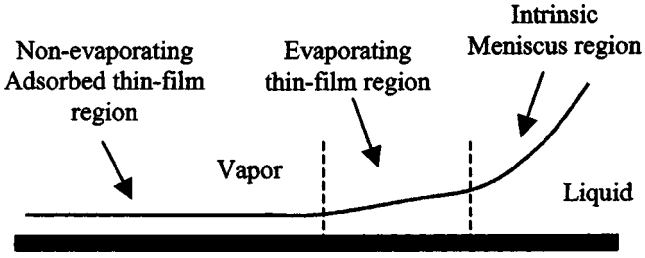

Fig. 2 Details of an evaporating meniscus region

Objectives of the Present Work

The objectives of the present work are as follows:

1. Develop an apparatus to investigate stationary and moving liquid-vapor interface formed by a meniscus on a heated surface
2. Study the interface characteristics such as the advancing and receding contact angles through high speed photographs
3. Obtain quantitative information on the size and shape of the meniscus as a function of meniscus velocity and heater surface temperature
4. Obtain quantitative information on the heat transfer rates from the heated surface to the meniscus base as a function of water flow rate, meniscus velocity, and heater surface temperature

Theoretical Analysis

The heat transfer in the meniscus region is modeled as consisting of three main features:

1. Transient heat conduction between the the heater surface and the water
2. Evaporation of water along the receding liquid-vapor interface
3. Recirculation and mixing of the unevaporated water behind the advancing liquid-vapor interface with the incoming water

The recirculated and fresh incoming water streams are mixed as they flow behind the advancing liquid-vapor interface. The temperature of this mixed stream depends on the recirculation rate and the temperature of the incoming water.

Figure 3 identifies different flow regions considered in the present model. The inlet stream is identified as stream A, the mixed stream is identified as stream B, while stream C represents the water flowing over the heater surface encountering transient heat conduction, stream D is the fluid flow behind the receding interface, and stream E represents the evaporating water. Since the meniscus is stable, the inlet and the evaporating streams (A and E) are equal.

The transient heat transfer between the heater surface and water is dictated by the relative thermal diffusivities of water and the heated copper block. The instantaneous temperature of the interface of two semi-infinite mediums is given by Schneider [26] in the following:

$$T_{ins,S-W}=\frac{(k\rho c_p)_S^{1/2}T_{S,i}+(k\rho c_p)_W^{1/2}T_{W,i}}{(k\rho c_p)_S^{1/2}+(k\rho c_p)_W^{1/2}} \quad (1)$$

For an initial surface temperature of copper block of 108°C, and a water temperature of 100°C, using Eq. (1) we obtain $T_{ins,S-W}=107.65$°C. Because of the large thermal diffusivity of copper, the surface temperature is found to be close to the initial temperature of the copper block. Therefore, the interface temperature to be the same as the initial temperature of the copper block, and the transient heat transfer is modeled as the semi-infinite medium in water coming in contact with a constant temperature of the heater surface.

A detailed numerical study of a two-dimensional moving and evaporating meniscus was conducted by Mukherjee and Kandlikar

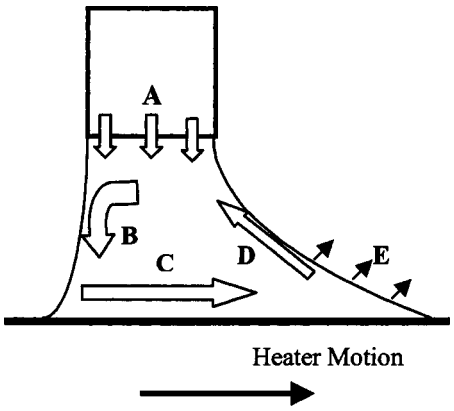

Fig. 3 Identifying various streams in a meniscus moving over a moving heater surface: (*a*) fresh water inlet, (*b*) recirculating mixed stream, (*c*) water stream in transient heat conduction with the heater surface, (*d*) water stream flowing behind the receding interface, and (*e*) evaporating vapor stream

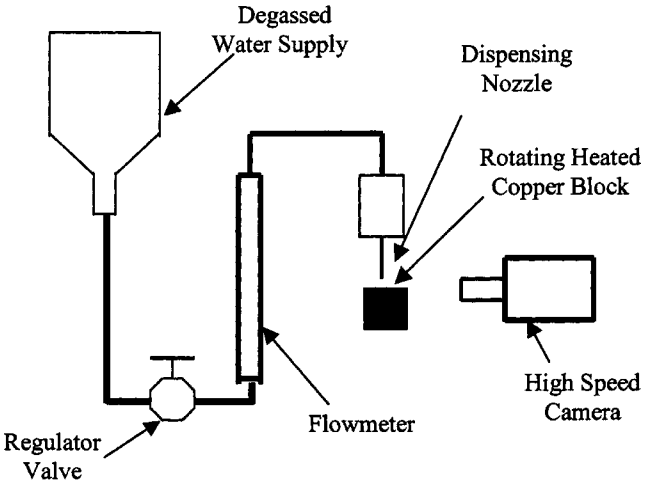

Fig. 5 Experimental setup

[27]. The complete Navier-Stokes equations along with continuity and energy equations were solved. Circulation of liquid was observed inside the meniscus. Figure 4 shows the numerical results for recirculation of liquid inside the meniscus. The circulation pattern is seen to be similar to that shown in Fig. 3. The numerical results also showed that the heat transfer rate near the advancing liquid front was the highest due to transient conduction between the heater and the recirculated liquid. In the present work, heat transfer rates are experimentally measured over the entire meniscus region.

Experimental Setup and Experimental Procedure

Figure 5 shows a schematic of the experimental setup with the water delivery system and the rotating heated copper block. The fluid delivery system is designed to deliver degassed and deionized water to the dispensing nozzle using gravitational head. The fluid delivery system includes a degassed water pouch, a flow meter with attached regulator valve, and a dispensing nozzle.

Figure 6 shows the schematic of the stationary test section used in the present study. A copper block with a 10 mm dia cylindrical extension is used as the heated surface. It is heated with the cartridge heater as shown. The top surface of the copper block is polished with 1 μm slurry in the final stage of polishing. The polished surface prevents any boiling inside the meniscus by removing large-sized nucleation cavities. This allows a superheat of around 8–10°C without nucleation occurring inside the meniscus, thus providing a stable evaporating meniscus.

Figure 7 shows the schematic of a rotating test section. A copper block 37 mm in diameter and 63 mm long is placed on an insulating and support disk with four screw attachments to minimize the conduction losses. The top surface of the copper block is also polished with the 1 μm slurry in the final stage of polishing. The assembly is then mounted on the shaft of an electric motor whose rotational speed can be closely controlled by supplying voltage from a digitally regulated power source. The test section is heated to the desired temperature by adjusting the temperature of an electric blower that blows hot air over the cylindrical surface of the copper block. The airflow is shielded from the heater surface as shown. A simple thermocouple probe is used to measure the temperature by stopping the rotation and inserting the probe in a hole made in the copper block. Because of the large mass of the copper block, the temperature does not change during the measurement. The copper surface is made level and true to the rotational axis so that the distance between the needle and the heater surface does not change as the motor turns the heater assembly. The needle is positioned at a certain radial distance from the center of rotation. This provides the necessary relative velocity as the

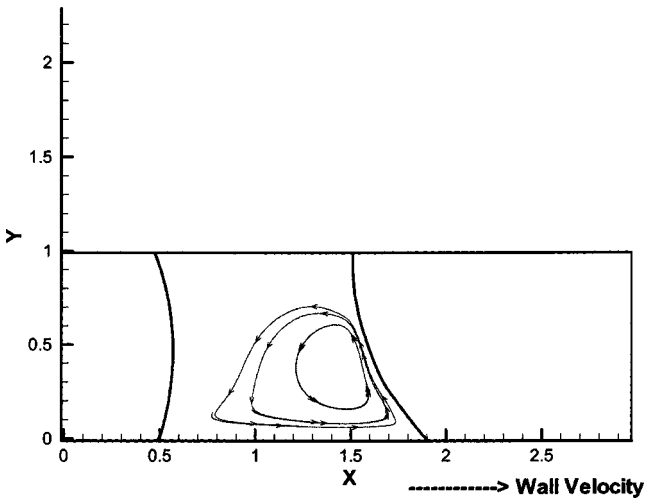

Fig. 4 Liquid circulation inside a moving and evaporating meniscus[27]

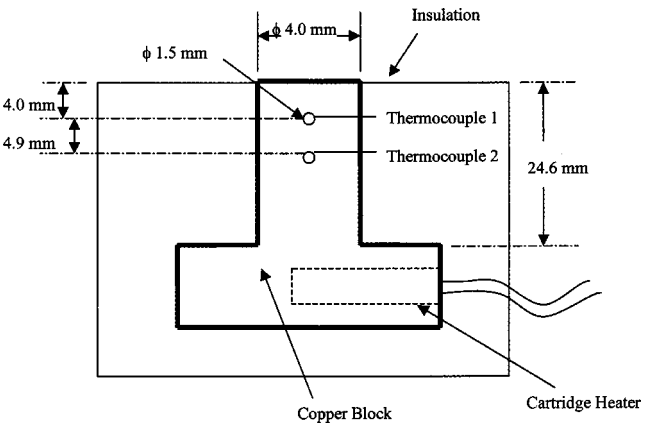

Fig. 6 Stationary test section schematic

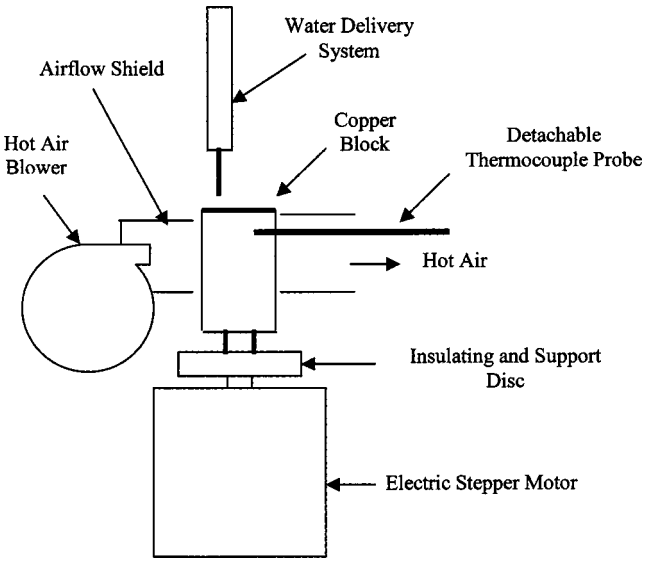

Fig. 7 Rotating test section schematic

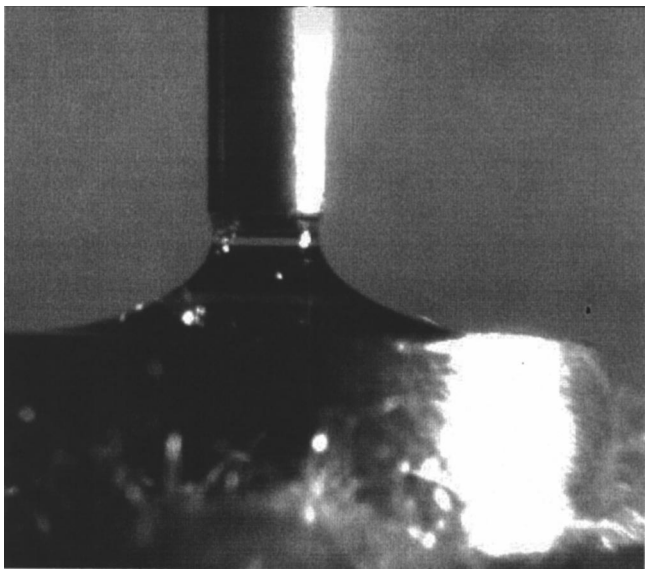

Fig. 8 Stationary meniscus at 108°C

heater surface turns. By adjusting the voltage to the electric motor, the rotational speed of the heated copper block can be closely controlled.

The images of the meniscus are obtained using a microscopic lens attached to two high-speed cameras that are both capable of recording frame rates of up to 8000 fps. The cameras are mounted on tripods and are located at an angle of 90 deg apart from each other. Using two cameras, we can obtain the width and length of the meniscus. Under stable operating conditions, all water supplied through the needle is evaporated; this provides accurate information regarding the heat transfer rate from the evaporating meniscus under various operating conditions.

Experimental Uncertainties

The velocity of the rotating surface, the heater surface temperature, and the flow rate of water are three major parameters in this study. The flow rate of water is measured using a precision flow meter that is calibrated by actual measurement of flow using a chemical weighing scale over a 5 min period. The accuracy of flow measurement is within $\pm 2\%$. The temperature measurement is accurate to within $\pm 0.1°C$. The rotational speed is measured by calibrating the speed versus supply voltage. This is done in the vision software using the time steps with an indicator located on the rotating copper block. The error in measuring the distance of meniscus from the center of rotation is estimated to be 0.5 mm. The overall error in velocity measurement is estimated to be $\pm 3\%$.

The accuracy of combined advancing contact line angle and receding contact angle measurement is within ± 1 deg. The error in measuring the area of meniscus that is in contact with the heated surface is estimated to be $\pm 8\%$. The error in measuring the heat flux is estimated to be $\pm 11\%$.

Results

The advancing and receding contact angles and heat transfer results for stationary and moving menisci are presented in this section. For the stationary meniscus, the contact angles are repre-

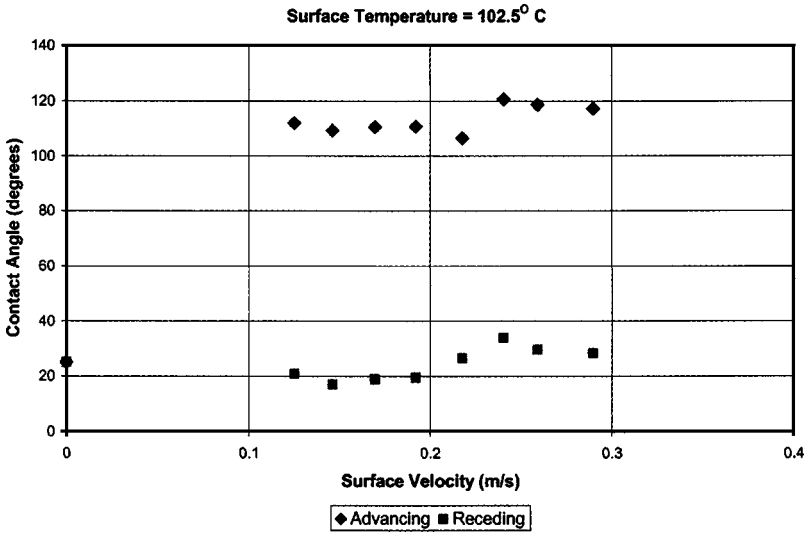

Fig. 9 Plot of receding and advancing contact angles versus surface velocity at 0.016 mL/min and surface temperature of 102.5°C

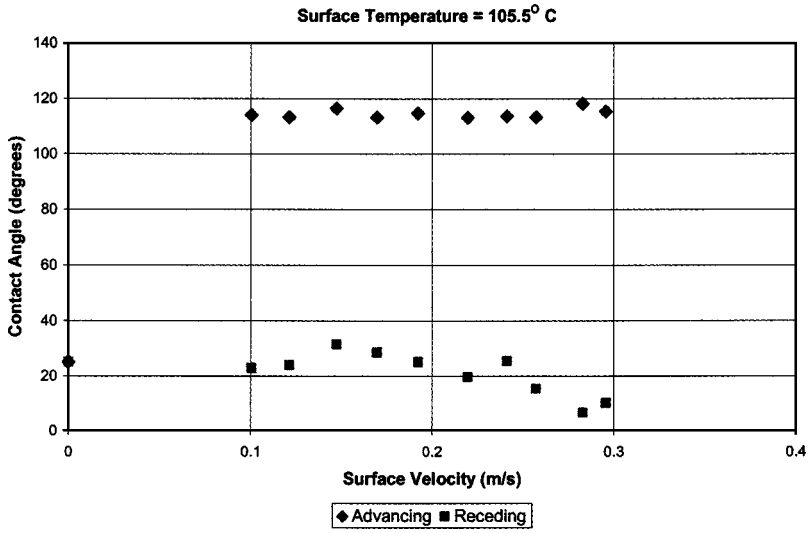

Fig. 10 Plot of receding and advancing contact angles versus surface velocity at 0.016 mL/min and surface temperature of 105.5°C

sentative of the equilibrium contact angle. These are expected to fall between the advancing and the receding contact angle values. Figure 8 shows a typical stationary meniscus at 8°C superheat.

In the case of the rotating heater, the moving meniscus presents dynamic advancing and dynamic receding contact angles. These are measured from the images obtained with the high-speed camera. These images are transported into PRO-Engineering software program and then the respective angles are measured.

Figures 9–11 show the plots of the advancing and receding contact angles as a function of the relative surface velocity. The water mass flow rate is at a constant value of 0.016 mL/min. The surface temperatures are 102.5°C, 105.5°C, and 108°C, respectively. The zero velocity point corresponds to the stationary meniscus. For the stationary meniscus, the contact angle is found to be almost independent of the wall superheat.

In Fig. 9 as the surface velocity increases, the advancing and receding contact angles are found to be almost constant. In Fig. 10 as the surface velocity increases, the receding contact angle remains almost constant in the beginning but then decreases for higher velocities. In Fig. 11, as the relative surface velocity increases, a larger scatter is seen in the contact angles. The operation became unstable at this temperature, with occasional meniscus breakage. The large scatter in contact angles seen in Fig. 11 are caused by interface instabilities set in by the high evaporation rate at the higher surface temperature of 108°C.

The surface heat flux under the meniscus area is calculated from the known water flow rate and the inlet temperature. Heat transferred in this region goes into heating the water from the inlet temperature to the saturation temperature of 100°C, and then evaporating it into steam at atmospheric pressure.

Thus q'' is given by

$$q''=\frac{[\dot{m}h_{fg}+\dot{m}C_p(100^\circ\mathrm{C}-T_{in})]}{A} \tag{2}$$

where A is the footprint area of the meniscus.

The inlet temperature of water T_{in} is 20°C. The area for stationary meniscus is πr^2, and for the moving meniscus, the base surface area is calculated from the measured length, width, and shape of the footprint of the meniscus base.

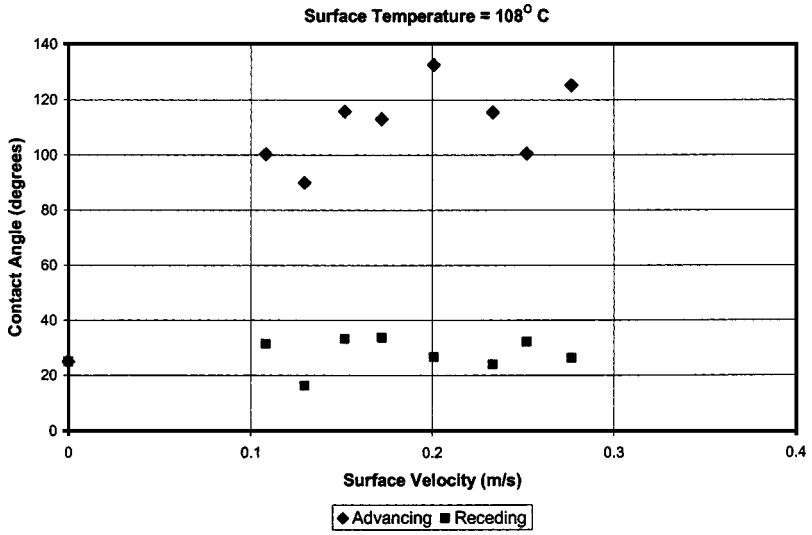

Fig. 11 Plot of receding and advancing contact angles versus surface velocity at 0.016 mL/min and surface temperature of 108°C

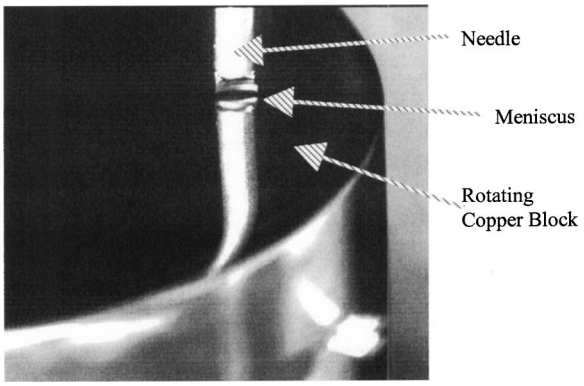

Fig. 12 Front view of moving meniscus

Figure 12 shows front view of the meniscus on the moving heated surface. The meniscus base width is measured at the contact line of the meniscus image and its reflection on the polished copper surface.

The length of the meniscus is obtained from Fig. 13, which shows the side view. The edge of the meniscus is found to be very clearly visible at both advancing and receding interfaces and no thin liquid films are observed. Presence of thin films in the contact regions is expected to show a change in reflected light from the copper surface. The top views of the receding interface shows a sharp and clear edge of the meniscus with no changes in reflectivity of light beyond it on the heater surface.

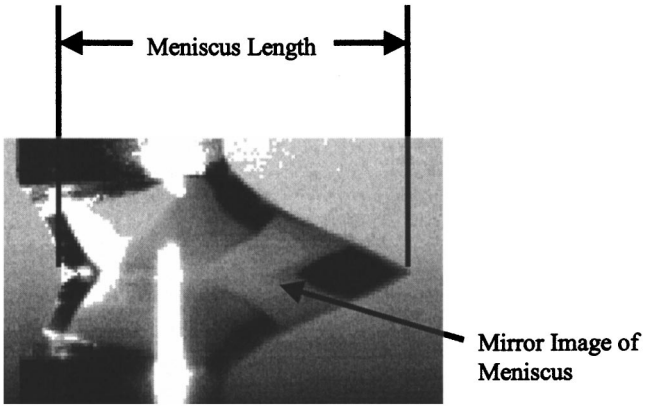

Fig. 13 Side view of moving meniscus

The meniscus base footprint is approximated as an ellipse with a major diameter given by its length and a minor diameter given by the width. The meniscus base area is thus calculated by measuring the length and width of the meniscus.

The heat transfer results are presented in terms of the measured heat flux as a function of surface velocity. Figures 14 and 15 show this variation for two different heater surface temperatures. It can be seen that there is a systematic dependence of heat flux on the surface velocity and surface temperature. At lower velocities, the heat flux is relatively insensitive to velocity. However, as the surface velocity increases the heat flux increases almost linearly as the transient conduction process becomes more efficient. Also, we note that the amount of scatter in the data increases with an increase in wall superheat, which is believed to be due to interface instability.

As seen in Figs. 16 and 17, the meniscus length decreases when the relative surface velocity increases because of increased transient conduction from the wall and subsequently higher evaporation rates.

Figure 18 shows the images of menisci for a constant surface temperature of 105.5°C and at a constant water mass flow rate of 0.016 mL/min with varying surface velocities. Note that the thin film region can be seen at the pointy edge in Figs. 18(*a*) and 18(*b*). This thin film region disappears from Fig. 18(*c*) to 18(*e*). The present visualization scheme allows for a detection of meniscus thickness of 1–2 μm.

Comparision with Bubble Dynamics in Pool Boiling

In our experiments, for the relative surface velocity of 0.1 m/s and with 8°C excess temperature, the experimentally obtained heat flux value is about 150 kW/m^2. The heat flux values taken from the boiling curve (e.g., Incropera [28]) for 110°C is 100 kW/m^2. Thus, the advancing and receding motion of the meniscus provides heat transfer rates that are higher than the nucleate boiling values.

In the present experimental setup, the advancing and receding interfaces are exposed to air. Although the high evaporation rate at the receding interface is not expected to be affected by this, the presence of air is expected to increase the evaporation rate from the advancing interface due to the low partial pressure of water vapor in the air. A mass transfer analysis is performed to estimate

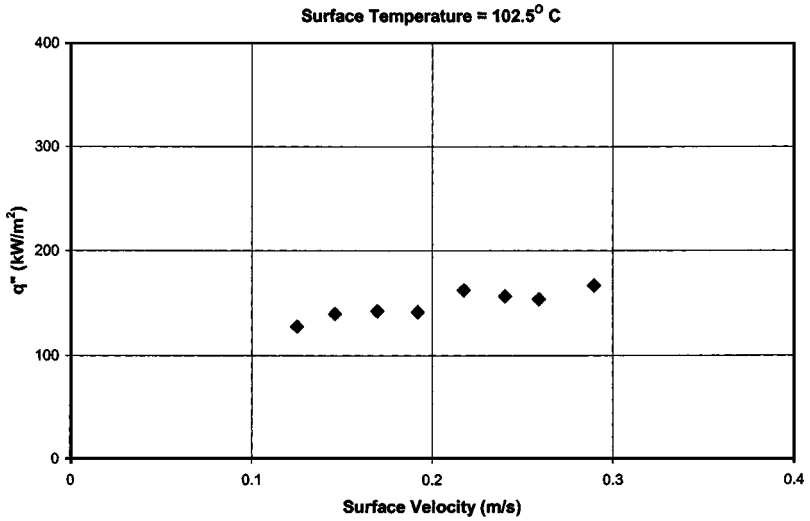

Fig. 14 Variation of heat flux with surface velocity at 0.016 mL/min for heater surface temperature of 102.5°C

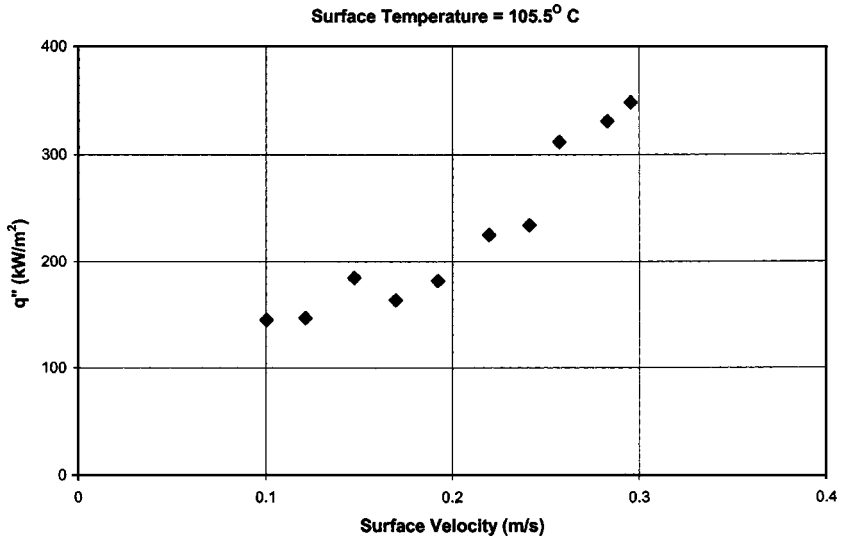

Fig. 15 Variation of heat flux with surface velocity at 0.016 mL/min for heater surface temperature of 105.5°C

this evaporative heat transfer rate from the advancing interface. The heat loss from the advancing interface to the air is estimated to be less than 10% of the total heat transfer rate under the present experimental conditions. In a pool boiling system, the heat transfer rate from the advancing interface will be lower as the interface is exposed to saturated steam and not the air. This could be one of the reasons why the experimental heat transfer rates obtained in the present work are higher than the pool boiling values. It is recommended that the surrounding air be replaced by a saturated vapor environment in future experiments to accurately simulate the pool boiling conditions.

Another reason for the discrepancy between the heat fluxes for meniscus and pool boiling system is that the present experimental system focuses only in the region bounded between the advancing and receding interfaces. In a boiling system, the actual liquid area contacting the heater surface would be quite different.

Conclusions

An experimental investigation is conducted to study the characteristics of an evaporating meniscus on a smooth heated surface. The heat transfer characteristics are also investigated for both stationary and moving menisci. The study provides an important insight on the role of transient conduction around a nucleating bubble in pool boiling. The following conclusions are drawn from the present study.

1. For the stationary meniscus, the contact angle is almost independent of the wall superheat in the range of parameters investigated. It is seen to be almost constant at an angle of 26 deg for deionized water on polished copper surface.

2. In the case of a moving meniscus, as the surface velocity increases, the receding contact angle is found to vary whereas the

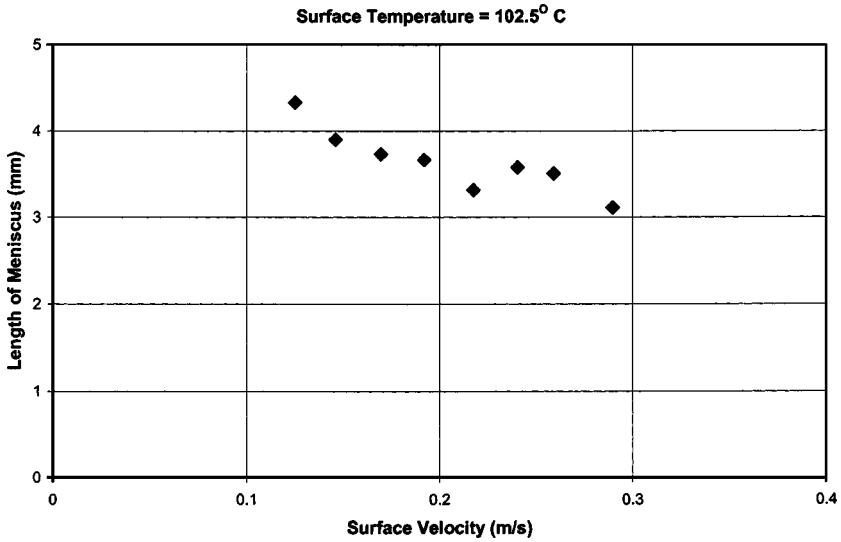

Fig. 16 Variation of meniscus length with surface velocity at 0.016 mL/min for heater surface temperature of 102.5°C

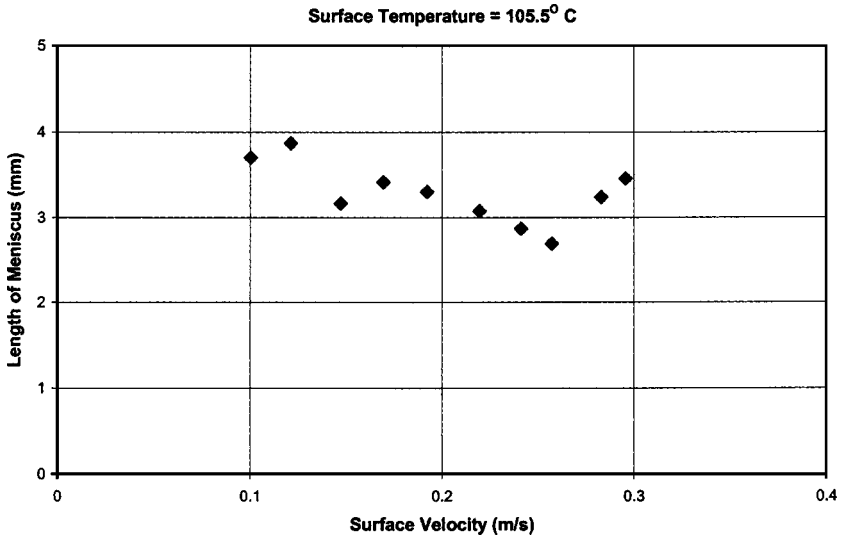

Fig. 17 Variation of meniscus length with surface velocity at 0.016 mL/min for heater surface temperature of 105.5°C

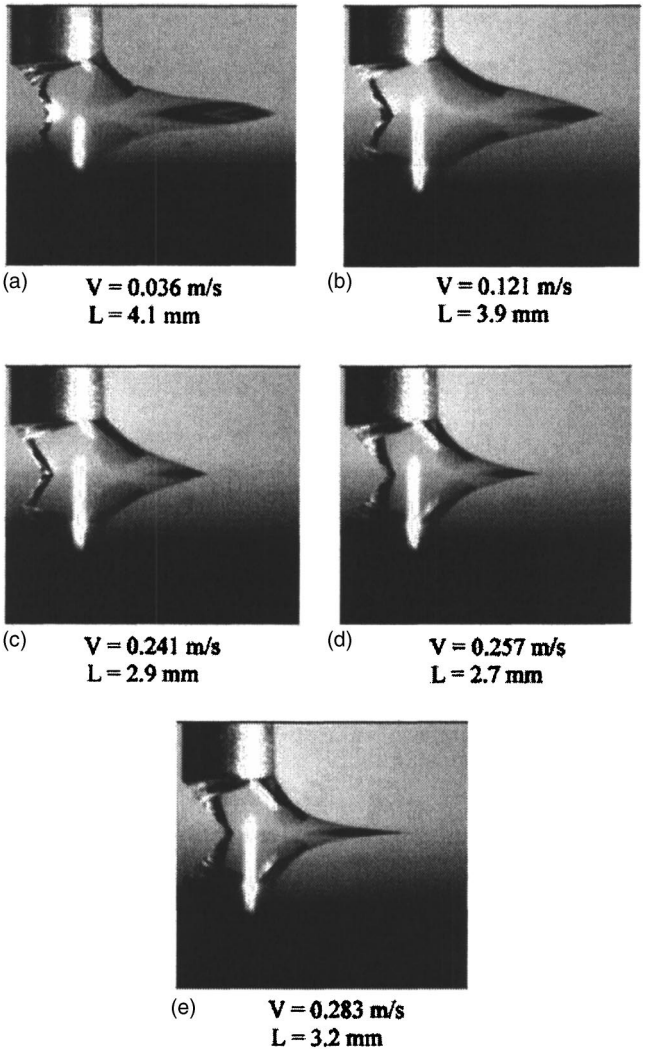

Fig. 18 Meniscus length *L* for different surface velocities at 0.016 mL/min at heater surface temperature of 105.5°C

advancing contact angle is found to remain almost constant. However, at high wall superheat of 108°C the meniscus became unstable and considerable scatter was observed in the contact angle measurements.

3. The heat flux at the meniscus footprint increases with the relative velocity.

4. The advancing and receding motion of the meniscus provides heat transfer rates that are higher than the average values during nucleate boiling.

Acknowledgment

All of the work was conducted in the Thermal Analysis Laboratory at RIT. The support provided by Rochester Institute of Technology is gratefully acknowledged.

Nomenclature

A = area, m^2
c_p = specific heat of water at constant pressure, J/kg-°C
h_{fg} = latent heat of vaporization, J/kg
k = thermal conductivity, W/m-°C
L = distance between the advancing and receding fronts along the heater surface, m
$\dot{m}$ = mass flow rate, kg/s
q'' = heat flux, W/m^2
r = radius of stationary meniscus base
T_{in} = water supply temperature, °C
$T_{W,i}$ = initial water temperature at the inlet to the transient conduction region, °C
$T_{S,i}$ = initial heater surface temperature at for the transient conduction, same as the heater block temperature, °C
$T_{ins,S-W}$ = instantaneous temperature of the interface of two semi-infinite medium, °C

Subscripts

i = initial
ins = instantaneous
s = solid
w = water

Greek Letters

α = thermal diffusivity, m^2/s
ρ = density, kg/m^3

References

[1] Wayner, Jr., P. C., 1978, ''The Effect of Thin Film Heat Transfer on Meniscus Profile and Capillary Pressure,'' AIAA J., **17**(7), pp. 772–776.

[2] Holm, F. W., and Golpen, S. P., 1979, ''Heat Transfer in the Meniscus Thin Film Transition Region,'' ASME J. Heat Transfer, **101**, pp. 543–547.

[3] Swanson, L. W., and Herdt, G. C., 1992, ''Model of the Evaporating Meniscus in a Capillary Tube,'' ASME J. Heat Transfer, **114**(2), pp. 434–441.

[4] Hallinan, K. P., Chebaro, H. C., Kim, S. J., and Chang, W. S., 1994, ''Evaporation from an Extended Meniscus for Non-isothermal Interfacial Conditions,'' J. Thermophys. Heat Transfer, **8**(4), pp. 709–716.

[5] Khrustalev, D., and Faghri, A., 1996, ''Fluid Flow Effects in Evaporation From Liquid Vapor Meniscus,'' ASME J. Heat Transfer, **118**(3), pp. 725–731.

[6] Kim, I. Y., and Wayner, Jr., P. C., 1996, ''Shape of an Evaporating Completely Wetting Extended Meniscus,'' J. Thermophys. Heat Transfer, **10**(2), pp. 320–326.

[7] DasGupta, S., Schonberg, J. A., and Wayner, P. C., 1993, ''Investigation of an Evaporating Extended Meniscus Based on the Augmented Young-Laplace Equation,'' ASME J. Heat Transfer, **115**, pp. 201–208.

[8] Derjaguin, B. V., 1940, ''A Theory of Capillary Condensation in the Pores of Sorbents and Other Capillary Phenomena Taking Into Account the Disjoining Action of Polymolecular Liquid Films,'' Acta Physicochim. URSS, **12**(1), pp. 181–200.

[9] Derjaguin, B. V., Nerpin, S. V., and Churaev, N. V., 1965, ''Effect of Film Transfer Upon Evaporating Liquids From Capillaries,'' RILEM Bull, **29**(1), pp. 93–98.

[10] Lay, J. H., and Dhir, V. K., 1995, ''Shape of a Vapor Stem During Nucleate Boiling of Saturated Liquids,'' ASME J. Heat Transfer, **117**, pp. 394–401.

[11] Nikolayev, V. S., and Beysens, D. A., 1999, ''Boiling Crisis and Non-equilibrium Drying Transitions,'' Europhys. Lett., **47**(3), pp. 345–351.

[12] Pierret, R. F., 1996, *Semiconductor Device Fundamentals, Solutions Manual*, Addison-Wesley, Reading, MA, pp. 6.12

[13] Potash, Jr., M., and Wayner, Jr., P. C., 1972, ''Evaporation From a Two-Dimensional Extended Meniscus,'' Int. J. Heat Mass Transfer, **15**, pp. 1851–1863.

[14] Schonberg, J. A., 1995, ''An Augmented Young-Laplace Model of an Evaporating Meniscus in a Microchannel With High Heat Flux,'' *Experimental Thermal and Fluid Science 1995*, Elsevier Science, New York, pp. 163–170.

[15] Sefiane, K., Benielli, D., and Steinchen, A., 1998, ''A New Mechanism for Pool Boiling Crisis, Recoil Instability, and Contact Angle Influence,'' Colloids Surf., A, **142**, pp. 361–373.

[16] Shoji, M., Mori, Y. H., and Maruyama, S., 1999, Representation of Solid-Liquid-Vapor Phase Interactions, *Handbook of Phase Change-Boiling and Condensation*, S. G. Kandlikar, M. Shoji, and V. K. Dhir, eds. Taylor and Francis, Philadelphia, Chap. 6, Sec. 2.2.6.

[17] Son, G., Dhir, V. K., and Ramanajapu, N., 1999, ''Dynamics and Heat Transfer Associated With a Single Bubble During Nucleate Boiling on a Horizontal Surface,'' ASME J. Heat Transfer, **121**, pp. 623–631.

[18] Sujanani, M., Wayner, Jr., P. C., 1992, ''Transport Processes And Interfacial Phenomena in an Evaporating Meniscus,'' Chem. Eng. Commun., **118**, pp. 89.

[19] Wayner, Jr., P. C., 1991, ''The Effect of Interfacial Mass Transport in Thin Liquid Films,'' Colloids Surf., **52**, pp. 71–84.

[20] Wayner, P. C., Jr., 1992, ''Evaporation and Stress in the Contact Line Region,'' *Proc. Conference on Pool and External Flow Boiling*, Santa Barabra, V. K. Dhir, and A. E. Bergles, eds., Engineering Foundation, New York, pp. 251–256.

[21] Wayner, Jr., P. C., 1994, ''Thermal and Mechanical Effects in the Spreading of a Liquid Film Due to a Change in the Apparent Finite Contact Angle,'' ASME J. Heat Transfer, **116**, pp. 938–945.

[22] Wayner, P. C., Jr., DasGupta, S., and Schonberg, J. F., 1991, ''Effect of Interfacial Forces on Evaporating Heat Transfer in a Meniscus,'' Technical Report WL-TR-91, Wright-Patterson AFB, Ohio.

[23] Wayner, Jr., P. C., Kao, Y. K., and Lacroix, L. V., 1976, ''The Interline Heat Transfer Coefficient of an Evaporating Wetting Film,'' Int. J. Heat Mass Transfer, **19**(2), pp. 487–492.

[24] Kandlikar, S. G., and Kuan, W. K., 2003, ''Circular Evaporating Meniscus: A New Way to Study Heat Transfer Mechanism During Nucleate Boiling,'' 5th International Conference on Boiling Heat Transfer 2003, Jamaica, May 4–8.

[25] Kandlikar, S. G., and Kuan, W. K., 2003, ''Heat Transfer From a Moving and Evaporating Meniscus on a Heated Surface,'' ASME Summer Heat Transfer Conference 2003, Las Vegas, July 20–23.

[26] Schneider, P. J., 1955, *Conduction Heat Transfer*, Addison-Wesley, Reading, MA.

[27] Mukherjee, A., and Kandlikar, S. G., 2004, ''Numerical Study of an Evaporating Meniscus on a Moving Heated Surface,'' ASME Summer Heat Transfer Conference 2004, Charlotte NC, July 11–15, HT-FED2004-56678.

[28] Incropera, F. P., and DeWitt, D. P., 2002, *Pool Boiling, Fundamentals of Heat and Mass Transfer*, John Wiley and Sons, Inc., New York, Chap. 10, Sec. 10.3.2.

J. Y. Tu
School of Aerospace, Mechanical, and Manufacturing Engineering,
RMIT University,
Vic. 3083, Australia

G. H. Yeoh
e-mail: Guan.Yeoh@ansto.gov.au
Australian Nuclear Science and Technology Organization (ANSTO),
PMB 1, Menai, NSW 2234, Australia

G.-C. Park

M.-O. Kim

Department of Nuclear Engineering,
Seoul National University,
San 56-1 Sinlim-dong, Gwanak-gu,
Seoul 151-742, Korea

On Population Balance Approach for Subcooled Boiling Flow Prediction

The capability of using the population balance approach combined with a three-dimensional two-fluid model for predicting subcooled boiling flow is investigated. Experiments were conducted to study the local flow characteristics of subcooled boiling flow and to provide measured local two-phase flow parameters. Calculations were performed using the newly developed population balance boiling model to study the effects of various factors on numerical predication of local two-phase flow parameters in the subcooled boiling regime. Comparison of model predictions against local measurements was made for the radial distribution of the bubble Sauter diameter and void fraction covering a range of different mass and heat fluxes and inlet subcooling temperatures. Additional comparison using recent active nucleation site density models and empirical relationships to determine the local bubble diameter adopted by other researchers was also investigated. Overall, good agreement was achieved between predictions and measurements using the newly formulated population balance approach based on the modified MUSIG (multiple-size-group) model for subcooled boiling and two-fluid model.
[DOI: 10.1115/1.1857952]

1 Introduction

Application of the population balance approach toward better describing and understanding complex industrial flow systems has received unprecedented attention and acceptance. Ramkrisha and Mahoney [1], in their review of population balance models, have highlighted a promising future adopting such an approach toward handling two-phase flow systems. Lately, mounting interest on population balances has resulted in a number of significant developments, especially toward modeling bubbly flows. Several studies that were conducted using the computational fluid dynamics (CFD) models with population balances have been reported in Krishna et al. [2], Shimizu et al. [3], Pohorecki et al. [4], and Olmos et al. [5]. The use of CFD and population balance models has been shown to expedite a more in-depth understanding of different flow regimes and further enhance the description of the bubble characteristics in the column volume for design, especially with the consideration of bubble coalescence and breakup mechanisms in the model simulations.

Although considerable efforts have been invested to develop more sophisticated models for bubble migration, attention of the transport processes is still very much focused on isothermal bubbly flow problems. Hence, there is an increasing need for further development toward a more robust mathematical model capable of handling complex phenomena associated with hydrodynamics, heat and mass transfer, and bubble coalescence and breakup. Subcooled boiling flow belongs to a specific category of bubbly flows where it embraces all the complex dynamic interaction of the aforementioned phenomena. Through fundamental experiments, an accurate knowledge of distributions of the local two-phase flow parameters can be obtained, which are crucial to the eventual understanding and modeling of interfacial transfer terms required for a mechanistic multidimensional analysis of a two-phase field. The majority of the fundamental experimental studies focused primarily on adiabatic two-phase flows [6–13]. Moreover, data measured from these experiments concerned only on the overall effects of the two-phase flow field domain instead of local behavior that would allow a more fundamental development of the mechanistic models for the bubble interaction with the fluid. Extensive local measurements are still very much in short supply, and there is an urgent need for a wide range of heat fluxes and flow conditions for subcooled boiling flows.

In our comprehensive investigation on axial void fraction distribution in channels, we achieved good agreement of the boiling flow model against a wide range of experimental data [14,15]. Improvements made to the boiling flow model include modifications to interphase heat transfer, mean bubble diameter in the bulk liquid and wall heat partition model. Further investigations in Yeoh et al. [16] for local radial measurements of a low-pressure subcooled boiling annular channel flow revealed significant weakness of the model, predominantly in the radial prediction of the bubble Sauter diameter and the liquid and vapor velocities. Empirical correlation applied for our axial comparison exercise that determines the bubble size in the bulk subcooled liquid was derived to only predict the macroscopic consideration of the boiling phenomenon. It is therefore not surprising that numerical models that employed this sort of relationship were unable to adequately represent the important complex mechanistic behaviors of bubble coalescence and condensation (microscopic in nature) as observed through experiments. The absence of the bubble mechanistic behavior, such as bubble coalescence clearly observed during experiments in the vicinity of the heated wall and the condensation on the unheated flow region, significantly compromised the model predictions especially the bubble Sauter diameter distribution. In the commonly used two-fluid CFD model for multiphase flow applications, the phase interaction terms appear in the field equations, which represent the contribution of the mass, momentum, and energy transfers through the interface between the phases. As the bubble Sauter diameter appears in the interfacial terms between the liquid and gas phases, an accurate determination of the bubble Sauter diameter is important as the bubble size significantly influences the interphase momentum, such as the drag force and heat and mass transfer through the interfacial area concentrations.

Because of the considerable success of employing population balances, especially the feasibility to accurately account the merging and fragmentation characteristics of bubbles in adiabatic bubbly flow systems, the approach presents great potential toward modeling and prediction of nonuniform bubble size distribution in subcooled boiling flows. Such capability does not exist in the

Manuscript received November 12, 2003; revision received November 17, 2004. Review conducted by: J. N. Chung.

current state of the art. An investigation on the capability of using the population balance approach for subcooled boiling flows was conducted. The aim is to develop a better understanding of the complex phenomena associated with hydrodynamics, heat and mass transfer, and bubble coalescence and condensation in subcooled boiling flow as observed through experimental observations. Numerical simulations using the population balance approach based on the MUSIG (multiple-size-group) model coupled with the two-fluid CFD boiling model in the generic computer code CFX4.4 are also conducted. This new MUSIG boiling model is evaluated through comparisons against experimental measurements of local two-phase quantities.

2 Numerical Formulation

2.1 Flow Equations. The two-fluid model, treating both the vapor and liquid phases as continua, solves two sets of conservation equations governing mass, momentum, and energy, which are written for each phase as

Continuity Equation of Liquid Phase

$$\frac{\partial \rho_l \alpha_l}{\partial t} + \nabla(\rho_l \alpha_l \vec{u}_l) = \Gamma_{lg} \tag{1}$$

Continuity Equation of Vapor Phase

$$\frac{\partial \rho_g \alpha_g f_i}{\partial t} + \nabla(\rho_g \alpha_g \vec{u}_g f_i) = S_i - f_i \Gamma_{lg} \tag{2}$$

Momentum Equation of Liquid and Vapor Phases

$$\begin{aligned}\frac{\partial \rho_k \alpha_k \vec{u}_k}{\partial t} &+ \nabla(\rho_k \alpha_k \vec{u}_k \vec{u}_k) \\ &= -\alpha_k \nabla P + \alpha_k \rho_k \vec{g} + \nabla\{\alpha_k \mu_k^e [\nabla \vec{u}_k + (\nabla \vec{u}_k)^T]\} \\ &+ \sum_{j=1, j\neq k}^{2} (\Gamma_{kj} \vec{u}_j - \Gamma_{jk} \vec{u}_k) \\ &+ \sum_{j=1, j\neq k}^{2} \mathrm{F}_{kj} \quad (kj = lg, jk = gl)\end{aligned} \tag{3}$$

Energy Equation of Liquid and Vapor Phases

$$\begin{aligned}\frac{\partial \rho_k \alpha_k H_k}{\partial t} &+ \nabla(\rho_k \alpha_k \vec{u}_k H_k) \\ &= Q_k + \nabla(\alpha_k \lambda_k^e \nabla T_k) \\ &+ \sum_{j=1, j\neq k}^{2} (\Gamma_{kj} H_j - \Gamma_{jk} H_k) \quad (kj = lg, jk = gl)\end{aligned} \tag{4}$$

In Eq. (1), Γ_{lg} represents the mass transfer rate due to condensation in the bulk subcooled liquid, which is expressed by

$$\Gamma_{lg} = \frac{h a_{if} (T_{sat} - T_l)}{h_{fg}} \tag{5}$$

where h is the interphase heat transfer coefficient and a_{if} is the interfacial area per unit volume. The heat transfer coefficient has been determined from Ranz and Marshall [17], Nusselt number correlation. The wall vapor generation rate is modeled in a mechanistic way, derived by considering the total mass of bubbles detaching from the heated surface as

$$\Gamma_{gl} = \frac{Q_e}{h_{fg} + C_{pl} T_{sub}} \tag{6}$$

where Q_e is the heat transfer due to evaporation. This wall nucleation rate is accounted in Eq. (6) as a specified boundary condition apportioned to the discrete bubble class or classes based on the size of the bubble departure criteria on the heated surface. On the right-hand side of Eq. (2), S_i represents the additional source terms due to coalescence and breakup based on the formulation, which are described in Section 2.2. The term $f_i \Gamma_{lg}$ represents the mass transfer due to condensation redistributed for each of the discrete bubble classes. The gas void fraction, along with the scalar fraction f_i, is related to the number density of the discrete bubble ith class n_i (similarly to the jth class n_j) as $\alpha_g f_i = n_i v_i$. The size distribution of the dispersed phase is therefore defined by the scalar fraction f_i. The formulation of the population balance equation for each of the discrete bubble classes n_i is provided in Section 2.2. Interphase transfer terms in the momentum and energy equations (Γ_{kj} and F_{kj}) denote the transfer terms from phase j to phase k. The mass transfer Γ_{lg} is already given in Eq. (5) while the total interfacial force F_{lg} considered in the present study includes the effects of

$$\mathrm{F}_{lg} = \mathrm{F}_{lg}^{drag} + \mathrm{F}_{lg}^{lift} + \mathrm{F}_{lg}^{lubrication} + \mathrm{F}_{lg}^{dispersion} \tag{7}$$

The terms on the right-hand side of Eq. (7) are the drag force, lift force, wall lubrication force, and turbulent dispersion force, respectively. Detail descriptions of these forces can be found in Anglart and Nylund [18] and Lahey and Drew [19] and will not be repeated here.

A two-equation κ-ε turbulence model is employed for the continuous liquid and dispersed vapor phases. The effective viscosity in the momentum and energy equations is taken as the sum of the molecular viscosity and turbulent viscosity. The turbulent viscosity is considered as the total of the shear-induced turbulent viscosity and Sato's bubble-induced turbulent viscosity [20].

Experimental and theoretical investigations for low-pressure subcooled boiling flow by Judd and Hwang [21] suggest that the wall heat flux Q_w can be divided into three components: heat transferred by conduction to the superheated layer next to the wall (nucleate boiling or surface quenching) Q_q, heat transferred by evaporation or vapor generation Q_e, and heat transferred by turbulent convection Q_c. The nucleate-boiling or surface-quenching heat flux is determined through the relationship

$$Q_q = \left[\frac{2}{\sqrt{\pi}} \sqrt{k_l \rho_l C_{pl}} \sqrt{f}\right] A_q (T_w - T_l) \tag{8}$$

where T_w is the wall temperature and f is the bubble generation frequency. A_q, the fraction of wall area subjected to cooling by quenching, is calculated from $A_q = N''(\pi d_{bw}^2/4)$. The heat flux due to vapor generation at the wall in the nucleate boiling region can be calculated from

$$Q_e = N'' f \left(\frac{\pi}{6} d_{bw}^3\right) \rho_g h_{fg} \tag{9}$$

The heat flux according to the definition of local Stanton number St for turbulent convection is

$$Q_c = \mathrm{St} \rho_l C_{pl} u_l (T_w - T_l)(1 - A_q) \tag{10}$$

It is noted that u_l is the local tangential liquid velocity adjacent to the heated surface. More details of the model can be found in Tu and Yeoh [14] and will not be repeated here.

The local bubble Sauter diameter based on the calculated values of the scalar fraction f_i and discrete bubble sizes d_i can be deduced from

$$D_s = \frac{1}{\sum_i \frac{f_i}{d_i}} \tag{11}$$

2.2 Bubble Population Balance Model. The implementation of population balance equations originally developed by Lo [22] for the generic computer code CFX4.4 is reformulated to account for wall nucleation and condensation in the subcooled boiling flow regime. To account for the nonuniform bubble size

Table 1 Diameter of each discrete bubble class

Class no.	Central class diameter d_i (mm)
1	0.503
2	1.040
3	1.644
4	2.265
5	2.889
6	3.512
7	4.141
8	4.771
9	5.402
10	6.033
11	6.665
12	7.297
13	7.929
14	8.562
15	9.194

distribution, in this present study, bubbles ranging from 0 mm to 9.5 mm dia are equally divided into 15 classes (see Table 1). Instead of considering 16 different complete phases, it is assumed that each bubble class travels at the same mean algebraic velocity to reduce the computational time. This therefore results in 15 continuity equations for the gas phase coupled with a single continuity equation for the liquid phase.

The coalescence of two bubbles is assumed to occur in three stages. The first stage involves the bubbles colliding, thereby trapping a small amount of liquid between them. This liquid film then drains until it reaches a critical thickness, and the last stage features the rupturing of the liquid film subsequently causing the bubbles to coalesce. The collisions between bubbles may be caused by turbulence, buoyancy, and laminar shear. Only the first cause of collision (turbulence) is considered in the present model. Indeed collisions caused by buoyancy cannot be accounted for here because all the bubbles from each class have been assumed to travel at the same speed. Moreover, calculations showed that laminar shear collisions are negligible because of the low superficial gas velocities considered in this investigation. The coalescence rate considering turbulent collision taken from Prince and Blanch [23] can be expressed as

$$\chi = \theta_{ij} \exp\left(- \frac{t_{ij}}{\tau_{ij}} \right) \tag{12}$$

where τ_{ij} is the contact time for two bubbles given by $(d_{ij}/2)^{2/3}/\varepsilon^{1/3}$ and t_{ij} is the time required for two bubbles to coalesce having diameter d_i and d_j, which has been estimated to be $[d_{ij}/2)^3 \rho_l/16\sigma]^{1/2} \ln(h_0/h_f)$. The equivalent diameter d_{ij} is calculated as suggested by Chesters and Hoffman [24]: $d_{ij}=(2/d_i + 2/d_j)^{-1}$. According to Prince and Blanch [23], for air-water systems, h_0, the initial film thickness, and h_f, the critical film thickness at which rupture occurs, are assumed to be 1×10^{-4} m and 1×10^{-8} m, respectively. The turbulent collision rate θ_{ij} for two bubbles of diameter d_i and d_j is given by

$$\theta_{ij} = \frac{\pi}{4}(d_i + d_j)^2 (u_{ti}^2 + u_{tj}^2) \tag{13}$$

The turbulent velocity u_t in the inertial subrange of isotropic turbulence [25] is

$$u_t = 1.4 \varepsilon^{1/3} d^{1/3} \tag{14}$$

The breakup of bubbles in turbulent dispersions employs the model developed by Luo and Svendsen [26]. Binary breakup of the bubbles is assumed, and the model is based on the theories of isotropic turbulence. For binary breakage, a dimensionless variable describing the sizes of daughter drops or bubbles (the breakage volume fraction) can be defined as

$$f_{BV} = \frac{v_i}{v} = \frac{d_i^3}{d^3} = \frac{d_i^3}{d_i^3 + d_j^3} \tag{15}$$

where d_i and d_j are diameters (corresponding to v_i and v_j) of the daughter particles in the binary breakage of a parent particle with diameter d (corresponding to volume v). The value interval of the breakage volume fraction is between 0 and 1. The breakup rate of bubbles of volume v_j into volume sizes of $v_i (= v f_{BV})$ can be obtained as

$$\frac{\Omega(v_j : v_i)}{(1-\alpha_g) n_j} = C \left(\frac{\varepsilon}{d_j^2} \right)^{1/3} \int_{\xi_{\min}}^{1} \frac{(1+\xi)^2}{\xi^{11/3}} \exp\left(- \frac{12 c_f \sigma}{\beta \rho_l \varepsilon^{2/3} d_j^{5/3} \xi^{11/3}} \right) d\xi \tag{16}$$

where $\xi = \lambda/d_j$ is the size ratio between an eddy and a particle in the inertial subrange and, consequently, $\xi_{\min} = \lambda_{\min}/d_j$. The constants β and C are determined, respectively, from fundamental consideration of drops or bubbles breakage in turbulent dispersion systems. The measured β value of 2.0, according to Kuboi et al. [27,28], is used while the constant C calculated from $C' \pi \beta^{1/2}/4$ with C' approximately evaluated by $15/2(2\pi)^{2/3}\Gamma(1/3) \approx 0.83$ in Luo and Svendsen [26] and employing the measured β value arrives at a value of 0.923. The increase coefficient of surface area c_f is given by

$$c_f = [f_{BV}^{2/3} + (1 - f_{BV})^{2/3} - 1] \tag{17}$$

The integration in Eq. (16) is numerically determined and approximated by Simpson's rule.

The general form for the population balance equation is

$$\frac{\partial n_i}{\partial t} + \nabla(\overline{u_g} n_i) = \sum_{j=1}^{4} R_j + R_{ph} \tag{18}$$

where $\Sigma_{j=1}^{4} R_j$ represents the net change in the number density distribution due to coalescence and breakup processes. This interaction term $\Sigma_{j=1}^{4} R_j (= P_C + P_B - D_C - D_B)$ contains the source rates of P_C, P_B, D_C, and D_B, which are, respectively, the production rates and the death rate due to coalescence and breakup of bubbles formulated as

$$\begin{gathered} P_C = \frac{1}{2} \sum_{k=1}^{N} \sum_{l=1}^{N} \chi_{i,kl} n_i n_j \quad \chi_{i,kl} = \chi_{kl} \quad \text{if } v_k + v_l = v_i \\ \text{else } \chi_{i,kl} = 0 \quad \text{if } v_k + v_l \neq v_i \\ P_B = \sum_{j=i+1}^{N} \Omega(v_j : v_i) n_j, \quad D_C = \sum_{j=1}^{N} \chi_{ij} n_i n_j, \quad D_B = \Omega_i n_i \end{gathered} \tag{19}$$

The term R_{ph} in Eq. (15) denotes the source rate due to phase change. For general boiling systems, R_{ph} represents the bubble nucleation in the bulk liquid due to the homogeneous and heterogeneous nucleation and the collapse rate due to condensation for the subcooled boiling flow. For the present investigation, only the latter is appropriately considered because of the attention on subcooled boiling flow. The source rate can be formulated as

$$R_{ph} = - \frac{1}{\rho_g \alpha_g} \left[\frac{h a_{if} (T_{sat} - T_l)}{h_{fg}} \right] n_i \tag{20}$$

The heated wall nucleation rate is not included in R_{ph} and has been specified as a boundary condition as described in Section 2.1.

2.3 Numerical Details. Solution to the two sets of governing equations for the balance of mass, momentum, and energy of each phase was sought. The conservation equations were discretized using the control volume technique. The discrete bubble sizes prescribed in the dispersed phase were further tracked by solving an additional set of 15 transport equations, which were progressively coupled with the flow equations during the simula-

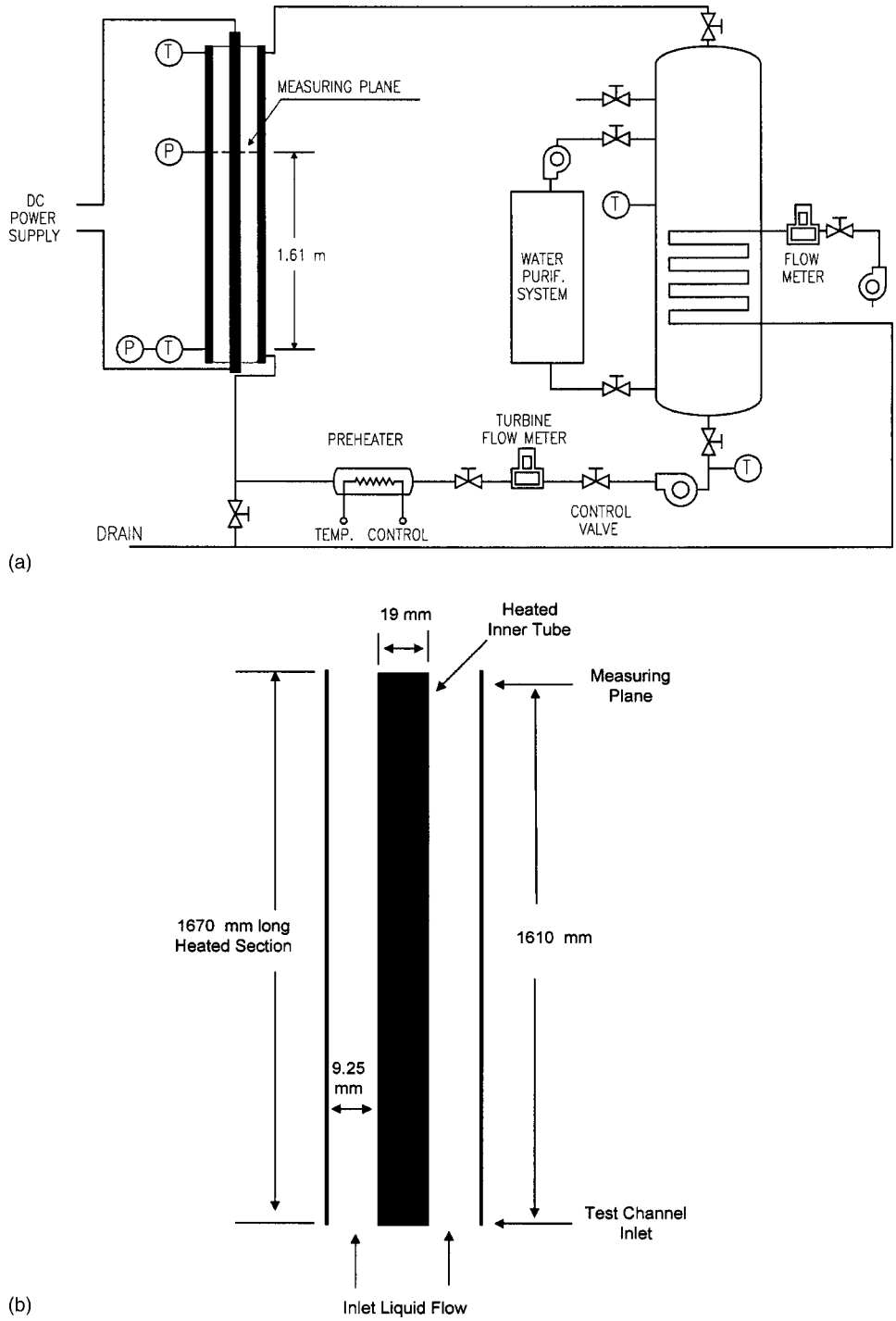

Fig. 1 Schematic drawing: (*a*) experimental setup details and (*b*) test channel

tions. The velocity-pressure linkage was handled through the SIMPLE procedure. The discretized equations were solved using Stone's Strongly Implicit Procedure [29]. Since the wall heat flux was applied uniformly throughout the inner wall of and taking advantage of the annular geometrical shape, only a quarter of it was considered as the domain for simulation. A body-fitted conformal system was employed to generate the three-dimensional mesh within the annular channel, resulting in a total of 13 (radial)$\times$30 (height)$\times$3 (circumference) control volumes. Grid independence was examined. In the mean parameters considered, further grid refinement did not reveal significant changes to the two-phase flow parameters. Convergence was achieved within 1500 iterations when the mass residual dropped below 1×10^{-7}. Global execution time on the Silicon Graphics machine was about 30 min.

3 Experimental Details

3.1 Test Rig. A schematic of the experimental rig is shown in Fig. 1. The test loop consists mainly of the test channel, water storage tank, circulating pump, preheater, and water purification unit. The test channel contains a heated section where the subcooled boiling flow occurs. The test channel is a 2.376 m long vertical concentric annulus with a heated inner tube. The inner

Table 2 Experimental conditions for C1, C2, C3, and C4 used for validating the two-fluid and population balance models

Run	P_{inlet} [Mpa]	T_{inlet} [°C]	T_{sub}(inlet) [°C]	Q_w [kW/m^2]	G [kg/m^{2}s]	α
C1	0.139	95.6	11.5	114.8	477.0	0.0399
C2	0.125	93.9	12.0	139.1	715.2	0.0373
C3	0.142	96.6	13.4	152.3	474.0	0.0816
C4	0.137	94.9	13.8	197.2	714.4	0.0724

tube of 19 mm in outer diameter is composed of a heated section and two unheated sections. The heated section is a 1.67 m long Inconel 625 tube with a 1.5 mm wall thickness, and it is filled with magnesium oxide powder insulation. The rod is uniformly heated by a DC power supply of 54 kW. The outer wall is comprised of two stainless steel tubes (with an inner diameter of 37.5 mm), which are connected by a transparent glass tube so that visual observations and photographs are made possible. The transparent glass tube is 50 mm long and is installed just below the measuring plane. It is noted that the curvature of circular tube may distort the images of the high-speed camera. However, depending on the purpose of experiment on the parameter to be measured, the images of the high-speed camera were utilized only to trace the presence of bubbles along the axial direction qualitatively, not quantitatively. Moreover, bubbles have been found to be sufficiently small (2~4 mm) compared to the flow path (8 mm) to be distorted. The measuring plane is located 1.61 m downstream of the beginning of the heated section. Demineralized water was used as the working fluid.

3.2 Experimental Conditions. Experiments were carried out at different levels of mass flux, heat flux, and inlet subcooling. The tested range of the parameters were 476~1061 kg/m^2 s for mass flux, 11.5~21.3°C for inlet subcooling temperatures, and 114.8~320.4 kW/m^2 for heat flux. The inlet flow rate was regulated by flow control valve, whereas the inlet subcooling temperature was controlled via the preheater. The heat flux was controlled by the DC power supply. The water temperatures at the test channel inlet and exit were measured using the calibrated platinum resistance temperature detectors within ±0.2°C, and the pressures at inlet and measuring plane were measured by absolute pressure transducers with the estimated error of ±0.001 MPa. The errors in mass flux, inlet subcooling temperatures, and heat flux measurements were estimated to be within ±1.8%, ±2.5%, and ±1.7% of the rated values, respectively. The system pressure was maintained at 1 bar to 2 bars and was not controlled, but was determined by the net volume expansion balanced by the bubble generation rate in the test channel and ventilation rate in the storage tank.

3.3 Local Measurements. Local void fraction and vapor velocity distributions were measured by the two-conductivity probe method. The two-conductivity probe in this study consisted of two sensors that were made of Teflon-coated stainless steel wire with a diameter of 0.076 mm. The two sensors were adjusted for a distance of 1.6 mm in the lengthwise direction and were aligned in the channel axial direction. The local liquid velocity was measured via the Pitot tube. The liquid velocity can be obtained by measuring the pressure difference ΔP between the stagnation pressure and static pressure at the tube. In two-phase flow, the velocity reduction model is needed to calculate local liquid velocity from the measured ΔP. In this study, the following model suggested by Reimann et al. [30] was applied

$$V_l = \frac{1}{\sqrt{(1-\alpha_g/2)}} \sqrt{\frac{2\Delta P}{K\rho_l}} \tag{21}$$

where ρ_l is liquid density and K is momentum transfer factor. The measurement of K is required for the local measurement in the low-velocity region because the drag force at the Pitot tube tip can change rapidly with the liquid velocity. This factor was determined in the pretest of single-phase liquid flow. In order to check the applicability of the Pitot tube method to the present boiling experiments, the global continuity check was carried out by comparing the inlet mass flow rate and the mass flow rate at measuring plane. Since the contribution of vapor mass flow rate to total mass flow rate at measuring plane is negligibly small compared to the liquid mass flow rate, the mass balance calculation can be a method for confirming the applicability of Pitot tube method in the average sense. The mean deviation between mass flow rates at inlet and those at measuring plane was found to be ±3.2%. However, the uncertainty of the bubble Sauter diameter values, applied equally to the interfacial area concentration, was difficult to ascertain and will, at present, be estimated to be lower than 27%. Experimental conditions that have been used for comparison with the simulated results are presented in Table 2.

4 Results and Discussion

4.1 Phenomenological Observation During Experiments. During the experiments, observations made through high-speed photography (see Fig. 2) revealed the presence of large bubbles away from the heated wall. In Fig. 2, the bottom vapor bubble at upstream was seen sliding along the heated surface until it was impeded by the downstream bubble. Experiments by Bonjour and Lallemand [31] and Prodanovic et al. [32] have clearly indicated the presence of bubbles sliding shortly after being detached from the heated surface cervices before lifting into the liquid core.

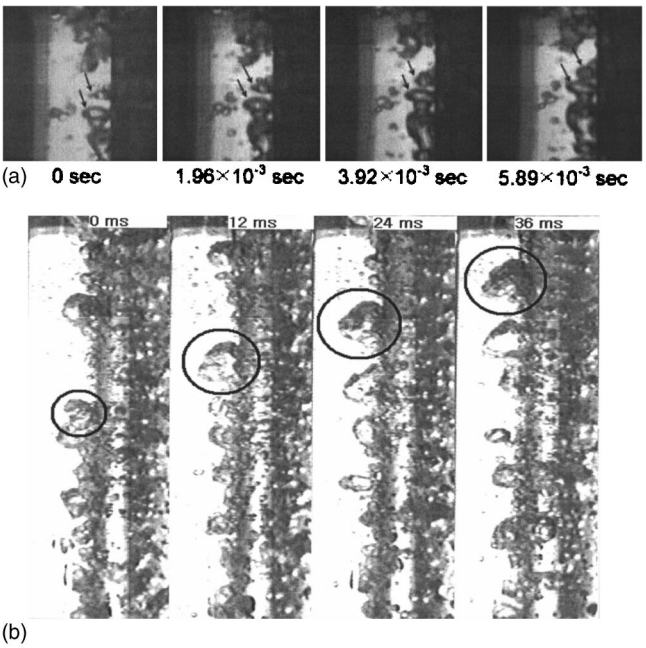

Fig. 2 Experimental observations: (*a*) bubble sliding along the heated wall and colliding with downstream bubble and (*b*) significant bubble coalescence of the bubble mushroom region as observed near the heated wall of an annular channel

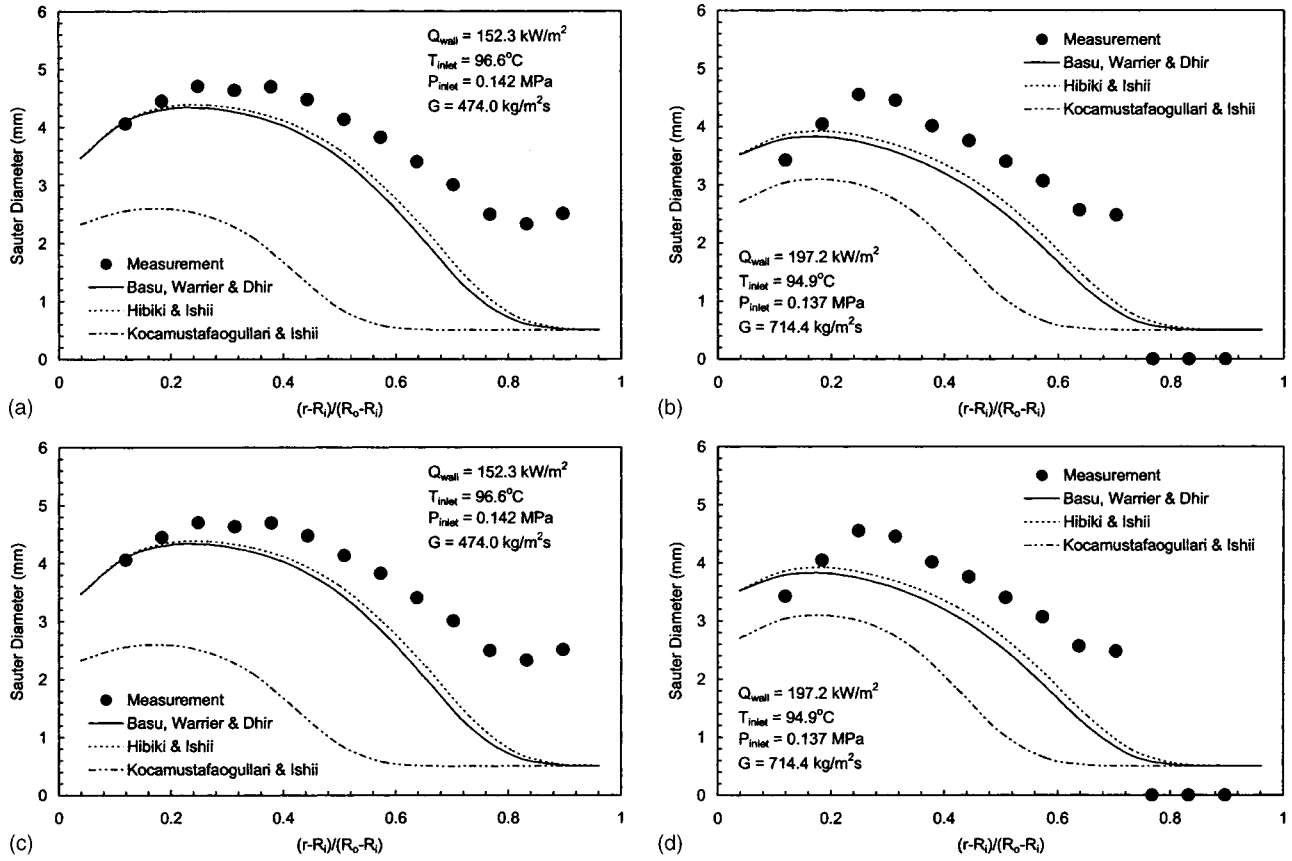

Fig. 3 Comparison of local mean radial profiles of bubble Sauter diameter between predictions of recent active nucleation stie density models and measurements: (*a*) C1, (*b*) C2, (*c*) C3, and (*d*) C4

These upstream bubbles traveling closely to the heated wall have the tendency of significantly colliding with any detached bubbles downstream and, subsequently, forming bigger bubbles due to the bubbles merging together. Away from the heated wall, the supposition of larger bubbles being present due to bubble coalescence was evidenced in Fig. 3. Focusing on the local bubble mushroom region as depicted in Fig. 3 and tracking its development through time, the region could be seen increasing in size along the heated wall downstream, confirming the significant merging intensity of the bubbles. Nevertheless, further away from the heated wall and in the proximity of the unheated wall of the annulus, there were relatively very few bubbles being present and traveling in the subcooled boiling flow as demonstrated in Fig. 2. Here, the condensation phenomenon dominated and the bubbles gradually decreased in size due to the increased condensation as they migrated toward the opposite end of the unheated wall of the annular channel. This supposition of the phenomenon predominant in subcooled boiling flows has been further confirmed by experimental observations of Gopinath et al. [33], which illustrated a bubble gradually being condensed in a subcooled liquid away from the heated surface.

4.2 Local Bubble Distribution at the Measuring Plane. The radial profiles of the bubble Sauter diameter for experimental conditions C1, C2, C3, and C4 located at 1.61 m downstream of the beginning of the heated section are predicted through the two-fluid and MUSIG boiling models. In all the figures presented henceforth, the dimensionless parameter $(r-R_i)/(R_o-R_i)=1$ indicates the inner surface of the unheated flow channel wall while $(r-R_i)/(R_o-R_i)=0$ indicates the surface of the heating rod in the annular channel.

In subcooled boiling flow, bubbles that form at cavities on the heated surface are known as nucleation sites. In Eq. (9), the heat transfer due to evaporation Q_e is expressed as a function of the active nucleation site density N''. The bubble departure in Eq. (9) was determined through the modified Fritz expression, which can be found in Kocamustafaogullari and Ishii [34]. The relationship is essentially a balance between the buoyancy and surface tension forces. The contact angle θ was assumed to be 65 deg for the current study. Realizing the significance of the active nucleation site density as an important parameter in the continuity equation of the gas phase, some recent correlations for predicting active nucleation site density were investigated.

Three relationships of the active nucleation site density from Kocamustafaogullari and Ishii [34], Basu et al. [35] and Hibiki and Ishii [36] were employed to determine their capability to accurately predict the local radial bubble Sauter distribution. Kocamustafaogullari and Ishii correlated existing active nucleation site density data by means of parametric study. They have assumed that the active nucleation site density in pool boiling by both surface conditions and thermophysical properties of the fluid. They also postulated that the active nucleation site density developed for pool boiling could be used in a forced convective system by the use of an effective superheat rather than the actual wall superheat. The active nucleation site density N'' is expressed as

$$N''=\frac{1}{d_{bw}^2}\left[\left(\frac{2\sigma T_{sat}}{\Delta T_{\text{eff}}\rho_g h_{fg}}\right)\Big/\,(0.5^* d_{bw})\right]^{-4.4} f(\rho^*) \qquad (22)$$

where $\rho^*=\Delta\rho/\rho_g$ and the function $f(\rho^*)$ is a known function of a density ratio described by $f(\rho^*)=2.157\times10^{-7}\rho^{*-3.2}(1+0.0049\rho^*)^{4.13}$ and ΔT_{eff} is the effective wall superheat, which is given by $\Delta T_{\text{eff}}=S\Delta T_w$; S is the suppression factor. Basu et al. [35]

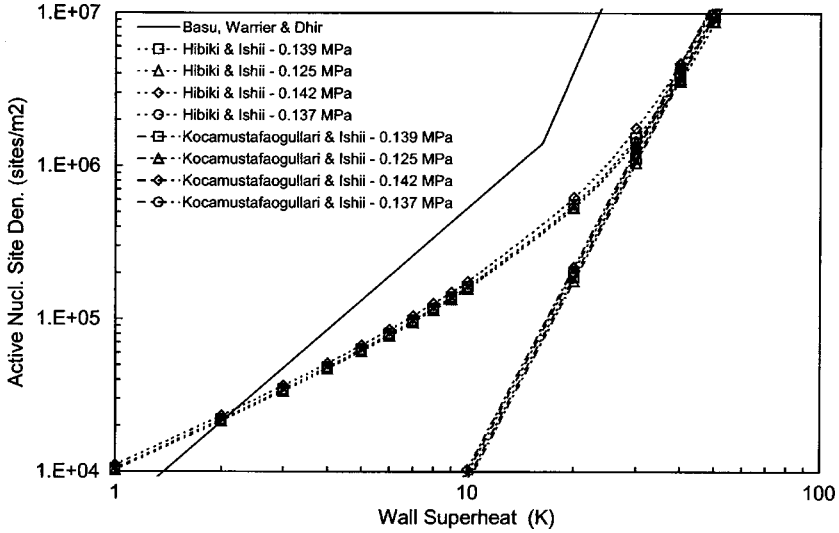

Fig. 4 Comparison of active nucleation site density models: Kocamustafaogullari and Ishii [34], Basu et al. [35], and Hibiki and Ishii [36]

proposed an alternative empirical correlation that included the effect of contact angle θ on the active nucleation site density, which is given by

$$N'' = 0.34\times 10^4(1-\cos\theta)\Delta T_w^{2.0} \quad \Delta T_{ONB} < \Delta T_w < 15 \text{ K}$$
$$N'' = 3.4\times 10^{-1}(1-\cos\theta)\Delta T_w^{5.3} \quad 15 \text{ K} \leqslant \Delta T_w \qquad (23)$$

Very recently, Hibiki and Ishii [36] modeled the active nucleation site density relationship mechanistically by knowledge of the size and cone angle distributions of cavities. In accordance with the Basu et al. [35] correlation, they have also formulated the nucleation site density as a function of contact angle. The correlation is given by

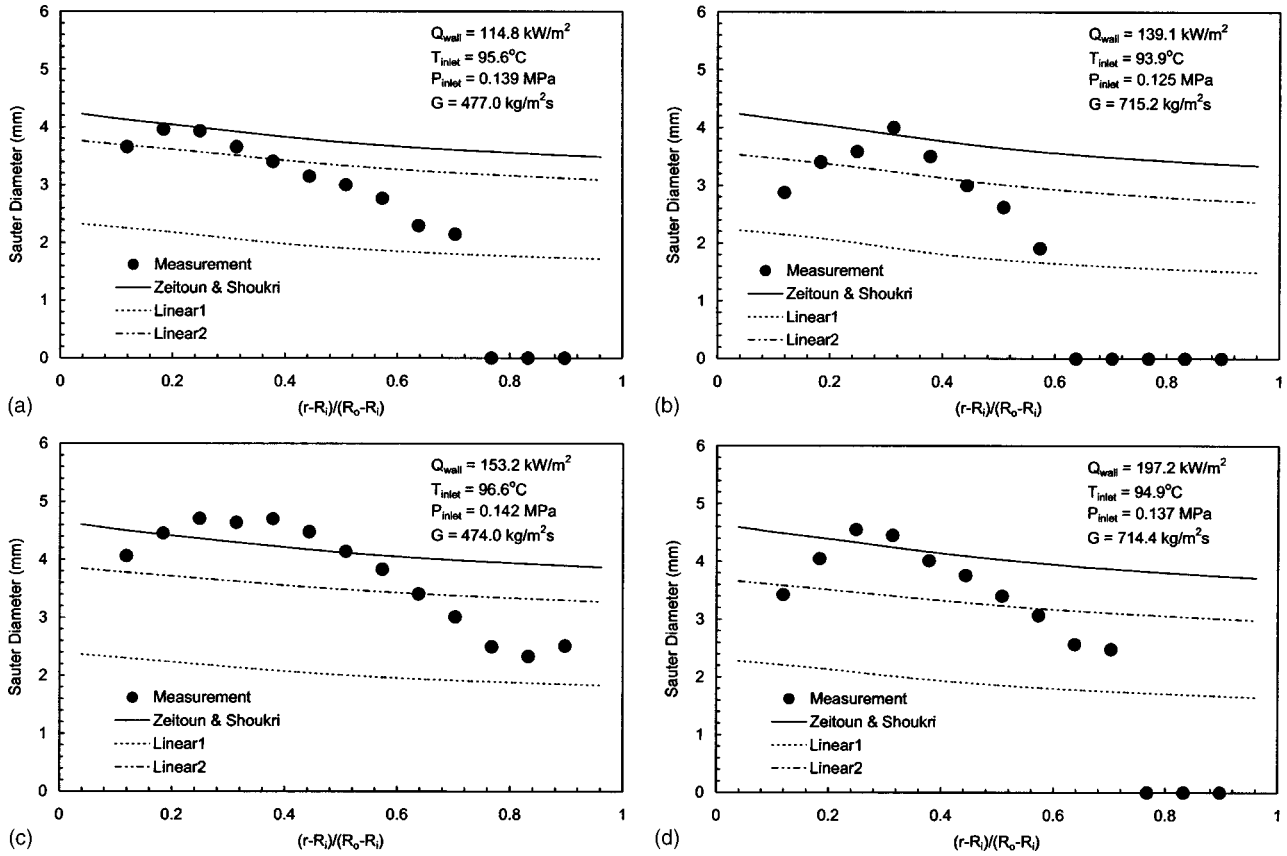

Fig. 5 Comparison of local mean radial profiles of bubble Sauter diameter between predictions of empirical bubble diameter relationships and measurements: (*a*) C1, (*b*) C2, (*c*) C3, and (*d*) C4

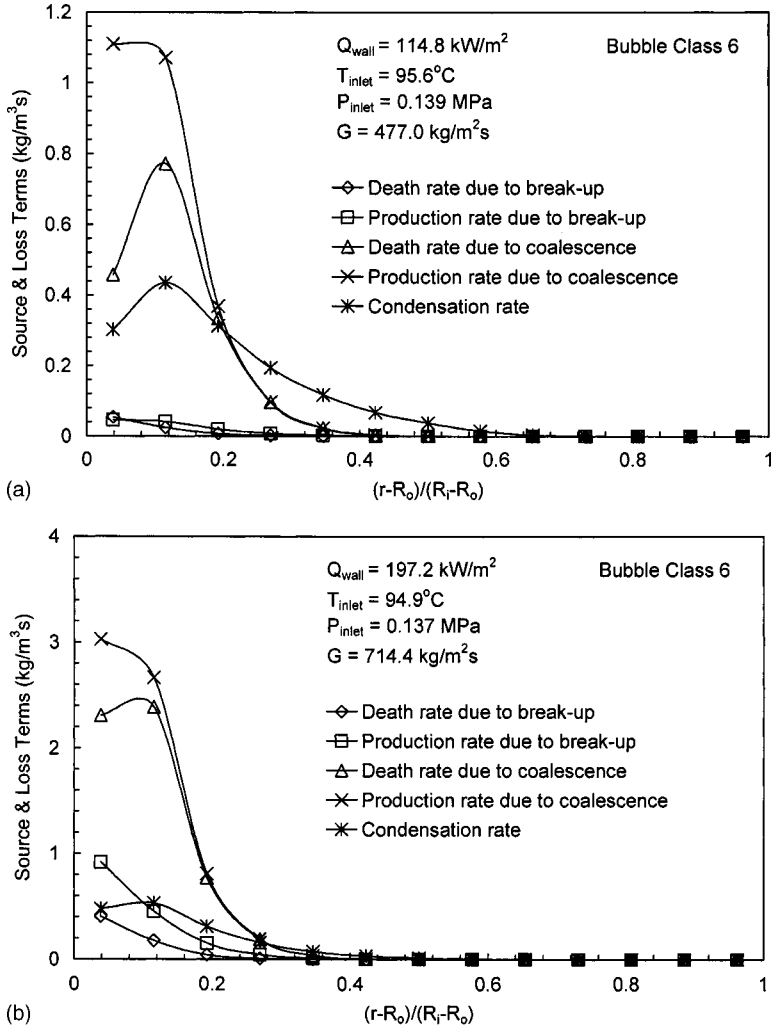

Fig. 6 Radial contributions of the production rates of P_C and P_B and death rates of D_C and D_B as well as the condensation rate R_{ph} of population balance equation for bubble class 6: (*a*) C1 and (*b*) C4

$$N'' = 4.72\times 10^5\left[1-\exp\left(-\frac{\theta^2}{4.17}\right)\right]\left\{\exp\left[2.5\times 10^{-6} f(\rho^+)\frac{\Delta T_w \rho_g h_{fg}}{2\sigma T_{sat}}\right]-1\right\} \quad (24)$$

where $\rho^+ = \log_{10}(\Delta\rho/\rho_g)$ and the function $f(\rho^+)$ is a function described by $f(\rho^+) = -0.01064 + 0.48246\rho^+ - 0.22712\rho^{+2} + 0.05468\rho^{+3}$.

Figure 3 presents the predicted bubble Sauter distributions employing the three correlations above against the locally measured bubble Sauter diameters for all four experimental conditions. Experimental photographs (see Fig. 2) clearly showed large bubble sizes being present away from the heated wall but not at the heated wall; this trend has been correctly modeled and predicted by the population balance model. In all four cases, the maximum predicted bubble Sauter diameters for C1, C2, C3, and C4 were obtained at about 3.8, 3.2, 4.3, and 3.9 mm, respectively, whereas the experimental maximum bubble sizes for C1, C2, C3, and C4 were measured at about 4.0, 4.1, 4.5, and 4.6 mm, respectively. Significant discrepancy of the bubble sizes between predictions and measurements could be found particularly for cases C2 and C4. It appeared that the predicted maximum bubble Sauter diameters for these two cases occurred much closer to the heated wall than the measurements. This could be possibly due to the static bubble departure relationship employed in the simulations where the contact angle was taken to be constant. In reality during the experiments, the contact angle continuously evolved in the subcooled boiling flow from the point of inception until point of departure.

In order to obtain the appropriate bubble nucleation rates for the evaluation of the heat transfer due to evaporation Q_e for Eq. (9), good agreement was achieved employing the active nucleation site density relationships of Basu et al. [35] and Hibiki and Ishii [36] instead of Kocamustafaogullari and Ishii [34] correlation. It was seen that the Kocamustafaogullari and Ishii model consistently predicted lower bubble Sauter diameter distributions. This could be explained by the relationship between the active nucleation site density and the wall superheat as illustrated in Fig. 4. In all the cases studied, the wall superheat was evaluated between 5 and 10 K. The empirically derived correlation of Kocamustafaogullari and Ishii [34] yielded much smaller active nucleation site densities at these wall superheats than those of the Basu et al. [35] and Hibiki and Ishii [36] models, which, therefore, resulted in lower bubble nucleation rates at the heated surface and smaller bubbles in the bulk liquid. Since it has been demonstrated that there was no significant appreciable differences between the Basu et al. [35] and Hibiki and Ishii [36] model results, the active nucleation site density correlation of Basu et al. was used to generate the rest of the predictions in the results presented henceforth.

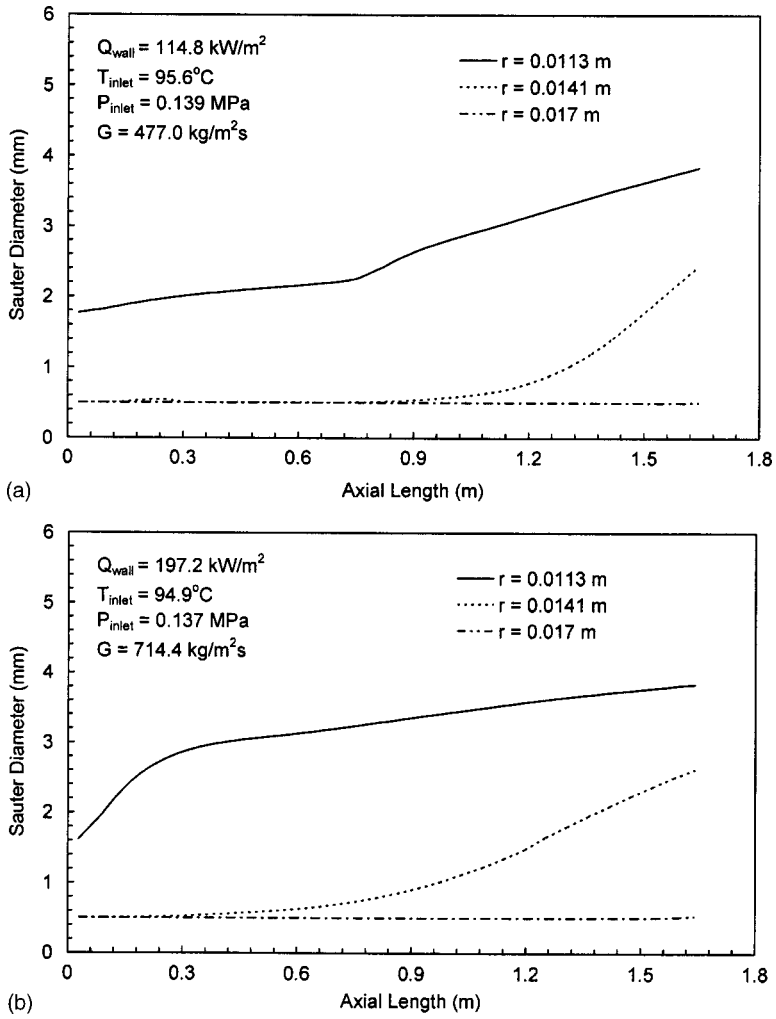

Fig. 7 Axial distribution of the bubble Sauter diameter—near the heated wall, middle and near the unheated wall—of the annular channel: (*a*) C1 and (*b*) C4

Figure 5 further demonstrates the boiling model predictions against local measurements determined through empirical relationships formulated for low-pressure subcooled boiling flow. Here, the correlation developed by Zeitoun and Shoukri [37] was adopted where they have correlated against measured data with

$$\frac{D_s}{\sqrt{\sigma/g\Delta\rho}} = \frac{0.0683(\rho_l/\rho_g)^{1.326}}{\mathrm{Re}^{0.324}\left(\mathrm{Ja} + \dfrac{149.2(\rho_l/\rho_g)^{1.326}}{Bo^{0.487}\,\mathrm{Re}^{1.6}}\right)} \tag{25}$$

where D_s is the mean Sauter diameter. The nondimensional parameters in Eq. (25) are defined as follows: Re is the flow Reynolds number; *Bo* is the boiling number; and Ja is the Jakob number. Comparison was also made with computational results determined through the empirical relationship of Anglart and Nylund [18] to determine the local bubble diameter. They have proposed to estimate the interfacial transfer terms through a bubble diameter relationship assuming a linear dependence with local liquid subcoolings, which can be expressed by

$$d = \frac{d_1(\theta_{sub} - \theta_0) + d_0(\theta_1 - \theta_{sub})}{\theta_1 - \theta_0} \tag{26}$$

This relationship is still currently being used and applied in many boiling studies through the CFX4.4 code. Application of this correlation for subcooled boiling flow at low pressures has recently been reported in the numerical investigations of Lee et al. [38]. Reference diameters of d_0 and d_1 in Eq. (26), corresponding to the reference subcooling temperatures at θ_0 and θ_1, are usually not known a priori. Calculations based on different reference diameters have been investigated in the present study. We have assumed for the first case—"Linear1"—the local bubble diameters were evaluated between $d_0 = 1.5\times10^{-4}$ m and $d_1 = 4.0\times10^{-3}$ m while for the second case—"Linear2"—they are determined between $d_0 = 1.5\times10^{-4}$ m and $d_1 = 7.0\times10^{-3}$ m, respectively. We further assumed that both of the reference diameters corresponded to identical reference subcooling temperatures of $\theta_0 = 13.0$ K and $\theta_1 = -5$ K.

The local radially predicted bubble diameter distributions determined through the empirical relationships were not consistent with those measured during the experiments. It should be noted that these empirical relationships have been correlated based on area-averaged experimental data. The deficiency of the correlations due to the absence of the mechanistic behavior of bubble coalescence and collapse due to condensation observed through experiments significantly compromised the model predictions. Evidently, the bubble size determination in the bulk liquid core was not strictly dependent on only local subcooling temperatures. It is clearly demonstrated in Fig. 5 that extending the use of the empirical bubble diameter correlations to predict local bubble sizes is invalid.

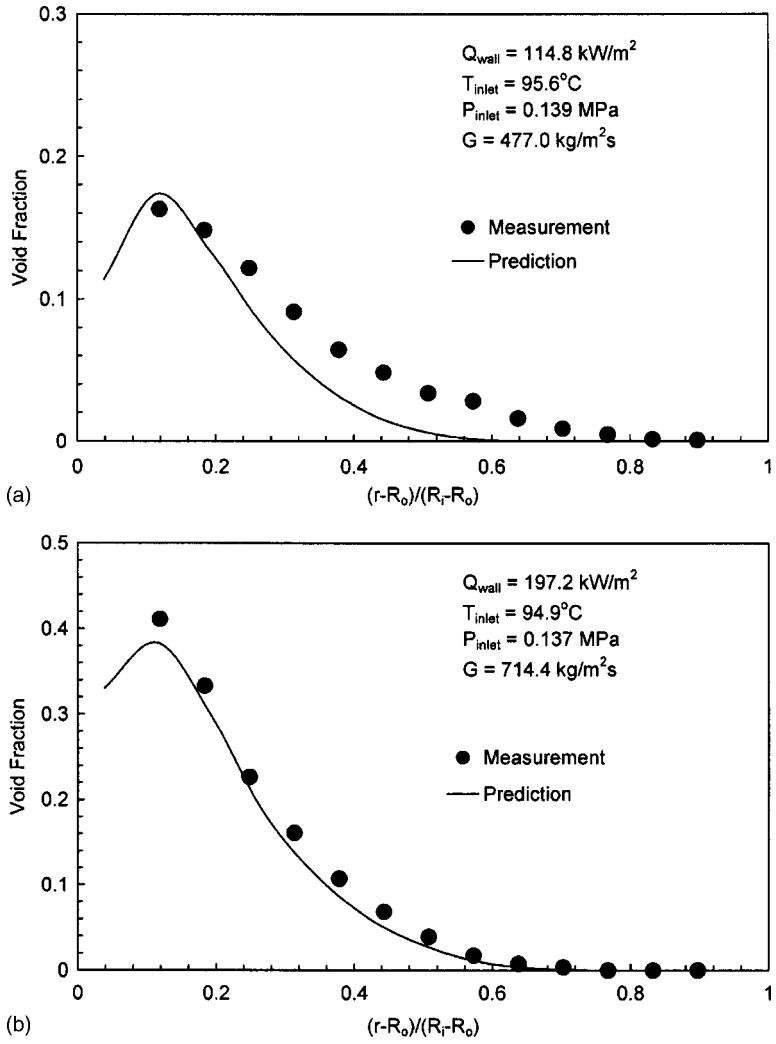

Fig. 8 Local mean radial profiles of void fraction: (*a*) C1 and (*b*) C4

4.3 Phenomenological Understanding of Source and Sink Rates in the Population Balance Equation Toward Modeling Subcooled Boiling Flow. In this section, a phenomenological understanding of the production, death, and condensation rates contributing toward the merging and fragmentation of bubbles in the bulk subcooled boiling flow through the population balance model is instigated. It was aforementioned that the nonuniform bubble size distribution has been accounted by equally dividing the bubble sizes into 15 classes ranging from 0 mm to 9.5 mm diam (see Table 1). For the purpose of illustration in order to gain some important insight into the relative contributions of the source and sink rates, we focused on bubble class 6 (diameter $\approx$3.5 mm) at experimental conditions of C1 and C4.

Figure 6 details the contributions of the production rates of P_C and P_B and death rates of D_C and D_B as well as the condensation rate R_{ph}. The dominant rate near the heated wall was the production rate due to coalescence. An important contribution through the death rate due to coalescence is also noted. The significance of the former indicated a source due to the merging of smaller bubbles forming bigger bubbles. Nevertheless, the latter indicated a source contribution due to the breakage of larger bubbles. The dominant coalescence rates found near the heated wall corresponded to the proper modeling of the physical bubble mechanisms that have been observed in experiments (see Fig. 2). The condensation rate residing away from the heated wall correctly modeled the condensation phenomenon as also observed through the experimental photographs and confirmed through the observations of Gopinath et al. [33]. Nevertheless, further away from the heated surface, with the condensation rate significantly higher than the net rate and the phenomenon dominating between $(r-R_i)/(R_o-R_i)=0.2$ and $(r-R_i)/(R_o-R_i)=0.5$, the model predicted the gradual fragmentation of bubbles as they migrated toward the unheated wall. Within this region it has been demonstrated in Fig. 5 that the predicted bubble Sauter diameter sizes were found to be lower than the measured bubble sizes. This was due to the condensation rate predicted through the Ranz and Marshall Nusselt number correlation [17] Gopinath et al. [33] has demonstrated that the original form of the Ranz and Marshall Nusselt number correlation has a tendency to underpredict the condensation Nusselt number. This underprediction could be explained by the fact that the thermal layer around the bubble thickens as the bubble shrinks in size. The net effect of the thickening of the boundary layer results in a decrease in the overall condensation rate. They modified the original form of the Ranz and Marshall Nusselt number expression to better predict the condensation Nusselt number by accommodating the observed effect. Further investigative studies will be performed to employ the modified Ranz and Marshall correlation [17] in the boiling model.

4.4 Axial Bubble Sauter Diameter Distributions and Local Void Fraction Distributions at Measuring Plane. Figure 7 illustrates the bubble Sauter diameter distributions along three axial locations—near the heated wall, middle, and near the unheated wall—of the annular channel for the four cases. The two distinct

flow regions where there were significant bubbles present near the heated surface and no bubbles near the unheated wall is a characterization of a typical subcooled flow boiling—a *high-temperature* two-phase region near the heated wall and a *low-temperature* single-phase liquid away from the heated surface. More importantly, this figure demonstrates the increasing bubble sizes along the height of the annular channel in the vicinity of the heated wall. This clearly confirmed the significant coalescence of bubbles as demonstrated through the predicted coalescence rates in Fig. 6 and similarly observed in experiments.

Figure 8 presents the locally predicted void fraction profiles against radial measured values. Good agreement was achieved between the predictions and measurements. The peak local void fraction was always observed in the vicinity of the heated surface in a typical subcooled boiling flow. The high local void fraction found here was explicitly due to the large number of bubbles generated from the active nucleation sites on the heated surface. Here, large amount of bubbles were generated from these nucleation sites when the temperature on the heated surface exceeded the saturation temperature. A proper prediction of the nucleation site densities is therefore crucial as already confirmed from the parametric study above (see Fig. 4). As these bubbles reached a critical size, they detached from the heated surface and migrated laterally toward the subcooled liquid core under the competing process of bubble coalescence and condensation as aforementioned.

5 Conclusion

A two-fluid model coupled with the population balance approach is presented in this paper to handle subcooled billing flows. The increase in complexity of modeling such flows derives from the additional consideration of the gas or liquid undergoing a phase transformation. Subcooled boiling flow embraces all the complex dynamic interaction of the phenomena associated with hydrodynamics, heat and mass transfer, and bubble coalescence and breakup. In this study, the range of bubble sizes in the subcooled boiling flow was distributed according to the division of 15 diam classes through the formulation of a MUSIG model. Each of them experiencing coalescence and breakup phenomena in the bulk subcooled liquid has been considered. In addition to the formulation of the bubble coalescence of Prince and Blanch [23] and bubble breakup of the Luo and Svendsen [26] mechanisms, the MUSIG model was further developed to account for the wall nucleation or vapor generation on the heated surface and condensation process in the subcooled liquid core. Comparison of the predicted results was made against local measurements. Parametric investigations of some recent active nucleation site density models and empirical relationships to determine the local bubble diameter were also performed. Overall, good agreement was achieved through the newly formulated population balance model for the local bubble Sauter diameter and void fraction profiles. Moreover, it has been demonstrated that the model correctly showed the significant bubble coalescence behavior near the heated wall and the fragmentation of bubbles due to condensation away from the heated wall as confirmed through experiments. Hence, modeling subcooled boiling flows using a two-fluid model coupled with the population balance approach, as demonstrated in this study, presents enormous potential.

Nomenclature

a_{if} = interfacial area concentration, 1/m
A_q = fraction of wall area subjected to quenching
Bo = boiling number
c_f = increase coefficient of surface area
C = constant in Eq. (16)
C_p = specific heat, J/kg K
d = parent particle diameter, m
d_{bw} = bubble departure diameter, m
d_i, d_j = daughter particle diameters, m
d_{ij} = equivalent diameter, m
d_0, d_1 = reference bubble diameters, m
D_B = death rate due to breakup, $1/m^3$ s
D_C = death rate due to coalescence, $1/m^3$ s
D_s = bubble Sauter diameter, m
f = bubble departure frequency, 1/s
f_{BV} = breakage volume fraction
f_i = scalar variable of the dispersed phase
F_{lg} = total interfacial force, N
F_{lg}^{drag} = drag force, N
F_{lg}^{lift} = lift force, N
$\mathrm{F}_{lg}^{lubrication}$ = wall lubrication force, N
$\mathrm{F}_{lg}^{dispersion}$ = turbulent dispersion force, N
$\underline{g}$ = gravitational acceleration, m/s^2
g = gravitational vector, m/s^2
h = interphase heat transfer coefficient, W/m^2 K
G = mass flux, kg/m^2 s
h_0 = initial film thickness, m
h_f = critical film thickness at rupture, m
h_{fg} = latent heat, J/kg
H = enthalpy, J/kg
Ja = Jakob number based on subcooling temperature
$\underline{K}$ = momentum transfer factor
$\overline{n}$ = normal to the wall surface
n_i = number density of the ith class, $1/m^3$
n_j = number density of the jth class, $1/m^3$
N = number of bubble classes, $1/m^3$
N'' = active nucleation site density, $1/m^2$
P = pressure, Pa
ΔP = pressure difference between stagnation and static pressures, Pa
P_B = production rate due to breakup, $1/m^3$ s
P_C = production rate due to coalescence, $1/m^3$ s
Q = heat source in Eq. (4), W
Q_w = wall heat flux, W/m^2
Q_c = heat transferred by convection, W/m^2
Q_e = heat transferred by evaporation, W/m^2
Q_q = heat transferred by quenching, W/m^2
r = radius, m
Re = flow Reynolds number
R_i, R_o = inner and outer radius of annular channel, m
R_{ph} = condensation rate, $1/m^3$ s
S = suppression factor
S_i = source term due to coalescence and breakup
St = Stanton number
t = thermofluid time scale, s
t_{ij} = coalescence time, s
T = temperature, K
T_{sat} = saturation temperature, K
T_{sub} = subcooling temperature, K
ΔT_{eff} = effective wall superheat, K
ΔT_{ONB} = wall superheat at onset of nucleate boiling, K
ΔT_w = wall superheat, K
$\underline{u}$ = velocity, m/s
$\overline{u}$ = velocity vector, m/s
u_t = velocity due to turbulent collision, m/s
v = volume corresponding to particle diameter d, m^3
V_l = local measured liquid velocity, m/s
y_w = adjacent point normal to the wall surface

Greek Symbols

α = void fraction
β = measured constant in Eq. (16)
χ = coalescence rate, $1/m^3$ s
ε = dissipation of kinetic energy, m^2/s^3
κ = turbulent kinetic energy, m^2/s^2
Γ = mass transfer, kg/m^3 s
λ = size of an eddy, m

λ^e = effective thermal conductivity, W/m K
μ^e = effective viscosity, kg/m s
θ = bubble contact angle, rad
θ_{ij} = turbulent collision rate, $1/m^3$ s
θ_{sub} = local subcooling temperature $= T_{sat} - T_l$, K
$\theta_0 \theta_1$ = reference subcooling temperatures, K
ρ = density, kg/m^3
$\Delta\rho$ = density difference $= \rho_l - \rho_g$, kg/m^3
σ = surface tension, kg/s^2
τ_{ij} = bubble contact time, s
Ω = breakup rate, $1/m^3$ s
ξ = size ratio between an eddy and a particle in the inertial subrange

Subscripts

g = vapor
gl = transfer of quantities from liquid phase to vapor phase
l = liquid
lg = transfer of quantities from vapor phase to liquid phase
min = minimum
w = wall

References

[1] Ramkrishna, D., and Mahoney, A. W., 2002, ''Population Balance Modeling: Promise for the Future,'' Chem. Eng. Sci., **57**, pp. 595–606.
[2] Krishna, R., Urseanu, M. I., van Baten, J. M., and Ellenberger, J., 1999, ''Influence of Scale on the Hydrodynamics of Bubble Columns Operating in the Churn-Turbulent Regime: Experiments vs. Eulerian Simulations,'' Chem. Eng. Sci., **54**, pp. 4903–4911.
[3] Shimizu, K., Takada, S., Minekawa, K., and Kawase, Y., 2000, ''Phenomenological Model for Bubble Column Reactors: Prediction of Gas Hold-Up and Volumetric Mass Transfer Coefficients,'' Chem. Eng. J., **78**, pp. 21–28.
[4] Pohorecki, R., Moniuk, W., Bielski, P., and Zdrojkwoski, A., 2001, ''Modelling of the Coalescence/Redispersion Processes in Bubble Columns,'' Chem. Eng. Sci., **56**, pp. 6157–6164.
[5] Olmos, E., Gentric, C., Vial, Ch., Wild, G., and Midoux, N., 2001, ''Numerical Simulation of Multiphase Flow in Bubble Column Reactors: Influence of Bubble Coalescence and Break-Up,'' Chem. Eng. Sci., **56**, pp. 6359–6365.
[6] Serizawa, A., Kataoka, I., and Michiyoshi, I., 1975, ''Turbulence Structure of Air-Water Bubbly Flow—I. Measuring Techniques,'' Int. J. Multiphase Flow, **2**, pp. 347–356.
[7] Heringe, R. A., and Davis, M. R., 1976, ''Structural Development of Gas-Liquid Mixture Flows,'' J. Fluid Mech., **73**, pp. 97–123.
[8] Welle, R. V., 1985, ''Void Fraction, Bubble Velocity and Bubble Size in Two-Phase Flow,'' J. Neurosurg., **11**, pp. 317–345.
[9] Kataoka, I., Ishii, M., and Serizawa, A., 1986, ''Local Formulation and Measurements of Interfacial Area Concentration in Two-Phase Flow,'' J. Neurosurg., **12**, pp. 505–529.
[10] Liu, T. J., 1989, ''Experimental Investigation of Turbulence Structure in Two-Phase Bubbly Flow,'' Ph.D. Thesis, Northwestern University, Evanston, IL.
[11] Kocamustafaogullari, G., and Wang, Z., 1995, ''An Experimental Study on Local Interfacial Parameters in a Horizontal Bubbly Two-Phase Flow,'' J. Neurosurg., **17**, pp. 553–572.
[12] Revankar, S. T., and Ishii, M., 1992, ''Local Interfacial Area Measurement in Bubbly Flow,'' Int. J. Heat Mass Transfer, **35**, pp. 913–925.
[13] Velidandla, V., Putta, S., and Roy, R. P., 1996, ''Velocity Field in Isothermal Turbulent Bubbly Gas-Liquid Flow Through a Pipe,'' Exp. Fluids, **21**, pp. 347–356.
[14] Tu, J. Y., and Yeoh, G. H., 2002, ''On Numerical Modelling of Low-Pressure Subcooled Boiling Flows,'' Int. J. Heat Mass Transfer, **45**, pp. 1197–1209.
[15] Yeoh, G. H., and Tu, J. Y., 2002, ''Implementation of a Two-Phase Boiling Model Into the RELAP/MOD2 Computer Code to Predict Void Distribution in Low-Pressure Subcooled Boiling Flows,'' Nucl. Sci. Eng., **140**, pp. 182–188.
[16] Yeoh, G. H., Tu, J. Y., Lee, T. H., and Park, G.-C., 2002, ''Prediction and Measurement of Local Two-Phase Flow Parameters in a Boiling Flow Channel,'' Numer. Heat Transfer, Part A, **42**, pp. 173–192.
[17] Ranz, W. E., and Marshall, W. R., 1952, Chem. Eng. Prog., **48**, pp. 141–148.
[18] Anglart, H., and Nylund, O., 1996, ''CFD Application to Prediction of Void Distribution in Two-Phase Bubbly Flows in Rod Bundles,'' Nucl. Sci. Eng., **163**, pp. 81–98.
[19] Lahey, Jr., R. T., and Drew, D. A., 2001, ''The Analysis of Two-Phase Flow and Heat Transfer Using Multidimensional, Four Field, Two-Fluid Model,'' Nucl. Eng. Des., **204**, pp. 29–44.
[20] Sato, Y., Sadatomi, M., and Sekoguchi, K., 1981, ''Momentum and Heat Transfer in Two-Phase Bubbly Flow-I,'' Int. J. Multiphase Flow, **7**, pp. 167–178.
[21] Judd, R. L., and Hwang, K. S., 1976, ''A Comprehensive Model for Nucleate Pool Boiling Heat Transfer Including Microlayer Evaporation,'' ASME J. Heat Transfer, **98**, pp. 623–629.
[22] Lo, S., 1996, ''Application of Population Balance to CFD Modelling of Bubbly Flow via the MUSIG Model,'' AEAT-1096, AEA Technology.
[23] Prince, M. J., and Blanch, H. W., 1990, ''Bubble Coalescence and Break-Up in Air-Sparged Bubble Column,'' AIChE J., **36**, pp. 1485–1499.
[24] Chesters, A. K., and Hoffman, G., 1982, ''Bubble Coalescence in Pure Liquids,'' Appl. Sci. Res., **38**, pp. 353–361.
[25] Rotta, J. C., 1972, *Turbulente Stromungen*, Teubner, Stuttgart.
[26] Luo, H., and Svendsen, H., 1996, ''Theoretical Model for Drop and Bubble Break-Up in Turbulent Dispersions,'' AIChE J., **42**, pp. 1225–1233.
[27] Kuboi, R., Komasawa, I., and Otake, T., 1972a, ''Behavior of Dispersed Particles in Turbulent Liquid Flows,'' J. Chem. Eng. Jpn., **5**, pp. 349–355.
[28] Kuboi, R., Komasawa, I., and Otake, T., 1972b, ''Collision and Coalescence of Dispersed Drops in Turbulent Liquid Flow,'' J. Chem. Eng. Jpn., **5**, pp. 423–424.
[29] Stone, H. L., 1968, ''Iterative Solution of Implicit Approximations of Multidimensional Partial Differential Equations,'' SIAM (Soc. Ind. Appl. Math.) J. Numer. Anal., **5**, pp. 530–558.
[30] Reimann, J., Kusterer, H., and Jhon, H., 1983, ''Two-Phase Flow Rate Measurements With Pitot Tube and Density Measurements,'' Symposium Measuring Techniques in Gas-Liquid Two-Phase Flows, Nancy, France.
[31] Bonjour, J., and Lallemand, M., 2001, ''Two-Phase Flow Structure Near a Heated Vertical Wall During Nucleate Pool Boiling,'' Int. J. Multiphase Flow, **27**, pp. 1789–1802.
[32] Prodanovic, V., Fraser, D., and Salcudean, M., 2002, ''Bubble Behavior in Subcooled Flow Boiling of Water at Low Pressures and Low Flow Rates,'' Int. J. Multiphase Flow, **28**, pp. 1–19.
[33] Gopinath, R., Basu, N., and Dhir, V. K., 2002, ''Interfacial Heat Transfer During Subcooled Flow Boiling,'' Int. J. Heat Mass Transfer, **45**, pp. 3947–3959.
[34] Kocamustafaogullari, G., and Ishii, M., 1995, ''Foundation of the Interfacial Area Transport Equation and its Closure Relations,'' Int. J. Heat Mass Transfer, **38**, pp. 481–493.
[35] Basu, N., Warrier, G. R., and Dhir, V. K., 2002, ''Onset of Nucleate Boiling and Active Nucleation Site Density During Subcooled Flow Boiling,'' ASME J. Heat Transfer, **124**, pp. 717–728.
[36] Hibiki, T., and Ishii, M., 2003, ''Active Nucleation Site Density in Boiling Systems,'' Int. J. Heat Mass Transfer, **46**, pp. 2587–2601.
[37] Zeitoun, O., and Shoukri, M., 1997, ''Axial Void Fraction Profile in Low Pressure Subcooled Flow Boiling,'' Int. J. Heat Mass Transfer, **40**, pp. 867–879.
[38] Lee, T. H., Park, G.-C., and Lee, D. J., 2002, ''Local Flow Characteristics of Subcooled Boiling Flow of Water in a Vertical Annulus,'' Int. J. Multiphase Flow, **28**, pp. 1351–1368.

Heat Transfer in Two-Pass Rotating Rectangular Channels (AR=1:2 and AR=1:4) With Smooth Walls

Wen-Lung Fu
Lesley M. Wright
Je-Chin Han[1]

Turbine Heat Transfer Laboratory,
Department of Mechanical Engineering,
Texas A&M University,
College Station, Texas 77843-3123

This paper reports the heat transfer coefficients in two-pass rotating rectangular channels [aspect ratio (AR=1:2 and AR=1:4)] with smooth walls. The experiments are conducted at four Reynolds numbers: 5000, 10,000, 25,000, and 40,000. The rotation numbers vary from 0.0 to 0.21 and 0.0 to 0.3 for AR=1:2 and AR=1:4, respectively. For each channel, two channel orientations are studied, 90° and 45° with respect to the plane of rotation. The results showed that the 180° sharp turn significantly enhanced heat transfer on both the leading and trailing surfaces in the turn region for both nonrotating and rotating channels. The results also showed that the rotation effect increased the heat transfer on the trailing surface in the first pass, but reduced the heat transfer on the leading surface. However, the heat transfer difference between the leading and trailing walls in the second pass is relatively small compared to the first pass due to strong turn effect. [DOI: 10.1115/1.1857946]

Introduction

Advanced gas turbines operate at high temperatures to improve thermal efficiency. The high inlet temperature creates thermal stresses on the blades which can be detrimental to the operation of the engine. In order to achieve reasonable durability goals, improved cooling techniques, such as film cooling and internal cooling, are applied to turbine blades. Internal cooling is achieved by circulating compressed air in multipass flow channels inside the blade structure. As Fig. 1 shows, the cross section of the internal cooling channels varies depending on their location in the blade. Cooling channels near the leading edge could be tall and narrow, and channels closer to the trailing edge are typically wide and short. The cooling channels are either single-pass (with radial outward flow) or multipass (both radial outward and radial inward flow) passages. To enhance the heat transfer from the walls of the channels, they are typically lined with ribs or other turbulence promoters.

The coolant flow through these internal cooling passages is complex and influenced by multiple parameters. The aspect ratio of the channels, 180° turns in the multipass channels, and the rib configurations all affect the level of heat transfer enhancement in nonrotating channels. However, the cooling channels in actual turbine blades are rotating. Rotation introduces the added complexities of Coriolis and buoyancy forces which also alter the coolant flow through the passages. Many studies are available which report the combined effect of selected parameters. The interested reader is referred to *Gas Turbine Heat Transfer and Cooling Technology* [1] for many published studies investigating internal cooling techniques.

Because the heat transfer distribution within the cooling channels is influenced by many factors, it is necessary to parametrically study these factors. Therefore, it is necessary to understand the behavior of the coolant through smooth, rotating channels (without turbulence promoters) before the more complicated behavior can be fully realized. Turbulent flow through nonrotating, circular tubes has been thoroughly investigated; Kays and Crawford [2] summarizes this work that considers the heat transfer in tubes with various entrance conditions. The Nusselt number in tubes with fully developed turbulent flow is also given by Kays and Crawford [2]. The widely accepted Dittus–Boelter correlation for fully developed turbulent flow was developed in circular tubes, but this correlation has also been applied to flow through channels with noncircular cross sections.

As stated above, the heat transfer coefficients in turbine blade cooling channels are influenced by the 180° turn. Fan and Metzger [3] and Han et al. [4] concentrated on the heat transfer in this turn region. Both studies indicated that the heat transfer coefficients in the turn and downstream of the turn are greater than the heat transfer coefficients before the turn. However, the overall level of heat transfer enhancement is dependent on the cross section (aspect ratio) of the channel.

Although straight forward expressions have been developed for turbulent flow through nonrotating, smooth passages, coolant flow in rotating passages with smooth walls lacks closure. Wagner et al. [5,6] was the first to show the heat transfer from the leading and trailing walls of a rotating channel are not symmetrical. In other words, in their square [aspect ratio (AR)=1:1] cooling channel with radially outward flow, the heat transfer from the trailing surface increases with rotation, while the heat transfer from the leading surface decreases. Due to the reversal of the Coriolis force, the leading surface of channels with radially inward flow experiences heat transfer enhancement while the trailing surface decreases.

Johnson et al. [7] extended this study of a square channel to investigate the effect of channel orientation with respect to the direction of rotation. When the channel is oriented nonorthogonally to the direction of rotation, the effect of rotation decreases; in other words, the difference between the heat transfer coefficients on the leading and trailing surfaces is reduced. Dutta and Han [8] confirmed this result in a rotating square channel. They also showed that the channel orientation has the greatest impact on the heat transfer in the first pass with radially outward flow, and the effect decreases in the subsequent passes.

When the impact of rotation was realized, researchers sought more detailed heat transfer measurements. Park and Lau [9] used naphthalene sublimation to obtain detailed heat/mass transfer distributions in a rotating two-pass square channel. The detailed distributions indicated the Coriolis forces create large spanwise

[1]Marcus Easterling Endowed Chair, jchan@mengr.tamu.edu

Manuscript received December 28, 2003; revision received September 8, 2004. Review conducted by: N. K. Anand.

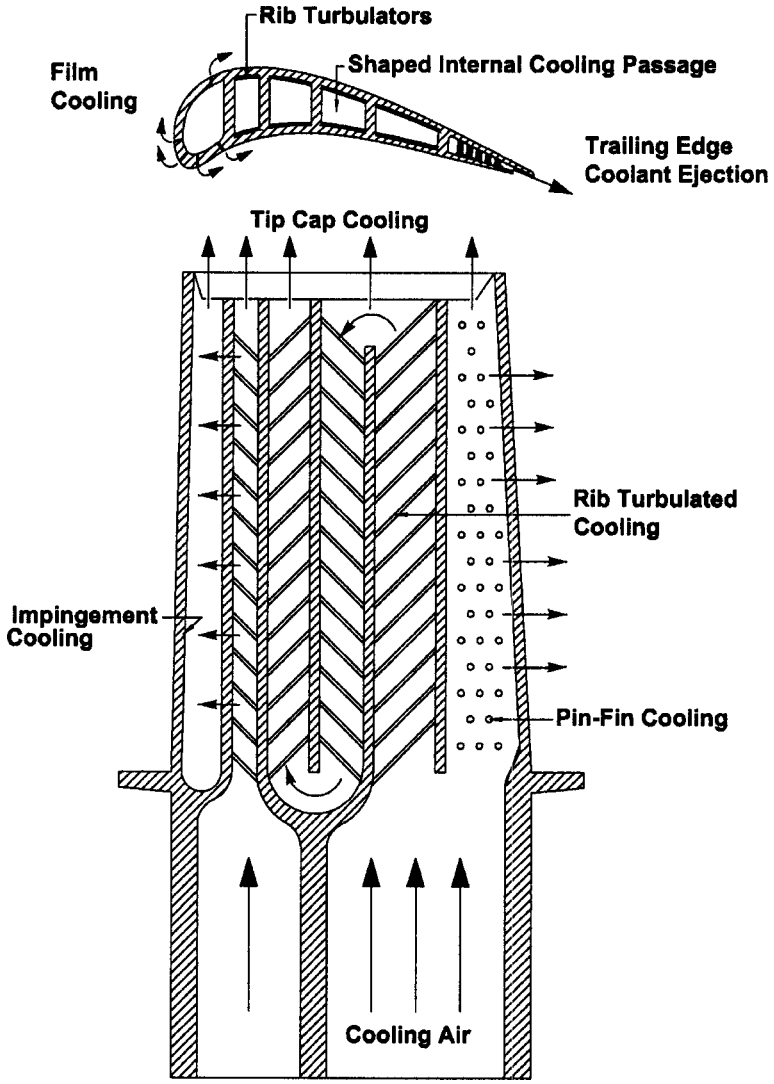

Fig. 1 Typical turbine blade internal cooling passages

variations on both the leading and trailing surfaces. Bons and Kerrebrock [10] gathered detailed heat transfer coefficient distributions using infrared thermography, and they complimented these heat transfer measurements with flow field measurements (particle image velocimetry). In this rotating single-pass square channel, they concluded that the reduced heat transfer from the leading wall is the result of the Coriolis force transporting the hot low momentum wall fluid from the trailing wall to the leading wall. They also showed that the Nusselt number on the trailing surface can be twice as great as that on the leading surface due to the combined effect of the Coriolis and buoyancy forces.

These studies aided designers in creating more efficient cooling channels, but these studies do not include the aspect ratio effect. As shown in Fig. 1, the cooling channels can consist of a variety of cross sections, and this must be considered. In recent years, several studies have emerged which investigate the effect of rotation in rectangular channels. Azad et al. [11] studied the combined effect of channel aspect ratio and channel orientation. Their findings for a 2:1 (width:height), two-pass channel were similar to a 1:1 channel: In the first pass with radially outward flow, the heat transfer from the leading surface decreased while the trailing surface increased, and the opposite occurs in the second pass. Also, the effect of rotation is reduced when the channel is skewed to the direction of rotation.

Channels located near the trailing edge of the blade have an even greater aspect ratio to fit into this narrow region of the blade. Several studies have focused on the effect of rotation in a 4:1 channel. Griffith et al. [12] observed significant spanwise variation in the heat transfer distributions due to rotation. Their results also showed that the channel orientation of the 4:1 channel has a small effect on the trailing and a large effect on the leading surface in this one-pass cooling channel. In the 4:1 channel oriented at 135° to the direction of rotation, the heat transfer from all surfaces in the channel is enhanced with rotation. Acharya et al. [13] used mass transfer to obtain detailed distributions in a two-pass 4:1 channel, and their findings were consistent with Griffith et al. [12]. Zhou et al. [14] considered the effect of rotation in a 4:1 channel with high rotation numbers. They concluded that there is a critical Reynolds number beyond which the expected heat transfer trends reverse. They also showed that increasing the density ratio increases the heat transfer enhancement. Willett and Bergles [15] studied the effect of rotation in a very narrow 10:1 channel. They independently controlled the rotation number and buoyancy parameter, and they showed the heat transfer coefficients increase on the trailing surface with increasing rotation and buoyancy while the heat transfer coefficients on the leading surface increase with increasing buoyancy.

Because the secondary flow patterns in rotating channels are strongly influenced by the cross section of the channel. It is imperative to investigate the effect of rotation in low aspect ratio

channels ($W/H<1$). Cho et al. [16] used a mass transfer method to study the effect of rotation in a rotating two-pass rectangular channel (AR=1:2). Their results showed that the rotation effect diminished in the second pass due the 180° turn effect. An experimental result for a 1:4 rotating two-pass channel was reported by Agarwal et al. [17] using the mass transfer method. For a smooth surface, they found that the 1:4 channel has lower heat/mass transfer compared to square channel.

From the above-mentioned research, it is clear that the majority of available studies involve square channels and channels located near the trailing edge of the blade. There is very limited data available for the lower aspect ratio (AR=1:2 and 1:4) channels with smooth walls. In addition, as the secondary flows resulting from rotational effects interact with the sharp 180° turn, new heat transfer characteristics in the lower aspect ratio ducts with rotation are expected. In order to understand the complex flow in low aspect ratio cooling channels with ribs, it is necessary to first understand the more fundamental flows in these smooth channels. Therefore, the objectives of this paper are to study:

1. The effects of rotation, channel orientation, and 180° sharp turn on the heat transfer distribution in two-pass low aspect ratio channels with smooth walls. The channels have aspect ratios of 1:2 and 1:4, and the channel orientation varies from 90° to 45°. Although these combinations of aspect ratio and channel orientation may not be directly applicable to current engines, it is important to investigate the effect of rotation at an alternate angle; and
2. The comparison of heat transfer enhancement between the low aspect ratio smooth channels and the published high aspect ratio smooth channels under rotating conditions.

Experimental Facility

The experimental test rig is shown in Fig. 2. This test rig was previously used by Azad et al. [11]. A variable frequency motor is connected via a gear-and-belt mesh to a hollow rotating shaft. This shaft runs from the base of the test rig to the work platform and is attached orthogonal to the hollow rotating arm. The test section is inserted inside the hollow rotating arm, which rotates in a plane orthogonal to the rotating shaft. A hand held optical tachometer is used to determine the rotation speed of the arm. Thermocouple and heater wires are connected to the slip-ring assembly mounted to the rotating shaft. The output of the thermocouples is transferred to a data acquisition system. Power input to the heaters from the variable transformers is also transmitted through the slip-ring assembly. Cooling air is pumped from a steady flow compressor through an ASME orifice flow meter and the hollow rotating shaft, turning 90°, passing into the rotating arm through the test section, and is finally expelled into the atmosphere.

This experiment contains two test sections. The geometry of the test sections are shown in Fig. 3. The 1:2 test section is 12.7 $\times$25.4 mm in cross section with a hydraulic diameter (D_h) of 16.93 mm. The test section contains a 222.25 mm unheated entrance length to provide a hydrodynamic fully developed flow condition. Each pass has a 152.4 mm long heating section. The clearance of the 180° sharp turn is 12.7 mm from tip to end wall. The divider wall has a thickness of 12.7 mm with a 6.35 mm radius at the tip. Cooling air is expelled to the atmosphere through a 6.35 mm radius hole in the second pass. The distance from the end of the heated section in the second pass to the exit hole is 152.4 mm. The 1:4 and 1:2 test sections are identical with the exception that the 1:4 test section has a cross section of 12.7 $\times$50.8 mm with a hydraulic diameter (D_h) of 20.32 mm. The mean rotating radius is 635 mm for both test sections.

A cross-sectional view of the AR=1:2 test section is shown in Fig. 4. Each pass is divided into six segments. Each segment contains six copper plates: One for the leading, one for the trailing, two for the outer, and two for the inner walls. The inner wall has only five segments in the flow direction because of the 180° turn. The copper plates are mounted in a nylon substrate, which is

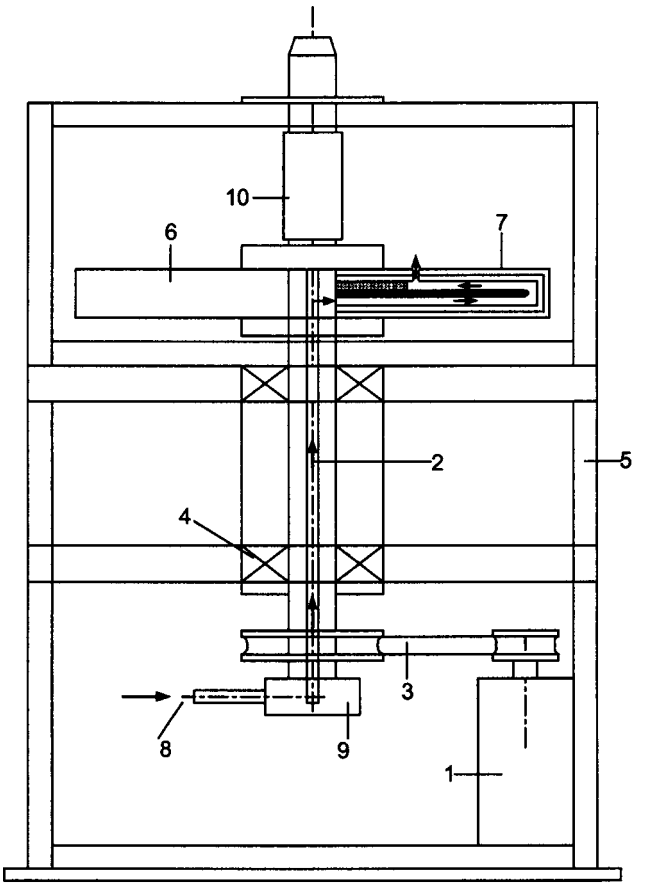

1. Electrical Motor with Controller
2. Rotating Shaft
3. Belt Drive Pulley System
4. Bearing Support System
5. Steel Table
6. Rotating Arm
7. Test Section
8. Compressor Air
9. Rotary Seal
10. Slip Ring

Fig. 2 Schematic of the test rig

comprised of the bulk of the test section. Prefabricated flexible heaters are installed beneath the copper plates. A total of 13 heaters are used for each test section. All heaters supply steady, uniform heat flux to the copper plates. Sufficient power is supplied in order to maintain a maximum wall temperature of nearly 65°C for the corresponding section. Thermal conducting paste is applied between the heater and copper plates to promote heat transfer from the heater to the plates. Each 3.18 mm thick copper plate has a 1.59 mm deep blind hole drilled in the back side, in which a copper-constantan thermocouple is installed 1.59 mm from the plate surface with thermal conducting glue. Thin nylon strips (1.59 mm) between the copper plates reduce the conduction effect between the plates.

The entire test duct is surrounded by insulating nylon material and fits in a hollow cylindrical aluminum alloy arm for structural rigidity. The AR=1:4 test section has an identical cross-sectional view except that the distance between the leading and trailing walls is twice that of the AR=1:2 test section. For both test sections, the experiments were conducted for Reynolds numbers of 5000, 10,000, 25,000 and 40,000. The test section rotates at a speed of 550 rpm, resulting in a range of rotation number (Ro) from approximately 0.026–0.2 and 0.038–0.3 for AR=1:2 and AR=1:4, respectively. This range of Reynolds number and rotation number is applicable to aircraft engines which typically have a Reynolds number of 10,000 to 50,000, and the rotation numbers can be as high as 0.25.

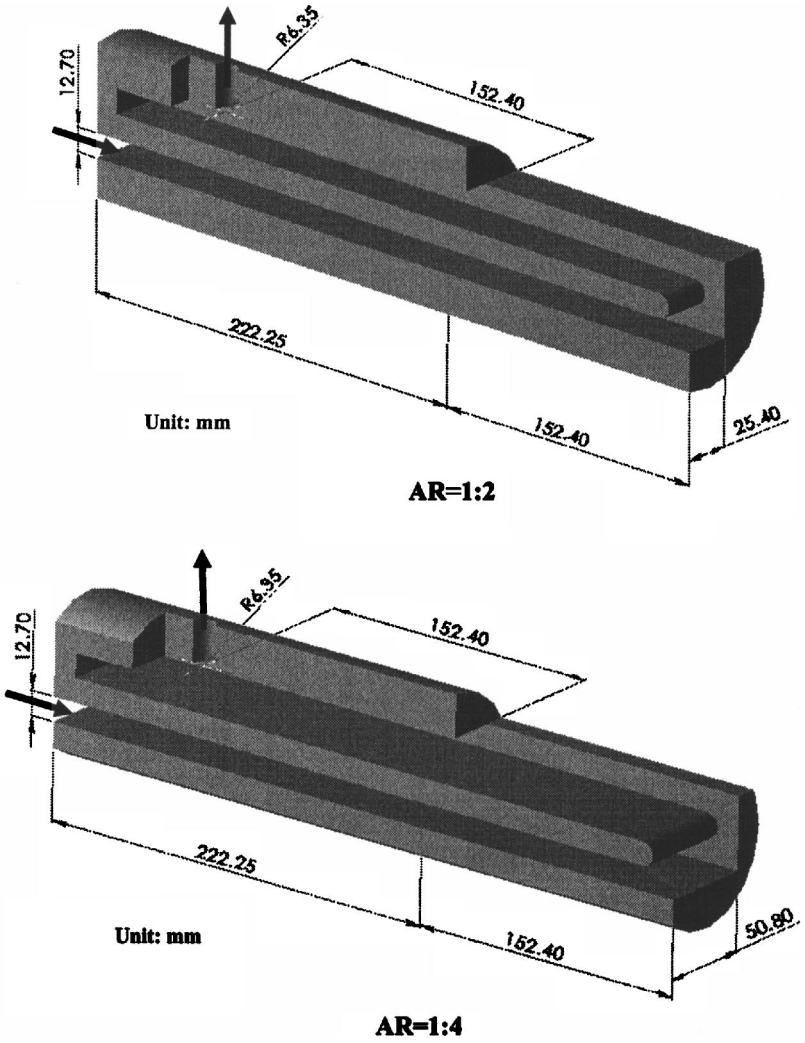

Fig. 3 Geometry of the test section: Smooth wall

Data Reduction

The regionally averaged heat transfer coefficient was calculated by dividing the net heat input to the coolant by the surface area and the temperature difference between the copper plate and air bulk mean temperature:

$$h = \frac{q - q_{\text{loss}}}{A \times (T_w - T_b)} \tag{1}$$

The net heat transfer rate is the electrical power supplied to the heater ($q = VI$) minus heat losses. Heat losses were determined by supplying power to the test section until a steady-state condition was achieved in a no-flow condition. Fiberglass insulation was inserted into the test channel to prevent convection between the channel walls. This is done for several power inputs to obtain a relation between the total heat loss from each wall and the corresponding wall temperature. The regionally averaged wall temperature is obtained from thermocouples that are embedded in each copper plate. The bulk mean air inlet and exit temperatures are measured by thermocouples. Because there is a long distance between leading and trailing walls, two thermocouples are placed at the exit to measure the bulk mean air temperature. The averaged value of these two measurements is used for the exit bulk mean temperature. However, the difference between these two measurements is less than 1°C for all cases. The local bulk mean air temperature (T_b) used in Eq. (1) is calculated by using linear interpolation between the measured inlet and exit bulk air temperatures. Another way to obtain the local bulk mean air temperature is by using the energy balance through the test channel. The difference between the linear interpolation and energy balance of bulk mean air temperature is 1 to 2°C in all cases.

The regionally averaged Nusselt number is normalized by the Nusselt number for fully developed turbulent flow in a smooth nonrotating circular pipe to reduce the influence of the flow Reynolds number on the heat transfer coefficient. The regionally averaged Nusselt number normalized by the Dittus–Boelter/McAdams correlation is

$$\frac{\text{Nu}}{\text{Nu}_o} = \frac{hD_h}{k_{\text{air}}} \frac{1}{(0.023\,\text{Re}^{0.8}\,\text{Pr}^{0.4})} \tag{2}$$

The Prandtl number (Pr) for air is 0.71. Air properties are taken based on the mean bulk air temperature. The estimated uncertainty for temperature measurement is 0.5°C. Based on the method described by Kline and McClintock [18], the uncertainty of the Nusselt number ratio is about 5% for the high Reynolds number. For the low Reynolds number (Re=5000), the maximum uncertainty is about 18% on the low heat transfer surfaces under the rotating condition.

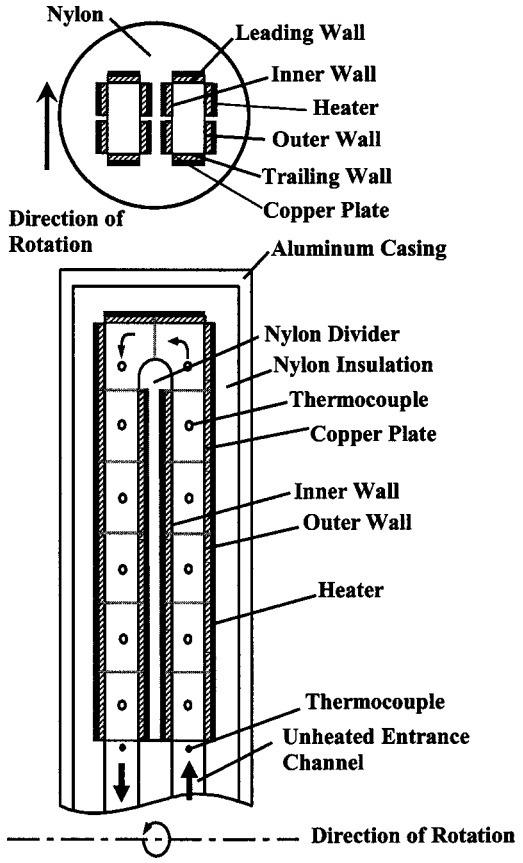

Fig. 4 Cross-sectional view of the two-pass rectangular test section (AR=1:2)

Results and Discussion

Rotation effect, turn effect, and buoyancy parameter are the most important factors in heat transfer in a two-pass rotating rectangular channel with smooth walls. The Coriolis force is known as the primary effect due to rotation. As shown in Figs. 5 and 6, with a 90° channel orientation, the Coriolis force induces a pair of vortices which circulate toward the trailing wall for radial outward flow and toward the leading wall for radial inward flow. This cross-stream secondary flow pattern significantly increases heat transfer on the trailing wall in the first pass (radial outward flow) and the leading wall in the second pass (radial inward flow), but reduces heat transfer on the opposite walls (leading wall in the first pass and trailing wall in the second pass). Therefore, rotation causes a difference in the heat transfer between the leading and trailing walls. When the channel orientation is rotated to 45°, the effect of rotation is reduced. The effect of rotation is evaluated by using the rotation number

$$\mathrm{Ro}=\frac{\Omega D_h}{V} \tag{3}$$

The 180° sharp turn creates additional secondary flows that affect heat transfer inside the turn and after the turn. A variety of different flow patterns can result depending on the turn geometry. For this case, when the flow passes through the 180° sharp turn (as shown in Figs. 5 and 6), the flow impinges on the outer wall due to the centrifugal force, then reattaches on the inner wall in the second pass. It creates a circulation zone right after the turn near the inner wall in the second pass. Two additional circulation zones occur in the outer corners of the turn because of the geometry. This type of flow behavior has been verified by numerical simulations, and the interested reader is referred to the work of Su et al. [19] for additional explanations of the flow physics. As one would anticipate, these flow structures, due to the turn, result in different heat transfer enhancements inside the turn and after the turn.

The buoyancy parameter due to the centrifugal force and temperature difference is important because of the high rotating speed and large temperature difference in the actual engine. For the radial outward flow, the rotation-induced buoyancy force aids the inertia force. This force opposes the inertia force in the second pass because the flow direction is reversed. A local buoyancy parameter is used to present the combined effects of the Coriolis and buoyancy forces.

$$Bo_x=\left(\frac{\Delta\rho}{\rho}\right)(\mathrm{Ro})^2\frac{R}{D_h} \tag{4}$$

This local buoyancy parameter can be rewritten incorporating the measured wall and coolant temperatures as shown in Eq. (5):

$$Bo_x=\frac{T_{w.x}-T_{b,x}}{T_{f,x}}(\mathrm{Ro})^2\frac{R_x}{D_h} \tag{5}$$

The local film temperature is the average of the local wall and the local coolant temperatures

$$T_{f,x}=\frac{T_{w.x}+T_{b,x}}{2} \tag{6}$$

Nusselt Number Ratio Distribution for an Aspect Ratio of 1:2

The experimental results are shown in Fig. 7 for the 1:2 channel. The figure contains both nonrotating and rotating ($\beta=90°$ and 45°) heat transfer distributions for both the leading and trailing surfaces. For the nonrotating case, the Nusselt number ratio is about one in the first pass as expected. It is apparent that the turn effect significantly enhances heat transfer on both the leading and trailing surfaces in the turn region. The enhancement decreases in the second pass. The Nusselt number ratio is above one due to the short length of the channel. If X/D_h were longer, the Nusselt number ratio would decrease to about one. At a Reynolds number equal to 40,000, the flow is reaching fully developed.

For the rotating case, as one would anticipate, the rotation effect enhances heat transfer on the trailing surface in the first pass, and the leading surfaces experiences a declination in heat transfer. As the Reynolds number increases, the variation between the leading and trailing surfaces decreases as both surfaces approach the nonrotating value of a Nusselt number ratio of about one. In the turn region, the heat transfer enhancement is greater than that of the nonrotating value due to the combined effect of rotation and 180° sharp turn. This heat transfer trend is true for both channel orientations ($\beta=45°$ and 90°). The Nusselt number ratio trends of the second pass are unlike those reported for square channels or channels with an aspect ratio of 2:1. In general, the Nusselt number ratios for both the leading and trailing surfaces under the rotating condition are higher than those of the nonrotating case in the second pass of present 1:2 channel. The only exception is the trailing surface with the 90° channel orientation at the lowest Reynolds number. As the Reynolds number increases (rotation number decreases), the variation between the leading and trailing surfaces decreases.

Not only is the enhancement on both the leading and trailing surfaces greater than that of the nonrotating channel, there is less difference between the leading and trailing surfaces of the second pass. The numerous studies involving square channels indicate that the leading surface of the second pass experiences heat transfer enhancement above that of a nonrotating channel, while the trailing surface experiences decreased heat transfer. For the present 1:2 channel, less variation between the leading and trailing surfaces is seen due to the strong turn. The 180° sharp turn has a more dominant effect on the heat transfer of the second pass than rotation. Therefore, the rotation-induced vortices, which result in

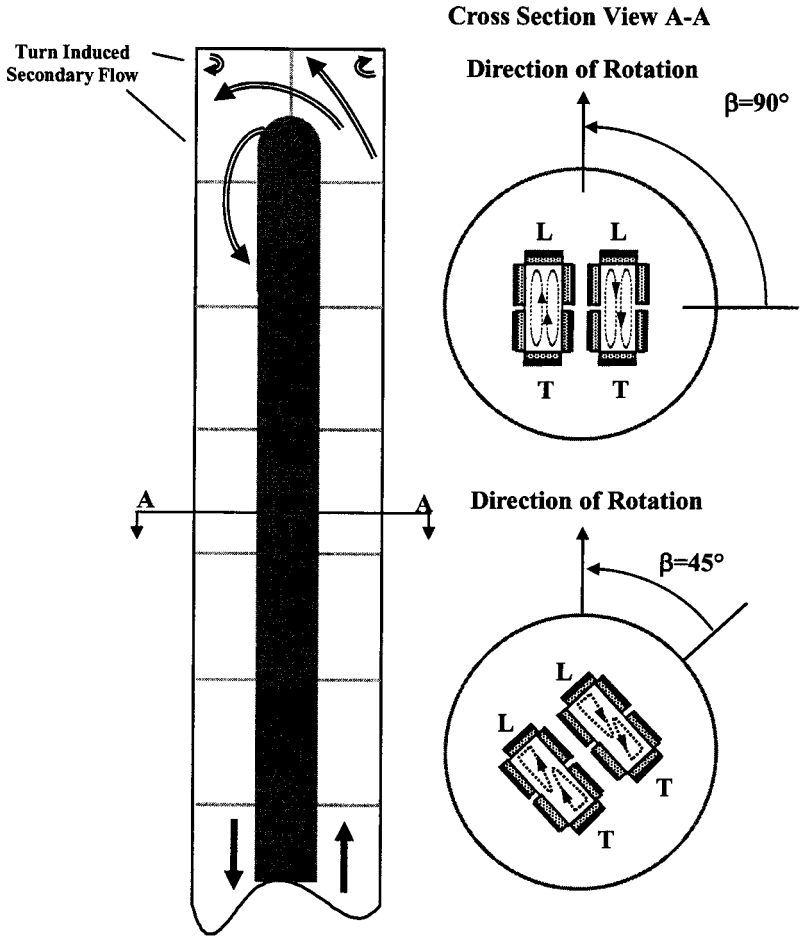

Fig. 5 Conceptual view of the secondary flow patterns (AR=1:2)

the heat transfer difference between the leading and trailing surfaces, are not as strong as the secondary flow induced by the turn. The second pass is approximately 9 hydraulic diameters long, and the strong turn dominates the heat transfer trends over this entire length.

Nusselt Number Ratio Distributions for an Aspect Ratio of 1:4

Figure 8 shows the Nusselt number ratio distributions for the 1:4 channel. Similar to the 1:2 channel, the Nusselt number ratio of the nonrotating channel is about one. As the Reynolds number increases, the enhancement decreases. Because the second pass is not long enough (about 7 D_h) for flow to develop, the Nusselt number ratio is always higher than one in the 1:4 channel.

Similar to the 1:2 channel (Fig. 7), significant variation due to rotation is observed in the first pass of the 1:4 channel. However, the difference between the leading and trailing surfaces is greater in this 1:4 channel than the 1:2 channel. Because the rotating experiments are conducted at a constant angular velocity of 550 rpm, the rotation numbers vary between the two channel sizes (the channels have different hydraulic diameters). Therefore, the rotation numbers of the 1:4 channel are greater than those of the 1:2 channel. As the rotation number decreases (Reynolds number increases), the difference between the leading and trailing surfaces decreases for both channel orientations ($\beta=90°$ and 45°).

Similar to the 1:2 channel (Fig. 7), the difference between the heat transfer from the leading and trailing surfaces decreases significantly in the second pass of the 1:4 channel (Fig. 8). At the higher rotation numbers (lower Reynolds numbers), variation between the leading and trailing surfaces can be observed, but this difference quickly diminishes as the rotation number decreases (Reynolds number increases). In this case, the flow has less than 7 hydraulic diameters to develop downstream of the turn. This short distance is insufficient for the rotation-induced vortices to overcome the dominant secondary flow induced by the 180° sharp turn.

The channel averaged Nusselt number ratios are shown in Fig. 9 for both channel aspect ratios under nonrotating and rotating conditions. The first pass average includes all regions in the first pass, including the region at the entrance of the 180° turn. The second pass average includes all regions in the second pass, including the region at the exit of the turn. The nonrotating curves are the average of the leading and trailing surfaces in the nonrotating channels. The effect of rotation is clearly seen in the first pass of both the 1:2 and the 1:4 channels: The leading surfaces experience decreased heat transfer while the trailing surfaces experience increased heat transfer. However, the variation is signifi-

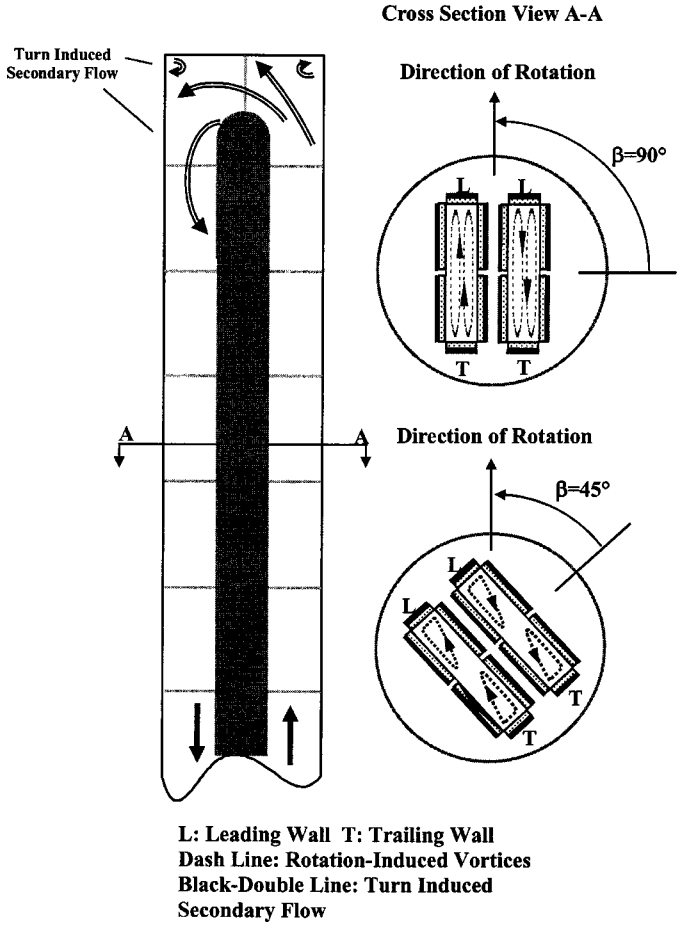

Fig. 6 Conceptual view of the secondary flow patterns (AR=1:4)

cantly reduced in the second pass, and this is clearly seen for both the 1:2 and 1:4 channels in Figs. 9(*b*) and 9(*d*), respectively. It can be seen that the rotation cases have higher heat transfer than the nonrotating case in the second pass. As the Reynolds number increases (rotation number decreases), the difference between the leading and trailing walls is reduced. In addition, the average Nusselt number ratio decreases with increasing Reynolds number.

Comparison with Previous Studies

The diminished variation between the leading and trailing surfaces of the second pass has also been observed by Cho et al. [16] and Agarwal et al. [17] in 1:2 and 1:4 rotating channels, respectively. Figure 10 compares the heat transfer coefficients in the smooth 1:2 channel of Cho et al. [16] to the smooth results of the present 1:2 channel. The Reynolds number of both the nonrotating and rotating channel is 10,000, and the rotation number of the rotating case is 0.1 for both the previous study and the present study.

As shown in Fig. 10, the present study is in close agreement with the previous study for the nonrotating smooth channel. The most significant difference between the two data sets is in the 180° turn. The study of Cho et al. [16] is performed using mass transfer; therefore, a detailed distribution can be obtained. With the copper plate method of the present study, only two regionally averaged points are recorded for the turn, so the detailed distribution cannot be obtained to capture the slightly higher values presented in the previous mass transfer study.

The rotating results of the present 1:2 channel are also very comparable to the previous study. As shown in Fig. 10, both studies (using different experimental methods) reveal the same results for both the leading and trailing surfaces of the first and second passes. This confirms that the heat transfer in the second pass is dominated by the 180° turn. As with the current study, Cho et al. [16] reported only negligible variation between the leading and trailing surfaces of the second pass.

Agarwal et al. [17] used naphthalene sublimation to investigate the effect of rotation in channels with an aspect ratio of 1:4. Because the entrance conditions of the two channels vary significantly (fully developed for the present study and sudden contraction for the previous study) and the flow conditions are different (Reynolds and rotation numbers), it is difficult to make direct comparisons between the two data sets. However, from the local distributions presented for the smooth rotating channels, the lack of variation between the leading and trailing surfaces is present at the beginning of the second pass of their 1:4 channel. Approximately 7 hydraulic diameters are required for a significant difference to appear between the leading and trailing surfaces, and as the channel continues to X/D_h of 30, the difference between the leading and trailing surfaces becomes more significant. The second pass of the present 1:4 channel has a length of less than 7 hydraulic diameters. In this short passage length, the effect of the turn is dominant, and as shown by Agarwal et al. [17] at least 7 hydraulic diameters are required for the turn effect to diminish.

The reduced effect of rotation in the second pass was also reported in square channels (Johnson et al. [7]) and 2:1 channels (Azad et al. [11]). Johnson et al. [7] attributed the lack of large variation in the second pass to the secondary flow induced by the turn. Although both of these studies show that the effect of rota-

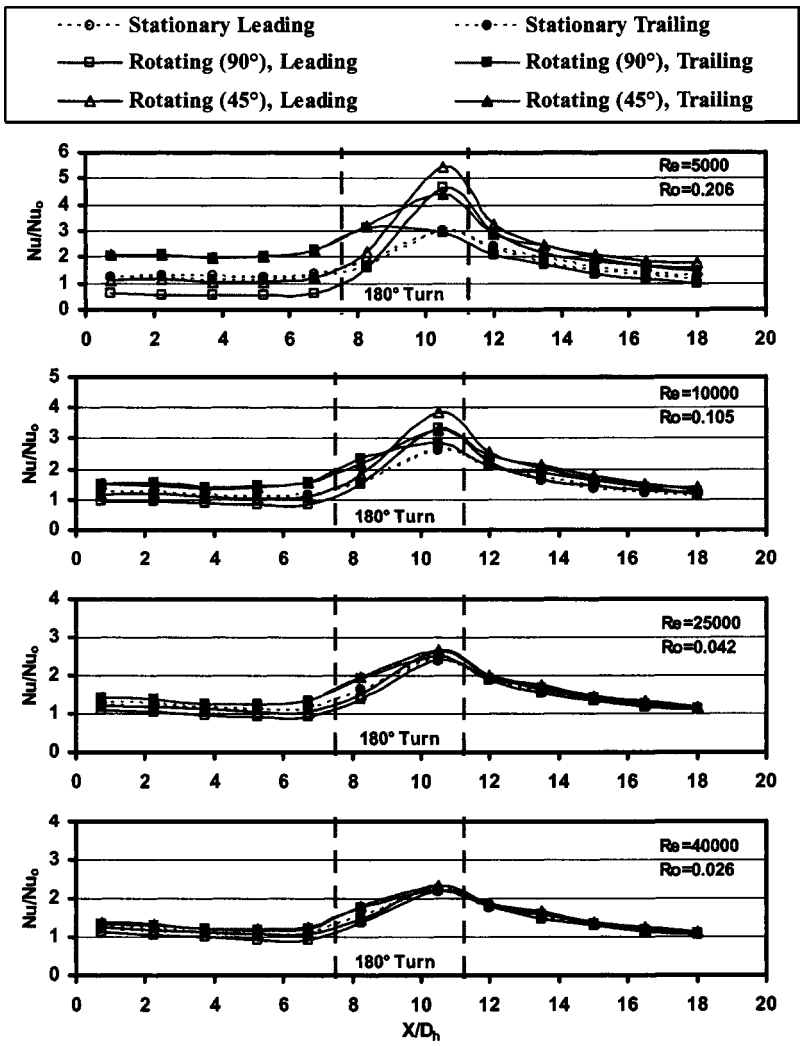

Fig. 7 Nusselt number ratio distribution for AR=1:2 with smooth wall

tion on the second pass is less than that of the first pass, the effect of rotation in both the square and 2:1 channels is significant; unlike the present 1:2 and 1:4 channels.

When considering the flow structure of the coolant in the rotating two-pass channels, it has been shown that the circulation direction of the rotation-induced vortices reverses in the second pass due to the reversed direction of the Coriolis force. The strength of the vortices begins growing just downstream of the turn. While the strength of the rotation-induced vortices is growing, the effect of the turn diminishes through the second pass. With a relatively large distance between the leading and trailing surfaces of the 1:2 and 1:4 channels (compared to square and 2:1 channels), more distance is required for the effect of the sharp 180° turn to diminish. Therefore, the length of the second pass of the present study is not long enough for the entrance effect to diminish and allow the effect of rotation to become more apparent. Therefore, the effect of rotation is significantly reduced in the second pass of the low aspect ratio channels.

Secondary Flow Effect on Circumferential Walls Heat Transfer

The rotation-induced secondary flow has a strong effect on the circumferential heat transfer of the channel. Figure 11 shows the rotation-induced secondary flow patterns, as well as the circumferential regionally averaged Nusselt number ratios at the Reynolds number of 10,000. The circumferential distribution is shown at two locations in the channel: At the fourth region in the first pass and the fifth region in the second pass (eleventh point overall). The numbers marked next to each surface of the different aspect ratios, orientations, and rotation numbers are the Nusselt number ratios on these surfaces.

For the nonrotating case (as shown in Fig. 11), the regionally averaged heat transfer is uniform around the perimeter walls in the first pass. In the second pass, it is generally true, except that the heat transfer level is slightly higher than in the first pass due to the 180° turn effect. As the channel is rotated, a pair of vortices induced by the Coriolis force enhances the heat transfer on the trailing surface, and reduces the heat transfer on the leading surface in the first pass. The effect is reversed in the second pass due to the reversed direction of the Coriolis force. Therefore, the trailing, outertrailing, and innertrailing surfaces in the first pass undergo a heat transfer enhancement under rotating conditions, while the leading, outerleading, and innerleading surfaces experience reduced heat transfer. In general, the heat transfer in the second pass follows this trend, however, the turn effect created a more complicated result. The difference between leading and trailing surfaces is relatively small in the second pass than that in the first pass. In addition, the outertrailing wall in the second pass has higher heat transfer than the outer-leading wall.

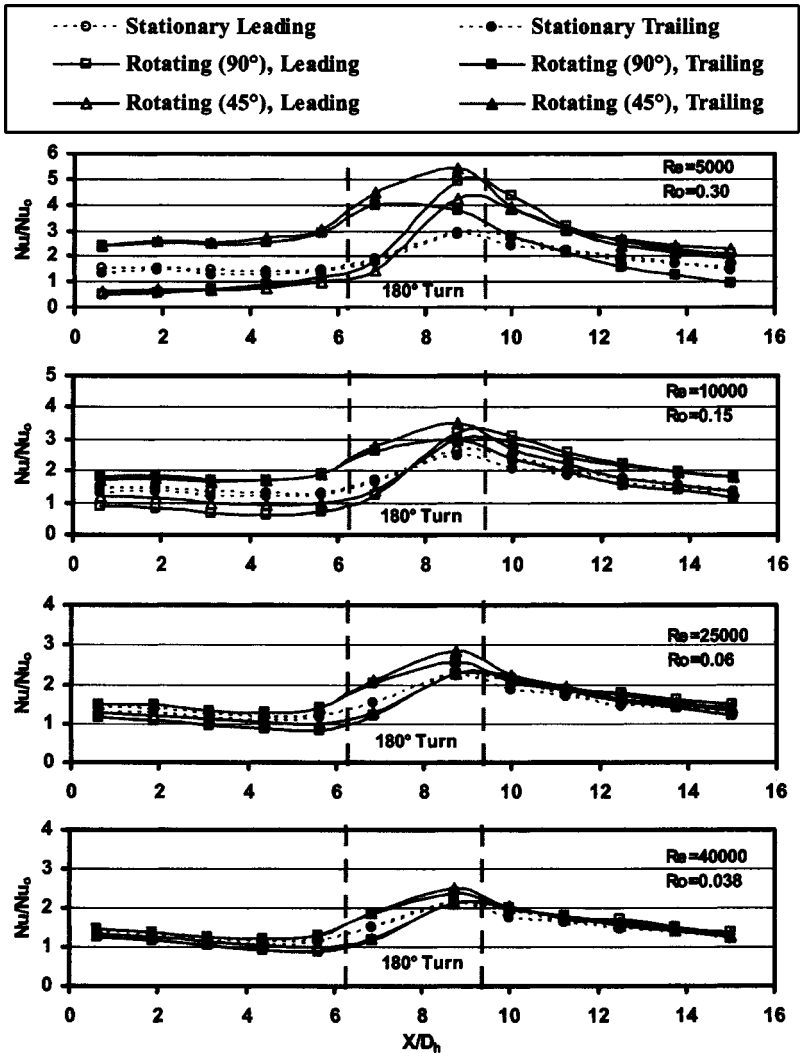

Fig. 8 Nusselt number ratio distribution for AR=1:4 with smooth wall

The rotation effect reduced for the channel orientation of 45° (when compared to $\beta=90°$). Therefore, the difference of heat transfer between the leading and trailing surfaces was reduced. Higher heat transfer enhancement can be seen on the side walls due to the rotation-induced secondary flow impinging on the side walls.

Aspect Ratio Effect on Heat Transfer

A channel aspect ratio comparison is shown in Fig 12. The figure compares the Nusselt number ratios of five channels of different aspect ratios ranging from 4:1 to 1:4; therefore, this range of channels can cover the entire cross section of an airfoil. All channels cover a range of Reynolds numbers varying from 5000 to 40,000. The square channel has a hydraulic diameter of 12.7 mm, the hydraulic diameter of the 1:2 and 2:1 channels is 16.93 mm, and the hydraulic diameter of the 1:4 and 4:1 channels is 20.32 mm. Because the channels have different hydraulic diameters but the same channel length, the comparisons are made at specific regions where the flow can be considered fully developed in both the first pass and the second pass. In the first pass, data are compared at the fourth copper plate, and compared at the eleventh copper plate in the second pass.

Figure 12(*a*) shows a comparison of the first pass of the rotating channels oriented at $\beta=90°$. This figure shows that the heat transfer from the trailing surface of all the channels increases with the increasing buoyancy parameter, and this should be anticipated as the core of the coolant is shifted toward the trailing surface with rotation. However, the heat transfer trends of the leading surface are more complex. At low buoyancy parameters, the heat transfer decreases as the buoyancy parameter increases for all channels. At high buoyancy parameters, the heat transfer from the leading surfaces of the 4:1 and 1:4 channels increases with the increasing buoyancy parameter. The heat transfer difference between the leading and trailing surfaces is about the same for 1:1, 2:1, and 1:2 channels; however, the difference in the 1:4 channel is much larger than the 4:1 channel. Figure 12(*b*) shows the aspect ratio comparison in the second pass of the two-pass channels. The heat transfer in the second pass of all channels has a decreasing trend for the trailing surface with the increasing buoyancy parameter. However, the Nusselt number ratio for all leading surfaces increases with the increasing buoyancy parameter.

In the actual turbine blades, the cooling channels have different orientations in order to fit the cross section of the airfoil; therefore, the channel orientation of 90° is not practical for all aspect ratio channels. Figure 13 takes the channel orientation into account by comparing the heat transfer enhancement of various aspect ratio channels at various orientation angles. The square channel (AR=1:1) maintains the orientation of 90°, the 1:4 and 1:2 channels which would likely be located near the leading edge of the blade are oriented at 45°, and the 2:1 and 4:1 channels are oriented at 135° to fit near the trailing edge of the blade. The behavior of the first pass is shown in Fig. 13(*a*) and is similar to

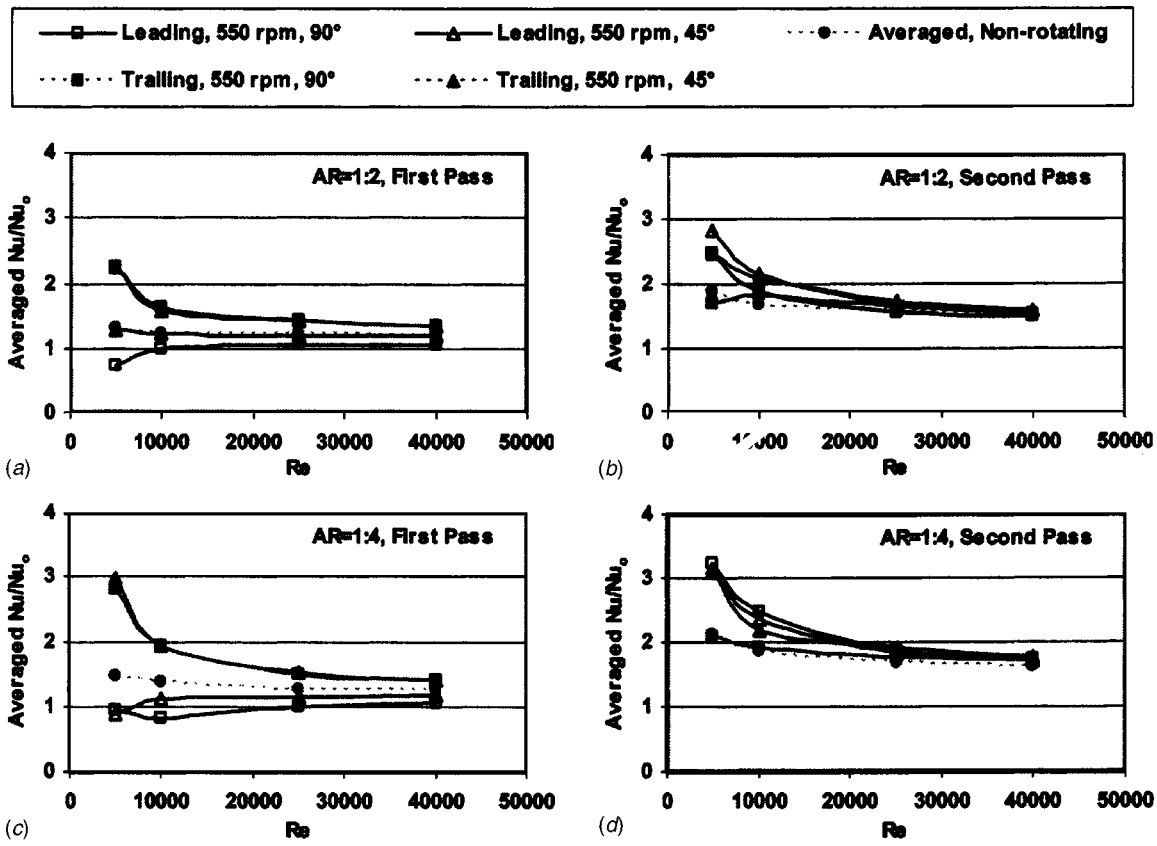

Fig. 9 Channel averaged Nusselt number ratio for both rotating and nonrotating cases

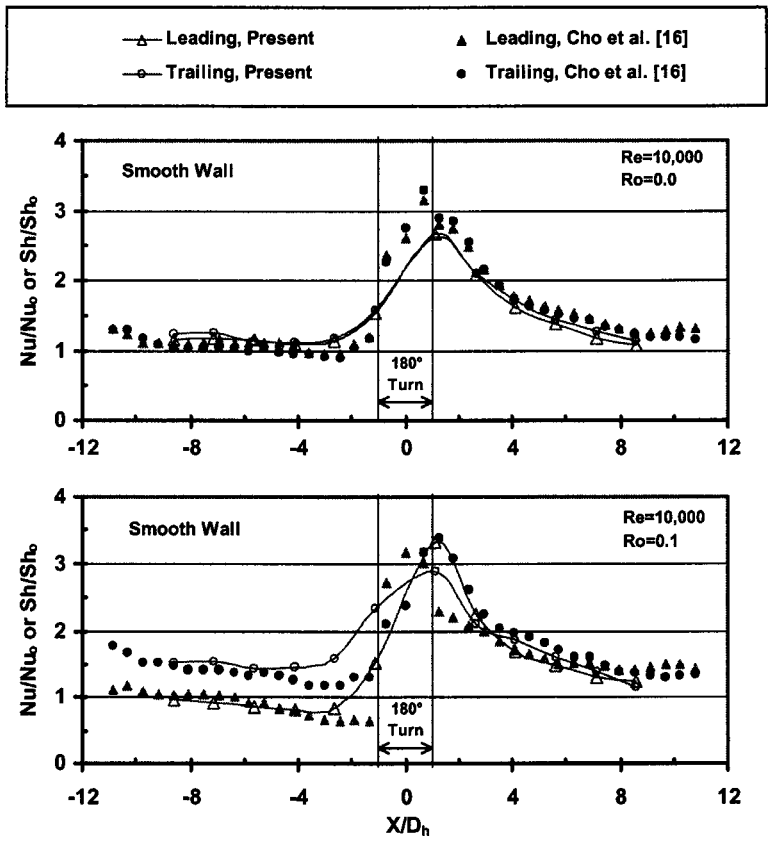

Fig. 10 Comparison of the Nusselt number ratio distributions for AR =1:2 with smooth walls

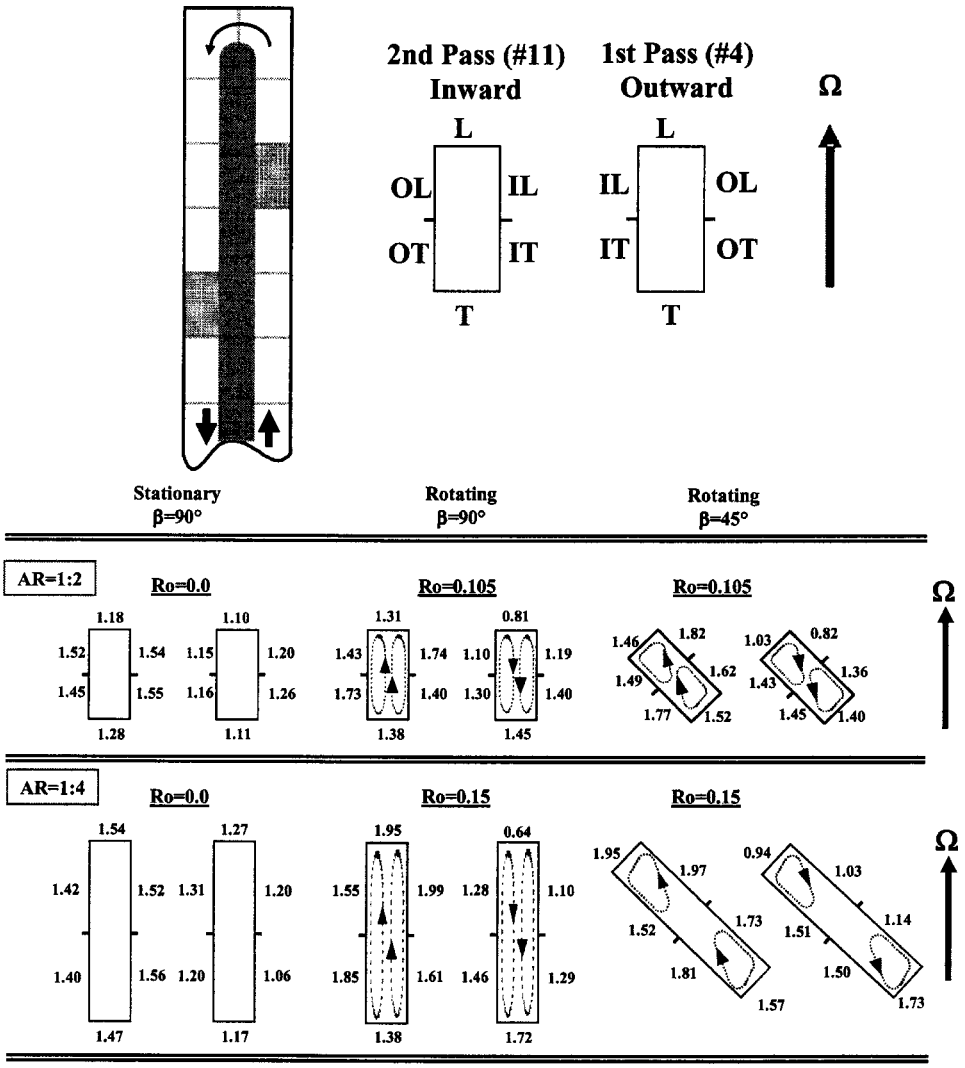

Fig. 11 Secondary flow effect on circumferential heat transfer (Re=10,000) (number represents the Nusselt number ratio)

the behavior shown in Fig. 12(*a*). For all channels, the heat transfer enhancement on the trailing surfaces increases with the increasing buoyancy parameter. However, the heat transfer decreases on the leading surface of the 1:1 and 1:4 channels, while it increases on the leading surfaces of the 4:1 channel. However, the declination of heat transfer on the leading surfaces is much less in these channels which account for the channel orientation effect than in the channels orientated at 90°. Similar results are shown for the second pass of these channels [Fig. 13(*b*)] as for the orthogonal rotating channels [Fig. 12(*b*)]: Both the leading and trailing surfaces of the 1:4 and 1:2 channels undergo heat transfer enhancement with the increasing buoyancy parameter, and the trailing surfaces of the 1:1 and 2:1 channels experience a decrease while the leading surfaces see an enhancement in the Nusselt number ratios.

Conclusions

In actual turbine blades, the internal cooling passages have a low aspect ratio near the leading edge of the airfoil. This study experimentally investigated the low aspect ratio two-pass rectangular channels under rotating conditions with smooth walls. Two aspect ratio channels were tested: AR=1:2 and AR=1:4. The results are comparable to the results of previous studies. The aspect ratio effect in two-pass rotating rectangular channels was considered. Based on the discussion, the main conclusions are:

1. The 180° sharp turn significantly increased heat transfer on both the leading and trailing surfaces in the turn region. As the Reynolds number increases, the Nusselt number ratio decreases in both nonrotating and rotating cases
2. The rotation effect increased heat transfer on the trailing surface but decreased the heat transfer on the leading surface in the first pass of both the 1:4 and 1:2 channels. Therefore, the rotation effect created a heat transfer difference between the leading and trailing surfaces. In the second pass, the rotation effect enhanced heat transfer on all surfaces except for the trailing surface at a channel orientation of 90°. The difference of heat transfer between the leading and trailing surfaces diminished in the second pass compared to that in the first pass. As the Reynolds number increased, the rotation effect decreased.
3. Rotation has a relatively small effect in the second pass of the 1:2 and 1:4 channels. In the present results, the second pass has a length about 9 and 7 hydraulic diameters for the 1:2 and 1:4 channels, respectively. It is believed that a clear rotation effect can be observed in a longer channel or at higher rotation numbers.

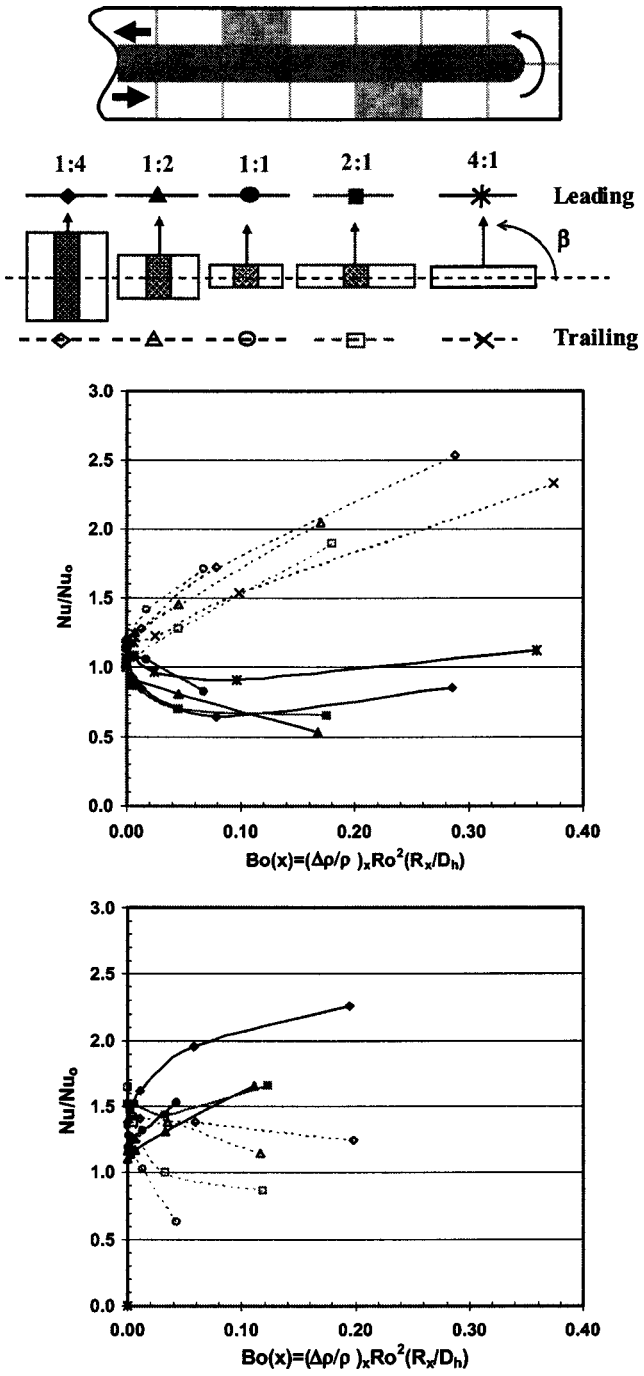

Fig. 12 Aspect ratio effect on heat transfer ($\beta=90°$)

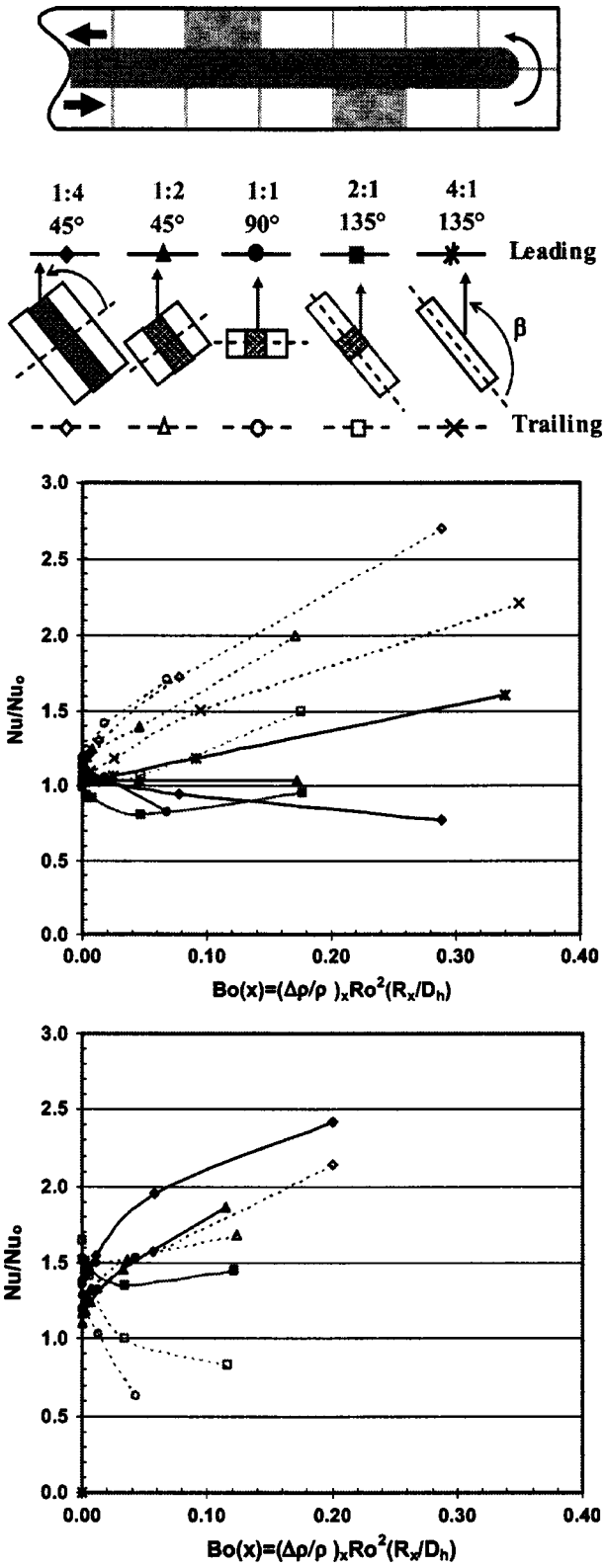

Fig. 13 Aspect ratio and channel orientation effect on heat transfer ($\beta=90°$, 45°, and 135°)

4. The 90° channel orientation creates a greater heat transfer difference between the leading and trailing walls than the 45° channel orientation for both aspect ratio ducts under rotating conditions.

5. The results of the circumferential wall heat transfer agree well with the secondary flow patterns in both the nonrotating and rotating cases.

6. A comparison of five different aspect ratio channels showed that increasing the buoyancy parameter enhanced the heat transfer on the trailing surface for all channels in the first pass. However, the heat transfer trends are different for different aspect ratios in the second pass. The square duct has the lowest heat transfer on both the leading and trailing surfaces compared to the other channels.

Acknowledgments

This publication was prepared with the support of the U.S. Department of Energy, Office of Fossil Energy, National Energy Technology Laboratory, through SCIES project 01-01-SR094.

However, any opinions, findings, conclusions, or recommendations expressed herein are those of the authors and do not necessarily reflect the views of the DOE.

Nomenclature

A = area of smooth wall
Bo_x = local buoyancy parameter
D_h = hydraulic diameter
h = heat transfer coefficient
k = thermal conductivity of coolant
Nu = local Nusselt number, hD_h/k
Nu_o = Nusselt number for fully-developed turbulent flow in a smooth pipe
Pr = Prandtl number
q_{net} = net heat transfer rate at the wall
R = mean rotating radius
R_x = local rotating radius
Re = Reynolds number, $\rho VD_h/\mu$
Ro = rotation number, $\Omega D_h/V$
$T_{b,x}$ = local coolant temperature
$T_{f,x}$ = local film temperature
$T_{w,x}$ = localwall temperature
V = bulk velocity in streamwise direction
β = angle of channel orientation with respect to the axis of rotation
Ω = rotational speed
μ = dynamic viscosity of coolant
ρ = density of coolant
$(\Delta\rho/\rho)$ = local coolant-to-wall density ratio, $(T_{w,x}-T_{b,x})/T_{f,x}$

References

[1] Han, J. C., Dutta, S., and Ekkad, S. V., 2000, *Gas Turbine Heat Transfer and Cooling Technology*, Taylor and Francis, New York.
[2] Kays, W. M., and Crawford, M. E., 1993, *Convective Heat and Mass Transfer*, 3rd ed., McGraw–Hill, New York, pp. 311–349.
[3] Fan, C. S., and Metzger, D. E., 1987, ''Effects of Channel Aspect Ratio on Heat Transfer in Rectangular Passage Sharp 180° Turn,'' ASME Paper No. 87-GT-113.
[4] Han, J. C., Chandra, P. R., and Lau, S. C., 1988, ''Local Heat/Mass Transfer in Distributions Around Sharp 180° Turns in Two-Pass Smooth and Rib-Roughened Channels,'' ASME J. Heat Transfer, **110**, pp. 91–98.
[5] Wagner, J. H., Johnson, B. V., and Hajek, T. J., 1991a, ''Heat Transfer in Rotating Passage with Smooth Walls and Radial Outward Flow,'' ASME J. Turbomach., **113**, pp. 42–51.
[6] Wagner, J. H., Johnson, B. V., and Kooper, F. C., 1991b, ''Heat Transfer in Rotating Passage with Smooth Walls,'' ASME J. Turbomach., **113**, pp. 321–330.
[7] Johnson, B. V., Wagner, J. H., Steuber, G. D., and Yeh, F. C., 1994, ''Heat Transfer in Rotating Serpentine Passage with Selected Model Orientations for Smooth or Skewed Trip Walls,'' ASME J. Turbomach., **116**, pp. 738–744.
[8] Dutta, S., and Han, J. C., 1996, ''Local Heat Transfer in Rotating Smooth and Ribbed Two-Pass Square Channels with Three Channel Orientations,'' ASME J. Heat Transfer, **118**, pp. 578–584.
[9] Park, C. W., and Lau, S. C., 1998, ''Effect of Channel Orientation of Local Heat (Mass) Distributions in A Rotating Two-Pass Square Channel with Smooth Walls,'' ASME J. Heat Transfer, **120**, pp. 624–632.
[10] Bons, J. P., and Kerrebrock, J. L., 1999, ''Complementary Velocity and Heat Transfer Measurements in a Rotating Cooling Passage with Smooth Walls,'' ASME J. Turbomach., **121**, pp. 651–662.
[11] Azad, G. S., Uddin, M. J., Han, J. C., Moon, H. K., and Glezer, B., 2002, ''Heat Transfer in a Two-Pass Rectangular Rotating Channel with 45° Angled Rib Turbulators,'' ASME J. Turbomach., **124**, pp. 251–259.
[12] Griffith, T. S., Al-Hadhrami, L., and Han, J. C., 2002, ''Heat Transfer in Rotating Rectangular Cooling Channels (AR=4) with Angled Ribs,'' ASME J. Heat Transfer, **124**, pp. 617–625.
[13] Acharya, S., Agarwal, P., and Nikitopoulos, D. E., 2004, ''Heat/Mass Transfer in a 4:1 AR Smooth and Ribbed Coolant Passage with Rotation in 90° and 45° Orientations,'' ASME Paper No. GT2004-53928.
[14] Zhou, F., Lagrone, J., and Acharya, S., 2004, ''Internal Cooling in 4:1 AR Passages at High Rotation Numbers,'' ASME Paper No. GT2004-53501.
[15] Willett, F. T., and Bergles, A. E., 2001, ''Heat Transfer in Rotating Narrow Rectangular Ducts with Heated Sides Orientated at 60° to the *R-Z* Plane,'' ASME J. Turbomach., **123**, pp. 288–295.
[16] Cho, H. H., Kim, Y. Y., Kim, K. M., and Rhee, D. H., 2003, ''Effects of Rib Arrangements and Rotation Speed on Heat Transfer in a Two-Pass Duct,'' ASME Paper No. 2003-GT-38609.
[17] Agarwal, P., Acharya, S., and Nikitopoulos, D. E., 2003, ''Heat/Mass Transfer in 1:4 Rectangular Passages with Rotation,'' ASME Paper No 2003-GT-38615.
[18] Kline, S. J., and McClintock, F. A., 1953, ''Describing Uncertainty in Single-Sample Experiments,'' Mech. Eng. (Am. Soc. Mech. Eng.), **75**, pp. 3–8.
[19] Su, G., Chen, H. C., Han, J. C., and Heidmann, D., 2004, ''Computation of Flow and Heat Transfer in Rotating Two-Pass Rectangular Channels (AR=1:1, 1:2, and 1:4) by a Reynolds Stress Turbulence Model,'' Int. J. Heat Mass Transfer, **47**, pp. 5665-5683.

Unsteady Heat Transfer Enhancement Around an Engine Cylinder in Order to Detect Knock

Khaled Loubar

Jérôme Bellettre

Mohand Tazerout

e-mail: jerome.bellettre@emn.fr

Ecole des Mines de Nantes, DSEE.,
4, rue Alfred Kastler, B.P. 20722,
44307 Nantes Cedex 3, France

This paper deals with the transient thermal signal around an engine cylinder in order to propose a new and nonintrusive method of knock detection. Numerical simulations of unsteady heat transfer through the cylinder and inside the coolant flow are carried out to account for heat flux variations due to normal and knocking combustion. The effect of rib roughened surfaces on thermal signal amplification is investigated. The geometric parameters are fixed at $Pi/h=10$ and $w/h=1$ with a Reynolds number based on hydraulic diameter of 12,000. The results reveal that square ribs give better performance in term of thermal signal amplification within the fluid. An amplification of the temperature variation up to 20 times higher is found. Finally, flow analysis shows that amplification depends on the position where the thermal signal is collected. [DOI: 10.1115/1.1857943]

1 Introduction

Modern engines control systems are designed to minimize exhaust emissions while maximizing power and fuel economy. The ability to maximize power and fuel economy by optimizing spark timing for a given air/fuel ratio is limited by the engine knock. Especially in gas spark ignition (SI) engines, composition, and the knocking properties of the fuel vary with time. Knock produces pressure waves that generate a rapid increase in cylinder pressure. If sustained heavy knock occurs, damage to pistons, rings, and exhaust valves can result.

There is currently no totally satisfactory means of detecting knock in spark ignition engines. Due to its simplicity, a vibration sensor (accelerometer, which uses the fact that the engine structure vibrates as it knocks), is the most common type of knock sensor [1,2]. Unfortunately, the output of the accelerometer is strongly affected by engine component parasitic noises. On the other hand, cylinder pressure data provide a direct and reliable way to analyze knock [3,4]. Pressure transducers work well, but they are expensive. Also, the insertion of a probe inside the cylinder may reduce the engine lifetime. Hence, an alternative to these two current methods is needed.

Knock occurrence is accompanied by an increase of the wall heat transfer inside the combustion chamber [5–9]. Harigaya et al. [8] measured the effect of knocking on the temperature rise of combustion chamber wall surfaces. They reported a heat transfer coefficient rise of about 260% for a knock intensity of 0.6 MPa. Lu et al. [9] calculated wall heat flux from measured temperature variations on the cylinder wall. Results show that near the knocking zone the maximum wall heat flux is more than four times that of the nonknocking case. Thus, the analysis of a thermal signal detected near the outer side of the cylinder could be a desirable alternative. This technique of detecting knock could be efficient if the thermal damping effect of the cylinder wall is not too important. Moreover, temperature should not be recorded on the wall but within the coolant duct because of technological constraints.

In the present paper, turbulent promoters are used on the external side of cylinder wall in order to compensate for cylinder wall damping effects. Heywood [10] states that temperature variation is damped out within a small distance (about 1 mm) from the wall surface and measurement would be made at the inner surface of the combustion chamber. Bellettre and Tazerout [11] showed that, for several kinds of steel, the thermal signal variation is maintained within the cylinder wall only if knock occurs. They stated that due to knocking combustion thermal signal amplitude of few Kelvin (about 3 K) can be observed at 2 mm from the combustion chamber wall.

The use of transverse ribs at regular intervals is often adopted for heat transfer enhancement [12–14]. Several studies show that the performance of that transfer surface with ribs depends significantly on the parameters of the flow structure, such as reattachment length of the separated streamline and turbulence intensities, as well as the rib geometry and dimensions. In this study, numerical simulations are carried out to investigate the effect of ribs on the unsteady heat transfer and flow structure in order to improve thermal signal detection.

2 Numerical Model

2.1 Geometrical Configuration. The present paper treats the case of a water-cooled engine cylinder. The geometrical characteristics of this cylinder are representative of those of a combined heat and power (CHP) gas engine (bore: 0.152 m, displacement 3 1). The engine speed is set constant at 1500 rpm, as in an actual CHP operation. The computational domain is two dimensional (2D) (Fig. 1). The cylinder wall (made in cast iron) thickness, e, is 0.003 m, and the coolant channel hydraulic diameter is 0.02 m. The geometry of the cylinder head (made in aluminum) is simplified because we just need to account for its effect on the vertical heat fluxes. Since the annular space is small in comparison with the cylinder diameter, the geometrical configuration is considered as 2D plane (preliminary results did not show any difference between 2D plane and 2D axysymmetric configuration).

Ribs with different shapes and dimensions are placed on the outer surface of the cylinder. The geometric variables of the ribs are the height h, the width w, and the pitch Pi. In this work, the ratio of width-to-height (w/h) and the ratio of pitch-to-height (Pi/h) are fixed to 1 and 10, respectively. These values are chosen to give an optimal heat transfer enhancement [15,16].

2.2 Governing Equations. The water flow is assumed to be incompressible and turbulent. Conduction in the solid part is unsteady due to heat flux variations on the internal side of the combustion chamber (Fig. 1). Thus, the governing equations can be written in Cartesian notation as:

Continuity:

$$\frac{\partial U_i}{\partial x_i}=0 \tag{1}$$

Manuscript received November 7, 2003; revision received October 22, 2004. Review conducted by: A. F. Emery.

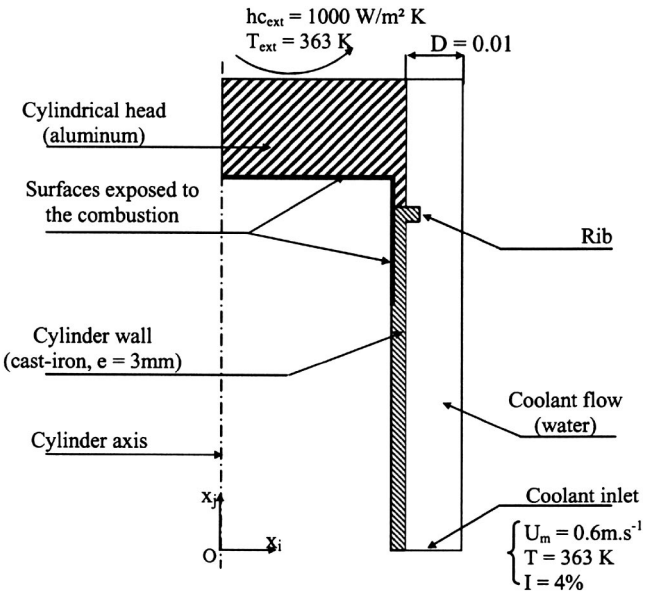

Fig. 1 Computational domain and boundary conditions

where U represents the mean value of the velocity in the i direction.

Momentum transport:

$$\frac{\partial}{\partial x_j}(\rho U_i U_j) = -\frac{\partial p}{\partial x_i} + \frac{\partial}{\partial x_j}\left[\mu\left(\frac{\partial U_i}{\partial x_j} + \frac{\partial U_j}{\partial x_i}\right) - \rho\overline{u_i u_j}\right] + \rho g_i \tag{2}$$

where p represents the mean value of the pressure, and u is the velocity fluctuation. g_i is the gravity in the i direction, ρ is the fluid density, and μ the dynamic viscosity.

Energy:

$$\frac{\partial}{\partial t}(\rho H) + \frac{\partial}{\partial x_j}(\rho U_j H) = \frac{\partial}{\partial x_j}\left[\lambda\frac{\partial T}{\partial x_j} - \rho\overline{u_j h'}\right] + U_j\frac{\partial p}{\partial x_j} \tag{3}$$

where H is the mean value of enthalpy. It is linked to the temperature T by the specific heat, c_p: $H = \int_{T_{\text{ref}}}^{T} c_p dT$, where $T_{\text{ref}} = 273\,\text{K}$. h' is the enthalpy fluctuation and λ is the thermal conductivity. The physical properties of the fluid are set constant because of the small variations of temperature observed outside the combustion chamber.

2.3 Turbulence Model. The turbulent stress and heat flux appearing in Eqs. (2) and (3) must be modeled in order to close the governing equations. The Reynolds stress model (RSM) is used as the turbulence model. This choice is based on comparison with other turbulence models (such as $k-\epsilon$, ReNormalization Group (RNG) $k-\epsilon$ and $k-\omega$, see discussion in Sec. 3.1.2).

Details and physical assumptions on RSM model can be found in Launder et al. [17]. A low-Reynolds number approach is retained to account for wall effects [18]. The transport equations for the Reynolds stresses can be written in the following form:

$$\frac{\partial}{\partial x_k}(\rho U_k\overline{u_i u_j}) = \frac{\partial}{\partial x_k}\left(\frac{\mu_t}{\sigma_k}\frac{\partial\overline{u_i u_j}}{\partial x_k}\right) + P_{ij} + \Phi_{ij} - \epsilon_{ij} \tag{4}$$

with

$$P_{ij} = -\rho\left(\overline{u_i u_k}\frac{\partial U_j}{\partial x_k} + \overline{u_j u_k}\frac{\partial U_i}{\partial x_k}\right),$$

$$\Phi_{ij} = -c_1\rho\frac{\epsilon}{k}\left(\overline{u_i u_j} - \frac{2}{3}\delta_{ij}k\right) - c_2\rho\left(P_{ij} + c_{ij} - \frac{2}{3}\delta_{ij}(P+C)\right),$$

$$c_{ij} = \frac{\partial U_k\overline{u_i u_j}}{\partial x_k}; \quad \epsilon_{ij} = \frac{2}{3}\delta_{ij}\rho\epsilon,$$

and

$$\sigma_k = 0.82; \quad P = \frac{1}{2}P_{ii}; \quad C = \frac{1}{2}C_{ii}; \quad c_1 = 1.8; \quad c_2 = 0.60.$$

The turbulent viscosity μ_t is given by $\mu_t = \rho C_\mu k^2/\epsilon$ with $C_\mu = 0.09$ and k, the turbulent kinetic energy is given by the trace of the Reynolds stress tensor: $k = 1/2\overline{u_i u_i}$. The turbulent kinetic energy dissipation rate ϵ is computed from a model transport equation (similar to that of the standard $k-\epsilon$ model):

$$\frac{\partial}{\partial x_j}(\rho U_j\epsilon) = \frac{\partial}{\partial x_k}\left[\left(\mu + \frac{\mu_t}{\sigma_\epsilon}\right)\frac{\partial\epsilon}{\partial x_k}\right] + c_{\epsilon 1}\frac{\epsilon P_{ij}}{2k} - c_{\epsilon 2}\frac{\epsilon^2}{k} \tag{5}$$

where $c_{\epsilon 1} = 1.44$ and $c_{\epsilon 2} = 1.92$.

The turbulent heat flux is obtained from

$$\rho\overline{u_i t'} = -\frac{\mu_t}{\sigma_T}\frac{\partial T}{\partial x_i} \tag{6}$$

with $\sigma_T = 0.9$ (the turbulent Prandtl number).

2.4 Boundary Conditions. The inlet conditions, deduced from literature [19], are an uniform velocity of 0.6 m/s corresponding to a Reynolds number Re_{Dh} of 12,000, a temperature of 363 K and a turbulent intensity of 4%. On the outer wall of the cylinder head (Fig. 1), a condition of external forced convection is imposed, namely a heat transfer coefficient, hc_{ext}, of 1000 $\text{W m}^{-2}\,\text{K}^{-1}$. This is a reasonable order of magnitude in convective heat transfer for water-cooled engines [20]. The external wall of the coolant duct and the bottom side of the cylinder liner are adiabatic. At the outflow, a zero normal gradient condition is assumed for all flow variables except pressure.

The heat flux is convected from the hot burnt gases to the combustion chamber wall, conducted through the wall and then convected from the wall to the coolant. On the combustion chamber wall, instantaneous local heat fluxes are imposed. Their values are deduced from literature for the cases of both normal and knocking combustion. The wall heat flux presents a sinusoidal variation with time during the combustion period. The combustion starts at the top dead center (TDC) and takes place during a crank angle of 30° (i.e., 3.33 ms at 1500 rpm). Among the different values of wall heat flux that are found in the literature [6,7,9], medium values are chosen in a first step (heat flux of 4 MW/m^2 and 16 MW/m^2, respectively, for normal and knocking combustion). A sensitivity study of this parameter is presented in Sec. 3.5.

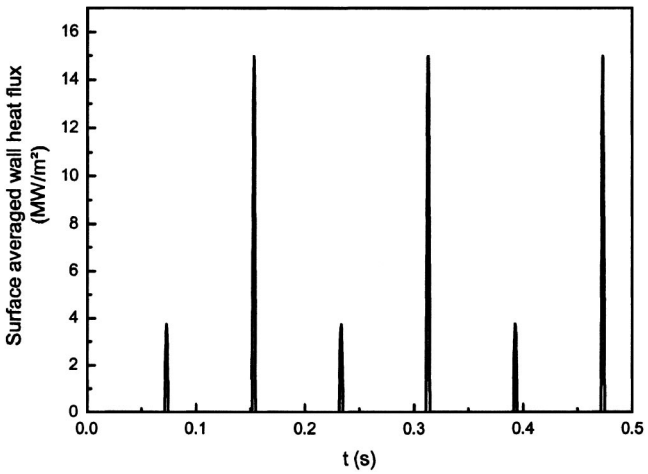

Fig. 2 Instantaneous heat flux on wall combustion chamber

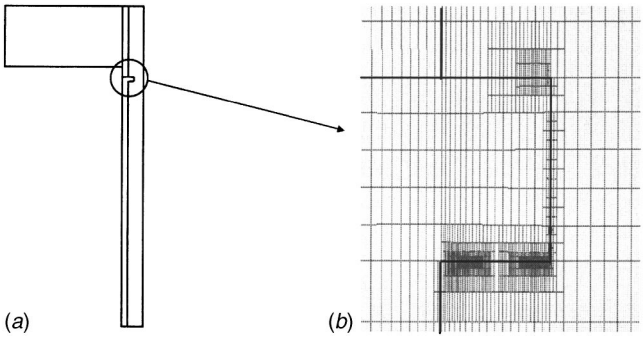

Fig. 3 Computational grid for a 2 mm square rib geometry (refined mesh around the rib)

Because of the continuous motion of the piston, the boundary conditions at the gas/wall interface are time dependent. The surface exposed to burnt gases varies as the combustion proceeds. Thus, the surface area of the combustion chamber wall subjected to the heat flux (shown in Fig. 1) is calculated using the equation of the piston movement:

$$x_j(\theta)=[r\cos\theta+\ell\sqrt{1-(r/\ell)^2\sin^2\theta}] \tag{7}$$

where x_j is the piston position, ℓ is the length of the connecting rod ($\ell=0.34$ m), r is the radius of the crankshaft ($r=0.08$ m), and θ is the crank angle.

An example of the instantaneous heat flux imposed on the upper region of the inner cylinder wall is presented in Fig. 2. In this example, the knock occurs one time every two cycles. The plotted flux is the value averaged on the total surface that will see the whole or a part of the combustion process (this explains why the maximal average value is slightly lower than the local peak value: 15 against 16 MW/m^2).

2.5 Numerical Method. The governing equations solved in the present study, using a Computational Fluid Dynamics (CFD) code, are the 2D incompressible continuity momentum and energy equations employing the RSM turbulence model. By the use of the control-volume based finite volume method, all equations are discretized according to the power-law scheme. Because of the unsteady thermal boundary conditions, the temperature field is time dependent while the flow in the coolant channel is steady. The time dependent terms in the energy equation are integrated using a first-order implicit scheme; the time step is fixed at 10^{-4} s (corresponding to 30 steps during one combustion period with engine cycle period of 0.08 s). Four iterations per time step are adopted because more iterations (up to ten iterations per time step were tested) do not improve the convergence of computations. This choice is justified by the low value of the time step (10^{-4} s); it allows one, therefore, to preserve a reasonable calculation time. The pressure—velocity coupling is carried out by the SIMPLE algorithm for the incompressible flow computation.

2.6 Mesh. Because of the geometry, the grid is structured. A wall model is employed to treat the near-wall regions. It consists of two different regions in the boundary layer: A viscosity-affected region and a fully turbulent region. Hence, the generated grid (Fig. 3) must have strong clustering close to the walls to ensure that the first computational node is at $y^+\approx 1$. Local grid refinement with hanging nodes is used near the rib walls. This approach allows for a more efficient distribution of the grid nodes and a more effective resolution of the near-wall regions and enables the features of the flow field to be better resolved. The coolant duct is subdivided into three regions; namely, a near entry region, a developing region, and an exit region—which include the rib and where the most of the heat transfer occurs. As shown in Fig. 4, three grids were used in order to carry out grid independent tests in the fluid flow. The selected optimum grid consisted of ~17,400 nodes. On the other hand, for each time step, the computed results are declared convergent when the total sum of absolute cell residues in the entire domain for each dependent variable was less than 10^{-6}.

3 Results and Discussion

3.1 Model Validation and Grid Independence

3.1.1 Unsteady Conduction. In the solid part of the studied domain, grid dependency is carried out to find an optimum grid. For an unsteady heat conduction problem in the cylinder wall, a one-dimensional case was considered in order to compare with the analytical solution (Heywood [10]). The majority of the heat transfer into the liner is in the radial direction [10]. Thus, the vertical heat transfer within the cylinder wall may be neglected in first approximation in this conduction validation step.

Figure 5 depicts a grid composed of 18 nodes across the wall thickness. It gives very good agreement with the analytical solution [10]. A denser grid of 32 nodes across the wall gave the same results (difference less than 0.1%). At the inner side of the combustion chamber ($x=0$), the thermal signal changes rapidly due to instantaneous heat flux variations. For other positions within

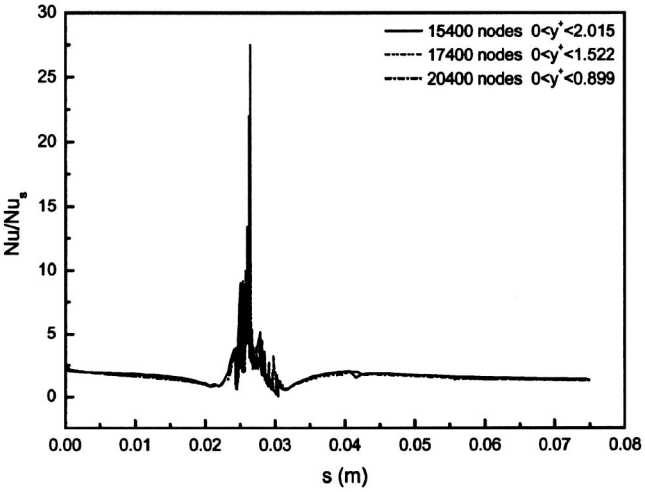

Fig. 4 Grid dependency test—local Nusselt number distributions (Re=12,600, $s=0$ at $x_j=0.133$ m on the cylinder wall)

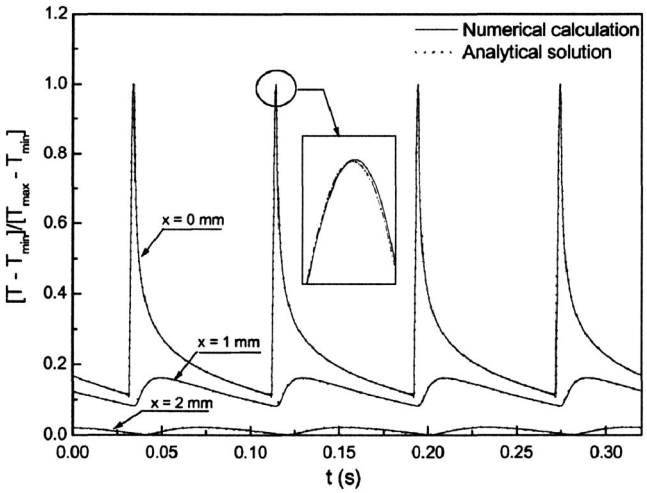

Fig. 5 Temperature signal across the cylinder wall (cast iron)

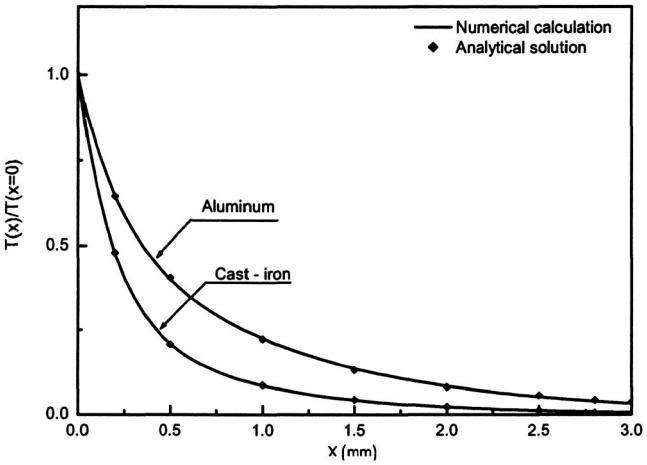

Fig. 6 Temperature amplitude attenuation along the cylinder wall thickness

the cylinder wall (made of cast iron), the amplitude of the signal decays drastically. We can also notice that the phase shift between the thermal signals is well predicted.

Figure 6 shows the amplitude of temperature variations as a function of the distance from the internal side of the cylinder, *x*. Due to the wall damping effects, this amplitude diminishes along the cylinder wall. Hence, thermal signal detection becomes difficult at the outer side of the combustion chamber. On the other hand, the effect of physical properties (diffusivity) on the amplitude of temperature variations is clearly shown on Fig. 6. Aluminum, with higher diffusivity, allows thermal signal variations to be maintained in the wall more than cast iron. Thus, in the following, the emphasis is made at the top of the cylinder where aluminum can be employed (as shown in Fig. 1).

3.1.2 Flow Field. As mentioned previously, the Reynolds stress model has been used. This choice is related to the comparative results reported in Fig. 7 relative to the distribution of the Nusselt number in a ribbed channel. RSM gives better agreement with experimental data from Liou et al. [21] than the other considered models, especially in the area that is going to be studied (i.e., in the recirculation region downstream the ribs, $s > 0.008$ m). At the leading edge of the rib ($s = 0$ m), simulations

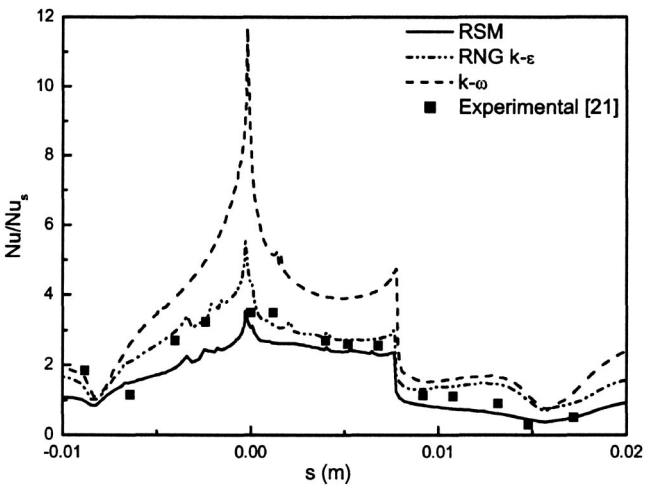

Fig. 7 Effect of turbulence model choice on the Nusselt number prediction (Re=12,600)

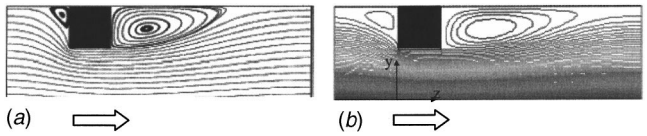

Fig. 8 Streamlines (Re=37,200); (a) Kim et al. [15] and (b) present calculations

achieved with the RSM approaches well with the experimental data while the relative error of 54% and 228% are noticed for respectively RNG $k-\epsilon$ and $k-\omega$ models.

Figure 8 shows streamlines of the flow field in a 2D channel with a single rib. By considering the same configuration examined by Kim et al. [15], it can be seen that both predict similar characteristics of the flow field. A small and a large recirculation are found upstream and downstream of the rib, respectively, as expected. Reattachment length ranging around three to four times the rib height is predicted for $Pi/h = 7.2$ which is in good agreement with that reported by O'Doherty et al. [22].

For the validation of numerical solution of the velocity field, the computed profiles of mean axial velocity are compared with measured profiles of Drain and Martin [23] (Fig. 9). The results are in close agreement with published data [23] for all positions. Maximum velocity locations are shifted to the bottom wall compared to a smooth channel case. At $z/h = 4.18$, the computed and measured profiles indicate that the flow is still separated near the upper wall.

3.1.3 Convective Heat Transfer. The results were first obtained for a smooth channel in the thermal entry region. By comparison with correlation for thermal development flow [24], the computed results are in very good agreement in terms of local Nusselt number (result not reported here). For the ribbed channel, the distributions of local Nusselt number in the vicinity of the rib are shown in Fig. 10. As mentioned earlier, the agreement with measured data [21] is good, especially in the recirculation region ($s > 0.008$ m); this is most important as shown later. Grid independence of the results was checked in the range $0 \leqslant y^+ \leqslant 2$ that corresponds to the validity range of the wall treatment model (shown in Fig. 4).

3.2 Thermal Signal Amplification and Flow Analysis. As presented in the Introduction, turbulent promoters are generally introduced in order to enhance heat transfer. In the present study, we especially focus on the recirculation zone that is generated by

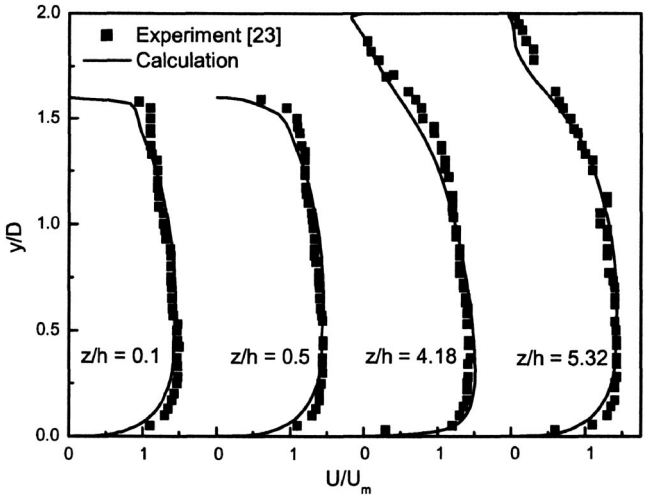

Fig. 9 Comparison of predicted and measured mean velocity profiles (Re=37,200)

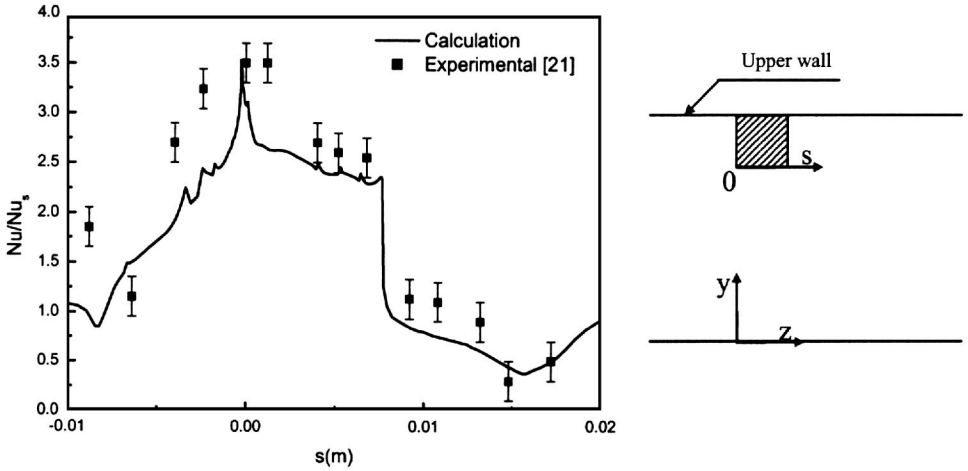

Fig. 10 Comparison of predicted and measured local Nusselt number (Re=12,600)

the rib in front of aluminum wall in order to compensate the cylinder wall damping effect. The recirculation regions upstream and downstream of the rib have opposite effects on the heat transfer. In the upstream bubble, the cold flow impinges on the rib side wall and then moves toward the cylinder wall. In the downstream bubble, the flow is reversed and the heated fluid is convected toward the rib side wall, then up and away from the floor. The obstruction in the flow would then increase transverse velocity and turbulence levels. Figure 11 presents the effect of a rib (h =2 mm), mounted on the outer surface of the cylinder wall, on the thermal signal variations at a position of 0.5 mm from the wall and located within the fluid (point 2, Fig. 12). Only oscillations due to knocking combustion can be seen. It is clear that a rib roughened surface gives good results in terms of amplitude amplification (approximately 20 times in comparison with smooth surface at the same location). The presence of recirculation downstream of the rib (Fig. 12) makes the residence time of the fluid in contact of the wall more important. Consequently, the fluid has more time to collect the thermal signal. In fact, in downstream of the rib, the flow is slowed down and the fluid is made stagnant. For example, at point 2 (Fig. 12), the vertical velocity is ten times smaller than the velocity for the smooth surface case at the same location (0.05 against 0.5 m/s). Thus, the passage of the fluid just behind the rib occurs after a larger residence time along the cylinder wall. These results are similar to those reported by Ollivier et al. [25] who studied recirculation inside a groove made in the cylinder wall. Indeed, they found that the enhancement of the variations was a function of both residence time and fluid velocity. On the other hand, the increase in turbulence, resulting from the obstruction of the boundary layer formation, intensifies the mixing of the fluid and gives rise to the effective conductivity of the cooling water in the region behind the rib. The higher effective thermal conductivity results in higher heat diffusion rates and improvement in temporal variations in temperature.

3.3 Effect of Rib Characteristics

3.3.1 Rib's Shape and Rib's Number. Two different rib shapes, square and cylindrical, are used to find the optimum rib geometry. A triangular geometry was not considered because it does not give good performance [26] in comparison with the others. Ribs with 2 mm of height are used for each situation. Figure 13 shows that the square rib gives more amplification of the thermal signal while the cylindrical one does not present any significant modification compared to the smooth wall configuration (recording point is shown in Fig. 14). Streamlines plotted in Fig. 14 can explain this behavior. We observe that very small recirculation is generated behind the cylindrical rib. Consequently, the flow downstream the rib is not disturbed enough, and turbulent intensity is very low to promote turbulent heat transfer.

The effect of two square ribs instead of one rib was examined (Figs. 15 and 16). The amplification of the thermal signal was about 10% higher in comparison with one rib. This small variation

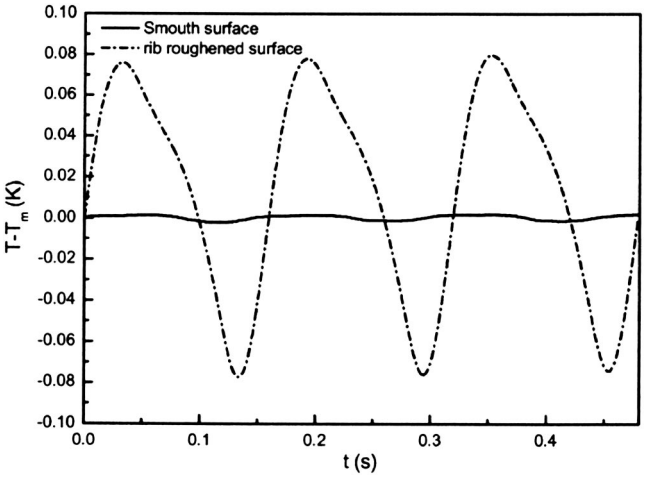

Fig. 11 Temporal variation of thermal signal in the fluid (0.5 mm from the wall)

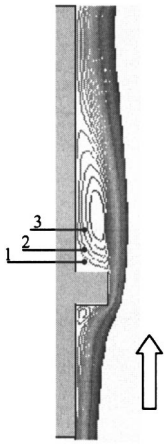

Fig. 12 Recirculation zone downstream the rib (Re=12,000)

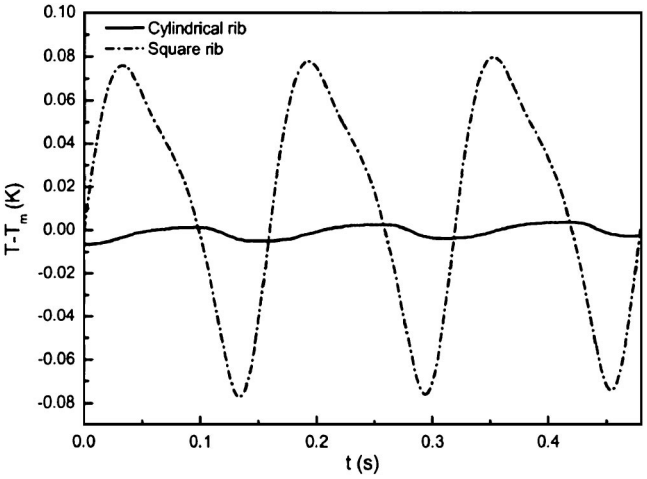

Fig. 13 Thermal signal variation for different rib geometries

is certainly due to the fact that the flow structure in the recirculation zone does not change significantly in downstream of the second rib as compared to the first one. Indeed, Lee and Abdel-Moniem [27] showed that for successive ribs, the reattachment

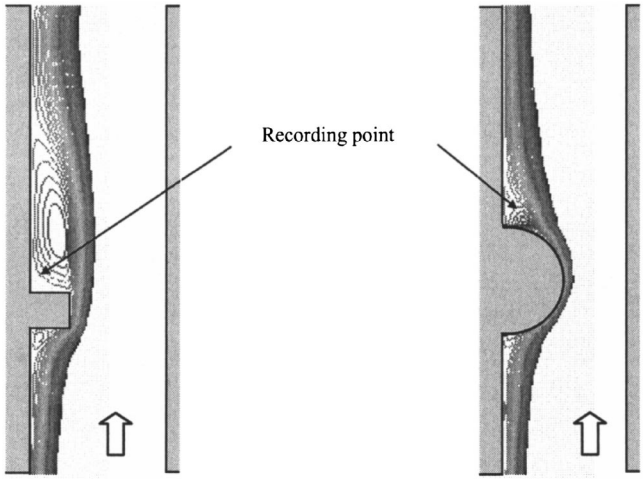

Fig. 14 Flow structure downstream of the ribs (Re=12,000)

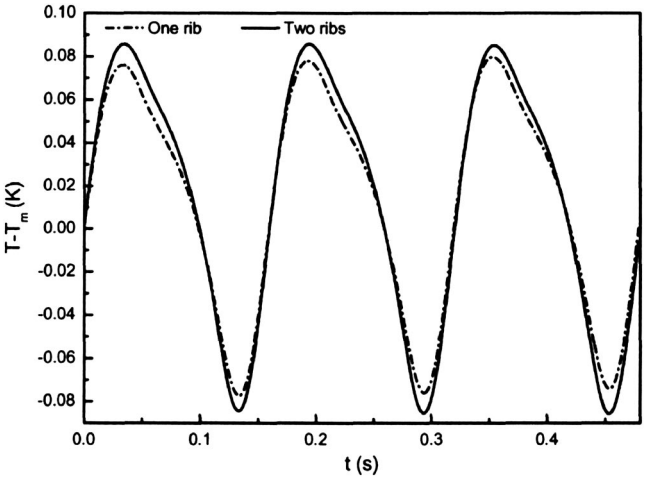

Fig. 15 Effect of rib number on thermal signal variations (h =2 mm)

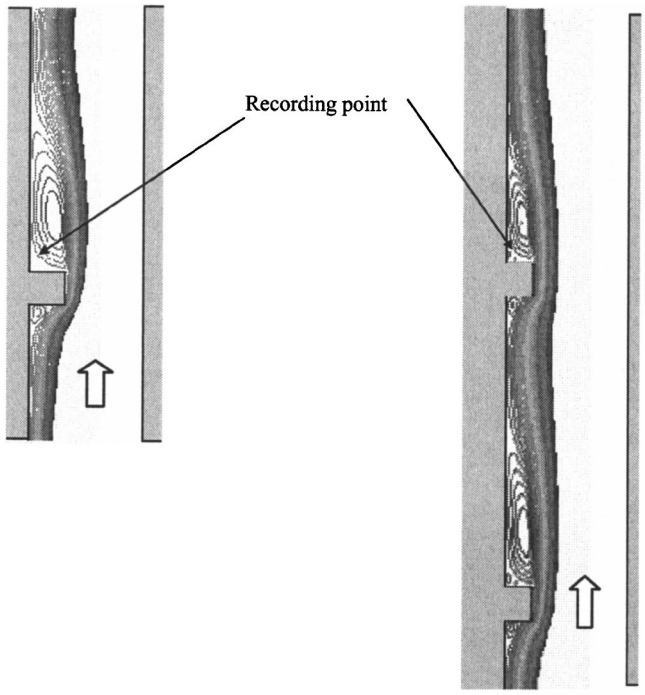

Fig. 16 Flow structure downstream of one or two ribs (Re=12,000)

length ranges around three times the rib height. Thus, the velocity and the turbulent intensity in the separation/reattachment region at the upper region of the cylinder wall do not vary greatly. At the recording point (Fig. 16) the velocity magnitude was around 0.05 m/s for both cases. We note that more than two ribs were not considered owing to the narrowness of the interesting cylinder region regarding the heat transfer (near the TDC).

3.3.2 Rib Dimensions. As presented previously, the thermal signal amplification depends on the flow structure. Thus, the effect of rib dimension is examined here. Two square rib situations are used with different heights ($h=1$ mm and 2 mm) while the ratio width-to-height is kept constant. As shown in Fig. 17, a rib with 1 mm height does not perform as well as the larger rib. This is due to the size of the bubble downstream of the rib, which depends

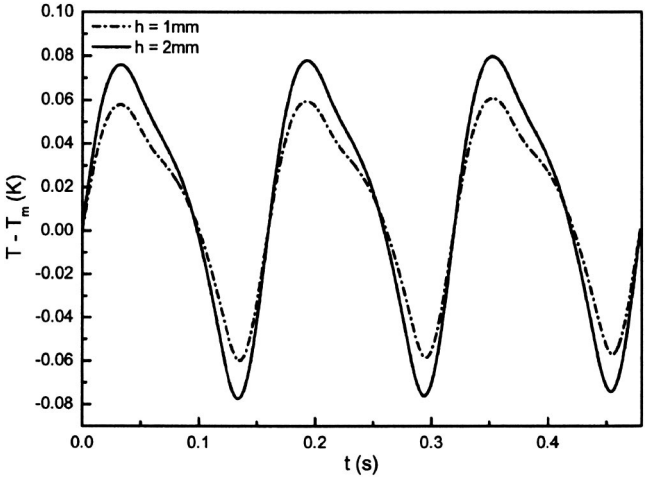

Fig. 17 Thermal signal variation for rib heights of 1 mm and 2 mm

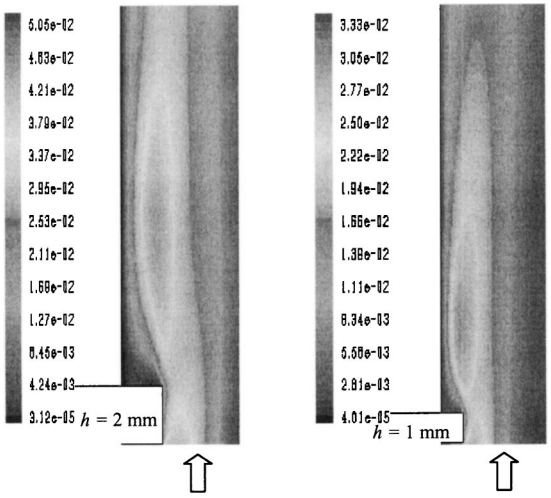

Fig. 18 Turbulent kinetic energy contours for square ribs (Re =12,000)

directly on the rib dimensions. Smaller recirculations generate smaller residence time for the fluid near the heated wall.

Figure 18 shows the profiles of the kinetic energy of turbulence for square ribs ($h=1$ mm, $h=2$ mm). High levels of turbulence were predicted close to the ribbed wall and in the recirculation region in comparison with the flow near the outer wall, and especially near the leading edge of the rib. This is due to the acceleration of the fluid and the strong shear at the rib top. The 2 mm rib increases the turbulence more than the other as expected. The increase in the turbulent kinetic energy yields an increase in the eddy diffusivity of the flow. Finally, we can state that both the increase of fluid residence time along the heated wall and the enhancement of the fluid effective diffusivity by the turbulence lead to the improvement of the thermal signal compared to the smooth wall case.

3.4 Effect of Recording Point Position in the Recirculation All the results presented previously are recorded at 0.5 mm from the wall and 1 mm behind the rib. To illustrate the influence of thermal signal recording location, three positions are studied. All are situated at 0.5 mm from the cylinder wall but at different distances from the rib (Fig. 12). Results show that the signal becomes increasingly weaker as one approaches the center of recirculation (Fig. 19). Indeed, the fluid particles at points 1, 2, and 3 (Fig. 12) have different trajectories and different levels of velocity. Moreover, the trajectory of Point 1 is very close to the wall, this makes it possible for fluid to better collect the signal. It is important to notice that Ollivier et al. [25] observed the same phenomenon in a recirculation zone generated inside a groove.

Table 1 Wall heat flux intensities for normal and knocking conditions

Reference	Normal combustion (MW/m^2)	Knocking combustion (MW/m^2)
Douaud [6]	10	40
Enomoto et al. [7]	4	16
Lu et al. [9]	2.5	8

3.5 Effect of Heat Flux Level. In the results presented previously, wall heat fluxes of 4 MW/m^2 and 16 MW/m^2 were used, respectively, for normal and knocking combustion. Table 1 presents several intensities of wall heat flux encountered in literature. These values were employed to analyze the effect of heat transfer intensity on the thermal signal within the fluid. Figure 20 shows that the thermal signal amplitude (Point 2, cf. Fig. 12) is proportional to the amount of heat exchange. This is due to the rise in temperature at the outer wall of the cylinder which is proportional to heat flux levels.

In all studied cases, while the presence of the rib amplifies the thermal signal, the total signal variation does not exceed 0.4 K (i.e., 2×0.2 K). For industrial applications, this magnitude may be difficult to detect in a noisy engine environment. However, Bauer et al. [28] showed that small temperature fluctuations (less than 1 K) of exhaust gas can be measured in an intake port of a SI engine. A new measuring technique was developed by Bourouga et al. [29], which has been used to evaluate the unsteady temperature distribution and the heat flux within the cylinder head of a diesel engine. It allows detecting thermal signal variations with less than 0.5 K of amplitude. This shows that the detection of knock occurrence can be achieved by the presently proposed method. The chosen instrumentation and its calibration has to be accurate enough.

The thermal signal may further be improved by the use of a liquid with a suspension of nanoparticles (called nanofluid), which offer a much higher effective thermal conductivity than normal fluids [30,31]. Roy et al. [31] found that, in a radial flow cooling systems, a nanoparticle volume fraction of 5% gives an increases of 30% in the average wall heat transfer coefficient for water/

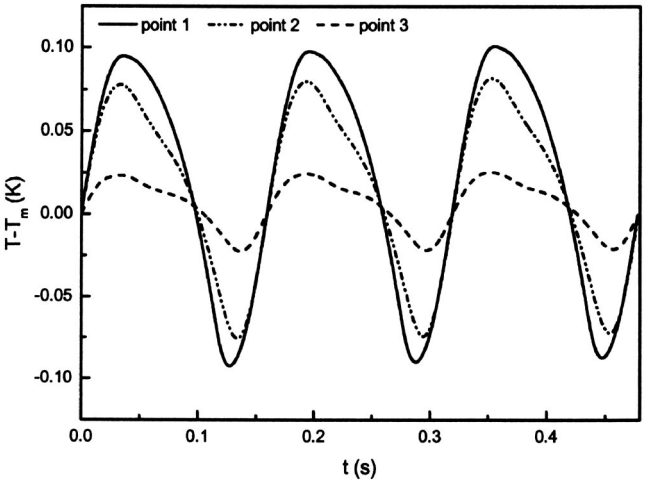

Fig. 19 Thermal signal variation at different locations within the fluid

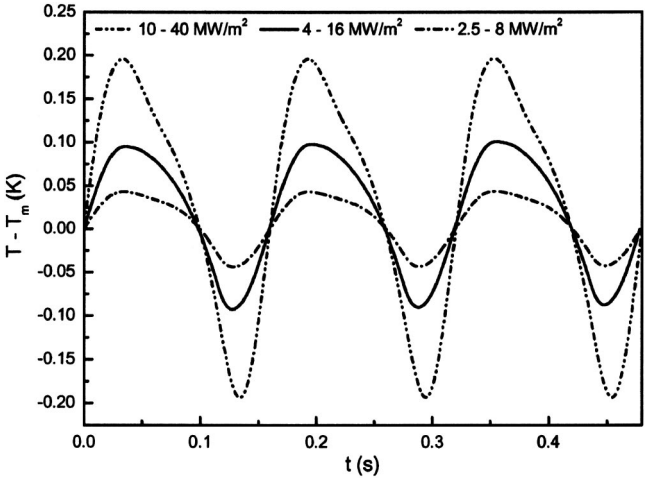

Fig. 20 Effect of heat transfer intensity on thermal signal amplitude

Al_2O_3 nanofluid. It is also shown that local heat transfer is noticeably changed with the behavior of the hydrodynamic field (i.e., flow separation areas). In the presently studied configuration, the use of 5% water/Al_2O_3 nanofluid increases the thermal signal variations by 20% over that predicted using water alone.

4 Conclusion

Numerical simulation of transient heat transfer around a water-cooled combustion chamber coupled with RANS flow analysis was carried out. Knocking combustion generates higher wall heat fluxes than normal combustion. A program that enables fixing instantaneous heat flux on the inner side of the cylinder was developed. Thermal signal is collected within the flow at a position of 0.5 mm from the wall relative to rib heights ranging from 1 to 2 mm. The results demonstrate the viability of a nonintrusive sensor implementation in order to detect knock appearance.

Thermal signal variations are found to be considerably amplified (about 20 times) when square ribs, acting as turbulent promoters, are used. Flow and thermal signal analyses show that signal amplification depends on the flow structure in the vicinity of the rib. The larger the circulation region, the higher the thermal signal variations. Several configurations, which account for rib shape and dimensions, were examined. Computed results show that the square rib situation, where $h=2$ mm, gives the best performance. Otherwise, it is shown that amplification magnitude depends on the position where the thermal signal is collected. To conclude, the present study showed that a rib, placed on the external side of the cylinder, in conjunction with thermal signal analysis outside the combustion chamber, enables knock to be detected.

Nomenclature

D = channel height, m
e = wall thickness, m
h = rib height, m
hc = heat transfer coefficient, $W\,m^{-2}\,K^{-1}$
h' = enthalpy fluctuation, $J\,kg^{-1}$
I = turbulence intensity
k = turbulent kinetic energy, $m^2\,s^{-2}$
ℓ = connecting rod length, m
Pi = pitch, m
r = crankshaft radius, m
s = curvilinear length, m
T_m = time average temperature, K
U = velocity, $m\,s^{-1}$
U_m = mean velocity, $m\,s^{-1}$
u = velocity fluctuation, $m\,s^{-1}$
w = rib width, m
x = spatial coordinate, m
y = spatial coordinate, m
y^+ = wall unit ($\delta\sqrt{\tau_w/\rho}/\nu$)
z = spatial coordinate, m

Greek Letters

δ = distance between the wall and the first node of the grid, m
δ_{ij} = Kronecker symbol
ϵ = turbulent kinetic energy dissipation rate, $m^2\,s^{-3}$
λ = thermal conductivity, $W\,m^{-1}\,K^{-1}$
μ = dynamic viscosity, $kg\,m^{-1}\,s^{-1}$
θ = crank angle, deg

Subscript

ext = external
i, j, k = i, j, and k directions
s = smooth
w = on the wall

References

[1] Decker, H., and Gurber, H., 1985, "Knock Control of Gasoline Engines, A Comparison of Solutions and Tendencies, With Special References to Future European Emission Legislation," SAE Paper No. 850298.
[2] Honig, G., Decker, H., and Rohde, S., 1981, "Electronic Spark Control Systems: Part I, Microcomputer Controlled Ignition System; Part II: Bosh Knock Control," SAE Paper No. 810059.
[3] Hudson, C., Gao, X., and Stone, R., 2001, "Knock Measurement for Fuel Evaluation in Spark Ignition Engines," Fuel, **80**, pp. 395–407.
[4] Brecq, G., Bellettre, J., and Tazerout, M., 2003, "A New Indicator for Knock Detection in Gas SI Engines," Int. J. Therm. Sci., **42**, pp. 523–532.
[5] Syrimis, M., 1996, "Characterization of Knocking Combustion and Heat Transfer in a Spark-Ignition Engine," Ph.D. thesis, University of Illinois.
[6] Douaud, A., 1983, "Eléments d'Analyze du Cliquetis et de ses Effets," Rev. Inst. Fr. Pet., **38**, pp. 665–674.
[7] Enomoto, Y., Kitahara, N., and Takai, M., 1994, "Heat Losses During Knocking in a Four-Stroke Gasoline Engine," JSME Int. J., Ser. B Fluids Therm. Eng., **37**(3), pp. 668–676.
[8] Harigaya, Y., Toda, F., Ohyagi, S., and Tsuji, H., 1989, "Surface Temperature and Wall Heat Flux in a Spark Ignition Engine Under Knocking and Non-Knocking Conditions," JSAE Paper, pp. 369–378.
[9] Lu, J. H., Ezekoye, D., Liyama, A., Greif, R., and Sawyer, R. F., 1989, "Effect of Knock on Time Resolved Engine Heat Transfer," SAE Paper No. 890158.
[10] Heywood, J. B., 1988, *Internal Combustion Engines Fundamentals*, McGraw–Hill, Singapore.
[11] Bellettre, J., and Tazerout, M., 2003, "Numerical Study of Unsteady Heat Transfer Around a Cylinder: Application to Knock Detection in Gas SI Engine," *Proc. Eurotherm Seminar74 Heat Transfer in Unsteady and Transitional Flows*, Endhoven, The Netherlands, edited by H. C. de Lange and A. A. Steenhoven, pp. 99–104.
[12] Ooi, A., Iaccarino, G., Durbin, P. A., and Behnia, M., 2002, "Reynolds Averaged Simulation of Flow and Heat Transfer in Ribbed Ducts," Int. J. Heat Fluid Flow, **23**, pp. 750–757.
[13] Liou, T. M., Chen, S. H., and Shih, K. C., 2002, "Numerical Simulation of Turbulent Flow Field and Heat Transfer in a Two Dimensional Channel With Periodic Slit Ribs," Int. J. Heat Mass Transfer, **45**, pp. 4493–4505.
[14] Iaccarino, G., Ooi, A., Durbin, P. A., and Behnia, M., 2002, "Conjugate Heat Transfer Predictions in Two Dimensional Ribbed Passages," Int. J. Heat Fluid Flow, **23**, pp. 340–345.
[15] Kim, K. Y., and Kim, S. S., 2002, "Shape Optimization of Rib Roughened Surface to Enhance Turbulent Heat Transfer," Int. J. Heat Fluid Flow, **45**, pp. 2719–2727.
[16] Iacovides, H., Kelemenis, G., and Raisee, M., 2003, "Flow and Heat Transfer in Straight Cooling Passages With Inclined Ribs on Opposite Walls: An Experimental and Computational Study," Exp. Therm. Fluid Sci., **27**, pp. 283–294.
[17] Launder, B. E., Reece, G. J., and Rodi, W., 1975, "Progress in the Development of a Reynolds Stress Turbulence Closure," ASME J. Fluids Eng., **68**, pp. 537–566.
[18] Launder, B. E., and Shima, N., 1989, "Second-Moment Closure for the Near-Wall Sublayer: Development and Application," AIAA J., **27**, pp. 1319–1325.
[19] Makkapati, S., Poe, S., Shaikh, Z., Cross, R., and Mikulec, T., 2002, "Coolant Velocity Correlations in an IC Engine Coolant Jacket," SAE Paper No. 011203.
[20] Pirotais, F., 2004, "Contribution à la Modélisation du Flux Thermique Disponible pour le Chauffage d'un Habitacle d'Automobile après un Démarrage à Froid," PhD thesis, University of Nantes (in French).
[21] Liou, T. M., Hwang, J. J., and Chen, S. H., 1993, "Simulation and Measurement of Enhanced Turbulent Heat Transfer in a Channel With Periodic Ribs on One Principal Wall," Int. J. Heat Mass Transfer, **36**, pp. 507–517.
[22] O'Doherty, T., Jolly, A. J., and Bates, C. J., 2001, "Optimization of Heat Transfer Enhancement Devices in a Bayonet Tube Heat Exchanger," Appl. Therm. Eng., **21**, pp. 19–36.
[23] Drain, L. E., and Martin, S., 1985, "Two-Component Velocity Measurements of Turbulent Flow in a Ribbed-Wall Flow Channel," *International Conference on Laser Anemometry—Advanced and Application*, Manchester, pp. 99–112.
[24] Kays, W., 1966, *Convective Heat Transfer*, McGraw–Hill, New York.
[25] Ollivier, E., Duma, B., Bellettre, J., and Tazerout, M., 2003, "Knock Detection in Gas Engine by Analysis of Transient Heat Transfer," *International Symposium on Transient Convective Heat and Mass Transfer in Single and Two-Phase Flows*, CESME, Turkey, ed., Begell House Inc.
[26] Kilicaslan, I., and Sarac, H. I., 1998, "Enhancement of Heat Transfer in Compact Heat Exchanger by Different Type of Rib With Holographic Interferometry," Exp. Therm. Fluid Sci., **17**, pp. 339–346.
[27] Lee, C. K., and Abdel-Moneim, S. A., 2001, "Computational Analysis of Heat Transfer in Turbulent Flow Past a Horizontal Surface With Two-Dimensional Ribs," Int. Commun. Heat Mass Transfer, **21**(2), pp. 161–170.
[28] Bauer, W., Heywood, J. B., Avanessian, O., and Chu, D., 1996, "Flow Characteristics in Intake Port of Spark Ignition Engine by CFD and Transient Gas Temperature Measurement," SAE Paper No. 961997.
[29] Bourouga, B., Lepaludier, V., and Bardon, J. B., 1998, "In Situ Measurement of Temperature and Surface Flux in Combustion Chamber of Diesel Engine,"

Congress of the SFT, Marseille, France, Elsevier, pp. 307–313 (in French).
[30] Wang, B., Zhou, L., and Peng, X., 2003, "A Fractal Model for Predicting the Effective Thermal Conductivity of Liquid With Suspension of Nanoparticles," Int. J. Heat Mass Transfer, **46**, pp. 2665–2672.
[31] Roy, G. C., Nguyen, C. T., and Comeau, M., 2004, "Electronic Component Cooling Enhancement Using Nanofluids in a Radial Flow Cooling System," *Proc. ASME—ZSIS International Thermal Science Seminar II*, ASME, New York, pp. 743–750.

Modulated Air Layer Heat and Moisture Transport by Ventilation and Diffusion From Clothing With Open Aperture

Nesreen Ghaddar[1]
ASME Fellow
e-mail: farah@aub.edu.lb
American University of Beirut,
Beirut, Lebanon

Kamel Ghali
e-mail: amro@aub.edu.lb
Beirut Arab University,
Beirut, Lebanon

Jihad Harathani
e-mail: jih01@aub.edu.lb
American University of Beirut,
Beirut, Lebanon

A two-dimensional model is developed for the modulated internal airflow, due to walking, in the gap between clothing and skin surface in the presence of clothing apertures. The normal airflow renewing the air layer through the fabric is modeled using the Ghali et al. three-node fabric ventilation model with corrected heat and moisture transport coefficients within the fabric voids to include the diffusion-dominated transport processes in the fabric at low normal flow rates that occur near the open aperture. The parallel flow is induced by a periodic pressure difference between environmental pressure at the aperture of the clothing system and trapped air layer pressure. The parallel flow in the trapped air layer is assumed to be locally governed by the Womersley solution of time-periodic laminar flow in a plane channel. The two-dimensional (2D) model that uses, in the parallel direction, the Womersley flow of the trapped air layer has predicted significantly lower flow rates than a model based on an inertia-free quasi-steady Poisueille flow model (valid only at low ventilation frequencies). In addition, the model predicted lower sensible and latent heat losses from the sweating skin in the presence of open apertures in the clothing system. The percentage drop in total heat loss due to open aperture is 7.52%, and 2.63%, at ventilation frequencies of 25, and 35 revolution per minute, respectively. The reported results showed that under walking conditions, a permeable clothing system with an open aperture reduced heat loss from the skin when compared to a normal ventilation model (closed aperture). These results were consistent with previously published empirical data of Lotens and Danielsson on air layer resistance for open and closed apertures in high air permeable fabrics. [DOI: 10.1115/1.1857949]

Keywords: Clothing Ventilation Model, Modulated Microclimate Air Layer, Womersley Flow, Steady Periodic Heat Transfer in Clothing

Introduction

Heat and moisture transport from the human skin are initiated by gradients of temperature and moisture concentration of the air within the fabric, the air space between the skin and the fabric, and the ambient air. The transport processes are not only of diffusion type but are enhanced by the ventilating motion of air through the fabric initiated by the relative motion of the human with respect to the surrounding environment. The size of the air spacing between the skin and the fabric varies continuously in time, depending on activity level and location, thus inducing variable airflow in and out of the fabric. The induced airflow ventilates the fabric and contributes to the augmentation of the rate of condensation and adsorption in the clothing system and to the amount of heat and moisture loss from the body. During body motion, air penetrates in and out and ventilation is obtained without gross environmental air movement [1,2].

For the past two decades, the so-called pumping or bellows effect has been studied, and its importance to the heat and mass transfer of the human body has often been discussed [3–6]. In order to describe the dynamic behavior, Jones et al. [7,8] described a model of the transient response of clothing systems, which took into account the sorption behavior of fibers, but assumed local thermal equilibrium with the surrounding air. They compared the prediction of heat loss by the model with experimental data from thermal manikin tests and found reasonable agreement. Recently, Li and Holcombe developed a mathematical model in which a human thermoregulatory model was combined with a kinetic sorption model of fabrics to study the transient thermal response of a clothed human [9]. Their model, however, neglected ventilation effects between the air passing through the fiber and the solid fiber. Ghali et al. [1] studied the effect of ventilation on heat and mass transport through a fibrous material to predict the transfer coefficients in a cotton fibrous medium. Their model was further developed and experimentally validated to predict temporal variations in temperature and moisture of the air within the fiber in a multilayer three-node model [10]. In realistic applications, ventilation of the clothing system during human motion occurs by periodic motion of air in and out of the air spacing as the fabric moves outward or inward towards the skin. Ghali et al. [11] reported experimental data on sensible and latent heat transport initiated by sinusoidal motion of a fabric plane about a fixed mean air spacing thickness above a sweating isothermal hot plate placed in a controlled environment. The periodic ventilation effect, according to Ghali et al. [11] causes a temperature change of about 2.5°C in the enclosed air layer temperature during one period of oscillation of the fabric. A numerical three-node-fabric model followed in the same work of Ghali et al. to analyze the effect of fabric motion on the sensible and latent heat transport from a wet isothermal skin. Their transient model predicted the heat loss from the wet boundary and agreed fairly well with the experimentally measured values. Ghaddar et al. [12] have later coupled the three-node fabric model with Gagge's two-node human thermoregulatory model [13] to predict the transient thermal response of a walking human at variable levels of activity and

[1]Author to whom correspondence should be addressed. Telephone: ++961-1-3500000 ext 3594/3590; Fax: ++961-1-744462. Web address: http://webfaculty.aub.edu.lb/~farah/

Manuscript received January 9, 2004; revision received December 13, 2004. Review conducted by: B. Farouk.

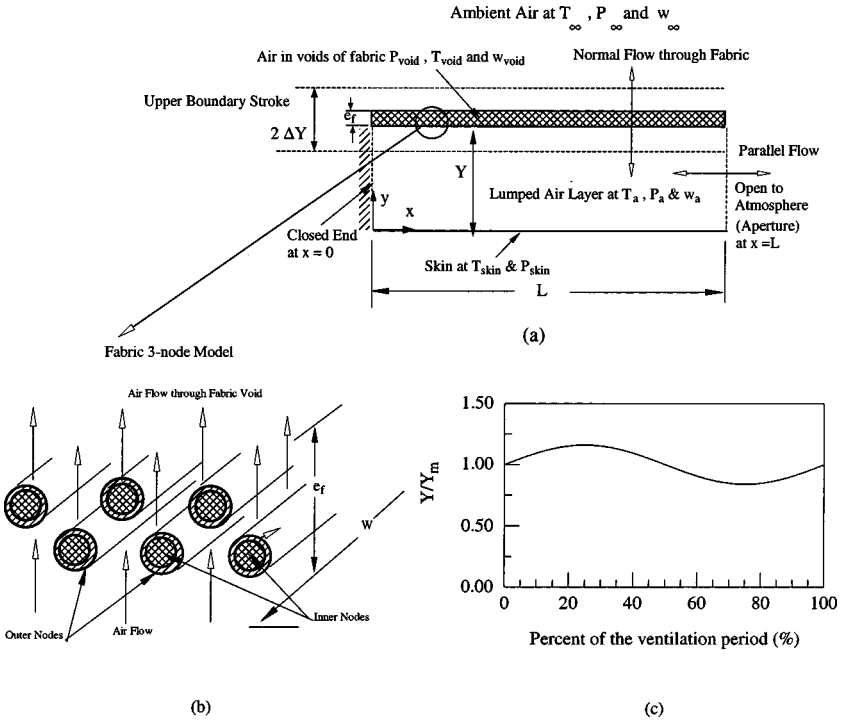

Fig. 1 Schematic of the physical domain of (*a*) the fabric-air layer-skin system; (*b*) the fabric model, and (*c*) the variation in time of the ratio of air layer thickness to the air layer mean thickness

ventilation frequencies. Ghaddar et al. [12] empirically derived correlation of the evaporative and dry convective heat transport coefficients from the skin to the lumped air layer as a function of ventilation frequency.

Previous periodic ventilation models of fibrous media of Lotens and Ghali et al. considered the impact of normal airflow [2,11]. However, Lotens' model was based on empirical equations that restricted its use. Ghali et al. normal periodic ventilation model is valid for normal airflow through the fabric, but is not applicable for parts of the body where there is a parallel airflow to the fabric at the sleeve and neck openings to the environment. A two-dimensional model was further developed by Ghali et al. [14] where parallel airflow to the fabric was present due to open apertures in clothed arms (sleeve end) or trunk (neck opening) using a locally fully developed Poiseuille model for the flow in the parallel direction. The reported reduction in sensible and latent heat loss of the Poiseuille flow model of Ghali et al. [14] due to an open aperture did not agree well with published experimental results of Lotens [2]. Ghali et al. [14] neglected the fluid inertia associated with the flow modulation and reversal during the flow cycle in the parallel direction and hence limited the model applicability to low Womersley number. The Ghali et al. model had another deficiency in the region close to the opening where the normal low flow rate is small. In that region, the mechanism of heat and mass transport through the fabric is dominated by diffusion and the fabric three-node ventilation model would not be accurate.

The objective of this work is to develop from first principles a realistic 2D model that can be used to predict air exchange rates within the internal air layer of a walking human at any speed in a loose-fitting one-layer ensemble with open or closed. The model will predict the skin heat and moisture transport resulting from the periodic motion of fabric with respect to the skin during walking. The periodic motion of the porous fabric above the skin induces air exchange rates with ambient air in the normal direction through the fabric and in the parallel direction through the open aperture. Inertia effects of the modulated parallel internal air layer flow to and from the ambient air through the aperture will be accounted for by assuming the flow to be locally a Womersley steady-periodic flow in a channel [15,16]. The air exchange in the normal direction through the fabric will use the Ghali et al. three-node absorption model [1]. In this work, the internal heat and moisture transport coefficients in the fabric void are modified to extend the applicability of the ventilation model to low normal flow rates region near the open clothing apertures to the atmosphere. The contribution of this work is in the novel approach to modeling of the internal air layer using Womersley flow and the extension of the 3-node fabric ventilation model of Ghali et al. [1,10] to low normal flow rates when diffusion of heat and moisture is dominant.

Mathematical Formulation of the Model

Figure 1(*a*) presents the schematic of the physical domain of the air-layer-fabric system where an enclosed air layer of thickness Y and length L separates the fabric and the human skin. The physical domain of the air-layer-fabric system represents a situation where skin is represented by a flat surface covered with clothing with one tight end (no air flow escapes) and the other end is open to the atmosphere such as loose clothing openings at the sleeves end or around the neck. The fabric upper boundary, represented by the Ghali et al. [10] fabric three-node model shown in Fig. 1(*b*), is assumed to have a sinusoidal up and down motion that induces air movement through the fabric. The variation of the height Y between is a periodic function of time at an angular frequency $\omega(=2\pi f/60)$ and amplitude ΔY given by

$$Y = Y_m + \Delta Y \sin(\omega t) \tag{1}$$

The time variation of Y/Y_m is shown in Fig. 1(*c*). The fabric does not touch the skin in the current study where the ratio of $\Delta Y/Y_m$ is less than unity. The sinusoidal motion is an approximate model of the periodic change of air spacing layer thickness for a walking person. Human gait analysis show repeated periodic pattern of limb motion as a function of walking speed that can be approxi-

mated as a sinusoidal pattern [17]. One end of the air layer physical domain at $x=0$ is impermeable to flow (closed) and the other end at $x=L$ is open to ambient air resembling the presence of a clothing open aperture. The fabric thickness is e_f. The presence of the open aperture at $x=L$ coupled with the fabric periodic motion will induce periodic flow exchange with the ambient air in the parallel direction. The frequency of the oscillating motion of the fabric is generally proportional to the activity level of the walking human. The air spacing layer beneath the fabric will be formulated as an incompressible layer.

In walking conditions, the clothed parts of the body such as arms or trunks with no openings at the sleeve or neck (closed apertures clothing) lose heat and moisture by ventilation of air through the fabric (bellows-ventilation). When open apertures are present in the clothing system, 2D airflow develops in the air layer during walking leading to both normal flow through the fabric and parallel flow convection to the skin and fabric. Reduced normal ventilation rates occur in the region close to the openings that require modification of the fabric ventilation model transport coefficients to accommodate the diffusion dominant mechanism of heat and moisture. In addition, the induced flow in the parallel direction exhibits periodic motion with complete reversal for flow from the atmosphere into the domain through the aperture during the fabric upward motion and out of the domain to the atmosphere during the fabric downward motion. At high frequency of motion, the flow inertia associated with high modulation rates of the air cannot be neglected.

In this section, the formulation of the periodic ventilation problem in the presence of an open aperture address: (i) The analysis of the air flow through the upper fabric boundary using the three-node fabric model [1]; and (ii) the modeling of the internal air layer motion and transport processes while accounting for the flow inertia in the parallel direction due to the periodic motion and flow reversal during the walking cycle.

Analysis of the Air Flow Through the Fabric. The analysis of the airflow through the fabric boundary of the physical domain depicted in Fig. 1(*b*) is based on the single lumped fabric layer of three-node adsorption model described in detail by Ghali et al. [1,11]. In summary, the three-node model lumps the fabric into an outer node, inner node, and an air void node. The fabric outer node represents the exposed surface of the yarns, which is in direct contact with the penetrating air in the void space (air void node) between the yarns. The fabric inner node represents the inner portion of the ''solid'' yarn, which is surrounded by the fabric outer node. The outer node exchanges heat and moisture transfer with the flowing air in the air void node and with the inner node, while the inner node exchanges heat and moisture by diffusion only with the outer node. The air flowing through the fabric void spaces does not spend sufficient time to be in thermal equilibrium with the fabric inner and outer nodes. The moisture uptake in the fabric occurs first by the convection effect from the air in the void node to the yarn surface (outer node), followed by sorption/diffusion to the yarn interior (inner node). The use of lumped parameters of the fabric model nodes is commonly used in thin permeable fabrics [18,19]. The mass and energy balances of the fabric three-node model are found in detail in Ref. [1] and will not be repeated here. According to Ghali et al. [11], the three-node fabric model predicted well the measured sensible and latent heat loss from the skin due to periodic normal air flow through the fabric induced by planer periodic up and down motion of the permeable fabric above the skin with closed clothing apertures. The presence of an open aperture in the system requires modifying internal fabric transport coefficients to extend the applicability of the normal ventilation model to low normal flow rates that will occur near the openings. The diffusion model of heat and moisture transport through the fabric is based on the effective dry and evaporative resistance across the fabric [18,19]. The bridging of both ventilation and diffusion models is done by updating the appropriate internal transport coefficients in the fabric to accurately predict the heat and moisture transport processes at zero and low flow rates. At significant normal air flow rates, the three-node ventilation model defines internal effective heat and mass transfer coefficients H_{co} and H_{mo} for the outer node of the fabric and void, and the heat and mass diffusion coefficients H_{ci} and H_{mi} from the outer to the inner nodes of the fabric. The modified effective heat transfer coefficient between the air flow in the fabric void and the outer node and their validation is given in the Appendix.

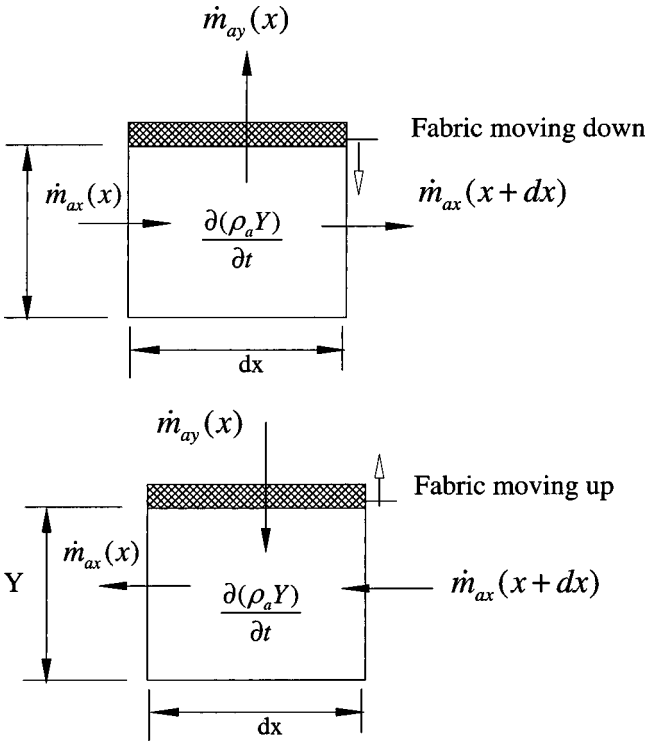

Fig. 2 Schematic representation of the air mass balance on element of thickness *dx*

Modeling of the Internal Modulated 2D Air Layer

Air Flow Mass Balance. The flow inertia due to the periodic oscillation of air in and out of the open aperture induced by the fabric up and down motion will be accounted for by assuming the flow to be locally a Womersley steady-periodic flow [15]. The air and the water vapor mass balances and the air energy balance are formulated in this section. The normal airflow passing through the fabric layer during ventilation has an obvious significant impact on the heat and mass transport at the fabric and from the skin.

In the presence of apertures in clothing systems, the flow of air will take place in both the normal and parallel directions to the fabric. The parallel flow is through the clothing open apertures (sleeves, skirts, neck) and the normal flow is through air spaces within the clothing void spaces. The parallel airflow is in contact with the environment at the opening at the $x=L$ boundary as was shown in Fig. 1. The airflow in the parallel direction x has a smaller pressure head loss compared with the flow through the fabric layer, and hence it is expected to result in a significant flow rate. Figure 2 shows the mass balance performed on an element of height Y and thickness dx. The general air layer mass balance can then be written as:

$$\frac{\partial(\rho_a Y)}{\partial t} = -\dot{m}_{ay} - \frac{\partial(Y\dot{m}_{ax})}{\partial x} \tag{2a}$$

where $\dot{m}_{ax}$ is the mass flux in the parallel direction in kg/m^2·s and $\dot{m}_{ay}$ is the normal air flow rate in the y direction. The x boundary conditions for the air flow are

$$\dot{m}_{ax}(x=0)=0 \tag{2b}$$

$$\dot{m}_{ax}(x=L)=C_D\left[\frac{2\rho_a}{|P_L-P_\infty|}\right]^{1/2}[P_\infty-P_L] \tag{2c}$$

where Eq. (2*c*) is derived from the pressure drop at the opening by applying Bernoulli's equation from P_∞ in the far environment ($x\rightarrow\infty$) to the opening at $x=L$, and C_D is the discharge loss coefficient at the aperture of the domain dependent on the discharge area ratio of the aperture to the air layer thickness Y. The mass flow rate in the x direction will be solved in terms of the driving pressure gradient in x, while the flow rate in the y direction is governed by the pressure differential across the fabric between the local air layer pressure at any x and the atmospheric pressure and depends on the permeability of the fabric material. The permeability is affected by the type of yarn, tightness of the twist in the yarn, yarn count, and fabric structure.

In this study the permeability of the fabric is considered constant at the standard experimentally measured value under the pressure difference $\Delta P_m=0.1245$ kPa [20]. To get the normal airflow passing through the fabric at other pressure differentials, other than 0.1245 kPa, the amount of airflow is proportional to the pressure differentials [1]. The normal airflow rate is then represented by

$$\dot{m}_{ay}=\frac{\alpha\rho_a}{\Delta P_m}(P-P_\infty)\ \ \mathrm{kg/m^2\cdot s} \tag{3}$$

where α is the fabric air permeability ($\alpha=4.99\ \mathrm{cm^3/cm^2\cdot s}$), and, P is the air pressure of the air layer between the skin and the fabric and P_∞ is the outside environment air pressure.

The flow in the x direction, driven by time-periodic pressure gradient, will be treated as locally governed by the Womersley time-periodic laminar channel base flow [15,16,21]. Given the oscillatory flow of the air, Womersley further simplifies the analysis by assuming the channel to be of sufficient length such that the flow is fully developed. With these simplifications, the governing momentum equations of the parallel velocity at any position x becomes

$$\frac{\partial u_x}{\partial t}=-\frac{1}{\rho_a}\frac{\partial P}{\partial x}+\nu\frac{\partial^2 u_x}{\partial y^2} \tag{4}$$

Note that if the inertia term $\partial u_x/\partial t$ is neglected in Eq. (4), then the momentum equation reduces back to a quasi-steady Poiseuille flow model for the parallel flow direction [14]. However, the driving pressure in the air layer is oscillating with the same frequency of the normal motion frequency of the upper fabric boundary but with a phase difference of $(\pi/2)$. At high normal fabric-ventilation frequencies, the inertia term is significant. At the minimum fabric position $Y_{\min}=Y_m-\Delta Y$ and the maximum fabric position $Y_{\max}=Y_m+\Delta Y$, the pressure in the air layer equalizes with P_∞ before the normal flow changes direction. The driving pressure gradient in the x direction is written as follows:

$$-\frac{1}{\rho_a}\frac{\partial P}{\partial x}=\Lambda_x\sin\left(\omega t+\frac{\pi}{2}\right)=\Lambda_x\cos(\omega t) \tag{5}$$

where Λ_x is the pressure gradient amplitude factor that can be solved to satisfy the air layer mass balance. Assuming a frequency-separable transient solution, Eq. (4) is written for an oscillating laminar flow in a channel as follows:

$$\frac{\partial u_x}{\partial t}=\Lambda_x\cos(\omega t)+\nu\frac{\partial^2 u_x}{\partial y^2},\qquad\text{and}\quad u_x\left(\pm\frac{Y}{2},t\right)=0 \tag{6}$$

A complete solution can be obtained analytically for $u_x(y,t)$ in dimensionless form $u'_x(y,t)$ as follows, [21]:

$$\begin{aligned}u'_x(y,t)=\frac{u_x(y,t)}{\Lambda_x/\omega}=\cos(\omega t)-\left(\frac{1}{x_1^2+x_2^2}\right)\\ \times\left\{\left[x_1\cos\left(y'\frac{Y}{2}\sqrt{\frac{\omega}{2\nu}}\right)\cosh\left(y'\frac{Y}{2}\sqrt{\frac{\omega}{2\nu}}\right)\right.\right.\\ +x_2\sin\left(y'\frac{Y}{2}\sqrt{\frac{\omega}{2\nu}}\right)\sinh\left(y'\frac{Y}{2}\sqrt{\frac{\omega}{2\nu}}\right]\cos(\omega t)\\ +\left[x_2\cos\left(y'\frac{Y}{2}\sqrt{\frac{\omega}{2\nu}}\right)\cosh\left(y'\frac{Y}{2}\sqrt{\frac{\omega}{2\nu}}\right)\right.\\ \left.\left.-x_1\sin\left(y'\frac{Y}{2}\sqrt{\frac{\omega}{2\nu}}\right)\sinh\left(y'\frac{Y}{2}\sqrt{\frac{\omega}{2\nu}}\right]\sin(\omega t)\right\}\end{aligned} \tag{7}$$

where

$$x_1=\cos(Y/2\sqrt{\omega/2\nu})\cosh(Y/2\sqrt{\omega/2\nu}),$$

$$x_2=\sin(Y/2\sqrt{\omega/2\nu})\sinh(Y/2\sqrt{\omega/2\nu}),$$

and

$$y'=2y/Y$$

where y origin is assumed at the center of the spacing height Y between the boundaries at $\pm Y/2$. Equation (7) expresses the dimensionless axial velocity as a function of y, t and the physical parameters ω and ν. By prescribing a flow condition such as pressure or volume flow rate in the x direction, with the same ventilation frequency, the value of Λ_x can be determined at any given height Y. The mass flow rate per unit area can be calculated as a function of time at any local position x by integrating the x velocity $u'_x(y,t)$ over the height analytically or numerically which will give the mass flow rate per unit depth as follows:

$$\dot{m}'_{ax}(t)=\dot{m}_{ax}Y=\rho_a\frac{Y\Lambda_x}{2\omega}\Phi(t) \tag{8a}$$

where Φ is the dimensionless flow rate given by:

$$\Phi(t)=\int_{-1}^{1}u'_x(y',t)dy' \tag{8b}$$

The air mass flow rate per unit depth $\dot{m}'_{ax}(t)$ is related to the pressure drop in the channel through Eq. (6). The pressure drop at the opening ($x=L$) can be calculated by applying Bernoulli's equation from P_∞ in the far environment to the opening at $x=L$ [see Eq. (2*b*)]. Since the mass flow rate is modeled as a function of pressure differences independently in the x and y directions, then the mass balance of the air layer would result in a pressure equation that can be solved numerically at any discrete location within the air layer as a function of time while satisfying the imposed boundary conditions given in Eqs. (2*b*) and (2*c*).

Water Vapor Mass Balance. Once the pressure and mass flow rates in the air layer are determined, the water vapor mass balance is performed on the air layer. During the oscillation cycle, the air from the environment will move through the fabric void into the air layer when the pressure in the air layer $P_a(x)$ is less than that of the environment P_∞. The airflow into the air spacing layer coming from the air void node of the fabric will have the same humidity ratio as the air in the void space of the fabric. The water vapor mass balance for the air spacing layer when $P_a(x)$ is less than P_∞ is given by

$$\frac{\partial(\rho_a Y w_a)}{\partial t} = h_{m(\text{skin-air})}[P_{sk} - P_a] - \dot{m}_{ay} w_{\text{void}} - \frac{\partial(Y \dot{m}_{ax} w_a)}{\partial x} + D\frac{\rho_a(w_{\text{void}} - w_a)}{e_f/2} \quad P_a(x) < P_\infty \tag{9a}$$

When the pressure in the air layer $P_a(x)$ is greater than P_∞, the airflow through the fabric void space leaving the internal air layer will carry the same humidity ratio of that air layer. Then the water vapor mass balance for the air spacing layer when $P_a(x)$ is greater than P_∞ is given by

$$\frac{\partial(\rho_a Y w_a)}{\partial t} = h_{m(\text{skin-air})}[P_{sk} - P_a] - \dot{m}_{ay} w_a - \frac{\partial(Y \dot{m}_{ax} w_a)}{\partial x} + D\frac{\rho_a(w_{\text{void}} - w_a)}{e_f/2} \quad P_a(x) > P_\infty \tag{9b}$$

where $h_{m(\text{skin-air})}$ is the mass transfer coefficient between the skin and the air layer, P_a is the water vapor pressure in the air layer, w_a is the humidity ratio of the air layer, P_{sk} is the vapor pressure at the skin solid boundary, w_{void} is the humidity ratio of the air void, e_f is the fabric thickness, and D is the diffusion coefficient of water vapor into air. The terms on the right hand side of Eqs. (9*a*) and (9*b*) are explained as follows: The first term represents the mass transfer from the skin to the trapped air layer where the mass transfer coefficient at the skin to the air layer is obtained from published experimental values of Ghaddar et al. [14]; the second term is the convective mass flow coming through the fabric voids; the third term represents the net flux in the parallel direction; and the last term is the water vapor diffusion term from the air layer to the air in the fabric void due to the difference in water vapor concentration.

Energy Balance of the Air Layer. The energy balance for the air–vapor mixture in the air spacing layer will be performed taking into account the parallel air motion, as well as the normal motion direction of the fabric and its effects on the properties of the air mass that enters the domain and leaves the domain during the oscillatory upward and downward motion of the fabric boundary. An energy balance of the air spacing of the fabric expresses the rate of change of the energy air–vapor mixture of the air-layer in terms of the external work done by the environment on the air layer, the evaporative heat transfer from the moist skin, the dry convective heat transfer from the skin, the convection of heat to the air layer associated with $\dot{m}_{ay}$ coming through the upper boundary, and the heat diffusion from void air to confined air layer due to gradients in temperature and water–vapor concentrations. The energy balance of the air layer when $P_a(x)$ is less than P_∞ is given by

$$\frac{\partial}{\partial t}[\rho_a Y(C_v T_a + w_a h_{fg})] + P_\infty \frac{\partial Y}{\partial t} = h_{m(\text{skin-air})} h_{fg}[P_{sk} - P_a] + h_{c(\text{skin-air})}[T_{sk} - T_a] - \dot{m}_{ay}[C_p T_{\text{void}} + w_{\text{void}} h_{fg}] - \frac{\partial Y[\dot{m}_{ax}(C_p T_a + w_a h_{fg})]}{\partial x} + h_{m(f\text{-air})} h_{fg}[P_o - P_a] + h_{c(f\text{-air})}[T_o - T_a] + D h_{fg}\frac{\rho_a(w_{\text{void}} - w_a)}{e_f/2} + k_a\frac{(T_{\text{void}} - T_a)}{e_f/2} \quad P_a(x) < P_\infty \tag{10a}$$

When $P_a(x)$ is greater than P_∞, the energy balance in the air spacing layer becomes

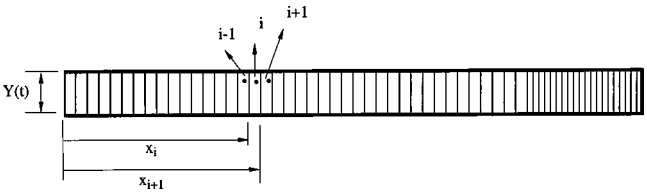

Fig. 3 Computational grid system

$$\frac{\partial}{\partial t}[\rho_a Y(C_v T_a + w_a h_{fg})] + P_\infty \frac{\partial Y}{\partial t} = h_{m(\text{skin-air})} h_{fg}[P_{sk} - P_a] + h_{c(\text{skin-air})}[T_{sk} - T_a] - \dot{m}_{ay}[C_p T_a + w_a h_{fg}] - \frac{\partial[Y \dot{m}_{ax}(C_p T_a + w_a h_{fg})]}{\partial x} + h_{m(f\text{-air})} h_{fg}[P_o - P_a] + h_{c(f\text{-air})}[T_o - T_a] + D h_{fg}\frac{\rho_a(w_{\text{void}} - w_a)}{e_f/2} + k_a\frac{(T_{\text{void}} - T_a)}{e_f/2} \quad P_a(x) > P_\infty \tag{10b}$$

where k_a is the thermal conductivity of air, $h_{c(f\text{-air})}$ is the convection coefficient from the fabric to air, and $h_{m(f\text{-air})}$ is the mass transport coefficient from the fabric to air. The fabric to air parallel transport coefficients can be taken similar to those from skin to air. Since the fabric void thickness is very small, conduction of heat from the fabric void air to the trapped air layer is represented by the law of the wall as shown in the last two terms of Eqs. (10*a*) and (10*b*).

Numerical Procedure

The control volume methodology is used to divide the air layer into grids of size Δx and height $Y(t)$ as shown in Fig. 3. Each grid volume contains a lumped adsorption system of fibrous inner, outer nodes and air void as the upper boundary. The discrete air pressure at the volume center is defined as:

$$P_i^n = P_a(n\Delta t, (x_i + x_{i+1})/2) \quad \{i = 0 \cdots N_x\} \tag{11}$$

where n is the discrete time step number. Note that Y is assumed to be constant in the x direction, but the formulation can easily be extended to a variable air layer thickness in x direction if quasi-parallel flow conditions are applicable ($dY/dx \ll 1$).

In this work, only the discrete model equations for the air mass balance are given to illustrate the methodology. There are two different airflows for each location: Airflow through the fabric in the y direction, $\dot{m}_{ay}$, and airflow parallel to the fabric layer in the x direction. At the end boundary $x = L$, there will be a flow direct to or from the environment, $\dot{m}_0$. The mass flow rates in x is dependent on the pressure gradient parameters Λ_x, while $\dot{m}_{ay}$ depends on pressure difference $(P_a - P_\infty)$. The integral in Eq. (8*b*) of the dimensionless volumetric flow rate Φ^n at $t^n = n\Delta t$ is evaluated analytically and numerically at the discrete times dictated by the numerical scheme stability and convergence conditions for the time step size Δt. The temporal integration of the air layer mass balance for an internal control volume node i is performed using a first order Euler–Forward scheme. The discrete form of the air mass balance is given by

$$\rho_a\left(\frac{dY^n}{dt}\right) = \gamma_{ay}(P_\infty - P_i^n) - \rho_a\frac{Y^n}{2\omega}\Phi^n\left[\frac{\Lambda_{x(i)} - \Lambda_{x(i-1)}}{\Delta x_i}\right] \tag{12a}$$

where γ_{ay} is a linearized coefficient in y direction, kg/kPa·s·m^2 obtained from Eq. (2) as:

$$\gamma_{ay} = \frac{\alpha \rho_a}{\Delta P_m} \tag{12b}$$

Equation (12) has two unknowns: P_i^n and $\Lambda_{x(i)}$. The gradient factor $\Lambda_{x(i)}$ is correlated to the pressure by

$$P_{i+1} = P_i + \rho_a \Lambda_{x(i)} \Delta x \sin(\omega t) \tag{13}$$

At the boundary node with no axial flow ($x=0$), the mass balance for the first node of the air layer is given by

$$\rho_a \frac{dY^n}{dt} = \gamma_{ay}(P_1^n - P_\infty) + \rho_a \frac{Y^n}{2\omega} \Phi^n \left(\frac{\Lambda_{x(1)}}{\Delta x} \right) \tag{14}$$

At the opening to atmosphere ($x=L$), the mass flow rate to the environment is governed by the Bernoulli equation giving

$$\dot{m}_o = \gamma_o (P_\infty - P_{N_x}^n) \tag{15a}$$

where $\gamma_o = C_D(2 * \rho_a / (|P_N^n - P_\infty|))^{1/2}$. At the boundary control volume, the mass balance is given by

$$\rho_a \frac{dY_x^n}{dt} = \gamma_o (P_N^n - P_\infty) + \gamma_{ay}(P_N - P_\infty) + \rho_a \frac{Y^n}{2\omega} \Phi^n \left(\frac{\Lambda_{x(N)}}{\Delta x} \right) \tag{15b}$$

The term $\Lambda_{x(N-1)}$ is omitted since a central node is used for the pressure and the open end is balanced by flow induced by the pressure gradient at node $N(\Lambda_{x(N)})$ and by $\dot{m}_o$ at the open boundary. The above equations will be solved at each time step for the pressure P_i^n and $\Lambda_{x(i)}$ at every node in the computational domain. Then the pressure is used to determine the air flow in each direction. The pressure and the airflow rates follow as direct inputs in the water vapor mass balances and the energy balances of the air layer control volume, and of the fabric nodes and void space. These equations will be integrated numerically using first-order Euler–Forward scheme in time and control volume methodology in space. The vapor pressure of the flowing air in the air spacing layer or in the fabric voids is related to the air relative humidity, RH, and temperature and is calculated using the psychometric formulas of Hyland and Wexler [22] to predict the saturation water–vapor pressure and hence the vapor pressure at the specified relative humidity. The regain R of the cotton material has a definite relation to the relative humidity of the water vapor through a property curve of regain versus relative humidity. The property curve is fitted with an interpolation function given by:

$$RH = -6.33 \times R^3 - 23.7337 \times R^2 + 10.42 \times R - 0.05 \tag{16}$$

The solution will proceed at each time step by assuming a value of the pressure at node N_x, calculating γ_o, solving the pressure equation for Λ_x in Eq. (12*a*) concurrently with the pressure recurrence formula in Eq. (13) at all the internal nodes. The solution will produce a new value of P_{Nx} which will be used again in the solution of Eqs. (12) and (13) until the solution converges where the percent error in the pressure between any two iterative steps is less than $10^{-5}\%$.

Several numerical tests were performed to assure a grid independent and stable numerical solution. For a domain of length $L = 0.5$ m $C_D = 1$, $Y_m = 38.1$ mm, and $\Delta Y = 6.35$ mm at different mesh size to get a grid independent solution in axial direction. Both the uniform and nonuniform grid distributions are tested for a domain length $L = 0.5$ m. The size of the uniform grid of $\Delta x = 0.01$, 0.005, and 0.004 m were used to generate the solution. The program was also run with a variable gird size; 0.005 at opening and 0.01 for inner parts since the higher gradient of parallel flow occurs near the opening. For our simulations, a variable grid size of 0.005 m at opening and 0.01 in the interior were used in the runs and produced grid independent results. The size of the time step was taken at 0.01 and 0.001 s over a total integration period of 3600 s. At low frequencies, the higher time step of 0.01 s was sufficient to produce a stable accurate solution with the selected grid size.

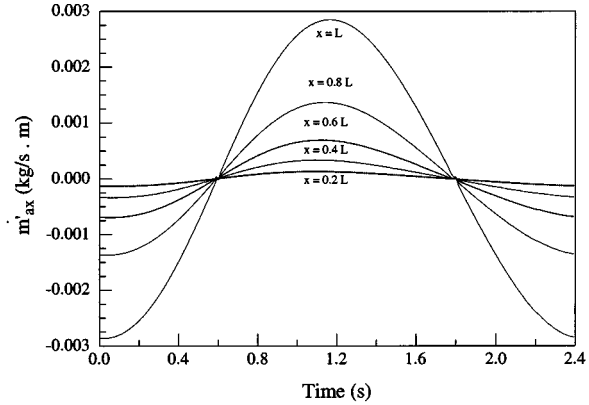

(*a*)

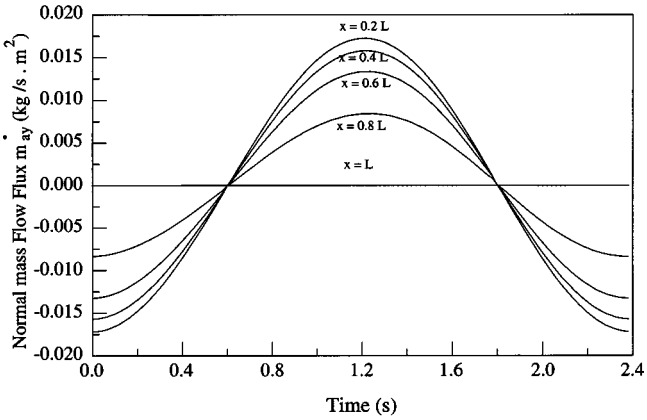

(*b*)

Fig. 4 The variation with time of the internal modulated air layer parallel flow rate and normal mass flux (*a*) $\dot{m}'_{ax}$ and (*b*) $\dot{m}_{ay}$, respectively, at $x = 0.2$ L, 0.4 L, 0.6 L, 0.8 L and L using the presented Womersley model for the parallel flow at the frequency of 25 rpm, $C_D = 1$, $Y_m = 38.1$ mm, and $\Delta Y = 6.35$ mm

Results and Discussion

Simulations are performed for a domain of length $L = 0.5$ m $C_D = 1$, $Y_m = 38.1$ mm, and $\Delta Y = 6.35$ mm at three different frequencies for the 2D normal-parallel flow model. The selection of the length is based on the realistic physical length of a sleeve, or cloth-covered trunk between the waist and the aperture at the neck. The mean spacing size and amplitude of oscillation replicate experimental values used in published work [11]. The ambient conditions are taken at 25°C and 50% RH and the skin condition is saturated at 35°C and 100% relative humidity. The numerical simulation results from the model predict transient steady periodic mass flow rates in normal and parallel direction, fabric regain, internal air layer temperature and humidity ratio, fabric outer node temperature and heat sensible and latent heat transfer quantities from the skin surface. Heat losses will be compared with the limiting case results of normal flow, 2D Poisueille flow model of Ghali et al. [14] and with published empirical results of Lotens [2].

Figures 4(*a*) and 4(*b*) show the variation in time of the internal modulated air layer parallel flow rate and normal mass flux [Fig. 4(a)] $\dot{m}'_{ax}$ and [Fig. 4(b)] $\dot{m}_{ay}$, respectively, at $x = 0.2L$, $0.4L$, $0.6L$, $0.8L$ and L using the Womersley model for the parallel flow at the frequency of 25 rpm, $C_D = 1$, $Y_m = 38.1$ mm, and $\Delta Y = 6.35$ mm. To study the extent of the rate of air renewal rates in the internal air layer, the time-averaged mass flow rate is calculated over half cycle period τ during upward motion or downward motion as the fabric moves from the lowest position with respect

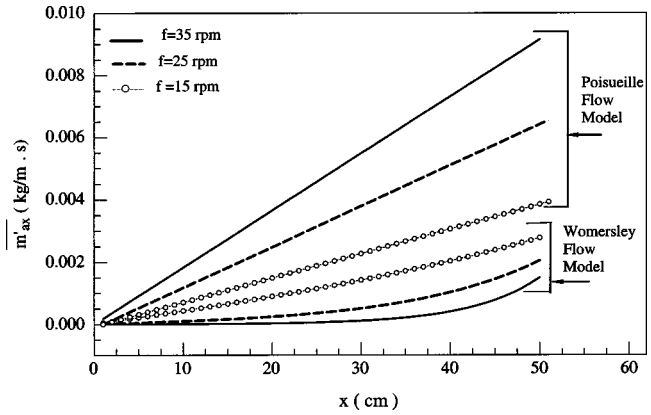

Fig. 5 The variation of the Womersley and Poisueille models time-averaged mass flow rates with x at three different ventilation frequencies of 15, 25, and 35 rpm for $C_D=1$, $Y_m=38.1$ mm, and $\Delta Y=6.35$ mm

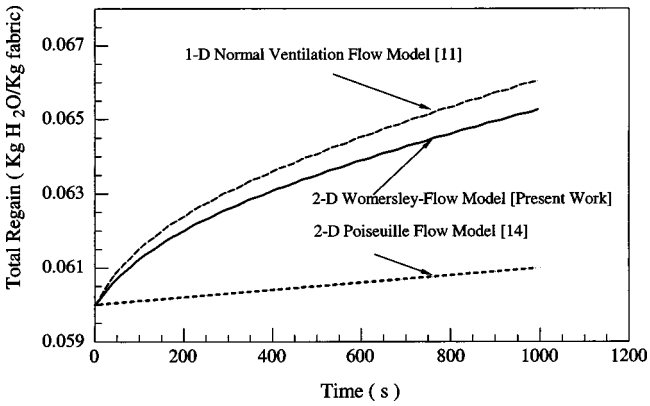

Fig. 6 The fabric space-averaged regain as a function of time for the both the Womersley and Poiseuille 2D models of parallel flow (open aperture), and the 1D normal flow model (closed aperture)

to the fixed skin surface to the highest position. The time-averaged mass flow rate per unit depth in the x direction is defined by

$$\overline{\dot{m}'_{ax}}=\frac{2}{\tau}\int_{\tau/4}^{3\tau/4}\dot{m}_{ax}(t)Y(t)dt \tag{17}$$

Figure 5 shows the variation of the parallel time averaged mass flow rate per unit depth for Womersley and Poiseuille models at three different ventilation frequencies of 15, 25, and 35 rpm for $C_D=1$, $Y_m=38.1$ mm, and $\Delta Y=6.35$ mm. The mean air mass flow rate in the x direction increases sharply close to the open boundary. The Womersley model parallel mass flow rate values approach the Poisueille model values as the ventilation frequency decreases ($W_o \ll 1$). The ratios in percentage of the parallel flow rate through the opening ($x=L$) of the Womersley-based model to the Poisueille-based model are 16.3%, 31.25%, 73.68% and corresponding to frequencies of 15, 25, and 35 rpm, respectively. In the Poiseuille flow, as the frequency increased, the flow rate increased. In the Womersley flow, as the frequency increased the flow rate decreased to approach that of Poiseuille at low frequency. This behavior is inherent in the solution of the momentum equation [Eq. (6)] where at a fixed amplitude of the driving pressure gradient, the channel maximum mass flow rate increases with the frequency up to a critical value of the Womersley number of $W_o=1.107$ and then the flow rate decreases with increased frequency [21]. As $W_o \to \infty$ (inertia prevails), the maximum mass flow rate approaches zero for any value of the driving pressure gradient.

Figure 6 shows the fabric space-averaged total regain as a function of time for the 2D Womersley-model (open aperture) compared to the one-dimensional (1D) Poisueille-model (open aperture) and the 1D normal flow model (closed aperture) at $f=25$ rpm, $C_D=1$, $Y_m=38.1$ mm, and $\Delta Y=6.35$ mm. Figure 7(a) shows the variation in time of the internal air layer temperature at $x=0$, 0.6 L, 0.8 L, and L, and for the 1D normal flow model at the frequency $f=25$ rpm, $C_D=1$, $Y_m=38.1$ mm, and $\Delta Y=6.35$ mm. The variation in amplitude of the air layer temperature at the opening is higher than that of internal nodes because of the difference between incoming fresh air at 25°C and the human skin temperature at 35°C. Figure 7(b) the space-averaged temperature over the length of the domain L of the internal air layer of the 2D model, and the air layer temperature of the 1D normal flow model are shown as a function of time. Similarly, the internal air layer space-averaged humidity ratios of the 2D and 1D models are plotted as a function of time at $f=25$ rpm in Fig. 7(c). The air layer space-average temperature of the 2D model modulates over a temperature difference (between maximum and minimum) of 1.825°C compared to 1.5°C for the 1D model. Figure 8(a) shows the spatial variation in x direction of the steady periodic temperatures of the outer node and the internal air layer. Maximum values of the outer node temperature and internal air layer temperature occur at $x=0.405$ m and $x=0.384$ m, respectively. The effect of parallel flow convection through the opening is to produce a net cooling effect close to the boundary better than 1D normal model, while ventilation is providing faster renewal of air by ventilation across the portion of length near the closed boundary. Since the peak ventilation normal mass flow rate through the fabric is almost twice that entering from the aperture, it is expected to have more influence to move the local peak of the outer node and air layer temperatures towards the open aperture. A similar behavior is observed in Fig. 8(b) of the internal air layer steady-periodic humidity ratio variation in x. The air layer temperature rises as the location is nearer the opening from 0.4 to 0.8 L and drops from 0.8 L to L. At the opening, the air layer temperature is lower as would be expected.

The presented results indicate that the presence of the opening has actually reduced the cooling effect on the internal air layer and consequently will reduce the sensible and latent heat losses. Figures 9(a) and 9(b) show the parallel Womersley flow model time-averaged [Fig. 9(a)] sensible and [Fig. 9(b)] latent heat losses from the skin in W/m^2 as a function of x at three different ventilation frequencies of 15, 25, and 35 rpm for $C_D=1$, $Y_m=38.1$ mm, and $\Delta Y=6.35$ mm. The Poiseuille model results of Ghali et al. at $f=25$ rpm is also shown in the figures for comparison. The heat losses are higher at the boundary open to atmosphere because of the big difference between the temperature and humidity ratio between room conditions and the skin condition. The local minimum heat loss occurs at $x=35.5$, 42, and 45 cm at $f=15$, 25, and 35 rpm, respectively. At higher frequencies, the effect of the opening on the heat loss is reduced. The Poiseuille model of the parallel flow results in artificially increased heat losses in the region close to the opening where 90% of the heat loss takes place between $x=30$ cm and $x=50$ cm while decreasing the normal ventilation effect to almost zero in the internal region next to the closed end ($x=0$ to $x=30$ cm). The time and space-averaged total heat loss of the current Womersley model of the parallel flow is calculated as 247.04 W/m^2 compared with 152 W/m^2 calculated using the Poiseuille parallel flow model. The Poiseuille flow model of the parallel air flow fails at high frequencies to predict the heat losses from a clothed skin with open aperture.

Heat losses predicted by the current Womersley model for the open aperture system are compared with the 1D ventilation model (close aperture). The time and space-averaged sensible and latent heat losses from the skin are calculated at frequencies of 15, 25, and 35 rpm, and the corresponding heat losses of the 1D normal flow model (closed aperture). Table 1 shows the time and space-

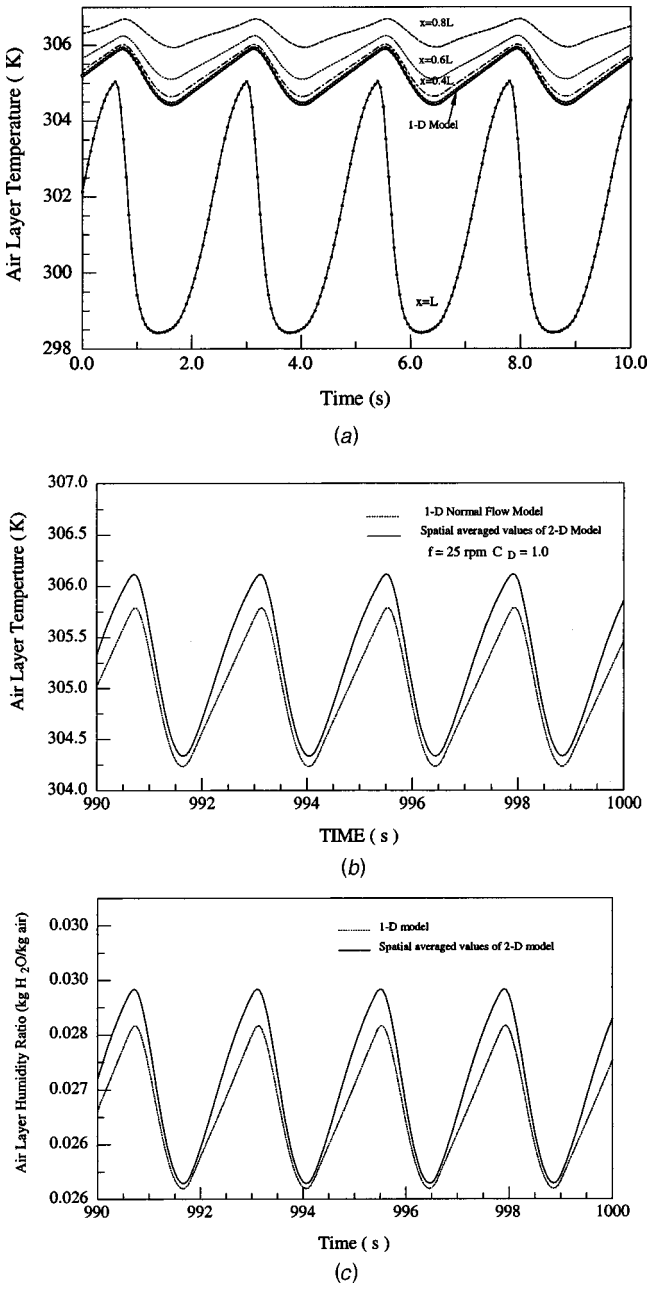

Fig. 7 The variation in time of (*a*) the internal air layer temperature at $x=0.4$, 0.6 L, 0.8 L and L, at $f=25$ rpm and $C_D=1$, and for the 1D normal flow model at $f=25$ rpm, (*b*) the 2D space-averaged internal air layer temperature over the length L and 1D normal flow model $f=25$ rpm, and (*c*) the 2D space-averaged humidity ratios of the 2D and 1D models at $f=25$ rpm

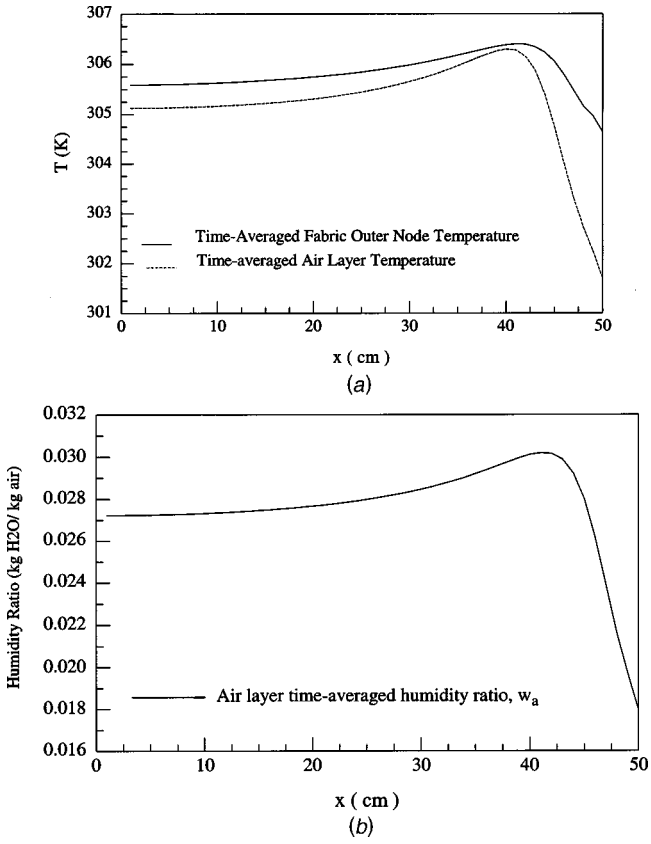

Fig. 8 The Womersley-based 2D model time-averaged (*a*) sensible and (*b*) latent heat losses from the skin in Watt/m^2 as a function of x at three different ventilation frequencies of 15, 25, and 35 rpm for $C_D=1$, $Y_m=38.1$ mm and $\Delta Y=6.35$ mm. The Poisueille-based 2D model at $f=25$ rpm is also shown.

averaged sensible and latent heat losses from the skin at ventilation frequencies of 15, 25, and 35 rpm, and the corresponding heat losses of the 1D normal flow model (closed aperture). The results show that the presence of the opening has resulted in lower sensible and latent heat loss than the 1D model representing the closed aperture. The percentage drop in total heat loss due to open aperture is 18.3%, 7.52%, and 2.63%, at ventilation frequencies of 15, 25, and 35 rpm, respectively. These results are consistent with published experimental data of Lotens [2] and Danielsson [3]. Lotens has reported experimental measurements of the internal air layer evaporative resistance at the skin and in the internal air layer as a function of open or closed apertures and walking speed for high air permeable clothing ensemble made of cotton fabric. He noticed that the resistance to vapor transfer with closed and open apertures are not very different regardless of the outside air velocity. His results show that vapor resistance from the body at zero walking speed and 0.2 m/s wind is slightly higher for closed aperture than for open aperture. However, as the walking speed is increased to 0.694 and 1.388 m/s, the evaporative resistance at the skin and in the internal air layer at the same wind speed of 0.2 m/s, decreased by 1.4% and 7.6%, respectively. Similar results have been reported by Danielsson [3] on higher heat loss and higher internal convective coefficients for closed aperture clothing over various body parts as compared to respective values for open aperture clothing at walking conditions. It is clear that for long domains, the presence of the openings will only have a local effect close to the boundary, while at the same time reducing the air renewal flow rate by normal ventilation due to reduced pressure difference through the fabric between the internal layer and the environment.

Conclusions

The coupled convection heat and moisture exchange within the clothing system subject to sinusoidal air layer thickness variation about a fixed mean is theoretically modeled to predict the fabric temperature and the transient conditions of the air layer located between the fabric and the skin. The developed mathematical model is based on the Womersley flow for the parallel flow direction and uses a three-node adsorption ventilation model for the fabric in the normal airflow direction. The ventilation model transport coefficients within the fabric have been modified to better

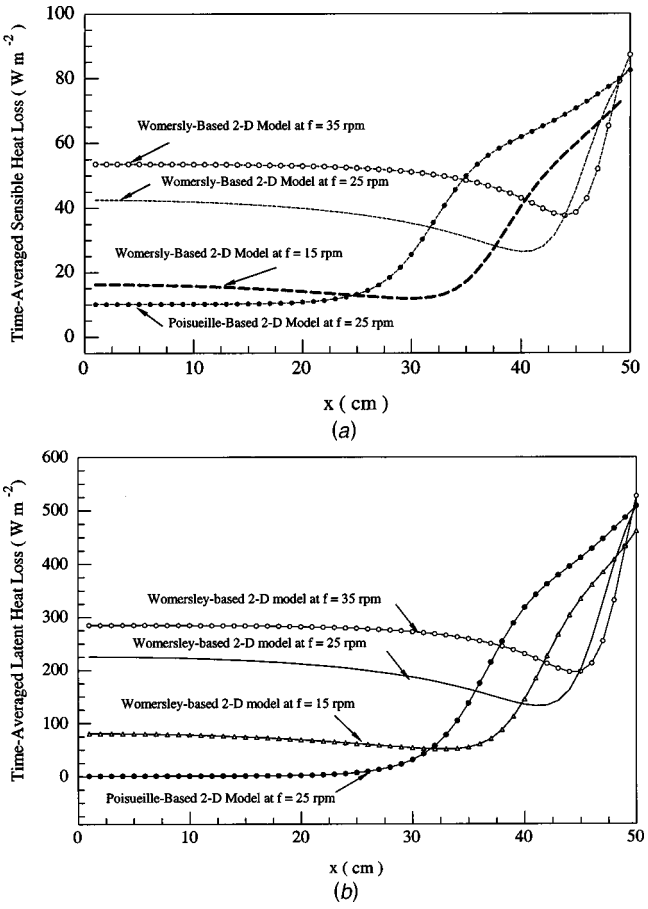

Fig. 9 The parallel Womersley flow model time-averaged (*a*) sensible and (*b*) latent heat losses from the skin in W/m^2 as a function of *x*

predict transport processes in the fabric when low normal ventilation flow rates exist near openings to the atmosphere.

The developed model of the internal air layer flow rates using locally the Womersley flow model shows that inertia term due to air modulation plays a significant role in reducing air mass flow rate in the direction parallel to the fabric and brings the results closer to the experimental findings of Loten [2] that show slight reduction in heat loss for closed aperture clothing. Neglecting air flow inertia, results in a significant reduction of the normal ventilation rate and an increase in the air layer temperature.

The current model approach is novel in its consideration of the periodic nature of air motion in the trapped layer between skin and fabric from first principles that capture all the physical parameters of the system. The model provides an effective and fast method of providing solution at low computational cost. This makes the model attractive for integration with human body thermal models to better predict human response under dynamic conditions. The 2D motion within the air layer and its interaction with the ambient air through the fabric and the aperture is a complex basic problem. The introduction of the Womersley flow in the parallel air flow has reduced the complexity of the solution and predicts realistic mass flow rate through the apertures. In long domains, the effect of the aperture is localized.

Table 1 The time-space averaged sensible and latent heat losses at various ventilation frequencies of the fabric and the corresponding heat losses of the 1D normal flow model

	$f=15$ rpm		$f=25$ rpm		$f=35$ rpm	
Model	Q_L (W/m^2)	Q_S (W/m^2)	Q_L (W/m^2)	Q_S (W/m^2)	Q_L (W/m^2)	Q_S (W/m^2)
Normal flow model (closed aperture)	154.5	28.7	225.3	41.9	280.97	52.81
2D Womersley Flow Model (open aperture)	124.48	25.24	207.99	39.06	273.61	51.39

Acknowledgment

The authors would like to acknowledge the financial support of the University Research Board of the American University of Beirut.

Nomenclature

A_f = area of the fabric (m^2)
C = specific heat (J/kg·K)
C_D = dimensionless flow discharge coefficient at the aperture
D = water vapor diffusion coefficient in air (m^2/s)
e_f = fabric thickness (m)
f = frequency of oscillation of the fabric boundary (ventilation frequency) (revolution per minute)
h_{fg} = heat of vaporization of water (J/kg)
h_{ad} = heat of adsorption (J/kg)
H_{ci} = conduction heat transfer coefficient between inner node and outer node (W/m^2·K)
H_{co} = convection heat transfer coefficient between outer node and air flowing through fabric (W/m^2·K)
$h_{c(f\text{-air})}$ = heat transport coefficient from the fabric outer node to the trapped air layer (W/m^2·K)
$h_{c(\text{skin-air})}$ = heat transport coefficient from the skin to the trapped air layer (W/m^2·K)
h_{ce} = heat transport coefficient from the fabric to the environment air at zero normal flow (W/m^2·K)
h_{ci} = heat transport coefficient from the fabric outer node to the trapped air layer (W/m^2·K)
h_{de} = mass transport coefficient from the fabric to the environment air at zero normal flow (W/m^2·K)
h_{ci} = mass transport coefficient from the fabric outer node to the trapped air layer at zero normal flow (W/m^2·K)
H_{mi} = diffusion mass transfer coefficient between inner node and outer node (kg/m^2·kPa·s)
H_{mo} = mass transport coefficient between outer node and air void in the fabric (kg/m^2·kPa·s)
$h_{m(f\text{-air})}$ = mass transfer coefficient between the fabric outer node and the air layer (kg/m^2·kPa·s)
$h_{m(\text{skin-air})}$ = mass transfer coefficient between the skin and the air layer (kg/m^2·kPa·s)
k_a = thermal conductivity of air (W/m·K)
L = fabric length in x direction (m)
$\dot{m}_{ax}$ = mass flow rate of air per unit area in x-direction (kg/m^2·s)
$\dot{m}'_{ax}$ = Parallel mass flow rate of air in x-direction per unit depth (kg/m·s)
$\dot{m}_{ay}$ = mass flow rate of air per unit area in y-direction (kg/m^2·s)
P_a = air vapor pressure (kPa)
P_i = vapor pressure of water vapor adsorbed in inner node (kPa)
P_o = vapor pressure of water vapor adsorbed in outer node (kPa)
R = total regain in fabric (kg of adsorbed H_2O/kg fiber)
R_v = water vapor gas constant (=0.461 kJ/kg·K)
RH = relative humidity (%)

rpm = revolution per minute
t = time (s)
T = Temperature (°C)
w = humidity ratio (kg of water/kg of air)
W_o = Womersley number ($W_o=(Y/2)\sqrt{\omega/2\nu}$)
x = x coordinate in the parallel direction to the fabric and skin
Y = instantaneous air layer thickness (m)
Y_m = mean air layer thickness (m)
y = y direction

Greek Symbols

ε = fabric emissivity
Φ = periodic dimensionless flow rate parameter in x-direction
ρ = mass density of fabric (kg/m^3)
ω = Angular frequency ($=2\pi f/60$) (rad/s)
Λ_x = Pressure gradient parameter in x-direction (Pa·m^2/kg)
α = fabric air permeability (cm^3/cm^2·s)
ν = *kinematic* air viscosity (m^2/s)
σ = Stefan Boltzman constant$=5.669\times10^{-8}$ W/m$^2\cdot$K^4

Subscript

a = conditions of air in the spacing between skin and fabric
i = inner node
o = outer node
sk = conditions at the skin surface
void = local air inside the void
∞ = environment condition

Appendix: Fabric Modified Ventilation Transport Coefficients

At significant normal air flow rates, the Ghali et al. [11] three-node ventilation model defines internal effective heat and mass transfer coefficients H_{co} and H_{mo} for the outer node of the fabric and void, and the heat and mass diffusion coefficients H_{ci} and H_{mi} from the outer to the inner nodes of the fabric [1]. The main parameter predicted by solving the conservation equations of mass and energy balances of the fabric nodes in the model is the fabric regain (amount of moisture retained by the fabric per kg of the fabric). The heat and mass transport coefficients, namely H'_{ci}, H'_{mi}, H'_{co} and H'_{mo} are modified in this work to account for the low flow rate range of the ventilation model when heat and moisture diffusion dominate. At zero normal flow rate, the time-dependent mass and energy balances for the diffusion model of a relatively dry fabric placed in humid environment are derived based on the dry and evaporative resistances of a lumped fabric model first introduced by Farnworth [18] and simplified by Jones and Ogawa [19]. The modeled fabric is cotton fabric with effective thermal conductivity of 0.042 W/m·K and is similar to the fabric used in the experiments of Ghali et al. [1] which had a thickness of 1 mm. The Biot number is equal 0.095 at $h=4$ W/m·K that justifies the lumped approach. The water vapor balance of a fabric placed in humid air is simply given by

$$\frac{dR}{dt}=\frac{1}{\rho_f e_f}\left[\frac{P_\infty-P_f}{R_E h_{fg}}+h_{Di}(P_f-P_\infty)+h_{De}(P_f-P_\infty)\right] \quad (A1)$$

where R is the fabric total regain, R_E is the fabric evaporative resistance, P_f is the vapor pressure in the fabric void space, and h_{Di} and h_{De} are the internal and external mass transfer coefficients with the air layer and with the environment, respectively. The energy balance in the fabric is

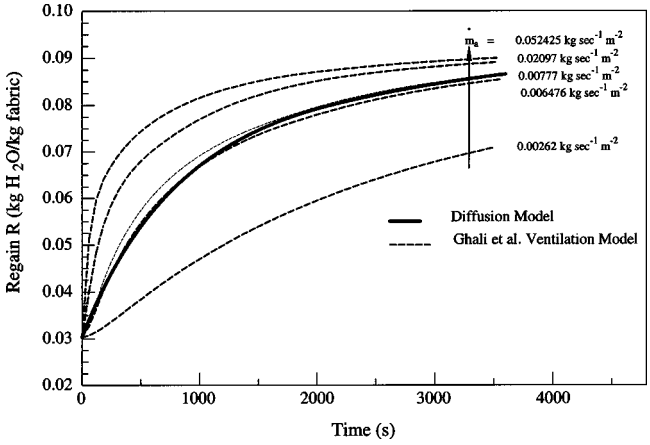

Fig. A1 The predicted fabric regain using ventilation model for the conditions of Ghali et al. experiment [1] at various air flow rates from zero to 0.05242 kg/m^2·s. On the same graph, the diffusion model regain in still air is shown.

$$\frac{dT_f}{dt}=\frac{1}{\rho_f C_{pf} t_f}\left[\frac{T_\infty-T_f}{R_D}+\rho_f t_f h_{ad}\frac{dR}{dt}+h_{ce}(T_\infty-T_f)+h_{ci}(T_\infty-T_f)+2h_r(T_\infty-T_f)\right] \quad (A2)$$

where R_D is the fabric dry resistance, h_r is the linearized radiation heat transfer coefficient based on average temperature given by Holman [23], h_{ad} is the heat of adsorption, h_{ci} and h_{ce} are the internal and external mass transfer coefficients with the air layer and with the environment, respectively. Data on h_{ad} as a function of relative humidity are found in the work of Morton and Hearle [24].

Equations (*A*1) and (*A*2) are solved numerically for the same fabric at conditions that replicate the reported original experimental data used for the development of Ghali et al. [1] three-node ventilation model, where the fabric was initially conditioned for 24 h in a dry climatic chamber at a temperature of 30°C and relative humidity of 30%. The same fabric was then transferred to the wet chamber at temperature of 30°C and relative humidity of 80%. For the cotton fabric used in previous work, the dry resistance is $R_D=0.029$ m$^2\cdot$K/W and the evaporative resistance is $R_E=0.00505$ m$^2\cdot$kPa/W. In still air, the internal and external heat convection coefficients h_{ci} and h_{ce} used in the diffusion model are the same as those reported by Lotens [2].

The transport coefficients H'_{mo} and H'_{co} were empirically derived by Ghali et al. [1] and are found to increase linearly with the air normal mass flow rate. The range of flow rates per unit area considered by the reported study was from 0.00777 to 0.045 kg/m^2·s. Human gait analysis [17] reports that a walking speed of 0.9 m/s corresponds to 70 steps/min (ventilation frequency is 35 rpm). The maximum mass flow rate during one walking cycle for air passing through the fabric is at 35 rpm is 0.027 kg/m^2·s, while at 25 rpm it is 0.0193 kg/m^2·s. The flow rate ranges studied here are practical for low to moderate walking speeds. It is of interest to find the minimum flow rate of the ventilation model that could reproduce the diffusion model results.

Figure A1 presents a plot of calculated fabric regain of the Ghali et al. [1] ventilation model at various air flow rates from zero to 0.05242 kg/m^2·s. On the same graph, the diffusion model regain in still air is plotted. At flow rates lower than 0.00777 kg/m^2·s, the ventilation model predicts lower regain than the diffusion model. The diffusion model produces the lowest regain that can physically take place in the fabric. However, at the mass flow rate of 0.00777 kg/m^2·s, the same value of the steady periodic regain is predicted by both the ventilation model based on 3

lumped nodes at different temperatures and humidity ratios and the diffusion model based on lumping the fabric as one node. At 0.00777 $kg/m^2 \cdot s$, the relative error between the calculated regain using the diffusion model and the regain using the ventilation model is less than 0.01% and the difference between the calculated fabric temperatures using both diffusion and ventilation models is less than 0.0005%. At low flow rates, the diffusion model can easily be replaced by the three nodes model using the lower bound of the values of transport coefficients at the flow rate of 0.00777 $kg/m^2 \cdot s$. The modified effective heat transfer coefficient between the air flow in the fabric void and the outer node is then given by

$$H'_{Co} = 495.72\dot{m}_a - 1.85693 \ \ W/m^2 \cdot K, \quad \dot{m}_a \geq 0.00777 \ \ kg/m^2 \cdot s \tag{A3a}$$

$$H'_{Co} = 2.0 \ \ W/m^2 \cdot K, \quad \dot{m}_a \leq 0.00777 \ \ kg/m^2 \cdot s \tag{A3b}$$

Similarly, the modified effective mass transfer coefficient between the water vapor in airflow in the fabric void and the outer node is given by

$$H'_{mo} = 3.408 \times 10^{-3}\dot{m}_a - 1.2766 \times 10^{-5} \ \ kg/m^2 \cdot kPa \cdot s, \quad \dot{m}_a \geq 0.00777 \ \ kg/m^2 \cdot s \tag{A4a}$$

$$H'_{mo} = 1.3714 \times 10^{-5} \ \ kg/m^2 \cdot kPa \cdot s, \quad \dot{m}_a \leq 0.00777 \ kg/m^2 \cdot s \tag{A4b}$$

A correlation factor of 0.999 is obtained for H'_{co} and H'_{mo} equations. The inner node transport coefficients used in the model development have not changed and are as reported by Ghali et al. [1] $H'_{ci} = 1.574 \ W/m^2 \cdot K$, and $H'_{mi} = 7.58 \times 10^{-6} \ kg/m^2 \cdot kPa \cdot s$.

To further validate the use of the above approach in simulating the ventilation speeds from zero to high rates, the ventilation model with the updated transport coefficients is used to predict the original experimental values of sensible and latent heat loss by ventilation due to fabric oscillating motion above a sweating hot plate [11]. The ventilation model with updated transport coefficients is used to predict the fabric regain and the heat loss from the skin due to the motion at $Y_m = 38.1$ mm and $\Delta Y = 6.35$ mm. The experimentally reported time-averaged total (sensible and latent) heat loss at $f = 25$ rpm was 235.88 W/m^2 and the reported three-node ventilation model time-averaged total heat loss was 273.5 W/m^2 [11]. The current modified transport coefficients of the normal ventilation model better predicts the total heat loss at 266.4 W/m^2, reducing the relative error to 12% between theoretical and experimental values compared to 16% reported previously.

References

[1] Ghali, K., Ghaddar, N., and Jones, B., 2002, "Empirical Evaluation of Convective Heat and Moisture Transport Coefficients in Porous Cotton Medium," ASME J. Heat Transfer, **124**(3), pp. 530–537.

[2] Lotens, W., 1993, "Heat Transfer From Humans Wearing Clothing," Doctoral Thesis, TNO Institute for Perception, Soesterberg, The Netherlands, 34–37.

[3] Danielsson, U., 1993, "Convection Coefficients in Clothing Air Layers," PhD thesis, The Royal Institute of Technology, Stockholm.

[4] McCullough, E. A., Jones, B. W., and Jones, B. W., 1989, "A Database for Determining the Evaporative Resistance of Clothing," ASHRAE Trans., **95**, pp. 316–328.

[5] Havenith, G., Heus, R., and Lotens, W. A., 1990, "Resultant Clothing Insulation: a Function of Body Movement, Posture, Wind Clothing Fit and Ensemble Thickness," Ergonomics, **33**(1), pp. 67–84.

[6] Havenith, G., Heus, R., and Lotens, W. A., 1990, "Clothing Ventilation, Vapor Resistance and Permeability Index: Changes Due to Posture, Movement, and Wind," Ergonomics, **33**(8), pp. 989–1005.

[7] Jones, B. W., Ito, M., and McCullough, E. A., 1990, "Transient Thermal Response Systems," Proceedings International Conference on Environmental Ergonomics, Austin, TX, pp. 66–67.

[8] Jones, B. W., and McCullough, E. A., 1985, "Computer Modeling for Estimation of Clothing Insulation," Proceedings of CLIMA 2000, World Congress on Heating, Ventilating, and Air Conditioning, Copenhagen, Denmark, **4**, pp. 1–5.

[9] Li, Y., and Holcombe, B. V., 1998, "Mathematical Simulation of Heat and Moisture Transfer in a Human-Clothing-Environment System," Text. Res. J., **68**(6), pp. 389–397.

[10] Ghali, K., Ghaddar, N., and Jones, B., 2002, "Multi-Layer Three-Node Model of Convective Transport Within Cotton Fibrous Medium," J. Porous Media, **5**(1), pp. 17–31.

[11] Ghali, K., Ghaddar, N., and Jones, B., 2002, "Modeling of Heat and Moisture Transport by Periodic Ventilation of Thin Cotton Fibrous Media," Int. J. Heat Mass Transfer, **45**, pp. 3703–3714.

[12] Ghaddar, N., Ghali, K., and Jones, B., 2003, "Integrated Human-Clothing System Model for Estimating the Effect of Walking on Clothing Insulation," Int. J. Therm. Sci., **42**(6), pp. 605–619.

[13] Gagge, A. P., Fobelets, A., and Berglund, L. G., 1986, "A Standard Predictive Index of Human Response to the Thermal Environment," ASHRAE Trans. 2B, PO-86-14.

[14] Ghali, K., Ghaddar, N., and Harathani, J., 2004, "Two Dimensional Clothing Ventilation Model for a Walking Human," Proceedings of the International Conference on Thermal Engineering: Theory and Applications. Paper No. ICEA-TF1-03, Beirut-Lebanon, May 31–June 4, 2004.

[15] Womersley, J. R., 1955, "Oscillatory Motion of Viscous Liquid in Thin-Walled Elastic Tube: I. The Linear Approximation for Long Waves," Philos. Mag., **46**, pp. 199–221.

[16] Womersley, J. R., 1957, "An Elastic Tube Theory of Pulse Transmission and Oscillatory Flow in Mammalian Arteries," Aeronautical Research Laboratory. WADC Technical Report TR 56-614.

[17] Lamoreux, L. W., 1971, "Kinematic Measurements in the Study of Human Walking," Bull. Prosthet. Res., pp. 3–86.

[18] Farnworth, B., 1986, "A Numerical Model of Combined Diffusion of Heat and Water Vapor Through Clothing," Text. Res. J., **56**, pp. 653–655.

[19] Jones, B. W., and Ogawa, Y., 1993, "Transient Interaction Between the Human and the Thermal Environment," ASHRAE Trans., **98**(1), pp. 189–195.

[20] American Society for Testing and Materials (1996), ASTM D737-96, Standard Test Method for Air Permeability of Textile Fabrics, (IBR) approved 1983.

[21] Straatman, A. G., Khayat, R. E., Haj-Qasem, E., and Steinman, D. A., 2002, "On the Hydrodynamic Stability of Pulsatile Flow in a Plane Channel," Phys. Fluids, **14**(6), pp. 1938–1944.

[22] Holman, J. P., 1997, *Heat Transfer*, McGraw-Hill, New York, 8th ed., Chap. 8, pp. 488–489.

[23] Hyland, R. W., and Wexler, A., 1983, "Formulations for the Thermodynamic Properties of the Saturated Phases of H_2O From 173.15 K to 473.15 K," ASHRAE Trans., **89**(2A), pp. 500–519.

[24] Morton, W. E., and Hearle, L. W., 1975, *Physical Properties of Textile Fibers*, Heinemann, London.

Simulation of Nanoscale Multidimensional Transient Heat Conduction Problems Using Ballistic-Diffusive Equations and Phonon Boltzmann Equation

Ronggui Yang
Mem. ASME

Gang Chen
Mem. ASME

Marine Laroche[1]

Mechanical Engineering Department,
Massachusetts Institute of Technology,
Cambridge, MA 02139-4307

Yuan Taur
Department of Electrical & Computer
Engineering, University of California,
La Jolla, CA 92093-0407

Heat conduction in micro- and nanoscale and in ultrafast processes may deviate from the predictions of the Fourier law, due to boundary and interface scattering, the ballistic nature of the transport, and the finite relaxation time of heat carriers. The transient ballistic-diffusive heat conduction equations (BDE) were developed as an approximation to the phonon Boltzmann equation (BTE) for nanoscale heat conduction problems. In this paper, we further develop BDE for multidimensional heat conduction, including nanoscale heat source term and different boundary conditions, and compare the simulation results with those obtained from the phonon BTE and the Fourier law. The numerical solution strategies for multidimensional nanoscale heat conduction using BDE are presented. Several two-dimensional cases are simulated and compared to the results of the transient phonon BTE and the Fourier heat conduction theory. The transient BTE is solved using the discrete ordinates method with a two Gauss-Legendre quadratures. Special attention has been paid to the boundary conditions. Compared to the cases without internal heat generation, the difference between the BTE and BDE is larger for the case studied with internal heat generation due to the nature of the ballistic-diffusive approximation, but the results from BDE are still significantly better than those from the Fourier law. Thus we conclude that BDE captures the characteristics of the phonon BTE with much shorter computational time. [DOI: 10.1115/1.1857941]

1 Introduction

The feature size of electronic devices in current integrated circuits has become comparable to or even smaller than the phonon mean-free path in the substrate that the devices are built on and is projected to be much smaller in the next ten years. For example, the mean-free path of the heat-carrying phonons in silicon is ~40–300 nm, depending on how it is estimated. The volumetric heat generation rate inside ultrasmall semiconductor devices can be expected to be very high because the device operating power cannot be reduced below a certain level [1]. In addition, the switching transient of these devices is approaching the phonon relaxation time, which is on the order of 10–100 ps in silicon. It is well recognized that heat conduction in micro- and nanoscale and in ultrafast processes may deviate significantly from the predictions of the Fourier law, due to the boundary and interface scattering and the finite relaxation time of heat carriers [2].

The phonon Boltzmann equation (BTE) and Monte Carlo simulation can be used for simulating heat conduction processes continuously from nanoscale to macroscale in the regime where the particle description of phonons is valid. For many nanostructures and heat transfer configurations, past solutions of the BTE for electron, neutron, and photon transport can be applied [3–5]. However, the solution of the phonon BTE has been limited to few simple geometrical configurations, such as thin films and superlattices [6,7]. The inherent difficulties associated with the solution of the phonon BTE have significantly limited the consideration of the size and transient effects in multidimensional real engineering problems. Fewer studies have gone beyond nonplanar and multidimensional geometries [8–11]. Approximate methods that are capable of capturing the major size effects but easier to implement are thus desirable.

Recently the transient ballistic-diffusive heat conduction equations (*BDE*) are derived from the phonon BTE under the relaxation time approximation [12,13]. The comparison of transient heat conduction in thin films using BDE and the phonon BTE shows that BDE can capture both the time retardation and the nonlocal process, and thus can be applied to the fast heat conduction process and to small structures. As an early stage of developing simulation techniques for heat transport in practical nanoscale devices, the BDE was applied to study the two-dimensional (2D) heat conduction in nanostructures [14,15]. In this paper, we generalize BDEs to study multidimensional nanoscale heat conduction, including different kinds of boundary conditions and the nanoscale heat source term. The numerical solution strategies for BDE are presented. We also developed parallel solution strategies for transient phonon BTE in multidimensional structures. Results obtained from BDE are compared to the solution from the transient phonon BTE and the Fourier heat conduction equation.

2 Ballistic-Diffusive Equations

It has been demonstrated in the last decade that the phonon BTE is a valid and useful tool for studying classical size effects on phonon transport. Under the relaxation time approximation, the phonon BTE can be written in the phonon intensity form as [16]

$$\frac{\partial I_\omega}{\partial t} + \vec{v}_\omega \cdot \nabla_{\vec{r}} I_\omega = -\frac{I_\omega - I_{0\omega}}{\tau_\omega} + S_\omega \tag{1}$$

where the phonon intensity $I_\omega(t,\vec{r},\hat{\Omega})$ is defined as

[1]Current address: Laboratoire d'Energétique Moléculair et Macroscopique, Combustion, Ecole Centrale Paris, Centre National de la Recherche Scientifique, Cedex, France.

Manuscript received October 30, 2003; revision received September 12, 2004. Review conducted by: C. P. Grigoropoulos.

$$I_\omega(t,\vec{r},\vec{\Omega}) = \vec{v}_\omega \hbar\omega f(t,\vec{r},\vec{\Omega}) D(\omega)/4\pi \tag{2}$$

In the above equations, $D(\omega)$ is the phonon density of states per unit volume, $f_\omega(t,\vec{r},\vec{\Omega})$ is the number of phonons in a given state described by the phonon circular frequency ω, the transient time t, the spatial coordinate $\vec{r}$, and the unit vector in the direction of carrier propagation $\vec{\Omega}$. $I_{0\omega}$ is the equilibrium phonon intensity, which is determined by the Bose-Einstein statistics for phonons. τ_ω is the phonon relaxation time, $\vec{v}_\omega$ is the carrier group velocity, and S_ω is the phonon source term, which is, for example, determined by electron-phonon scattering and often assumed to be isotropic.

Heat conduction in most devices is multidimensional and involves length scales from nanoscale to macroscale. Modeling the heat conduction processes in such multiple length scale devices is very challenging. Direct numerical solution of the phonon BTE is preferred, but it is usually slow. Approximate methods that are capable of capturing the major size effects but easier to implement are thus desirable. One such method, for example, is to focus on the interface region only by introducing appropriate boundary conditions, while away from the boundaries the usual diffusion or drift-diffusion equations are used (e.g., Ref. [17]).

Another approximation that provides further improvements, compared to the introduction of special interface conditions, is the ballistic-diffusive approximation, which splits the carriers inside the medium into two groups—a ballistic component and a diffusive component [12,13,18,19]. Recently the idea itself has been further explored to combine with the discrete ordinates method to reduce the ray effect in solving the photon radiative transport equation (RTE) in optically thin media [20,21].

This work further develops the ballistic-diffusive equations for phonons [12,13] to include the nanoscale heat source term. The carrier generation term is grouped into the ballistic component for studying the nanoscale heat source. Thus the governing equation for the ballistic part is

$$\frac{\partial I_{b\omega}}{\partial t} + \vec{v}_\omega \cdot \nabla_{\vec{r}} I_{b\omega} = -\frac{I_{b\omega}}{\tau_\omega} + S_\omega \tag{3}$$

where the ballistic intensity $I_{b\omega}(t,\vec{r},\hat{\Omega})$ represents carriers originating from the boundaries and/or the carrier generation source and experiencing outscattering only.

For the diffusive part, the governing equation is

$$\frac{\partial I_{m\omega}}{\partial t} + \vec{v}_\omega \cdot \nabla_{\vec{r}} I_{m\omega} = -\frac{I_{m\omega} - I_{0\omega}}{\tau_\omega} \tag{4}$$

where $I_{m\omega}(t,\vec{r},\hat{\Omega})$ is the diffusive component that represents carriers scattered or emitted into this direction from other internal points.

Following Ref. [22], the general solution for the ballistic part [Eq. (3)] is

$$\begin{aligned} I_{b\omega}(t,\vec{r},\vec{\Omega}) = {} & \int_0^\infty S_\omega(t-s/|\vec{v}_\omega|,\vec{r}-s\vec{\Omega},\vec{\Omega}) \cdot \exp\left[-\int_0^s \frac{ds'}{|\vec{v}_\omega|\tau}\right] ds \\ & + I_{w\omega e}(t-|\vec{r}-\vec{r}_s|/|\vec{v}_\omega|,\vec{r}_s,\vec{\Omega}) \exp\left[-\int_0^{|\vec{r}-\vec{r}_s|} \frac{ds'}{|\vec{v}_\omega|\tau}\right] \\ & \cdot H(|\vec{v}_\omega|t-|\vec{r}-\vec{r}_s|) + I_{i\omega}(\vec{r}-|\vec{v}_\omega|t\vec{\Omega},\vec{\Omega}) \\ & \times \exp\left[-\int_0^{|\vec{v}_\omega|t} \frac{ds'}{|\vec{v}_\omega|\tau}\right] \cdot H(|\vec{r}-\vec{r}_s|-|\vec{v}_\omega|t) \end{aligned} \tag{5}$$

where s is the distance along the direction of propagation, $I_{w\omega e}$ is the phonons entering the system through the boundary surface, and $I_{i\omega}$ is due to the initial distribution condition inside the system. The Heaviside or unit step function $H(\xi)$ indicates that $I_{w\omega e}$ should be taken as zero for negative time and $I_{i\omega}$ should be taken as zero for points outside the system. The integral equation simply follows the fact that phonons of direction $\hat{\Omega}$, which are at point $\vec{r}$ at time t, must have originated at some point $\vec{r}-s\hat{\Omega}$ at time $t - s/|\vec{v}_\omega|$ due to the finite speed of phonon (i.e., the time retardation). The exponential in the equation accounts for the outscattering.

The spherical harmonic expansion of the intensity is applied to the diffusive carriers because those carriers experience lots of scattering and the transport are more isotropic

$$I_{m\omega}(t,\vec{r},\vec{\Omega}) = J_{0\omega}(t,\vec{r}) + \vec{J}_{1\omega}(t,\vec{r}) \cdot \vec{\Omega} \tag{6}$$

where $\vec{J}_{1\omega}$ is a vector.

Based on the decomposition of intensity, the heat flux can be expressed as

$$\vec{q}(t,\vec{r}) = \int \left[\int_{4\pi} I_\omega(t,\vec{r},\vec{\Omega}) \cdot \vec{\Omega} d\Omega \right] d\omega = \vec{q}_b + \vec{q}_m \tag{7}$$

where the ballistic and diffusive heat flux are defined as

$$\vec{q}_b(t,\vec{r}) = \int \left[\int_{4\pi} I_{b\omega}(t,\vec{r},\vec{\Omega}) \cdot \vec{\Omega} d\Omega \right] d\omega,$$

$$\vec{q}_m(t,\vec{r}) = \frac{4\pi}{3} \int \vec{J}_{1\omega}(t,\vec{r}) d\omega \tag{8}$$

The energy conservation equation, which can be obtained by the integration of Eq. (1), gives

$$-\nabla \cdot \vec{q} + \dot{q}_h = \frac{\partial u}{\partial t} \tag{9}$$

where $\dot{q}_h$ is heat generation per unit volume due to phonon generation and u is the internal energy of the heat carriers per unit volume, which can be written as

$$u = \int_\omega \int_{4\pi} \frac{I_{b\omega}}{|\vec{v}|} d\vec{\Omega} d\omega + \int_\omega \frac{4\pi J_{0\omega}}{|\vec{v}|} d\omega = u_b + u_m \tag{10}$$

where u_b and u_m are the internal energy of the ballistic and the diffusive components, respectively. The total internal energy is related to the equivalent temperature through

$$\frac{\partial u}{\partial t} = C\frac{\partial T}{\partial t} = \frac{\partial u_m}{\partial t} + \frac{\partial u_b}{\partial t} \tag{11}$$

where C is the specific heat capacity. In our simulation, a temperature-independent specific heat capacity value is used for simplification. It should be noted again that in the ballistic regime, the statistical distribution of heat carriers deviates far from equilibrium. The local temperature is best considered as a measure of the local internal energy. We also introduced temperatures $T_m = u_m/C$ and $T_b = u_b/C$, which represent only the local internal energy constitutions. The total internal energy (temperature) is an additive of these two terms.

Following the derivation of a previous paper [13], the following constitutive relation for the diffusive component and ballistic component are obtained

$$\tau\frac{\partial q_m}{\partial t} + q_m = -\frac{k}{C}\nabla u_m \tag{12}$$

$$\tau\frac{\partial u_b}{\partial t} + \nabla \cdot \vec{q}_b = -u_b + \dot{q}_h \tag{13}$$

where k is the thermal conductivity. Taking the divergence of Eq. (12) and utilizing Eqs. (9) and (13) lead to the governing equation of the diffusive component

$$\tau\frac{\partial^2 u_m}{\partial t^2} + \frac{\partial u_m}{\partial t} = \nabla\left(\frac{k}{C}\nabla u_m\right) - \nabla \cdot \vec{q}_b + \dot{q}_h \tag{14}$$

For the boundary and initial conditions for diffusive component, interested readers are referred to Ref. [13]. It is worth mentioning that the input material properties are bulk properties because the derivation of the BDE starts from the relaxation time in bulk materials. Depending on whether the phonon dispersion is accounted for or not, the specific heat, group velocity, and phonon mean-free path varies several times [23]. In this work, we do not emphasize the dispersion relation and use $|\vec{v}|=3000$ m/s, phonon mean-free path $\lambda=100$ nm, $C=1.5\times10^6$ J/m^3 K as the input bulk properties. Most results, however, are expressed in nondimensional form that is independent of such input values.

2.1 Boundary Conditions for the Phonon BTE and BDE. The Boltzmann transport equation is a first-order partial differential equation in spatial coordinate and thus needs only part of the boundary conditions specified in the spatial coordinate. For example, the boundary condition is needed in one end and the other end can be left free in one-dimensional examples. However, this boundary condition must specify the intensity in all solid angle directions, including those entering the domain (leaving the boundary) and those leaving the domain (entering the boundary). In most literature, particularly for photon radiation transport, only the intensity distribution entering the domain is given, however, over all boundaries, which is equivalent to specifying the intensity distribution over all 4π solid angle directions on part of the boundary. In radiation heat transfer, the temperature representing the distribution of the photons entering the domain is specified as the temperature at the boundary. This is justified because most of these boundaries are solid boundaries and the temperature actually represents the local solid temperature. For phonons, a similar treatment will cause misinterpretation because the temperature representing phonons entering the domain covers only half of the solid angle in space and is called the emitted phonon temperature [24]. Phonons leaving the boundary, which cover the other half of the solid angle, may have a different characteristic temperature. The local energy density (and thus the corresponding temperature, which represents the sum of the phonons leaving and entering the boundary) is different from the emitted phonon temperature; it is called the equivalent equilibrium temperature. Because the temperature distribution inside the calculation domain obtained from the phonon BTE or BDE represents the local energy phonon density, it is consistent only with the equivalent equilibrium temperature used in boundaries. If the emitted phonon temperature is used to represent the local temperature in boundaries, then an artificial temperature jump develops there for ''black'' surfaces that have no phonon reflection. The temperature concept used in Fourier law is a local equilibrium quantity. It represents the local energy density. Thus a comparison between the Fourier-law-based heat conduction equation with the phonon BTE or BDE would be meaningful only when the equivalent equilibrium temperature boundary conditions are used in the phonon BTE or BDE. This consistent use of temperatures excludes the nonphysical temperature jump at ''black'' boundaries as shown in Cases II and III. The use of the consistent temperature definition, however, makes the simulation more demanding because the phonon characteristics entering a boundary are usually unknown, making iteration necessary.

2.2 Numerical Calculation Scheme. In this paper we studied the transient phonon transport in 2D geometry as shown in Figs. 1(*a*) and 1(*b*). In Fig. 1(*a*), a heater is deposited on a substrate and the heater width can be varied to control the phonon Knudsen number (Kn), which is defined as $\mathrm{Kn}=\Lambda/L_h$, where Λ is the phonon mean-free path and L_h is the heater width. The substrate is initially at the ambient temperature T_0. At time $t=0$, the heater is suddenly increased to temperature T_1. T_1 and T_0 represent the emitted temperature in case I and the equivalent equilibrium temperature in case II. The calculation is normalized to the temperature difference $\Delta T=T_1-T_0$ as discussed in Ref.

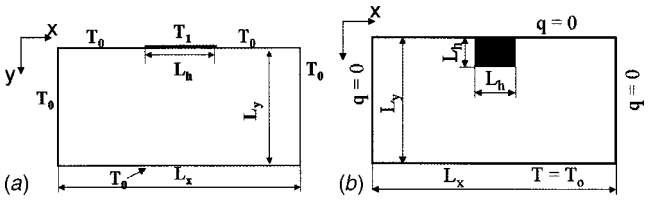

Fig. 1 Schematic drawing of device geometry simulated in this paper: (*a*) confined surface heating at $y=0$, T_1, and T_0 represents emitted temperature in case I and equivalent equilibrium temperature in case II; and (*b*) a nanoscale heat source embedded in the substrate, which is similar to the heat generation and transport in the MOSFET device

[14]. $\gamma_{xh}=L_X/L_h=10$ and $\gamma_{yh}=L_Y/L_h=5$ are set in cases I and II, and the following nondimensional parameters are introduced to present the results

$$\theta=\frac{T}{\Delta T},\quad q^*=\frac{q}{C|\vec{v}|\Delta T},\quad t^*=\frac{t}{\tau},\quad x^*=\frac{x}{L_x},\quad y^*=\frac{y}{L_y} \tag{15}$$

Case III investigates the size effect of a nanoscale heat source inside the medium as shown in Fig. 1(*b*). The heat source is similar to that generated in a MOSFET device.

From the above derivation, we know that the ballistic term in BDEs can be expressed explicitly in terms of the values at the boundaries, the heat source, and the initial distribution inside the system. Solving Eq. (14) is much simpler than solving the phonon BTE, which involves seven coordinates in the phase space (three spatial, three momentum, and one time), because Eq. (14) is averaged over the momentum space and thus involves only three spatial coordinates plus time, as in the Fourier equation. This equation can be solved using standard finite difference or finite elements methods.

Nanoscale heat conduction problems often involve multiscale modeling. For example, heat is generated in a nanoscale source region and is eventually conducted to a much larger substrate. In order to accurately capture the physics of the transport phenomena and minimize the calculation time, a nonuniform grid system is used in this paper. Fine grids are used close to the heating region. In the x direction, the length underneath [refer to Fig. 1(*a*)] or inside [refer to Fig. 1(*b*)] the heating area L_h is divided uniformly into N_h grids. The grids outside the heater area are increased in size using a geometric series with each consecutive grid size increased by grid size ratio χ_x. For Fig. 1(*b*), the length inside the heating region is divided uniformly into N_h grids and the rest is divided non-uniformly with an increase in size by grid size ratio χ_y. The total grids in the x direction are N_x-2, and the total grids in y are N_y-2. The total calculation points are $N_x\times N_y$ since the additional points with zero volume are added at all the boundaries. For Fig. 1(*a*), a simpler division in y with nonuniform division starting just underneath the heating region has also been tested. The results presented in this paper use the same set of grid systems as that used for Fig. 1(*b*). The grid size dependence of the simulation results has been studied. The results presented in the paper used $N_x=151$, $N_y=81$, $N_h=31$, $\chi_x=1.05$, and $\chi_y=1.05$, which give convergent results for all the cases studied.

A general numerical calculation block diagram is shown in Fig. 2. From Eq. (5), it is not difficult to understand that the ballistic term can be subdivided into a source term, a boundary emission term, and an initial condition term. At each time step, calculation of the ballistic component induced by the internal heat source and initial condition is straightforward since the internal heat generation and initial condition are known. The ballistic term from the boundaries depends on whether the emitted temperatures at the boundaries are known or not. In case I, the calculation is easier because the emitted temperatures at the boundaries are predefined.

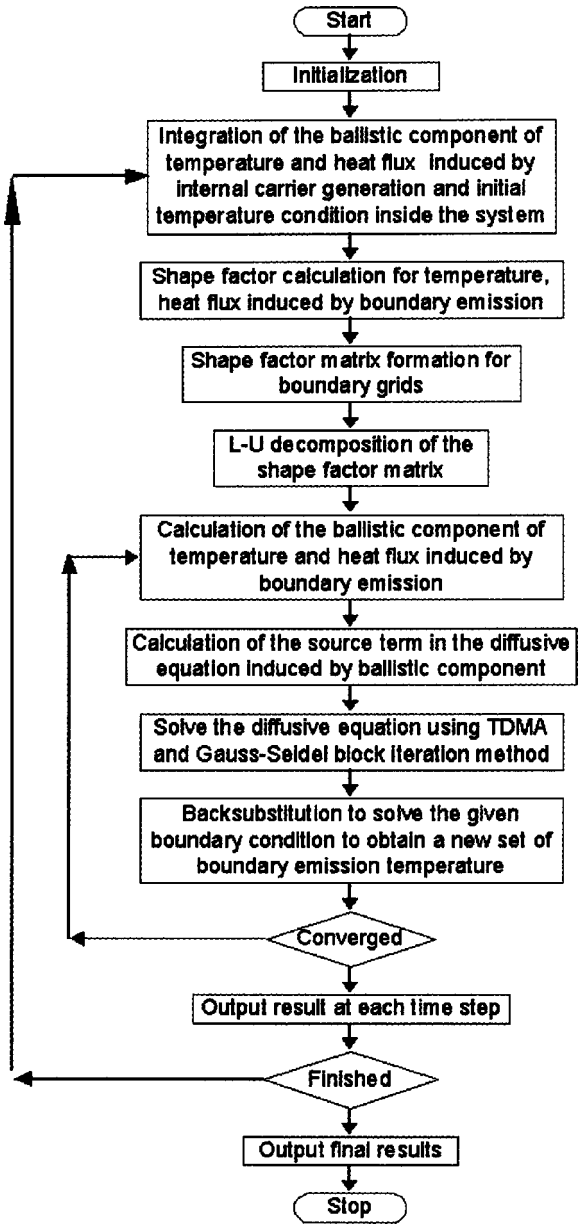

Fig. 2 Numerical solution scheme of the ballistic-diffusive equations

However, the emitted phonon temperatures at the boundaries are unknown for most practical engineering problems (e.g., cases II and III). Thus we used an iteration scheme to obtain the emitted phonon temperatures at the boundaries in each time step. The Gauss-Legendre integration scheme is used to calculate the ballistic components, and the conventional finite difference technique is used to solve the governing equation for the diffusive component. For comparison, the diffusion heat conduction equation based on the Fourier law is also solved using the finite difference method for identical geometry and boundary conditions.

3 Two-Dimensional Transient Phonon BTE Solver

To validate the simulation results of BDE in multidimension, the transient phonon BTE is also numerically solved in 2D structures, as shown in Figs. 1(*a*) and 1(*b*). To be rigorous, phonon transport simulations should incorporate the frequency dependence of phonon relaxation time and group velocity and thus account for interactions among phonons of different frequencies.

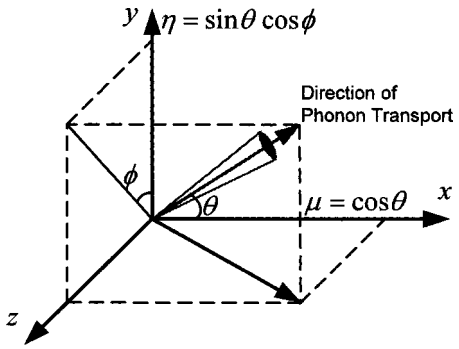

Fig. 3 Local coordinate used in phonon Boltzmann transport simulation

This requires solution of the phonon BTE [i.e. Eq. (1)] for many different frequencies, which has been performed for one-dimensional transport by several authors before [16,23,25]. Again the present study focuses on the complexity of two-dimensional transport, thus the frequency dependence of the phonon properties are neglected. Integrating Eq. (1) over frequency, we obtain the same equation as (1) in form without the frequency as subscripts.

From the first law of thermodynamics, we obtain the expression of the equilibrium intensity as [26]

$$I_0(t,\vec{r}) = \frac{1}{4\pi}\int_{4\pi} I(t,\vec{r},\vec{\Omega})d\Omega \tag{16}$$

Equation (1) is similar to the photon radiative transport equation (RTE) [16]. The key is to solve $I(t,\vec{r},\vec{\Omega})$. A variety of solution methods is available in the thermal radiative transfer literature [4,27]. The discrete ordinates method (DOM) achieves a solution by solving exact RTE for a set of discrete directions spanning of 4π. The discrete ordinates method has received considerable attention and development in the last decade because of its ability to solve many radiative transport problems with relatively good accuracy and moderate computing resources. Different sets of directions and weights have been tabulated and may result in considerably different accuracy [28,29]. The most serious drawback of the method is that it does not ensure conservation of radiative energy [30]. The finite volume method (FVM) was first proposed by Briggs et al. [31] in 1975 using the exact integration to evaluate solid angle integrals. The method is fully conservative in radiative energy and recently reviewed by Raithby [30]. However, both methods suffer from two shortcomings: ray effects and false scattering. Ray effects are related to the angular discretization, whereas false scattering is related to spatial discretization. Several proposals to overcome these numerical inaccuracies have been proposed [20,21,32–34].

We focused our solution method on the discrete ordinates method. Similar to the solution of BDE, the nonuniform grid system has been used. The grid size dependence of the simulation results has been studied with the combination of the choice of the discrete directions. The results presented in the paper used $N_x = 121$, $N_y = 71$, $N_h = 21$, $\chi_x = 1.05$, and $\chi_y = 1.05$, which give convergent results for all the cases studied. Figure 3 shows the direction cosines projecting the path of phonon transport onto the x-y plane using polar and azimuthal angles θ and φ. For the angular discretization, the conventional S_{12} quadrature [35] has also been examined. The "ray effect" is found to be very serious for Kn=10 (acoustic thin limit) case though it gives enough accuracy for small Knudsen numbers (acoustic thick limit). We, therefore, used two Gauss-Legendre quadratures to increase the discretized direction points: one to discretize the cosine μ into N_μ points from -1 to 1 and the other to discretize φ into N_ϕ points for $0\sim\pi$ (not $0\sim2\pi$ due to symmetry). Thus we present only the results using two Gauss-Legendre quadratures in the rest of this paper. We have

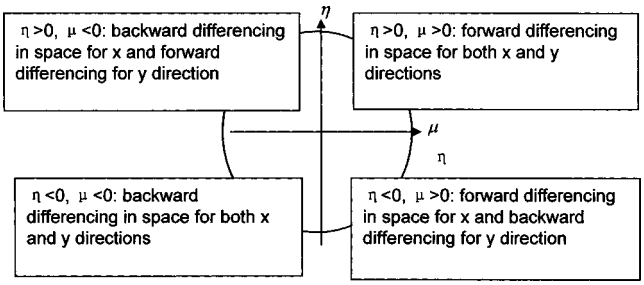

Fig. 4 Directions of phonon transport in two-dimensional planes as given by different combinations of the directional cosines and corresponding differencing schemes used for the BTE solver

tested the dependence of simulation results with the number of discrete directions. For the spatial grids presented in this paper, the change of the simulated results is negligible when $N_\mu > 100$ and $N_\phi > 12$. For example, the maximum relative difference of temperature distribution for using $N_\mu = 100$ and $N_\phi = 12$ discrete directions and using $N_\mu = 160$ and $N_\phi = 16$ discrete directions is less than 0.02%. The reported simulation results used $N_\mu = 120$ and $N_\phi = 16$. Fewer points can be used for faster calculation. Then Eq. (16) can be written as

$$I_0(t,x,y) = \frac{2}{4\pi} \sum_n \sum_m I(t,x,y,\mu_n,\varphi_m) w_n w'_m \tag{17}$$

the factor 2 in the denominator is due to the symmetry. The weights satisfy $\Sigma_n \Sigma_m w_n w'_m = 2\pi$. The diamond scheme and the step scheme are the two most popular schemes for spatial discretization [36]. The step scheme is the counterpart of the upwind in computational fluid dynamics, and it is well known that it tends to smooth steep gradients yielding the so-called false diffusion (i.e., false scattering). The diamond scheme reduces false scattering, but it may yield unphysical results. Following the recommendation by Chai et al. [36], the step scheme has been used for spatial discretization in this work. As shown in Fig. 4, spatial differencing depends on the directions of phonon transport in the two-dimensional plane. As an example, we show here the discretized equation for the case $\eta > 0$ and $\mu > 0$. For a given direction (μ_n, φ_m), we have

$$\frac{I^{k+1}_{i,j,n,m} - I^k_{i,j,n,m}}{\Delta t} + |\vec{v}|\mu \frac{I^{k+1}_{i,j,n,m} - I^{k+1}_{i-1,j,n,m}}{\Delta x} + |\vec{v}|\eta \frac{I^{k+1}_{i,j,n,m} - I^{k+1}_{i,j-1,n,m}}{\Delta y} = -\frac{I^{k+1}_{i,j,n,m} - \frac{1}{4\pi}\Sigma_n \Sigma_m I^{k+1}_{i,j,n,m} w_n w'_m}{\tau} + S_\omega \tag{18}$$

where k is the time index, i the index in the x direction, and j the index in the y direction. As shown in Eq. (18), the transient equation is solved using an implicit scheme in time marching. The equation is solved by iteration on the value of the equilibrium intensity $I_0(t,x,y) = 1/2\pi \Sigma_m \Sigma_n I(t,x,y,\mu_n,\varphi_m) w_n w'_m$. At each time step, the initial value of equilibrium intensity is guessed by setting it equal to the value of the previous time step and then the intensity field inside the medium for every direction is calculated. The iteration advances by taking the values of intensity $I^{k+1}_{i,j,n,m}$ in $\Sigma_n \Sigma_m I^{k+1}_{i,j,n,m} w_n w'_m$ equal to its previous iteration to calculate the equilibrium intensity I_0. We would like to note that although the implicit scheme for the transient calculation has been used, the nature of the BTE equation involves the iteration for I_0 term. Thus the so-called implicit scheme is not a "full" implicit scheme. The time step for a stable calculation should be $\Delta t < \min[(\Delta x/|v|),(\Delta y/|v|)]$. For transient simulation, one needs to consider the change of value in each time step when a convergence criterion is selected. In our calculation, the maximum relative error of the equilibrium intensity between two iteration steps is selected to be 2×10^{-6}. That is, when the relative error of the calculated value of the equilibrium intensity between two iteration steps is less than 2×10^{-6}, the calculation advances to the next time step. This convergence criterion gives convergent transient results for all the cases presented in the paper although it might be too strict for some cases and consumed longer computational time as necessary. For equivalent equilibrium temperature cases, the relative error for the iterations of the emitted temperature at the boundaries is also controlled to be less than 2×10^{-6}.

Although at nanoscale, temperature cannot be defined as a measure of equilibrium, we can use it to reflect the local energy density inside the medium. Assuming constant specific heat over a wide temperature range, we can write

$$T(t,x,y) = \frac{4\pi I_0(t,x,y)}{C|\vec{v}|} = \frac{1}{C|\vec{v}|} \sum_n \sum_m I(t,x,y,\mu_n,\varphi_m) w_n w'_m \tag{19}$$

The heat flux can be accordingly written as

$$q_x(t,x,y) = \sum_m \sum_n I(t,x,y,\mu_n,\varphi_m) \mu_n w_n w'_m \tag{20}$$

$$q_y(t,x,y) = \sum_m \sum_n I(t,x,y,\mu_n,\varphi_m) \sqrt{1-\mu_n^2} \cos\varphi_m w_n w'_m \tag{21}$$

4 Results and Discussions

Several two-dimensional cases have been simulated. In case I, the boundary conditions are specified as emitted phonon temperature boundary conditions in Fig. 1(*a*) to compare the simulation results of the Boltzmann transport equation and BDE. Case II assumes the equivalent equilibrium temperature boundary condition to compare the BTE results with those of BDE and the Fourier law. Case III investigates the size effect of a nanoscale heat source inside the medium as shown in Fig. 1(*b*).

Case I: Emitted Temperature Boundary Condition. To compare the simulation results of the phonon BTE and BDE, the emitted phonon temperatures are assumed at the boundaries of the simulation geometry shown in Fig. 1(*a*). The detail formulation and results are documented in a previous paper [14].

Figure 5 shows a comparison of the transient temperature and the heat flux in the y direction at the centerline of the geometry for Kn=10. It shows that BDEs can capture the characteristics of the phonon BTE in the multidimension case. However, it takes an Intel P4 800 MHz PC only around a 20 min calculation to reach the steady state for BDE as compared to 100 min for the phonon BTE. For small Knudsen numbers (i.e., the acoustic thick limit), the calculation time of the BTE solver can be much longer, but the calculation time of BDEs does not change much.

Very often, the results of the phonon BTE are compared to those obtained from the Fourier heat conduction theory. From the discussion above, it is clear that the comparison might not be meaningful without consistent use of the temperature concept. But the comparison gives a sense of how heat conduction based on Fourier law and the BTE might differ. Figure 6(*a*) shows the comparison of steady-state temperature distribution at the centerline using the Fourier theory, the phonon BTE, and BDE for different Knudsen numbers. As we can see, BDE agrees well with the phonon BTE for all the Knudsen numbers. When the Knudsen number is small, results of both the ballistic-diffusive results and the phonon BTE become very close to those of the Fourier theory. Figure 6(*b*) shows the heat flux comparison at the centerline for Kn=0.1 at $t^*=100$. Apparently, BDE agree well with the pho-

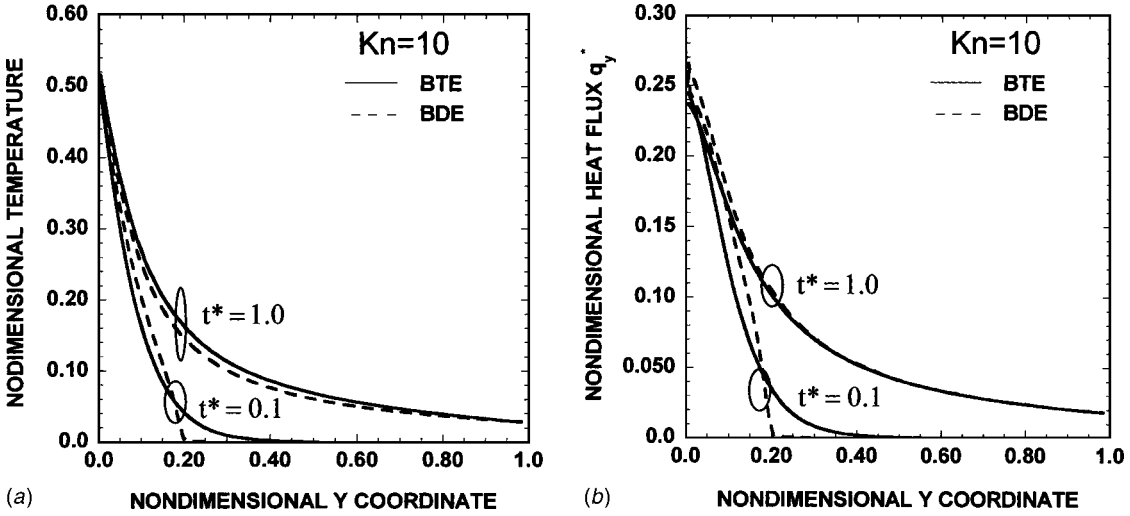

Fig. 5 Comparison of the transient temperature and heat flux in *y* direction at the centerline of the geometry for Kn=10 based on emitted temperature condition: (*a*) temperature and (*b*) heat flux q_y^*

non BTE. There is again a slight difference between the Fourier theory and the phonon BTE even in the small Knudsen number limit (acoustic thick limit). The underlying physics is due to the subtle difference in boundary conditions.

Case II: Equivalent Equilibrium Temperature Boundary Condition. As explained before, the emitted phonon temperatures in case I do not represent the local energy density at the boundaries. To compare with results obtained from the diffusion heat conduction equation based on the Fourier law, the boundaries in Fig. 1(*a*) are set as the equivalent equilibrium temperature in case II. Though the results are presented in temperature, it should be properly interpreted as energy density. As discussed earlier, iteration is needed to obtain transient emitted phonon temperatures at the boundaries from given equivalent equilibrium temperature boundary conditions. The calculation time for both BTE and BDE can be 4–5 times longer than the corresponding emitted temperature boundary conditions.

Figures 7(*a*) and 7(*b*) compare the transient nondimensional heat flux in the *y* direction calculated using the phonon BTE, BDE, and the Fourier law. The BDE has very good agreement with the phonon BTE. However, the Fourier law overpredicts the heat flux by several times compared to the prediction by the phonon BTE. These results indicate that the suppressed heat conduction in nanostructures will lead to a larger temperature rise than that obtained from the Fourier law if a heat flux is specified at the boundary. Figure 7(*c*) shows the comparison of the transient temperature distribution along the centerline. Comparing to case I, no temperature jump is observed at the boundary because of the consistent use of temperature there. Both the phonon BTE and BDE show time retardation due to the finite propagation speed of the phonons, which cannot be predicted by the Fourier law. The temperature distribution predicted by Fourier heat conduction theory is very close together for $t^*=0.1$ and $t^*=1.0$, as shown in Fig. 7(*b*).

Case III: Nanoscale Volumetric Heat Generation. In case III, we investigate the size effect of a nanoscale heat source inside the medium, as shown in Fig. 1(*b*). The heat source is similar to that generated in a metal oxide semiconductor field effect transistor (MOSFET), which is the backbone of microelectronics. A 10 nm×10 nm×1 μm hot strip is embedded in the silicon substrate.

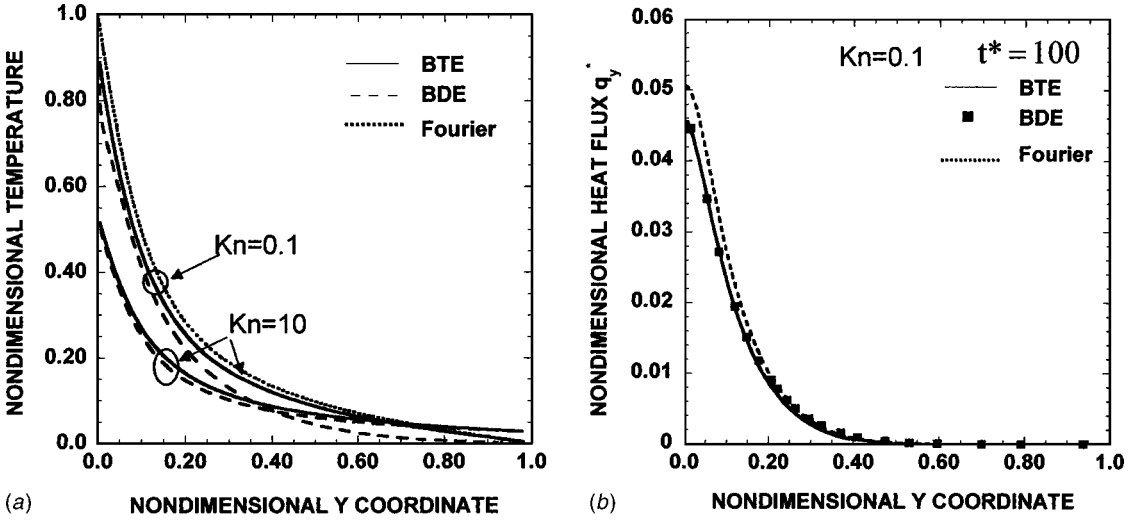

Fig. 6 (*a*) Comparison of steady-state temperature distribution at the centerline using the Fourier theory, the Boltzmann equation, and the ballistic-diffusive equations for different Knudsen numbers. (*b*) Comparison of the heat flux q_y^* at the centerline for Kn=0.1 at $t^*=100$.

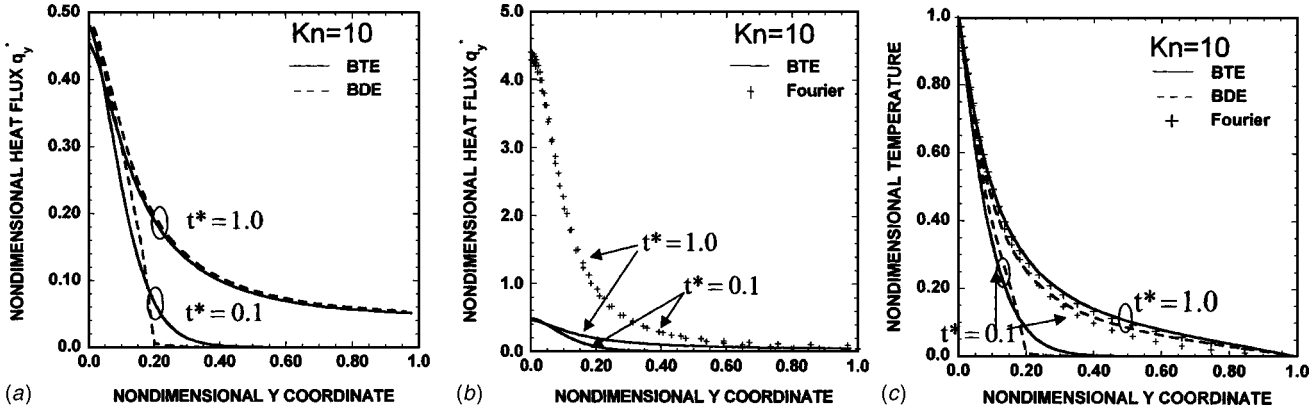

Fig. 7 Comparison of transient temperature and heat flux distribution at the centerline using the Fourier theory, the Boltzmann equation, and the ballistic-diffusive equations based on thermalized temperature boundary conditions: (*a*) and (*b*) heat flux q_y^*, and (*c*) temperature

The power generation rate is 1×10^{19} W/m^3, typically for a period of 10 ps [1]. We are interested in finding out the temperature rise ~10 ps after the device is turned on. With the given input properties stated in Sec. 2, we can model the problem as a two-dimensional nanoscale heat conduction problem because 1 μm in the length direction (z) is much longer than the phonon traveling length 30 nm in 10 ps. We know that the geometric parameter L_x and L_y will not affect much on results by the phonon BTE and BDE when the surrounding length is larger than 30 nm, thus $L_x = 10L_h$ and $L_y = 5L_h$ is used in the calculation.

Figure 8 shows the source, boundary emission and the diffusive component contribution to the total temperature and the heat flux in y direction at the centerline. The region close to the heater is dominated by the ballistic part. The ballistic component of the temperature rise induced by the heat source reaches a maximum while the ballistic component of the heat flux induced by the heat source is zero at the center of the heat source because the carrier is propagating in both directions. The ballistic component induced by the boundary emission decays exponentially from the boundary. The region far away from the heater is dominated by the diffusive part. There is bending for the diffusive component in both the temperature and heat flux profile because the carriers are treated as ballistic components out of the boundary once they are diffused into the boundary. A small wave front is also observed where the boundary emission component decays to zero. This wave front is believed to be artificial because it does not appear in the solution of the Boltzmann equation.

Figure 9 shows the comparison of temperature distribution obtained by the phonon BTE, BDE, and the Fourier law. The peak temperature predicted by the Fourier law is much smaller than that predicted by the phonon BTE and BDE. However, Fourier law predicts a broader temperature-affected region because Fourier law assumes a very large thermal conductivity and an infinite phonon propagation speed. The heat flux distribution shown in Fig. 10(*a*) explains the difference in Fig. 9. The Fourier law overpredicts the heat flux by many times especially in the short time scale than those obtained by the phonon BTE. Localized nanoscale heating is clearly shown in the results, and the phonon BTE and BDE captures such an effect fairly well. Figure 10(*b*) shows the peak temperature rise in the device as a function of time. A saturation of temperature rise after 10 ps is predicted by all the methods although the magnitudes are different.

From the cases studied, we also note that the relative difference between the BDE and phonon BTE is case specific. Without a heat source inside the medium, the relative difference between the BDE and BTE is negligible. The difference between the BTE and BDE is larger when an internal heat source exists, but the results

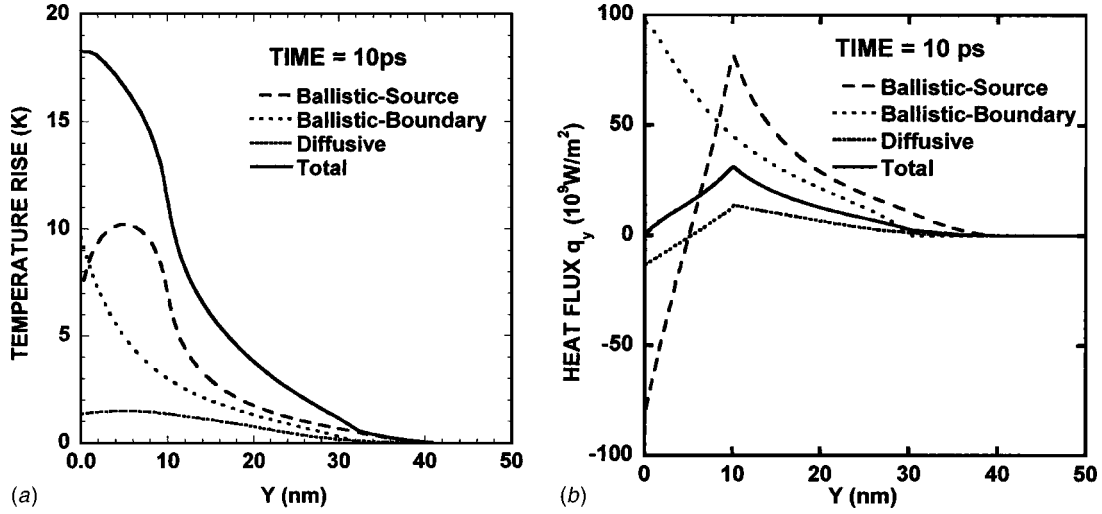

Fig. 8 The ballistic and diffusive component contributions to the total temperature and heat flux at the centerline: (*a*) temperature and (*b*) heat flux q_y^*

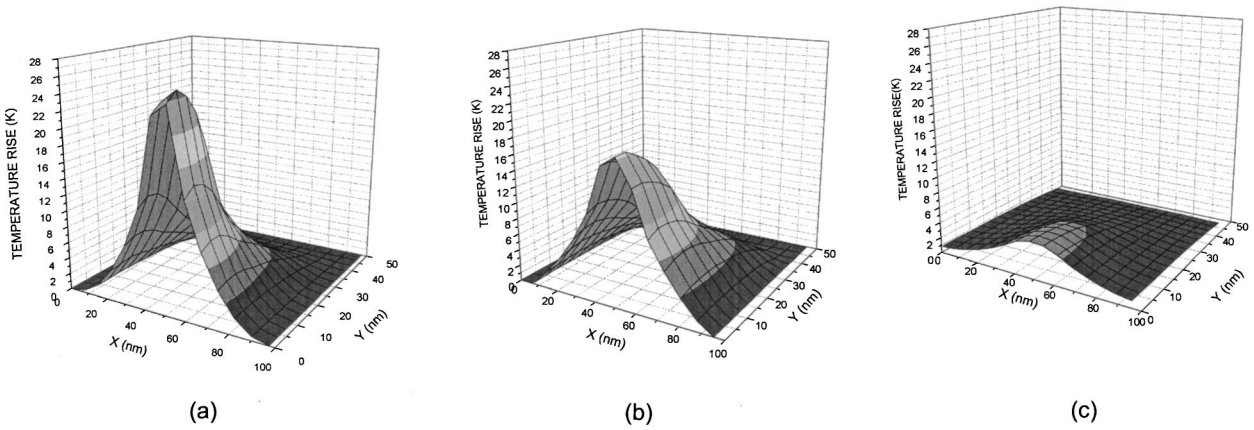

Fig. 9 Comparison of two-dimensional temperature rise distribution after the device is operated for 10 ps: (*a*) the Boltzmann equation, (*b*) the Ballistic-diffusive equations, and (*c*) the Fourier law

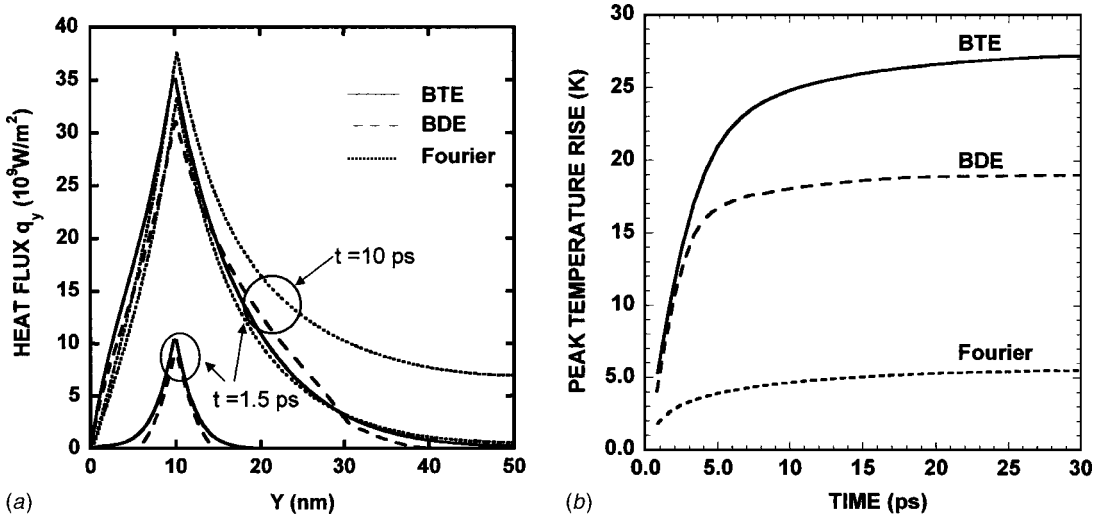

Fig. 10 (*a*) Comparison of the heat flux obtained by the Boltzmann equation, the ballistic-diffusive equations, and the Fourier law at the centerline. (*b*) Comparison of the peak temperature rise inside the device obtained by the Boltzmann equation, the Ballistic-diffusive equations and the Fourier law.

from BDE are still significantly better than those from the Fourier law. For example, the relative errors are 25% and 85% for the BDE and the Fourier law, respectively, compared to the phonon BTE in case III.

5 Conclusions

In this paper, we further developed BDE for multidimensional heat conduction, including nanoscale heat source terms and different boundary conditions. The numerical solution strategies for multidimensional nanoscale heat conduction using BDE are presented. The transient Boltzman equation is solved using the discrete ordinates method with the two Gauss-Legendre quadratures. Several 2D cases are simulated to compare the results of the transient phonon BTE, BDE, and the Fourier law. Special attention has been paid to the boundary conditions. Compared to the cases without internal heat generation, the difference between the BTE and BDE is larger for the case studied with internal heat generation due to the nature of the ballistic-diffusive approximation, but the results from the BDE are still significantly better than those from the Fourier law. Overall, the BDE captures the characteristics of the phonon BTE with much shorter computational time.

Acknowledgments

This work is supported by the DOE (SE-FG02-02ER45977) and NSF (CTS0129088).

Nomenclature

C = volumetric specific heat, $\mathrm{JK^{-1}\,m^{-3}}$
D = density of states per unit volume, $\mathrm{m^{-3}}$
f = carrier distribution function
g = source term in the Boltzmann equation
$\hbar$ = Planck constant divided by 2π, $\mathrm{J\,s^{-1}}$
I = intensity, $\mathrm{Wm^{-2}\,sr^{-1}}$
J_0 = first term in the spherical harmonics expansion, $\mathrm{Wm^{-2}\,sr^{-1}}$
$\vec{J}_1$ = second term in the spherical harmonics expansion, $\mathrm{Wm^{-2}\,sr^{-1}}$
k = thermal conductivity, $\mathrm{Wm^{-1}\,K^{-1}}$
Kn = carrier Knuden number ($=\Lambda/L_h$)
L = geometric dimension, m
N = number of discrete points in spatial or angular coordinates
q, $\vec{q}$ = heat flux, $\mathrm{Wm^{-2}}$
$\dot{q}_h$ = volumetric heat generation rate, $\mathrm{Wm^{-3}}$

s = distance along direction of propagation, m
S = source term in phonon intensity Boltzmann equation
t = time, s
T = temperature, K
u = volumetric internal energy, Jm^{-3}
$\vec{v}$ = group velocity, ms^{-1}
w = weight factor of Guass-Legendre quadrature
x = coordinate
y = coordinate
z = coordinate
χ = grid size ratio
γ = aspect ratio
φ = azimuthal angle, rad
θ = polar angle, rad
Λ = mean-free path, m
μ = directional cosine
τ = relaxation time, s
ω = angular frequency, Hz
Ω = solid angle, sr
$\vec{\Omega}$ = unit vector along solid-angle direction

Subscripts

b = ballistic
BTE = Boltzmann equation based quantities
h = heat source
m = diffusive or directional cosine index
n = azimuthal angular index
o = equilibrium quantities, boundary points
r = coordinate
ω = frequency dependent quantities
o = equilibrium quantities, boundary points
x = coordinate
y = coordinate
z = coordinate
μ = directional cosine
φ = azimuthal angle

Superscripts

$*$ = nondimensional
k = time index

References

[1] Taur, Y., Wann, Ch. H., and Frank, D. J., 1998, ''25 nm CMOS Design Considerations,'' *Electron Devices Meeting, Tech. Digest., Intl.*, Dec. 6–9 pp. 789–792.
[2] Tien, C. L., Majumdar, A., and Gerner, F. M., 1998, *Microscale Energy Transport*, Taylor & Francis, Washington, DC.
[3] Lewis, E., 1984, *Computational Methods of Neutron Transport*, Wiley, New York.
[4] Modest, M. F., 2003, *Radiative Heat Transfer*, 2nd ed., Academic Press, New York.
[5] Tellier, C. R., and Tosser, A. J., 1982, *Size Effects in Thin Films*, Elsevier, Amsterdam.
[6] Goodson, K. E., and Ju, Y. S., 1999, ''Heat Conduction in Novel Electronic Films,'' Annu. Rev. Mater. Sci., **29**, pp. 261–293.
[7] Chen, G., 2000, ''Phonon Heat Conduction in Low-Dimensional Structures,'' Semicond. Semimetals, **71**, pp. 203–259.
[8] Chen, G., 1996, ''Nonlocal and Nonequilibrium Heat Conduction in the Vincinity of Nanoparticles,'' ASME J. Heat Transfer, **118**, pp. 539–545.
[9] Sverdrup, P. G., Ju, Y. S., and Goodson, K. E., 2001, ''Sub-Continuum Simulations of Heat Conduction in Silicon-on-Insulator Transistors,'' ASME J. Heat Transfer, **123**, pp. 130–137.
[10] Murthy, J. Y., and Mathur, S. R., 2003, ''An Improved Computational Procedure for Sub-Micron Heat Conduction,'' ASME J. Heat Transfer, **125**, pp. 904–910.
[11] Narumanchi, S. V. J., Murthy, J. Y., and Amon, C. H., 2003, ''Simulation of Unsteady Small Heat Source Effects in Sub-Micron Heat Conduction,'' ASME J. Heat Transfer, **125**, pp. 896–903.
[12] Chen, G., 2001, ''Ballistic-Diffusive Heat Conduction Equations,'' Phys. Rev. Lett., **86**, pp. 2297–2300.
[13] Chen, G., 2002, ''Ballistic-Diffusive Equations for Transient Heat Conduction From Nano to Macroscales,'' ASME J. Heat Transfer, **124**, pp. 320–328.
[14] Yang, R. G., and Chen, G., 2001, ''Two-Dimensional Nanoscale Heat Conduction Using Ballistic-Diffusive Equations,'' Proc. of Int. Mechanical Engineering Conference and Exhibition, New York, **369**, pp. 363–366.
[15] Yang, R. G., Chen, G., and Taur, Y., 2002, ''Ballistic-Diffusive Equations for Multidimensional Nanoscale Heat Conduction,'' Proc. of International Heat Transfer Conference, Grenoble, France, Elsevier, Paris, Vol. 1, pp. 579–584.
[16] Majumdar, A., 1993, ''Microscale Heat Conduction in Dielectric Thin Films,'' ASME J. Heat Transfer, **115**, pp. 7–16.
[17] Chen, G., 2003, ''Diffusion-Transmission Condition for Transport at Interfaces and Boundaries,'' Appl. Phys. Lett., **82**, pp. 991–993.
[18] Olfe, D. B., 1967, ''A Modification of the Differential Approximation for Radiative Transfer,'' AIAA J., **5**, pp. 638–643.
[19] Modest, M. F., 1989, ''The Modified Differential Approximation for Radiative Transfer in General Three-Dimensional Media,'' J. Thermophys. Heat Transfer, **3**, pp. 283–288.
[20] Ramankutty, M., and Crosbie, A., 1997, ''Modified Discrete Ordinates Solution of Radiative Transfer in Two-Dimensional Rectangular Enclosures,'' J. Quant. Spectrosc. Radiat. Transf., **57**, pp. 107–140.
[21] Sakami, M., and Charette, A., 2000, ''Application of a Modified Discrete Ordinates Method to Two-Dimensional Enclosures od Irregular Geometery,'' J. Quant. Spectrosc. Radiat. Transf., **64**, pp. 275–298.
[22] Pomraning, G. C., 1973, *The Equation of Radiation Hydrodynamics*, Pergamon, New York.
[23] Chen, G., 1997, ''Size and Interface Effects on Thermal Conductivity of Superlattices and Periodic Thin-Film Structures,'' ASME J. Heat Transfer, **119**, pp. 220–229.
[24] Chen, G., 1998, ''Thermal Conductivity and Ballistic Phonon Transport in Cross-Plane Direction of Superlattices,'' Phys. Rev. B, **57**, pp. 14958–14973.
[25] Goodson, K. E., 1996, ''Thermal Conductivity in Nonhomgeneous CVD Diamond Layers in Electronic Microstructures,'' ASME J. Heat Transfer, **118**, pp. 279–336.
[26] Joshi, A. A., and Majumdar, A., 1993, ''Transient Ballistic and Diffusive Heat Transport in Thin Films,'' J. Appl. Phys., **74**, pp. 31–39.
[27] Siegel, R., and Howell, J. R., 2001, *Thermal Radiation Heat Transfer*, 4th ed, Taylor & Francis, Washington DC.
[28] Fiveland, W. A., 1987, ''Discrete Ordinate Methods for Radiative Heat Transfer in Isotropically and Anisotropically Scattering Media,'' ASME J. Heat Transfer, **109**, pp. 809–812.
[29] Truelove, J. S., 1987, ''Discrete-Ordinate Solutions of the Radiation Transport Equation,'' ASME J. Heat Transfer, **109**, pp. 1048–1051.
[30] Raithby, G. D., 1994, ''Discussion of the Finite-Volume Method for Radiation, and Its Application Using 3D Unstructured Meshes,'' Numer. Heat Transfer, Part B, **35**, pp. 389–405.
[31] Briggs, L. L., Miller, W. F., and Lewis, E. E., 1975, ''Ray-Effect Mitigation in Discrete Ordinate-Like Angular Finite Element Approximations in Neutron Transport,'' Nucl. Sci. Eng., **57**, pp. 205–217.
[32] Chai, J. C., Lee, H. S., and Patankar, S. V., 1993, ''Ray Effect and False Scattering in the Discrete Ordinates Method,'' Numer. Heat Transfer, Part B, **24**, pp. 373–389.
[33] Coelho, P., 2002, ''The Role of Ray Effect and False Scattering on the Accuracy of the Standard and Modified Discrete Ordinates Methods,'' J. Quant. Spectrosc. Radiat. Transf., **73**, pp. 231–238.
[34] Murthy, J., and Mathur, S., 1998, ''Finite Volume Method for Radiative Heat Transfer Using Unstructured Meshes,'' J. Thermophys. Heat Transfer, **12**, pp. 313–321.
[35] Fiveland, W. A., 1991, ''The Selection of Discrete Ordinate Quadrature Sets for Anisotropic Scattering,'' *Fundamentals of Radiation Heat Transfer*, ASME, New York, HTD-Vol. 160, pp. 89–96.
[36] Chai, J. C., Patankar, S. V., and Lee, H. S., 1994, ''Evaluation of Spatial Differencing Practices for the Discrete-Ordinates Method,'' J. Thermophys. Heat Transfer, **8**, pp. 140–144.

Absence of Oscillations and Resonance in Porous Media Dual-Phase-Lagging Fourier Heat Conduction

Peter Vadasz
Fellow ASME
Professor and Chair
Department of Mechanical Engineering,
Northern Arizona University,
P.O. Box 15600,
Flagstaff, AZ 86011-5600

The approximate equivalence between the dual-phase-lagging heat conduction model and the Fourier heat conduction in porous media subject to lack of local thermal equilibrium suggested the possibility of thermal oscillations and resonance. The present investigation demonstrates that the physical conditions necessary for such thermal waves and, possibly resonance, to materialize are not attainable in a porous slab subject to constant temperature conditions applied on the boundaries. [DOI: 10.1115/1.1860567]

Keywords: Dual-Phase-Lagging, Hyperbolic Heat Conduction, Local Thermal Equilibrium, Porous Media, Thermal Waves

1 Introduction

The problem of heat transfer in a fluid-saturated porous domain subject to lack of local thermal equilibrium (La Lotheq) has been the subject of wide interest due to its theoretical as well as practical appeals. As long as the application of porous materials proliferates, including, for example, recent interest in metal foams as well as the investigation of biotissues, a more accurate understanding of the heat transfer phenomena in porous media will continue to attract attention. Tzou [1] showed that the system of governing equations for Fourier conduction in porous media subject to La Lotheq is approximately equivalent to the dual-phase-lagging (DuPhlag) model of heat conduction. The latter can produce thermal waves in the form of oscillations. As a result the DuPhlag model can yield thermal resonance when periodically forced by a periodic heat source or a periodic boundary condition with a forcing frequency that is equal to one of the natural frequencies of the system. Tzou [1–3] presents applications of the DuPhlag model to a wide variety of fields from ultrafast (femtosecond) pulse-laser heating of metal films, phonon-electron interaction at nano- and micro-scale heat transfer, temperature pulses in superfluid liquid helium, thermal lagging in amorphous materials, and thermal waves under rapidly propagating cracks.

The particular application of the DuPhlag model to porous media Fourier heat conduction subject to La Lotheq is the focus of the present paper. Tzou [1] refers to experimental results in porous media heat conduction identifying thermal oscillations and overshooting, and explains them by applying the DuPhlag model. Analytical solutions as well as analysis of the DuPhlag heat conduction was presented among others in excellent papers by Xu and Wang [4], Wang et al. [5], Wang and Xu [6], and Antaki [7]. The special case of dual-phase-lagging heat conduction in a one-dimensional slab subject to Dirichlet boundary conditions studied by Xu and Wang [4] is of special interest. The authors show that thermal oscillations are possible solutions if the ratio between the temperature gradient time lag τ_T and the heat flux time lag τ_q is less than 1 (i.e., if $\tau_T/\tau_q<1$). Consequently, thermal resonance may occur subject to the same condition of $\tau_T/\tau_q<1$ due to a periodic heat source with a forcing frequency that is identical to one of the natural frequencies of the system.

Applications of porous media heat transfer subject to La Lotheq were undertaken among others by Nield [8], Minkowycz et al. [9], Banu and Rees [10], Baytas and Pop [11], Kim and Jang [12], Rees [13], Alazmi and Vafai [14], and Nield et al. [15]. In particular Minkowycz et al. [9] link the La Lotheq model with the DuPhlag model in a manner similar to the one presented by Tzou [1]; however, they impose rather than derive the DuPhlag model for the particular La Lotheq application to porous media heat transfer by using a non-Fourier constitutive relationship between the heat flux and temperature gradient. As a result they do not obtain accurate relationships for the two time lags τ_T and τ_q, but rather approximated expressions. In addition, Minkowycz et al. [9] use imposed heat flux boundary conditions quite distinct from the imposed temperature boundary conditions used in the present paper; hence, the conclusions of the present paper do not apply to the results presented by Minkowycz et al. [9]. The present paper's conclusions also do not imply that the lack of thermal waves challenges the La Lotheq model. While the significance of practically obtaining the same temperature solution for each phase in a porous medium subject to a lack of local thermal equilibrium (La Lotheq) is discussed by Vadasz [16] identifying conditions for which the traditional formulation of the La Lotheq model is not adequate, the conditions used in the present paper are not identical to those identified by Vadasz [16]. Other examples of conditions that are not affected by the conclusions of the present paper are problems of convection subject to La Lotheq, such as those presented by Spiga and Morini [17], Kuznetsov [18], Amiri and Vafai [19], and Kuznetsov [20].

The present paper deals with Fourier heat conduction in a porous medium subject to La Lotheq. It aims at demonstrating that the condition required for oscillatory solutions, $\tau_T/\tau_q<1$, is not physically attainable in a porous slab conduction subject to Dirichlet boundary conditions. As a consequence thermal waves cannot materialize, nor resonance, in a porous slab heat conduction subject to constant temperatures imposed on the boundaries. It should be emphasized that the latter result is obtained based on physical conditions pertaining to valid porous media properties, and it is not just a mathematical curiosity nor dependent on the method of solution. The result is accurate and absolutely based on the physical reality. The mathematical derivations are being used only as tools to prove it. While the results of the present paper may provide a useful guide among others to pulsed laser processing of nanofilms (e.g., [21]), the problem presented here is essentially distinct and deals with the application to porous media. There are major distinctions as well as similarities between the two. The similarities are linked to the two-phase coupled equations used to represent the ''absorption of photon energy by elec-

Manuscript received May 24, 2004; revision received December 2, 2004. Review conducted by: R. P. Roy.

trons and the heating of the lattice through electron-phonon coupling'' [22]. The distinctions are mainly in two aspects. Although energy transport by phonons (heat conduction in the metal lattice) is neglected, because heat flux is carried mainly by free electrons for metals, the heat conduction in the solid phase in a porous medium cannot be generally neglected. Therefore, in order to obtain the equivalence between the porous media La Lotheq conduction equations to small scale (micro- or nanoscales) and ultrafast (picoseconds) conduction in metals, the thermal conductivity of the solid phase in the porous medium (which is equivalent to the thermal conductivity of the metal lattice for the micro-nanoscale effects in metals) has to vanish (i.e. $k_s=0$). In addition, because of the small scale in the ultrafast heating of metals or thin films, it is legitimate to use a non-Fourier constitutive model to represent the relationship between the heat flux and the temperature gradient, such as the application of the dual-phase-lagging for each phase [21]. In porous media because of the typical macroscopic scale of both phases, the latter is not applicable. In the present paper Fourier law was employed for the heat flux mechanism at each phase. Nevertheless, the coupling between the phases in terms of the heat conduction at the solid-fluid interface leads to a formulation that is approximately equivalent to dual-phase-lagging. The latter is a result of the analysis and not an imposed constitutive relationship. To add to the latter the limitations to Dirichlet boundary conditions, the specific geometry, and substantial distinctions between the traditional formulation of La Lotheq in porous media and the conditions pertaining to nanofilms, call for caution when the conclusions of this paper are applied to other fields. Specific and critical analyses for distinct applications need to be separately undertaken prior to reaching general conclusions.

2 Problem Formulation

2.1 Governing Equations for Lack of Local Thermal Equilibrium. Consider the heat conduction equations for the two phases that compose an isotropic and homogeneous porous medium, which are obtained as phase averages over a representative elementary volume (REV) following Fourier's law, in the form

$$\gamma_s\frac{\partial T_s}{\partial t_*}=k_s\nabla_*^2T_s-h(T_s-T_f) \tag{1}$$

$$\gamma_f\frac{\partial T_f}{\partial t_*}=k_f\nabla_*^2T_f+h(T_s-T_f) \tag{2}$$

where $\gamma_s=(1-\varphi)\rho_s c_s$ and $\gamma_f=\varphi\rho_f c_{p,f}$ are the solid phase and fluid phase effective heat capacities, respectively, φ is the porosity, k_s and k_f are the effective thermal conductivities of the solid and fluid phases, respectively, and h represents an integral heat transfer coefficient for the heat conduction at the solid-fluid interface within an REV. As correctly pointed out by Lage [23] " . . . the heat transfer coefficient h should not be confused with the heat transfer coefficient used in convection heat transfer analysis . . . For one reason h is defined independently of fluid motion, i.e., h is not necessarily zero when the fluid saturated porous medium is stationary. Moreover, by definition the units of h are . . . " $\mathrm{W\,m^{-3}\,K^{-1}}$ and not $\mathrm{W\,m^{-2}\,K^{-1}}$, which are applicable to the convection heat transfer coefficient. Generally, in a stationary fluid saturated porous medium (i.e., without fluid flow) as considered in the present paper, h is anticipated to depend on the thermal conductivities of both phases, on the porosity, on the heat transfer surface area, and on the tortuousity of the interface between the solid and fluid phases [23,24]. In the case of fluid flow the value of h will depend also on local Reynolds and Prandtl numbers of the fluid as presented by Alazmi and Vafai [14].

When the local thermal equilibrium assumption is not valid, conditions appropriate for the case when the temperature difference between the two phases is not small, both Eqs. (1) and (2) are to be solved simultaneously. The diffusion terms in these equations are a result of replacing the $-\nabla_*\cdot\boldsymbol{q}_s$ and $-\nabla_*\cdot\boldsymbol{q}_f$ terms by using Fourier's law in the form $\boldsymbol{q}_s=-k_s\nabla_*T_s$ and $\boldsymbol{q}_f=-k_f\nabla_*T_f$ to yield the Laplacian terms. The coupling between the two equations can be resolved by presenting them in the equivalent operator form

$$\begin{bmatrix}\left(\gamma_s\dfrac{\partial}{\partial t_*}-k_s\nabla_*^2+h\right) & -h\\ -h & \left(\gamma_f\dfrac{\partial}{\partial t_*}-k_f\nabla_*^2+h\right)\end{bmatrix}\begin{bmatrix}T_s\\T_f\end{bmatrix}=0 \tag{3}$$

Then, their uncoupled form is obtained by evaluating the operator determinant leading to

$$\left[\left(\gamma_s\frac{\partial}{\partial t_*}-k_s\nabla_*^2+h\right)\left(\gamma_f\frac{\partial}{\partial t_*}-k_f\nabla_*^2+h\right)-h^2\right]T_i=0\quad\forall i=s,f \tag{4}$$

where the index i can take the values s representing the solid phase or f standing for the fluid phase. Equation (4) can be presented explicitly, after dividing it by $h(\gamma_s+\gamma_f)$ in the form

$$\tau_q\frac{\partial^2T_i}{\partial t_*^2}+\frac{\partial T_i}{\partial t_*}=\alpha_e\nabla_*^2T_i+\delta_e\nabla_*^2\frac{\partial T_i}{\partial t_*}-\beta_e\nabla_*^4T_i\quad\forall i=s,f \tag{5}$$

where the following notation was used:

$$\tau_q=\frac{\gamma_s\gamma_f}{h(\gamma_s+\gamma_f)},\quad\alpha_e=\frac{k_s+k_f}{\gamma_s+\gamma_f},$$

$$\delta_e=\frac{\gamma_sk_f+\gamma_fk_s}{h(\gamma_s+\gamma_f)},\quad\beta_e=\frac{k_sk_f}{h(\gamma_s+\gamma_f)} \tag{6}$$

Note the negative sign in front of the biharmonic term as distinct from Tzou [1], which shows incorrectly a positive sign in front of this term. Alternatively, the same Eq. (5) can be obtained by isolating T_f in Eq. (1) to obtain $T_f=(\gamma_s/h)\partial T_s/\partial t_*-(k_s/h)\nabla_*^2T_s+T_s$ and substituting it into Eq. (2), regrouping the terms and dividing the resulting equation by $(\gamma_s+\gamma_f)$. The expression for τ_q in Eq. (6) is identical to the corresponding expression for τ_e in Hays-Stang and Haji-Sheikh [21] with the following equivalent notations for the lag/thermalization time $\tau_q\rightarrow\tau_e$, fluid/electron gas heat capacities $\gamma_f\rightarrow C_e$, solid/metal lattice heat capacities $\gamma_s\rightarrow C_l$, fluid-solid interface heat transfer coefficient/electron-phonon coupling factor $h\rightarrow G$, and $(\gamma_f+\gamma_s)\rightarrow C=(C_e+C_l)$ where the first terminology and symbols belong to the porous medium problem, whereas the second ones belong to the micro-/nano-scale ultrafast heat transfer in metals (see text following Eq. (3b) in [21]).

Similarly, by using Eqs. (1) and (2) in the form

$$\gamma_s\frac{\partial T_s}{\partial t_*}+\nabla_*\cdot\boldsymbol{q}_s+h(T_s-T_f)=0 \tag{7}$$

$$\gamma_f\frac{\partial T_f}{\partial t_*}+\nabla_*\cdot\boldsymbol{q}_f-h(T_s-T_f)=0 \tag{8}$$

applying the gradient operator (∇_*) on Eqs. (7) and (8) and the Fourier law expressed in the form

$$\nabla_*T_s=-\boldsymbol{q}_s/k_s,\quad\nabla_*T_f=-\boldsymbol{q}_f/k_f \tag{9}$$

to replace the ∇_*T_s and ∇_*T_f terms, produces the following system:

$$\begin{bmatrix}\left(\dfrac{\gamma_s}{k_s}\dfrac{\partial}{\partial t_*}-\nabla_*(\nabla_*\cdot)+\dfrac{h}{k_s}\right) & -\dfrac{h}{k_f}\\ -\dfrac{h}{k_s} & \left(\dfrac{\gamma_f}{k_f}\dfrac{\partial}{\partial t_*}-\nabla_*(\nabla_*\cdot)+\dfrac{h}{k_f}\right)\end{bmatrix}\begin{bmatrix}\boldsymbol{q}_s\\\boldsymbol{q}_f\end{bmatrix}=0 \tag{10}$$

Following a similar process as for the temperature one obtains the uncoupled equation for the heat flux in the form

$$\tau_q \frac{\partial^2 \boldsymbol{q}_i}{\partial t_*^2} + \frac{\partial \boldsymbol{q}_i}{\partial t_*} = \alpha_e \nabla_*(\nabla_* \cdot \boldsymbol{q}_i) + \delta_e \frac{\partial \nabla_*(\nabla_* \cdot \boldsymbol{q}_i)}{\partial t_*} - \beta_e \nabla_*[\nabla_*^2(\nabla_* \cdot \boldsymbol{q}_i)] \quad \forall i = s,f \tag{11}$$

where the definitions of the parameters are identical to Eq. (6).

2.2 Governing Equations for Dual-Phase-Lagging Heat Conduction. The dual-phase-lagging model applied to porous media conduction was introduced by Tzou [1], and its solution was presented among others by Xu and Wang [4]. In the dual-phase-lagging model, the following formulation is suggested to replace the classical Fourier law [1]:

$$\boldsymbol{q}_i(\boldsymbol{x}_*, t_* + \tau_q) = -k_i \nabla_* T_i(\boldsymbol{x}_*, t_* + \tau_T) \quad \forall i = s,f \tag{12}$$

where the relationship between the heat flux and temperature gradient is not instantaneous but rather affected by two time lags, a heat flux lag $\boldsymbol{\tau}_q$, and a temperature gradient time lag $\boldsymbol{\tau}_T$. Tzou [1] indicates that "*the lagging response, in general, describes the heat flux vector and the temperature gradient occurring at different instants of time in the heat transfer process. If the heat flux precedes the temperature gradient in the time history, the heat flux is the cause and the temperature gradient is the effect of heat flow. If the temperature gradient precedes the heat flux, on the other hand, the temperature gradient becomes the cause and the heat flux becomes the effect.*" The latter means that for $\tau_q < \tau_T$ the heat flux is the *cause* and the temperature gradient is the *effect*, whereas for $\tau_q > \tau_T$ the temperature gradient is the cause and the heat flux is the effect. By expanding Eq. (12) in a Taylor series in time, one obtains

$$\boldsymbol{q}_i(\boldsymbol{x}_*, t_*) + \tau_{qi} \frac{\partial \boldsymbol{q}_i}{\partial t_*}(\mathbf{x}_*, t_*) + \frac{\tau_{qi}^2}{2!} \frac{\partial^2 \boldsymbol{q}_i}{\partial t_*^2}(\boldsymbol{x}_*, t_*) + \ldots = -k_i \left[\nabla T_i(\boldsymbol{x}_*, t_*) + \tau_{Ti} \frac{\partial (\nabla_* T)_i}{\partial t_*}(\boldsymbol{x}_*, t_*) + \frac{\tau_{Ti}^2}{2!} \frac{\partial^2 (\nabla_* T)_i}{\partial t_*^2}(\boldsymbol{x}_*, t_*) + \ldots \right] \quad \forall i = s,f \tag{13}$$

Upon truncating the Taylor series at the first-order approximation, it yields to order $O(\tau_{qi})$ and $O(\tau_{Ti})$

$$\boldsymbol{q}_i + \tau_{qi} \frac{\partial \boldsymbol{q}_i}{\partial t_*} = -k_i \left[\nabla_* T_i + \tau_{Ti} \frac{\partial (\nabla_* T_i)}{\partial t_*} \right] \quad \forall i = s,f \tag{14}$$

This dual-phase-lagging formulation is applied to the thermal conduction energy equation

$$\gamma_i \frac{\partial T_i}{\partial t_*} + \nabla_* \cdot \boldsymbol{q}_i = 0 \quad \forall i = s,f \tag{15}$$

by replacing the fluid-solid interface heat transfer term with the dual-phase-lagging formulation. Applying now the $(\nabla_* \cdot)$ operator on Eq. (14) produces

$$\left[1 + \tau_{qi} \frac{\partial}{\partial t_*} \right] \nabla_* \cdot \boldsymbol{q}_i = -k_i \left[1 + \tau_{Ti} \frac{\partial}{\partial t_*} \right] \nabla_*^2 T_i \quad \forall i = s,f \tag{16}$$

Substituting $\nabla_* \cdot \boldsymbol{q}_i = -\gamma_i \partial T_i / \partial t_*$ from Eq. (15) into Eq. (16) and dividing the resulting equation by γ_i yields one equation for the temperature of each phase due to dual-phase-lagging, in the form

$$\tau_{qi} \frac{\partial^2 T_i}{\partial t_*^2} + \frac{\partial T_i}{\partial t_*} = \alpha_i \nabla_*^2 T_i + \alpha_i \tau_{Ti} \nabla_*^2 \frac{\partial T_i}{\partial t_*} \quad \forall i = s,f \tag{17}$$

Applying now the operator $k_i[1 + \tau_{Ti} \partial / \partial t_*] \nabla_*$ on Eq. (15) and the operator $\gamma_i \partial / \partial t_*$ on Eq. (14) yields, respectively,

$$\gamma_i k_i \left[1 + \tau_{Ti} \frac{\partial}{\partial t_*} \right] \frac{\partial (\nabla T_i)}{\partial t_*} + k_i \left[1 + \tau_{Ti} \frac{\partial}{\partial t_*} \right] \nabla (\nabla_* \cdot \boldsymbol{q}_i) = 0 \quad \forall i = s,f \tag{18}$$

$$\gamma_i \left[1 + \tau_{qi} \frac{\partial}{\partial t_*} \right] \frac{\partial \boldsymbol{q}_i}{\partial t_*} + \gamma_i k_i \left[1_i + \tau_{Ti} \frac{\partial}{\partial t_*} \right] \frac{\partial (\nabla_* T_i)}{\partial t_*} = 0 \quad \forall i = s,f \tag{19}$$

Subtracting Eq. (18) from Eq. (19) and dividing the result by γ_i yields finally one equation for the heat flux due to dual-phase-lagging in the form

$$\tau_{qi} \frac{\partial^2 \boldsymbol{q}_i}{\partial t_*^2} + \frac{\partial \boldsymbol{q}_i}{\partial t_*} = \alpha_i \nabla_*(\nabla_* \cdot \boldsymbol{q}_i) + \alpha_i \tau_{Ti} \frac{\partial [\nabla_*(\nabla_* \cdot \boldsymbol{q}_i)]}{\partial t_*} \quad \forall i = s,f \tag{20}$$

Equations (17) and (20) are the conduction dual-phase-lagging equations for the temperature and heat flux, respectively, and for each phase of a porous medium. It is not clear from Tzou [1] precisely to what part of the REV the dual-phase-lagging applies, whether to each phase separately or to the bulk. Whichever the case may be, equations similar to (17) and (20) are the result. Comparing Eqs. (17) and (20) to the uncoupled equations obtained from applying the Fourier law to each phase, while including the fluid-solid interface heat transfer term, Eqs. (5) and (11) show that they are equivalent, provided the biharmonic term in Eqs. (5) and (11) is negligibly small (i.e., if $\beta_e \sim 0$) and provided the following equivalency of parameters is enforced:

$$\tau_{qi} = \tau_q = \frac{\gamma_s \gamma_f}{h(\gamma_s + \gamma_f)}, \quad \alpha_i = \alpha_e = \frac{k_s + k_f}{\gamma_s + \gamma_f}, \quad \delta_e = \alpha_e \tau_T = \frac{\gamma_s k_f + \gamma_f k_s}{h(\gamma_s + \gamma_f)} \quad \forall i = s,f \tag{21}$$

Therefore, the consequent definition of the temperature gradient lag τ_{Ti} that is consistent with dual-phase-lagging is

$$\tau_{Ti} = \tau_T = \frac{\delta_e}{\alpha_e} = \frac{\gamma_s k_f + \gamma_f k_s}{h(k_s + k_f)} \quad \forall i = s,f \tag{22}$$

This result is identical to the corresponding expression for τ_l in Hays-Stang and Haji-Sheikh [21] when considering that for the micro-nanoscale ultrafast heat transfer in metals the thermal conductivity of the metal lattice is taken as zero, corresponding to an equivalent value of $k_s = 0$ in Eq. (22). Then for micro-/nanoscale ultrafast heat transfer in metals, Eq. (22) leads to $\tau_T = \gamma_s / h$ with the following equivalent notations for $\tau_T \rightarrow \tau_l$, solid/metal lattice heat capacities $\gamma_s \rightarrow C_l$, fluid-solid interface heat transfer coefficient/electron-phonon coupling factor $h \rightarrow G$, where the first terminology and symbols belong to the porous medium problem, whereas the second ones belong to the micro-nanoscale ultrafast heat transfer in metals (see text following Eq. (6b) in [21]). Similarly, Eq. (22) is identical to the expression for τ_t obtained by Minkowycz et al. [9] for investigating the effect of a rapidly changing heat source in porous media with the following equivalent notations $\tau_T \rightarrow \tau_t$, $\gamma_s \rightarrow C_f$, $h \rightarrow \bar{h}/r_h$, and $k_f = 0$ (the latter is a result of the assumption made by the authors that the conduction in the fluid is negligible at the short time scales considered prior to the onset of equilibrium, see Eq. (2) in [9]). (Note the distinction between the definitions of the heat transfer coefficients in the present paper and [9], h and $\bar{h}$, respectively). With these equivalent notations for the same parameters substituted into (22), one obtains $\tau_t = r_h C_f / \bar{h}$, a result that is identical to Minkowycz et al. [9] result (see text following Eq. (6) in [9]). Since Hays-Stang and Haji-Sheikh [21] introduce a dual-phase-lagging constitutive relationship to replace the Fourier law because of the ultrafast and micro-nanoscale problem while Minkowycz et al. [9] introduce the dual-phase-lagging constitutive relationship to replace the Fourier law because of the rapidly changing heat source the similarities between their results and those presented in the present

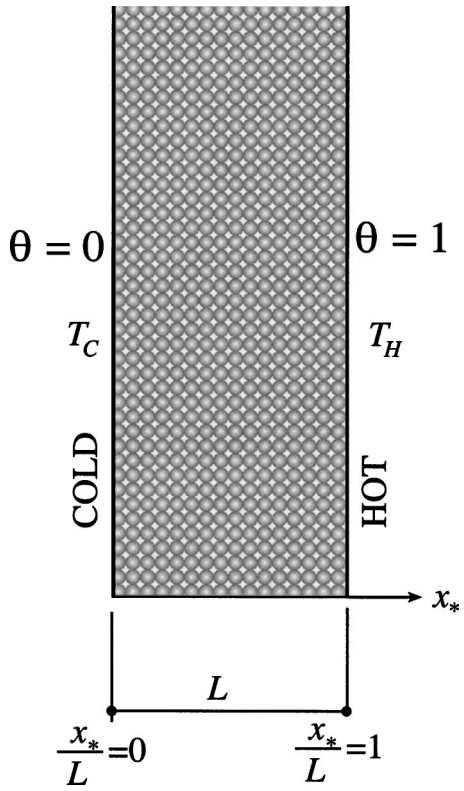

Fig. 1 Fluid saturated porous slab subject to constant temperature conditions at the walls

paper end at the model formulation. In the present paper, Fourier law was invoked at all stages and the approximate dual-phase-lagging was obtained as a result of the heat transfer interaction between the phases, not imposed as a constitutive relationship instead of Fourier law.

A direct property of these parameters is by evaluating the ratio τ_T/τ_q by using (21) and (22), which leads to the following result:

$$\frac{\tau_T}{\tau_q}=1+\frac{\gamma_s^2 k_f+\gamma_f^2 k_s}{\gamma_s\gamma_f(k_s+k_f)}>1 \tag{23}$$

Since the combination of positive valued properties in the second term of Eq. (23) is always positive, the time lags ratio is always greater than 1 (i.e. $\tau_T/\tau_q>1$). The latter conclusion, which is based on a physical argument and is accurately derived, has a profound impact on the following results. It applies generally to Fourier heat conduction in porous media subject to La Lotheq and is not restricted to any specific geometry nor boundary conditions. In addition, inequality (23) implies, by virtue of the dual-phase-lagging, that the heat flux is the cause and the temperature gradient is the effect in porous media two-phase heat conduction. The strength of the DuPhlag formulation is in the fact that it approximates the accurate behavior obtained by using the Fourier Law for each phase. Note that although each one of the time lags τ_T and τ_q depends on the interface heat transfer coefficient h as observed in Eqs. (21) and (22), their ratio τ_T/τ_q in Eq. (23) is independent of this coefficient, making its evaluation simpler as it depends on the effective properties of each phase and is independent of the interaction between the phases.

3 Analytical Solution

In order to analyze the characteristic behavior of the dual-phase-lagging model for porous media conduction, a particular solution of Eq. (5) for the one-dimensional heat conduction in a porous slab of length L (as presented in Fig. 1) is being considered. Since the equations for each phase are identical, the indices $i=s, f$ are being dropped from the following derivations subject to the understanding that the results apply equally well to both phases. The significance of practically obtaining the same temperature solution for each phase in a porous medium subject to a lack of thermal equilibrium is discussed elsewhere (see [16]). It is sufficient to mention that initial conditions, which are different for each phase, are sufficient to produce different phase solutions. Transforming Eq. (5) into a dimensionless form by using L to scale the independent length variable x_* (i.e. $x=x_*/L$), by using L^2/α_e to scale the time (i.e. $t=t_*\alpha_e/L^2$) and introducing the dimensionless temperature θ defined in the form

$$\theta=\frac{T-T_C}{T_H-T_C} \tag{24}$$

leads to

$$\mathrm{Fo}\frac{\partial^2\theta}{\partial t^2}+\frac{\partial\theta}{\partial t}=\nabla^2\theta+N_\delta\nabla^2\frac{\partial\theta}{\partial t}-N_\beta\nabla^4\theta \tag{25}$$

where the Fourier number Fo and two additional dimensionless groups arise

$$\mathrm{Fo}=\frac{\alpha_e\tau_q}{L^2},\quad N_\delta=\frac{\delta_e}{L^2}=\frac{\alpha_e\tau_T}{L^2},\quad N_\beta=\frac{\beta_e}{\alpha_e L^2} \tag{26}$$

The consistency between the dual-phase-lagging and the two-phase porous media equations require that $N_\beta\ll 1$, a requirement that is typically fulfilled if the effective thermal conductivities of the two phases differ substantially (i.e., either $k_s\ll k_f$ or $k_f\ll k_s$). Then, the biharmonic term in Eq. (25) can be neglected, leading to

$$\mathrm{Fo}\frac{\partial^2\theta}{\partial t^2}+\frac{\partial\theta}{\partial t}=\nabla^2\theta+N_\delta\nabla^2\left(\frac{\partial\theta}{\partial t}\right) \tag{27}$$

For the one-dimensional slab presented in Fig. 1, Eq. (27) becomes

$$\mathrm{Fo}\frac{\partial^2\theta}{\partial t^2}+\frac{\partial\theta}{\partial t}=\frac{\partial^2\theta}{\partial x^2}+N_\delta\frac{\partial^3\theta}{\partial t\partial x^2} \tag{28}$$

and their corresponding boundary and initial conditions are

$$x=0:\ \theta=0,\quad x=1:\ \theta=1 \tag{29}$$

$$t=0:\ \theta=\theta_o=\text{const}\quad\text{and}\quad \dot{\theta}=\dot{\theta}_o=\text{const} \tag{30}$$

Different values of the constants for θ_o and $\dot{\theta}_o$ applied to the solid and fluid phases will produce different solutions for each phase, hence, $T_s\neq T_f$. The solution to Eq. (28) is separated into steady-state θ_{ss} and transient θ_{tr} parts in the form $\theta=\theta_{ss}+\theta_{tr}$. The steady state is the linear solution $\theta_{ss}=x$, which satisfies the boundary conditions Eq. (29). The transient solution θ_{tr} has to fulfill the equation

$$\mathrm{Fo}\frac{\partial^2\theta_{tr}}{\partial t^2}+\frac{\partial\theta_{tr}}{\partial t}=\frac{\partial^2\theta_{tr}}{\partial x^2}+N_\delta\frac{\partial^3\theta_{tr}}{\partial t\partial x^2} \tag{31}$$

and the following boundary and initial conditions:

$$x=0:\ \theta_{tr}=0,\quad x=1:\ \theta_{tr}=0 \tag{32}$$

$$t=0:\ \theta_{tr}=(\theta_o-x)\quad\text{and}\quad \dot{\theta}_{tr}=\dot{\theta}_o \tag{33}$$

The solution is obtained by separation of variables in the form of two equations for $\theta_{tr}=\phi_n(t)u_n(x)$ presented in the form

$$\frac{d^2\phi_n}{dt^2}+c_{f,n}\frac{d\phi_n}{dt}+\omega_n^2\phi_n=0 \tag{34}$$

$$\frac{d^2u_n}{dx^2}+\kappa_n u_n=0 \tag{35}$$

The solution of Eq. (35) subject to the homogeneous boundary conditions $u_n=0$ at $x=0$ and at $x=1$ is $u_n=a_1\sin(n\pi x)$, and the resulting eigenvalues are $\kappa_n=n\pi\ \forall n=1,2,3,\ldots$. As a result, the coefficients $c_{f,n}$ and ω_n^2 in Eq. (34) are being defined in the form

$$c_{f,n}=\mathrm{Fo}^{-1}(1+N_\delta n^2\pi^2),\quad \omega_n^2=\mathrm{Fo}^{-1}n^2\pi^2 \tag{36}$$

Equation (34) represents a linear damped oscillator. Its eigenvalues are

$$\lambda_{1n}=-\frac{c_{f,n}}{2}\left(1+\sqrt{1-4\frac{\omega_n^2}{c_{f,n}^2}}\right) \tag{37}$$

$$\lambda_{2n}=-\frac{c_{f,n}}{2}\left(1-\sqrt{1-4\frac{\omega_n^2}{c_{f,n}^2}}\right) \tag{38}$$

The solution for ϕ_n is overdamped if for some values of n the condition $4\omega_{n_{cr}}^2<c_{f,n_{cr}}^2$ is satisfied, leading to

$$\theta_{tr,n}=(A_{1n}e^{\lambda_{1n}t}+A_{2n}e^{\lambda_{2n}t})\sin(n\pi x) \tag{39}$$

It is critically-damped if for some value of $n=n_{cr}$ the condition $4\omega_{n_{cr}}^2=c_{f,n_{cr}}^2$ is satisfied, i.e., $\lambda_{1n}=\lambda_{2n}=\lambda_{n_{cr}}=-c_{f,n_{cr}}/2$, leading to

$$\theta_{tr,n_{cr}}=(A_{1n_{cr}}e^{\lambda_{n_{cr}}t}+A_{2n}te^{\lambda_{n_{cr}}t})\sin(n_{cr}\pi x) \tag{40}$$

and it is underdamped if for some values of n the condition $4\omega_n^2>c_{f,n}^2$ is satisfied, i.e., $\lambda_{1n}=\lambda_r-i\lambda_i$ and $\lambda_{2n}=\lambda_r+i\lambda_i$, where $\lambda_r=-c_{f,n}/2$ and $\lambda_i=\sqrt{4\omega_n^2-c_{f,n}^2}/2$, leading to decaying standing thermal waves in the form

$$\theta_{tr,n}=e^{-c_{f,n}t}\{A_{1n}[\cos(\lambda_i t-n\pi x)-\cos(\lambda_i t+n\pi x)] -A_{2n}[\sin(\lambda_i t-n\pi x)-\sin(\lambda_i t+n\pi x)]\} \tag{41}$$

4 Lack of Oscillations and Lack of Resonance

The condition for an underdamped solution and its associated oscillations can be further explored to obtain explicit criteria in terms of the primitive parameters of the original system. By using the definitions from Eq. (36) it produces the condition for an underdamped solution in the form

$$\frac{c_{f,n}^2}{4\omega_n^2}=\frac{(1+N_\delta n^2\pi^2)^2}{4\,\mathrm{Fo}\,n^2\pi^2}<1 \tag{42}$$

An analysis of inequality (42) presented in the Appendix produces the following necessary and sufficient condition for the underdamped solution to materialize:

$$\frac{N_\delta}{\mathrm{Fo}}=\frac{\tau_T}{\tau_q}<1 \tag{43}$$

However, Eq. (23) shows that based on physical arguments the lag ratio τ_T/τ_q is always greater than 1 (i.e., $\tau_T/\tau_q>1$). Therefore, underdamped solutions, which require according to Eq. (43) that $\tau_T/\tau_q<1$, are being ruled out. Similarly, since the condition for critically damped solutions is $N_\delta/\mathrm{Fo}=\tau_T/\tau_q=1$, but in reality this ratio is greater than 1 (i.e., $\tau_T/\tau_q>1$), critically damped solutions are ruled out as well. One can, therefore, conclude that underdamped and critically damped solutions are not possible, and hence, oscillations cannot occur in dual-phase-lagging application to porous media conduction subject to the specified geometry and boundary conditions. Since resonance would have been possible due to a forced periodic source or alternatively due to periodic boundary conditions at a forcing frequency that is identical to one of the natural frequencies of the system, the lack of possibility for underdamped solutions prevents resonance from occurring as well in dual-phase-lagging application to porous media conduction subject to the specified geometry and boundary conditions.

5 Results and Discussion

The possible solution is therefore the one corresponding to overdamped conditions for all values of n as presented by Eq. (39), leading to the complete solution in the form

$$\theta=x+\sum_{n=1}^{\infty}(A_{1n}e^{\lambda_{1n}t}+A_{2n}e^{\lambda_{2n}t})\sin(n\pi x) \tag{45}$$

By using the initial conditions specified in Eq. (33) with $\theta_o=0$, representing a step temperature change of the hot wall at $x=1$ (to $T=T_H$ or $\theta=1$) from an initial uniform temperature in the slab $T=T_C$ (or, $\theta=0$), one obtains the following expressions for the coefficients A_{1n} and A_{2n}:

$$A_{1n}=\frac{2}{(\lambda_{2n}-\lambda_{1n})n\pi}\{\dot{\theta}_o[(-1)^n-1]+\lambda_{2n}(-1)^n\} \tag{46}$$

$$A_{2n}=\frac{-2}{(\lambda_{2n}-\lambda_{1n})n\pi}\{\dot{\theta}_o[(-1)^n-1]+\lambda_{1n}(-1)^n\} \tag{47}$$

A different constant value of θ_o for the other phase will produce a different coefficient.

A combination of three different cases is being considered. The first case corresponds to moderate values of Fo and N_δ while the initial condition for the temperature rate of change in time is $\dot{\theta}_o=0$, a condition that applies if the slab was initially exposed to the surroundings for a sufficient relaxation time in order to reach thermal equilibrium with the environment. The temperature solution as a function of $x=x_*/L$ for the latter case of dual-phase-lagging heat conduction in the porous slab corresponding to Fo=1, $N_\delta=1.1$, $\theta_o=0$, and $\dot{\theta}_o=0$, is presented in Fig. 2 for different values of time. From Fig. 2, a typical feature of the dual-phase-lagging conduction can be observed in the temperature jump at the hot wall where $x=x_*/L=1$. While Fourier conduction is capable of quickly smoothing out any initial temperature discontinuity [see Fig. 5, which describes essentially a typical Fourier solution where the initial ($t=0$) discontinuity at $x=x_*/L=1$ disappears at all subsequent times $t>0$], the dual-phase-lagging retains this discontinuity for all times until steady state is achieved (as observed in Fig. 2 at the location $x=x_*/L=1$), the latter steady

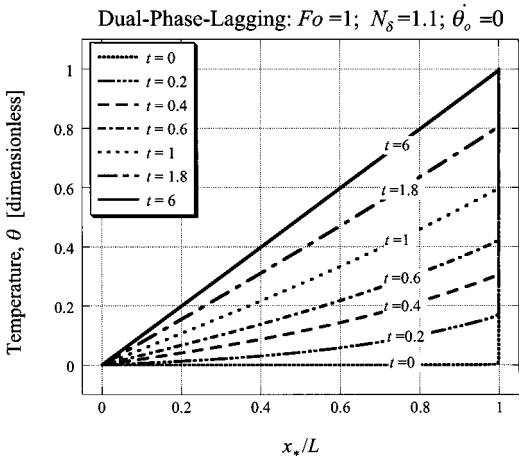

Fig. 2 Temperature solution of dual-phase-lagging thermal conduction in a porous slab as a function of $x=x_*/L$ for different values of time and corresponding to Fo=1, $N_\delta=1.1$, $\theta_o=0$, and $\dot{\theta}_o=0$

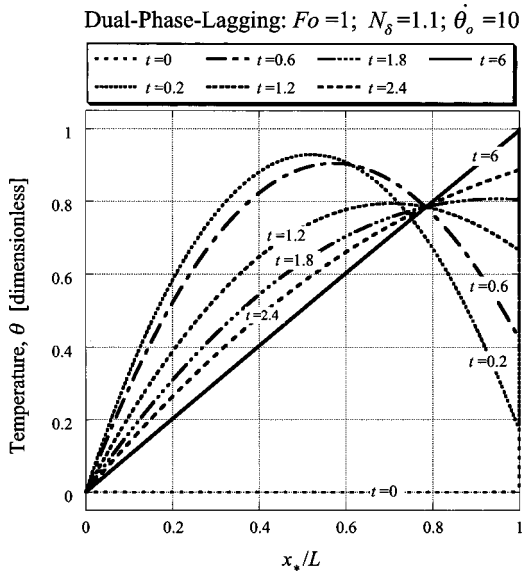

Fig. 3 Temperature solution of dual-phase-lagging thermal conduction in a porous slab as a function of $x=x_*/L$ for different values of time and corresponding to Fo=1, $N_\delta=1.1$, $\theta_o=0$, and $\dot{\theta}_o=10$

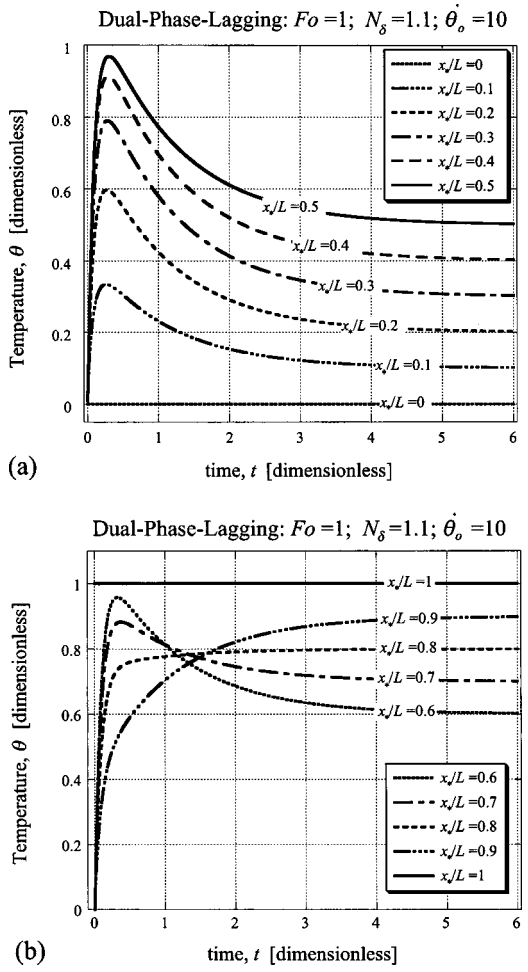

Fig. 4 Temperature solution of dual-phase-lagging thermal conduction in porous media as a function of time for different values of $x=x_*/L$ and corresponding to Fo=1, $N_\delta=1.1$, $\theta_o=0$, and $\dot{\theta}_o=10$: (*a*) the solution for $x=0$, 0.1, 0.2, 0.3, 0.4, 0.5; (*b*) the solution for $x=0.6$, 0.7, 0.8, 0.9, 1

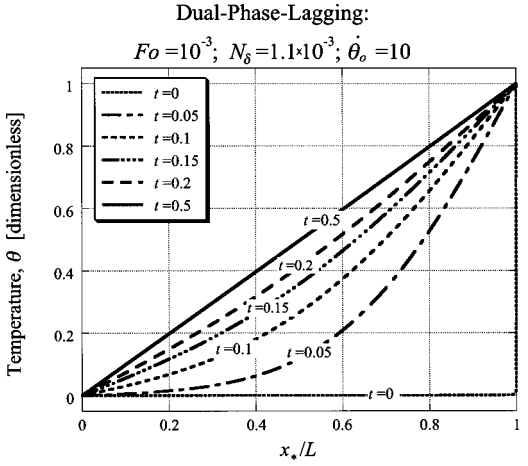

Fig. 5 Temperature solution of dual-phase-lagging thermal conduction in a porous slab as a function of $x=x_*/L$ for different values of time and corresponding to small values of Fo $=10^{-3}$ and $N_\delta=1.1\times10^{-3}$ and to $\theta_o=0$ and $\dot{\theta}_o=10$. The parameter values correspond to small dual-phase-lagging effect leading approximately to a local thermal equilibrium (Lotheq) conduction solution (Fourier diffusion).

state only being capable of removing the discontinuity. Overshooting is not possible if the initial rate of temperature change vanishes (i.e., if $\dot{\theta}_o=0$).

The second case applies to the same moderate values of Fo=1 and $N_\delta=1.1$, whereas the initial condition for the temperature rate of change in time is $\dot{\theta}_o=10$. The latter applies to strong initial thermal inertia, a condition that is expected to produce an overshooting solution in time. The temperature solution as a function of $x=x_*/L$ for the latter case of dual-phase-lagging heat conduction in the porous slab, corresponding to Fo=1, $N_\delta=1.1$, $\theta_o=0$, and $\dot{\theta}_o=10$, is presented in Fig. 3 for different values of time. The temperature discontinuity at $x=x_*/L=1$ is maintained here as well until steady state is reached. The same solution in the time domain (i.e., the temperature solution as a function of time for different values of $x=x_*/L$) is presented in Fig. 4, where the overshooting is apparent. Such an overshooting is not possible in a Fourier heat conduction solution nor in DuPhlag heat conduction when $\dot{\theta}_o=0$.

In order to observe how the solution of the dual-phase-lagging conduction degenerates to the Lotheq heat conduction solution (Fourier diffusion) a third case was considered, corresponding to very small values of Fo and N_δ. The temperature solution as a function of $x=x_*/L$ for dual-phase-lagging heat conduction in the porous slab corresponding to the limiting case of approximate Lotheq (Fourier) conduction (i.e., Fo$=10^{-3}$, $N_\delta=1.1\times10^{-3}$, and for $\theta_o=0$ and $\dot{\theta}_o=10$) is presented in Fig. 5 for different values of time, where the typical Fourier thermal diffusion evolution toward the steady state is identified. An evaluation of the maximum absolute temperature difference between this solution and the accurate Fourier conduction solution shows that the difference is about 5×10^{-3}.

6 Conclusions

The approximate equivalence between the dual-phase-lagging (DuPhlag) heat conduction model and the Fourier heat conduction in porous media subject to lack of local thermal equilibrium (La Lotheq) suggested the possibility of thermal waves and resonance. It was demonstrated that the conditions necessary for such thermal oscillations and possibly resonance to materialize are not physically attainable in a porous slab subject to Dirichlet boundary conditions. Nevertheless, temperature overshooting in time is pos-

sible and can occur if the initial rate of change of the temperature with time is nonzero, $\dot{\theta}_o \neq 0$. As the temperature gradient time lag τ_T is always larger than the heat flux time lag τ_q, the heat flux is the cause and the temperature gradient is the effect in a porous slab heat conduction subject to constant temperatures on the walls. These results suggest the need for a critical reevaluation of the DuPhlag model as used in other applications along similar lines as presented here in order to establish the physical realization of thermal waves and resonance via the dual phase lagging model.

Nomenclature

Latin Symbols

$c_{p,f}$, c_s = fluid and solid phase specific heat, respectively (dimensional)
$\hat{\boldsymbol{e}}_x$ = unit vector in the x direction.
$\hat{\boldsymbol{e}}_y$ = unit vector in the y direction.
$\hat{\boldsymbol{e}}_z$ = unit vector in the z direction.
Fo = Fourier number, equals $\alpha_e \tau_q / L^2$
N_δ = dual-phase-lagging mixed term dimensionless group, equals $\delta_e / L^2 = \alpha_e \tau_T / L^2$
N_β = dual-phase-lagging biharmonic term dimensionless group, equals $\beta_e / \alpha_e L^2$
h = integral heat transfer coefficient for the heat conduction at the solid-fluid interface (dimensional)
k_s = effective thermal conductivity of the solid phase, equals $(1-\varphi)\tilde{k}_s$ (dimensional)
$\tilde{k}_s$ = thermal conductivity of the solid phase, (dimensional)
k_f = effective thermal conductivity of the fluid phase, equals $\varphi \tilde{k}_f$ (dimensional)
$\tilde{k}_f$ = thermal conductivity of the fluid phase, (dimensional)
L = length of the porous slab (dimensional)
$\boldsymbol{q}$ = heat flux vector (dimensional)
t_* = time (dimensional)
T = temperature (dimensional)
T_C = coldest wall temperature (dimensional)
T_H = hottest wall temperature (dimensional)
x_* = horizontal coordinate (dimensional)
$\boldsymbol{x}$ = position vector, equals $x\hat{\boldsymbol{e}}_x + y\hat{\boldsymbol{e}}_y + z\hat{\boldsymbol{e}}_z$

Greek Symbols

α_e = effective thermal diffusivity, defined by Eq. (6) (dimensional)
β_e = effective property coefficient to the dual-phase-lagging biharmonic term, defined in Eq. (6) (dimensional)
γ_s = solid phase effective heat capacity, equals $(1-\varphi)\rho_s c_s$ (dimensional)
γ_f = fluid phase effective heat capacity, equals $\varphi \rho_f c_{p,f}$ (dimensional)
δ_e = effective property coefficient to the dual-phase-lagging mixed term, defined in Eq. (6) (dimensional)
θ = dimensionless temperature, equals $(T-T_C)/(T_H - T_C)$
φ = porosity.
ρ_s = solid phase density
ρ_f = fluid phase density
τ_q = time lag associated with the heat flux, defined by Eq. (6) (dimensional)
τ_T = time lag associated with the temperature gradient, equals δ_e / α_e (dimensional)
ω_n = dimensionless natural thermal frequency defined by Eq. (36)

Subscripts

$*$ = corresponding to dimensional values of the independent variables
s = related to the solid phase
f = related to the fluid phase

Appendix

The condition for underdamped solutions to materialize was presented in Eq. (42) in the form

$$\frac{(1+N_\delta n^2 \pi^2)^2}{4\,\mathrm{Fo}\, n^2 \pi^2} < 1 \tag{A1}$$

The inequality presented in Eq. (*A*1) can be expanded to produce the following inequality which applies to the values of n:

$$y \equiv n^4 + bn^2 + c < 0 \tag{A2}$$

where

$$b = \frac{2(N_\delta - 2\mathrm{Fo})}{\pi^2 N_\delta^2}, \quad c = \frac{1}{\pi^4 N_\delta^2} > 0 \tag{A3}$$

By treating n^2 as a continuous variable, the function $y(n^2) = n^4 + bn^2 + c$ represents a parabola which has a minimum at $n^2 = (-b/2)$. For obtaining real and positive values of n the roots, n^2, of the equation $y \equiv n^4 + bn^2 + c = 0$ have to be real and positive. The plot of $y(n^2)$ as a function of n^2 is presented in Fig. 6, identifying the cases where $c > 0$, while the cases when $c < 0$ are not presented as they are not applicable here according to Eq. (*A*3). The two typical curves presented in Fig. 6 correspond to $b < 0$ $(N_\delta/\mathrm{Fo} < 2)$ and $b > 0$ $(N_\delta/\mathrm{Fo} > 2)$. For $b > 0$ $(N_\delta/\mathrm{Fo} > 2)$ the negative part of the curve corresponds to negative values of n^2 and, therefore, cannot accommodate real values of n. For $b < 0$ $(N_\delta/\mathrm{Fo} < 2)$, an underdamped solution is, in principle, possible provided the roots of the quadratic equation $y \equiv n^4 + bn^2 + c = 0$ are real. The latter implies that the following roots $n_{1,2}^2 = -b[1 \pm \sqrt{1 - 4c/b^2}]/2$ have to be real for obtaining two real and positive values of n^2 as presented in Fig. 6. For the latter to occur the discriminant $(b^2 - 4c)$ must be positive. By substituting the parameters from Eq. (*A*3) into this condition, it yields

$$\frac{4}{\pi^4 N_\delta^2}\left[\frac{(N_\delta - 2\mathrm{Fo})^2}{N_\delta^2} - 1\right] > 0 \tag{A4}$$

Further derivation of the square brackets in Eq. (*A*4) leads to

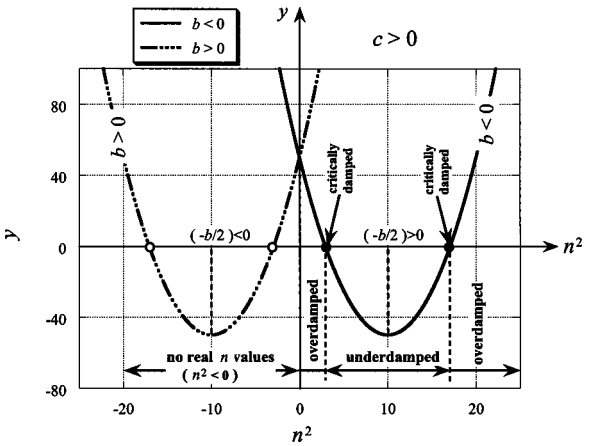

Fig. 6 Graphical representation of the conditions for underdamped, critically damped, and overdamped solutions in terms of the function $y(n^2) = n^4 + bn^2 + c$, for $c > 0$

$$-\frac{4\,\mathrm{Fo}}{N_\delta}\left[1-\frac{\mathrm{Fo}}{N_\delta}\right]>0 \tag{A5}$$

For positive values of $\mathrm{Fo}>0$ and $N_\delta>0$ Eq. (*A*5) requires

$$\frac{N_\delta}{\mathrm{Fo}}=\frac{\tau_T}{\tau_q}<1 \tag{A6}$$

Inequality (*A*6) represents a necessary and sufficient condition for underdamped solutions to materialize.

References

[1] Tzou, D. Y., 1997, *Macro-to-Microscale Heat Transfer: The Lagging Behavior*, Taylor & Francis, Washington, D.C.

[2] Tzou, D. Y., 1995, ''A Unified Field Approach for Heat Conduction From Macro-to-Micro-Scales,'' ASME J. Heat Transfer, **117**, pp. 8–16.

[3] Tzou, D. Y., 2001, ''Temperature-Dependent Thermal Lagging in Ultrafast Laser Heating,'' Int. J. Heat Mass Transfer, **44**, pp. 1725–1734.

[4] Xu, M., and Wang, L., 2002, ''Thermal Oscillation and Resonance in Dual-Phase-Lagging Heat Conduction,'' Int. J. Heat Mass Transfer, **45**, pp. 1055–1061.

[5] Wang, L., Xu, M., and Zhou, X., 2001, ''Well-Posedness and Solution Structure of Dual-Phase-Lagging Heat Conduction,'' Int. J. Heat Mass Transfer, **44**, pp. 1659–1669.

[6] Wang, L., and Xu, M., 2002, ''Well-Posedness of Dual-Phase-Lagging Heat Conduction Equation: Higher Dimensions,'' Int. J. Heat Mass Transfer, **45**, pp. 1165–1171.

[7] Antaki, P. J., 1998, ''Solution for Non-Fourier Dual-Phase-Lag Heat Conduction in a Semi-Infinite Slab With Surface Heat Flux,'' Int. J. Heat Mass Transfer, **41**, pp. 2253–2258.

[8] Nield, D. A., 2002, ''A Note on the Modeling of Local Thermal Non-Equilibrium in a Structured Porous Medium,'' Int. J. Heat Mass Transfer, **45**, pp. 4367–4368.

[9] Minkowycz, W. J., Haji-Shiekh, A., and Vafai, K., 1999, ''On Departure From Local Thermal Equilibrium in Porous Media Due to a Rapidly Changing Heat Source: The Sparrow Number,'' Int. J. Heat Mass Transfer, **42**, pp. 3373–3385.

[10] Banu, N., and Rees, D. A. S., 2002, ''Onset of Darcy-Benard Convection Using a Thermal Non-Equilibrium Model,'' Int. J. Heat Mass Transfer, **45**, pp. 2221–2238.

[11] Baytas, A. C., and Pop, I., 2002, ''Free Convection in a Square Porous Cavity Using a Thermal Nonequilibrium Model,'' Int. J. Therm. Sci., **41**, pp. 861–870.

[12] Kim, S. J., and Jang, S. P., 2002, ''Effects of Darcy Number, the Prandtl Number, and the Reynolds Number on Local Thermal Non-Equilibrium,'' Int. J. Heat Mass Transfer, **45**, pp. 3885–3896.

[13] Rees, D. A. S., 2002, ''Vertical Free Convective Boundary-Layer Flow in a Porous Medium Using a Thermal Nonequilibrium Model: Elliptical Effects,'' ZAMP, **53**, pp. 1–12.

[14] Alazmi, B., and Vafai, K., 2002, ''Constant Wall Heat Flux Boundary Conditions in Porous Media Under Local Thermal Non-Equilibrium Conditions,'' Int. J. Heat Mass Transfer, **45**, pp. 3071–3087.

[15] Nield, D. A., Kuznetsov, A. V., and Xiong, M., 2002, ''Effect of Local Thermal Non-Equilibrium on Thermally Developing Forced Convection in a Porous Medium,'' Int. J. Heat Mass Transfer, **45**, pp. 4949–4955.

[16] Vadasz, P., 2004, ''Conditions for Local Thermal Equilibrium in Porous Media Conduction,'' Transp. Porous Media, accepted for publication, in press.

[17] Spiga, M., and Morini, G. L., 1999, ''Transient Response of Non-Thermal Equilibrium Packed Beds,'' Int. J. Eng. Sci., **37**, pp. 179–188.

[18] Kuznetsov, A. V., 1998, ''Thermal Nonequilibrium Forced Convection in Porous Media,'' in *Transport' Phenomena in Porous Media*, D. B. Ingham and I. Pop, eds., Elsevier, Oxford, pp. 103–129.

[19] Amiri, A., and Vafai, K., 1994, ''Analysis of Dispersion Effects and Non-Thermal Equilibrium, Non-Darcian, Variable Porosity Incompressible Flow Through Porous Media,'' Int. J. Heat Mass Transfer, **37**, pp. 934–954.

[20] Kuznetsov, A. V., 1997, ''A Perturbation Solution for Heating a Rectangular Sensible Heat Storage Packed Bed With a Constant Temperature at the Walls,'' Int. J. Heat Mass Transfer, **40**, pp. 1001–1006.

[21] Hays-Stang, K. J., and Haji-Sheikh, A., 1999, ''A Unified Solution for Heat Conduction in Thin Films,'' Int. J. Heat Mass Transfer, **42**, pp. 455–465.

[22] Qiu, T. Q., and Tien, C. L., 1992, ''Short-Pulse Laser Heating of Metals,'' Int. J. Heat Mass Transfer, **35**, pp. 719–726.

[23] Lage, J. L., 1999, ''The Implications of the Thermal Equilibrium Assumption for Surrounding-Driven Steady Conduction Within a Saturated Porous Medium Layer,'' Int. J. Heat Mass Transfer, **42**, pp. 477–485.

[24] Quintard, M., and Whitaker, S., 1995, ''Local Thermal Equilibrium for Transient Heat Conduction: Theory and Comparison With Numerical Experiments,'' Int. J. Heat Mass Transfer, **38**, pp. 2779–2796.

Robert J. Stevens
Department of Mechanical and Aerospace Engineering
University of Virginia
Charlottesville, VA 22904

Andrew N. Smith
Department of Mechanical Engineering
United States Naval Academy
Annapolis, MD 21402

Pamela M. Norris
Department of Mechanical and Aerospace Engineering
University of Virginia
Charlottesville, VA 22904
e-mail: pamela@virginia.edu

Measurement of Thermal Boundary Conductance of a Series of Metal-Dielectric Interfaces by the Transient Thermoreflectance Technique

Measurement of the thermal boundary conductance (TBC) by use of a nondestructive optical technique, transient thermoreflectance (TTR), is presented. A simple thermal model for the TTR is presented with a discussion of its applicability and sensitivity. A specially prepared sample series of Cr, Al, Au, and Pt on four different substrates (Si, sapphire, GaN, and AlN) were tested at room temperature and the TTR signal fitted to the thermal model. The resulting TBC values vary by more than a factor of 3 (0.71 $\times 10^8 - 2.3 \times 10^8$ *W/m*^{2} *K). It is shown that the diffuse mismatch model (DMM) tended to overpredict the TBC of interfaces with materials having similar phonon spectra, while underpredicting the TBC for interfaces with dissimilar phonon spectra. The DMM only accounts for diffuse elastic scattering. Other scattering mechanisms are discussed which may explain the failure of the DMM at room temperature.* [DOI: 10.1115/1.1857944]

Introduction

Thermal management of micro- and optoelectronics is becoming more critical as device sizes decrease and new materials are employed. For this reason, there has been a growing interest in the determination of the thermophysical properties of thin-film materials. Significant attention has been given to the thermal diffusivity of thin-film materials, which often differs from bulk materials. Perhaps more critical to the thermal management of superlattice and future nanoscale devices is the thermal boundary resistance (TBR), which is frequently approximated or neglected leading to significant uncertainties in design and performance. Specific applications for which TBR is currently being considered are thermionic refrigeration [1], thermoelectrics [2], thin-film high-temperature superconductors [3,4], heterostructure field-effect transistors [5], and optical data storage media [6]. More applications are sure to follow. The TBR can vary widely depending on the deposition technique and types of materials utilized. Precise knowledge of the TBR is required in order to fully understand the thermal characteristics of multilayer thin-film devices. The ability to determine the TBR between thin metal films and different substrate materials will become increasingly critical to both the design and selection of innovative dielectric materials and the selection of deposition techniques.

TBR creates an abrupt change in temperature, ΔT, across an interface between two different materials. This was first observed by Kapitza for a solid and liquid helium interface in 1941 [7]. The inverse of TBR is often referred to as Kapitza conductance, σ_k or thermal boundary conductance (TBC). The heat flux, q'', across an interface can be expressed by the following equation:

$$q'' = \sigma_k \Delta T \tag{1}$$

The primary energy carriers in dielectric materials are acoustic phonons. Consequently, the TBR of dissimilar dielectric materials is often attributed to the reflection of phonons at the interface. There have been several theoretical models developed to estimate the TBR. The first of these theories is the acoustic mismatch model (AMM) developed by Little for the interface of dissimilar solids at low temperatures [8]. This model assumes that each solid can be treated as a continuum with a perfect interface. The incident phonons are treated as plane waves, for which transmission and reflection probabilities are calculated, and there is no scattering at the interface. The AMM assumptions are generally reasonable at low temperatures and for perfect interfaces. A more recent model, called the diffuse mismatch model (DMM), was developed and is generally more applicable for nonperfect interfaces, where at higher temperatures, higher-frequency acoustic phonons are expected to scatter. This model assumes complete diffuse scattering at the interface [9]. The transmission probability is then related to the density of phonon states on both sides of the interface. Diffuse scattering is more important at higher temperatures and for nonperfect interfaces. Swartz and Pohl [9] conducted experiments comparing the two models. A review of both mismatch theories and their comparison to experimental observations was compiled by Swartz and Pohl [7].

More recent theoretical efforts have utilized lattice-dynamical calculations to numerically determine the TBR. Young and Maris calculated theoretical Kapitza resistances using three-dimensional lattices [10]. Experimental data was later compared to this lattice-dynamical model over various materials and over a range of temperatures [11]. Pettersson and Mahan altered the model to account for dissimilar lattices [12]. More elaborate lattice-dynamical models have been developed by Kechrakos [13] and Fagas et al. [14] in attempts to account for phonon scattering at disordered interfaces. For a more recent review of the theoretical methods for calculating the TBR, see Cahill et al. [15].

TBR measurements have been made using a few different techniques. One technique employed by Swartz and Pohl [9] utilizes two thin-film microbridges deposited close to one another on a dielectric substrate. One microbridge is used as both a heat source and thermal sensor on the metal side and the other microbridge is a thermal sensor for the dielectric side. This technique requires that the mean-free path of the phonon is larger than the spacing between the microbridges, and is therefore only applicable at low temperatures. A second technique, called modulated thermoreflectance microscopy, examines the propagation of thermal waves generated by a laser pulse [16,17]. The wave propagation is de-

Manuscript received December 12, 2003; revision received September 21, 2004. Review conducted by: K. Kihm.

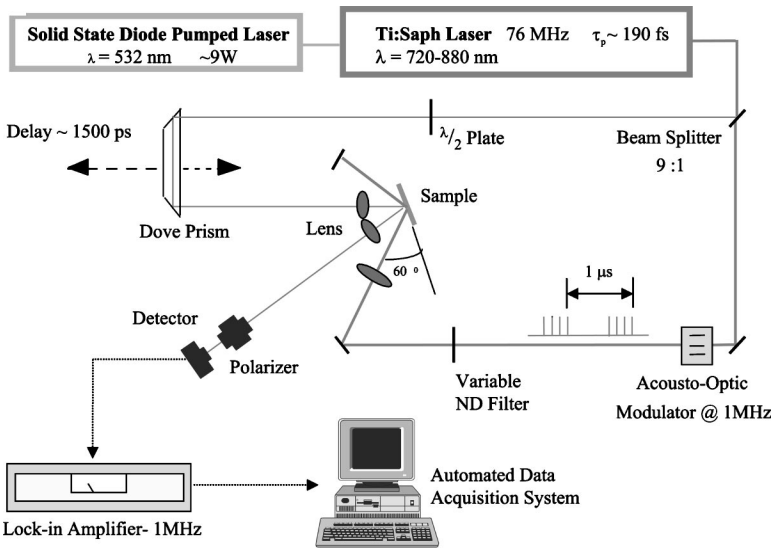

Fig. 1 TTR experimental setup

termined by measuring the reflectance of a probe beam that is rastered around the heating location. The phase of the probe is measured and compared to a thermal model where the thermal boundary resistance is treated as a free parameter [18,19]. A third technique, the 3ω method, uses an ac hot-wire setup to measure apparent thermal conductivity of a film and interface system. The TBR is extracted from data taken on a series of films while varying thickness [20,21].

A fourth technique is the transient thermoreflectance technique (TTR) where a short-pulsed laser beam is used to heat a thin metal film. The thin metal film is then probed with a weaker laser pulse after a known time delay in order to measure the transient temperature change of the metal film. This technique was used by Stoner and Maris [11] and Costescu et al. [22] to measure the TBR of metal films and dielectric substrates. One distinct advantage of this technique is the ability to directly measure the thin-film TBR of films with thicknesses on the order of the optical penetration depth. This paper describes the TTR technique and its application to a specially prepared set of metal films and dielectric interfaces. Several issues associated with using TTR for measuring the TBR will be discussed. The systematic set of data collected as part of this investigation will hopefully be used in future developments of more sophisticated models for the TBR of interfaces, which to date are still lacking.

Transient Thermal Reflectance Technique

The TTR method uses an intense ultrashort laser pulse to generate a transient thermal response, and a weaker probe pulse to monitor the reflectivity response of the surface. Changes in reflectively can be related to the change in temperature for most metals. A schematic of the experimental setup is shown in Fig. 1. The pulses from a 76 MHz Ti:Sapphire laser with a full width at half maximum (FWHM) pulse width of 200 fs are separated into two beams with an intensity ratio of 9:1 by a nonpolarizing beam splitter. The intense ''pump'' beam is used to heat the film while the low power ''probe'' beam is used to monitor the reflectivity. The pump beam passes through an acousto-optic modulator, which creates a pulse train at a frequency of 1 MHz. The pump beam is focused to $\sim 80\ \mu$m at an incident angle of 30 deg with an estimated fluence of ~ 2 J/m^2. The probe beam passes through a dovetail prism mounted on a variable delay stage that is used to increase the optical path length of the probe beam and hence the time delay between the pump and probe pulses. A half-wave plate rotates the probe beam's polarization parallel to the plane of incidence. The probe, which is centered in the heated area, is focused to $\sim 15\ \mu$m at near-normal incidence to minimize the illuminated area. A polarizer, oriented such that only the probe light passes and not the pump, is positioned before a silicon photodiode, which monitors the probe beam's reflection off the sample. The reflectivity of metals is assumed to be linearly related to temperature for small changes in temperature, which creates an amplitude modulation in the probe beam. A lock-in amplifier set at a frequency of 1 MHz monitors the photodiode response to the modulation in intensity of the probe beam. The probe pulse is delayed in time allowing for the transient cooling profile of the sample to be recorded.

For long scans and samples where residual heating cannot be neglected, data must be phase corrected as described by Smith et al. [23]. Alignment of the pump and probe spots for long scans can be an issue as pointed out by Capinski and Maris [24]. To avoid the misalignment problems, the probe beam was collimated before the stage and the probe spot was profiled using a sweeping knife edge for all time delays. For the pump-probe diameter ratios utilized in this investigation and for less then the measured 5 μm overlap error, the errors in signal at any given delay time are less than 1% due to misalignment.

Thermal Model and Analysis

The heat transfer within the metal film and the substrate material heated by a short-pulsed laser on a timescale greater than ~ 100 ps is governed by the time dependent heat conduction equation, which describes the thermal diffusion in the metal film and substrate, respectively:

$$C_f \frac{\partial \theta_f}{\partial t} = k_f \frac{\partial^2 \theta_f}{\partial x^2} \tag{2}$$

$$C_s \frac{\partial \theta_s}{\partial t} = k_s \frac{\partial^2 \theta_s}{\partial x^2} \tag{3}$$

where θ is the temperature above ambient, C is the thermal capacitance, and k is thermal conductivity.

Upon absorption of a laser pulse, there is an immediate temperature gradient in the metal film given by Eq. (4) and a negligible temperature rise in the substrate. Therefore, initial conditions for the metal film and the substrate are:

$$\theta_f(x) = \frac{F(1-R)}{C_f \delta} e^{-x/\delta} \tag{4}$$

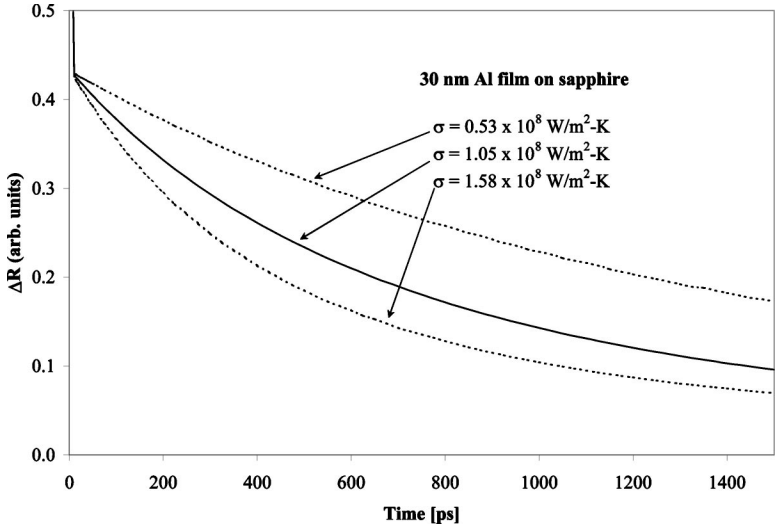

Fig. 2 Modeled thermal response of 30 nm Al film on a sapphire substrate with $\sigma = 1.05 \times 10^8$ W/m^2 K. The dotted lines are the thermal response for the same film with ±50% change in σ.

$$\theta_s(x) = 0 \tag{5}$$

where F is the fluence, R is the reflectance, and δ is energy deposition depth. In reality, the initial temperature profile will be more uniform across the metal film due to increased thermal diffusion that results from nonequilibrium heating during the first few picoseconds [25]. To account for the initial nonequilibrium between electron and phonon systems, a more sophisticated model could be used, but it turns out to have little impact on the decay after 100 ps, which is of interest for measuring the TBR. Equation (5) assumes that the initial heating of the substrate is negligible. This assumption is valid when the metal film thickness is two or more times greater than the optical penetration depth and the substrate has a small optical absorption coefficient and a significant thermal conductivity.

At the interface ($x = d$), the conductive heat flux of the substrate and film are equal to the heat transport across the interface, so the system is subject to the following boundary conditions:

$$-k_f \frac{\partial \theta_f}{\partial x}(x = d) = \sigma(\theta_f - \theta_s) \tag{6}$$

$$-k_s \frac{\partial \theta_s}{\partial x}(x = d) = \sigma(\theta_f - \theta_s) \tag{7}$$

where σ is the TBC. For the nanosecond time regime considered, the convective and radiative losses from the surface of the metal film (at $x = 0$) are negligible. The substrate is treated as semi-infinite, because less than 2 μm of the substrate are influenced by the temperature rise on the 1–2 ns timescale of the experiment.

In order to resolve the thermal boundary conductance, the time constant for the film should be significantly smaller than the time constant associated with the interface, otherwise it will be difficult to extract the TBC from the thermal diffusion in the film. The time constant, τ, associated with diffusion of heat in the film can be approximated using:

$$\tau \approx \frac{d^2}{\alpha} \tag{8}$$

where α is the effective diffusivity of the metal film, and d is the film thickness. The interface time constant is given by

$$\tau_i = \frac{C_f d}{\sigma} \tag{9}$$

for highly conductive substrates [11]. Thus, this model and experimental technique is limited to situations in which the following applies:

$$\frac{\tau}{\tau_i} = \frac{d\sigma}{k_f} < 1 \tag{10}$$

Practically, this means that for metals with interfaces having $\sigma \approx 2 \times 10^8$ W/m^2 K, films are restricted to thicknesses less than 100 nm. Also, the interface time constant, τ_i, should be less than or on the order of the TTR scan length in order to resolve the TBR. Thus, for scan lengths of 1–2 ns, metal films should be 100 nm thick or less.

Another criteria for the applicability of using the TTR method to resolve the TBC is that the substrate must have a significant thermal conductivity [26]. Energy transferred across the interface should not induce a large temperature change in the substrate; otherwise the decay observed will be dominated by the thermal resistance of the substrate and not the thermal boundary resistance. High thermal conductivity also reduces issues associated with steady-state heating. This criterion eliminates the use of glasses for substrate materials.

Equations (2) and (3) subject to Eqs. (4)–(7) are numerically solved using the Crank–Nicolson method. Figure 2 shows the temperature response of a 30 nm thick aluminum film on a sapphire substrate using a TBC of 1.05×10^8 W/m^2 K reported by Stoner and Maris [11]. The dashed lines show the change in the cooling profile resulting in a change in the TBC of ±50% indicating how sensitive the model is to the value used for the TBC even for a fairly low thermal conductance substrate, such as sapphire. Because the model is sensitive to the TBC, it should provide a high degree of confidence in determining the TBR from experimental data assuming all other inputs are well known. For substrates with higher thermal conductivities compared to sapphire, the differences between the cooling profile for a given TBC and uncertainty of ±50% is even more significant.

In addition to being sensitive to the TBR, the model is also sensitive to uncertainties in the film heat capacity and thickness. The thermal response is only weakly dependent on the uncertainties of thermal conductance and capacitance of the substrate and the thermal conductance of the film. This is discussed in more detail in the Results section.

Table 1 Debye temperatures (θ_D) of materials used in sample series [27–29]

Material	θ_D (K)
Au	165
Pt	240
Al	428
Cr	630
GaN	600
Si	645
Sapphire	1035
AlN	1150

Samples

The current theory for TBR is primarily concerned with phonon transmission across an interface and is therefore dependent on the differences in the phonon densities of states of both materials at the interface. Two sample series were selected to cover a wide range of interface conditions in a systematic way. The series consisted of 30 nm thick Al and Cr films deposited on Si, sapphire, AlN, and GaN substrates. In addition, Au and Pt were deposited only on Si substrates. The Si substrates were factory polished at (100) orientation. The AlN substrates were single crystalline and factory polished but had an unknown orientation. The GaN substrate consisted of a 2 μm polycrystalline layer of GaN metal-organic vapor phase epitaxy deposited on the *a* plane of a polished single-crystalline sapphire substrate. The Debye temperatures (θ_D) for the materials used in the sample series are listed in Table 1.

The Cr and Al films were deposited by rf diode sputtering with 5 in. 99.995% purity targets in a single sputter-down target system with a base pressure of 8×10^{-7} Torr. For each run, the substrates were first spin cleaned in ethanol, trichloroethylene (TCA), and methanol and then hot-plate baked at 120°C for 5 min before being loaded into the deposition system. The samples were mounted onto a glass carrier with Apiezon-L high-vacuum grease, and the carrier was in turn mounted with Apiezon-L to the water-cooled substrate table. The samples were lightly sputter etch cleaned at 300 V removing approximately 5 nm of material, including the native oxide layer. The deposition rates, with a 600 V target bias, were 4.60 nm/min and 6.77 nm/min for the Cr and Al targets, respectively. The ''30 nm'' Cr samples were deposited in two separate runs due to substrate size limitations. With an expected thickness of 30 nm, the two Cr and Al film thicknesses subsequently measured from the glass carriers were 29.5 nm, 29.0 nm, and 28.0 nm, respectively. The film thicknesses were measured using a Tencor surface profiler, using a multiple (five) scan method where the scans are averaged. The two subsequent measurements (from the expected rate versus the measured carrier) agreed to better than 5%.

The Au and Pt films were deposited using a Temescal BJD-1800 evaporator. The deposition chamber was evacuated to a pressure of $\sim6\times10^{-7}$ Torr. The Au films were deposited at a rate of 60 nm/min and the Pt films were deposited at a rate of 30 nm/min. The rate of deposition was monitored using a vibrating quartz crystal, and the thickness of each film was measured using a profilometer to confirm the accuracy of the quartz crystal. The thickness presented for each film is the value measured using the Tencor surface profiler. These values were consistent to within 10% of the thickness predicted by the quartz crystal. Prior to deposition, each substrate was cleaned using a solvent wash of ethanol, TCA, and methanol. The substrates were also cleaned using a plasmaline O_2 cleaner.

Although much care was taken in making the samples, it should be noted that the interfaces are more than likely not abrupt junctions and possibly two phase, this can especially be the case for metals on Si. Franciosi et al. experimentally determined that Cr deposited on Si substrates at room temperature resulted in a Si-rich intermixed layer on the order of 10 monolayers [30]. The intermixed layer was not believed to be a silicide ($CrSi_2$) which typically forms at higher temperatures. Although Al and Si do not form silicides, interdiffusion can occur at room temperature. In the case of the Au and Pt samples, the native oxide layer suppresses diffusion across the interface. Hiraki et al. showed that Au deposited on SiO_2 results in a sharp interface [31].

Results

Several TTR scans were taken for each of the samples described above. The TBC of each was determined by fitting the model described in Eqs. (2)–(7) to TTR data. The proportionality constant relating the measured changes in reflectance to the changes in temperature was determined by fitting the TTR data to the model at approximately 100 ps, when the temperature gradient in the metal film is negligible and the film electrons and lattice are in local equilibrium.

Figure 3 shows the best fit for a 29 nm thick Pt film on a Si substrate, with $\sigma=1.45\times10^8$ W/m^2 K and all other inputs set to bulk values [32]. Although Fig. 3 does appear to have an excellent fit, it was found that in most cases a better fit was achieved by allowing the thermal conductivity of the substrate, k_s, to be a free

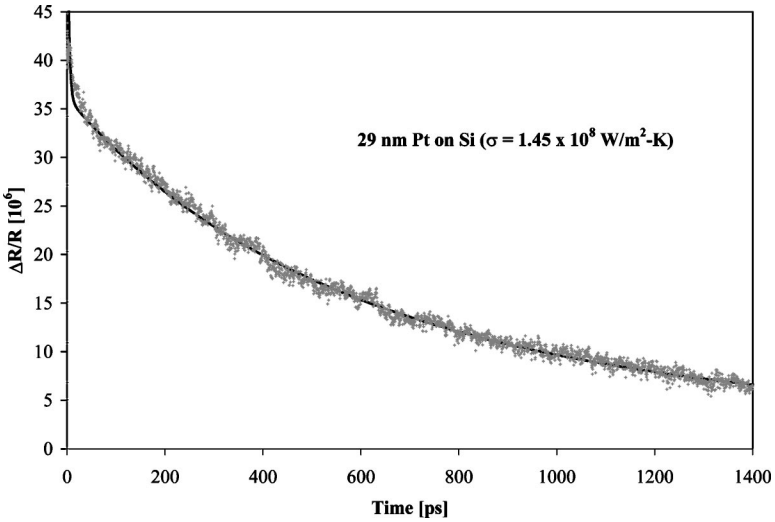

Fig. 3 Experimental results for 29 Pt film on Si

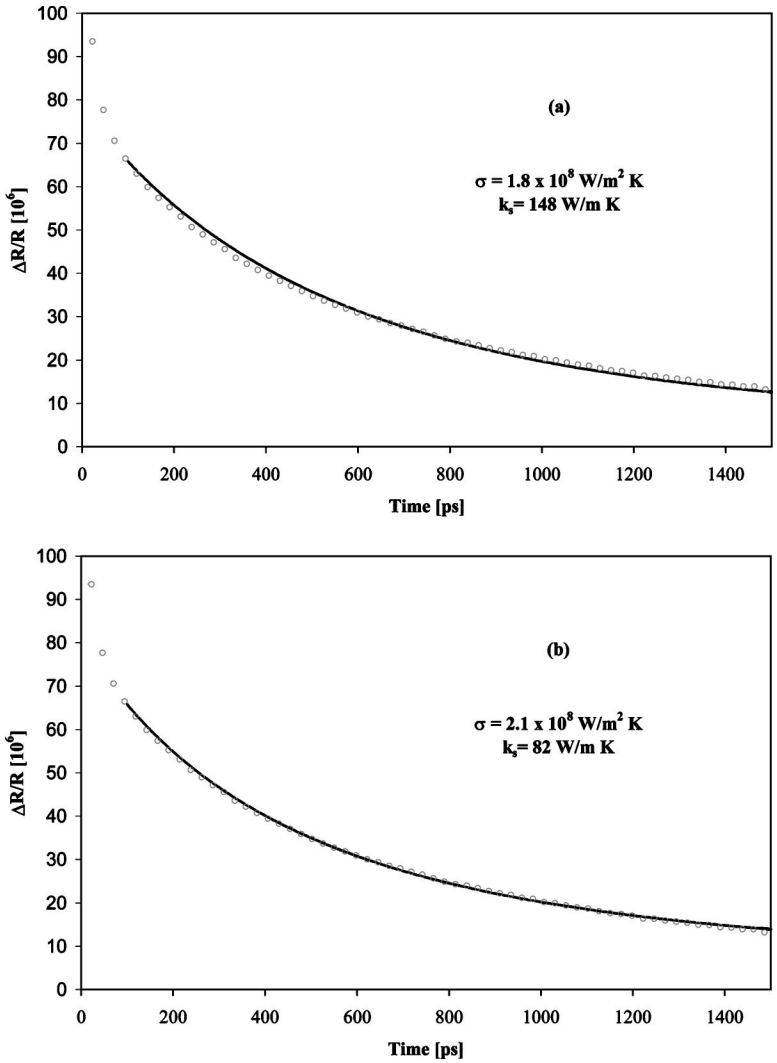

Fig. 4 Experimental results for 30 nm Cr film on Si with (a) bulk value used for k_s; and (b) k_s treated as a free parameter

parameter. The model is relatively insensitive to k_s. This method was employed by Stoner and Maris with the explanation that there is possibly a small damaged layer remaining near the surface of the substrate from predeposition processing and this causes the thermal conductivity to deviate from the bulk value [11]. In most cases, the model fits best when the assumed value of k_s is less than the bulk value by approximately a factor of 2 or more. Figure 4 shows a fit for a 30 nm Cr film on a Si substrate. Cr samples tended to give scans with little noise compared to Pt and other films, which can be seen by comparing Figs. 3 and 4. Figure 4(a) shows the results when the bulk value of $k_s = 148$ W/m K is employed, giving rise to a curve fit value of $\sigma = 1.8 \times 10^8$ W/m^2 K. Figure 4(b) shows the results obtained when k_s is treated as a free parameter. The best fit is obtained with a k_s of 82 W/m K and the resulting value of $\sigma = 2.1 \times 10^8$ W/m^2 K. The difference in the best fit for σ between using bulk values as opposed to allowing k_s to be a free parameter was less than 20% in most cases. Several scans were taken and fitted to the model described above with k_s treated as a free parameter. The averaged values for σ for the films tested can be found in Table 2.

As mentioned earlier, the model is also sensitive to uncertainties in the film heat capacity and thickness. The film thickness was measured, but bulk values were used for the film heat capacity, which is the product of the density and specific heat. Assuming an uncertainty in the total heat capacity of the film of 10%, uncertainties in σ are between 10–20% for the samples listed in Table 2. The uncertainty has a stronger impact for less conducting substrates, such as sapphire. Due to the sensitivity of the model to the heat capacity of the film, a significant effort should be made to measure film thickness and the density of the film to a greater degree of accuracy to gain greater confidence in the measured value of σ.

One possible explanation for the TBR and the reduced transmission of phonons across an interface is the discontinuity in the phonon density of states across the interface. If it is assumed that phonons of a particular frequency in the metal film can only couple with the same frequency phonons in the substrate, then the transmission probability will be small if the number of states in the substrate is small compared to those in the metal film or vice versa. Following this line of reasoning, one would expect that

Table 2 The average of best TBC, σ(10^8 W/m^2 K)

Substrate\Film	Au	Pt	Al	Cr
GaN			1.9	2.3
Si	0.71	1.4	1.2	2.0
Sapphire			2.0	1.9
AlN			2.3	2.0

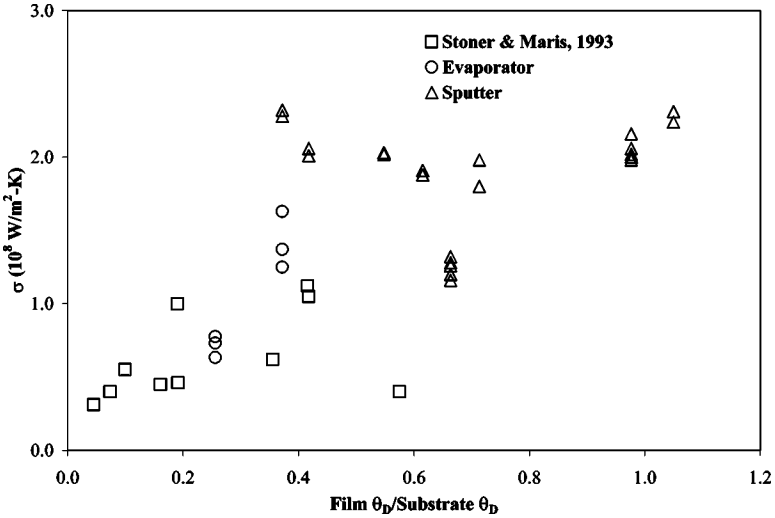

Fig. 5 TBC versus the ratio of Debye temperatures of the metal film and dielectric substrate. Some data are from Stoner and Maris [11].

materials with significantly different Debye temperatures would have a smaller phonon transmission probability compared to materials with similar Debye temperatures. Figure 5 shows the TBC data obtained from all scans performed for this study and data collected by Stoner and Maris [11] versus the film-substrate Debye temperature ratio. In general, for poorly overlapping film-substrate interfaces, where the Debye temperature ratio is small, there tends to be lower TBC values, while for better overlapping film-substrate interfaces there tends to be higher TBC values. Although this is not a conclusive trend, it is strong evidence that the phonon spectra disparity between two materials has a significant impact on the TBR of the interface. The DMM, which is the model often used in engineering analysis [2,3,5], accounts for the differences in the phonon spectra across interfaces.

To compare the DMM with the measured TBC, the TBC is calculated using the DMM assuming isotropic Debye solids for each sample. The ratios of the measured to the calculated DMM TBC versus the film-substrate Debye temperature ratio are presented graphically in Fig. 6. It is apparent from Fig. 6 that the DMM does not completely account for the trend for the room-temperature TBCs of the sample series. For interfaces with Debye temperature ratios greater than 0.4, the model overpredicts the TBC, while for dissimilar materials, the DMM underpredicts the TBC. For a more accurate application of the DMM, a realistic phonon density of states as opposed to the Debye model could be used, which was suggested by Swartz and Pohl [7]. When the realistic phonon density of states as opposed to the Debye model is used, the room-temperature DMM TBC is reduced as noted by Stoner and Maris [11] for Pb and Au on diamond and sapphire substrates and by Cahill et al. [20] for Al on a sapphire substrate. This may explain a portion of the overprediction of the Debye-based DMM for Debye-like interfaces. Unfortunately, the measured phonon density of states is not readily available in tabular form and it is rarely separated into the different phonon modes, making it difficult to use the DMM with realistic phonon density of states.

Another possible explanation for the overprediction of the Debye-based DMM is due to possible substrate damage and poor

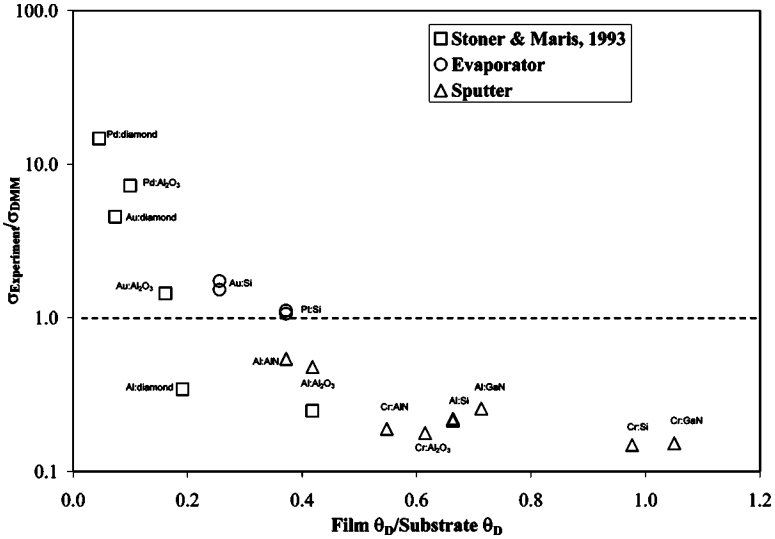

Fig. 6 Ratio of measured to theoretical DMM TBC versus the ratio of Debye temperatures of the metal film and dielectric substrate. Some data is from Stoner and Maris [11].

interface quality as suggested by Swartz and Pohl [9,11] and Stoner and Maris [11]. Substrate damage is a strong possibility for the Cr and Al samples which were sputtered etched. Just a 3–5 nm damage thickness with thermal conductivities on the order of amorphous materials (~1.5 W/m K) will result in thermal resistances ($2-3\times10^{-9}$ m^2 K/W) that are on the order of those measured for low mismatch interfaces (5×10^{-9} m^2 K/W). These large resistances associated with substrate damage could partially explain why there are little differences in the TBC for the samples with Debye temperature ratios above 0.4. The TBC for these Debye-type materials appear to be restricted due to some interface condition rather than the interface materials.

Costescu and Cahill measured TBC epitaxial interfaces with low mismatch materials [22]. For these interfaces, substrate damage and poor interfaces are not the issue [22]. Majumdar and Reddy suggested that a thermal resistance associated with electron-phonon coupling on the metal side of the interface accounted for the difference between the DMM and measured data [33]. Although, Majumdar's model appears to provide a good explanation for epitaxial interfaces, the effective electron-phonon resistance is small ($\sim<0.3\times10^{-9}$ m^2 K/W for Cr) for most metals. The effective electron-phonon resistance is negligible compared to the overall resistance measured for the Cr and Al interfaces. Therefore, the primary reason for overprediction of the TBC by the DMM appears to be related to defects at the interface. Future experiments are planned to investigate the effect of substrate damage and poor interfaces on the effective TBC.

Although the above explanations may account for the discrepancies between the DMM and experimental data for Debye-type interfaces, other explanations are needed to describe the large experimental TBC compared to the DMM TBC for dissimilar material interfaces. Embedded in the DMM is the assumption that only elastic phonon scattering occurs, in other words, phonons scattering at the interface maintain the same frequency and do not scatter into multiple phonons. Kosevich considered the role of subharmonic and multiharmonic phonon transmission on TBC [34]. By using both a harmonic and anharmonic model, Kosevich was able to show for a highly theoretical case that inelastic (subharmonic and multiharmonic) scattering makes a greater contribution to the TBC than elastic scattering for interfaces with very different vibrational spectra. Another mechanism for increased energy transport across mismatch interfaces, proposed by Sergeev, is due to inelastic scattering of electrons at the interface [35,36]. Sergeev's theoretical work focused on thin metal films on insulating substrate in the low-temperature limit, ($T<\theta_D$). It was assumed that a portion of the electron scattering around the interface released energy into the substrate phonon system. This TBC low-temperature model approximates the electronic scattering portion of the TBC to be $2-6\times10^7$ W/m^2 K, which is on the order of the measured TBC for dissimilar material interfaces. Huberman and Overhauser considered electrons in Pb transferring some of the electrons' energy to joint vibrational modes of a Pb–diamond interface and then to the diamond substrate [37]. Although the above theories appear plausible, they have been developed for highly theoretical or material specific interfaces. Unfortunately, to date, these theories have not been developed for a range or real interfaces. There also has been little experimental data to verify these proposed models. Further systematic testing is planned to test some of the theories in hopes of developing a practical and comprehensive model that can be applied to room-temperature interfaces.

Conclusions

A description of the TTR technique for measuring TBRs of thin metal film and dielectric substrates has been presented. The sensitivity and applicability of the TTR technique was discussed based on thermal properties of the interfacial materials. In particular, the technique is limited to thin metal films on substrates with thermal conductivities of approximately 25 W/m K or greater. The model is most sensitive to the TBC and the heat capacity of the film and only slightly sensitive to the thermal properties of the substrate.

A series of Cr, Al, Au, and Pt samples were carefully prepared to supplement existing TBR data in developing improved TBR theories. Scans of all the samples were conducted over several sessions and at different pump intensities to verify the repeatability of the TTR technique. The scans were fitted to the thermal model to determine the TBC. It was found that best fits were obtained by reducing the thermal conductivity of the substrate from book values. The TBC generally increases as the phonon density of states spectra of the metal film and dielectric substrate are better overlapped. It was shown that the DMM using the Debye solid approximation did not adequately account for the range of measured TBC. Brief explanations and potential transport mechanisms were presented to describe the discrepancies.

Acknowledgments

One of the authors (R. S.) would like to thank the UVA's Science and Engineering of Laser Interaction with Matter: NSF IGERT fellowship program for supporting his work. The authors also acknowledge financial support of the NSF (Grant No. CTS-9908372). Another author (A. S.) greatly appreciates the financial support of the Office of Naval Research. The authors give special thanks to Dr. Richard Henry of the Naval Research Lab for providing the GaN samples and Arthur Lichtenberger for making many of the samples.

Nomenclature

C = heat capacitance, J/(m^3 K)
d = film thickness and location of interface, m
F = laser fluence, J/m^2
q'' = heat flux across interface, W/m^2
R = reflectance of metal film
t = time, s
x = coordinate from top of film surface, m
δ = energy deposition depth into the film, m
ΔT = temperature drop across film-substrate interface, K
θ = temperature above ambient, K
θ_D = Debye temperature under the low-temperature limit, K
κ = thermal conductivity, W/(m K)
σ = thermal boundary conductance, W/(m^2 K)
τ = thin film diffusion time constant, s
τ_i = interface time constant, s

Subscripts

f = thin film
s = substrate

References

[1] Mahan, G. D., and Woods, L. M., 1998, ''Multilayer Thermionic Refrigeration,'' Phys. Rev. Lett., **80**, pp. 4016–4019.
[2] da Silva, L. W., and Kaviany, M., 2002, ''Miniaturized Thermoelectric Cooler,'' *Proc. 2002 ASME International Mechanical Engineering Congress and Exposition*, ASME, New York, pp. IMECE2002-32437 1–15.
[3] Phelan, P. E., 1998, ''Application of Diffuse Mismatch Theory to the Prediction of Thermal Boundary Resistance in Thin-Film High-*Tc* Superconductors,'' ASME J. Heat Transfer, **120**, pp. 37–43.
[4] Phelan, P. E., Song, Y., Nakabeppu, O., Ito, K., Hijikata, K., Ohmori, T., and Torikoshi, K., 1994, ''Film/Substrate Thermal Boundary Resistance for an Er–Ba–Cu–O High-*Tc* Thin Film,'' ASME J. Heat Transfer, **116**, pp. 1038–1041.
[5] Filippov, K. A., and Balandin, A. A., 2003, ''The Effect of the Thermal Boundary Resistance on Self-Heating of AlGaN/GaN HFETs,'' MRS Internet J. Nitride Semicond. Res., **8**, pp. 1–4.
[6] Kim, E.-K., Kwun, S.-I., Lee, S.-M., Seo, H., and Yoon, J.-G., 2000, ''Thermal Boundary Resistance at Ge2Sb2Te5/ZnS:SiO2 Interface,'' Appl. Phys. Lett., **76**, pp. 3864–3866.
[7] Swartz, E. T., and Pohl, R. O., 1989, ''Thermal Boundary Resistance,'' Rev. Mod. Phys., **61**, pp. 605–668.

[8] Little, W. A., 1959, ''The Transport of Heat Between Dissimilar Solids at Low Temperatures,'' Can. J. Phys., **37**, pp. 334–349.
[9] Swartz, E. T., and Pohl, R. O., 1987, ''Thermal Resistance at Interfaces,'' Appl. Phys. Lett., **51**, pp. 2200–2202.
[10] Young, D. A., and Maris, H. J., 1989, ''Lattice-Dynamical Calculation of the Kapitza Resistance Between fcc Lattices,'' Phys. Rev. B, **40**, pp. 3685–3693.
[11] Stoner, R. J., and Maris, H. J., 1993, ''Kapitza Conductance and Heat Flow Between Solids at Temperatures From 50 to 300 K,'' Phys. Rev. B, **48**, pp. 16373–16387.
[12] Pettersson, S., and Mahan, G. D., 1990, ''Theory of the Thermal Boundary Resistance Between Dissimilar Lattices,'' Phys. Rev. B, **42**, pp. 7386–7390.
[13] Kechrakos, D., 1991, ''The Role of Interface Disorder in Thermal Boundary Conductivity Between Two Crystals,'' J. Phys.: Condens. Matter, **3**, pp. 1443–1452.
[14] Fagas, G., Kozorezov, A. G., Lambert, C. J., and Wigmore, J. K., 1999, ''Lattice-Dynamical Calculation of Phonon Scattering at a Disordered Interface,'' Physica B, **263–264**, pp. 739–741.
[15] Cahill, D. G., Ford, W. K., Goodson, K. E., Mahan, G. D., Majumdar, A. M., Humphrey, J., Merlin, R., and Phillpot, S. R., 2003, ''Nanoscale Thermal Transport,'' J. Appl. Phys., **93**, pp. 793–818.
[16] Rosencwaig, A., Opsal, J., Smith, W. L., and Willenborg, D. L., 1985, ''Detection of Thermal Waves Through Optical Reflectance,'' Appl. Phys. Lett., **46**, pp. 1013–1015.
[17] Pottier, L., 1994, ''Micrometer Scale Visulatization of Thermal Waves by Photoreflectance Microscopy,'' Appl. Phys. Lett., **64**, pp. 1618–1619.
[18] Li, B., and Zhang, S., 1997, ''The Effect of Interface Resistances on Thermal Wave Propagation in Multilayered Samples,'' J. Phys. D, **30**, pp. 1447–1454.
[19] Li, B., Roger, J. P., Pottier, L., and Fournier, D., 1999, ''Complete Thermal Characterization of Film-on-Substrate System by Modulated Thermoreflectance Microscopy and Multiparameter Fitting,'' J. Appl. Phys., **86**, pp. 5314–5316.
[20] Cahill, D. G., Bullen, A., and Lee, S.-M., 2000, ''Interface Thermal Conductance and the Thermal Conductivity of Multilayer Thin Films,'' High Temp. - High Press., **32**, pp. 135–142.
[21] Lee, S.-M., and Cahill, D. G., 1997, ''Heat Transport in Thin Dielectric Films,'' J. Appl. Phys., **81**, pp. 2590–2595.
[22] Costescu, R. M., Wall, M. A., and Cahill, D. G., 2003, ''Thermal Conductance of Epitaxial Interfaces,'' Phys. Rev. B, **67**, pp. 054302 1–5.
[23] Smith, A. N., Caffrey, A. P., Klopf, M. J., and Norris, P. M., 2001, ''Importance of Signal Phase on the Transient Thermoreflectance Response as a Thermal Sensor,'' *Proc. of the 35th National Heat Transfer Conference*, ASME, New York, pp. NHTC01 11221 1–6.
[24] Capinski, W. S., and Maris, H. J., 1996, ''Improved Apparatus for Picosecond Pump-and-Probe Optical Measurements,'' Rev. Sci. Instrum., **67**, pp. 2720–2726.
[25] Qiu, T. Q., and Tien, C. L., 1992, ''Short-Pulse Laser Heating of Metals,'' Int. J. Heat Mass Transfer, **35**, pp. 719–726.
[26] Smith, A., Hostetler, J. L., and Norris, P. M., 2000, ''Thermal Boundary Resistance Measurements Using a Transient Thermoreflectance Technique,'' Microscale Thermophys. Eng., **4**, pp. 51–60.
[27] Kittel, C., 1996, *Introduction to Solid State Physics*, 7th ed., Wiley, New York.
[28] Fugate, R. Q., and Swenson, C. A., 1969, ''Specific Heat of Al2O3 From 2 to 25 K,'' J. Appl. Phys., **40**, pp. 3034–3036.
[29] Levinshtein, M. E., Rumyantsev, S. L., and Shur, M. S., eds., 2001, *Properties of Advanced Semiconductor Materials: GaN, AlN, InN, BN, SiC, SiGe*, Wiley-Interscience, New York, p. 216.
[30] Franciosi, A., Peterman, D. J., Weaver, J. H., and Moruzzi, V. L., 1982, ''Structural Morphology and Electronic Properties of the Si–Cr Interface,'' Phys. Rev. B, **25**, pp. 4981–4993.
[31] Hiraki, A., Shuto, S., Kim, S., Kammura, W., and Iwami, M., 1977, ''Room-Temperature Interfacial Reaction in Au-Semiconductor,'' Appl. Phys. Lett., **31**, pp. 611–612.
[32] Touloukian, Y. S., 1970, *Thermophysical Properties of Matter*, Plenum, New York.
[33] Majumdar, A., and Reddy, P., 2004, ''Role of Electron-Phonon Coupling in Thermal Conductance of Metal-Nonmetal Interfaces,'' Appl. Phys. Lett., **84**, pp. 4768–4770.
[34] Kosevich, Y. A., 1995, ''Fluctuation Subharmonic and Multiharmonic Phonon Transmission and Kapitza Conductance Between Crystals With Very Different Vibrational Spectra,'' Phys. Rev. B, **52**, pp. 1017–1024.
[35] Sergeev, A., 1999, ''Inelastic Electron-Boundary Scattering in Thin Films,'' Physica B, **263**, pp. 217–219.
[36] Sergeev, A. V., 1998, ''Electronic Kapitza Conductance Due to Inelastic Electron-Boundary Scattering,'' Phys. Rev. B, **58**, pp. R10199–10202.
[37] Huberman, M. L., and Overhauser, A. W., 1994, ''Electronic Kapitza Conductance at a Diamond-Pb Interface,'' Phys. Rev. B, **50**, pp. 2865–2873.

Jader R. Barbosa, Jr.[1]
Department of Mechanical Engineering,
Federal University of Santa Catarina,
Florianópolis—SC—88040900,
Brazil
e-mail: jrb@nrva.ufsc.br

Geoffrey F. Hewitt
Department of Chemical Engineering and
Chemical Technology, Imperial College,
London,
Prince Consort Road,
London, SW7 2BY, UK
e-mail: g.hewitt@imperial.ac.uk

A Thermodynamic Nonequilibrium Slug Flow Model

This paper presents a calculation methodology to predict the peaks in heat transfer coefficient at near zero equilibrium quality observed in forced convective boiling in vertical conduits. The occurrence of such peaks is typical of low latent heat, low thermal conductivity systems (such as refrigerants and hydrocarbons), and of systems in which the vapor volume formation rate for a given heat flux is large (low-pressure water). The methodology is based on a model that postulates that the mechanism behind the heat transfer coefficient enhancement is the existence of thermodynamic nonequilibrium slug flow, i.e., a type of slug flow in which rapid bubble growth in subcooled boiling leads to the formation of Taylor bubbles separated by slugs of subcooled liquid. Results are compared with experimental data for forced convective boiling of pure hydrocarbons and show considerable improvement over existing correlations. [DOI: 10.1115/1.1857945]

1 Introduction

Several classes of heat transfer equipment operate at moderate exit qualities and low-to-moderate mass and heat fluxes [1,2]. Under these conditions, intermittent flow patterns, such as slug flow and churn flow, are more likely to prevail than annular flow. Wadekar and Kenning [1] and Wadekar [2] explored the reasons for the lack of experimental data and of suitable predictive methods, despite the industrial significance of such flows.

As pointed out by Collier and Thome [3] and by Hewitt [4,5], the classical representation of forced convective boiling under low wall heat flux conditions implies that the heat transfer coefficient rises in the subcooled boiling region, and then is roughly constant until the point where the convective boiling dominant region is reached. Nevertheless, a number of studies demonstrate that, under some conditions, a very distinctive departure from the classic behavior takes place. For example, recent experimental work on the boiling of pure hydrocarbons (*n*-pentane and iso-octane) in a vertical electrically heated test section [6,7] showed that the heat transfer coefficient is locally enhanced in the region near zero equilibrium quality.

The objective of this paper is to examine the mechanisms which can lead to this local heat transfer enhancement and to present a methodology capable of predicting the heat transfer coefficient behavior near zero quality [6]. The postulated mechanism is the existence of local thermal nonequilibrium instabilities leading to an abrupt flow pattern transition in the subcooled region [8,9]. As will be seen, conditions of the experimental data against which the present method will be compared are favorable to the occurrence of such types of instability.

This paper is organized as follows. In Sec. 2, an account of the experimental observations of the peaks in heat transfer coefficient is made together with possible explanations for the heat transfer enhancement. The proposed calculation methodology is described in detail in Sec. 3. Results are presented in Sec. 4, where the present method is compared with experimental data for two hydrocarbons and with predictions from existing correlations. Finally, conclusions are presented in Sec. 5.

2 Heat Transfer Coefficient Peaks Near Zero Quality

2.1 Experimental Observations. A detailed compilation of experimental data showing near zero equilibrium quality heat transfer coefficient peaks has been presented by Hewitt [4,5]. Cheah [10] observed peaks in the heat transfer coefficient in boiling water in vertical tubes at subatmospheric pressures (250 mbar). The peaks were not observed at atmospheric pressure. Similar behavior has been reported by Thome [11] for the boiling of refrigerants in horizontal tubes.

The first systematic investigation of the heat transfer enhancement near zero qualities was made by Kandlbinder [6], who conducted experiments on flow boiling of pentane and iso-octane in a (0.0254 mm inner diameter, 8.5 m long) vertical tube. Kandlbinder's experiments covered ranges of mass flux from 140 to 510 kg/m^2 s, of heat flux from 10 to 60 kW/m^2, of inlet subcooling from 40°C to 10°C, and of pressure from 2.4 to 10 bar. A typical example of the heat transfer coefficient enhancement phenomenon observed by Kandlbinder is depicted in Fig. 1. Here, the time-averaged local heat transfer coefficient is defined as

$$\overline{\alpha} = \frac{\dot{q}_w}{T_w - T_b} \tag{1}$$

Figure 1 also shows the profiles of local thermodynamic equilibrium quality and of local equilibrium subcooling (the difference between the saturation temperature corresponding to the local pressure and the thermodynamic equilibrium bulk temperature).

Figure 2 shows the axial distribution of temperatures measured at the center of the pipe by Kandlbinder [6] for the same case depicted in Fig. 1. Profiles of calculated thermodynamic equilibrium bulk temperature, saturation temperature, and slug temperature (to be defined in Sec. 3) are also presented. As can be seen, the existence of thermal nonequilibrium (characterized by the difference between the equilibrium temperature and the experimental values) persists over some distance downstream of the theoretical point of net vapor generation (NVG) [12]. Allowing for some experimental uncertainty, this distance is of the order of 2 m in the case of Fig. 2. More recently, Urso et al. [7] extended Kandlbinder's database by conducting experiments using iso-octane over a lower range of mass fluxes (70 to 300 kg/m^2 s). The objective of Urso et al.'s work was to obtain a wider range of qualities over which the subannular regimes (bubble, slug, and churn) would persist. The heat transfer coefficient peaks at near zero quality were also observed consistently.

2.2 Prediction Efforts. As yet, no calculation method satisfactorily predicts the trends of heat transfer coefficient leading to an enhancement near zero quality. Kandlbinder [6] compared his data for the saturated boiling region ($\overline{T_b} = T_{sat}$) with the correlations of Chen [13], Shah [14], Kandlikar [15], and Steiner and Taborek [16]. Although the correlations performed satisfactorily over the whole saturated data range (average errors less than 25%

[1]Author to whom correspondence should be addressed.

Manuscript received December 22, 2003; revision received September 10, 2004. Review conducted by: J. Chung.

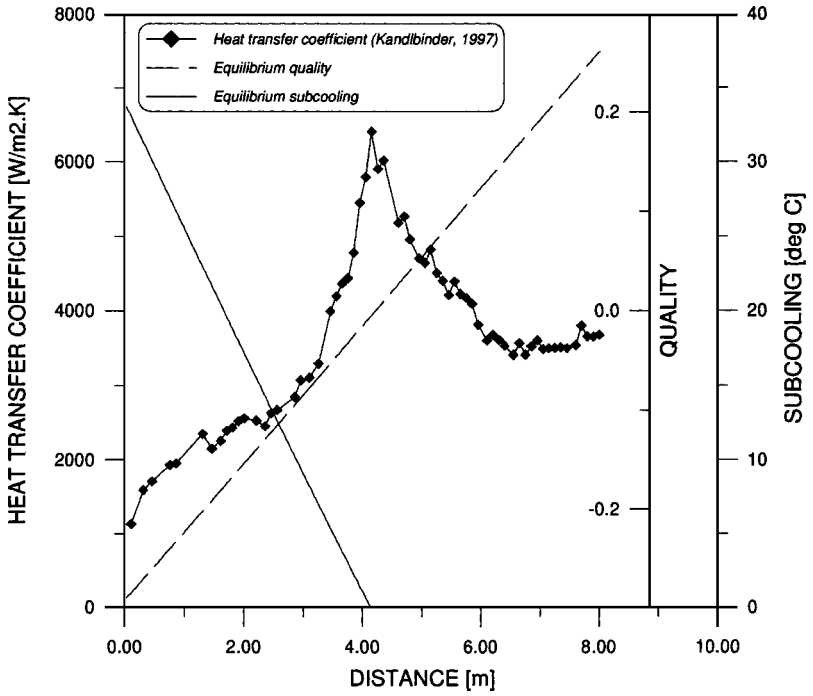

Fig. 1 Heat transfer coefficient enhancement near zero quality. Experimental conditions: fluid: *n*-pentane, inlet pressure: 6.0 bar, total mass flux: 377.4 kg/m^2 s, wall heat flux: 49.9 kW/m^2, inlet temperature: 67.5°C.

and standard deviations of the order of 20% to 30%), they have severely underpredicted the experimental heat transfer coefficient in the region near zero quality.

Urso et al. [7] were the first to include some mechanistic insight into the calculation procedure. They made use of a modified version of a model for slug flow heat transfer [1,2]. No attempt, however, was made to take account of thermal nonequilibrium effects (see Sec. 2.3. below) in the methodology. Their model provided results which generally agreed with their own data, but failed to predict the heat transfer coefficient behavior near zero vapor qualities.

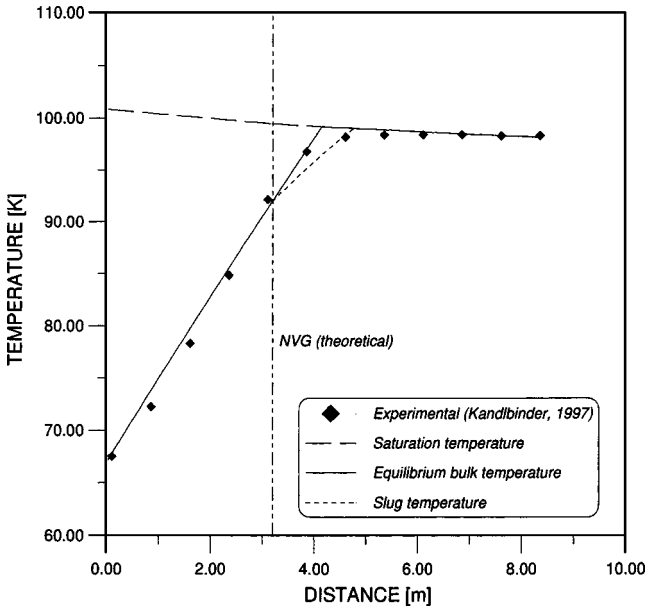

Fig. 2 Profiles of experimental (center line), saturation, equilibrium bulk and liquid slug temperature profiles. Experimental conditions: fluid: n-pentane, inlet pressure: 6.0 bar, mass flux: 377.4 kg/m^2 s, wall heat flux: 49.9 kW/m^2, inlet temperature: 67.5°C.

2.3 Discussion of Mechanisms. Hewitt [4,5] suggested that the most probable explanation for the occurrence of the near zero quality peak in heat transfer coefficient was the existence of a local thermal instability of the type observed by Jeglic and Grace [8] and Ishii [9]. Basically, in a situation where the conditions for bubble nucleation at the wall are poor, the layer of fluid adjacent to the wall becomes highly superheated. Therefore, once a bubble is nucleated, it grows rapidly, suddenly releasing the thermal energy stored in the surrounding liquid. Jeglic and Grace [8] showed that the rate of change in void fraction in the subcooled region was high and abrupt and that it was associated with the formation of a vapor slug. In summary, there are four aspects that favor the occurrence of the observed enhancement mechanism. These are as follows:

1. *Large vapor formation for a given superheat*. This implies high liquid-to-gas density ratios and/or low latent heat of vaporization;
2. *Low liquid thermal conductivity leading to large differences between the wall temperature and the local saturation temperature*. This explains the occurrence of this type of enhancement in flows of organic fluids and refrigerants;
3. *High subcooling*. In light of their experimental results, Jeglic and Grace [8] concluded that the abrupt transition associated with the formation of a vapor plug took place when the subcooling was significant. One, therefore, expects that at low subcooling, nucleate boiling at the wall initiates early in the test section, thus preventing excessive superheats in the liquid; and
4. *Low mass transfer resistance to bubble growth*. In mixture systems, the less volatile material concentrates on the liquid side of the interface and offers an additional resistance to rapid bubble growth. This is probably the reason for near zero quality enhancement observed by Kandlbinder [6] only during the single component boiling experiments.

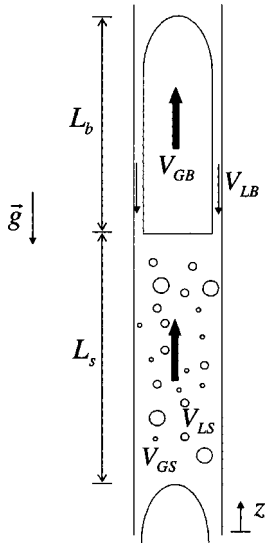

Fig. 3 A schematic representation of real slug flow

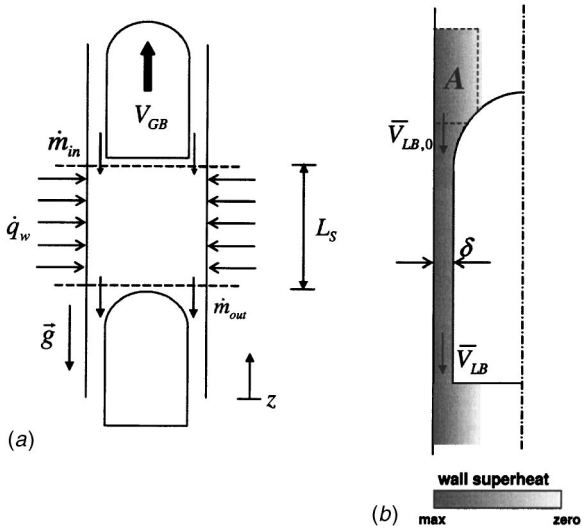

Fig. 4 (*a*) A schematic representation of the transfer of energy into the liquid slug; (*b*) illustration of the wall superheat and the liquid shedding into the film region

3 The Methodology

3.1 Slug Flow and Thermal Nonequilibrium. The basic structure of the present model is a slug unit that consists of a Taylor bubble surrounded by a falling liquid film and a liquid slug, as seen in Fig. 3. Theoretical models for the prediction of adiabatic slug flows [17–20] rely on solutions of time- and area-averaged mass and momentum conservation equations for the Taylor bubble and liquid slug regions using appropriate closure relations. A similar approach will be pursued here taking account of nonequilibrium effects on the structure of the flow.

It is assumed that the abrupt vapor growth in the subcooled region gives rise to the formation of Taylor bubbles. As they are formed, the Taylor bubbles become separated by regions of subcooled liquid (slugs). The falling film surrounding the Taylor bubble is presumed saturated, i.e., a considerable portion of the energy associated with the high wall temperatures in the near-wall region is used up during the process of generation of the Taylor bubble. Phase change and gas holdup within the liquid slug are assumed negligible.

An energy balance over the slug unit gives

$$\frac{dm_G}{dt}\Delta h_v + m_S c_{pL}\frac{d\overline{T}_S}{dt} = \dot{Q} \tag{2}$$

where m_G is the mass of vapor in the Taylor bubble, and m_s is the mass of the liquid slug. As $\dot{Q}=\pi\dot{q}_w d_T(L_B+L_S)$ and $m_S=\pi\rho_L L_S d_T^2/4$, Eq. (2) becomes

$$\frac{dm_G}{dt} = \frac{\pi d_T}{\Delta h_v}\left[\dot{q}_w(L_B+L_S) - \frac{d_T}{4}\rho_L c_{pL}\frac{d\overline{T}_S}{dt}\right] \tag{3}$$

The masses of vapor and liquid within the slug unit are given by

$$m_G = \rho_G L_B \frac{\pi(d_T-2\delta)^2}{4} \tag{4}$$

$$m_L = \rho_L\frac{\pi}{4}\{L_S d_T^2 + L_B[d_T^2-(d_T-2\delta)^2]\} \tag{5}$$

By combining the overall mass conservation

$$dm_G = -dm_L \tag{6}$$

with Eqs. (3) to (5) assuming that: (i) The thickness of the liquid film surrounding the Taylor bubble is small compared with the pipe diameter, (ii) the mass of the liquid film is small compared with that of the slug, and (iii) that the densities do not vary strongly with time/distance, one obtains

$$\frac{dL_B}{dt} = \frac{1}{\rho_G\Delta h_v}\left[\frac{4\dot{q}_w(L_B+L_S)}{d_T} - \rho_L c_{pL}L_S\frac{d\overline{T}_S}{dt}\right] \tag{7}$$

$$\frac{dL_S}{dt} = \frac{1}{\Delta h_v}\left[c_{pL}L_S\frac{d\overline{T}_S}{dt} - \frac{4\dot{q}_w(L_B+L_S)}{\rho_L d_T}\right] \tag{8}$$

As a *system*, the slug unit moves at a velocity equal to the rise velocity of the (center of mass of the) Taylor bubble through the pipe. Therefore, for a stationary observer assuming that $V_{GB} \gg dL_B/dt$, then $dt/dz=1/V_{GB}$ and Eqs. (7) and (8) become

$$\frac{dL_B}{dz} = \frac{1}{\rho_G\Delta h_v}\left[\frac{4\dot{q}_w(L_B+L_S)}{d_T V_{GB}} - \rho_L c_{pL}L_S\frac{d\overline{T}_S}{dz}\right] \tag{9}$$

$$\frac{dL_S}{dz} = \frac{1}{\Delta h_v}\left[c_{pL}L_S\frac{d\overline{T}_S}{dz} - \frac{4\dot{q}_w(L_B+L_S)}{\rho_L d_T V_{GB}}\right] \tag{10}$$

The average slug temperature profile $d\overline{T}_S/dz$ is determined through an energy balance in the liquid slug. This can be written as follows [see Fig. 4(a)]

$$\dot{Q}_S = \frac{d}{dt}(e_S m_S) - \dot{m}_{\text{in}}h_{\text{in}} + \dot{m}_{\text{out}}h_{\text{out}} \tag{11}$$

where e_S is the internal energy of the liquid slug, and $\dot{m}_{\text{in}}$ and $\dot{m}_{\text{out}}$ are the mass flow rates entering and leaving the liquid slug, respectively. It is assumed that compressibility effects in the liquid slug are negligible ($c_p \approx c_v$). In light of previous hypotheses, the combination of overall mass conservation and mass conservation in the Taylor bubble region gives

$$\frac{d}{dt}m_S = -\frac{d}{dt}m_G = \dot{m}_{\text{in}} - \dot{m}_{\text{out}} \tag{12}$$

Preliminary calculations, of the same nature of those performed in [18], showed that the fraction of the liquid slug cross section from which liquid is drawn into the falling film, is relatively thin. Given that the superheat in the fluid layers adjacent to the wall is considerably high, the liquid in the fraction of the slug cross section that supplies liquid to the film [region "A" of Fig. 4(b)] is likely to have an average temperature close to the saturation temperature. Thus, since saturation has been assumed in the Taylor bubble

region, it is hypothesized that $h_{in} \approx h_{out}$. Following the above simplifications, and substituting $\dot{Q}_S = \dot{q}_w L_S \pi d_T$ and $m_G = \pi \rho_G L_B d_T^2/4$, Eq. (11) becomes

$$\frac{d\overline{T}_S}{dt} = \frac{4}{d_T}\frac{\dot{q}_w}{\rho_L c_{pL}} - \frac{\rho_G}{\rho_L}\frac{1}{L_S}\frac{dL_B}{dt}(T_{sat} - \overline{T}_S) \tag{13}$$

Since the liquid slug travels at a velocity V_{LS}, the above equation can be written as

$$\frac{d\overline{T}_S}{dz} = \frac{4}{d_T}\frac{\dot{q}_w}{\rho_L c_{pL} V_{LS}} - \frac{\rho_G}{\rho_L}\frac{1}{L_S}\frac{dL_B}{dz}(T_{sat} - \overline{T}_S) \tag{14}$$

In the thermal nonequilibrium region, i.e., $\overline{T}_S(z) < T_{sat}$, the liquid slug temperature gradient, the Taylor bubble growth rate, and the liquid slug contraction rate are given by the simultaneous solution of Eqs. (9), (10), and (14). A stepwise solution of this system of equations gives local values of L_B, L_S, and $\overline{T}_S$ along the thermal nonequilibrium region. Calculation of additional slug flow parameters and determination of boundary conditions are addressed in the next section.

3.2 Modeling

3.2.1 Slug Flow Parameters. In this work, ideal slug flow (no vapor entrainment in the liquid slug) is assumed. Although this is an oversimplification of the real situation and may lead to some discrepancies, it does not alter qualitatively the main results and conclusions of the present formulation.

As can be seen from several models available in the literature [17–20], under the ideal slug flow assumption and for steady-state conditions, the overall vapor mass balance and the mass conservation equations for the mixture in the Taylor bubble and liquid slug regions become

$$U_{GS} = \beta \epsilon_B V_{GB} \tag{15}$$

$$\epsilon_B V_{GB} + (1-\epsilon_B) V_{LB} = U_M \tag{16}$$

$$V_{LS} = U_M \tag{17}$$

where $U_M = U_{GS} + U_{LS} = G[(1-x_G)/\rho_L + x_G/\rho_G]$ is the mixture velocity, $\beta = L_B/(L_B+L_S)$, and the film thickness and the void fraction in the Taylor bubble region are related by $\delta = d_T(1-\epsilon_B^{1/2})/2$. The Taylor bubble velocity is given by the expression of Nicklin et al. [21]

$$V_{GB} = 1.2U_M + V_0 \tag{18}$$

where $V_0 = \gamma(g d_T)^{1/2}$ is the rise velocity of a Taylor bubble in quiescent liquid given by Wallis [22]. The parameter γ was correlated by

$$\gamma = 0.345\left[1 - \exp\left(-\frac{0.01 N_f}{0.345}\right)\right]\left[1 - \exp\left(\frac{3.37 - Bo}{m}\right)\right] \tag{19}$$

where

$$m = \begin{cases} 10 & \text{when } N_f > 250 \\ 69/N_f^{-0.35} & \text{when } 18 < N_f < 250 \\ 25 & \text{when } N_f < 18 \end{cases} \tag{20}$$

The falling film velocity is given by [22]

$$V_{LB} = \begin{cases} -0.333\left(\dfrac{g d_T^2 \rho_L}{\eta_L}\right)(1-\epsilon_B^{1/2})^2, & \text{when } \mathrm{Re}_f < 750 \\ -11.2[g d_T (1-\epsilon_B^{1/2})]^{1/2}, & \text{when } \mathrm{Re}_f > 750 \end{cases} \tag{21}$$

where $\mathrm{Re}_f = |V_{LB}|\rho_L \delta/\eta_L$ is the falling film Reynolds number. In the present methodology, Eqs. (15)–(21) are solved together with Eqs. (9), (10), and (14). At each step Δz, a value of β is calculated and introduced together with the physical properties in Eqs. (15)–(21) to give the local value of the real quality, x_G, and also other slug flow parameters.

3.2.2 Boundary Conditions. The distance from the pipe inlet up to the point where slug flow takes place, z_0, must be defined along with boundary conditions for Eqs. (9), (10), and (14). In the present work, it is believed that the classical (i.e., textbook) representation of the onset of the boiling and phase change (see Fig. 5.1 of Collier and Thome, [3]) is not applicable and the onset of nucleation is associated with a sudden increase in void fraction associated with the formation of a vapor plug [8]. In the absence of a specific method to determine z_0, the Saha and Zuber [12] NVG model was employed. Although Saha and Zuber's correlation is not strictly applicable to the present situation (boiling of hydrocarbons), it remains the most accurate of its kind [3] and is, to the authors' judgement, the best approximation given the current resources. The model of Saha and Zuber [12] also provides the liquid slug temperature at the onset of slug flow, $\overline{T}_{S,o}$.

The specification of the lengths of the liquid slug and Taylor bubble regions at the onset of slug flow, $L_{S,o}$ and $L_{B,o}$, is somewhat arbitrary. Values of L_S in equilibrium slug flow reported in the literature range from $12d_T$ to $20d_T$ [23,24]. Equilibrium slug flow models usually employ an intermediate value, i.e., $16d_T$ [25,26]. Here, for consistency, it has been assumed that $L_{S,o} = 16d_T$. The length of the Taylor bubble region at the onset of slug flow was specified based on an estimate of the minimum stable Taylor bubble length, $L_{B,\min}$, which would enable bubble growth with distance. $L_{B,\min}$ was determined by a search for the local minimum of Eq. (9) through $d^2L_B/dz^2 = 0$. In the present calculations, the value of $L_{B,o}$ was taken as $1.2L_{B,\min}$. As no direct experimental data on the initial bubble length were available to confirm this hypothesis, several values of $L_{B,o}$ were tested, and the value which provided the best agreement in terms of calculated heat transfer coefficient was selected. Nevertheless, results showed that the sensitivity of the calculated heat transfer coefficient to the choice of $L_{B,o}$ was marginal and even variations as high as 50% of $L_{B,\min}$ did not affect the results significantly. This is, however, an aspect of the methodology which certainly deserves further investigation.

3.3 Time-Averaged Local Heat Transfer. The time-averaged local heat transfer coefficient has been defined by Eq. (1). In the slug flow regime, the local time-averaged wall temperature is given by (disregarding the thermal capacity of the heated wall)

$$\overline{T}_w = \frac{1}{t_{sp}}\int_0^{t_{sp}} T_w dt \tag{22}$$

Taking into account the existence of a Taylor bubble region and a liquid slug region, one can write

$$\overline{T}_w = \frac{1}{t_{sp}}\left[\int_0^{t_{sf}} T_w dt + \int_{t_{sf}}^{t_{sf}+t_{ss}} T_w dt\right] = \frac{1}{t_{sp}}(t_{sf}\overline{T}_{w,f} + t_{ss}\overline{T}_{w,S}) \tag{23}$$

As mentioned before, as a system, the slug unit moves at a uniform velocity V_{GB}. Thus, $t_{ss} = L_S/V_{GB}$, $t_{sf} = L_B/V_{GB}$, and $t_{sp} = (L_S+L_B)/V_{GB}$. In terms of the length fraction of the slug unit occupied by the Taylor bubble region, Eq. (23) can be written as

$$\overline{T}_w = \beta\overline{T}_{w,f} + (1-\beta)\overline{T}_{w,S} \tag{24}$$

3.4 Heat Transfer in the Liquid Slug. Heat transfer in the liquid slug region is calculated using a superposition model [13], assuming slug body subcooling. Thus

$$\dot{q}_w = \overline{\alpha}_{fc,S}(\overline{T}_{w,S} - \overline{T}_S) + \overline{\alpha}_{nb,S}(\overline{T}_{w,S} - T_{sat}) \tag{25}$$

or, in terms of $\overline{T}_{w,S}$

$$\overline{T}_{w,S}=\frac{\dot{q}_w+\overline{\alpha}_{fc,S}\overline{T}_S+\overline{\alpha}_{nb,S}T_{\text{sat}}}{\overline{\alpha}_{fc,S}+\overline{\alpha}_{nb,S}} \tag{26}$$

The forced convective heat transfer coefficient in the liquid slug is given by

$$\overline{\alpha}_{fc,S}=F\overline{\alpha}_{c,S} \tag{27}$$

where

$$\overline{\alpha}_{c,S}=0.023\frac{\lambda_L}{d_T}\text{Re}_{LS}^{0.8}\text{Pr}_L^{0.4} \tag{28}$$

and $\text{Re}_{LS}=\rho_L V_{LS} d_T/\eta_L$ is the Reynolds number associated with the liquid slug. F is the Chen [13] two-phase enhancement factor. In the subcooled slug region, F is set equal to unity [3,27], since the slug void fraction is disregarded. The nucleate boiling heat transfer coefficient was calculated from $\overline{\alpha}_{nb,S}=S\overline{\alpha}_{n,S}$, where

$$\overline{\alpha}_{n,S}=0.00122\frac{\lambda_L^{0.79}c_{pL}^{0.45}\rho_L^{0.49}(\overline{T}_{w,S}-T_{sat})^{0.24}(p_{w,S}-p_{sat})^{0.75}}{\sigma^{0.5}\eta_L^{0.29}\rho_G^{0.24}h_{LG}^{0.24}} \tag{29}$$

is the Forster and Zuber [28] correlation and

$$S=(1+2.53\times 10^{-6}\,\text{Re}_{LS}^{1.17})^{-1} \tag{30}$$

is the Chen [13] nucleate boiling suppression factor.

3.5 Heat Transfer in the Taylor Bubble. Heat transfer in the Taylor bubble region is modeled assuming superposition of heat transfer mechanisms [13] and saturation in the vicinity of the Taylor bubble. Thus

$$\dot{q}_w=(\overline{\alpha}_{fc,f}+\overline{\alpha}_{nb,f})(\overline{T}_{w,f}-T_{\text{sat}}) \tag{31}$$

or

$$\overline{T}_{w,f}=T_{\text{sat}}+\frac{\dot{q}_w}{\overline{\alpha}_{fc,f}+\overline{\alpha}_{nb,f}} \tag{32}$$

In the film region, the heat transfer coefficient is calculated using the correlation of Chun and Seban [29]

$$\frac{\overline{\alpha}_{fc,f}}{\lambda_L}\left(\frac{\eta_L^2}{\rho_L^2 g}\right)^{1/3}=0.0038(4\,\text{Re}_f)^{0.4}\text{Pr}_L^{0.65} \tag{33}$$

In the falling film region, the nucleate boiling coefficient is calculated through the Forster and Zuber [28] correlation—Eq. (29) using $\overline{T}_{w,f}$—and the suppression factor, S, is estimated using Re_F in Eq. (30).

4 Results

Figure 5 exhibits, together with the heat transfer coefficient distribution, the difference between the equilibrium bulk temperature, $\overline{T}_b$, and the calculated liquid slug temperature, $\overline{T}_S$. In this particular case, the difference increases from zero up to approximately 3°C at the point where $\overline{T}_b=T_{\text{sat}}$ and then decreases in the equilibrium saturated region ($z>z_{\text{sat}}$). The slug temperature profile is illustrated in Fig. 2, together with the saturation and equilibrium bulk temperature profiles. The two vertical lines in Fig. 5 represent the NVG point [12] (which in the present model corresponds also to the point of onset of slug flow) and the point of transition from slug flow to churn flow. The transition from slug flow to churn flow was calculated using the model of Jayanti and Hewitt [23], who associated this transition to flooding in the Taylor bubble region.

It is interesting to note that the peak in the temperature difference distribution somewhat coincides with that of the heat transfer coefficient. This result has been observed consistently in our simulations and goes a long way toward explaining the near zero quality heat transfer coefficient enhancement. Once the large nucleated bubble fills the pipe cross section, it continues to grow (as will be shown below), increasing the fluid velocity and reducing the residence time in the channel of the liquid slugs between successive bubbles. This reduced residence time implies that the

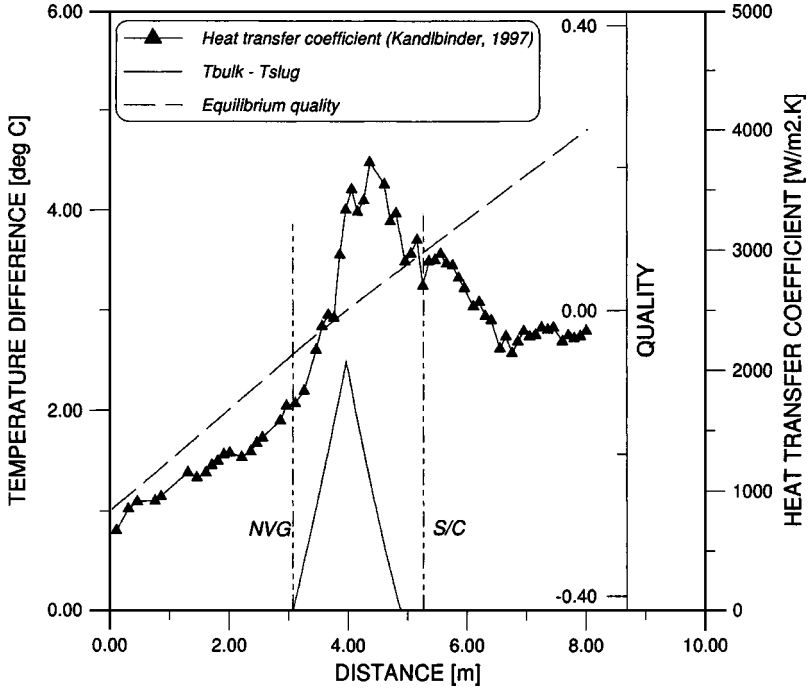

Fig. 5 Variation of the difference between the equilibrium and slug temperatures as a function of distance. Coincidence of temperature difference and heat transfer coefficient peaks. Experimental conditions: fluid: iso-octane, inlet pressure: 3.1 bar, total mass flux: 200.8 kg/m^2 s, wall heat flux: 19.5 kW/m^2, inlet temperature: 117.4°C.

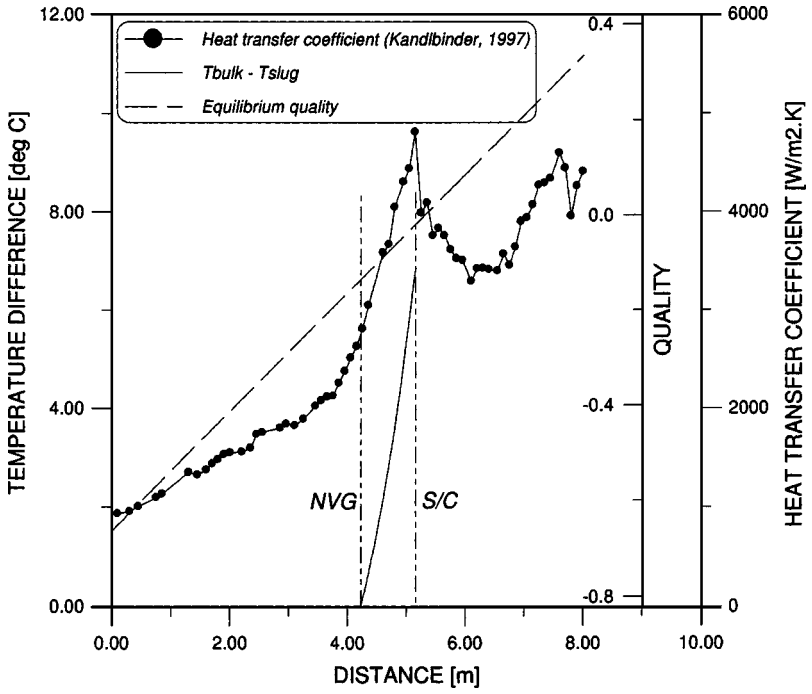

Fig. 6 Variation of the difference between the equilibrium and slug temperatures as a function of distance. Experimental conditions: fluid: iso-octane, inlet pressure: 2.2 bar, total mass flux: 296.7 kg/m^2 s, wall heat flux: 60.1 kW/m^2, inlet temperature: 55.3°C.

liquid in the slug remains subcooled at any given position and, therefore, the actual quality (and hence the heat transfer coefficient) is much higher than that calculated on a thermodynamic basis (see Fig. 1). As can be seen from the liquid slug temperature profile in Fig. 2, since the slug velocity is ever increasing (as will be shown below), the subcooling is reduced much more slowly as a function of distance than would be the case for an equilibrium flow [7]. Moreover, Fig. 5 shows that the decay of the heat transfer coefficient back toward the classical behavior of forced convective boiling [3–5] corresponds to the region of breakdown of slug flow into churn flow (S/C), predicted by the model of Jayanti and Hewitt [23]. Since this transition is related to the collapse of the slug unit, the mixing of the phases would result in the attainment of thermodynamic equilibrium, thus eliminating remaining local subcooling effects.

A further example of the variation of the difference between the equilibrium and slug temperatures as a function of distance is given in Fig. 6. In this figure, contrary to the example of Fig. 5, the transition to churn flow takes place before the liquid slug reaches saturation, i.e., the point at which $T_{\text{sat}}-\overline{T}_S=0$. It is also interesting to observe that, as the S/C transition takes place, the heat transfer coefficient decreases sharply, reiterating the fact that the subsistence of liquid subcooling is responsible for the local heat transfer enhancement.

Figure 7 shows the variation with distance of the length of the Taylor bubble and liquid slug regions and of the Taylor bubble length fraction, β. As can be seen, the length of the liquid slug remains approximately constant while the Taylor bubble length virtually doubles along the distance over which the slug flow regime prevails. As expected, the Taylor bubble length fraction somehow follows the trend of the Taylor bubble length. It is the increase in vapor mass fraction resulting from the growth of the Taylor bubble shown in Fig. 7 that may trigger an early transition to churn flow.

Calculated Taylor bubble and liquid slug velocities are plotted in Fig. 8 as function of distance in the region of occurrence of slug flow, i.e., between the NVG point and the S/C transition. Both velocities increase as a result of the increase in real quality associated with the increase in Taylor bubble length depicted in Fig. 7. The velocity of the liquid phase in a hypothetical situation in which complete thermodynamic equilibrium takes place is also shown in Fig. 8 (''Liquid equilibrium velocity''). In the region upstream of the point at which the equilibrium quality is zero (marked by X in the figure), this velocity is equal to the liquid superficial velocity, G/ρ_L. As equilibrium phase change takes place, the liquid velocity is estimated through

$$V_L=\frac{G(1-x_{G,\text{eq}})}{\rho_L(1-\epsilon_{G,\text{eq}})} \tag{34}$$

where $x_{G,\text{eq}}$ is the equilibrium quality and $\epsilon_{G,\text{eq}}$ is the void fraction calculated based on the equilibrium quality. Here, $\epsilon_{G,\text{eq}}$ was estimated using the Chexal–Lellouche [30,31] correlation. The equilibrium quality (also shown in Fig. 1) was calculated through a heat balance. As can be seen, in the region of occurrence of slug flow, the velocity of the subcooled slug is considerably higher than the velocity of the liquid phase in a thermodynamic equilibrium situation.

An illustration of the local heat transfer coefficient prediction capability of the model is provided in Figs. 9 and 10 for typical *n*-pentane and iso-octane runs. The trend of the experimental data is well picked up by the correlation in both cases. Although it systematically underpredicts the data in the whole subcooled region (the point of saturation is marked by X) and part of the equilibrium saturated region of the case shown in Fig. 9, the correlation exhibits an excellent agreement with the data in the subcooled region of Fig. 10.

Analogous to the T_b-T_S profile (see Fig. 5), the peaks in the calculated heat transfer coefficient profiles somewhat coincide with those in the experimental data. Results obtained using the Chen [13] correlation are also shown in Figs. 9 and 10. In the subcooled region, the corrections suggested by Butterworth and co-worker [3,27] were applied to the Chen [13] correlation. As can be seen, the nonequilibrium slug model performs better than

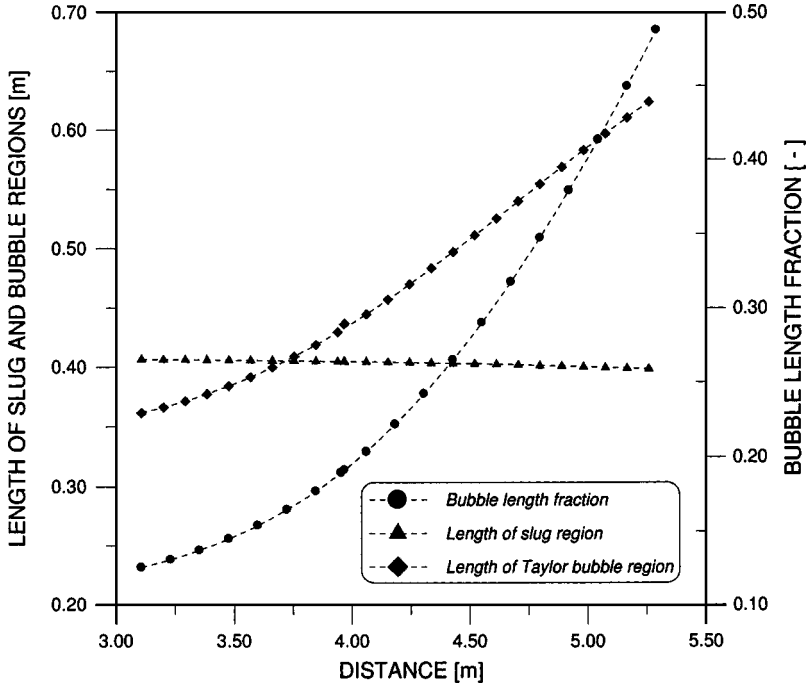

Fig. 7 Variation of L_S, L_B, and β. Experimental conditions: fluid: iso-octane, inlet pressure: 3.1 bar, total mass flux: 200.8 kg/m^2 s, wall heat flux: 19.5 kW/m^2, inlet temperature: 117.4°C.

the Chen model in this region in both cases. In the equilibrium saturated region (downstream of the X point), the Chen model predicts a sharp increase in the heat transfer coefficient, in contrast with the decreasing trend exhibited by the nonequilibrium slug flow model. In short, as has been observed by Kandlbinder [6], the Chen [13] model, together with other correlations [14–16, underpredicts the data in the near zero quality region and fail to identify a point of maximum in the heat transfer coefficient profiles. The general heat transfer behavior illustrated in Figs. 9 and 10 is typical of the conditions investigated here for both hydrocarbons.

Figure 11 presents a general comparison between experimental and calculated heat transfer coefficients for both *n*-pentane and iso-octane for six runs that represent the range of parameters as-

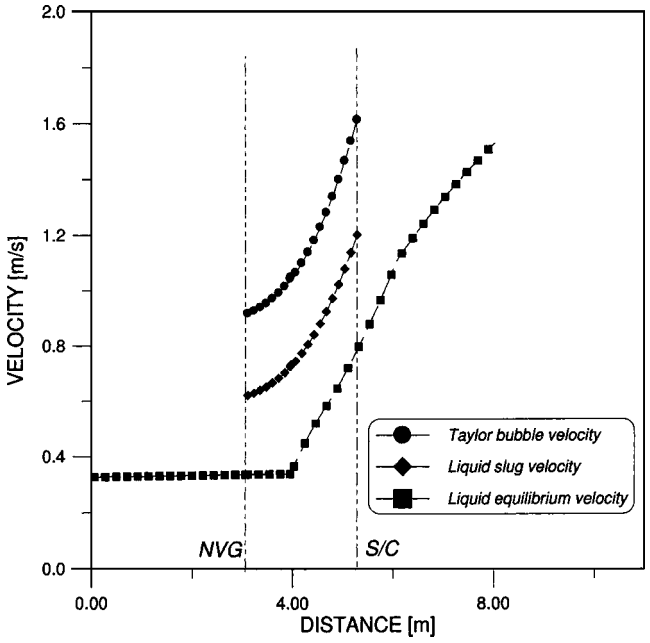

Fig. 8 Taylor bubble and liquid slug velocity profiles as a function of distance in the region of occurrence of slug flow. The equilibrium liquid velocity is shown for comparison. Experimental conditions: fluid: n-pentane, inlet pressure: 4.9 bar, total mass flux: 376.0 kg/m^2 s, wall heat flux: 50.0 kW/m^2, inlet temperature: 60.7°C.

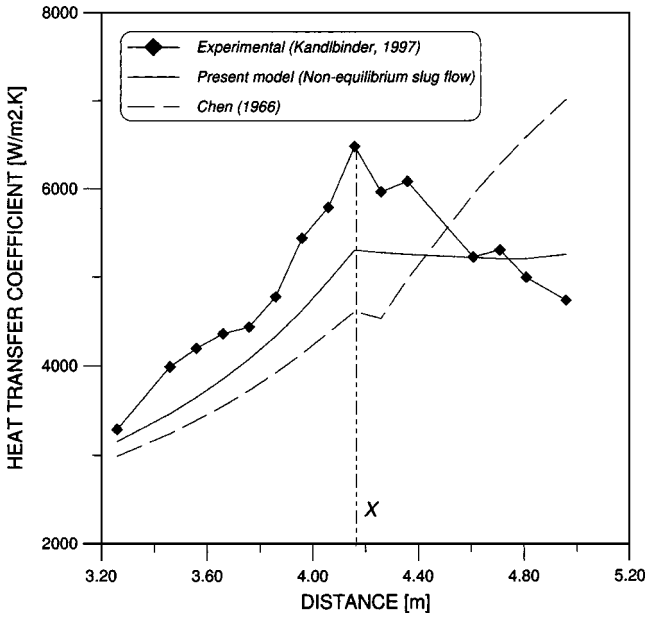

Fig. 9 Local heat transfer coefficient prediction. Experimental conditions: fluid: n-pentane, inlet pressure: 6.0 bar, total mass flux: 377.4 kg/m^2 s, wall heat flux: 49.9 kW/m^2, inlet temperature: 67.5°C.

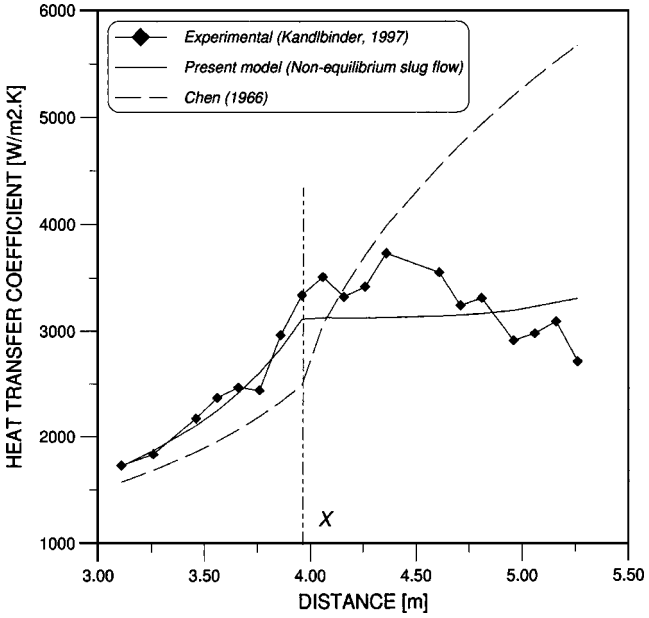

Fig. 10 Local heat transfer coefficient prediction. Experimental conditions: fluid: iso-octane, inlet pressure: 3.1 bar, total mass flux: 200.8 kg/m^2 s, wall heat flux: 19.5 kW/m^2, inlet temperature: 117.4°C.

sessed by Kandlbinder [6]. The performance of the proposed nonequilibrium slug flow model is superior to that of the Chen [13] correlation and 95% of the data fall the ±18% relative error band. The largest deviations between the Chen correlation and the experimental data take place in the equilibrium saturated region as observed in Figs. 9 and 10.

As far as the local heat transfer coefficient prediction is concerned, the performance of the nonequilibrium model could have been improved by selecting a more appropriate and up-to-date set of relationships to replace, for example, Eqs. (28)–(30) and (33). In particular, it has been shown [32] that the Forster and Zuber [28] correlation for the nucleate boiling contribution [Eq. (29)] is

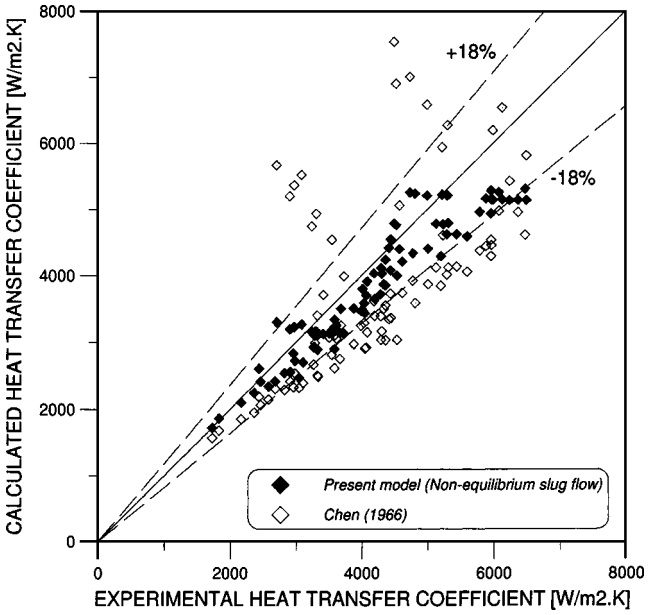

Fig. 11 Overall comparison of local heat transfer coefficient predictions

"subject to considerable uncertainty". Nevertheless, we opted for an adaptation of the Chen [13] model to better demonstrate the effect of the proposed thermal nonequilibrium phenomenon in comparison with the original and well-accepted Chen formulation. The aim of the paper is not to put together the more accurate correlation, but to point out and predict the underlying phenomena through a set of physically consistent conservation equations. Limitations and inconsistencies related to the definition and the application of the two-phase enhancement and nucleate boiling suppression factors in several widely used correlations have been addressed in a recent paper by Webb [33].

5 Conclusions

This paper presented a model for predicting the heat transfer coefficient peaks observed in the near zero quality region in boiling of hydrocarbons in a vertical pipe [6,7]. The principle of the model is the occurrence of thermal nonequilibrium effects [8,9] associated with the formation of a type of slug flow in which the Taylor bubbles are separated by subcooled liquid slugs. The main conclusions arising from this work are as follows:

1. It was shown that the heat transfer coefficient peaks coincide with the peaks in the calculated difference between the equilibrium bulk and average slug temperatures, $\overline{T}_b - \overline{T}_S$. Thus, slugs remain subcooled for distances longer than would be the case for equilibrium flow situations. A consequence of this effect is that the wall temperature in the liquid slug region is lower than that in the equilibrium case. As the heat transfer coefficient is defined in terms of an equilibrium relationship [Eq. (1)], the net result is an increase in the heat transfer coefficient.
2. In addition to the apparent increase described in Eq. (1) above, the increasing velocity of the subcooled liquid slugs resulting from the acceleration of the Taylor bubbles predicted by the model may contribute to the local enhancement of the heat transfer coefficient in the near zero quality region.
3. This is the first model to predict the local heat transfer enhancement in the near zero quality region. In the portion of the pipe over which nonequilibrium slug flow takes place (between the NVG point and the point of transition to churn flow [23]), the heat transfer coefficient was predicted within error limits to be lower than those by established methodologies [6,13].
4. Further experiments are needed to provide support for future developments in the proposed model, such as the determination of boundary conditions at the onset of nonequilibrium slug flow and the inclusion of a model to predict the gas holdup in the subcooled liquid slug.

Acknowledgments

One of the authors (J. R. B.) thanks CNPq (Conselho Nacional de Desenvolvimento Científico e Tecnológico) and FUNCITEC (Fundação de Ciência e Tecnologia do Estado de Santa Catarina) for financial support.

Nomenclature

Bo = $(\rho_L - \rho_G) g d_T^2 / \sigma$—Bond number
c_p = specific heat capacity (J/kg K)
d_T = pipe diameter (m)
g = acceleration due to gravity (m/s^2)
h = enthalpy (J/kg)
L_S = length of the liquid slug region (m)
L_B = length of the Taylor bubble region (m)
m = mass (kg)
$\dot{m}$ = Mass flow rate (kg/s)
N_f = $[d_T^3 g(\rho_L - \rho_G)\rho_L]^{1/2} / \eta_L$—viscosity number
p = pressure (Pa)
Pr = $\eta c_p / \lambda$—Prandtl number
$\dot{q}_w$ = wall heat flux (W/m^2)

t_{sp} = time period during which a slug unit is seen at a fixed location (s)
t_{sf} = time period during which a Taylor bubble (falling film) is seen at a fixed location (s)
t_{ss} = time period during which a liquid slug is seen at a fixed location (s)
T_b = equilibrium bulk temperature (K)
T_s = liquid slug bulk temperature (K)
$\underline{T}_w$ = wall temperature (K)
$\underline{T}_{w,f}$ = local wall temperature averaged over t_{sf} (K)
$T_{w,S}$ = local wall temperature averaged over t_{ss} (K)
U_{GS} = superficial velocity of the vapor (m/s)
U_{LS} = superficial velocity of the liquid (m/s)
V_{GB} = rise velocity of the center of mass of the Taylor bubble (m/s)
V_{LB} = falling film velocity (m/s)
V_{LS} = rise velocity of the center of mass of the liquid slug (m/s)
x_G = vapor mass fraction (quality) (-)
z = distance along the pipe (m)

Greek

α = heat transfer coefficient ($W/m^2 K$)
$\alpha_{fc,S}$ = heat transfer coefficient due to forced convection in the liquid slug ($W/m^2 K$)
$\alpha_{nb,S}$ = heat transfer coefficient due to nucleate boiling in the liquid slug ($W/m^2 K$)
β = length fraction of the slug unit occupied by the Taylor bubble region (-)
Δh_v = latent heat of vaporization (J/kg)
δ = falling film thickness (m)
λ = thermal conductivity (W/m K)
η = viscosity (kg/m s)
ϵ = void fraction (-)
ρ = density (kg/m^3)
σ = surface tension (N/m)

Subscript

B = Taylor bubble
f = falling film
G = vapor
L = liquid
S = slug
sat = saturation

Superscript

$\overline{\ }$ = time averaging

References

[1] Wadekar, V. V., and Kenning, D. B. R., 1990, ''Flow Boiling Heat Transfer in Vertical Slug and Churn Flow Region,'' *Proc. 9th International Heat Transfer Conference*, Vol. 3, Hemisphere, pp. 449–454.
[2] Wadekar, V. V., 1991, ''Vertical Slug Flow Heat Transfer With Nucleate Boiling,'' ASME Phase Change Heat Transfer, **159**, 157–161.
[3] Collier, J. G., and Thome, J. R., 1994, *Convective Boiling and Condensation*, 3rd ed., Oxford University Press, Oxford, UK.
[4] Hewitt, G. F., 2000, ''Challenges in Boiling Research,'' *Keynote Lecture, Boiling 2000: Phenomena and Emerging Applications*, United Engineering Foundation, Anchorage, AK.
[5] Hewitt, G. F., 2001, ''Deviations From Classical Behavior in Vertical Channel Convective Boiling,'' Multiphase Sci. Technol., **13**(3 & 4), pp. 341–371.
[6] Kandlbinder, T. K., 1997, ''Experimental Investigation of Forced Convective Boiling of Hydrocarbons and Hydrocarbon Mixtures,'' Ph.D. thesis, Imperial College, University of London.
[7] Urso, M. E., Wadekar, V. V., and Hewitt, G. F., 2002, ''Flow Boiling at Low Mass Flux,'' *Proc. 12th International Heat Transfer Conference*, Elsevier Science, pp. 803–808.
[8] Jeglic, F. A., and Grace, T. M., 1965, ''Onset of Flow Oscillations in Forced Flow Subcooled Boiling,'' NASA Technical Note TN D-2821, Lewis Research Center, Cleveland, Ohio.
[9] Ishii, M., 1982, ''Wave Phenomena and Two-Phase Flow Instabilities,'' *Handbook of Multiphase Systems*, edited by G. Hetsroni, Hemisphere Publishing Co, Washington DC.
[10] Cheah, L. W., ''Forced Convective Evaporation at Subatmospheric Pressure,'' Ph.D. thesis, Imperial College, University of London.
[11] Thome, J. R., 1995, ''Flow Boiling in Horizontal Tubes: A Critical Assessment of Current Methodologies,'' *Proc. 1st Symposium on Two-Phase Flow Modeling and Experimentation Conference*, Vol. 1, Edizioni, Rome, pp. 41–52.
[12] Saha, P., and Zuber, N., 1974, ''Point of Net Vapor Generation and Vapor Void Fraction in Subcooled Boiling,'' *Proc. 5th International Heat Transfer Conference*, Paper B4.7.
[13] Chen, J. C., 1966, ''A Correlation for Boiling Heat Transfer to Saturated Fluids in Convective Flow,'' Ind. Eng. Chem. Process Des. Dev., **5**(3), pp. 322–329.
[14] Shah, M. M., 1982, ''Chart Correlation for Saturated Boiling Heat Transfer: Equations and Further Study,'' ASHRAE Trans., **88**(1), pp. 185–196.
[15] Kandlikar, S., 1990, ''A General Correlation for Saturated Two-Phase Flow Boiling Heat Transfer Inside Horizontal and Vertical Tubes,'' ASME J. Heat Transfer, **112**, pp. 219–228.
[16] Steiner, D., and Taborek, J., 1992, ''Flow Boiling Heat Transfer in Vertical Tubes Correlated by an Asymptotic Model,'' Heat Transfer Eng., **13**(2), pp. 43–69.
[17] Fernandes, R. C., Semiat, R., and Dukler, A. E., 1983, ''Hydrodynamic Model for Gas-Liquid Slug Flow in Vertical Tubes,'' AIChE J., **29**(6), pp. 981–989.
[18] Orell, A., and Rembrand, R., 1986, ''A Model for Gas-Liquid Slug Flow in a Vertical Tube,'' Ind. Eng. Chem. Fundam., **25**, pp. 196–206.
[19] Sylvester, N. D., 1987, ''A Mechanistic Model for Two-Phase Vertical Slug Flow in Pipes,'' J. Energy Resour. Technol., **109**, pp. 206–213.
[20] De Cachard, F., and Delhaye, J. M., 1996, ''A Slug-Churn Flow Model for Small-Diameter Airlift Pumps,'' Int. J. Multiphase Flow, **22**(4), pp. 627–649.
[21] Nicklin, D. J., Wilkes, J. O., and Davidson, J. F., 1962, ''Two-Phase Flow in Vertical Tubes,'' Trans. Inst. Chem. Eng., **40**, pp. 61–68.
[22] Wallis, G. B., 1969, *One-Dimensional Two-Phase Flow*, McGraw–Hill, New York.
[23] Jayanti, S., and Hewitt, G. F., 1992, ''Prediction of the Slug-to-Churn Transition in Vertical Two-Phase Flow,'' Int. J. Multiphase Flow, **18**(6), pp. 847–860.
[24] Costigan, G., 1997, ''Flow Pattern Transitions in Vertical Gas-Liquid Flows,'' D.Phil. thesis, Oxford University.
[25] Taitel, Y., Barnea, D., and Dukler, A. E., 1980, ''Modeling Flow Pattern Transition for Steady Upward Gas-Liquid Flow in Vertical Tubes,'' AIChE J., **26**, pp. 345–354.
[26] Barnea, D., and Yacoub, N., 1983, ''Heat Transfer in Vertical Upwards Gas-Liquid Slug Flow,'' Int. J. Heat Mass Transfer, **26**(9), pp. 1365–1376.
[27] Butterworth, G., and Shock, R. A. W., 1982, ''Flow Boiling,'' *Proc. 7th International Heat Transfer Conference*, Vol. 1, McGraw-Hill, pp. 11–30.
[28] Forster, H. K., and Zuber, N., 1955, ''Dynamics of Vapor Bubbles and Boiling Heat Transfer,'' AIChE J., **1**(4), pp. 531–535.
[29] Chun, K. R., and Seban, R. A., 1971, ''Heat Transfer to Evaporating Liquid Films,'' ASME J. Heat Transfer, **93**, pp. 391–396.
[30] Chexal, B., 1991, ''The Chexal-Lellouche Void Fraction Correlation for Generalized Applications,'' Electric Power Research Institute Report (EPRI) NSAC/139.
[31] Levy, S., 1999, *Two-Phase Flow in Complex Systems*, Wiley Interscience, NY.
[32] Aounallah, Y., and Kenning, D. B. R., 1987, ''Nucleate Boiling and the Chen Correlation for Flow Boiling Heat Transfer,'' Exp. Heat Transfer, **1**, pp. 87–92.
[33] Webb, R. L., 2003, ''Commentary on Correlations for Convective Vaporization in Tubes,'' ASME J. Heat Transfer, **125**, pp. 184–185.

B. Prabhakara Rao
Heat Transfer and Thermal Power Laboratory,
Department of Mechanical Engineering,
Indian Institute of Technology-Madras,
Chennai—600 036, India

Bengt Sunden
Division of Heat Transfer,
Department of Heat and Power Engineering,
Lund Institute of Technology, Lund, Sweden

Sarit K. Das[1]
Heat Transfer and Thermal Power Laboratory,
Department of Mechanical Engineering,
Indian Institute of Technology-Madras,
Chennai—600 036, India
e-mail: skdas@iitm.ac.in or
sarit_das@hotmail.com

An Experimental and Theoretical Investigation of the Effect of Flow Maldistribution on the Thermal Performance of Plate Heat Exchangers

An experimental and theoretical study of the effect of flow maldistribution from port to channel on the thermal performance of single and multipass plate heat exchangers is presented. In general, flow maldistribution brings about an increase in pressure drop and decrease of the thermal performance in heat exchangers. This deterioration is found to depend on flow rate, number of channels, and port size. Experiments show that analytical predictions of pressure drop and thermal performance in presence of flow maldistribution are quite accurate for practical purposes. The results indicate that under identical conditions, maldistribution is more severe in Z-type plate heat exchanger compared to U type. Multipassing is found to reduce the maldistribution effect significantly. An insight to the physical aspects of maldistribution and its possible reduction through proper design strategy are also presented. [DOI: 10.1115/1.1860568]

1 Introduction

Plate heat exchangers (PHE) are used in a variety of industries, such as breweries, food processing, pharmaceutical, and dairy industries as well as in the chemical process and metallurgical industry and even in thermal power plants. A large amount of literature is available on the thermal performance of plate heat exchangers, such as those by Focke et al. [1] and Muely and Manglik [2]. However, these works considered equal flow in each channel, indicating an ideal case of no flow maldistribution. In the direction of multipass flow arrangements, Jackson and Troupe [3] analyzed the 1-1 and 2-2 pass arrangements with overall counterflow and parallel flow, and 4-4 arrangements with overall counterflow. Kandlikar [4] numerically analyzed 1-1, 2-1, 2-2, and 3-1 counterflow arrangements and 1-1 and 2-2 parallel flow arrangements. His results were extended by Shah and Kandlikar [5] for 1-1, 2-1, and 3-1 flow arrangements where the total number of channels N was systematically varied from 3 to ∞, and detailed tabular results were provided for temperature effectiveness, P_1 and LMTD correction factor F. It was shown that the ''end effect'' due to a small number of thermal plates is important only for $N < 40$ for 1-1, 2-1, and 3-1 arrangements. Pignotti and Tamborena [6] classified the plate heat exchangers and showed two methods of analysis: the numerical solution for the finite number of thermal plates and the exact solution of an infinite number of thermal plates. They found that the asymptotic behavior ($N \rightarrow \infty$) is, in fact, realized with only a small number of thermal plates, depending on the number of passes.

Toward flow maldistribution in plate heat exchangers, the effect of unequal distribution of the fluid inside the channels was analyzed by Datta and Majumdar [7]. This work brought up the difference between U- and Z-type plate exchangers and expressed the distribution in the channels in the form of a closed-form equation using the general flow channeling and unification concept of Bajura and Jones [8]. In Bassiouny [9], even though flow distribution from channel to channel was explained excellently, this distribution was not used for the thermal analysis, which prevented assessment of the effect of this distribution on the thermal performance of the plate heat exchanger. This created an inspiration of the present work.

An analytical study has been made by Bassiouny and Martin [10,11] to calculate the axial velocity and pressure distributions in both the inlet and outlet conduits of plate heat exchangers as well as the flow distribution in the channels between the plates and the total pressure drop. From the analysis a general flow maldistribution characteristic parameter (m^2) has been derived from the mass and momentum formulation for inlet and exit port flows for all the plate heat exchangers. With this parameter the flow behavior is determined. The flow distribution tends to be uniform for low values of $m^2 (\leqslant 0.01)$. If m^2 is kept equal to zero, the flow distribution will be purely uniform. The sign of m^2 may be controlled by the area ratio of the inlet and outlet conduits, whereas its magnitude is affected by the shape and the number of plates. Thonon et al. [12] presented a numerical model for flow distribution in PHE and showed that pressure drop is significantly affected by the flow maldistribution. They showed that thermal influence is limited to nonuniformity in channel outlet temperature while overall thermal performances are less affected. Another important study by Heggs and Scheidat [13] developed a mathematical model which couples the maldistribution of flow within a plate heat exchanger to the heat transfer rate occurring in individual plate channels. Flow maldistribution was found to be insignificant in exchangers with less than 20 plates, but they found that the adverse effect on the thermal performance by the end channels must be accounted for in design. An analytical study of the effect of maldistribution on only single-pass plate heat exchangers was carried out by Rao et al. [14] but it was based on a large number of simplifying assumptions, which were not verified experimentally. Similar studies with multipass exchangers were carried out by Rao and Das [15], using a numerical method. The only experimental study on flow maldistribution in PHEs is by Rao and Das [16] considering the effect of maldistribution on pressure drop for both isothermal and nonisothermal flow.

Thus, in general, very little attention has been paid to flow maldistribution in plate heat exchangers even though the usage of these is extensive. Recently some research efforts have been di-

[1]Corresponding Author.

Manuscript received May 25, 2004; revision received December 22, 2004. Review conducted by: P. M. Ligrani.

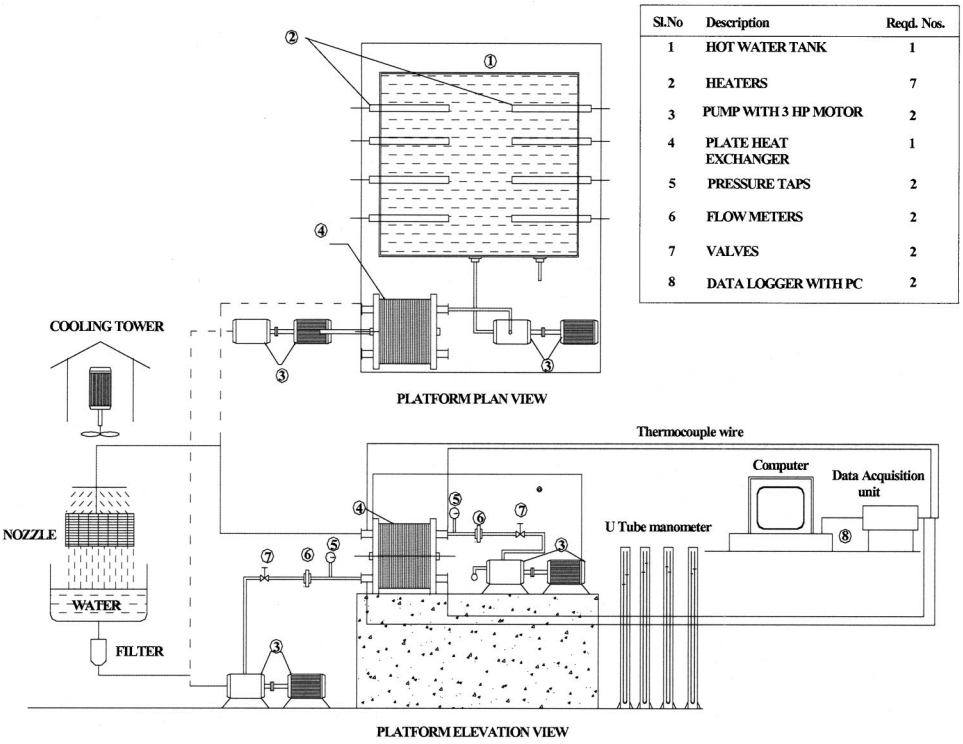

Fig. 1 Schematic view of experimental test facility (layout)

rected toward the flow maldistribution in plate heat exchangers, however, reliable experimental and theoretical predictions of the hydraulic and thermal performance in the presence of port-to-channel flow maldistribution, which provide a complete picture of the flow distribution and heat transfer in a real plate heat exchanger, are scare in literature. In the present work, the port-to-channel flow maldistribution and its effects on the thermal performance of plate heat exchangers have been studied. The experiments have been carried out to validate the analytical models considering port-to-channel flow distribution and channel-to-channel variable heat transfer coefficient as a function of a variable channel Reynolds number for single and multipass plate heat exchangers. A complete analytical treatment in contrast to available numerical approaches [13,14] has been adopted, and the comparison with carefully designed experiments makes the present study significant both fundamentally and with respect to applications.

2 Experimental Apparatus and Procedures

The layout of the experimental setup is shown in Fig. 1. It consists of a test plate heat exchanger, hot water storage tank, two circulation pumps, cooling tower with storage tank, and computerized data-acquisition unit. The plate heat exchanger consists of 40 corrugated steel plates. The detail of the plates is shown in Fig. 2. Differential manometers are connected to read the pressure drop across an orifice flow meter and also across the test plate heat exchanger. T-type thermocouples are used to measure the inlet/outlet temperatures of the plate heat exchanger. The thermocouples were placed close to the PHE ports in the well-insulated pipe sections. A temperature controller was used to maintain a constant temperature in the storage hot water tank, which has several heating elements. The given plate heat exchanger can be modified according to the requirement of pass arrangements by changing special plates that have one or more ports closed to change the fluid passes. Both U- and Z-type plate heat exchanger configurations can be obtained in the same setup by regulating the valves alone without the need for changing the end or frame plates. The area ratio of channel to port has been reduced to one-fourth by inserting a wooden mandrel inside the ports, which is shown in Fig. 3. The mandrel is so designed that the port effective diameter reduces to half and the port area reduces to one-fourth.

For evaluating the channel heat transfer coefficient, the tests were conducted with three channels with a counterflow arrangement with an equal Reynolds number on both the sides. During the measurements, the cold fluid was always kept on the side having more channels, in case of an odd number of channels, to minimize end heat loss. Cold process fluid was pumped out of the feed water tank and into the plate heat exchanger where heat is transferred from the hot to the cold fluid. The cold fluid then enters a cooling tower where it is cooled before returning to the plate heat exchanger. The hot fluid was pumped with the help of a 3 HP pump into the plate heat exchanger where it transfers heat to the cold fluid prior to flowing back into the storage tank heated by

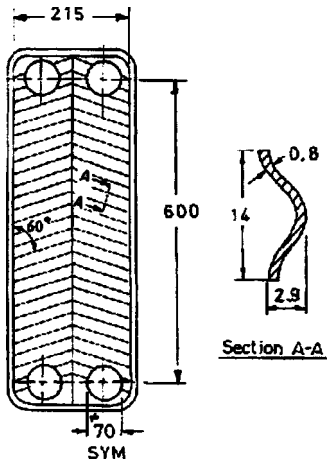

Fig. 2 Details of test plate

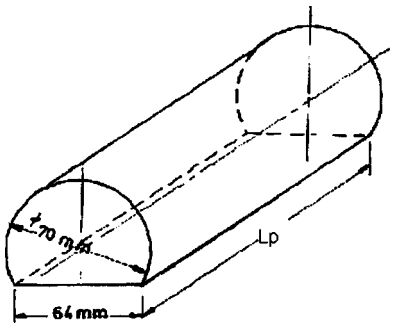

Fig. 3 Schematic view of the mandrel

seven submerged water heaters. Electrical power at 220–240 V was supplied to the heating elements through the AC mains. Temperatures were continuously recorded until steady state was reached by a Hewlett Packard Data Acquisition Unit (Serial No. 34970A). The flow rate and temperature limits were determined by the maximum allowable heat transfer to the cooling tower and by the system's ability to achieve steady state within a reasonable time. The flow rate and temperature data are used to check the energy balance, and the aim is to keep the losses within 2%. A series of experiments has been conducted for different flow rates, pass arrangements, number of channels, and area ratio. The three-pass arrangements chosen are representatives of $1-N$, $N-N$, and $M-N$ pass arrangements.

3 Data Reduction

3.1 Evaluation of Heat Transfer Coefficient and Thermal Effectiveness. All of the thermal data were obtained under steady-state conditions, and the range of operating conditions and flow variables covered in these experiments were as follows:

$$6.5\times 10^3 W < Q < 2.2\times 10^4 W$$

$$600 < \mathrm{Re} < 6000$$

$$3.5 < \mathrm{Pr} < 5.7$$

The four terminal temperatures have been denoted as $T_{c,i}$, $T_{c,o}$, $T_{h,i}$, and $T_{h,o}$. From the measured values of temperatures and flow rates, the dimensionless parameters, such as Reynolds number and Nusselt number, were calculated based on the characteristic length selected as the hydraulic diameter, d_e (=2b for $H \gg b$) based on the projected plate area suggested by Shah and Wanniarachchi [17].

$$\mathrm{Nu} = \frac{h(2b)}{\lambda}, \quad \mathrm{Re} = \frac{U_c(2b)}{\upsilon} \tag{1}$$

For the experiments the usual logarithmic mean temperature difference (LMTD) for the countercurrent flow plate heat exchanger was used in the form

$$\Delta T_{lm} = \frac{\Delta T_1 - \Delta T_2}{\ln\left(\frac{\Delta T_1}{\Delta T_2}\right)} \tag{2}$$

where $\Delta T_1 = T_{h,in} - T_{c,o}$ and $\Delta T_2 = T_{h,o} - T_{c,in}$. All fluid properties are evaluated at the mean temperature given by

$$T_m = (T_{c,in} + T_{c,o})/2 \tag{3}$$

Thus the overall heat transfer coefficient can be calculated from

$$U = \frac{\dot{m} c_p (T_{c,o} - T_{c,in})}{A_t \Delta T_{lm}} \tag{4}$$

From the overall heat transfer coefficient U, the heat transfer coefficients on the two sides are evaluated by using a correlation of the form

$$\mathrm{Nu} = C\ \mathrm{Re}^a\ \mathrm{Pr}^{1/3} \tag{5}$$

If the same heat transfer area is valid on the hot and cold water sides, then the relation between the overall heat transfer coefficient and the convective heat transfer coefficient on both sides can be expressed as

$$\frac{1}{h_{hot}} = \frac{1}{U} - \frac{1}{h_{cold}} - R_{wall} A \tag{6}$$

Thus, the individual heat transfer coefficients are calculated by taking care of the resistance due to the solid wall in between. However, in order to calculate h_{hot}, the cooling water side heat transfer coefficient h_{cold} is needed. This was determined from a correlation derived from experiments by employing the modified Wilson Plot technique [18].

The ε was calculated as a measure of the thermal performance. The overall energy balance between the hot and cold fluids is given by

$$Q = (\dot{m} c_p)_h (T_{h,in} - T_{h,o}) = (\dot{m} c_p)_c (T_{c,o} - T_{c,in}) \tag{7}$$

and was kept within 2%, after accounting for end-plate heat losses. The calculated heat exchanger effectiveness is given by

$$\varepsilon = \frac{(\dot{m} C_p)_h (T_{h,in} - T_{h,o})}{(\dot{m} C_p)_{\min} (T_{h,in} - T_{c,in})} \tag{8}$$

3.2 Evaluation of Flow Maldistribution Parameter. In this analysis, the flow maldistribution parameter m^2, as introduced by Bassiouny and Martin [10,11] has been taken as principal parameter to designate port to channel maldistribution. The physical significance of the maldistribution parameter is the index of deviation of the flow from the mean channel velocity in a plate packed heat exchanger. It is a function of the momentum correction factor, the plate channel flow geometry, and the resistance to flow in the channel, which results in the overall pressure drop from inlet to outlet. Flow maldistribution can be induced by: (*a*) heat exchanger geometry and (*b*) heat exchanger operating conditions. The Geometry-induced flow maldistribution can be classified into three categories named (i) gross flow, (ii) passage to passage, and (iii) manifold-induced flow maldistribution. Port-to-channel flow maldistribution belongs to the manifold-induced flow maldistribution, and it is mainly depending on port and channel geometries and channel friction coefficient ζ_c. This parameter can be calculated as reported by Bassiouny and Martin [10,11]. For identical inlet and exit port dimension, this value reduces to

$$m^2 = \left(\frac{nA_c}{A_p}\right)^2 \frac{1}{\zeta_c} \tag{9}$$

Here ζ_c is the overall frictional resistance of the channel.

In this equation, m^2 serves as the parameter quantifying the flow maldistribution. The value of m^2 approaches zero when the flow is uniformly distributed among the channels. The more flow maldistribution, the higher is the value of m^2. The theoretical values of m^2 calculated from Eq. (9) for the present PHE are shown in Table 1.

The overall channel pressure drop data was used in the following equation to obtain the overall channel friction coefficient ζ_c, according to

$$\zeta_c = \frac{2(\Delta P_{ch})_{overall}}{\rho U_c^2} \tag{10}$$

where $\zeta_c = f(l/d_e) +$ loss factors including turning, etc.

Table 1 The parameter m^2 for the flow distribution in the tested PHE

Re	$N=10$	$N=33$	$N=100$
500	0.0078	0.0852	0.7825
1000	0.0096	0.1050	0.9640
2000	0.0118	0.1293	1.1878
3000	0.0134	0.1461	1.3419
5000	0.1560	0.1704	1.5649
10,000	0.1920	0.2099	1.9280

The overall pressure drop data has been obtained for a single channel, and the friction factor was calculated and correlated as a function of Reynolds number. This correlation has been found to be

$$f=21.41\,\mathrm{Re}^{-0.301} \quad \text{for } 1000<\mathrm{Re}<7000 \tag{11}$$

A regression analysis was used for this purpose.

The nondimensional pressure drop can be written as

$$\Delta p^*=\frac{P-P^*}{\rho W_o^2} \tag{12}$$

The flow maldistribution was calculated from the experimental data using the following nondimensional overall pressure drop equations, which are taken from the Bassiouny and Martin [10,11] model for U- and Z-type PHE (flow arrangement shown in Fig. 4) given by

U-type PHE

$$\Delta p=\left(\frac{m^2}{\tanh^2 m}\right)\left(\frac{A_p}{nA_c}\right)^2\frac{\zeta_c}{2} \tag{13a}$$

Z-type PHE

$$\Delta p=\left[\left(\frac{m^2}{\tanh^2 m}\right)+c_2\left(1+\frac{c_2}{m^2}\right)\frac{(1-\sec hm)^2}{\tanh^2 m}\right]\left(\frac{A_p}{nA_c}\right)^2\frac{\zeta_c}{2} \tag{13b}$$

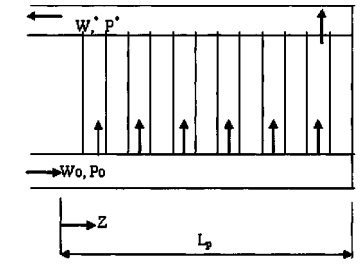

(a) U- type plate heat exchanger

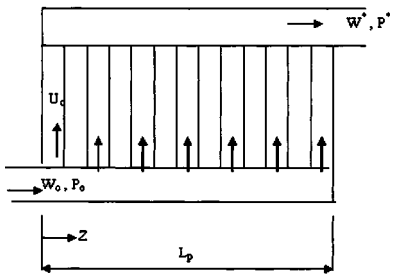

(b) Z – type plate heat exchanger

Fig. 4 Schematic views of U- and Z-type arrangements

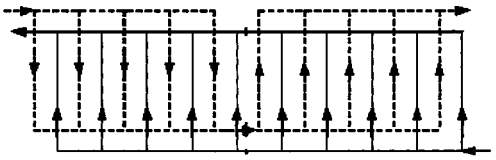

(a) 1-N pass flow configuration

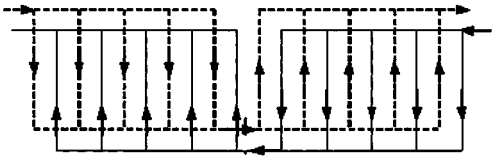

(b) N-N pass flow configuration

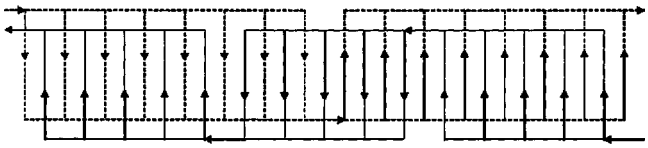

(c) M-N pass flow configuration

Fig. 5 Flow configurations of multipass plate heat exchangers: (*a*) 1−*N* pass, (*b*) *N*−*N* pass, and (*c*) *M*−*N* pass flow configurations

For each case the above equations were solved iteratively using measured value of total pressure drop on the left-hand side of the equations. This gives the actual effective value of maldistribution parameter m^2, which can be compared to the theoretical value given by Eq. (9).

3.3 Uncertainty in Measurements. The uncertainty analysis for the derived quantities was carried out following the procedure given in Moffat [19]. The uncertainty of the flow rate measurement was estimated to be maximum 3.1%. The uncertainty in the measurement of pressure was found to be 5% max. The uncertainty in temperature measurement was within ±0.5°C. The maximum errors in measurements of the primitive variable ΔT, ΔP and m were ±5%, ±5.1%, and ±1.1%, respectively. More than ±80% of the heat transfer data have an energy balance within 1.5%. Using the above values of measured quantities, the maximum uncertainty in the values of Re, f, Q, and Nu were calculated to be ±3.7%, ±5.8%, ±6.3%, and ±11.7%, respectively. The uncertainty in thermal effectiveness ε was found to be ±5.7%.

4 Mathematical Model

The mathematical model has been developed with the following assumptions: (i) the thermophysical properties of fluids are considered to be independent of temperature and pressure, (ii) heat transfer is assumed to take place only between the channel and not between the channel and ports or through the seal and gaskets, (iii) the flow distribution inside the channel is taken to be uniform giving a ''plug flow'' in each channel, and (iv) fluid is considered to be adiabatically mixed after every pass. Considering a small control volume of fluid inside the channel and a control volume of solid plate as shown in Fig. 6, the governing equations can be formulated for energy transfer depending on whether channels are located inside a pass or at the pass boundary.

For fluid 1,

$$(\dot m C_p)_1\frac{dT_i}{dx}=\frac{h_iA}{2L}(T_{wi}-T_i)+\frac{h_iA}{2L}(T_{wi+1}-T_i) \tag{14}$$

For fluid 2, two possibilities occur:

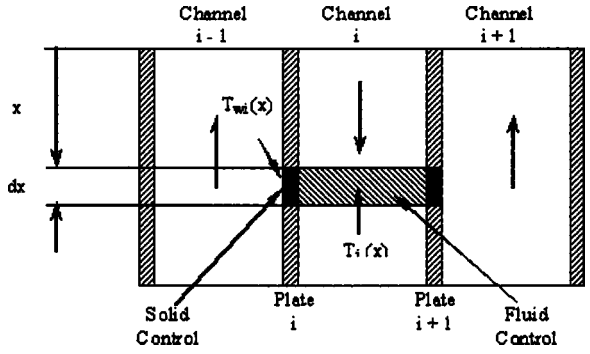

Fig. 6 Control volume of fluid inside the channel

i. channel inside a counter flow pass or pass boundary giving consecutive opposing flow

$$(\dot{m}C_p)_2\frac{dT_i}{dx}=(-1)^{i-1}\left[\frac{h_iA}{2L}(T_{wi}-T_i)+\frac{h_iA}{2L}(T_{wi+1}-T_i)\right] \tag{15}$$

ii. channel inside a parallel flow or pass boundary giving consecutive parallel flow

$$(\dot{m}C_p)_2\frac{dT_i}{dx}=\left[\frac{h_iA}{2L}(T_{wi}-T_i)+\frac{h_iA}{2L}(T_{wi+1}-T_i)\right] \tag{16}$$

For the plate

$$\frac{h_{i-1}A}{2L}(T_{i-1}-T_{wi})+\frac{h_iA}{2L}(T_i-T_{wi})=0 \tag{17}$$

In the multipass arrangement both fluid flow directions will be changed according to pass arrangement, while the outlet of one pass to inlet of the subsequent pass has to be considered. Therefore the signs of first two equations would be changed according to flow direction in a given pass arrangement.

In order to enable us to compare with the case of uniform flow in all the channels, Eqs. (14)–(17) may be written as

For individual counter flow pass $i=2,3,\ldots N-1$

$$\frac{dt_i}{dX}=\pm(-1)^{i-1}NTUrh(i)rv(i)\left[\left(\frac{u_{i-1}^a}{u_{i-1}^a+u_i^a}\right)t_{i-1}+\left(\frac{u_i^a}{u_i^a+u_{i+1}^n}+\frac{u_i^a}{u_i^a+u_{i-1}^a}-2\right)t_i+\left(\frac{u_i^a+1}{u_i^a+u_{i+1}^a}\right)t_{i+1}\right] \tag{18}$$

For individual parallel flow pass $i=2,3,\ldots N-1$

$$\frac{dt_i}{dX}=\pm(-1)^{i-1}NTUrh(i)rv(i)\left[\left(\frac{u_{i-1}^a}{u_{i-1}^a+u_i^a}\right)t_{i-1}+\left(\frac{u_i^a}{u_i^a+u_{i+1}^n}+\frac{u_i^a}{u_i^a+u_{i-1}^a}-2\right)t_i+\left(\frac{u_i^a+1}{u_i^a+u_{i+1}^a}\right)t_{i+1}\right] \tag{19}$$

The $\pm$ signs indicate whether the flow directions are in the same or opposite direction with respect to the chosen coordinate.

For first channel, i.e., $i=1$

$$\frac{dt_1}{dX}=NTUrv(1)rh(1)\left[\left(\frac{u_1^a}{u_1^a+u_2^a}-1\right)t_1+\left(\frac{u_2^a}{u_1^a+u_2^a}\right)t_2\right] \tag{20}$$

For last channel, i.e., $i=N$

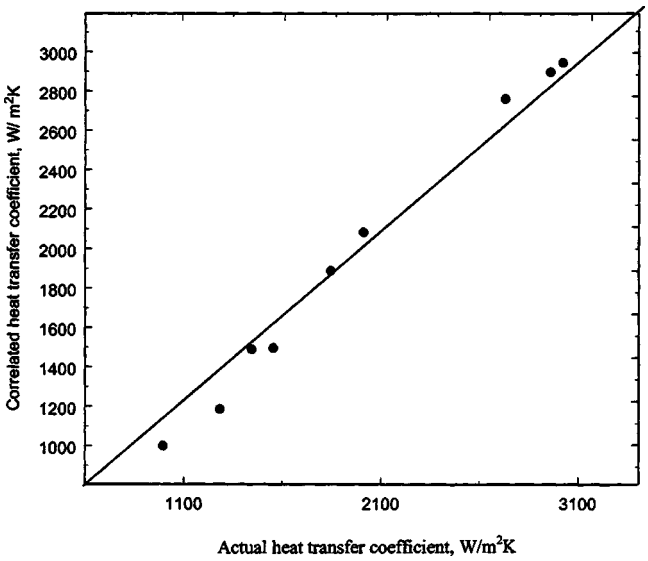

Fig. 7 Parity plot of Nusselt number correlation

$$\frac{dt_N}{dX}=NTUrv(N)rh(N)\left[\left(\frac{u_{N-1}^a}{u_{N-1}^a+u_N^a}\right)t_{N-1}+\left(\frac{u_N^a}{u_{N-1}^a-u_N^a}-1\right)t_N\right] \tag{21}$$

The flow distribution from port to the channels has been taken from Bassiouny and Martin [10,11]. Therefore, the nondimensional channel velocity can be computed as

$$\text{U-type}\quad u=\left(\frac{A_p}{nA_c}\right)m\frac{\cosh m(1-z)}{\sin hm} \tag{22a}$$

$$\text{Z-type}\quad u=\left(\frac{A_p}{nA_c}\right)m\frac{\cosh mz}{\sin hm} \tag{22b}$$

4.1 Boundary Conditions. For the above governing differential equations, the boundary conditions can be set as

$$\text{at } X=0,\ t_i=0 \quad \text{for } i=1,3,5,\ldots N$$

$$\text{at } X=1,\ t_i=1 \quad \text{for } i=2,4,6,\ldots N-1$$

In case of multipass plate heat exchangers, the boundary conditions depend on the type of pass arrangement. The multipass heat exchanger can be divided into a number of heat exchangers as shown in Fig. 5. Table 1 shows the flow arrangement in these sector exchangers.

For 1-2 pass PHE, here, it has been divided into two heat exchangers (HXs): HX1, and HX2, as shown in Fig. 5(*a*). The boundary conditions can be written as

$$\text{at } X=0,\quad t_i=0 \quad \text{for } i=1,3,\ldots N_1,\ N_1=N/2$$

$$\text{at } X=1,\quad t_i=t_{m1} \quad \text{for } i=N_1+2,\ N_1+4,\ldots N$$

$$t_i=1 \quad \text{for } i=2,4,\ldots N-1$$

For 2-2 pass PHE, similarly for the 2-2 pass arrangement, each pass can be considered as one counterflow heat exchanger giving

$$\text{at } X=0 \quad t_i=0 \quad \text{for } i=1,3,\ldots N_1=1$$

$$\text{for } i=N_1+1,\ N_1+3,\ldots N-1$$

$$\text{at } X=1,\quad t_i=t_{m1} \quad \text{for } i=N_1+2,\ N_1+4,\ldots N=t_{m2}$$

$$\text{for } i=2,4,\ldots N_1-1$$

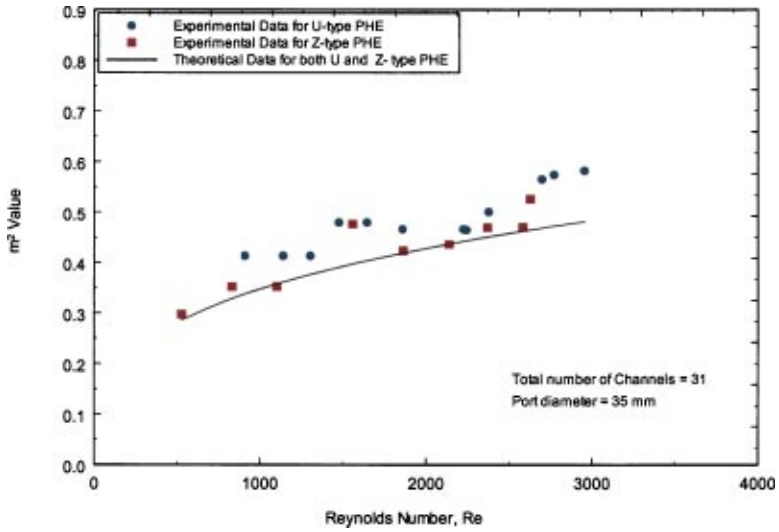

Fig. 8 Comparison of theoretical and experimental data of m^2 for both U- and Z-type plate heat exchangers

For 3-2 pass PHE, in the case of the 3-2 pass arrangement, it has been divided into heat exchangers as HX1, HX2, and HX3, as shown in Fig. 5(*c*). The first and third heat exchangers are counter and parallel flow, respectively, and the central one can be considered as a mixed flow heat exchanger. The boundary conditions can be set as

$$\text{at } X=0, \quad t_i=0 \quad \text{for } i=1,3,\ldots N_1=t_{m1}$$

$$\text{for } i=2,4,\ldots N_2;\ N_2=N/3$$

$$\text{at } X=1, \quad t_i=t_{m2} \quad \text{for } i=N_2+2,\ N_2+4,\ldots N_3-1$$

$$=t_{m3} \quad \text{for } i=N_1+2,\ N_1+4,\ldots N-1=1$$

$$\text{for } t=N_2+2,\ N_2+4,\ldots N_3,\ (N_3=N/6)$$

The system of first-order ordinary differential equations, (18)–(21), can be solved by the method of eigenvalues analytically. The most important requirement for this solution is a proper distribution of fluid in the channels from the port.

5 Solution Procedure

For solution, the set of differential equations given by Eqs. (18)–(21) can be cast into a matrix differential equation of the form

$$\frac{d\bar{t}}{dX}=\bar{c}\bar{t} \tag{22c}$$

where $\bar{t}=[t_1,t_2,t_3,\ldots t_N]^T$ and $\bar{c}$ is the coefficient matrix.

The solution to this matrix equation is given by

$$\bar{t}=\bar{F}\bar{B}(X)\bar{K} \tag{23}$$

$\bar{B}$ is the diagonal matrix given by

$$\bar{B}(X)=\text{diag}(e^{\beta_1 X},e^{\beta_2 X},e^{\beta_3 X}\ldots e^{\beta_N X})$$

where $\beta_1,\ \beta_2,\ldots\beta_N$ are the eigenvalues of the matrix $\bar{c}$ and $\bar{F}$ is the matrix containing the eigenvectors of $\bar{c}$.

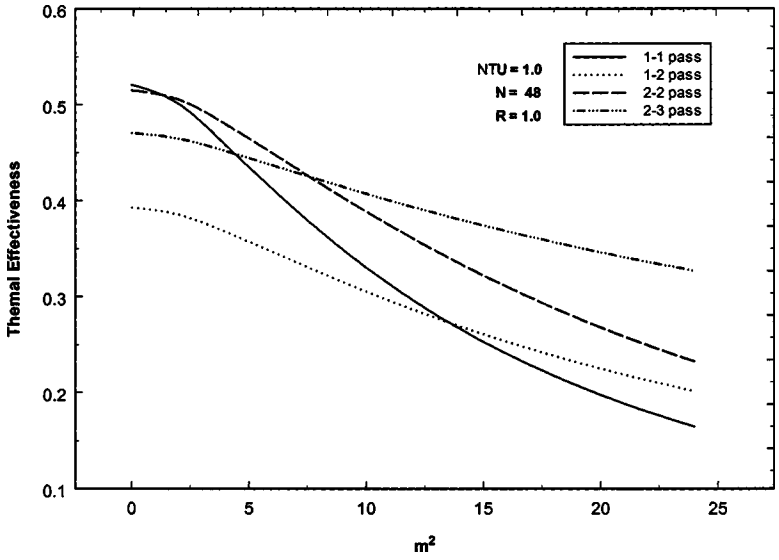

Fig. 9 Effect of flow maldistribution parameter m^2 on the thermal performance of plate heat exchanger

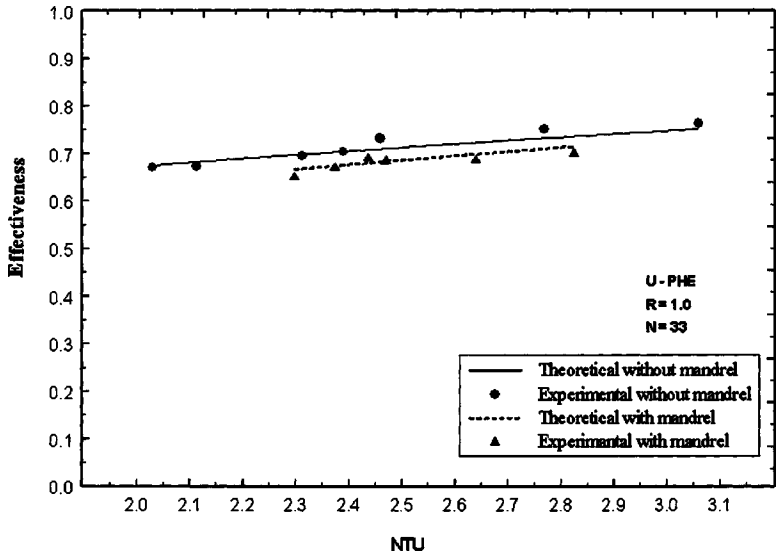

Fig. 10 Effect of port diameter on the thermal performance of U-type plate heat exchanger

$$\overline{F}=[e_{ij}],\quad i=1,2,\ldots N \quad \text{and} \quad j=1,2,\ldots N$$

and $\overline{K}$ is a coefficient matrix. The temperature distribution of the individual channels is given by

$$T_i=\sum_{j=1}^{N}\overline{K}_j e_{ij}\exp(\beta_j X) \tag{24}$$

Using the boundary conditions, a matrix equation of the following form can be formed and from this the coefficient matrix $\overline{D}$ can be evaluated:

$$\overline{y}\overline{K}=\overline{S} \tag{25}$$

For single-pass U- and Z-type plate heat exchangers

$$\overline{S}=(0\ \ 1\ \ 0\ \ 1\ldots\rightarrow N\ \ terms)^T$$

The above matrix $\overline{S}$ will be changed according to pass arrangement for multipass PHEs. The coefficient matrix $\overline{y}$ is generated by putting $X=0$ and $X=1$, respectively, in Eq. (25) to become

$$\overline{y}_{ij}=e \quad \text{for } i=1,3,5,\ldots N$$

$$=e_{ij}\exp(\beta_j) \quad \text{for } i=2,4,6,\ldots N-1$$

The system of linear equations given by Eq. (25) can be solved by any standard matrix solver.

6 Results and Discussion

6.1 Determination of Heat Transfer Coefficient. In order to establish the present method of analysis of maldistribution, the measured values of heat exchanger thermal performance are to be compared to those of the model for different values of parameters

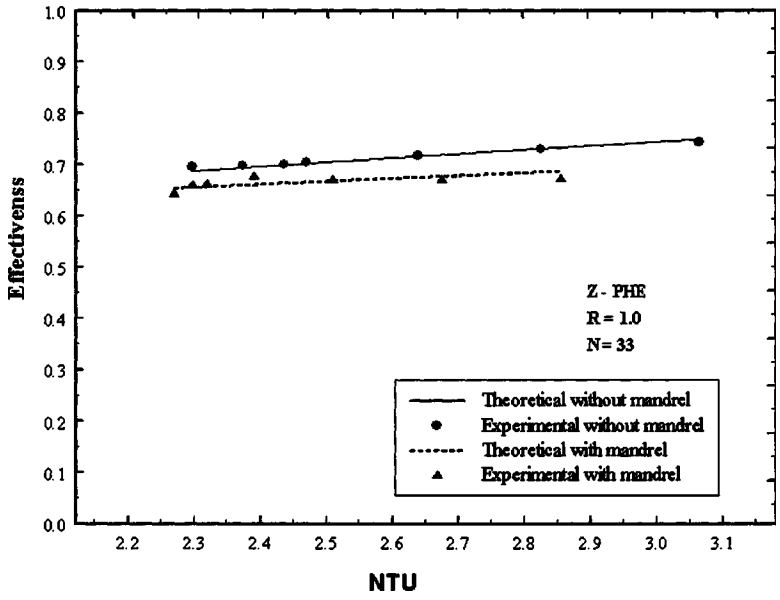

Fig. 11 Effect of port diameter on the thermal performance of Z-type plate heat exchanger

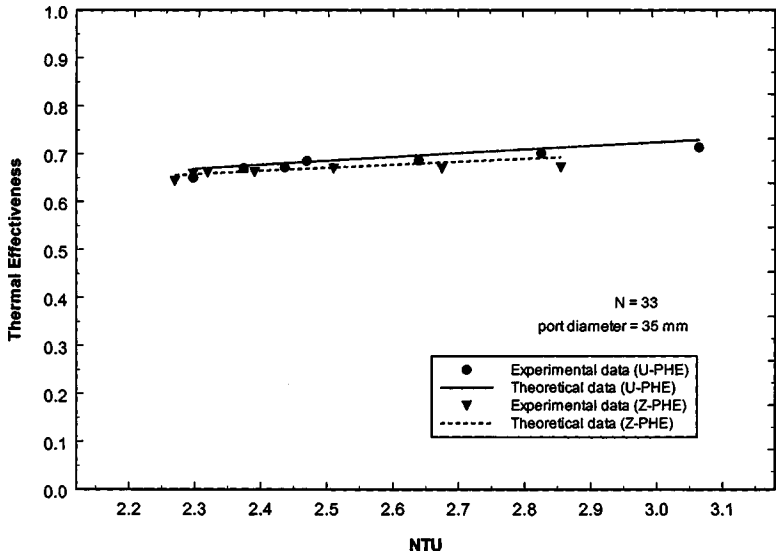

Fig. 12 Comparison of the effectiveness with NTU for U- and Z-type plate heat exchangers at port diameter, $D_p = 35$ mm

and pass arrangement like 1-1, 1-2, 2-2, and 2-3 passes. One of the most important inputs to the plate heat exchanger performance evaluation is the knowledge of the heat transfer coefficient. In dimensionless form, it is presented in terms of the Nusselt number versus Reynolds number.

Forced convection heat transfer coefficients for fully developed turbulent liquid flow in plate heat exchanger are usually correlated as

$$\mathrm{Nu} = C\,\mathrm{Re}^{a}\,\mathrm{Pr}^{a1} \tag{29}$$

where the empirical constants C, a, and a_1 depend on the plate pattern and geometrical parameters. No published information is available on the effect of systematic variation of fluid Prandtl number on the Nusselt number, particularly for plate heat exchangers. However, until actual performance data are reported, the exponent on Pr can be taken to be 1/3, as many investigators already used it in literature.

With a Pr exponent of 1/3 for both fluid streams, the Re exponent a and the constant C were evaluated from the multivariable regression analysis using a modified Wilson plot technique as described in Sec. 4. The iterative procedure, with regression fit through the data, as shown in Fig. 7, yielded $a = 0.651$ and $C = 0.218$. Thus, the correlation for the heat transfer coefficient recommended for high transient and turbulent flow is

$$\mathrm{Nu} = 0.218\,\mathrm{Re}^{0.65}\,\mathrm{Pr}^{1/3}$$

6.2 Determination of the Flow Maldistribution Parameter m^2. A series of experiments have been carried out to find out the value of the flow distribution parameter m^2 for both U and Z configurations of single-pass plate heat exchangers. The experiments were conducted for the range of Reynolds numbers from 600 to 5500 (for chevron plate heat exchangers turbulent flow occurs above Re=500). Figure 8 shows the comparison of theoretical and experimental value of m^2 over a wide range of Reynolds number for both U- and Z-type 31 channel plate heat exchanger with 35 mm port diameter and the ratio of the cross-sectional area of channel to port area of 0.162. The experimental

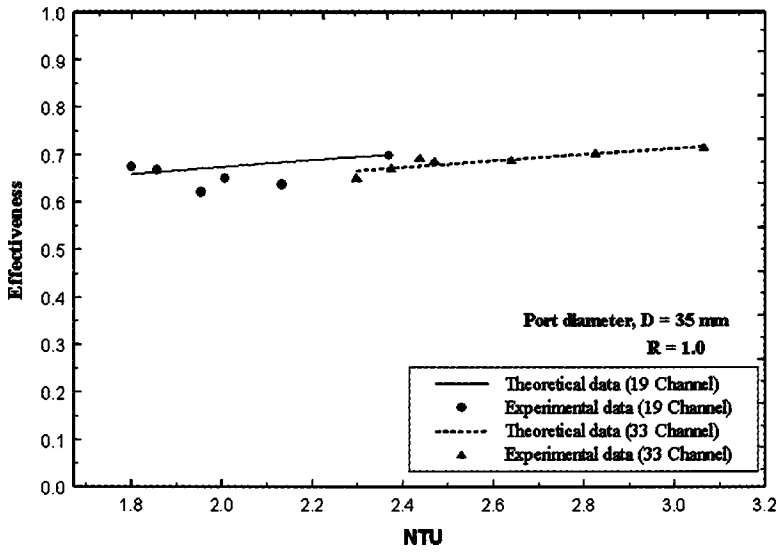

Fig. 13 Effect of number of channels on thermal performance with NTU for U-type plate exchanger at port diameter, $D_p = 35$ mm

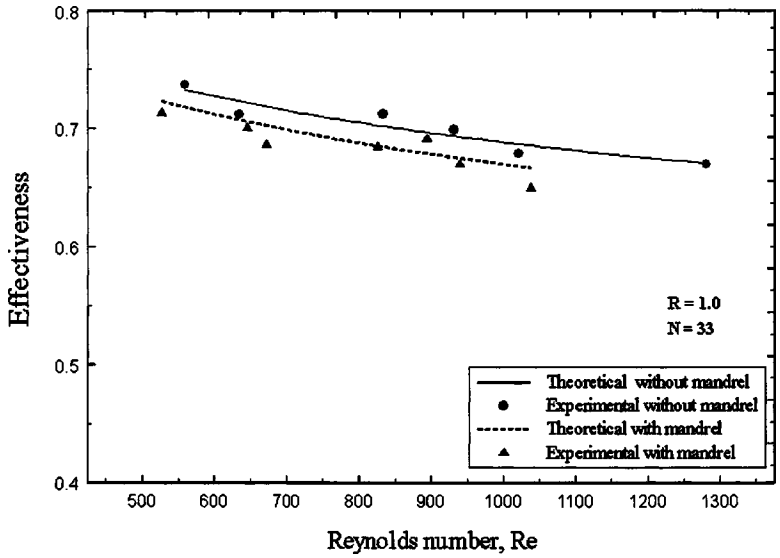

Fig. 14 Effect of Reynolds number on the thermal performance of U-type plate heat exchangers with and without mandrel

values of m^2 have been obtained from the measured overall pressure drop by iterating Eq. (14) for values of m^2. The flow distribution parameter m^2 is a function of number of channels per fluid, the area ratio of channel to port [i.e., (A_c/A_p)], and the channel resistance in terms of frictional coefficient ζ_c. The theoretical value of m^2 was obtained by substituting the respective values of these parameters into Eq. (10). The two values match closely, but the experimental one is higher than the theoretical value because of port resistance and other unaccountable minor losses. The theoretical correlation given by Eq. (10) was derived while neglecting the port resistance and the other unaccountable losses, such as the losses due to sudden enlargement and contraction as well as losses due to sharp edges.

6.3 Effect of Maldistribution on Single and Multipass PHE. In order to obtain the effect of flow maldistribution on the thermal performance of single and multipass plate heat exchangers, a mathematical model has been developed as described in the previous section. A typical plot of the effect of maldistribution on the thermal performance of plate heat exchangers calculated using this model is shown in Fig. 9. It shows the variation of the effectiveness for the range of the flow maldistribution parameters of a plate heat exchanger with 48 plates. Here the flow misdistribution parameter m^2 has been varied from 0.0 (uniform distribution) to a value of 25.0. The figure shows that, generally, the flow distribution affects the thermal performance. The performance is influenced adversely with increasing value of m^2. Except for very close to a uniform distribution $(m^2 \sim 0)$, the decrease is almost exponential with the flow maldistribution parameter m^2. The figure clearly indicates that the deterioration of the performance is more severe with an equal number of passes and single pass being the worst.

In the present study, the experiments were conducted for the number of channels, $N=33$ and 19, the heat capacity flow rate ratio, $R=1$, and the channel-to-port area ratio, $(A_c/A_p)=0.6172$ and 0.1543. The area ratio has been changed with the help of a wooden mandrel to reduce the port area of the plate heat ex-

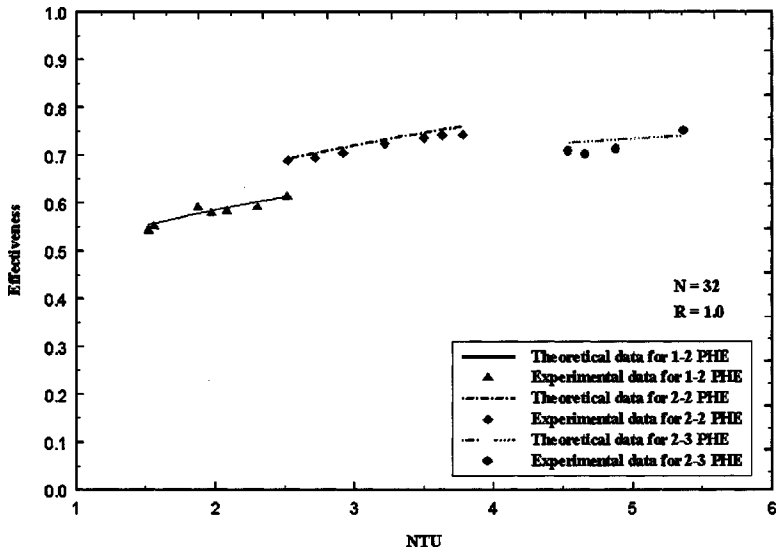

Fig. 15 Comparison of the performance of various multipass arrangements of plate heat exchangers at port diameter, $D_p=70$ mm

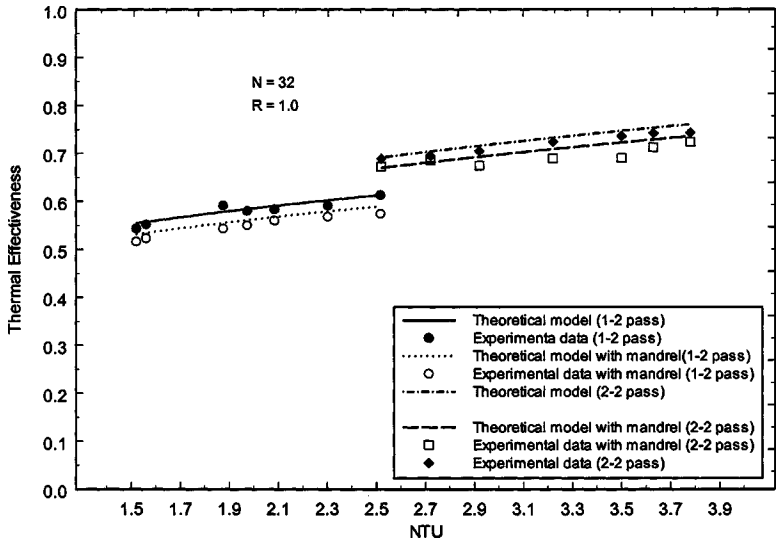

Fig. 16 Effect of flow maldistribution on thermal performance of multipass PHE

changer. By changing the area ratio, the flow maldistribution can be increased so that the net effect of flow maldistribution on the thermal performance of a U-type plate heat exchanger can be observed as shown in Fig. 10. The figure shows that the maldistribution deteriorates the effectiveness of the U-type plate heat exchanger. It also reconfirms that even though the range of maldistribution parameters is very low for the present case (due to difficulty of changing m^2 at laboratory level by changing the number of plates and flow rate), its effect on heat exchanger performance is not negligible. In the present analysis, the maldistribution has been brought about by reducing the port size, hence, the choice of port area seems to be vital as maldistribution in a plate heat exchanger is considered. The larger the port cross-sectional area is, the less the maldistribution is; but also, the area available for heat transfer in the plates is less. Thus one needs to meet the balance between reduction of NTU due to plate area reduction and decrease of maldistribution when the port is made larger. Figure 10 presents the effectiveness data for both experimental measurements and theoretical calculations. Excellent agreement is found. This clearly indicates that although the present theoretical model is based on a number of simplifying assumptions, it describes the flow distribution and heat transfer behavior in plate heat exchangers quite accurately. The same effect can be seen in Fig. 11 for the Z-type configuration. Here also the experiments and computations seem to match closely. However, for the present range of maldistribution parameters, the Z-type PHE appears to be less affected by maldistribution, which is concluded from the closeness of the effectiveness curves both with and without the mandrel. The comparison of both U- and Z-type plate heat exchangers can be found in Fig. 12 while plotting the data under the same conditions of port diameter, $D_p = 70$ mm and $R = 1.0$. It shows that the Z-type plate exchanger is inferior to the U-type plate heat exchanger with respect to flow maldistribution effects for the given NTU and maldistribution. However, for the present range of parameters the difference is found to be not very significant, primarily due to small values of m^2. Apart from reduction of port size, the other parameter increasing the maldistribution is the number of channels. Figure 13 shows the comparison for U-type plate heat exchangers having 19 and 33 plates, respectively. The results clearly indicate that with an increasing number of plates, the effectiveness decreases due to increasing maldistribution. This is very important, from a practical point of view, because in industrial plate heat exchangers the number of plates are much higher, some times on the order of hundreds. Hence, this aspect of flow maldistribution dealing with the number of plates is of great significance in practical applications. Finally, maldistribution is also related to the frictional resistance inside the channel. For this reason, Rao and Das [15,16] found theoretically that soft plates ($\alpha \sim 30$ deg) bring about more maldistribution than hard plates ($\alpha \sim 70°$). For a given plate heat exchanger, the channel resistance varies with flow rate. The higher the flow rate, the lower the overall channel friction coefficient, and the higher the flow maldistribution is. In addition to this, an increase in flow rate also reduces NTU. Hence, with increasing flow rate the effectiveness of the heat exchanger will decrease. Figure 14 reconfirms this.

To observe the effect of maldistribution on the multipass arrangements of 1-2, 2-2, and 2-3 pass plate heat exchangers, experimental data were obtained for $N = 32$, $R = 1.0$, and port diameter, $D_p = 70$ mm at different flow rates, and these are compared to theoretical predictions as shown in Fig. 15. It is found that the multipass arrangement with an equal number of passes on both sides gives higher thermal effectiveness than any other multipass arrangement. It is also found that the experimental data for all the multipass arrangements agree well with the present theoretical model. The results indicate that the 2-2 pass PHE has the best performance because the countercurrent flow in all the passes in contrast to 1-2 and 2-3 passes where some passes of the heat exchanger are co-current. Figure 16 also shows the effect of flow maldistribution in multipass plate heat exchanger. It is found that even though flow maldistribution affects the thermal performance of multipass PHEs of both cases, this deterioration is small compared to that of single-pass plate heat exchangers (Figs. 10 and 11) with comparable port dimensions. Particularly at higher NTU, multipass plate heat exchanger seems to be more advantageous with respect to flow maldistribution. Thus, apart from increasing port dimensions and decreasing flow rate and number of plates, which may not be possible for hydraulic and thermal constraints, multipassing is an alternative through which the maldistribution effect can be reduced.

7 Conclusions

An investigation of the effect of flow maldistribution on the thermal performance of plate heat exchangers has been carried out. An analytical model for both single and multipass plate heat exchangers with an extensive validation through carefully designed experiments has been presented. The results clearly indicate that even though the model uses a port-to-channel flow dis-

tribution correlation based on continuous flow of fluid out of the manifold, it can predict the performance in the presence of maldistribution in PHE quite accurately. The parameters (which are found to influence the maldistribution and, as a consequence, the thermal performance of plate heat exchangers) are flow or pass arrangement, port dimension, number of channels, and fluid flow rate. It is found that the flow maldistribution decreases with increasing port dimension, suggesting use of larger port diameter as can be accommodated by sacrificing acceptable loss of heat transfer area. The flow rates are also to be kept to the minimum possible for a given heat duty to avoid maldistribution. An important alternative to reduce maldistribution, particularly at higher NTU, is to use multipass arrangements, which might be more relevant for an industrial heat exchanger with a larger number of operating plates.

Acknowledgments

The authors gratefully acknowledge the financial support from SIDA-Swedish Research Links and Swedish Research Council (VR) for the project under which the present collaborative research was carried out. Some funding was also provided by the Swedish Energy Agency.

Nomenclature

$\underline{a}$ = exponent of Re Eq. (5), [-]
$\overline{a}$ = coefficient matrix, Eq. (22)
a_1 = exponent of Pr in Eq. (29), [-]
A = heat transfer area for effective plate, m^2
A_c = cross-sectional area of the channel, m^2
A_p = cross-sectional area of the port, m^2
A_t = total heat transfer surface area, m^2
$\underline{b}$ = plate spacing in packed plates, m
$\overline{B}$ = diagonal matrix, Eq. (23)
$\overline{c}$ = coefficient matrix, Eq. (22)
C = constant in Eq. (5)
C_p = isobaric specific heat of the fluid, $J\,kg^{-1}\,K^{-1}$
D_p = port diameter, m
$\overline{e}$ = matrix of eigen vector in Eq. (24)
$\overline{K}$ = the coefficient of matrix, [-]
d_e = equivalent diameter of port, 2b, m
h = heat transfer coefficient, $W\,m^{-2}\,K^{-1}$
l = vertical distance between two ports, m
L = fluid flow length in a channel, m
L_p = length of port of the plate package, m
$\dot{m}$ = mass flow rate, $kg\,s^{-1}$
m = flow distribution parameter which is the square root of m^2, [-]
m^2 = maldistribution parameter, [-]
n = number of channels per fluid, [-]
N = total number of channels, [-]
NTU = number of transfer units, [-]
Nu = Nusselt number, [-]
p = dimensionless pressure in the port, $P/\rho W_o^2$, [-]
P = pressure in the port, N/m^2
ΔP = dimensionless pressure drop across a plate heat exchanger, [-]
Pr = Prandtl number, [-]
R = heat capacity flow rate ratio= $(\dot{m}C_p)_1/(\dot{m}C_p)_2$, [-]
Re = Reynolds number, Re=$[U_c(2b)]/\upsilon$, [-]
rh = ratio of heat transfer coefficients, [-]
rv = ratio of velocity, [-]
R_{wall} = thermal resistance of plate, mK/W
t = non dimensional temperature of fluids $=(T-T_{2,in})/(T_{1,in}-T_{2,in})$, [-]
T = temperature of fluid, K
$T_{h,in}$ = inlet temperature of the hot fluid, K
$T_{h,o}$ = outlet temperature of the hot fluid, K
$T_{c,in}$ = inlet temperature of the cold fluid, K
$T_{c,o}$ = outlet temperature of the cold fluid, K
ΔT_{lm} = logarithmic mean temperature difference, K
S = matrix of differential temperatures, K
u = dimensionless channel velocity, U_c/U_m, [-]
U = overall heat transfer coefficient, $W/m^2\,K$
U_c = channel velocity, m/s
U_m = mean channel velocity, m/s
F = matrix of eigen values of the matrix $\overline{a}$
H = width of the plate, m
w = dimensionless velocity in the port, W/W_o, [-]
W = velocity of port, [m/s]
W_c = axial component of the inlet flow velocity of channel, m/s
W_o = port inlet velocity, [m/s]
y = coefficient matrix in Eq. (25)
x = axial distance of fluid flow in the channel, m
X = non-dimensional axial distance of fluid flow in the channel=x/L, [-]
Z = position of channel along the port, m
z = dimensionless position of channel along the port, $[Z/L_p]$, [-]

Greek Symbols.

α = the corrugation angle of chevron plate, [-]
β_j = jth eigen value of matrix A, [-]
ν = kinematic viscosity of the fluid, $m^2\,s^{-1}$
ε = effectiveness of a heat exchanger= $[(\dot{m}C_p)_h(T_{h,in}-T_{h,o})]/[(\dot{m}C_p)_{\min}(T_{h,in}-T_{c,in})]$
ζ_c = overall head loss friction coefficient for channel flow, [-]
ρ = density of fluid, kg/m^3
λ = thermal conductivity of fluid, W/mK

Subscripts.

c = cold fluid
ch = channel
h = hot fluid
i = ith channel
in = at inlet
o = at outlet
$*$ = exhaust port
m_1, m_2, m_3 = adiabatically mixed values from HX1, HX2, and HX3, respectively
min = fluid with minimum heat capacity rate
uniform = case of uniform flow distribution among channels
w = plate
w_i = ith plate
(without subscript) = intake port (in pressure terms shown in Fig. 1)
1 = the fluid in odd channel
2 = the fluid in even channel

References

[1] Focke, W. W., Zachariades, J., and Olivier, I., 1985, "The Effect of the Corrugation Angle on the Thermodynamic Performance of Plate Heat Exchangers," Int. J. Heat Mass Transfer, **28**(8), pp. 1469–1479.
[2] Muley, A., and Manglik, R. M., 1999, "Experimental Study of Turbulent Flow Heat Transfer and Pressure Drop in a Plate Heat Exchanger With Chevron Plates," ASME J. Heat Transfer, **121**(1), pp. 110–117.
[3] Jackson, B. W., and Troupe, R. A., 1966, "Plate Heat Exchanger Design by ε-NTU Method," Chem. Eng. Prog., Symp. Series No. 64, **62**, pp. 185–190.
[4] Kandlikar, S., 1984, "Performance Curves for Different Plate Heat Exchanger Configurations," ASME, New York, ASME Paper No. 84-HT-26.
[5] Shah, R. K., and Kandlikar, S. G., 1988, "The Influence of the Number of Thermal Plates on Plate Heat Exchangers Performance," in *Current Researches in Heat and Mass Transfer, A Compendium and A Festschrift for Professor Arcot Ramachandran*, Hemisphere, Washington, DC, pp. 267–288.
[6] Pignotti, A., and Tamborenea, P. I., 1988, "Thermal Effectiveness of Multipass Plate Heat Exchangers," Int. J. Heat Mass Transfer, **31**(10), pp. 1983–1991.
[7] Datta, A. B., and Majumdar, A. K., 1980, "Flow Distribution in Parallel and

Reverse Flow Manifolds,'' Int. J. Heat Fluid Flow, **2**(4), pp. 253–262.
[8] Bajura, R. A., and Jones, Jr., E. H., 1976, ''Flow Distribution Manifolds,'' ASME J. Fluids Eng., **98**, pp. 654–666.
[9] Bassiouny, M. K., 1985, ''Experimentelle und theoretische Untersuchungen ueber Mengentromverteilung, Druckverlust und Waermeuebergang in Platten Waermeaustauschern,'' Forsch-Ber, VDI, Reihe 6, Ni 181, VDI-Verlag, Dusseldorf.
[10] Bassiouny, M. K., and Martin, H., 1984, ''Flow Distribution and Pressure Drop in Plate Heat Exchangers-I, U-Type Arrangement,'' Chem. Eng. Sci., **39**, pp. 693–700.
[11] Bassiouny, M. K., and Martin, H., 1984, ''Flow Distribution and Pressure Drop in Plate Heat Exchangers-II, Z-Type Arrangement,'' Chem. Eng. Sci., **39**(4), pp. 701–704.
[12] Thonon, B., Mercier, P., and Feidt, M., 1992, ''Flow Distribution in Plate Heat Exchangers and Consequences on Thermal and Hydraulic Performances,'' *Design and Operation of Heat Exchangers*, Springer-Verlag, Berlin, pp. 245–254.
[13] Heggs, P. J., and Scheidat, H. J., 1992, ''Thermal Performance of Plate Heat Exchangers With Flow Maldistribution,'' *Compact Heat Exchanger for Power and Process Industry*, ASME, HTD, Vol. 201, pp. 87–93.
[14] Prabhakara Rao, B., Krishna Kumar, P., and Das, S. K., 2002, ''Effect of Flow Distribution to the Channels on the Thermal Performance of a Plate Heat Exchanger,'' Chem. Eng. Process., **41**, pp. 49–58.
[15] Prabhakara Rao, B., and Das, S. K., 2004, ''Effect of Flow Distribution to the Channels on the Thermal Performance of a Multi-Pass Plate Heat Exchanger,'' Heat Transfer Eng., **25**(8), pp. 1–16.
[16] Prabhakara Rao, B., and Das, S. K., 2004, ''Experimental and Analytical Studies on the Influence of Flow Maldistribution on the Pressure Drop Across a Plate Heat Exchanger,'' ASME J. Fluids Eng., **126**, pp. 680–691.
[17] Shah, R. K., and Wanniarachchi, A. S., 1991, ''Plate Heat Exchanger Design Theory,'' in: Buchlin, J.-M., ed., *Industrial Heat Exchangers*, von Karman Institute Lecture Series 1991-04.
[18] Shah, R. K., 1990, ''Assessment of Modified Wilson Plot Techniques for Obtaining Heat Exchanger Design Data,'' *Heat Transfer 1990*, Hetsroni, ed., Hemisphere, New York, pp. 51–56.
[19] Moffat, R. J., 1988, ''Describing the Uncertainties in Experimental Results,'' Exp. Therm. Fluid Sci., **1**, pp. 3–17.

Frost Temperature Relations for Defrosting Sensing System

J. Iragorry

Y.-X. Tao

Department of Mechanical and Materials Engineering,
Florida International University,
Miami, Florida 33174

To develop a better defrosting control system on finned evaporators of a refrigeration system, a study is conducted to better quantify the frosting and defrosting processes by using an infrared thermometer to determine the frost surface temperature. For gradual frost deposition a slow variation in surface emissivity is expected, while the defrosting process is characterized by a sudden change of this property. As an indicator for the defrosting initiation control mechanism, the times at which the IR signals stabilize at different conditions (Reynolds number, cold surface temperature, and ambient temperature) are reported along with the terminal mass concentration of a defined frosting process. On the other hand, the abrupt variation of surface emissivity indicates the termination of the defrosting process. Removable fins are used to measure frost weight, and a video microscope is used to determine the frost thickness. Defrosting initiation time and durations marked by melting, temperature are reported as a function of initial mass concentration and defrosting base surface temperature. The presented results could be used to design a better defrosting control system with better accuracy and energy saving features. [DOI: 10.1115/1.1860566]

Introduction

Under design and operation conditions of various freezers and refrigeration systems, frost formation on evaporator surfaces (i.e., air-refrigerant heat exchangers) occurs inevitably. The consequence of frost formation is well known, that is reducing the heat transfer rate of the evaporator and blocking the air passage (or increase the flow resistance through fin structure.), reducing the cooling capacity of the equipment. In order to restore the original heat exchange conditions, the heat exchanger is periodically defrosted.

Different analytical models and experimental correlations have been developed in the last 20 years; nevertheless the problem of frost formation on evaporators is still affecting the regular operation of this equipment. The mathematical models and correlations can be used during the design phase of the equipment, in order to predict frost formation and establish the critical conditions used to set up the defrosting cycle. Surface treatment can also reduce frost deposition and extend the frost growth time. However, the most effective method that would ensure the maximum overall equipment efficiency is in situ defrosting control. The effect of defrosting on the equipment efficiency depends mainly on the excess heat introduced to the system, or the mass of frost left on the fins due to an incomplete defrosting cycle. Both insufficient and excessive defrosting will result in a poor performance of the equipment and a waste of energy.

From the available literature, significant efforts have been committed to frost formation on a flat plate configuration and above freezing air conditions. One of the earliest works on finned surface is the one by Tao, Mao, and Besant [1], where they also mentioned the importance of the frost surface temperature (T_f) as an indicator of the heat transfer characteristics, and presented a set of curves based on numerical modeling of the relationship between this parameter and the frost layer density and thickness. A frost growth model for heat exchanger fins was presented by Chen et al. [2], where the frost thickness (δ_f) is calculated at different locations along the fin surface. In this model, the required frost surface temperature is ''calculated'' in an intermediate step, and later used to determine the frost height. This data can be compared to the values obtained in the present work. This model was further used in modeling the heat exchanger performance [3]. Another model for frost growth on heat exchanger fins was presented by Martines-Frias and Aceves [4]. An evaluation of the overall performance effect of frost formation on an air-to-air heat pump was obtained by combining the frost growth model in a heat pump model. As before, the frost surface temperature (T_f) is found in an intermediate step from the energy balance relation.

The importance of the temperature difference between the air-frost interface and the cooling surface (T_w), was also addressed in the work by Hao et al. [5], where they introduced the holographic interferometry technique to measure the frost surface temperature. The method proved to be appropriate for the case of natural convection, especially when the temperature distribution of the surrounding air over the cold surface is stratified. For forced convection, the thermal boundary layer over the finned surface is very thin, limiting the resolution required for the holographic interferometry to be effective.

In this paper, the use of infrared thermometry is proposed as an alternative temperature measurement method. A series of experiments was conducted to investigate the relation of the frost surface temperature, T_f, and the frost layer characteristics, namely frost layer average thickness, δ_f, and density, ρ_f. The special attention is given to the possibility to use this method as a tool to monitor and control defrosting processes. Here, our focus is on the relatively long period of frost formation period, which is up to 25 h and often defined as a densification and bulk-growth period (DBG [6]). The resulted frost properties will also be used as the initial conditions for investigating the defrost processes for which the feasibility of using infrared signals as a sensing and control signal is discussed.

Theoretical Background

Under a forced convection ambient condition, a frost growth process on the fin surface is influenced by a number of variables that make the functional generalization of frost properties such as frost thickness and density complicated. From a heat transfer process point of view, we may choose frost thickness, δ_f, and density, ρ_f, as two fundamental indicators of the measure of heat transfer degradation. It has been shown [7] that the following phenomenological relations exist:

$$\delta_f = f_1(t; T_w, T_o, \mathrm{Re}, \mathrm{geometry}) \quad (1)$$

$$\rho_f = f_2(t; T_w, T_o, \mathrm{Re}, \mathrm{geometry}) \quad (2)$$

Manuscript received April 27, 2004; revision received December 2, 2004. Review conducted by: J. N. Chung.

It has also been known that the functions f_1 and f_2 are very much dependent on particular operating conditions. It is very difficult, if not impossible, to have an exhaustive list of the above functions to cover all the possible operating conditions, especially when it deviates from the steady-state design conditions. Ideally, it will be desirable to determine δ_f and ρ_f from an easily measured parameter such as a frost surface temperature because a measured cold surface temperature T_w does not necessarily detect the presence of frost. From Fourier's law of conduction, we may arrive at the following,

$$\delta_f \propto k_{\text{eff}}(T_f - T_w) \tag{3}$$

where T_w can be reasonably assumed as constant. Since $k_{\text{eff}}=f$ (ρ_f; operational condition) [8], we may infer that

$$\dot{m}'' = \rho_f \delta_f = f[T_f(t)] \tag{4}$$

If we can directly measure the frost mass concentration, $\dot{m}''$, from a sensing signal, Δp,

$$\dot{m}'' = g(\Delta p) \tag{5}$$

then, Eqs. (4) and (5) will yield a simple direct sensing system that could lead to a more accurate, energy saving defrosting control solution. This study attempts to explore such a scenario by developing the underlying relation leading to Eq. (4).

Numerous correlations for the frost thermal conductivity (k_{eff}) are available in the literature. A good collection of these correlations is presented in Ref. [8]. In order to evaluate the applicability of these correlations, two of the most commonly used equations are compared with the experimentally obtained thermal conductivity. The correlations by Sanders et al., and Lee et al. [8], which apply for the same geometrical configuration and operational conditions used in this work, were selected for this matter.

The frost layer's transport properties depend on its microgeometry, which in turn is a function of the operational conditions. A classification of the frost formation types was first introduced by Hayashi [9], who also identified two main phases in the frosting process. The frosting process starts with the dropwise condensation of water vapor on the cold plate (DWC period). Part of the heat removed from the plate is released by the droplet until a critical time is reached when the condensate freezes. The solidification and tip-growth period starts (STG period), which is characterized by a vertical crystal growth on top of the initial droplet. After a transition period, which depends on the heat transfer characteristics, branching of the ice column starts, and a uniform porous layer forms underneath the column-tip interface. This period is known as the densification and bulk-growth period (DBG period).

Infrared Thermometer

Radiation temperature sensors operate with electromagnetic radiation with a wavelength from 0.75 to 1000 μm. Infrared radiation obeys all the laws of light. The Stephan Boltzmann law gives infrared radiation flow between two bodies:

$$Q_{rad} \propto A_{cool}(T_{hot}^4 - T_{cool}^4) \tag{6}$$

The object whose temperature is being measured is considered a ''gray'' body, in other words, the radiation emitted is a fraction of the radiation emitted by a ''black body'' at the same temperature, defined by the *emissivity*, $\varepsilon = W_{GB}/W_{BB}$.

The basic design of an IR thermometer includes a lens, a detector element, an emissivity adjustment button, and a circuit to compensate for changes in ambient temperature. The radiation from the target body is focused on the radiation detector, causing an increment in the detector's temperature, until the losses (to the surroundings) balance with the heat input. The heat losses are proportional to the temperature difference between the element and the surroundings. This temperature difference can be measured using a thermocouple, and the output voltage is then proportional to the target's body temperature.

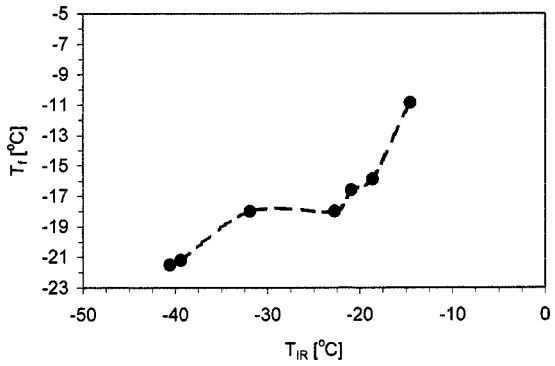

Fig. 1 Infrared sensor calibration chart, low and high temperature range

The radiation thermometer includes an emissivity adjustment pin, with a range from 0.01 to 0.99.

The emissivity value is a function of the body's temperature and surface characteristics; therefore the reading of the thermometer can change due to variation of this parameter, and a calibration function is required. In order to obtain the relation between the IR signal and the actual temperature, the emissivity is fixed to the largest value (0.99), a set of tests at different surface temperatures (and different frost temperatures) is performed, and the relation is tabulated. Surface thermocouples are used to measure the temperature at the point when the frost layer begins the growth process (and the temperature is close to the surface value).

The calibration chart is presented in Fig. 1. Two temperature ranges are identified, low temperature (IR signal from -30 to -45°C) and high temperature (IR signal from -15 to -25°C) and a corresponding function to each range. Equations (7*a*) and (7*b*) are the functions for the low- and high-temperature ranges, respectively. For a single function to cover the entire range, a combination of the last two was used:

$$T_f = 0.4109(T_{IR}) - 4.9056 \tag{7a}$$

$$T_f = 0.8584(T_{IR}) + 1.1343 \tag{7b}$$

Experimental Setup and Procedure

The experimental setup is presented in Fig. 2. The air inside a cold chamber ($1.83\times1.83\times2.44$ m^3), where temperature is maintained between -15°C and -20°C by means of a HEATCRAFT compact chiller (PTN031L6B), is forced by a centrifugal forward curved variable speed fan to pass by the test section. The test section consists of a finned test surface, an aluminum block, a thermoelectric cooling module, a heat-sink heat exchanger, and the insulation layers, as shown in Fig. 1(*c*). In the test section, the temperature of an aluminum plate (40×40 mm^2) with equally spaced fin inserts is reduced using a thermoelectric cooling module (Magaland $40\times40\times3.8$ mm^3). The thermoelectric cooling module is mounted on the heat-sink heat exchanger using the thermally conductive double-sided adhesive tape. The heat extracted by the module is then rejected to a thermal sink, where temperature is kept constant by a flow of a solution of water and ethylene glycol (50-50) from a refrigerated circulator. An OMEGA thin film heat flux sensor (HFS-3) measures the heat removal from the plate, while a set of T-type thermocouples (copper-constantan) measures the temperature of the plate and the airflow. High thermal conductivity paste (Omegatherm 201) is used between each one of the elements. A microscope/camera arrangement is used to collect images during the experiments. A PULNIX TMC-1000 digital camera is attached to an INFINIVAR zoom microscope, and a capture board (IMAQ PCI-1428) collects

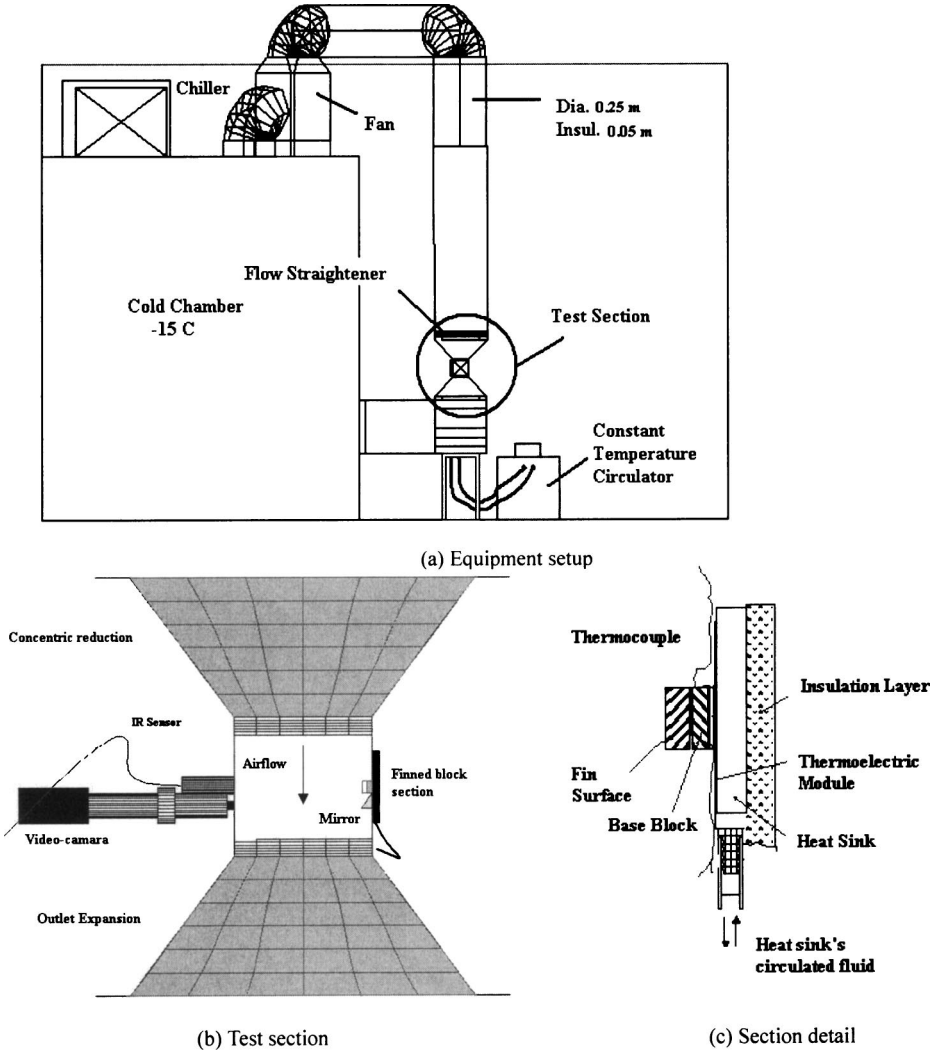

Fig. 2 Schematics of experimental apparatus

the signal from the camera to the PC. An infrared thermometer (Omega O565) with thermocouple output is used to measure the temperature of the frost top temperature. All of the signals from thermocouples are recorded and monitored by a PC computer through an OMEGA OMB-DS-16-8-TC data shuttle.

The temperature on the plate can be controlled by the temperature on the heat sink and by the power supplied to the cooling module. The fluid temperature can be controlled with a measured fluctuation of ± 0.1°C during a typical experiment. A bypass loop is set to allow that the cold fluid circulates outside the heat-sink heat exchanger before the fluid temperature reaches the desired value. For this set of experiments, the temperature at the heat sink is set up at -10°C.

Three levels of defrosting power are studied. The output of a variable voltage power supply is set to yield a heat flux of 31,500, 50,000, and 60,000 (w/m^2), respectively, at a low air velocity of 3.3 m/s corresponding to Reynolds numbers of 1400, and 45,000, 63,000 and 75,000 (w/m^2), respectively, for a high air velocity of 10 m/s, which corresponds to the Reynolds number of 4500. The range selected for this study covers the maximum and minimum values found in actual applications. The power supply set point also determines the final fin base temperatures, which end up being approximately -20°C, -23°C, and -26°C, respectively.

The density and thickness of frost are measured (or calculated) at different points during the frost and defrosting processes to arrive at the correlations of these properties with the frost surface effective temperature. Removable fins are used to obtain the weight of a frost layer at a specific time during the frost growth process. Figures 3 and 4 present two pictures of the removable fins arrangement. Figure 4 shows the frost layer formed on the fins for a typical case of Re=1400 and wall temperature of -23°C.

In order to obtain the frost thickness, the software MatLab is used to process and analyze the digital images taken during the frost growth. The fin area from a picture at the initial time is subtracted from the total frost area obtained from the final picture. The average thickness is obtained by integration over the fin perimeter. With the average thickness and the net frost weight, the average density is obtained for the case of study. This procedure is repeated for each of four experiments at a specified time during a frost growth process under the same ambient and cold surface conditions. For the low Reynolds number (Re=1400), the four time segments are 6, 12, 18, and 24 h, while for the high Reynolds number (Re=4500), the time segments are 3, 6, 12, and 24 h of frost growth.

The instrument uncertainty for the infrared meter output is 1°C, which corresponds to 5% of the average measurement, and the uncertainty for thermocouple measurements is 0.5°C (2.5% of average temperatures for the present study). The voltage output of the heat flux meter has a sensitivity of 3 mV, which represents an uncertainty that varies from 2% to 5% for the maximum and mini-

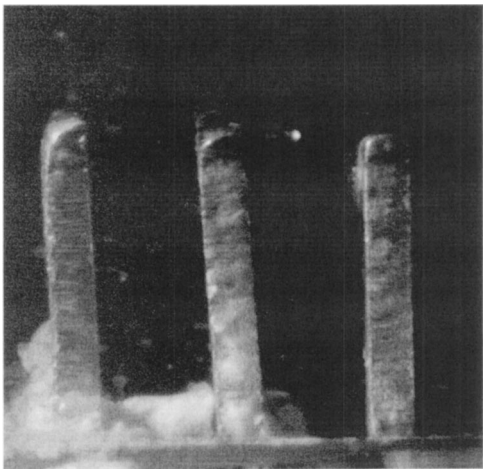

Fig. 3 Removable fins (aluminum 38×38×1.6 mm). Thermal conductive paste is used between fins and base.

mum operational heat removal rates. Minimum and maximum measurement uncertainties are combined in frost density calculation. A measurement uncertainty of only 0.005% for the frost mass is obtained with a high precision balance with a standard error of 0.001 g. The values of frost cross-section area obtained by image analysis have a variation of 5% of the average value, which is transferred to a total of 7.5% uncertainty for the frost density. The frost thickness measurement bears a 2.5% uncertainty resulting from image analysis.

Table I summarizes the cases of study for the present work. The cases are classified by airflow regime (laminar or turbulent) and heat extraction rate (or base temperature), and four time segments for each case.

Results and Discussion

In the following, we first discuss the results obtained during a series of frosting processes. The relation derived from the results can be used as an indicator (input data) for the defrosting control purpose. We then present results that correspond to the defrosting processes.

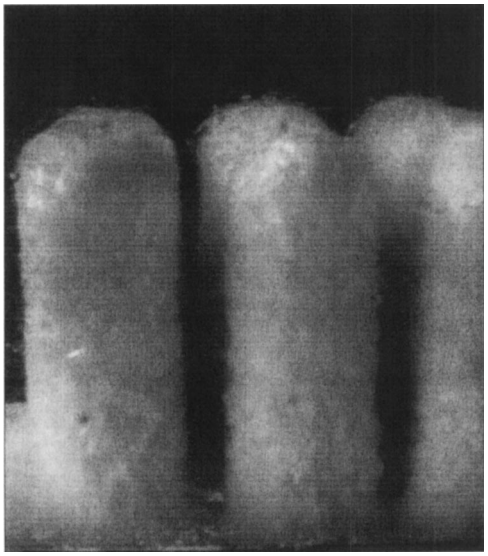

Fig. 4 Frost layer developed on fin surface: $T_a=-7°C$, $T_w=-23°C$, $q_w=31{,}500\ W/m^2$

Table 1 Test matrix

Case no.	Reynolds no.	Wall temperature (°C)	q_w (W/m^2)	Frost growth (h)
1	1400	−20	31,500	6,12,18,24
2	1400	−23	50,000	6,12,18,24
3	1400	−26	60,000	6,12,18,24
4	4500	−20	31,500	3,6,12,24
5	4500	−23	50,000	3,6,12,24
6	4500	−26	60,000	3,6,12,24

Frosting Processes. The results for the low Reynolds number (Re=1400) are presented in Figs. 5–8. At this airflow, frost thickness is a linear function and higher values of thickness are obtained as the fin base temperature is reduced. This result is presented in Fig. 5. A similar trend is observed for the tree cases, meaning that after the early stage of droplet condensation and freezing, the frost nucleation rate is independent of the base temperature. The critical time (freezing of condensed droplets) is a direct function of the wall temperature, and, as a result of longer condensation period, a denser initial layer is obtained for the cases of wall temperatures −20°C and −23°C, compared to a less dense and thicker layer obtained at a wall temperature of −26°C. The variation of the temperature difference between the fin base and frost surface is presented in Fig. 6. Frost growth for low airflows is characterized for an earlier vertical growth, also known as the solidification and tip-growth period (STG), followed by a horizontal growth stage (or frost layer development) and a final frost layer growth stage, or densification and bulk growth (DBG) period. A detailed explanation of the frost growth process for these conditions is presented in Ref. [8]. The curves on Fig. 6 start at a point during the STG period, and, as it can be seen, there is a reduction in this temperature difference, reaching a minimum point at the end of this period. The wall-frost temperature difference then increases during the DBG period, and finally stabilizes and increases gradually at the end. This decrease and increase in tem-

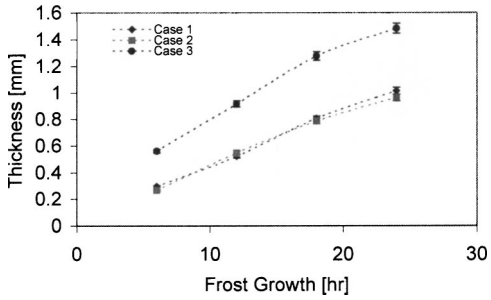

Fig. 5 Frost layer thickness history for different base temperatures and heat flux removal rates: Re=1400

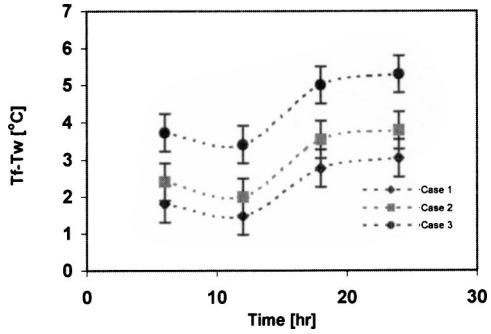

Fig. 6 Base-frost temperature difference history for different base temperatures and heat flux removal rates, Re=1400

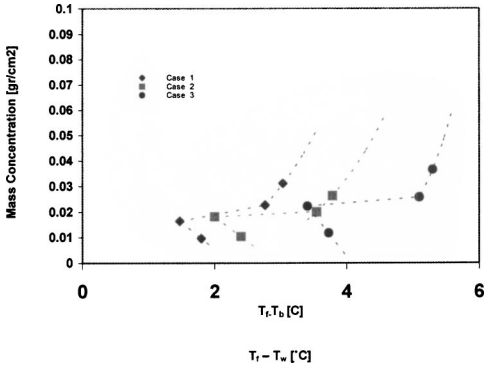

Fig. 7 Mass concentration on fin surface as a function of frost-wall temperature difference for different heat removal rates, Re=1400

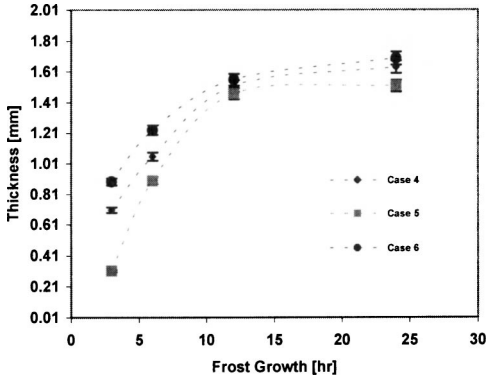

Fig. 9 Frost layer thickening history for different base temperatures and heat removal rates, Re=4500

perature difference explains the "zigzag" curve of Figs. 7 and 8. These figures illustrate the variation of mass concentration and thickness, respectively, with the surface-frost temperature difference. If we take the value of the thickness at the end of the vertical growth period to be the minimum, we note that even though the thickness increases to a certain degree during the DBG period, the base-frost temperature difference will decrease (see the section to the left of the minimum on the curves). On the other hand, during the DBG period this temperature difference increases as the thickness increases, which represents the right sides of those curves. The effect of a reduction on the base surface temperature is an increase of temperature difference values, due mainly to an increase in thickness. The mass concentration, however, is not significantly affected by this change.

For a high Reynolds number, on the other hand (Re=4500 in Figs. 9–12), there is a more uniform frost nucleation than with low airflow regime. The STG period is negligibly short, and essentially there is only one frost growth period (the DBG period) after nucleation. There is a rapid frost layer thickening at the beginning of the frost growth process followed by a reduction in the curve slope as the maximum value (half of the space between fins) is approached. This trend is presented in Fig. 9 for three different cases, where the curve with higher values corresponds to the lower surface temperature. In contrast to the low Reynolds figures, the initial thickness is different in the tree cases, meaning that each one has a different critical time (initiation of DBG period). At the end of this period (around 12 h), there is not a significant difference in the layer thickness, and the difference shown at later times could be attributed to measurement error. Figure 10 shows the variation of the temperature difference between the fin base and the frost surface for the turbulent case. These curves present a trend similar to that obtained in the thickness curves, with the difference of a noticeable reduction on the slope as the heat removal rate is reduced. Figures 11 and 12 show the variation of mass concentration and thickness with the surface-frost temperature difference. In these two figures, an exponential increase in the value of the parameters with the base-frost temperature difference is observed and, similarly as in the case of laminar Reynolds number, the main effect of surface temperature reduction is to increase the values of the base-frost surface temperature difference.

The effect of increasing the airflow (Reynolds) can also be depicted from this set of plots. In general, higher values of thickness and mass concentrations will be found at high Reynolds regimes.

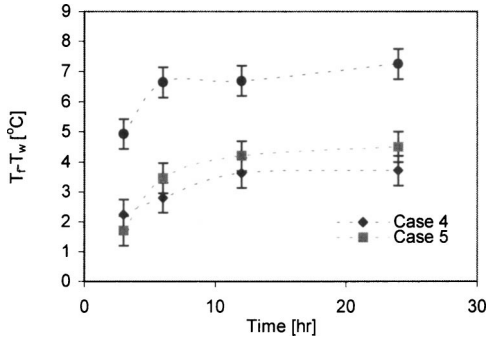

Fig. 10 Base-frost temperature difference history for different base temperatures and heat flux removal rates, Re=4500

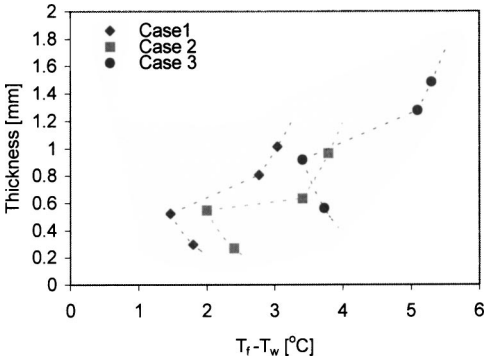

Fig. 8 Frost thickness as a function of frost-wall temperature difference for different heat removal rates, Re=1400

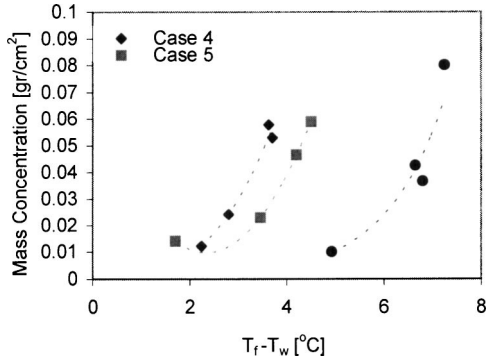

Fig. 11 Mass concentration on fin surface as a function of frost-wall temperature difference for different heat removal rates, Re=4500

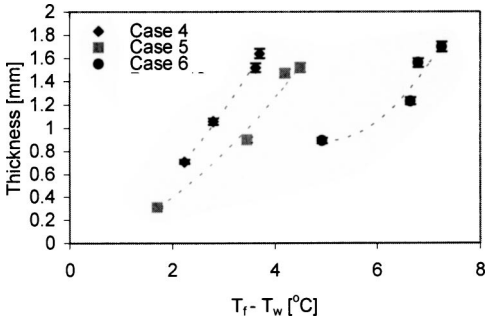

Fig. 12 Frost thickness as a function of frost-wall temperature difference for different heat removal rates, Re=4500

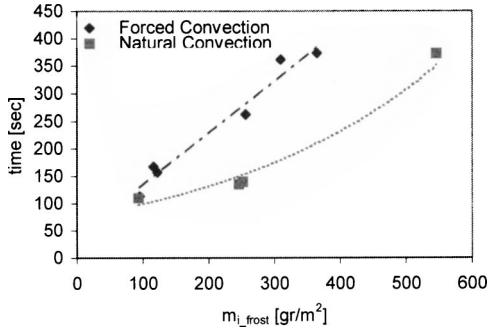

Fig. 14 Required defrosting time as a function of initial mass concentration. Forced convection versus natural convection. Defrosting temperature of 40°C.

Defrosting Processes. Another important part of this study is dedicated to the defrosting processes. The variation of the frost surface temperature can be used as an indicator (and control signal) of the defrosting process.

In order to simulate a hot gas defrosting process, a valve arrangement was installed in order to switch between two constant temperature circulators, one of which was set at 0°C to be used for frost growth in combination with the thermoelectric module, while the other one was set at a higher defrosting temperature (20°C, 40°C, or 60°C). Both the thermoelectric module and the variable speed fan should be turned off prior to defrosting. The initial mass concentration was measured, using the method discussed in the previous section, in order to obtain a set of relations of required defrosting time for an initial mass concentration at different defrosting temperatures. Figure 13 shows the defrosting temperature history for a frost layer initially of 0.03 g/cm^2 using a defrosting temperature of 40°C. In this plot, the wall temperature (base) increases from −27°C to 25°C at the end of the defrosting process, while the surrounding air is maintained at −7°C. The most interesting curves in this plot correspond to the IR reading and the heat flux. A first heat flux pulse is related to the cooling module shut-off, and higher values are obtained as the heating flow circulates trough the heat sink, reaching a maximum value at the point where the wall temperature matches the air temperature, and reduces as the wall temperature increases beyond that value. The IR signal's curve, on the other hand, presents a gradual increase from −20°C to a steady −8°C corresponding to an equilibrium point with the surrounding air. A sudden increase in the signal appears when the layer finally melts.

In order to study the effect of leaving the fan on during the defrosting (forced convection with air stream), two cases will be studied. The required defrosting time as a function of the initial mass concentration (at the defrosting initiation) was obtained for the cases of forced and natural convection with the air stream. Figure 14 shows a linear relation of the defrosting time required as the initial mass concentration increases, for the case of forced convection and defrosting temperature of 40°C. The energy required for this case also increases linearly with the mass concentration as presented in Fig. 15. In this figure, the energy required to melt the initial mass of ice is compared to the total energy required which includes the sensible heating of the heat transfer surface. It can be seen that approximately 70% of energy supplied to the surface is used to heat the heat exchanger material and surrounding air and only 30% is used to melt the ice.

The results obtained for natural convection surrounding conditions are presented in Figs. 16 and 17. The required time and energy for this case are in general much lower than for forced convection. The most important result was obtained for low mass concentration (below 400 g/m^2), where the major fraction of energy is used to heat the surface, and therefore there is almost no variation of energy and time as the concentration increases. In other words, setting the maximum (allowable) concentration below 400 g/m^3 will have almost no effect in the required defrost time and energy.

Another alternative for the effective frost temperature is the air-frost temperature difference. This value reduces as the frost thickness increases, and a minimum point could be set for defrosting initiation. An historical variation of this temperature difference is presented in Fig. 18 for the turbulent case and two different heat removal rates. The simulated heat gain due to door openings can also be observed in this figure as frequent temperature increments.

Bulk Effective Thermal Conductivity of Frost. The insulation effect of the frost layer can be measured by the following bulk effective thermal conduction of frost:

$$\overline{k}_{\text{eff}} = \frac{q_w}{(T_f - T_w)/\delta_f}. \tag{8}$$

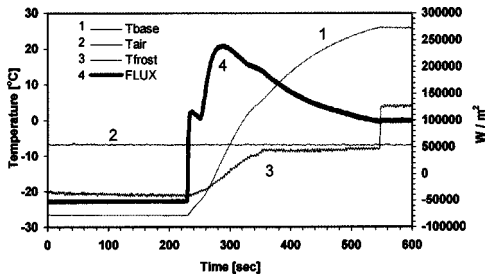

Fig. 13 Defrosting process with an initial mass concentration (m_i) of 0.030966 (g/cm^2), and defrosting temperature of 40°C

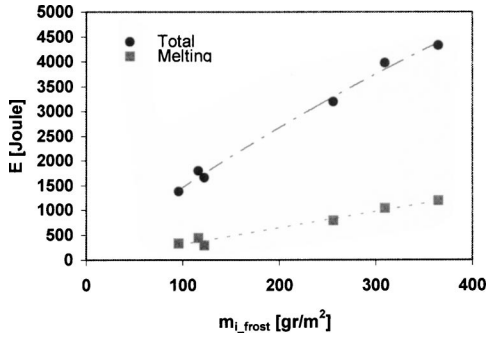

Fig. 15 Required defrosting energy as a function of initial mass concentration. Forced convection at low Reynolds number and defrosting temperature of 40°C.

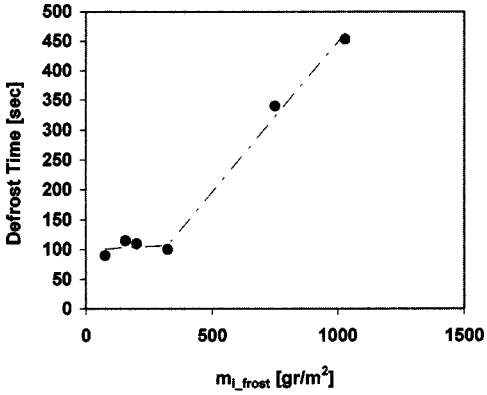

Fig. 16 Required defrosting time as a function of initial mass concentration. Natural convection and defrosting temperature of 60°C.

In this study, we determine $\overline{k}_{\text{eff}}$ from the measured q_w during a frosting process, which varies with time, and, therefore, by definition it is different from the local frost effective thermal conductivity defined in many models [10,11]. Figure 19 shows the results as a function of frost density for two different Reynolds numbers. The results reported by Sanders [12] and Lee et al. [13] are also shown for comparison. It can be seen that the measured results from all the cases in this study generally follow the trend of increasing in value with frost density, although a scattering trend is observed because of additional variables associated with processes under different ambient conditions and total frosting time. In general, the reported data are higher than those reported in

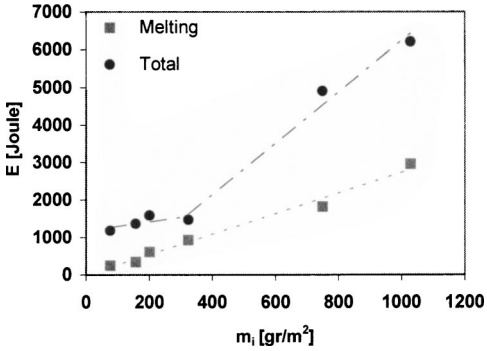

Fig. 17 Required defrosting energy as a function of initial mass concentration. Natural convection and defrosting temperature of 60°C.

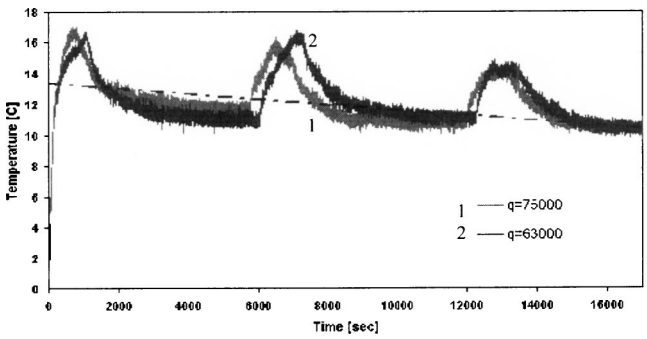

Fig. 18 Reduction of air-frost temperature difference at high Reynolds number. Heat flux in W/m^2.

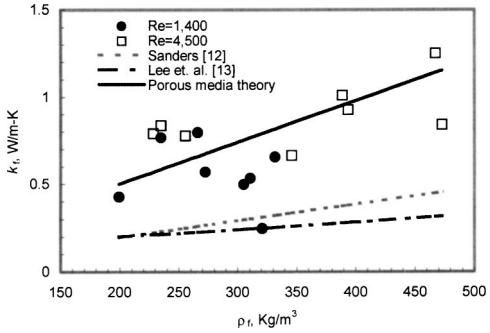

Fig. 19 Average effective frost thermal conductivity

[12,13]. It is interesting see that the measured data do follow the trend predicted by the theoretical approximation of thermal conductivity of a porous matrix consisting of ice and air:

$$\overline{k}_{\text{eff}} = \varepsilon_i k_i + (1-\varepsilon_i) k_a \,, \tag{9}$$

where $\varepsilon_i = (\rho_f - \rho_a)/(\rho_i - \rho_a)$ is the volume fraction of ice phase in frost. This observation may lead to a reasonable assumption that a simple model such as Eq. (9) can be sufficiently used to in a distributed analysis that treats the frost layer during the bulk growth period as a porous medium.

Comparison Between Frosting and Defrosting Processes. Except for a transient period of dropwise condensation (DWC period) and solidification and tip-growth (STG period), a frosting process is typically characterized by a quasi-steady deposition (layer formation) of ice crystals under a relative constant temperature difference between the refrigerant and ambient air. On the other hand, the defrosting process is a transient process where the temperature of refrigerant (hot gas) or ambient air increases rapidly. After the ice changes to liquid, the process becomes more unstable. The major difference in the frosting and defrosting time scales also result in the significant difference in the heat transfer flux through the heat exchanger surface. From the practical standpoint, it is desired to shorten the defrosting process with minimum heating energy consumption and prolong a frosting process if possible. Therefore, different modeling techniques may be sought to analyze those different processes. However, there is a strong dependency of a defrosting process on the preceding frosting process because both involve cumulative phenomena of a frost layer. The initial condition of a defrosting process is the final condition of the preceding frosting process. Using a frost surface temperature sensor, such as the one proposed in this study, along with other means, one may better characterize the linkage between a frosting and a defrosting process and ultimately improve the overall effectiveness and efficiency of a refrigeration system.

Summary

In this study, infrared thermometry is presented as an alternative method to obtain the frost surface temperature. A set of experiments was conducted in order to obtain the relation of the effective frost surface temperature with the thickness and mass concentration of the frost layer. These results could be used in conjunction with the sensing equipment as a defrosting control system. During frost growth, the relations of thickness and density could control the frost initiation time, while the defrosting termination will be given by the sudden change in the sensor signal.

Acknowledgments

The support from FIU Foundation and NSF (Award No. 0206028) are greatly appreciated. Additional support from Dr. Busby at Tennessee State University is also acknowledged. J. Iragorry thanks the FIU Latin American and Caribbean Center (LACC) for the additional scholarship support. The authors also thank HeatCraft, Inc., for their equipment support.

Nomenclature

A = heat transfer area, m^2
k = thermal conductivity, W/(m·°C)
L = length of object, m
m = mass concentration, g/m^2
P = pressure, Pa
Q = total heat rate, W
q = heat flux, W/m^2
Re = Reynolds number
RH = relative humidity, %
T = temperature, °C
t = time, s
W = total emitted power, W

Greek Symbols

δ = frost thickness, m
ρ = density, kg/m^3
ε = emissivity

Subscripts

a = air
BB = black body
base = aluminum base
cool = cold body's surface
eff = effective
f = frost surface
frost = frost layer
GB = gray body
hot = hot body's surface
i = ice
IR = infrared
o = ambient
w = cold surface

References

[1] Tao, Y. X., Mao, Y., and Besant, R. W., 1994, ''Frost Growth Characteristics on Heat Exchanger Surfaces: Measurement and Simulation Studies,'' Proceedings of the 1994 ASME International Mechanical Engineering Congress and Exposition, Chicago, IL, Nov. 1994, HTD-Vol **286**, pp. 29–38.
[2] Chen, H., Thomas, L., and Besant, R. W., 2000, ''Modeling Frost Characteristics on Heat Exchanger Fins: Part I. Numerical Model,'' ASHRAE Trans., **106**(Pt. A), pp. 357–367.
[3] Chen, H., Thomas, L., and Besant, R. W., 2000, ''Modeling Frost Characteristics on Heat Exchanger Fins: Part II. Model Validation and Limitations,'' ASHRAE Trans., **106**(Pt. A), pp. 368–376.
[4] Martinez-Frias, J., and Aceves, S. M., 1999, ''Effects of Evaporator Frosting on the Performance of a Air-To-Air Heat Pump,'' J. Energy Resources Technology, **121**, pp. 60–65.
[5] Hao, Y. L., Iragorry, J., Castro, D., Tao, Y.-X., and Jia, S., 2002, ''Microscopic Characterization of Frost Surface During Liquid-Ice Phase Change Period,'' Proceedings of the 2002 ASME International Mechanical Engineering Congress & Exposition, New Orleans, LA, November 17–22, 2002, Paper No. IMECE2002-32797.
[6] Kaviany, M., 1993, *Principles of Heat Transfer in Porous Media*, Springer Verlag, New York, p. 471.
[7] Mao, Y., Besant, R. W., and Chen, H., 1999, ''Frost Characteristics and Heat Transfer on a Flat Plate Under Freezer Operating Conditions: Part I, Experimentation and Correlations,'' ASHRAE Trans., **105**(Pt. A), pp. 231–251.
[8] Iragorry, J., Tao, Y.-X., and Jia, S., 2004, ''A Critical Review of Properties and Models for Frost Formation Analysis,'' HVAC&R Res., **10**(4), pp. 393–420.
[9] Hayashi, Y., Aoki, A., Adachi, A., and Hori, K., 1977, ''Study of Frost Properties Correlating With Frost Formation Types,'' Trans. ASME, Series C: J. Heat Transfer, **99**, pp. 239–245.
[10] Tao, Y.-X., Besant, R. W., and Rezkallah, K. S., 1993, ''Mathematical Model for Predicting the Densification and Growth of Frost on a Flat Plate,'' Int. J. Heat Mass Transfer, **36**(2), pp. 353–363.
[11] Chen, H., Thomas, L., and Besant, R. W., 2002, ''Fan Supplied Heat Exchanger Fin Performance Under Frosting Conditions,'' Int. J. Refrig., **26**, pp. 140–149.
[12] Sanders, C. T., 1974, ''The Influence of Frost Formation and Defrosting on the Performance of Air Coolers,'' Ph.D. thesis, Delf Technical University.
[13] Lee, K. S., Lee, T. H., and Kim, W. S., 1994, ''Heat and Mass Transfer of Parallel Plates Heat Exchanger Under Frosting Condition,'' SAREK J., **6**, pp. 155–165.

Heat Transfer for Laminar Flow in Spiral Ducts of Rectangular Cross Section

Michael W. Egner
e-mail: nfsd@swbell.net

Louis C. Burmeister
Professor, Mem. ASME
e-mail: mrub@ku.edu
Department of Mechanical Engineering,
University of Kansas, 1530 W. 15th St.,
Lawrence, KS 66045

Laminar flow and heat transfer in three-dimensional spiral ducts of rectangular cross section with aspect ratios of 1, 4, and 8 were determined by making use of the FLUENT *computational fluid dynamics program. The peripherally averaged Nusselt number is presented as a function of distance from the inlet and of the Dean number. Fully developed values of the Nusselt number for a constant-radius-of-curvature duct, either toroidal or helical with small pitch, can be used to predict those quantities for the spiral duct in postentry regions. These results are applicable to spiral-plate heat exchangers.* [DOI: 10.1115/1.1857950]

Keywords: Spiral, Heat Exchanger, Curved Duct, Dean Number

Introduction

The concept of the spiral-plate heat exchanger was apparently first proposed late in the 19th century, according to Hewitt et al. [1], and was reinvented in Sweden in the 1930s. Early experiments by Coons et al. [2], Tangri and Jayaraman [3], Hargis et al. [4], and Buonapane and Troupe [5] resulted in correlations for the overall heat transfer coefficients and pressure drops for spiral ducts that are similar to those for straight ducts. But, even though more recent correlations reported by Minton [6] and Martin [7] account for the average curvature of the spiral-plate heat exchanger, no information is in the open literature on the variation of heat transfer coefficients along a spiral duct of rectangular cross section. Minton [6] suggested the Graetz form

$$\mathrm{Nu} = 1.86(\mathrm{Re}\,\mathrm{Pr} D_h/L)^{1/3}(\mu/\mu_w)^{0.4}$$

with $D_h/L = (a/d)^{1/2}$ where d is the local diameter of the spiral and a is the channel width, reasoning that flow is continually developing. Although he did not do so, this correlation can be rewritten in terms of the Dean number K that is descriptive of swirling flow as

$$\mathrm{Nu} = 1.32 K_{av}^{1/3}\mathrm{Pr}^{1/3}(\mu/\mu_w)^{0.4}$$

Two related geometries have received considerable attention. Dean [8,9] established that steady laminar flow in a toroidal (in-plane) constant-radius-of-curvature (CRC) duct, the first geometry, of circular cross section has a secondary flow pattern when the Dean number K exceeds a critical value. Ghia et al. [10], Soh [11], Sankar et al. [12], Cheng et al. [13,14], Ghia and Sokhey [15], and Humphrey et al. [16] numerically determined the secondary flow vortex patterns and the Dean number ranges within which each occurs for the rectangular cross section. Ligrani and Niver [17] and Bolinder and Sundén [18] experimentally confirmed predictions for flow patterns and friction coefficients for the rectangular cross section.

Heat transfer was numerically investigated by Cheng and Akiyama [19] for steady fully developed laminar flow in toroidal CRC ducts of rectangular cross section with an axially uniform wall heat flux and a peripherally uniform wall temperature. Akiyama and Cheng [20] solved the corresponding Graetz problem for fully developed laminar flow. Both found the effect of secondary flow on the developing temperature field to be substantial. Mori et al. [21] conducted both analytical and experimental heat transfer investigations for the square cross section with constant wall heat flux. Yee et al. [22] performed a numerical study of heat transfer in a 90 deg channel with constant wall temperature.

The second geometry is a CRC duct that forms a helix of constant pitch. In this geometry, establishment of the fully developed conditions that often require more than a 360 deg turn can be studied in a physically meaningful way. Thangam and Hur [23] and Thomson et al. [24] established that the velocity distribution for the helical CRC duct is nearly the same as for a toroidal CRC duct.

In the following, a computational fluid dynamics investigation of developing flow and heat transfer for laminar flow in a spiral duct of rectangular cross section with an axially and peripherally uniform wall heat flux and a peripherally uniform wall temperature is described. The results obtained are compared to those for a helical CRC duct.

Formulation

The geometry of a spiral-plate heat exchanger is illustrated in Fig. 1. The centerline radius R of the spiral duct through which a fluid flows is represented by an Archimedean spiral whose radius varies with angle ϕ from the origin, a is the constant duct width and R_i is the minimum centerline radius of the spiral, as

$$R(\phi) = a\phi/\pi + R_i$$

The parameter values used for the rectangular cross section of this study are similar to those encountered in spiral-plate heat exchangers. For each aspect ratio γ (=1,4,8) the duct width a was 0.02 m, the innermost radius of curvature R_i was 0.06 m, the outermost radius of curvature R_o was 0.2 m, and the centerline length S was 2.86 m. The number, 3.5, of spiral turns is less than the 15 of some spiral-plate heat exchangers to keep the size of the computational fluid dynamics problem within the computational resources available. The largest aspect ratio of 8 is lower than the maximum value of about 80 that can be encountered, but it is large enough to enable discernment of essential differences between the square and the high-aspect-ratio case.

The hexahedral mesh for the FLUENT computational fluid dynamics program used to obtain solutions was constructed with the aid of the GAMBIT program. The symmetry of the flow and thermal fields was used to advantage by constructing a mesh only for the upper half of the rectangular cross section. For the square cross section, a uniform mesh of 30×60 cells was employed; for the 8/1 aspect ratio, a uniform mesh of 32×128 cells was used. Along the length of the channel, 84 separate zones were formed as illustrated in Fig. 1. For aspect ratios of 1 and 8 there were 864,000 hexahedral cells and 1,720,320 hexahedral cells, respectively. The mesh was graded in the streamwise direction so that cells were more closely spaced near the inlet. Convergence was detected by monitoring a physical quantity, such as shear stress, at one location; about 100 iterations were performed after it ceased to change. Uniform inlet velocity and temperature conditions were used. For the thermal boundary conditions, equal and constant heat fluxes were assigned to the inner and outer radial walls while the top wall was made adiabatic.

Manuscript received January 5, 2004; revision received December 13, 2004. Review conducted by: V. Prasad.

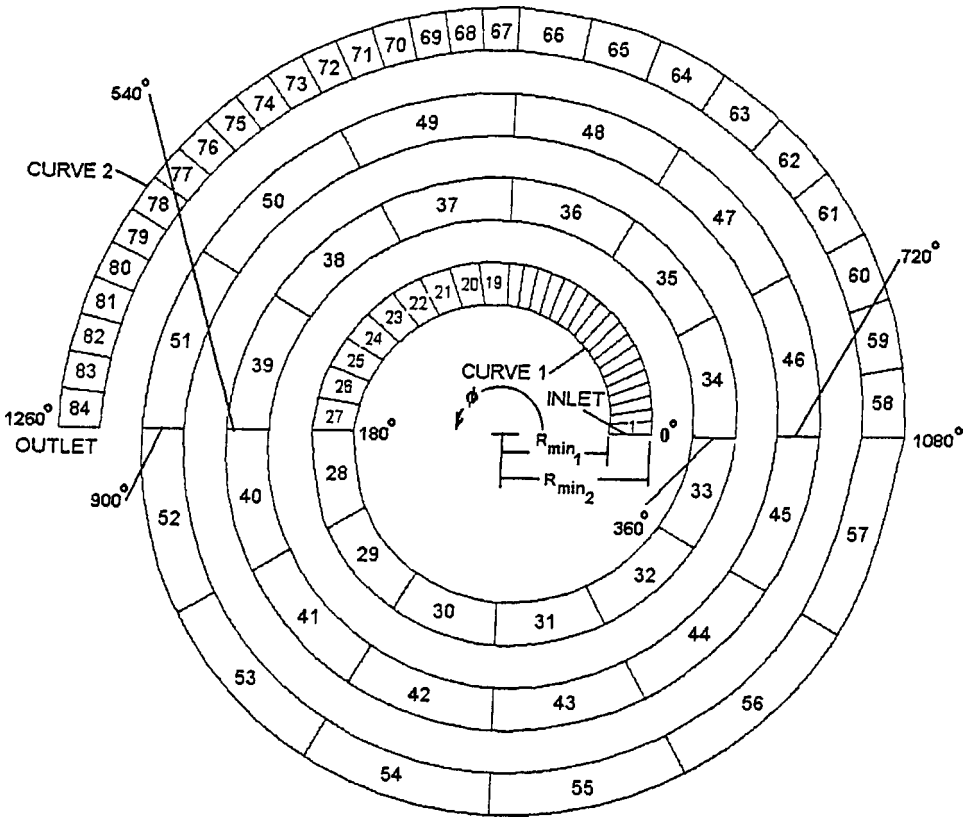

Fig. 1 Zone locations in the spiral duct

The procedures described above were applied to the test case of a laminar flow developing from uniform inlet conditions in a helical CRC duct with constant pitch and rectangular cross section. A mesh-refinement study established that the results for both the velocity and temperature distributions are nearly independent of the mesh size. Asymptotic values of C_f/C_{fo} and $\mathrm{Nu}/\mathrm{Nu}_o$ compare well to those from other studies.

Results

The velocity distribution was determined first. With it in hand, the temperature distribution was then obtained.

Secondary Flow. The evolution of the secondary flow structure for outward spiraling flow is shown in Fig. 2 for $\gamma=8$ and with Re=100 and 500. The stream function contour lines represent the secondary flow above the symmetry plane, a matching set of vortices lying below. As the Reynolds number increases from 100 to 500, the secondary flow field changes from a single-vortex pair to a double-vortex pair. The maximum secondary velocity is 8–35% of the average streamwise velocity, depending on the Reynolds number and aspect ratio. The stability map of Re versus curvature ratio given by Thangam and Hur [23] for the helical CRC duct predicts the onset of instability, secondary flow, in the spiral duct. As can be seen in the adaptation in Fig. 3, the stability boundary depends on both Reynolds number and curvature ratio, explaining the different critical Dean numbers of 142 reported by Joseph et al. [25], 150 by Cheng et al. [14], and 143 by Ghia and Sokhey [15]. The region below the boundary represents the conditions in which a single-vortex pair occurs while the region above the boundary represents the conditions in which either a double-vortex pair or roll cells occur. The combination of Reynolds number and curvature ratio on the stability boundary identifies the critical Dean number at which the secondary flow changes over from one pattern to the other.

Heat Transfer Coefficient. The Nusselt number Nu is based on the inner and outer wall areas at which heat transfer occurs and is peripherally averaged. The Nu variation versus Dean number

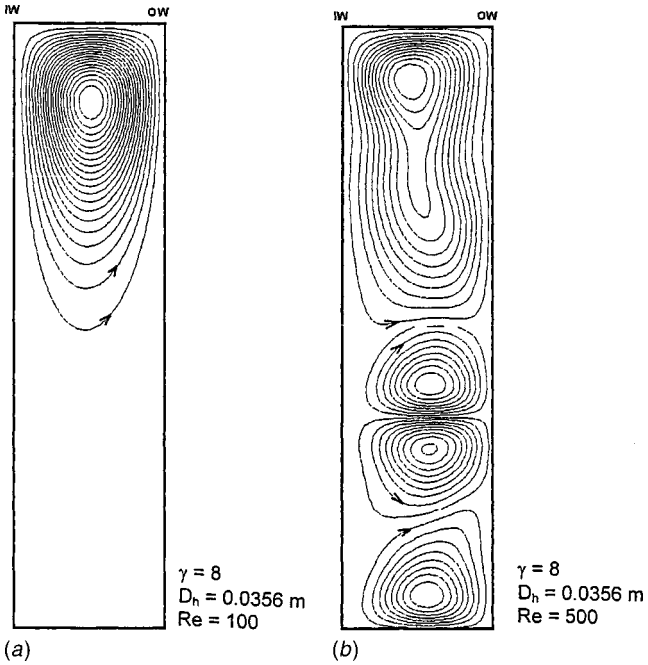

Fig. 2 Secondary flow streamlines for spiraling-outward flow at the 1080 deg slice plane: (*a*) $\gamma=8$, Re=100; (*b*) $\gamma=8$, Re=500. Only the upper half of the duct cross section is shown above the symmetry plane

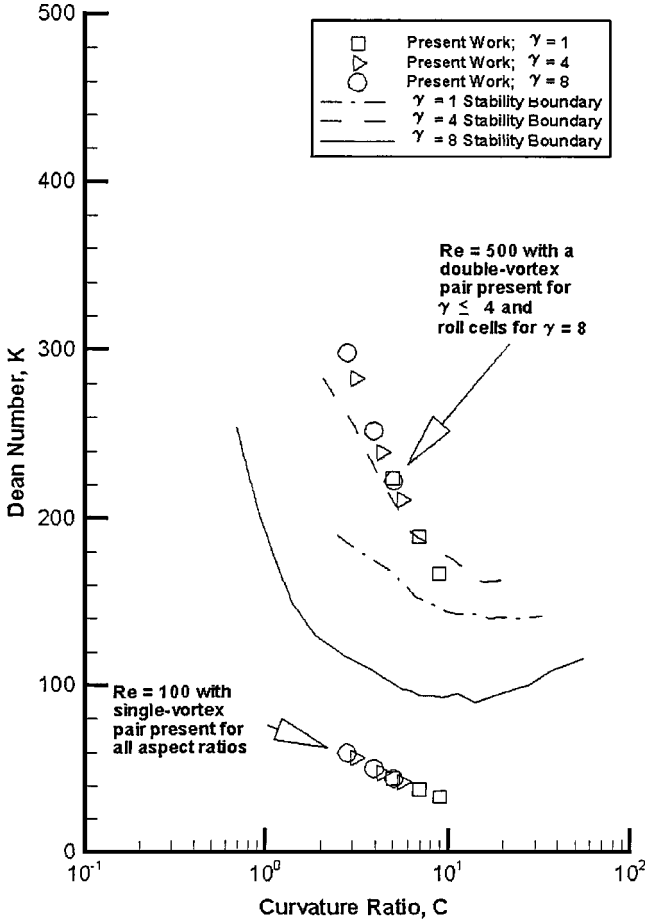

Fig. 3 Stability diagram in the Dean-number–curvature-ratio plane for curved and spiral ducts for outward-spiraling flow (adapted from [23])

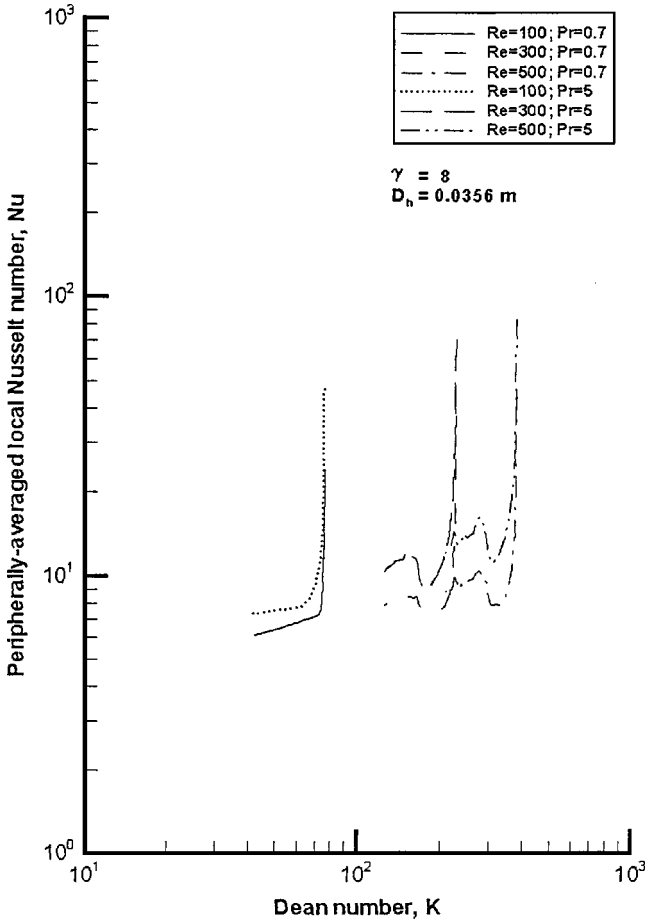

Fig. 4 Variation of the peripherally averaged local Nusselt number for outward-spiraling flow with Dean number for γ=8, Pr=0.7 and 5, and Re=100, 300, and 500

for outward spiraling flows is shown in Fig. 4 for γ=8. The high Nusselt number at the entrance is due to the uniform temperature at the entrance, a boundary condition whose effect dies away in the streamwise direction, leaving what is termed a ''regular'' variation. It is seen that Nu increases as Dean number increases, the Nu values for a spiral duct being 6% larger than the fully developed values in the helical CRC channel. As for the friction coefficient, local Nu values in a spiral duct are closely predicted by those for the fully developed CRC helical duct.

The Nu variation versus dimensionless distance from the entrance along the centerline is shown in Fig. 5 for outward spiraling flows for γ=8. The oscillations in the developing Nu at the end of the entrance region, where the Dean number is the highest, are consistent with the observation by Thomson et al. [24]. They have been observed for all cross sections and boundary conditions considered by other investigators.

The thermal entrance length L_t was measured from the inlet to the location at which the Nu began to follow a ''regular'' variation, close to the asymptotic Nu value for a CRC helical duct that depends on the local Dean number. A general conclusion is that

$$0.005 \leqslant L_t/\mathrm{Re}\,\mathrm{Pr} D_h \leqslant 0.04$$

for $100 \leqslant \mathrm{Re} \leqslant 500$. The thermal entry lengths for a spiral duct were about 10–80% of that for a straight channel and about 20–100% of that for a CRC helical duct.

The average Nusselt number Nu of the present study for spiral ducts is correlated for the uniform wall heat flux condition by

$$\overline{\mathrm{Nu}}/\overline{\mathrm{Nu}}_o = 1 + 0.0429(K_{av}/\gamma)^{0.68}\mathrm{Pr}^{0.4},$$

$$1 \leqslant \gamma \leqslant 4,\ 0 \leqslant K_{av} \leqslant 364,\ 0.7 \leqslant \mathrm{Pr} \leqslant 5 \quad (1)$$

$$\overline{\mathrm{Nu}}/\overline{\mathrm{Nu}}_o = 1 + 0.0767(K_{av}/\gamma)^{0.57}\mathrm{Pr}^{0.4},$$

$$1 \leqslant \gamma \leqslant 8,\ 0 \leqslant K_{av} \leqslant 384,\ 0.7 \leqslant \mathrm{Pr} \leqslant 5 \quad (2)$$

with 13% and 15% maximum error for Eqs. (1) and (2), respectively. Here, $K_{av}=(K_i+K_o)/2$ and Nu_o is the fully developed value due to Savino and Siegel [26] and Siegel and Savino [27] for a straight duct of the same aspect ratio: for γ=1, $\overline{\mathrm{Nu}}_o$=4.08; for γ=4, $\overline{\mathrm{Nu}}_o$=5.64; for γ=8, $\overline{\mathrm{Nu}}_o$=6.01. Comparisons of average Nusselt number downstream of the entrance region from the present study with correlations for the fully developed Nusselt number in a CRC helical duct due to Cheng and Akiyama [19] and Cheng et al. [13] are shown in Fig. 6. The average Nusselt number for a spiral duct is within 10% of that for a helical CRC duct, higher in some cases and lower in others.

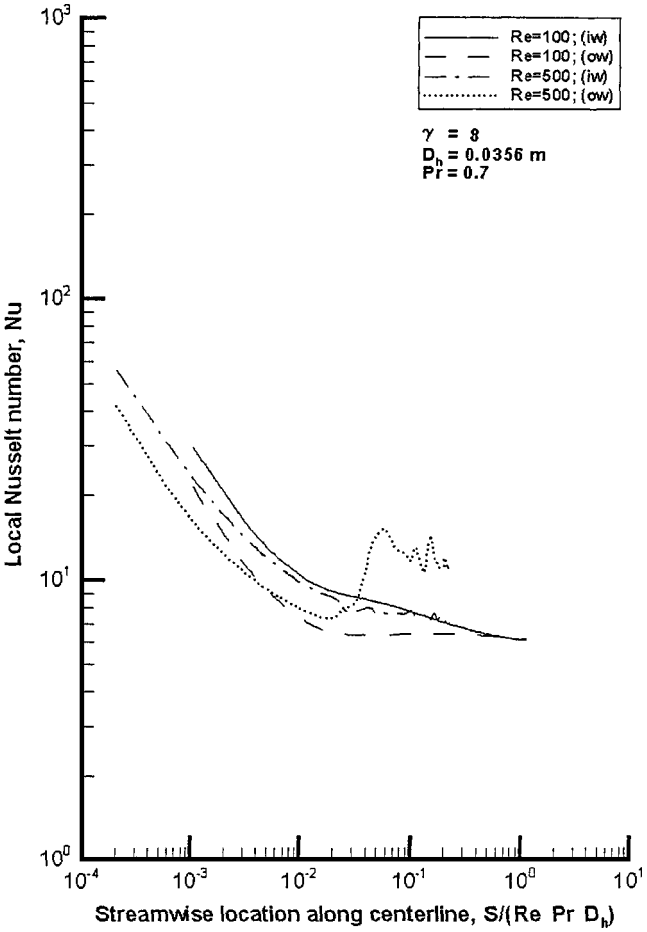

Fig. 5 Variation of local Nusselt number with streamwise distance along the centerline for γ=8 and spiraling-outward flow

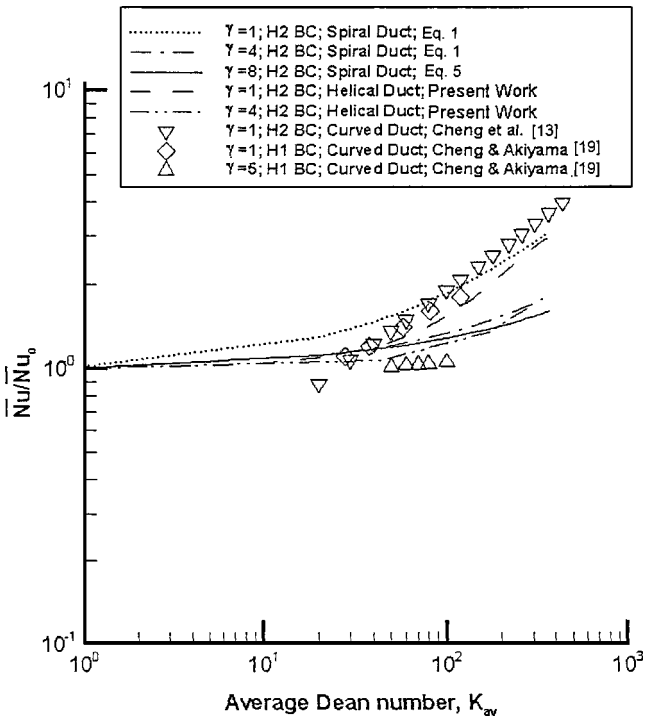

Fig. 6 Comparison of present correlations for average Nusselt number (Pr=0.7) versus average Dean number with those of previous studies (boundary conditions: H1 is constant axial wall heat flux and constant peripheral wall temperature, H2 is constant axial wall heat flux and constant peripheral wall heat flux)

Previous numerical studies of SPHE performance have taken the overall heat transfer coefficient U to be constant, which is seen to be correct within about 10% if entrance regions are excluded; in an entrance region U can vary by as much as 50% from the fully developed value. This information can be applied to studies of spiral-plate heat exchanger performance, such as those performed by Buonopane and Troupe [5], Chowdhury et al. [28], Zhang et al. [29], and Bes and Roetzel [30]. Additional details of method and result, especially with regard to coefficient of friction, are given by Egner [31].

Conclusion

The fully developed, peripherally averaged Nusselt number for a spiral duct of rectangular cross section is only 5–15% higher than the values for a constant-radius-of-curvature helical duct.

Nomenclature

a = channel spacing, m
b = channel height, m
C = curvature ratio, $=R/D_h$
C_p = specific heat at constant pressure, J/kg K
d = local diameter of spiral
D_h = hydraulic diameter, $=2ab/(a+b)$
h = local convective heat transfer coefficient, $=q_w/(T_w - T_b)$, W/m$_2$ K
$\bar{h}$ = peripherally averaged convective heat transfer coefficient, $=(1/A_h)\int h dA_h$, W/m^2 K
k = thermal conductivity
K = Dean number, $=\mathrm{Re}(D_h/R)^{1/2}$
L_t = thermal entrance length, m
Nu = peripherally averaged Nusselt number, $=hD_h/k$
$\overline{\mathrm{Nu}}_o$ = fully developed, peripherally averaged Nusselt number for straight duct of same cross section
Nu = streamwise-averaged Nusselt number, $=(1/S)\int$ NudS
Pr = Prandtl number, $=\mu C_p/k$
q_w = uniform wall heat flux, W/m^2
R = radius of curvature, m
R_{av} = average radius of curvature to channel centerline, $=(R_i+R_o)/2$, m
Re = Reynolds number, $=\rho w_{av} D_h/\mu$
S = length along the channel centerline
T_b = bulk fluid temperature, $=(\int TwdA/\int wdA)$, K
T_w = peripherally averaged wall temperature, $=(1/A)\int T_w dA$, K
w = tangential velocity, m/s
U = overall heat transfer coefficient, $=(h_i^{-1}+h_o^{-1})^{-1}$, W/m^2 K

Greek Symbols

γ = channel aspect ratio, $=b/a$
μ = dynamic viscosity, kg/ms
ρ = mass density, kg/m^3
π = natural number, π=3.1415 . . .
ϕ = angle

Subscripts

av = average
i = inside
min = minimum
max = maximum
o = outside
w = wall

References

[1] *International Encyclopedia of Heat and Mass Transfer*, Hewitt, G., Shires, G., and Polezhaev, Y. (eds.), 1997, CRC Press, New York, p. 1044.

[2] Coons, K., Hargis, A., Hewes, P., and Weems, F., 1947, ''Spiral Heat Exchanger–Heat Transfer Characteristics,'' Chem. Eng. Prog., **43**, pp. 405–414.

[3] Tangri, N., and Jayaraman, R., 1962, ''Heat Transfer Studies on a Spiral Plate Heat Exchanger,'' Trans. Inst. Chem. Eng., **40**, pp. 161–168.

[4] Hargis, A., Beckmann, A., and Loiacono, J., 1967, ''Applications of Spiral Plate Heat Exchangers,'' Chem. Eng. Prog., **63**, pp. 62–67.

[5] Buonopane, R., and Troupe, R., 1970, ''Analytical and Experimental Heat Transfer Studies in a Spiral Plate Heat Exchanger,'' *Proc. of 4th Int. Heat Transfer Conf*, Paris, Elsevier Publishing Co., Amsterdam, Paper No. HE 2.5.

[6] Minton, P., 1970, ''Designing Spiral Plate Heat Exchangers,'' Chem. Eng. (Rughy, U.K.), **77**, pp. 103–112.

[7] Martin, H., 1992, *Heat Exchangers*, Hemisphere Publishing, Washington, DC, pp. 73–82.

[8] Dean, W., 1927, ''Note on the Motion of Fluid in a Curved Pipe,'' Philos. Mag., **4**, pp. 208–223.

[9] Dean, W., 1928, ''The Stream-Line Motion of Fluid in a Curved Pipe,'' Philos. Mag., **5**, pp. 673–695.

[10] Ghia, K., Ghia, U., and Shin, C., 1987, ''Study of Fully Developed Incompressible Flow in Curved Ducts, Using a Multi-Grid Technique,'' ASME J. Fluids Eng., **109**, pp. 226–236.

[11] Soh, W., 1988, ''Developing Fluid Flow in a Curved Duct of Square Cross Section and Its Fully Developed Dual Solutions,'' J. Fluid Mech., **188**, pp. 337–361.

[12] Sankar, S., Nandakumar, K., and Masliyah, J., 1988, ''Oscillatory Flows in Coiled Square Ducts,'' Phys. Fluids, **31**, pp. 1348–1359.

[13] Cheng, K., Lin, R., and Ou, J., 1975, ''Graetz Problem in Curved Square Channels,'' J. Heat Transfer, **97**, pp. 244–248.

[14] Cheng, K., Lin, R., and Ou, J., 1976, ''Fully Developed Laminar Flow in Curved Rectangular Channels,'' ASME J. Fluids Eng., **98**, pp. 41–48.

[15] Ghia, K., and Sokhey, J., 1977, ''Laminar Incompressible Viscous Flow in Curved Ducts of Regular Cross-Sections,'' ASME J. Fluids Eng., **99**, pp. 640–648.

[16] Humphrey, J., Taylor, A., and Whitelaw, J., 1977, ''Laminar Flow in a Square Duct of Strong Curvature,'' J. Fluid Mech., **83**, Pt. 3, pp. 509–527.

[17] Ligrani, P., and Niver, R., 1988, ''Flow Visualization of Dean Vortices in a Curved Channel With 40 to 1 Aspect Ratio,'' Phys. Fluids, **31**, pp. 3605–3617.

[18] Bolinder, C., and Sundén, B., 1995, ''Flow Visualization and LDV Measurements of Laminar Flow in a Helical Square Duct With Finite Pitch,'' Exp. Therm. Fluid Sci., **11**, pp. 348–363.

[19] Cheng, K., and Akiyama, M., 1970, ''Laminar Forced Convection Heat Transfer in Curved Rectangular Channels,'' Int. J. Heat Mass Transfer, **13**, pp. 471–490.

[20] Akiyama, M., and Cheng, K. C., 1974, ''Graetz Problem in Curved Pipes With Uniform Wall Heat Flux,'' Appl. Sci. Res., **29**, pp. 401–417.

[21] Mori, Y., Uchida, Y., and Ukon, T., 1971, ''Forced Convective Heat Transfer in a Curved Channel With a Square Cross Section,'' Int. J. Heat Mass Transfer, **14**, pp. 1787–1805.

[22] Yee, G., Chilukuri, R., and Humphrey, J., 1980, ''A Computational Method for Thermal Design of Spiral Plate Heat Exchanger,'' *Proc. 1988 Heat Transfer Conference*, ASME, New York, HTD-96, Vol. 1, pp. 445–449.

[23] Thangam, S., and Hur, N., 1990, ''Laminar Secondary Flows in Curved Rectangular Ducts,'' J. Fluid Mech., **217**, pp. 421–440.

[24] Thomson, D., Bayazitoglu, Y., and Meade, A., 1998, ''Low Dean Number Convective Heat Transfer in Helical Ducts of Rectangular Cross Section,'' ASME J. Heat Transfer, **120**, pp. 84–91.

[25] Joseph, B., Smith, E., and Adler, R., 1975, ''Forced Laminar Convection in a Curved Isothermal Square Duct,'' ASME J. Heat Transfer, **113**, pp. 48–55.

[26] Savino, J., and Siegel, R., 1964, ''Laminar Forced Convection in Rectangular Channels With Unequal Heat Addition on Adjacent Sides,'' Int. J. Heat Mass Transfer, **7**, No. 7, pp. 733–741.

[27] Siegel, R., and Savino, J. M., 1965, ''An Analytical Solution of the Effect of Peripheral Wall Conduction on Laminar Forced Convection in Rectangular Channels,'' ASME J. Heat Transfer, **87**, pp. 59–67.

[28] Chowdhury, K., Linkmeyer, H., Bassiouny, M., and Martin, H., 1985, ''Analytical Studies on the Temperature Distribution in Spiral-Plate Heat Exchanger,'' Chem. Eng. Process., **19**, pp. 183–190.

[29] Zhang, N., Jiao, Z., and Ni, Z., 1988, ''A Computational Method for Thermal Design of Spiral Plate Heat Exchanger,'' *Proc. of 1988 Heat Transfer Conference*, ASME, New York, HTD-96, Vol. 1, pp. 445–449.

[30] Bes, T., and Roetzel, W., 1992, ''Distribution of Heat Flux Density in Spiral Heat Exchangers,'' Int. J. Heat Mass Transfer, **35**, pp. 1331–1347.

[31] Egner, M., 2003, ''Computation of Fluid Flow and Heat Transfer in Spiral and Constant-Radius Curved Channels,'' Ph.D. thesis, University of Kansas, Lawrence, KS.